

Copyright

by

Steven Michael Fulk

2016

The Dissertation Committee for Steven Michael Fulk Certifies that this is the approved version of the following dissertation:

Measuring and Modeling Aerosols in Carbon Dioxide Capture by Aqueous Amines

Committee:

Gary T. Rochelle, Supervisor

Roger T. Bonnecaze

Eric Chen

Lea Hildebrandt Ruiz

Elena McDonald-Buller

**Measuring and Modeling Aerosols in Carbon Dioxide Capture by
Aqueous Amines**

by

Steven Michael Fulk, B.S.

Dissertation

Presented to the Faculty of the Graduate School of

The University of Texas at Austin

in Partial Fulfillment

of the Requirements

for the Degree of

Doctor of Philosophy

The University of Texas at Austin

August 2016

Dedication

To Joy Desta Fulk

Acknowledgements

First, I would like to thank Dr. Gary Rochelle for his continued flexibility and understanding as an advisor. My transition into graduate school was anything but a smooth landing, but he continued to gently guide, and at times negotiate, my path to professional development and becoming a critical thinker while always providing room for life outside of the lab. His seemingly infinite well of ideas is inspirational and taught me a lot about higher level problem solving and how to not get so caught up in the weeds of excessive detail. I am tremendously grateful for his influence in my life.

Dr. Eric Chen was a valuable mentor in my development when I began working out at the Pickle Research Center with seemingly no hands-on skills. I learned a lot about being organized, how to manage projects, and getting my hands dirty. He also managed an endless army of undergraduates who contributed greatly to the pilot plant work in this study; special thanks go to Yong Kim for his work on the rack-mount FTIR.

I would like to acknowledge the numerous members of the Rochelle group who came before me, worked beside me, and those with some time still to go. We got to travel to many international conferences, problem solve, and talk about sports way too much; I'm grateful for it all. To the people following in my project's footsteps, I'd like to extend my gratitude for providing me feedback from modeling work and for your help finding mistakes in my data: Conlin Kang and Yue Zhang. I'd also like to give special thanks to my on-campus officemates for their friendship, great conversation (both research and non-research related), and numerous coffee runs: David Van Wagener, Jorge Plaza, Peter Frailie, Darshan Sachde, and Brent Sherman. And to my Pickle compatriots, thank you for endlessly entertaining me and your help with running

experiments or simply carrying things around for me: Matt Beaudry and Di Song. Most importantly, I want to thank Stephanie Freeman and Fred Closmann for pulling me aside, unsolicited, to give me encouragement when I need it the most.

For their financial support, I would like to thank the members of the Luminant Carbon Management Program, the Texas Carbon Management Program, the John L. Gidley Endowed Graduate Fellowship in Engineering, and the Department of Energy under Award Number DE-FE0005654.

I would also like to thank several industry partners and vendors who helped during pilot plant campaigns and development of the PDI. AECOM provided manual sampling data and project support during SRP pilot campaigns. Southern Company allowed us to sample at NCCC and provided support for those measurements. And Artium, specifically Chad Sipperley and Will Bachalo, did demonstrations and ultimately designed the custom PDI used in this work.

I owe gratitude for the numerous staff, both on-campus and at the Separations Research Program, that have helped me in multiple facets. Special thanks to Maeve Cooney for her endless work on quarterly reports and for keeping the lab organized and moving. Frank Seibert, Steve Briggs, Robert Montgomery, and Micah Perry of SRP played major roles in running the PRC pilot plant and taking data.

To my family, thank you for your years of love and support. Thank you to my parents for encouraging me to work hard and keep a positive attitude. And to my siblings, John and Erin, thank you all of the fun we've had together, our great stories, and for the phone calls. I'm incredibly lucky to have you all in my life.

I'd personally like to thank my Gateway family for all the amazing opportunities and support they've shown me. I'm incredibly blessed to have people who give me no excuses to be a better person, give me a place to serve, and are always glad to see me.

Special thanks to Tracy Guthrie for giving me a door, Karin Harper who helped me stumble through, and Steven Mary getting me back on my feet. And for their time and great life lessons, Rick Wells and Nathan Collins. I'd also like to thank the Greens, not only for opening their home for small group, but for their interest in my life and consistent encouragement for me and those who mean the most to me.

Victoria, thank you for your constant grace, kindness, optimism, and encouragement. Though we are still new to each other, you feel like an old friend. I hope to continue this incredible season of growth and adventure with you well into the future. I'm tremendously grateful for you.

Finally, thank you to God for His continuous grace, courage, and wisdom as well as His endless work in my life. Thank you for giving me life, sustaining me in health, and providing me with a good future.

Measuring and Modeling Aerosols in Carbon Dioxide Capture by Aqueous Amines

Steven Michael Fulk, Ph.D.

The University of Texas at Austin, 2016

Supervisor: Gary T. Rochelle

Pilot scale CO₂ capture plants have shown that amine condensation onto seed nuclei results in very high amine emissions which are very difficult to control using traditional aerosol removal techniques. Aerosol emissions can be suppressed by adjusting operating conditions such that drops evaporate, or, alternatively, grow to a size that can be efficiently captured by low cost methods. The effects of operating conditions on aerosol growth were investigated by experimental measurement and numerical modeling with sensitivity analyses.

Total particle densities and particle size distributions (PSDs) were measured using a custom-built phase Doppler interferometer (PDI) on bench and pilot scale CO₂ absorbers. Seed nuclei were generated using vaporized H₂SO₄, gaseous SO₂, and flue gas from a coal-fired power plant. PSDs were used to calculate the aerosol amine concentration when compared to total phase (gas and aerosol) measurements collected by FTIR.

The effects of operating conditions on aerosol growth were simulated in a combined heat and mass transfer model coded in MATLAB[®]. Aerosol transport equations included corrections for surface curvature and transport length scale regimes. Absorber and water wash models were simulated using Aspen Plus[®].

Inlet CO₂ is crucial in creating supersaturation in the absorber; the loading difference between the aerosol and bulk solvent creates an amine driving force for condensation. Aerosols grow faster in non-intercooled columns due to differences in solvent composition (CO₂ loading) and temperature.

H₂O condensation is the primary growth mechanism in the water wash. Reducing the water wash amine concentration and providing additional residence time leads to more aerosol growth. Doubling the water wash height results in a 13.7 % increase in the final aerosol diameter for a generic 8 m PZ absorber.

Similar to some other volatile amines, PZ forms 1–5 μm aerosols because its amine volatility is a strong function of CO₂ loading. The amine concentration in measured aerosol distributions, calculated by PDI/FTIR comparison, was one-to-two orders of magnitude lower than the bulk solvent.

SO₂ forms aerosol with PZ. 65 % of injected SO₂ leaves in the aerosol phase. Therefore, SO₂ polishing scrubbers are essential and systems should not be designed for simultaneous absorption of CO₂ and SO₂.

Table of Contents

Dedication	iv
Acknowledgements	v
Table of Contents	x
List of Tables	xxi
List of Figures	xxvi
Chapter 1: Introduction	1
1.1.1 CO ₂ Capture by Amine Absorption/Stripping	1
1.1.2 Volatile Losses	3
1.2 Aerosols at Pilot Plants	5
1.2.1 Mitsubishi Heavy Industries	5
1.2.2 SINTEF and TNO	6
1.2.3 National Carbon Capture Center	8
1.3 Aerosols at the Bench Scale	8
1.3.1 Laborelec, KIT, and TNO	8
1.3.1.1 Brachert et al. (2014)	9
1.3.1.2 Mertens et al. (2014)	9
1.3.2 Khakharia (2015)	10
1.3.2.1 Particle Concentration	10
1.3.2.2 Supersaturation	10
1.3.2.3 Amine Reactivity	10
1.3.2.4 Overall Theory	11
1.3.3 Key Findings	11
1.4 Abatement Strategy	12
1.5 Research Scope	13
1.5.1 Aerosol Analytical Development	13
1.5.2 Experimental Measurements	14
1.5.3 Numerical Modeling	15

Chapter 2: General Aerosol Theory and Equations	16
2.1 Particle Size Distributions (PSDs)	17
2.1.1 Distribution Averages	23
2.2 General Dynamic Equation.....	24
2.3 Particle Dynamics	27
2.3.1 Length Scales	27
2.3.2 Single Particle Motion	30
2.3.3 Cunningham Slip Correction	33
2.4 Particle Diffusion: Brownian Diffusion Coefficient.....	35
2.4.1 Thermodynamics: Surface Curvature Effects	36
2.4.2 Mass and Heat Transfer	38
2.5 Sampling and Removal	43
2.5.1 Total Sampling Efficiency	45
2.5.2 Inlet losses.....	47
2.5.2.1 Anisoaxial Sampling Aspiration Efficiency.....	47
2.5.2.2 Transmission Efficiency: Gravitational Settling	49
2.5.2.3 Transmission Efficiency: Inertial Deposition	50
2.5.3 Transfer Efficiency	51
2.5.3.1 Transfer Efficiency: Gravitational Settling	51
2.5.3.2 Transfer Efficiency: Diffusional Deposition.....	52
2.5.3.3 Transfer Efficiency: Turbulent Inertial Deposition.....	53
2.5.3.4 Transfer Efficiency: Inertial Deposition in Bends	54
2.5.3.5 Transfer Efficiency: Inertial Deposition in Contractions	55
Chapter 3: Analytical Methods and Supporting Equipment	57
3.1 Fourier Transform Infrared Spectroscopy (FTIR)	57
3.1.1 Reference Spectra	63
3.1.2 Multicomponent Spectra Analysis.....	65
3.1.2.1 Baseline Corrections	65
3.1.2.2 Analysis Regions.....	66
3.1.2.3 Pressure Compensation	67

3.1.2.4	Voice Coil Pressure.....	68
3.1.3	FTIR Hardware	68
3.1.3.1	DX4000 Sample Pump.....	70
3.1.3.2	CX4000 Sample Pump.....	71
3.1.3.3	Heated Sampling Lines	72
3.1.3.4	Heated Connection Blankets	73
3.1.3.5	Heated Sampling Probes (Stingers).....	74
3.1.4	Multipoint Heated Stream Switcher (MSSH).....	78
3.2	Phase Doppler Interferometry (PDI).....	81
3.2.1	Theory of Operation.....	81
3.2.2	Safety	86
3.2.3	Hardware Setup and Connections	86
3.2.3.1	Power Supply	87
3.2.3.2	Advanced Signal Analyzer (ASA)	87
3.2.3.3	Transmitter	88
3.2.3.4	Receiver.....	88
3.2.3.5	Temperature and Humidity Control	90
3.2.4	Test Cell.....	90
3.2.5	Software	95
3.2.5.1	Acquisition Control.....	95
3.2.5.2	Auto-Setup	95
3.2.5.3	Phase Calibration and Laser Alignment.....	95
3.2.5.4	Validation Criteria.....	99
3.2.5.5	Velocity Filter	99
3.2.5.6	Maximum Diameter Difference	99
3.2.5.7	Maximum Phase Pair Difference	99
3.2.5.8	Signal Processing	100
3.2.5.9	Fast Fourier Transform (FFT) Bins.....	100
3.2.5.10	Analog Filter	103
3.2.5.11	Mixer	103

3.2.5.12	Variable Mixer	103
3.2.5.13	Burst Detection (BD) Decimation.....	103
3.2.6	Optics	103
3.2.6.1	PMT Gain.....	104
3.2.6.2	Index of Refraction.....	105
3.2.6.3	Scattering Mode	105
3.2.6.4	Data Exporting	105
3.2.7	PDI Calculations	107
3.2.7.1	Velocity	107
3.2.7.2	Size Determination.....	108
3.2.7.3	Probe Volume Correction.....	110
3.2.7.4	Number Density	111
3.3	Supporting Equipment	112
3.3.1	Pilot Plant Sample Blower.....	112
Chapter 4:	Aerosol Growth Column (AGC) – Experimental Methods	114
4.1	Need for AGC Experiments.....	114
4.1.1	Aerosol Study Historical Development	114
4.1.2	Early UT Aerosol Work.....	116
4.2	Aerosol Growth Column.....	117
4.2.1	Nitrogen (N ₂)	118
4.2.2	Carbon Dioxide (CO ₂)	119
4.2.3	H ₂ O Presaturator	123
4.2.4	Absorber Column.....	123
4.2.5	Solvent Loop.....	124
4.2.6	Condenser	127
4.2.7	Liquid Sampling.....	128
4.2.7.1	AGC Thermocouple Calibration.....	128
4.2.8	AGC Controls and Data Acquisition	129
4.3	Aerosol Losses	131
4.4	Liquid Vaporizer and Injector (LVI)	133

4.4.1 Safety	133
4.4.2 Hardware and Operating Modes	134
4.5 FTIR Sampling.....	140
4.6 Aerosol Losses	143
4.7 PDI Sampling.....	145
4.8 Operating Procedures.....	146
4.9 Data Interpretation	151
4.9.1 Data Types	151
4.9.1.1 PDI Data.....	151
4.9.2 Data Algorithm	152
4.9.2.1 Aerosol Statistics.....	153
4.9.2.2 Aerosol to Total Phase Conversion.....	153
4.9.2.3 Aerosol Amine Concentration Optimization.....	155
4.10 Acknowledgements.....	155
Chapter 5: Aerosol Growth Column (AGC) – Results	156
5.1 AGC Experiments.....	156
5.1.1 Experiment Limitations	156
5.1.2 LVI Stability Tests.....	158
5.2 CO ₂ Capture Tests.....	161
5.2.1 Operating Conditions Tests.....	166
5.2.1.1 Effect of Inlet CO ₂	167
5.2.1.2 Effect of L/G	168
5.2.1.3 Effect of Temperature	170
5.3 PDI Tests.....	174
5.3.1 PDI Gen. 2	174
5.3.2 PDI Gen. 3	176
5.3.2.1 The Effect of CO ₂	183
5.3.2.2 The Effect of L/G	191
5.3.2.3 Particle Density Comparison.....	192
5.3.2.4 PDI/FTIR Fitting.....	193

5.3.2.5	Density, Diameter, and Emissions	196
5.4	Summary/Contribution	199
5.4.1	The Effect of CO ₂	200
5.4.2	The Effect of Solvent Rate.....	201
5.4.3	FTIR and Integrated PDI Comparison.....	201
5.4.4	Diameter/Total Density Relationship	202
5.5	Acknowledgements.....	202
Chapter 6:	Pilot Plant Measurements.....	203
6.1	NCCC – June 5, 2013 - PDI Generation 1 Test.....	203
6.1.1	Pilot Plant Setup.....	204
6.1.2	Sample Location	206
6.1.3	Equipment.....	208
6.1.4	Results.....	210
6.1.5	PDI Improvements.....	211
6.2	PRC – November, 2013 Campaign – PDI Generation 2 Test.....	211
6.2.1	Pilot Plant Setup.....	211
6.2.2	Sample Locations.....	214
6.2.3	Equipment.....	217
6.2.3.1	FTIR Sampling.....	217
6.2.3.2	PDI Sampling	217
6.2.3.3	Aerosol Sources.....	219
6.2.4	Results.....	221
6.2.4.1	Steady State Conditions	221
6.2.4.2	Manual Sampling	223
6.2.4.3	FTIR	223
6.2.4.4	PDI	229
6.2.5	PDI Improvements.....	232
6.3	PRC – March, 2015 Campaign – PDI Generation 3 Test.....	232
6.3.1	Equipment.....	233
6.3.1.1	FTIR Sampling.....	233

6.3.1.2	PDI Sampling	234
6.3.1.3	Aerosol Sources.....	236
6.3.2	Results.....	236
6.3.2.1	Steady State Conditions	236
6.3.2.2	Physical Observations	238
6.3.2.3	Manual Sampling	240
6.3.2.4	FTIR	241
6.3.2.5	PDI	249
6.3.3	PDI Improvements	256
6.4	NCCC – December, 2015 – PDI Generation 3.1 Test	256
6.4.1	Equipment	257
6.4.2	Results.....	261
6.4.2.1	Sampling Error	276
6.5	Conclusions.....	279
6.5.1	PDI and FTIR Measurement.....	279
6.5.2	Aerosol Characteristics	280
6.5.3	PDI/FTIR Fitting.....	282
6.5.4	SO ₂ /H ₂ SO ₄ Nucleation.....	284
6.5.5	Pilot Plant Observations.....	285
6.6	Acknowledgements.....	286
Chapter 7: Aerosol Growth Modeling		288
7.1	Basic Phase Modeling Concepts.....	289
7.2	Thermodynamics.....	293
7.2.1	Universal and Component Constants.....	294
7.2.2	Equilibrium Partial Pressures.....	295
7.2.3	Heats of Absorption and Vaporization	298
7.2.4	Liquid Heat Capacity	299
7.3	Physical Properties.....	300
7.3.1	Molecular Volume	300
7.3.2	Density	301

7.3.3	Surface Tension	301
7.4	Mass Transfer/Kinetics	302
7.4.1.1	Gas Film Limited Components	302
7.4.1.2	Reaction/Liquid Film Limited Components	302
7.5	Aerosol Dimensions.....	304
7.6	Absorber Input Profiles, Parameters, and Calculations	305
7.6.1	Input Parameters	305
7.6.2	Input Profiles.....	306
7.6.3	Calculations.....	309
7.7	Differential Equations	309
7.7.1	Component Mole Balances	309
7.7.2	Enthalpy Balance	310
7.7.3	Momentum Balance	311
7.8	Initial Conditions	312
7.9	Integration Algorithm	312
7.10	Program Structure	313
7.11	Results.....	315
7.11.1	Sensitivity Analysis: k'_g	315
7.11.2	Growth in the Water Wash	323
7.11.3	Water Wash Design Effects	329
7.11.3.1	Increasing Packed Height.....	329
7.11.3.2	Changing Water Wash Solvent Concentration.....	331
7.11.4	Growth Rate Extrapolation	332
7.11.4.1	Maxwell Solution – Continuum Approximation ($Kn \rightarrow 0$) 333	
7.11.4.2	Maxwell Solution – Kinetic Approximation ($Kn \rightarrow \infty$)	333
7.11.4.3	CO ₂ Reaction/Diffusion Limited (k'_g).....	334
7.11.4.4	Extrapolation Case Study	334
7.11.5	Growth Rate Theory – Absorber Driving Forces	335
7.11.5.1	Case 1 – Generic Absorber.....	336

7.11.5.2	Case 2 and 3 – The Effect of Intercooling	342
7.12	Aerosol Growth Hypothesis.....	350
7.13	Emissions Modeling.....	355
7.14	Conclusions.....	358
7.14.1	Parameter Sensitivity: k'_g	358
7.14.2	Growth in the Water Wash	359
7.14.2.1	Packing Height	359
7.14.2.2	Water Wash Concentration	359
7.14.3	Growth Rate Theory	360
7.14.3.1	The Effect of Intercooling.....	361
7.14.4	Emissions Modeling.....	361
7.14.5	Recommendations.....	362
7.15	Acknowledgements.....	363
Chapter 8:	Conclusions and Recommendations	364
8.1	Aerosol Growth Theory	364
8.1.1	Necessity of CO ₂	365
8.1.2	Water Wash Growth	365
8.1.3	PZ Makes Aerosol.....	366
8.2	Pilot Plant Observations.....	366
8.2.1	Amine Concentration in the Aerosol	366
8.2.2	SO ₂ and H ₂ SO ₄ Cause Aerosols.....	367
8.2.3	Aerosols Plug Filter Devices	367
8.3	Phase Doppler Interferometry.....	368
8.3.1	Field Demonstration.....	368
8.3.2	Density and Size Measurements	368
8.3.2.1	Density and Size Correlation	368
8.3.2.2	Aerosol Concentration Estimation	369
8.3.2.3	Aerosol Abatement Testing.....	369
8.4	Recommendations.....	369
8.4.1	Aerosol Generation	369

8.4.2 Aerosol Growth Column.....	370
8.4.3 Phase Doppler Interferometer	371
8.4.3.1 Installation Improvements.....	371
8.4.3.2 Portability	371
8.4.3.3 Condensate Control.....	371
8.4.3.4 Data Analysis	372
8.4.4 Aerosol Modeling	373
8.4.4.1 Mass Balance Incorporation.....	373
8.4.4.2 CO ₂ Mass Transfer Rate.....	373
8.4.4.3 Thermodynamics.....	373
8.4.4.4 Emissions Predictions	374
Appendix A: AGC and PDI/FTIR Data Algorithm	375
A.1 AGC Experiment Data Algoritihm	375
A.1.1 Analysis.xlsm.....	375
A.2 FTIR/PDI Pilot Experiment Data Algorithm for PM Data Sets	403
A.2.1 PM_PDI_FTIR_Analysis.xlsm.....	403
Appendix B: PDI Supporting Documentation	418
B.1 Aerosol Analyzer Selection	418
B.1.1 Aerosol Analyzer Selection	419
B.1.2 Instrument Review and Known Limitations	422
B.1.2.1 ELPI Errors and Limitations.....	422
B.1.2.2 PDI Errors and Limitations.....	426
B.1.3 PDI Rationale.....	427
Appendix C: LVI Supporting Documentation.....	428
C.1 LVI Performance Data.....	428
C.1.1 Eductor Flow and Vacuum	428
C.1.2 Pump Calibration	431
C.2 LVI Troubleshooting and Modifications	433
C.2.1 November, 2013 Campaign	434

C.2.1.1	First Upgrades – Coating and Increased Temperature	434
C.2.2	LVI Rebuild	440
C.2.2.1	Thermodynamic Analysis	440
C.2.2.2	Second Upgrades – Acid Concentration, Tube Heater, and Enclosure	443
C.2.3	March, 2015 Campaign	447
C.2.3.1	Furnace Bypass	448
C.3	Recommendations	448
C.4	Supporting Figures	450
Appendix D:	FTIR Connections/Assignments and DeltaV™ Code	453
D.1	FTIR/DeltaV™ Physical Connection	453
D.2	FTIR Menu Assignments	454
D.3	CALC1 DeltaV™ Code	459
Appendix E:	Aerosol Integration Code	462
E.1	Aerosol Integration Algorithm Overview	462
E.2	Aerosol_x.m	462
E.3	Initialize_x.m	476
E.4	Diffeql_x.m	480
E.5	Events_x.m	497
References		499
Vita		507

List of Tables

Table 2.1: Particle statistical averaging subscript definitions	24
Table 3.1: Analysis regions used for FTIR spectral analysis	67
Table 3.2: Temet Gasetm™ CX4000 Analyzer Technical Specifications.....	69
Table 3.3: Gasetm™ Portable Sampling Unit (PSU) Technical Specifications	70
Table 3.4: Baldor® Super-E® VEM3538 FTIR Sample Pump Motor Technical Specifications	71
Table 3.5: Air Dimensions, Inc.® Dia-Vac-R181® FTIR Heated Sample Pump Head Technical Specifications	72
Table 3.6: CleanAir® SKU 1233 heated/insulated electrical blanket technical specifications.....	73
Table 3.7: Universal Analyzers, Inc. Model 277S Heated Probe Technical Specifications	75
Table 3.8: MSSH-7 Stream Switcher Terminal Block Assignments	80
Table 3.9: PDI transmitter and receiver optical parameters.....	89
Table 3.10: Ametek® Rotron® EN303AG58L Regenerative Blower Technical Specifications	113
Table 4.1: AGC thermocouple calibration raw data and linear fitting parameters. All temperature are in °C.	129
Table 5.1: 06/24/14 AGC operation data	163

Table 5.2: Calculated k'_g values for cases 1–3 assuming constant inlet loading and an effective mass transfer area of $315 \text{ m}^2/\text{m}^3$. The k'_g value was adjusted to match the packing height by calculating the HTU and NTU of the AGC. The rich loading was calculated by mass balance.	163
Table 5.3: 06/25/14 AGC operation data	165
Table 5.4: 06/25/2014 CO₂ Stripping operation data	166
Table 5.5: LVI compositions produced using 0.5 m PZ and 0.05 vol % H₂SO₄, respectively. The LVI product gas is mixed with the process gas (20 SLPM) which is saturated to H₂O at 40 °C.	167
Table 5.6: PSD statistics for H₂SO₄ aerosols on the AGC. LVI flowrate: 2.0 mL/min of 10 vol % H₂SO₄. AGC solvent is H₂O.	175
Table 5.7: PDI data imported and calculated from raw PDI file output. The integrated volume is the total volume of liquids in the aerosol phase.	177
Table 5.8: Upstream gas mixing and presaturator temperature data.	178
Table 5.9: AGC inlet and outlet flowrate, temperatures, and solvent concentration.	179
Table 5.10: Calculated inlet and measured (FTIR) outlet gas concentrations.	180
Table 5.11: Calculated PZ volatility, integrated aerosol PZ content, and the absolute relative error between the integrated PDI PSD and the measurement made by FTIR.	181
Table 6.1: Generation 1 PDI optical and geometric parameters.	208
Table 6.2: Generation 1 and 2 PDI optical and geometric parameters.	218

Table 6.3: Absorber steady state conditions during the November, 2013 PRC pilot plant campaign.	222
Table 6.4: Manual sampling data provided by AECOM (formerly URS Corp.)	223
Table 6.5: Possible NH₃-SO₂-H₂O vapor-phase reactions and solubility product constants (Bai et al., 1994). Partial pressures used in K_{sp} expressions are atm.	228
Table 6.6: PDI data for Figure 6.17. Subscript definitions are in Table 2.1.	232
Table 6.7: Generation 1, 2, and 3 PDI optical and geometric parameters. ..	235
Table 6.8: Absorber steady state conditions during the March, 2015 PRC pilot plant campaign.	237
Table 6.9: Manual sampling data provided by AECOM (formerly URS Corp.)	241
Table 6.10: Aerosol injection and outlet PZ response data for the March, 2015 PRC pilot plant campaign. DeltaVTM run numbers are the closest matching steady state points to the injection time periods. The last column recalculates the PZ/SO₂ ratio using an absorption fraction of 34.9% (65.1% SO₂ is nucleated).	248
Table 6.11: Distribution statistics for the PSD measured at the PRC pilot plant with H₂SO₄ aerosol. The “Fine” and “Coarse” modes are approximating curves of the Total (Measured) distribution. ...	255
Table 6.12: PSD statistics for each sampling day at the SSTU at NCCC. PDI/FTIR error is the average absolute relative error.	265
Table 7.1: Universal constant parameters	294
Table 7.2: Component-specific constants	295

Table 7.3: Aerosol model input parameters from Aspen Plus®	305
Table 7.4: Aspen Plus® parameter definitions and units	306
Table 7.5: Reformatted sample absorber profile input data taken from a custom Aspen Plus® property set	307
Table 7.6: Reformatted sample absorber profile input data taken from a custom Aspen Plus® property set (cont'd.)	308
Table 7.7: Final diameter, growth ratio, and growth per packed height for aerosols passing through an absorber and water wash for $k'_g = 10^{-8}$, 10^{-7}, and 10^{-6} mol/s·Pa·m². The initial diameter d_i^D into the absorber was 3 μm.	326
Table B.1: Review of Analytical Instruments Capable of Measuring Particle Size Distributions. ^[1] (Kulkarni et al., 2011b); ^[2] (Biswas, 1985); ^[3] (Dekati Ltd., 2014); ^[4] (O'Hern et al., 1993); ^[5] (Artium Technologies, 2015); ^[6] (Stark et al., 2008); ^[7] (Mazumder et al., 2007); ^[8] (Malvern Instruments, 2007).	423
Table B.2: Review of Analytical Instruments Capable of Measuring Particle Size Distributions. ^[1] (Kulkarni et al., 2011b); ^[2] (Biswas, 1985); ^[3] (Dekati Ltd., 2014); ^[4] (O'Hern et al., 1993); ^[5] (Artium Technologies, 2015); ^[6] (Stark et al., 2008); ^[7] (Mazumder et al., 2007); ^[8] (Malvern Instruments, 2007).	424
Table B.3: Review of Analytical Instruments Capable of Measuring Particle Size Distributions. ^[1] (Kulkarni et al., 2011b); ^[2] (Biswas, 1985); ^[3] (Dekati Ltd., 2014); ^[4] (O'Hern et al., 1993); ^[5] (Artium Technologies, 2015); ^[6] (Stark et al., 2008); ^[7] (Mazumder et al., 2007); ^[8] (Malvern Instruments, 2007).	425

Table C.1: Flowrate and vacuum catalog data for Air-Vac model HAVR093SS and HAVR062SS eductors and actual measured values for the eductor system used in the LVI. P_{set} is the upstream motive fluid pressure.....	431
Table C.2: LVI pump calibration raw data.....	432
Table C.3: LVI Sampling train flow measurements to determine system leaks	438
Table D.1: FTIR RS-232 Cable to DeltaV™ S-Series Serial Interface Terminal Block Crossover Pinout.....	453

List of Figures

- Figure 1.1: CO₂ absorber (with water wash)/stripper process flow diagram under typical coal-fired flue gas conditions.....3**
- Figure 1.2: Total (aerosol and gas phase) amine emissions measured at the outlet of the water wash column are a function of the inlet SO₃ content and the amine system employed in the CO₂ capture process (Kamijo et al., 2013).....6**
- Figure 2.1: Bimodal PDF constructed from independent monomodal PDFs. **Coarse Mode:** $N_{Tot} = 5,000$, $d_G = 1 \mu\text{m}$, $\sigma_G = 2 \mu\text{m}$. **Fine Mode:** $N_{Tot} = 10,000$, $d_G = 0.15 \mu\text{m}$, $\sigma_G = 1.5 \mu\text{m}$20**
- Figure 2.2: Bimodal CDF constructed from independent monomodal PDFs. **Coarse Mode:** $N_{Tot} = 5,000$, $d_G = 1 \mu\text{m}$, $\sigma_G = 2 \mu\text{m}$. **Fine Mode:** $N_{Tot} = 10,000$, $d_G = 0.15 \mu\text{m}$, $\sigma_G = 1.5 \mu\text{m}$21**
- Figure 2.3: Bimodal surface area distribution constructed from independent monomodal PDFs. **Coarse Mode:** $N_{Tot} = 5,000$, $d_G = 1 \mu\text{m}$, $\sigma_G = 2 \mu\text{m}$. **Fine Mode:** $N_{Tot} = 10,000$, $d_G = 0.15 \mu\text{m}$, $\sigma_G = 1.5 \mu\text{m}$22**
- Figure 2.4: Bimodal volume distribution constructed from independent monomodal PDFs. **Coarse Mode:** $N_{Tot} = 5,000$, $d_G = 1 \mu\text{m}$, $\sigma_G = 2 \mu\text{m}$. **Fine Mode:** $N_{Tot} = 10,000$, $d_G = 0.15 \mu\text{m}$, $\sigma_G = 1.5 \mu\text{m}$23**
- Figure 2.5: Physical approximation regimes of particle-fluid interactions. As a particle approaches the mean free path of the surrounding fluid, the interactions more closely approximate kinetic/free-molecular theory of collisions in rarefied media.28**

Figure 2.6: Force diagram for a particle suspended in an upward moving fluid.	30
Figure 2.7: Approximation equations for the drag coefficient of a sphere with a smooth surface. Stokes' Law applies at small length scales or when inertial forces are much smaller than viscous forces.	33
Figure 2.8: Cunningham slip correction factor for several mean free paths.	35
Figure 2.9: Fuchs' correction factor for mass transfer in the continuum limit for several accommodation coefficients and a mean free path at STP $\lambda_{MFP} = 60.5 \text{ nm}$	40
Figure 2.10: Parameter and geometric definitions for calculating particle losses are defined for sampling from a horizontal process duct.	46
Figure 3.1: Flow chart of the operation sequence and optical information for FTIR using a Michelson-type interferometer.	58
Figure 3.2: GasetTM Calibrator, supplied by Air Quality Analytical, Inc.	64
Figure 3.3: Pin assignments and standard wire colors for 120 VAC power/Thermocouple connectors as viewed from behind (soldered ends). A separate standard K-type thermocouple connector is used in combination with Amphenol[®] power connectors. Both connectors are keyed, as indicated by the outer notch.	73
Figure 3.4: Mechanical and electrical drawing for the Universal Analyzers, Inc. Model 277S (no blowback) NEMA7 heated and filtered stack sampling "Stinger" probe. The high temperature (350 °F) thermomechanical switch was converted to PID control after the November 2013 SRP pilot campaign.	76

Figure 3.5: Heated sample probe side-view dimension diagram for connection of the stinger probe at the SRP pilot plant. The stinger probe depth into the process duct is set by a 1” Swagelok® to 1” MNPT adapter fitting using graphite ferrules. The tube adapter fitting connects to a 1” half-coupling welded to a short section of 1 ¼” S10 piping which is welded at approximately 135° with respect to the flow direction.77

Figure 3.6: Process flow diagram of the MSSH. The common bypass manifold is sent to waste/vent. The common sample manifold is sent to the FTIR for analysis.79

Figure 3.7: Schematic of geometric parameters, important measurement substeps, and data flow for a forward scattering PDI.83

Figure 3.8: Phase shifts between photodetectors are caused by magnification of the interference fringe pattern due to the particle curvature.85

Figure 3.9: PDI Transmitter and Receiver housing without mounting brackets and laser alignment port.89

Figure 3.10: The PDI test cell mounts to the PDI housing using swivel brackets. Channels for the 1/8” vacuum and purge tubing are inlayed in the mounting face plate of the PDI enclosure.92

Figure 3.11: Cutaway view of the test cell window and protection cone collar body. The windows are fixed in place using Silicone sealant.92

Figure 3.12: Engineering drawings for the PDI Transmitter laser protection cones.93

Figure 3.13: Engineering drawings for the PDI Receiver laser protection cones.94

- Figure 3.14: Doppler bursts for multiple particle trajectories. Particles passing through both beams in alignment produce a Gaussian pedestal with a thick, high frequency Doppler burst (1). Particles passing through a single beam will only contain a Gaussian pedestal and noise (2).**98
- Figure 3.15: Properly aligned Doppler burst with gate signal detection.**.....98
- Figure 3.16: Phase difference plots for all three combinations of detectors A,B, and C. The black lines show the exact phase difference expected from an ideal refracting aerosol. The top plots show raw data with no applied validation criteria. The bottom plots show the data with a 20° phase difference criteria (orange lines).**101
- Figure 3.17: A raw phase difference plot for two photodetector pairs operating in refraction mode. The black line represents the exact phase difference for ideal refracting aerosol. Aerosols passing on trajectories which cause pure reflection or mixed mode scattering have phase shift differences which fall in the regions between refraction lines, as indicated in the figure above.**102
- Figure 3.18: A plot of detector intensity versus particle diameter. The intensity of scattered light is assumed to occur by pure refraction and is proportional to the square of the particle diameter (Lorenz-Mie scattering). The maximum intensity line refers to a particle passing through the center of the beams. The minimum intensity line is for a particle crossing the minimum detection threshold (otherwise the edge of the sample volume).**106
- Figure 3.19: Doppler wavelength calculation schematic using the phase difference and the receiver geometry.**.....109

Figure 3.20: Probe volume is a function of particle diameter due to the Gaussian beam intensity profile and the scattering dependency on the square of the particle diameter. The detection volume, and probe width, decreases with decreasing particle diameter.	110
Figure 4.1: AGC P&ID #1. Gas distribution and LVI (bypass).	120
Figure 4.2: AGC P&ID #2. Inlet gas presaturation and mixing. Outlet gas condensation and vent.	121
Figure 4.3: AGC P&ID #3. Absorber column, solvent loop, and analysis locations.	122
Figure 4.4: AGC control enclosure and wiring diagram.	130
Figure 4.5: Calculated particle passage efficiency for the AGC assuming a total gas flowrate of 60 SLPM and a particle density of 1100 kg/m³. The total efficiency is the product of the individual efficiencies.	131
Figure 4.6: LVI control enclosure P&ID.	136
Figure 4.7: LVI injection enclosure P&ID.	137
Figure 4.8: Heated manual multipoint switching box. An external manifold with an isolation valve controls N₂ and Air flow used to purge the system. Heated sample lines connect to the top of the box.	141
Figure 4.9: FTIR and multipoint sample switcher PFD for the AGC	142
Figure 4.10: Front and back view of the rackmount FTIR and sampling system.	143
Figure 4.11: Aerosol sampling efficiency for FTIR analysis on the AGC. A particle density of 1,100 kg/m³ was assumed.	144
Figure 4.12: Front and back view of PDI mounted on the AGC outlet.	145
Figure 4.13: VBA Data processing algorithm for AGC experiments.	152

Figure 5.1: FTIR measurements of H₂O with varying solvent T and LVI flowrates. LVI Flowrates: 1.5 mL/min, 1.0 mL/min.	159
Figure 5.2: FTIR measurements of PZ with varying solvent T and LVI flowrates. LVI Flowrates: 1.5 mL/min, 1.0 mL/min.	160
Figure 5.4: 06/24/14 CO₂ Capture test. Inlet and outlet CO₂ concentrations. Solvent: 0.3 m PZ.	162
Figure 5.5: 06/25/14 CO₂ Capture test. Inlet and outlet CO₂ concentrations. Solvent: 0.3 m PZ.	164
Figure 5.6: 06/25/2014 CO₂ stripping operation outlet CO₂ FTIR measurements	165
Figure 5.7: Outlet PZ measurements for variable AGC operating conditions with injection of 0.5 m PZ by the LVI operating in bypass mode. Outlet PZ increases sharply with CO₂, but is not correlated to the concentration. PZ is inversely related to solvent rate. Inlet solvent T is 40 °C and nominally 1 m PZ at 0.18 CO₂ loading. (08/14/14)	171
Figure 5.8: Absorber outlet emissions under PZ aerosol load in response to changing solvent flowrate; CO₂ flow is zero. Outlet PZ is inversely proportional to the solvent rate. L/G varies from 9.5-57.0 mol/mol. Inlet solvent T is 40 °C and nominally 1 m PZ at 0.3 CO₂ loading. (08/15/14).	172
Figure 5.9: Absorber outlet emissions under PZ aerosol load in response to changing the solvent inlet temperature from 40 to 50 °C. The solvent is nominally 1 m PZ at 0.3 CO₂ loading Outlet PZ is inversely proportional to the solvent temperature. (08/15/14).	173

Figure 5.10: Outlet PZ measurements for variable AGC operating conditions with injection of 0.05 vol/vol H₂SO₄ by the LVI operating in bypass mode. Outlet PZ shows a weak, inverse correlation to CO₂ concentration and is positively correlated to solvent flowrate. Inlet solvent T is 40 °C and nominally 1 m PZ at 0.3 CO₂ loading.

(08/19/14).....174

Figure 5.11: Consecutive PDI analyses taken on the AGC outlet at an H₂SO₄ injection rate of 2 mL/min. and a solvent temperature of 40 and 50 °C. The solvent is DDI H₂O.....175

Figure 5.12: The measured outlet PZ is correlated with the inlet CO₂, the lean solvent rate, and the lean solvent temperature. The solvent was nominally 5 m PZ and 0.2 CO₂ loading. The LVI flowrate was set to 0.42 mL/min of H₂O. The inlet gas temperature ranged between 42 and 45 °C.....182

Figure 5.13: The aerosol particle size distribution shifts to the right (growth by condensation) with the addition of CO₂. Lean Solvent: 40 °C, 0.2 GPM. Inlet CO₂: 0 and 3 SLPM.....184

Figure 5.14: The measured count-average particle diameter (●) and total particle density changes (●) with inlet CO₂ content. No control for operating conditions other than inlet CO₂ was made.....185

Figure 5.15: The measured count-average particle diameter (●) and total particle density (●) changes with inlet CO₂ content. All other process conditions kept constant. The spread in data for constant inlet CO₂ content indicates repeatability of the measurement. 186

Figure 5.16: Outlet PZ measured by FTIR shows a maximum as the inlet CO₂ content is increased. All other process conditions are kept constant.	186
Figure 5.17: Normalized amine emissions for varying inlet CO₂ concentrations from this study (●) and the work of Khakharia (2015). This study used 5 m PZ. Khakharia used a mixed solvent system composed of 2.6 M AMP (●) and 0.9 M PZ (●).	189
Figure 5.18: The average particle diameter and the logarithm of particle density are correlated linearly for variable inlet CO₂. All other process conditions kept constant.	190
Figure 5.19: The measured count-average particle diameter (●) and total particle density increases (●) with the solvent rate. All other process conditions kept constant (inlet CO₂ is 10 vol %).	191
Figure 5.20: The average particle diameter and the particle density are positively correlated for variable lean solvent rate. All other process conditions kept constant.	192
Figure 5.21: Measured outlet amine concentration data for the AGC (PZ solvent, ◆) plotted against data collected by Khakharia (2015) (MEA solvent, ●) as a function of the measured particle density.	193
Figure 5.22: Calculated volatility (●), integrated aerosol volumetric PZ concentration (●), and outlet PZ measured by FTIR (black line). The solvent concentration was assumed to be 5 m at 0.25 lean loading.	195

Figure 5.23: Outlet PZ is linearly correlated to particle density above 2×10^6 part./cm³. Below 2×10^6 part./cm³, the PZ contained in the aerosol is an insignificant contributor to the total outlet PZ content.196

Figure 5.24: Outlet PZ is correlated to the count-average particle diameter.197

Figure 5.25: The count-average diameter and the total particle density are positively correlated across the experiment.198

Figure 6.1: Flue gas from Unit #5 (880 MWe) is drawn off after the Chiyoda SO₂ scrubber (shown in the left picture) and is piped into the PSTU (shown on the right) and other smaller pilot plants, test skids, and bench-top apparatuses located at PC4. The feed rate to PSTU is equivalent to a 0.5 MWe scrubbing system (10 tpd CO₂ captured).205

Figure 6.2: Equipment and optical setup of the Generation 1 PDI test on the water wash outlet duct of the PSTU at NCCC. The PDI transmitter and receiver are 140 ° apart on a 12” duct. The gas flow is oriented downward.207

Figure 6.3: Dimensions of the optical access windows on the PSTU. The viewing cones are designed to accommodate the crossing angles of the transmitter and receiver.207

Figure 6.4: Receiver output to an oscilloscope. The oscilloscope display shows a noisy baseline for both detectors with no discrete Doppler bursts, indicating a high concentration of particles $\leq 1 \mu\text{m}$209

Figure 6.5: Close-up view of the transmitted beam crossing. The intersection of the laser beams is where the gas is sampled for moving particles. 50 μm diameter beams were used in this test.210

Figure 6.6: Front view of the PRC pilot plant. PDI and FTIR sample points and the LVI injection point are shown as well.213

Figure 6.7: Side view of the PRC pilot plant detailing the locations of the inlet and outlet FTIR sampling points. The picture on the right shows a detail view of an FTIR sampling location stinger probe (absorber inlet).....214

Figure 6.8: Absorber outlet sampling location proximity for FTIR, PDI, and manual impinger sampling for amines (and H₂O).....215

Figure 6.9: Locations of sampling and aerosol injection points at the PRC pilot plant. The knockout location was not sampled during the November, 2013 campaign. Vaisala probes measure CO₂ content by IR.....216

Figure 6.10: The second generation PDI was oriented vertically to accommodate the modular PDI setup. An airbrush operated with H₂O was used to generate test aerosol for this picture. The PSD and velocity histogram are shown on the computer monitor.....218

Figure 6.11: PDI sampling and return PFD for the second generation PDI test.219

Figure 6.12: SO₂ injection location (left picture) downstream of the absorber blower. The LVI injection enclosure (right picture) was located upstream of the absorber inlet port, the inlet FTIR sampling point, and the SO_x manual sampling point.....221

Figure 6.13: FTIR (UT/SRP) and manual sampling (URS) data taken 11.21.2013.

Dashed lines with circle points are manual sampling PZ concentrations averaged over a 30-minute interval adjusted for moisture content. The LVI was in operation between the dotted gray lines. PDI sampling occurred inside the red circle.....225

Figure 6.14: FTIR (UT/SRP) and manual sampling (URS) data taken

11/22/2013. Dashed lines with circle points are manual sampling PZ concentrations averaged over a 30-minute interval adjusted for moisture content. SO₂ was injected during the period containing URS-7 and URS-8. Spray intercooling was turned on in between URS-7 and URS-8.226

Figure 6.15: FTIR analysis of SO₂ at the absorber inlet heated probe. SO₂ was

injected at a targeted concentration of 25 ppmv.....227

Figure 6.16: Consecutive PDI analyses taken on 11/19/2013 starting at 08:27 at

an H₂SO₄ injection rate of 1.5 mL/min. All data sets are 10,000 total counts.230

Figure 6.17: Consecutive PDI analyses taken on 11/21/2013 starting at 14:30 at

an H₂SO₄ injection rate of 2 mL/min. All data sets are 10,000 total counts.231

Figure 6.18: MSSH manual sampling switcher box. The switcher box selects the

sample solenoid which then activates the heated pneumatic valve.234

Figure 6.19: PDI weatherproof enclosure. The PDI power box, ASA, and computer are contained in the enclosure on rackmount railing. The oscilloscope can be set on the shelf for signal observation during calibration and analysis.	235
Figure 6.20: SO₂ (left) and H₂SO₄ (right) plumes at the absorber outlet vent stack.	238
Figure 6.21: The knockout filter pressure drop increased across the campaign following SO₂ injections due to accumulation of H₂O/PZ/CO₂ liquid and solids.	239
Figure 6.22: The knockout tank consists of an upstream coarse wire mesh pad (left) and a 0.3 μm filter (right). The filter and mesh were periodically rinsed with warm water to re-dissolve collected material.	240
Figure 6.23: FTIR response to MSSH sample switching (03/25/2015). The FTIR reaches steady state after five minutes between sample point switches.	242
Figure 6.24: FTIR measurements compared to CO₂ inlet and outlet measurements using Vaisala CO₂ probes and H₂O by Raoult's Law	243
Figure 6.25: Vaisala and FTIR CO₂ calibration comparison. Error bars are the maximum standard deviation for each data set.	244
Figure 6.26: Response of outlet PZ to SO₂ injection #1 using a mass flow controller (03/13/15)	245
Figure 6.27: Response of outlet PZ to SO₂ injection #2-3 using a rotameter (03/13/15)	245

Figure 6.28: Response of outlet PZ to H₂SO₄ injection #2 (03/20/15)246

Figure 6.29: Response of outlet PZ to H₂SO₄ injection #3 (03/20/15)246

Figure 6.30: Sulfate accumulates in the PRC pilot plant solvent proportionally to the SO₂ injection rate and time. The calculated SO₂ absorption percent is 34.9% assuming a total solvent inventory is 1,400 kg over the duration of the campaign.....249

Figure 6.31: Velocity distribution measured in the PDI analysis cell with purge and flush gas. The total data set is 15,802 counts. Negative velocities indicate back-mixing and turbulence in the cell.....251

Figure 6.32: PSD measured during H₂SO₄ injection at the PRC pilot plant. The total particle density is 9.9x10⁵ part./cm³. The total data set is 15,802 counts. The dashed lines indicate the quantification limits for the **generation #2 and **generation #3** PDI showing the marked improvement.....252**

Figure 6.33: A bimodal-lognormal distribution constrained to a total particle density of 9.9x10⁵ part./cm³. The individual distribution mode parameters were optimized to match the measured PSD in Figure 29. **Fine Mode parameters: $\sigma_G = 1.60 \mu\text{m}$, $d_G = 0.21 \mu\text{m}$, $7.0 \times 10^5 \text{ part./cm}^3$. **Coarse Mode** parameters: $\sigma_G = 1.25 \mu\text{m}$, $d_G = 0.86 \mu\text{m}$, $2.9 \times 10^5 \text{ part./cm}^3$253**

Figure 6.34: Measured and **approximated PSD at the PRC pilot plant.254**

Figure 6.35: Cumulative distributions for the **diameter, **surface area**, and **volume** of the measured PSD. The black line is the diameter cumulative distribution using the fitting curve from Figure 30.255**

- Figure 6.36: SSTU process flow diagram with FTIR/PDI sample/return loop.**
 The physical piping distance between the top of the water wash column and the sample port is 55 feet.....258
- Figure 6.37: Simultaneous FTIR/PDI sampling unit located at the outlet of the SSTU water wash operating at NCCC.....259**
- Figure 6.38: Calculated transmission efficiency (see Section 2.5 for equations) for the PDI/FTIR simultaneous sampling system assuming a flow rate of 125 SLPM. The aerosol density was 1,000 kg/m³ and the gas properties were calculated at 40 °C and 1 psig.....260**
- Figure 6.39: PDI/FTIR comparison data for December 5, 2015 measured at the water wash outlet of the SSTU at NCCC. C_{MEA} = 0.084 m MEA261**
- Figure 6.40: PDI/FTIR comparison data for December 7, 2015 measured at the water wash outlet of the SSTU at NCCC. C_{MEA} = 0.023 m MEA262**
- Figure 6.41: PDI/FTIR comparison data for December 8, 2015 measured at the water wash outlet of the SSTU at NCCC. C_{MEA} = 0.035 m MEA262**
- Figure 6.42: PDI/FTIR comparison data for December 9, 2015 measured at the water wash outlet of the SSTU at NCCC. C_{MEA} = 0.036 m MEA263**
- Figure 6.43: PDI/FTIR comparison data for December 10, 2015 measured at the water wash outlet of the SSTU at NCCC. C_{MEA} = 0.260 m MEA263**
- Figure 6.44: PDI/FTIR comparison data for December 11, 2015 measured at the water wash outlet of the SSTU at NCCC. C_{MEA} = 0.081 m MEA264**
- Figure 6.45: PDI/FTIR comparison data for December 12, 2015 measured at the water wash outlet of the SSTU at NCCC. C_{MEA} = 0.120 m MEA264**

Figure 6.46: Calculated MEA concentration in the aerosol required to perfectly fit the FTIR data for December 5, 2015 measured at the water wash outlet of the SSTU at NCCC.	267
Figure 6.47: Calculated MEA concentration in the aerosol required to perfectly fit the FTIR data for December 7, 2015 measured at the water wash outlet of the SSTU at NCCC.	267
Figure 6.48: Calculated MEA concentration in the aerosol required to perfectly fit the FTIR data for December 8, 2015 measured at the water wash outlet of the SSTU at NCCC.	268
Figure 6.49: Calculated MEA concentration in the aerosol required to perfectly fit the FTIR data for December 9, 2015 measured at the water wash outlet of the SSTU at NCCC.	268
Figure 6.50: Calculated MEA concentration in the aerosol required to perfectly fit the FTIR data for December 10, 2015 measured at the water wash outlet of the SSTU at NCCC.	269
Figure 6.51: Calculated MEA concentration in the aerosol required to perfectly fit the FTIR data for December 11, 2015 measured at the water wash outlet of the SSTU at NCCC.	269
Figure 6.52: Calculated MEA concentration in the aerosol required to perfectly fit the FTIR data for December 12, 2015 measured at the water wash outlet of the SSTU at NCCC.	270
Figure 6.53: Count-average diameter and total particle density on December 7, 2015. Both the diameter and density increase after switching from the PSTU to the SSTU blower.	271

Figure 6.54: Count-average diameter and total particle density on December 8, 2015. The diameter increase after switching from the PSTU to the SSTU blower; however, the density is not affected by the blower change.....272

Figure 6.55: Count-average diameter and total particle density on December 11, 2015 at NCCC. The aerosol removal device is in operation as indicated by the dashed black lines.....273

Figure 6.56: Count-average diameter and total particle density on December 12, 2015 at NCCC. The aerosol removal device is in operation as indicated by the dashed black lines.....274

Figure 6.57: The average diameter and particle density relationship depends on sampling day (left) and the location of the blower (right). The **PSTU blower shows an inverse relationship. The **SSTU** blower shows a positive correlation between the average diameter and the total particle density.275**

Figure 6.58: As window attenuation increases due to condensation, the maximum intensity of the initial laser beams decreases. As a result, the minimum detectable particle diameter (and the probe volume) as well as the total particle density decreases.....277

Figure 6.59: The normalized average diameter to total particle density ratio plotted against the absolute sampling time. If condensation attenuated the signals from the smaller droplets and was systematic in time, the curves would trend upwards. No such correlation is apparent.....278

Figure 7.1: Three phase mass and heat transfer schematic for a single calculation stage.	290
Figure 7.2: Simplified three phase mass and heat transfer schematic for a single calculation stage. The mass and energy balance between the aerosol and gas phase is neglected. The aerosol is assumed to contribute negligibly towards the total material and energy balance. A monomodal distribution is assumed and the calculation is performed for a single droplet.	291
Figure 7.3: The absorber (Eulerian) and aerosol (Lagrangian) reference states are linked by the momentum balance. Absorber calculations are performed in Aspen Plus® and the aerosol integration and interpolation are performed in MATLAB®.	293
Figure 7.4: CO₂ solubility comparison between Aspen Plus® (solid lines) and the empirical correlation (dashed lines).	297
Figure 7.5: PZ volatility comparison between Aspen Plus® (solid lines) and the empirical correlation (dashed lines).	297
Figure 7.6: Percent difference in $P^*_{H_2O}$ between Aspen Plus® and Raoult's Law for 1–12 m PZ at 40 (solid lines) and 60 °C (dashed lines) and 0.30–0.45 CO₂ loading.	298
Figure 7.7: k'_g experimental data taken from Dugas (2009) for 2–12 m PZ at 40 (solid lines) and 60 °C (dashed lines).	304
Figure 7.8: Aerosol integration program flow chart	314
Figure 7.9: Absorber and initial aerosol conditions for the sensitivity case study. The PZ concentration in the aerosol is not independent since H₂O and CO₂ are set by the bulk gas concentration.	315

Figure 7.10: Particle growth curves as a function of normalized column position for $k'_g = 10^{-6}$, 10^{-7} , and 10^{-8} mol/Pa·m²·s. Column input and aerosol initial conditions are given in Figure 7.9.....317

Figure 7.11: Bulk gas temperature profile and the temperature difference between the gas and aerosol for $k'_g = 10^{-6}$, 10^{-7} , and 10^{-8} mol/Pa·m²·s.318

Figure 7.12: Aerosol CO₂ loading as it passes through the absorber for $k'_g = 10^{-6}$, 10^{-7} , and 10^{-8} mol/Pa·m²·s. The initial aerosol diameter is 3 μm. The black curve represents the CO₂ loading which produces an equilibrium partial pressure equivalent to the bulk gas CO₂ concentration.....319

Figure 7.13: Aerosol PZ equilibrium partial pressure as it passes through the absorber for $k'_g = 10^{-6}$, 10^{-7} , and 10^{-8} mol/Pa·m²·s. The black curve is the bulk gas PZ partial pressure.....320

Figure 7.14: Driving forces to maintain aerosol loading: $D_{PZ,Mix}^G = 10^{-5}$ m²/s, $T^G = 40$ °C, $\lambda_{MFP} = 66$ nm, and $k'_g = 10^{-6}$, 10^{-7} , and 10^{-8} mol/Pa·m²·s.322

Figure 7.15: Absorber and water wash conditions for growth analysis between the two unit operations. The column heights were set by 90 % CO₂ removal (absorber) and 1 ppm PZ in the outlet gas (water wash).324

Figure 7.16: Particle growth curves as a function of normalized column position (normalized to the total column height) for $k'_g = 10^{-6}$, 10^{-7} , and 10^{-8} mol/Pa·m²·s.....325

Figure 7.17: Bulk gas temperature profile and the temperature difference between the gas and aerosol for $k'_g = 10^{-6}$, 10^{-7} , and 10^{-8} mol/Pa·m²·s.327

Figure 7.18: Aerosol CO₂ loading as it passes through the absorber and water wash for $k'_g = 10^{-6}$, 10^{-7} , and 10^{-8} mol/Pa·m²·s. The black curve represents the CO₂ loading which produces an equilibrium partial pressure equivalent to the bulk gas CO₂ concentration.328

Figure 7.19: Aerosol PZ equilibrium partial pressure as it passes through the absorber and water wash for $k'_g = 10^{-6}$, 10^{-7} , and 10^{-8} mol/Pa·m²·s. The black curve is the bulk gas PZ partial pressure.329

Figure 7.20: The addition of more packing height in the water wash can significantly increase the final diameter of aerosols leaving the amine scrubbing system. Condensation of H₂O continues with increased residence time.330

Figure 7.21: Variations in the water wash solvent concentration alter the aerosol growth rate. Dilution of the solvent increases the activity of H₂O and therefore the driving force for condensation onto the amine/CO₂ concentrated aerosol. $k'_g = 10^{-6}$ mol/s·Pa·m².332

Figure 7.22: The square of the final and initial aerosol diameters are linearly related for the sensitivity case study with the included water wash tower. The squared relationship indicates a gas-side component transfer limitation in the growth rate.335

- Figure 7.23: The temperature bulge location is a function of L/G, phase heat capacities, inlet temperatures, and the reaction rate and enthalpy. A large L/G (8 mol/mol) moves the temperature bulge towards the bottom of the column.....338**
- Figure 7.24: The partial pressure of PZ is a strong function of the liquid loading and temperature. The temperature bulge is directly reflected in the P_{PZ} curve. The inflection at the top of the column is caused by the rapid decrease in loading.339**
- Figure 7.25: Condensation onto aerosols requires a continuous driving force. Accumulation of salts (CO_2 and PZ) increases the driving force for H_2O condensation. Areas in the column with the highest CO_2 and PZ content will grow the fastest.....340**
- Figure 7.26: The gradient blocks indicate regions of high concentration of CO_2 and PZ which is theorized to cause aerosol growth. The aerosol actually shrinks at the top of the absorber where P_{CO_2} is lowest, even though P_{PZ} is still relatively high.341**
- Figure 7.27: The PZ concentration in the aerosol droplet changes as it moves through areas of changing saturation in the absorber. In the water wash, accumulation of H_2O occurs very rapidly which is reflected in the **molality** curve. The dilution suppresses PZ volatility such that PZ does not transfer readily out of the aerosol. The **total moles** of PZ remains relatively constant in the water wash.342**
- Figure 7.28: IC/NIC input conditions and simulated rich loading and CO_2 removal percentages. In-and-out intercooling was added to the NIC case without any parameter changes to yield the IC case.343**

Figure 7.29: Temperature profiles for the NIC and IC SRP absorber cases.
Intercooling suppresses temperature bulging throughout the entire column.....345

Figure 7.30: P_{PZ} and P_{CO2} curves for the NIC (solid lines) and IC (dashed lines) cases. Intercooling suppresses PZ volatility over the solvent due to the increased loading (faster absorption) and reduced temperatures.346

Figure 7.31: Droplets in non-intercooled columns grow larger due to the increased availability of condensable amine. The lower CO₂ capture rate also supplies more CO₂ for acid-base reaction with the amine.347

Figure 7.32: More PZ accumulates in the non-intercooled case. However, PZ accumulates for both absorber cases due to the PZ driving force created by the loading difference between the aerosol and the bulk liquid.....348

Figure 7.33: Growth curves for the NIC and IC cases show that the NIC cases grow at a faster rate. The availability of more condensable species (CO₂ and PZ) increases the driving forces throughout the column.349

Figure 7.34: The final total moles of PZ depends on the initial diameter for both the NIC and IC cases. The molality is constant for a given initial diameter, but is higher for the IC case: NIC = 6.4 m PZ, IC = 8.3 m PZ. The dashed lines are for the NIC case, the solid lines are for the IC case.....350

Figure 7.35: Amine driving forces between the gas and aerosol at the absorber rich (left) and lean (right) ends for 8 m PZ, 9 m MEA, and 4.8 m AMP at 40 °C. ($P_{CO_2,Rich} = 12,000$ Pa, $P_{CO_2,Lean} = 1,200$ Pa, $P^*_{CO_2,Rich} = 5,000$ Pa, $P^*_{CO_2,Lean} = 500$ Pa)......352

Figure 7.36: Three phase film diagram for mass transfer between an aerosol, gas, and bulk liquid. Temperature and CO₂ loading affects the transport between the liquid phases and the gas acts as a temperature and mass buffer......355

Figure 7.37: Bimodal-lognormal PSD composed of two individual (Coarse and Fine Modes) lognormal distributions weighted 0.1:0.9 (Coarse:Fine). The total particle density calculated by mass balance of 3 ppmv SO₃ assuming a liquid H₂SO₄ concentration of 0.1 mol/L is 4.58x10⁶ part./cm³......356

Figure 7.38: Initial and final PSDs using growth curves for the IC and NIC case studies......357

Figure B.1: Reported size ranges and total particle densities in CO₂ capture pilot plants and bench scale units. Size determination method is contained in parentheses.419

Figure B.2: Operating windows for aerosol size analysis instruments. *In situ* instruments are defined as non-interfering although a sample often requires extraction from a measurement point......421

Figure C.1: Measured LVI carrier gas flow rate compared to manufacturer data. The measured flow rate was compensated for density using P = 100 psig and T = 21 °C. The black curve (●) is the measured values for the eductor in the LVI system......429

Figure C.2: LVI eductor vacuum as a function of the inlet pressure. The reported data (● blue curve) is digitized from a catalog curve while the black points (●) are measured values.430

Figure C.3: LVI pump calibration curve with a new pump sleeve.433

Figure C.4: LVI fittings are coated in Dursan® polymer435

Figure C.5: LVI acid scrubbing sampler train flow diagram.....436

Figure C.6: First LVI test with downstream acid collection in stack sampling impinger train. Additional impingers were added after the first test which match the configuration shown in Figure C.5.....437

Figure C.7: Aerosols condensing through the first and second impinger cause an increase in opacity. Pulsation in aerosol production was directly observable by opacity fluctuations.439

Figure C.8: 3D drawing of the upgraded LVI with added tube furnace. Acid is injected at the green fitting. Carrier N₂ passes through the preheater and in all of the orange fittings. The hot, gaseous H₂SO₄ mixes at the intersection of the yellow tubing and the red eductor.445

Figure C.9: Condensate collected during H₂SO₄ injection in the first impinger showed significant accumulation of stainless steel corrosion products.446

Figure C.10: The tube furnace quartz wool packing holder with accumulated stainless steel corrosion products after operation on the SRP pilot plant.....447

Figure C.11: Rebuilt LVI control enclosure. A second liquid reservoir was added for H₂O to use during startup and shutdown.450

Figure C.12: Rebuilt LVI control enclosure wiring and electrical terminations.	451
Figure C.13: Simplified schematic of the original LVI system provided by Mark Nelson of AQA.	452
Figure D.1: DeltaV™ S-Series terminal block pin connections for FTIR input	454
Figure D.2: Top and bottom views of the RS-232 DB9 cable pins and wire colors	454
Figure D.3: Modbus output channels are configured in the analysis settings window under the Modbus tab. Up to 30 channels are configurable for any component order. The channel number corresponds to the output registry order.	456
Figure D.4: Double-clicking a ModBus output channel brings up the Output Channel Select Window where the component or on-board measurement can be selected as an output. The channel number and label on the Output Channel Select window correspond to the Gas Components Analysis Settings numbering. The ModBus and the Output channel numbers do not have to be the same.	457
Figure D.5: The RS-232 serial output to DeltaV™ has to be configured in Calcmet. The RS-232 Serial port corresponds to the physical communications port on the FTIR computer. The baud rate is set to match DeltaV™ and the protocol is set to ModBus. Cyclic Redundancy Check (CRC) is set to standard representation. The address is the RS-232 (serial) input card address in DeltaV™.	458

Figure D.6: I/O diagram for the FTIR in DeltaV™ Control Studios. The module is configured to card 11, port 1. The FTIR output registries begin at address 30001 which corresponds to the ModBus Output Channel 1 which is configured in Calcmet™. Seven ModBus channels are configured in this diagram. The read input values are converted to concentration numbers in the CALC1 calculation block.....459

Chapter 1: Introduction

Rapidly expanding populations and increasingly globalized economies have intensified demand for transportation fuels, manufacturing power, and residential amenities. Over the past two centuries, combustion of fossil fuels has met much of the global energy demand at the detriment of the environment. Climate change assessment reports from the Intergovernmental Panel on Climate Change (IPCC, 2007), and more recently the Berkeley Earth Project (Rohde et al., 2012), have created and renewed debate over economically viable solutions to reduce particulate and greenhouse gas (GHG) emissions, particularly CO₂, in an effort to mitigate the harmful effects of anthropogenic pollution. Transitioning to sustainable sources of energy will be a long and costly endeavor; abandoning the existing power infrastructure is infeasible if CO₂ reduction targets are to be met, while matching energy demand, within the next few decades. Therefore, bridging technologies, or short-to-near future GHG reduction solutions, are a critical piece in the long-term portfolio of useful strategies to abate climate change. This work focuses on the most mature and cost-effective bridging technology which can be implemented quickly and at a large scale: retrofit aqueous alkanolamine absorption/stripping on coal-fired power plants.

1.1.1 CO₂ Capture by Amine Absorption/Stripping

Alkanolamine scrubbing, patented by Bottoms (1930), is a robust and well-practiced industrial acid gas removal technology that has been in use for over 80 years (Kohl et al., 1997). The first CO₂ specific capture and sequestration plant was built on the Sleipner West gas field in Norway in 1996 and remains operational today (Rao et al., 2002). The process (shown below in **Figure 1.1**) begins by removing acidic components from flue gas blown into a counter-current, packed-bed absorber through reactive

absorption into an alkaline, aqueous solvent. The exiting liquid, now rich in absorbed species, is sent to another separation column (stripper) where heat is added to reverse the exothermic absorption step, thereby stripping out the desired components at high purity. Regenerated lean solvent is pumped through a series of heat exchangers to recover sensible heat before returning to the absorber to repeat the absorption/stripping cycle. The stripped CO₂ may then be compressed to 150 bar for subsequent use in enhanced oil recovery (EOR) or sequestration in underground geologic formations.

Figure 1.1 shows a typical process flow diagram of an amine absorber/stripper system capturing CO₂ from a typical coal-fired flue gas composition and state. CO₂ capture units would be added to the tail end of a power plant's pollution control system by re-routing the duct-work prior to the exhaust stacks. The flue gas would typically be preconditioned by undergoing adiabatic saturation in a spray tower with H₂O and SO₂ polishing to prevent significant sulfate build-up in the solvent.

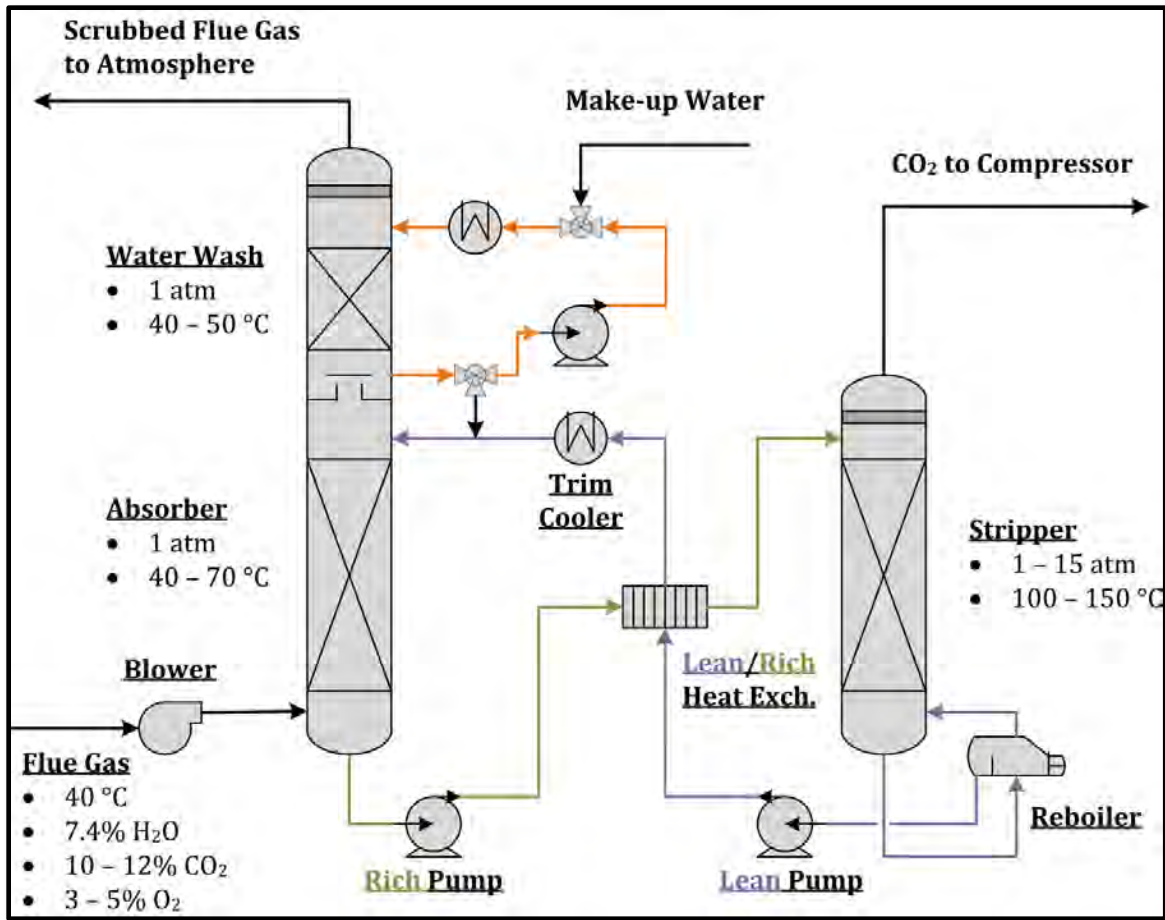


Figure 1.1: CO₂ absorber (with water wash)/stripper process flow diagram under typical coal-fired flue gas conditions.

1.1.2 Volatile Losses

Although amine scrubbing is a well-suited and characterized method for gas separation, it is not without its drawbacks. Continued exposure of solvent to O₂ (3-5 vol%) and pollutants (SO_x, NO_x, NH₃, PM) in the treated gas as well as elevated temperatures during stripping (100-150 °C) leads to poor performance via oxidation (Sexton, 2008; Freeman, 2011; Closmann, 2011), thermal degradation (Davis, 2009; Freeman, 2011; Closmann, 2011), contamination, corrosion, and foaming. Direct contact

of solvent and flue gas provides a pathway for carry-over of amine and degradation products into the exhaust gas as either vapor or suspended liquid.

Managing releases from a CO₂ capture facility is important both economically and environmentally. Solvent must be continually replenished due to volatile amine loss and purging degradation products/heat-stable salts during solvent reclamation.

Thitakamol and co-authors estimate these losses to be as much as 15.65 kg waste/ton CO₂ captured for a nominal 30 wt% monoethanolamine (MEA) process including fugitive emissions (Thitakamol et al., 2007). Making up amine is an important financial consideration which is often addressed by identifying robust solvents with low volatility. More importantly, reactions with flue gas components and degradation derivatives from oxidative and thermal decomposition create numerous classes of compounds possessing a wide range of phase partitioning behavior and toxicity at variable rates of formation (Azzi et al., 2010). Many emittable components are stable to biodegradation (Eide-Haugmo et al., 2011) and some reaction products, specifically nitrosamines, are known carcinogens (Jackson et al., 2010; Fine et al., 2013). Containing these emissions and reducing their environmental impact is therefore a crucial piece of large-scale deployment of amine scrubbers for carbon capture. Three points are evident from literature: (1) the breadth of possible species emitted from amine-based CO₂ capture systems is extensive and chemically varied, (2) little is known about the toxicology of these species, and (3) little, if any, regulation exists for many of these compounds.

Presently, a short section of packing, called a water wash, is added to the top of the absorption column for two purposes: (1) to reduce emitted compounds by absorption and (2) to control the H₂O balance in the overall system. Since the majority of washed components are highly soluble in aqueous media, WW's are effective at removing most volatile and semi-volatile species out of the gas phase; however, recent pilot plant studies

have shown poor pollution control out of the WW due to slippage of aerosols containing condensed amine and byproduct species.

1.2 AEROSOLS AT PILOT PLANTS

The following section highlights three pilot plant observations of aerosols, their impact on total emission rates, and aerosol analysis techniques.

1.2.1 Mitsubishi Heavy Industries

In 2011, MHI presented pilot test results for both KS-1TM (a proprietary solvent) and MEA which showed that emissions were proportional to inlet SO₃ concentration (Kamijo et al., 2013). SO₃ was created by oxidizing a metered stream of SO₂ in an upstream catalyst bed. Amine levels out of the wash section (WW) were 0.4-23.2 ppmv and 0.8-67.5 ppmv for KS-1TM and MEA, respectively for 0-3 ppmv inlet SO₃ (**Figure 1.2**). Mist was visually present at the upstream H₂O cooling tower and WW outlets. MHI showed that the total emissions (aerosol and gas phase) were a function of the inlet SO₃ content as well as the amine used in the capture process.

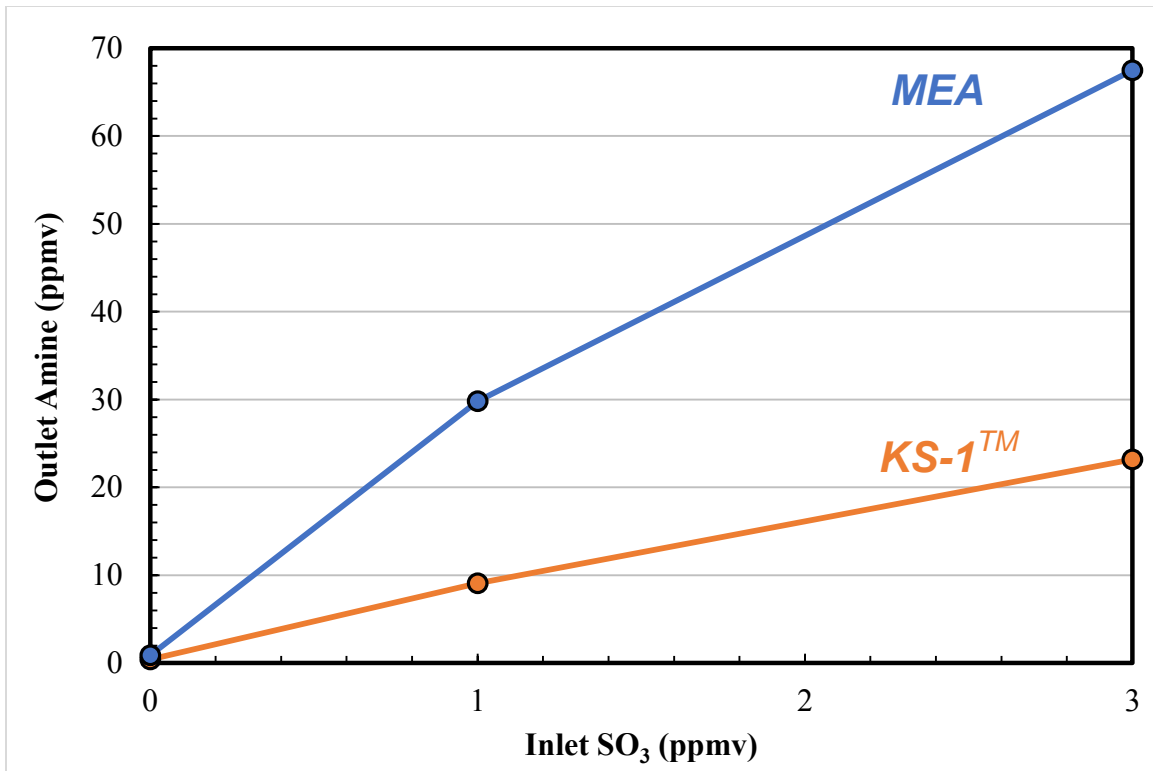


Figure 1.2: Total (aerosol and gas phase) amine emissions measured at the outlet of the water wash column are a function of the inlet SO₃ content and the amine system employed in the CO₂ capture process (Kamijo et al., 2013).

1.2.2 SINTEF and TNO

At the Maasvlakte pilot plant, the Netherlands Organisation for Applied Scientific Research (TNO) and The Foundation for Scientific and Industrial Research (SINTEF) jointly tested a 30 wt% MEA CO₂ capture unit with a downstream WW complete with online gas and aerosol phase sampling (van der Gijp et al., 2012; Kolderup et al., 2012).

The presence of aerosol-bound amine emissions was confirmed by the addition of lithium and rubidium carbonate (Li₂CO₃, Rb₂CO₃) tracers in the absorber solvent and water wash loops; physical entrainment of the solvent and wash streams was found to be negligible.

Detailed characterization of the particle phase was attempted using a combination of light extinction measurements, a Dekati Electrical Low-Pressure Impactor (ELPI™) with a pre-impactor plate (Anderson D50 of ca. 11 μm), a TSI Aerodynamic Particle Sizer (APS®) sampled isokinetically, installation of a high efficiency droplet capture device called the Brownian Demister Unit (BDU), and mass balances using condensate collection (van der Gijp et al., 2012; Kolderup et al., 2012). The sample gas line was maintained at ±1–2 °C relative to the extraction point temperature to prevent condensation or evaporation in the line. The BDU was installed downstream of the water wash.

The Sauter-mean droplet diameter (D_{32}) at top of the water wash tower prior to the BDU was reported to be 0.76–7.88 μm and decreased to 0.2–1.74 μm at the BDU outlet. The total particle density at the BDU inlet was 2.4×10^5 – 3.9×10^6 part./cm³ and 1.4×10^4 – 9.4×10^4 part./cm³ for the ELPI and APS, respectively, showing a large discrepancy between the two analytical techniques.

It was noted that the use of diluters, impaction pre-stages, vibrational sensitivity of the ELPI, and the well documented large particle bias of the APS led to quantification differences between the methods as well as increased absolute error of each individual measurement technique. The ELPI condensed too much H₂O to be operable in a short time (~1 min) which required the pre-impactor plate to reduce the amount of H₂O by removing the larger droplets which contain appreciable liquid-water content; however, the impactor led to an underestimation of total amine content of 20% prior to the BDU. The APS required a diluter, which precluded measurement of particles larger than 2.5 μm. Evaporation and signal response significantly affected large particle measurements. Further, deposition of particles on the nozzle upstream of the measurement region lead to

severe underestimation of particle count. They concluded that the quality of the inlet flue gas and the absolute temperature inside of the absorber influenced the emission rate.

Another practical observation was that the BDU was effective at removing nearly all of the emissions in the aerosol phase. However, for a flow rate of 900 m³/h, an additional 50 mbar (20 in H₂O) of pressure drop was created. For a CO₂ capture plant, including compression, 50 mbar of additional pressure drop increases the capture electricity consumption by 7 % (32 % not including compression) (van der Gijp et al., 2012). Physical means of capturing aerosols are likely to be economically unfeasible for CO₂ capture plants.

1.2.3 National Carbon Capture Center

A baseline study using MEA at the National Carbon Capture Center (NCCC) in Wilsonville, Alabama saw higher amine emissions than expected (Carter, 2012). The number of absorber beds (2-3), intercoolers (0-2), and inlet SO₃ concentration (1.8 and 3.2 ppmv) were varied as part of a parametric test on emission rate. Their work concluded that carry-over was proportional to inlet SO₃ (the same as that in Kamijo et al. (2010)), and also to the concentration of MEA in the wash water. Emissions were said to be inversely related to the absorber temperature. In all of their studies, aerosols increased emissions roughly 1-2 orders of magnitude above thermodynamic calculations.

1.3 AEROSOLS AT THE BENCH SCALE

1.3.1 Laborelec, KIT, and TNO

A series of papers from Laborelec, Karlsruhe Institute of Technology, and TNO discussed measurement of aerosol particle size distributions (PSDs) and total particle densities using an ELPI⁺ and condensation particle counters (CPCs) on a small scale

mobile pilot plant removing CO₂ from a synthetic flue gas with injected SO₃ and fly ash (Brachert et al., 2014; Mertens et al., 2014).

1.3.1.1 Brachert et al. (2014)

In the first paper by Brachert and co-authors, they investigated the effect of the dilution ratio ranging between 10 to 10⁴ (using a PALAS GmbH DC10000 cascade diluter) on the PSD measured by the ELPI⁺ at the inlet of the absorber (outlet of the quench section of the SO₃ injector) at different SO₃ injection rates. They also compared the total particle densities measured by the ELPI⁺ and the PALAS GmbH UF-CPC 200 CPC.

In their experiments, the total particle density ranged 1–7×10⁸ part./cm³ across both measurement techniques; the CPC required a dilution factor of 10⁴, while the ELPI⁺ dilution factor was varied from 10–10⁴. For dilution factors greater than 10, the ELPI⁺ measures 2–3 times the particle density of the CPC. The discrepancy between the measurements was explained by the PSD change due to the dilution used prior to the ELPI⁺ analysis section. This finding impacts both the PSD and total particle densities which are crucial parameters when designing particle removal devices and simulating aerosol growth and collection models. The dilution error increases as the volatile content in the aerosol increases; larger aerosols with significant H₂O content would experience significant evaporation and over-counting when using an ELPI⁺ alone.

1.3.1.2 Mertens et al. (2014)

The follow-up paper by Mertens et al. continued PSD and total particle density measurements, but at the absorber outlet operating with monoethanolamine (MEA). The measurements in that study confirmed the finding in Brachert et al., that the dilution ratio greatly impacts the PSD at the absorber outlet where the liquid content of the aerosol is

significantly higher than that at the inlet, where the droplets are nearly at their dry droplet diameter.

They also found that, although the submicron mode has a higher total particle density, the micron modes contain the most mass. Nearly all of the aerosol mass is contained between 0.5 and 2 μm .

1.3.2 Khakharia (2015)

The dissertation by Khakharia presented several hypotheses about aerosol growth and data measured at multiple pilot plants and bench scale systems. His findings will be summarized briefly here.

1.3.2.1 Particle Concentration

Amine emissions in the aerosol phase is a strong function of the inlet nuclei density which offer significant surface area for condensation (heterogeneous nucleation). This was the case for both fly ash and SO_3 .

1.3.2.2 Supersaturation

Increasing the supersaturation in the gas phase increases the growth of aerosols. This can be accomplished by increasing the temperature difference between the inlet gas and solvent, increasing the temperature gradient by changing the CO_2 loading (pH), and the relationship between the CO_2 loading, amine volatility, and reaction enthalpy.

1.3.2.3 Amine Reactivity

Aerosol-bound amine emissions were found to be a function of the promoter. Two promoted 2-Amino-2-methyl-1-propanol (AMP) systems were tested: (1) piperazine (PZ) promoted AMP, and (2) potassium taurate (KTau) promoted AMP. Khakharia theorized that the difference in the reaction kinetics between the promoters explained the

lack of aerosols for the K τ system but the large amount of aerosols found in the PZ promoted system.

1.3.2.4 Overall Theory

Khakharia's overall explanation of aerosol-based amine emissions is that a supersaturation zone is created just above the temperature bulge which creates a driving force for condensation onto heterogeneous nuclei present in the inlet flue gas. The rate of growth is determined by the overall mass transfer rate of CO₂, including the reaction and diffusion resistances. The differences in amine systems is thought to be caused by the reaction rates and the relationship between CO₂ solubility and amine volatility

1.3.3 Key Findings

It is clear from pilot plant observations and emission studies that removing aerosols is a key part of reducing possible releases from amine-based CO₂ capture plants. Aerosols of interest are 0.1–10 μm : common demisters will remove larger particles while smaller drops are insignificant to the cumulative emitted mass. The total particle density may span several orders of magnitude: 10^4 – 10^8 part./cm³ across the reported literature. The source of aerosols is variable; particles may carryover from the upstream Flue Gas Desulfurization (FGD) unit in the form of submicron H₂SO₄ mist, condensation may occur on flyash or other heterogeneous nucleation sites, or rapid temperature fluctuations in the absorber (i.e. cold lean solvent feed or intercooling) could lead to homogeneous nucleation. Many sources of aerosols from upstream coal combustion may contribute to the severity of aerosolized emissions from the absorber (Damle et al., 1982).

Discrepancy between measurement techniques and physical limitations greatly inhibit the study of aerosol growth and the relationship between total emissions (aerosol

and gas) measurements and PSD analytical techniques. Better measurement techniques require exploration for more rigorous analysis.

Overall, the failure of conventional wash columns and the potential financial impact of particle collection devices necessitate fundamental research to identify more practical means of controlling emissions for large-scale processes. Understanding interdependencies of the bulk CO₂ removal process operating conditions and aerosol dynamics can provide the necessary insight required to either design or operate a system with the intention of suppressing droplet growth; or conversely, to condition aerosols for easier removal.

1.4 ABATEMENT STRATEGY

This work began by studying the aerosol problem from a fundamental viewpoint through development of a simplified heat and mass transfer model for aerosols in CO₂ capture systems. It was theorized that by altering the operating conditions or physical design of the CO₂ capture plant, aerosol capture could be facilitated by condensational growth or evaporative shrinking; condensational growth is often used as a conditioning step for total particle density measurements by CPCs which pass nanometer sized particles through a chamber saturated by a condensable vapor, usually H₂O or butanol, where the particles grow to sizes that can be detected using optical techniques.

Moreover, several aerosol researchers in literature have pointed to efficient removal of high density aerosols in packed columns by heterogeneous nucleation (condensation) (Heidenreich et al., 2000; Johannessen et al., 1997; Calvert et al., 1984). By effectively selecting operating conditions, they argue, and experimentally confirm, that high degrees of supersaturation can be achieved which can “activate” aerosol growth and subsequently increase their capture in randomly packed columns. The degree of supersaturation, and the influence of operating conditions is characterized by the ratio of

heat and mass transfer rates, given by the Lewis number. In the work by Heidenreich and co-authors, they demonstrated that high concentrations (10^6 particles/cm³) of submicron particles of variable starting composition can be efficiently collected using a two-stage cascade counter-current contactor by increasing the temperature difference between the inlet fluids (Heidenreich et al., 2000). Cascaded column designs to remove aerosols through growth conditioning would be readily incorporated into existing water wash and acid wash tower configurations.

1.5 RESEARCH SCOPE

The overall scope of this work is broken up into three major components: (1) aerosol analytical measurement development, (2) experimental measurements of aerosol growth in aqueous amine absorber columns and (3) mathematical model development to explain measurements made at the bench and pilot scale.

1.5.1 Aerosol Analytical Development

One of the major accomplishments of this work was the application of an *in situ* aerosol measurement technique for PSD and total particle density determination at both the bench and pilot scale. *In situ* measurements were selected to eliminate the known biases of duct sampling systems and dilution effects commonly found in *ex situ* particle analysis.

A custom-built phase Doppler interferometer (PDI) and supporting peripherals were modified over the course of this study and tested at two pilot plants and one bench scale unit. The PSD and total particle density information expanded the understanding of the aerosol growth phenomena by discriminating the effect of the particle density and the PSD on the emission quantity. Furthermore, estimates of the aerosol liquid composition are made possible by integrating the PSD and total density.

The PDI sampling system with accompanying hot-gas Fourier Transform Infrared Spectroscopy (FTIR) total phase analysis, provides a transportable, direct technique for phase discrimination and real-time observation of process effects on aerosolized emissions.

1.5.2 Experimental Measurements

To confirm the theorized influence of operating parameters on aerosol growth and capture, an experimental apparatus (Chapters 4 and 5) capable of generating and analyzing aerosols at relevant concentrations and size ranges was designed and constructed. The Aerosol Growth Column (AGC) was developed as a CO₂ absorber analog, the Liquid Vaporizer and Injector (LVI) was built to produce homogeneously nucleated submicron seed nuclei, and the PDI was selected to analyze particle fields *in situ* to reduce extractive sampling errors.

The AGC allows for rapid testing of steady state absorber cases for aerosol growth measurement. Data acquisition and process control are done in LabVIEW™. Data algorithms for post-processing and data concatenation were written in Microsoft® Visual Basic® for applications (VBA).

The algorithms used in bench scale testing on the AGC were modified for pilot scale aerosol measurements (Chapter 6) performed at the Pickle Research Campus pilot plant (PRC) and the National Carbon Capture Center (NCCC) pilot plant.

Relationships between operating conditions and aerosols PSDs were measured at both CO₂ capture scales. This study presents the first data set with direct linkages between FTIR measurements and both PSDs and total particle densities.

1.5.3 Numerical Modeling

A numerical model (Chapter 7) was developed for simulating particle growth by heat and mass transfer, including corrections for Knudsen effects, in packed, counter-current CO₂ absorber and water wash columns. The model developed in this work represents the first application of aerosol dynamic equations to a CO₂ capture system in an attempt to predict amine emissions.

The model was used to investigate the effect of process configurations (water wash design) and operating conditions (intercooling) on the growth of heterogeneous nuclei. The foundation of the model allows for relaxation of assumptions for more rigorous future development.

Chapter 2: General Aerosol Theory and Equations

The study of airborne particles is an extremely broad subject spanning many areas of science including air pollution, cloud formation, climate impact studies, as well as general physiology of respirable aerosol. Hundreds of techniques, based on the physical response of either a single particle or particle ensembles, have been used to study the dynamics of aerosols which scale several orders of magnitude in size and volumetric density across many different applications. Decades of scientific progress and ever-improving analytical techniques have led to a deeper understanding of the complexity of interactions in a particle field. Particle-fluid(molecules) processes, interparticle collisions, phoretic effects (thermophoresis, diffusiophoresis, electrophoresis, and photophoresis), electromagnetic scattering (Lorenz-Mie, Rayleigh, diffraction, etc.), and many other physicochemical processes are all important particle-media interactions that fully characterize particle dynamics.

This chapter provides a library of equations used throughout this study that were gleaned from the extensive knowledge base of aerosol science. The equations presented here are general in nature; species-dependent correlations and mixing rules used for modeling or experimental applications will be presented in subsequent chapters. The scope, therefore, of the following sections is to provide definitions of commonly used terms, first-principle equations with generic property variables, and illustrative examples where warranted for clarity, not for the purposes of quantitative detail. Physical processes that are neglected from generalized equations are covered thoroughly in standard particle science texts (Seinfeld et al., 1998; Kulkarni et al., 2011a; Friedlander, 2000; Reist, 1993; Fuchs, 1959).

2.1 PARTICLE SIZE DISTRIBUTIONS (PSDs)

In order to provide a framework for discussing the characteristics of an inhomogeneous particle phase, a fundamental quantity defining the set of distributed physicochemical properties must be selected. The quantity most commonly chosen is the particle diameter, since all other quantities of interest (surface area, volume, and mass) can be readily calculated using well-defined intensive and extensive properties. Particle diameter is also chosen as the fundamental descriptor since it is a directly measurable quantity and most physical theory of aerosol dynamics is a direct function of the shape-adjusted, or aerodynamic, diameter.

Particle fields are typically polydisperse by nature, owing to the multiplicity of factors affecting their formation, interaction, growth, and transport which lead to significant spread of particle sizes. Their formation mechanisms alone often cause multimodal distributions: homogeneous nucleation produces nanometer-sized aerosol through condensation of supersaturated gases created by process gradients or gas-phase reactions and heterogeneous nucleation can yield both submicron ($< 1 \mu\text{m}$) and supermicron ($> 1 \mu\text{m}$) aerosols by bursting, shedding, and cenosphere formation. In most cases, these formation mechanisms occur simultaneously in vaporization-condensation systems. Damle et al. identify 14 generalized, but separate pathways for particle formation from combustion of a coal particle (Damle et al., 1982). Due to the polydisperse, multimodal nature of aerosol populations, statistical distribution functions are used to describe their properties.

A common distribution used to describe particle fields is the lognormal distribution, written in the form of a normalized probability density function (PDF) in Equation (2.1). The lognormal distribution is obtained from the normal, or Gaussian, distribution using lognormal parameters (Kulkarni et al., 2011a). The mean diameter is

given by μ , whereas the peak of the distribution is the mode. The spread of the peak is determined by the standard deviation σ ; larger σ equates to broader peaks. The cumulative distribution function, Equation (2.4), describes the probability that the distributed variable will be less than some specified value.

$$PDF = f(x) = \frac{1}{x \sigma \sqrt{2\pi}} \exp\left\{\frac{-[\ln(x) - \mu]^2}{2 \sigma^2}\right\} \quad (2.1)$$

$$\mu = \ln(\mu_g) = \frac{\sum[n_i \ln(x_i)]}{\sum n_i} \quad (2.2)$$

$$\sigma = \ln(\sigma_i) = \sqrt{\frac{\sum\{n_i [\ln(x_g) - \ln(x_i)]^2\}}{\sum(n_i) - 1}} \quad (2.3)$$

where:

$f(x)$ = Lognormal probability distribution function [--]

x = Randomly distributed variable [--]

σ = Natural logarithm of the geometric standard deviation of randomly distributed variable, x [--]

μ = Natural logarithm of the geometric mean of randomly distributed variable, x [--]

$$CDF = \int_0^{\infty} f(x) dx \quad (2.4)$$

where:

CDF = Cumulative distribution function [--]

The lognormal distribution can be related to a non-normalized quantity by multiplying the PDF by a scaling factor, which is the total events of a distributed variable in the sample set. For example, the number of particles in a differential size class can be

determined by multiplying the PDF of particle size by the total number of sampled particles, given in Equation (2.5).

$$dN(d^P) = \frac{N_{Tot}}{x \sigma \sqrt{2\pi}} \exp\left\{\frac{-[\ln(d^P) - \mu]^2}{2 \sigma^2}\right\} \quad (2.5)$$

where:

dN = Particle count distribution function [part.]

N = Total particle density [part./cm³]

Multimodal distributions are summations of monomodal distributions; the total size of a monomodal sample set determines the relative magnitudes of the composite distribution. Therefore, a single PDF can be used to describe multiple modes by renormalizing each individual PDF by the entire multimodal sample set, as shown in Equation (2.6). An example bimodal distribution composed of two monomodal distributions is shown in **Figure 2.1**.

$$f_{Tot}(x) = \frac{\sum[N_i f_i(x)]}{\sum N_i} \quad (2.6)$$

where:

f_{Tot} = Total, multimodal, probability distribution function [--]

f_i = Total, monomodal, probability density function of distribution mode i [--]

N_i = Total particle density for distribution mode i [part./cm³]

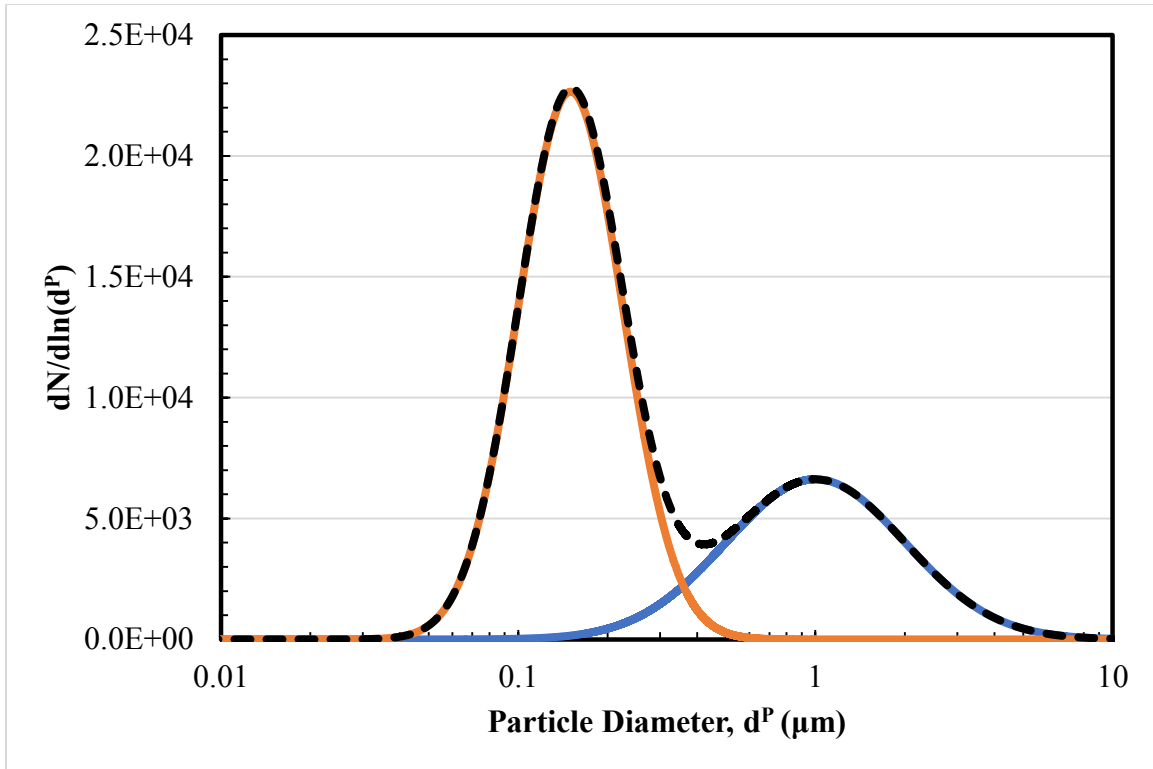


Figure 2.1: Bimodal PDF constructed from independent monomodal PDFs. Coarse Mode: $N_{\text{Tot}} = 5,000$, $d_G = 1 \mu\text{m}$, $\sigma_G = 2 \mu\text{m}$. **Fine Mode:** $N_{\text{Tot}} = 10,000$, $d_G = 0.15 \mu\text{m}$, $\sigma_G = 1.5 \mu\text{m}$.

Figure 2.2 shows the CDFs for each PDF and the resulting bimodal CDF. The weighting factors of the individual monomodal distributions and their standard deviations vary the concavity and position of the inflection points. 50% of the measured particles are under $0.15 \mu\text{m}$ and $1 \mu\text{m}$ for the fine and coarse modes, respectively. 50% of the total, bimodally distributed, aerosol exists under $0.2 \mu\text{m}$.

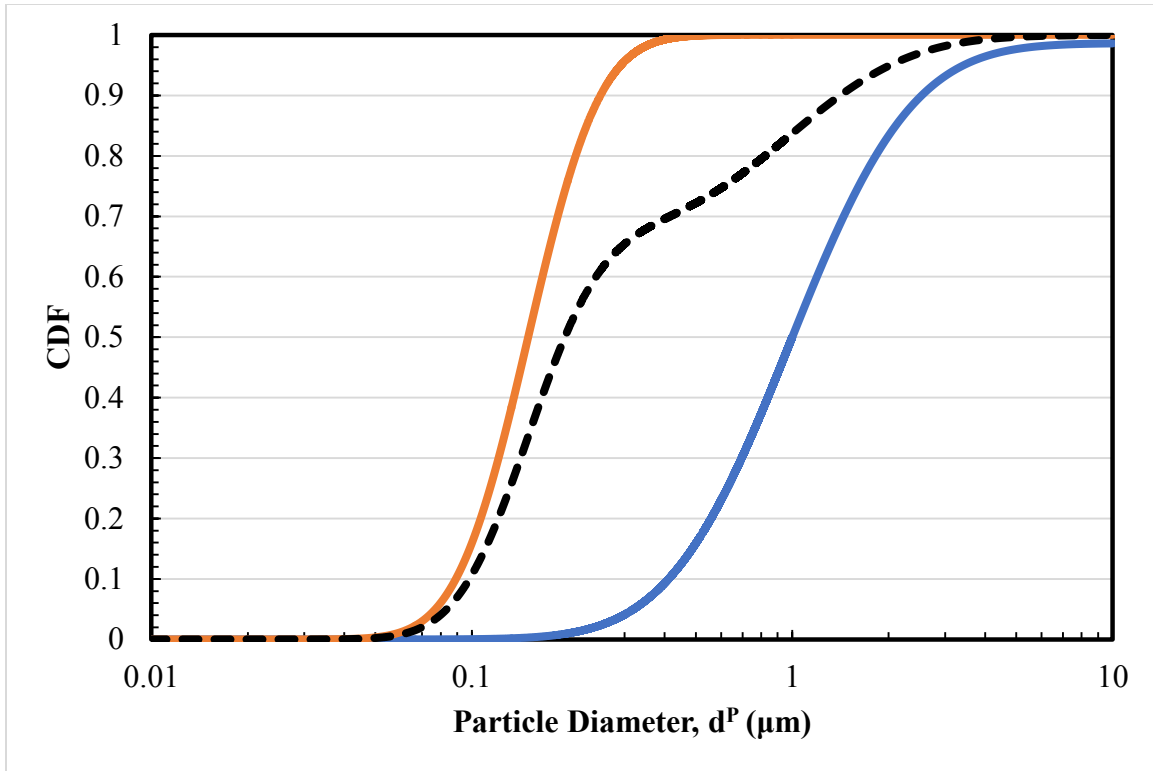


Figure 2.2: Bimodal CDF constructed from independent monomodal PDFs. Coarse Mode: $N_{\text{Tot}} = 5,000$, $d_G = 1 \mu\text{m}$, $\sigma_G = 2 \mu\text{m}$. **Fine Mode:** $N_{\text{Tot}} = 10,000$, $d_G = 0.15 \mu\text{m}$, $\sigma_G = 1.5 \mu\text{m}$.

The particle size PDF can be converted to a surface area, volume, or mass PDF using Equations (2.7)–(2.9). The surface area and volume distributions are shown in **Figure 2.3–Figure 2.4**, respectively. The mass distribution is just the volume distribution scaled by the particle phase density, assuming the aerosol field has a homogeneous composition and temperature, independent of the particle size.

$$dS = \pi(d^P)^2 dN \quad (2.7)$$

$$dV = \left(\frac{\pi}{6}\right) (d^P)^3 dN \quad (2.8)$$

$$dM = \rho^P \left(\frac{\pi}{6}\right) (d^P)^3 dN \quad (2.9)$$

where:

dS = Surface area probability distribution function [m^2]

d^P = Particle diameter [m]

dV = Volume probability distribution function [m^3]

dM = Mass probability distribution function [kg]

ρ^P = Particle density [kg/m^3]

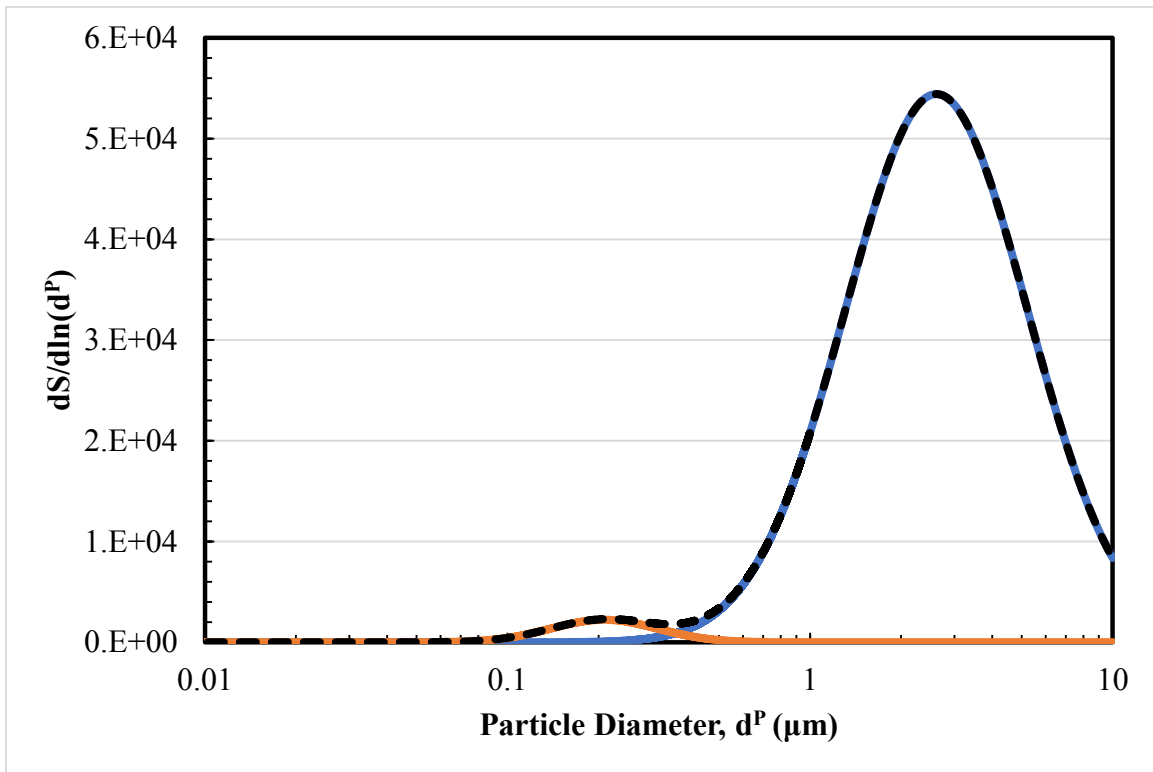


Figure 2.3: Bimodal surface area distribution constructed from independent monomodal PDFs. Coarse Mode: $N_{Tot} = 5,000$, $d_G = 1 \mu m$, $\sigma_G = 2 \mu m$. **Fine Mode:** $N_{Tot} = 10,000$, $d_G = 0.15 \mu m$, $\sigma_G = 1.5 \mu m$.

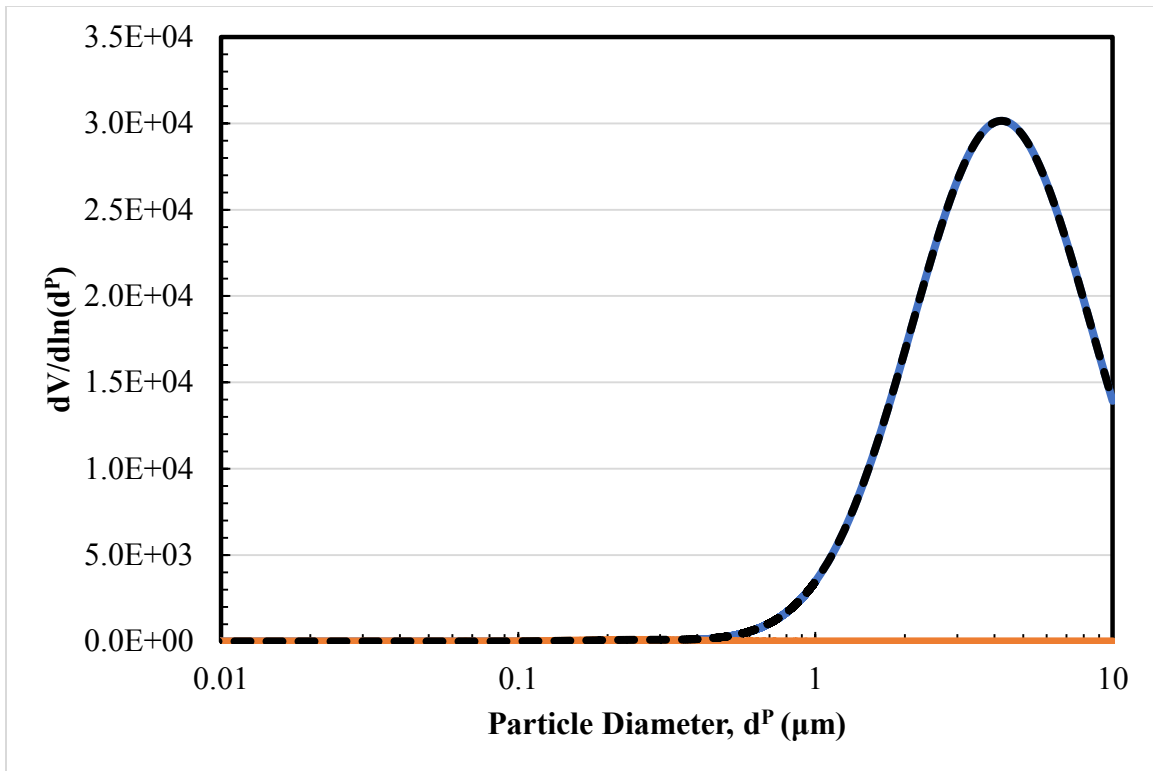


Figure 2.4: Bimodal volume distribution constructed from independent monomodal PDFs. Coarse Mode: $N_{\text{Tot}} = 5,000$, $d_G = 1 \mu\text{m}$, $\sigma_G = 2 \mu\text{m}$. Fine Mode: $N_{\text{Tot}} = 10,000$, $d_G = 0.15 \mu\text{m}$, $\sigma_G = 1.5 \mu\text{m}$.

Figure 2.3–Figure 2.4 highlight the impact of the order dependence of the particle diameter on distributed quantities. The surface area, most important in mass transfer, of the particle scales with the square of diameter; whereas the volume, otherwise the total emitted mass of the aerosol phase, scales with the cube of diameter. Therefore, an order of magnitude change in particle size changes the surface area and volume by a factor of 100 and 1,000, respectively. The count PDF is needed for removal calculations and the volume PDF is needed to assess total emissions reduction.

2.1.1 Distribution Averages

Moments, or various averages, of the particle size distribution are calculated using the generalized expression given by Equation (2.10).

$$d_{jk}^P = \left[\frac{\sum (d_i^P)^j}{\sum (d_i^P)^k} \right]^{(k-j)} \quad (2.10)$$

where:

d_i^P = Diameter of the i th particle [m]

Commonly reported averages of various powers of j and k are contained in **Table 2.1**, below. For clarification, the use of the D_{50} nomenclature follows the ISO guidelines for reporting the median diameter (ISO, 2014).

Table 2.1: Particle statistical averaging subscript definitions

d_{jk}^P		Reported average definition
j	k	
1	0	Arithmetic mean diameter
3	2	Sauter-mean diameter: the diameter of a particle with the same volume/surface area ratio as the averaged particle population.
4	3	De Brouckere diameter: volume mean diameter.
5	0	Median diameter (ISO, 2014)

2.2 GENERAL DYNAMIC EQUATION

Aerosol population dynamics are described by spatially homogeneous conservation equations, collectively called the General Dynamic Equation (GDE). The GDE provides a complete description of the temporal evolution of particle size distributions starting with gas-to-particle conversion (nucleation) and includes gas-particle (condensation and evaporation), particle-particle (agglomeration), and, in some formulations, sink terms accounting for removal through gravity settling, impaction, interception, Brownian diffusion, and turbophoresis. We will follow the convention of

Gelbard in defining agglomeration as the combined process of cluster/particle collision followed by coalescence and mixing of the two collided bodies (Gelbard, 1979). Coagulation and condensation are specific cases of agglomeration describing collisions between particles larger than the critical size and monomer-particle collisions, respectively.

The most intuitive form of the GDE is built from fundamental relationships involving the smallest structural unit, a gas molecule (or monomer). Complete aerosol population dynamics are modeled by an infinite number of nonlinear, ordinary differential equations formulated on the principle of integer multiples of molecular building blocks (discrete elements). Governing mechanisms are written in rate formulations using forward and reverse rate constants to describe the physical processes. The interaction of multiple chemical components and particle/cluster sizes forms a multidimensional, birth-death chain process. Equation (2.11) details particle processes occurring in a differential elemental volume using the discrete GDE (Friedlander, 2000). Though very useful in describing small bands of particle size distributions, especially in the case of classical nucleation, the discrete formulation of the GDE quickly becomes intractable as the aerosol population spreads many orders of magnitude in size scale. Simulation is usually limited to a subset of the total population and is limited to a finite number of particle size bins.

$$\frac{\partial n_k}{\partial t} = -\nabla \cdot n_k \bar{\mathbf{v}} + \nabla \cdot D^P \nabla n_k + \left[\frac{\partial n_k}{\partial t} \right]_{Growth} + \left[\frac{\partial n_k}{\partial t} \right]_{Coag.} - \nabla \cdot \bar{\mathbf{C}} n_k \quad (2.11)$$

where:

n_k = Density of particles containing k monomers [part/cm³]

$\bar{\mathbf{v}}$ = Gas flow velocity vector [m/s]

D^P = Brownian diffusion coefficient [N]

$\bar{\mathbf{c}}$ = Particle velocity resulting from external forces (electrophoresis, thermophoresis, etc.) [m/s]

The first two terms on the right-hand side of Equation (2.11) are the familiar convective-diffusion transport of material, in this case aerosol, across the boundary of the differential elemental volume. The third term describes monomer-particle events including evaporation and condensation. The fourth term describes particle-particle collision and coalescence, or, agglomeration. Finally, the fifth term in Equation (2.11) is a sink term which includes external forces resulting in a change in the particle's velocity vector. In this study, phoretic effects (thermophoresis, diffusiophoresis, electrophoresis, and photophoresis) are neglected. For particle removal processes relating to collection on surfaces, the GDE is translated to an Eulerian reference frame and the particle size distribution is cast as a function of a characteristic length.

Other descriptions of the GDE include the continuous form, and an integro-differential form of the GDE called the Discrete-Continuous GDE. The continuous (or integral) GDE is useful for describing aerosol fields spanning several orders of magnitude as the particle size distribution is described by a single equation. However, it inaccurately describes processes between very small particles, specifically the gas-to-particle nucleation events. Various formulations of the continuous GDE can be found in detail in Friedlander (2000). The Discrete-Continuous GDE divides the particle size distribution into two regions. The first region, smaller than some specified diameter, is described using a set of discrete equations while particles larger than the specified

diameter are represented by the continuous form of the GDE. The reader is referred to Gelbard for additional development, and ultimately the final derived working equations for the Discrete-Continuous GDE (Gelbard, 1979).

For the purposes of this work, the discrete GDE will be used as the starting point, neglecting coagulation and nucleation, for development of case-specific modeling activities; explicitly, aqueous aerosol dynamics in packed bed absorbers and optimization and data post-processing of particle sampling systems. Nucleation and coagulation are assumed to occur to a relatively high degree of completion prior to entering the CO₂ absorber; the nuclei, most likely (and most significantly) condensed H₂SO₄ from coal combustion, has already passed through FGD towers, additional SO₂ polishers, and a DCC as well as other possible abatement equipment. The residence time from formation by crossing the dew point in the FGD to the CO₂ absorber is on the order of many seconds and possibly up to a few minutes depending on proximity of the CO₂ capture facility to that of the FGD system.

2.3 PARTICLE DYNAMICS

2.3.1 Length Scales

The rate of momentum, mass, and energy transfer to a particle is a function of the size of the aerosol relative to the surrounding media. Each of the aforementioned processes is assumed to occur on the order of a characteristic length, of which a physical description of the interaction is based. If a particle is much larger than the mean free path of the gas molecules, the fluid appears to be a continuous media relative to the aerosol. Conversely, if a particle is on the same order in size as the surrounding molecules, then the aerosol undergoes collisions and diffusion in the manner described in free-molecular, or kinetic theory. Particles of intermediate size are in the transition regime. **Figure 2.5**

provides an illustration of the three described regimes. Since aerosol particles span many orders of magnitude in size from nanometers to as large as several hundred microns, the size of the particle relative to the molecular interaction scale of the surrounding fluid is an important characteristic quantity. The dimensionless group used to describe the regime of the suspending fluid-particle interactions is the Knudsen number (Equation (2.12)). The range of the Knudsen number is zero (continuum limit) to infinity (kinetic/free-molecular limit). Though there are no definitive boundaries between the regimes, transition mechanics are generally applicable for particle sizes ranging from 0.01–0.2 μm at atmospheric conditions (Seinfeld et al., 1998).

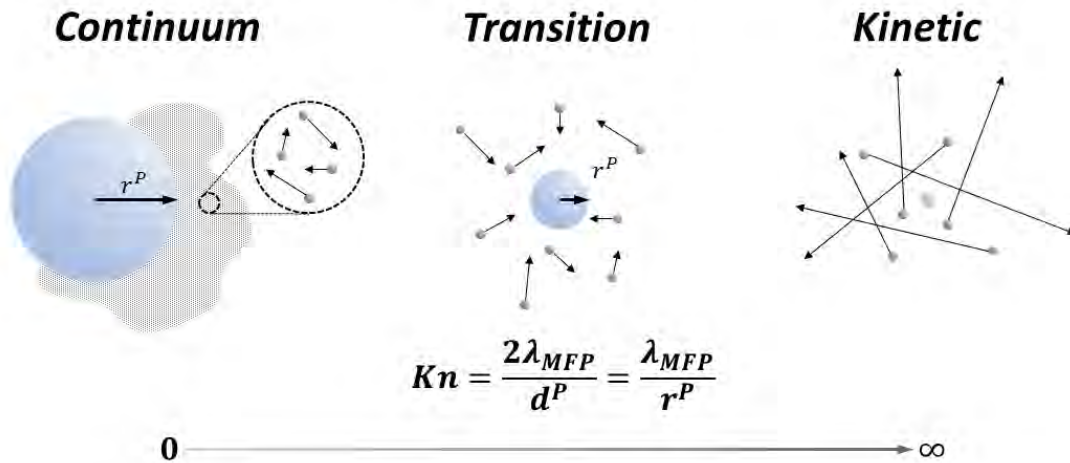


Figure 2.5: Physical approximation regimes of particle-fluid interactions. As a particle approaches the mean free path of the surrounding fluid, the interactions more closely approximate kinetic/free-molecular theory of collisions in rarefied media.

$$Kn = \frac{2\lambda_{MFP}}{d^P} \tag{2.12}$$

where:

Kn = Knudsen number [--]

λ_{MFP} = Mean free path of the surrounding fluid molecules [m]

d^P = Diameter of a particle [m]

The mean free path is the average distance traveled between molecular collisions in a gas, which is a function of the molecule size, the total molecular density, and, in the case of a multicomponent gas, the molecular weights of the colliding species. The mean free path can be related to macroscopic properties of a gas as defined in Equation (2.13).

$$\lambda_{MFP} = \frac{2\mu^G}{P \sqrt{\frac{8MW^G}{1000 \times \pi RT^G}}} \quad (2.13)$$

Where:

μ^G = Dynamic viscosity of the gas [Pa·s]

MW^G = Molecular weight of the gas [g/gmol]

P = Absolute pressure of the gas [Pa]

R = Universal gas constant [m³·Pa/K·mol]

T^G = Absolute temperature of the gas [K]

In this work, the relationship developed by Fuchs and Sutugin (1971) is used to calculate the mean free path (Equation (2.14)). The velocity of a gas molecule is calculated (Equation (2.15)) as the first moment of a Gaussian velocity distribution. Another commonly used velocity, the root-mean squared (RMS) velocity, is 8.5% higher. The binary diffusion coefficient can be calculated using either the Chapman-Enskog or the Fuller-Schettler-Giddings equations.

$$\lambda_{MFP} = \frac{3D_{ij}^G}{v_{AV}^G} \quad (2.14)$$

$$v_{AV}^G = \sqrt{\frac{8RT^G}{\pi MW^G}} \quad (2.15)$$

where:

D_{ij}^G = Gas-phase binary diffusion coefficient [m²/s]

v_{AV}^G = Average velocity of a gas molecule [m/s]

2.3.2 Single Particle Motion

The direction and velocity of a particle relative to a viscous surrounding media is dictated by a force balance at the particle's center of mass (**Figure 2.6**). The forces active on the particle include the force of gravity, buoyant lift, and a force induced by relative motion between the fluid and the particle called the drag force. Saffman lift is neglected in this work. Equation 2.16 is used to calculate the net force experienced by a particle in viscous flow.

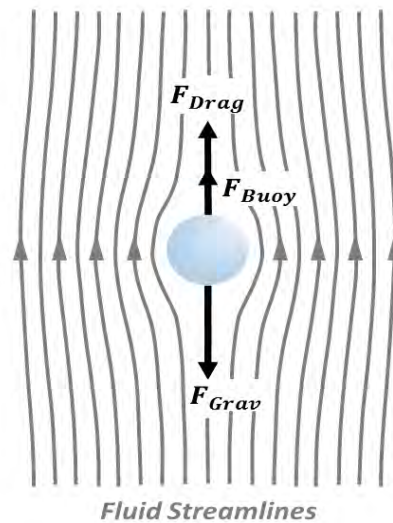


Figure 2.6: Force diagram for a particle suspended in an upward moving fluid.

$$F_{Part} = F_{Grav} - F_{Buoy} - F_{Drag} \quad (2.16)$$

where:

- F_{Part} = Net force on a particle [N]
- F_{Grav} = Force of gravity on a particle [N]
- F_{Buoy} = Buoyant force on a particle [N]
- F_{Drag} = Drag force on a particle [N]

Substituting the appropriate expressions for the body forces results in Equation (2.17). The Cunningham Slip correction will be covered in the next section.

$$\frac{\pi}{6}(d^P)^3\rho^P a^P = \frac{\pi}{6}(d^P)^3\rho^P g - \frac{\pi}{6}(d^P)^3\rho^G g - \frac{\pi C_D \rho^P (v_{Rel})^2 (d^P)^2}{8C_C} \quad (2.17)$$

where:

- d^P = Particle diameter [m]
- ρ^P = Particle density [kg/m³]
- a^P = Particle acceleration [m/s²]
- g = Acceleration of gravity [m/s²]
- ρ^G = Gas-phase density [kg/m³]
- C_D = Drag coefficient [--]
- v_{Rel} = Velocity of a particle relative to the gas phase [m/s]
- C_C = Cunningham Slip Correction factor [--]

Finally, assuming that viscous forces dominate over inertial forces and that the surrounding fluid is a continuous media, the Navier-Stokes equations of motion can be solved in the creeping flow limit to determine the pressure gradient around the particle as it moves relative to the fluid. Integrating the pressure gradient across the surface yields the force of drag. The drag force at the low Reynolds number limit is called Stokes'

Law. The drag coefficient under this set of circumstances is calculated exactly by using Equation (2.18).

$$C_D = \frac{24}{Re^P} \quad (2.18)$$

where:

Re^P = Reynolds number of a particle moving in a surrounding fluid [--]

Substituting in Equation (2.18) for the drag coefficient and also the macroscopic quantities for the Reynolds number, Equation (2.18) can be rearranged to give the acceleration of a particle moving through a fluid (Equation (2.19)).

$$a^P = g \left[1 - \left(\frac{\rho^G}{\rho^P} \right) \right] - \frac{18v_{Rel}\mu^G}{(d^P)^2\rho^P C_C} \quad (2.19)$$

where:

μ^G = Gas-phase dynamic viscosity [Pa·s]

For a non-accelerating, free-falling particle, the terminal velocity (relative to the fluid) can be calculated by Equation (2.20).

$$v_{Rel} = \frac{(d^P)^2 C_C \rho^P g}{18\mu^G} \left[1 - \left(\frac{\rho^G}{\rho^P} \right) \right] \quad (2.20)$$

In this work, Stokes' Law is assumed for nearly all studied conditions. Aerosols are on the order of 0.1–10 μm ; at standard conditions, the relative velocity would have to be 150–1.5 m/s to exceed a Reynolds number of one for the listed size domain. Even so, a first order approximation for the drag coefficient was added so that larger particles could be simulated. **Figure 2.7** shows the drag coefficient for a smooth sphere as a function of the Reynolds number and the curves of the approximating equations. The expected range of Reynolds number for the aerosol size range of interest is plotted as

well. Equation (2.21) shows the first approximation correction to Stokes' Law (Seinfeld et al., 1998).

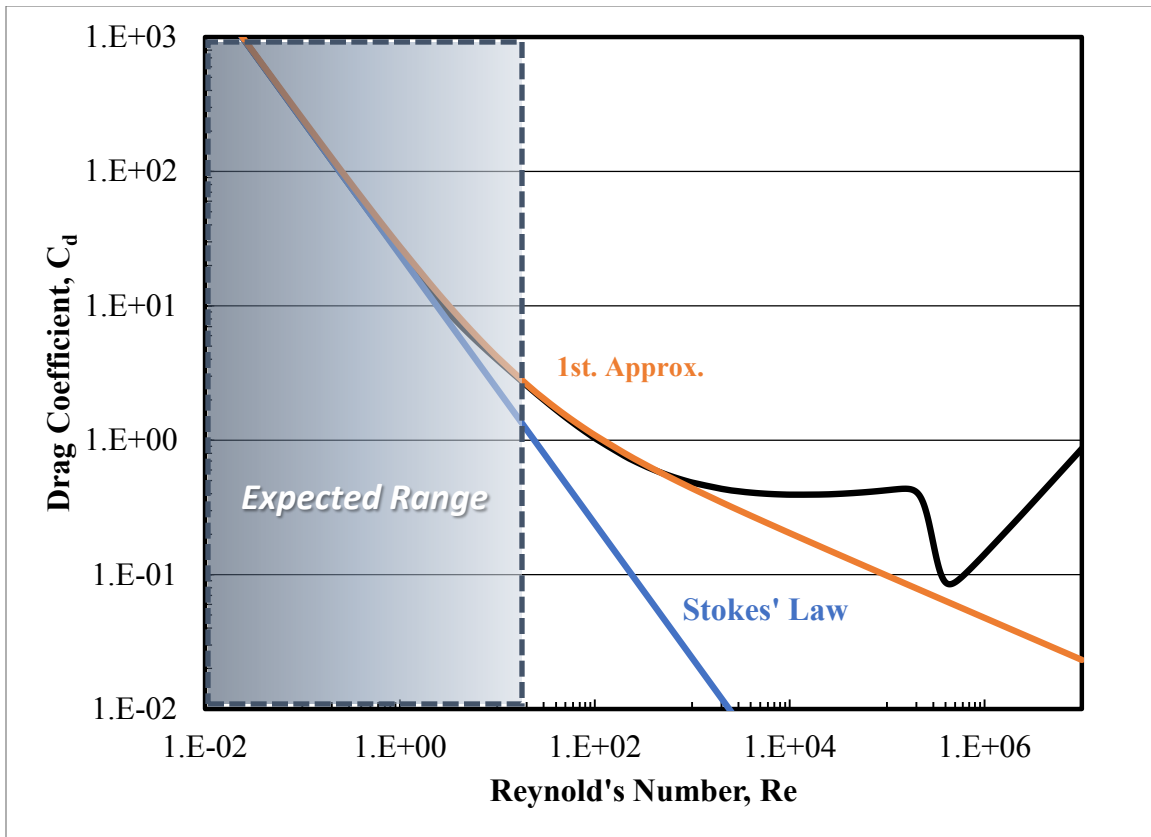


Figure 2.7: Approximation equations for the drag coefficient of a sphere with a smooth surface. Stokes' Law applies at small length scales or when inertial forces are much smaller than viscous forces.

$$C_D = \frac{24}{Re^P} [1 + 0.15(Re^P)^{0.687}] \quad (2.21)$$

2.3.3 Cunningham Slip Correction

In the derivation of Stokes' Law, the surrounding fluid was assumed to behave as a continuum, or in the limit of Kn approaching zero. The continuum approximation allows the use of the no-slip boundary condition used in common fluid mechanics

problems. However, as the particle dimension approaches that of the fluid mean free path, the drag force decreases due to the non-continuous nature of the media at the microscopic scale. A slip correction factor proposed by Cunningham and Millikan, commonly called the Cunningham Slip correction factor, is used to account for the physical nature of the fluid-particle interaction. The correction is a function of the Knudsen number and asymptotes at a value of one in the continuum limit. The functional form of the slip correction is shown in Equation (2.22). Several sets of parameters are reported in literature; those of Davies, Fuchs, Allen and Raabe, and Jennings are compiled in Reist (1993). The set of parameters determined by Fuchs are used in this study and are given below.

$$C_c = 1 + Kn \left[A + B \exp\left(-\frac{C}{Kn}\right) \right] \quad (2.22)$$

Where:

$$A = 1.246$$

$$B = 0.418$$

$$C = 0.867$$

Figure 2.8 shows the calculated values for the slip correction factor at three assumed mean free paths. For reference, the mean free path in air at standard conditions (STP: 273.15 K and 100,000 Pa, 28.96 g/gmol [Air]) is 0.0605 μm (60.5 nm).

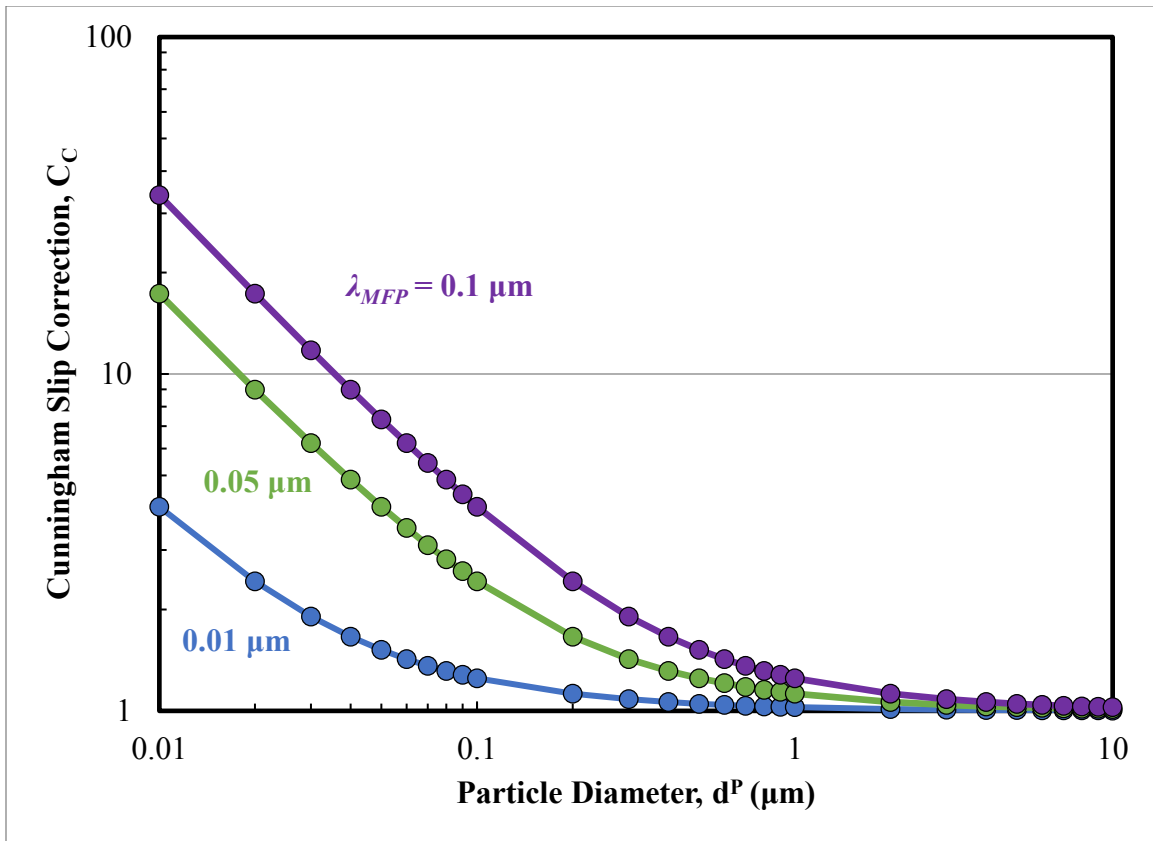


Figure 2.8: Cunningham slip correction factor for several mean free paths.

2.4 PARTICLE DIFFUSION: BROWNIAN DIFFUSION COEFFICIENT

Diffusion of particles by random motion (Brownian motion) is an important transport mechanism for very small aerosol particles. Random bombardment of molecules from the surrounding fluid, much the same as molecular diffusion, is a stochastic process. If we calculate the macroscopic flux and relate this to the mean square displacement of a particle, given by the isotropic Langevin equation, the particle diffusion coefficient can be found directly using Equation (2.23).

$$D^P = \frac{k_B T^G C_C}{3\pi\mu^G d^P} \quad (2.23)$$

where:

k_B = Boltzmann constant [$\text{m}^2 \cdot \text{kg}/\text{s}^2 \cdot \text{K}$]

2.4.1 Thermodynamics: Surface Curvature Effects

In order to discuss rate transfer processes, the bounds, or final states, of the system must be established thermodynamically. If the studied aerosols are liquid, in this case aqueous, then they will act as small parcels of fluid subject to the same chemical and thermal equilibrium treatment applied to larger gas-liquid unit operations. However, an additional term appears in the energy balance, which is often neglected in traditional “unbounded” thermodynamics: the surface energy of the gas-liquid interface.

Starting with a closed system containing only vapor, the change in the Gibbs energy upon formation of a droplet can be written as shown in Equation (2.24).

$$\Delta G = G^P - G^V \quad (2.24)$$

Where:

ΔG = Change in the total system’s Gibbs energy [J/gmol]

G^P = Gibbs energy of the droplet/vapor (two-phase) system [J/gmol]

G^V = Gibbs energy of the initial pure vapor phase [J/gmol]

Next, intensive quantities for the phase-specific Gibbs energy, a total mole balance, and an expression for surface energy (assuming a perfectly spherical droplet) are substituted into Equation (2.24) to give Equation (2.25).

$$\Delta G = N^P \overline{G^P} + (N^T - N^P) \overline{G^V} + 4\pi(r^P)^2 \sigma - N^T \overline{G^V} \quad (2.25)$$

where:

N^P = Number of molecules in the formed droplet phase [molec.]

\overline{G}^P = Gibbs energy of a liquid molecule [J/molec.]

N^T = Initial number of molecules in the pure vapor phase [molec.]

\overline{G}^V = Gibbs energy of the vapor phase [J/gmol]

r^P = Radius of the droplet phase [m]

σ = Surface tension between the vapor and droplet phase [J/m²]

Assuming the vapor to be an ideal gas (and also an ideal mixture), the liquid is incompressible, relating the number of molecules in the droplet to the liquid molecular volume, neglecting the Gibbs energy change of the liquid with pressure, and setting the differential of the total Gibbs energy change with respect to particle radius to zero (equilibrium), all result in Equations (2.26)–(2.27), which show the relationship between the saturation or equilibrium partial pressure for a curved surface relative to a flat surface. Equation (2.26), and recast as Equation (2.27), is referred to as the Kelvin equation. A more thorough derivation can be found in Vehkamäki (2006).

$$P_i^{*,C} = P_i^{*,F} \exp\left(\frac{4\sigma v_i^L}{d^P k_B T^G}\right) \quad (2.26)$$

$$P_i^{*,C} = \alpha_i(x^L, T^L) P_i^{Sat}(T^L) \exp\left(\frac{4\sigma v_i^L}{d^P k_B T^G}\right) \quad (2.27)$$

where:

$P_i^{*,C}$ = Equilibrium partial pressure of component i above a curved surface [Pa]

$P_i^{*,F}$ = Equilibrium partial pressure of component i above a flat surface [Pa]

v_i^L = Partial molar volume of component i in the liquid-phase [m³/mol]

T^G = Gas-phase temperature [K]

α_i = Activity of species i in the droplet phase [--]

x^L = Composition of the droplet phase, mole fraction [--]

T^L = Droplet phase temperature [K]

2.4.2 Mass and Heat Transfer

As aerosols move through soluble media, their size distribution changes by growth and evaporation due to concentration and temperature gradients along their trajectories. Transport to particles approaching the mean free path of the surrounding gas must be corrected for length scale effects in the manner described previously for momentum transfer. The Knudsen number will again be used as the scaling parameter.

Langmuir showed that large gradients of temperature and velocity exist next to heated or cooled bodies at a distance on the order of the mean free path of the gas (Fuchs, 1959). The gradients observed were much larger than those calculated using the normal microscopic balance equations. It was concluded that the exchange of molecules at a distance less than a few mean free paths (Δ) from a phase interface is unhindered, as in a vacuum. The rate of evaporation is described in this small layer using kinetic theory shown in Equation (2.28). Physically, the accommodation coefficient is the probability of a molecule sticking to a particle upon collision. The kinetic mass transfer rate equation is derived from the average number of molecular collisions on a unit area per time for random, three-dimensional motion.

$$J_{K,i} = \frac{dn_i}{dt} = \frac{\pi(d^P)^2}{2} \sqrt{\frac{2000 RT^G}{\pi MW_i}} \alpha (C_i^{Int} - C_i^\Delta) \quad (2.28)$$

where:

- $J_{K,i}$ = Molar condensation rate of species i given by kinetic theory [mole/s]
 n_i = Moles of species i [mole]
 α = Accommodation coefficient [--]
 C_i^Δ = Concentration of species i at a distance Δ from the gas-liquid interface [mol/m³]
 C_i^{Int} = Concentration of species i at the gas-liquid interface [mol/m³]

At a distance beyond Δ , the mass transfer gradient is accurately described by normal microscopic balances, the solution to which is the Maxwell equation (Equation (2.29)).

$$J_{C,i} = \frac{dn_i}{dt} = 2\pi D_i^G d^P (C_i^G - C_i^\Delta) \quad (2.29)$$

where:

- $J_{C,i}$ = Molar condensation rate of species i given by continuum theory [mole/s]
 D_i^G = Gas-phase diffusion coefficient of species i [m²/s]
 C_i^G = Concentration of species i in the bulk gas [mol/m³]

The total mass transferred across the boundary at Δ must be conserved. By applying the interface and bulk gas concentrations and by preserving the flux at the regime transition boundary Δ , the mass transfer to a spherical particle can be described using the Maxwell equation with a correction for the Knudsen number, known as the Fuchs' modification (Seinfeld et al., 1998). The modification is shown in Equation (2.30). The particular form of the transition regime formula is that of Fuchs and Sutugin (1971).

$$\phi_i = \frac{J_i}{J_{C,i}} = \frac{0.75\alpha(1 + Kn)}{Kn^2 + Kn + 0.283 Kn \alpha + 0.75 \alpha} \quad (2.30)$$

where:

ϕ_i = Fuchs' correction for species i [--]

J_i = Actual molar condensation rate of species i [mole/s]

Figure 2.9 shows the magnitude of the Fuchs' correction factor for different accommodation coefficients assuming a mean free path of 0.06 μm . Mass transfer slows significantly for particles below one micron, even if the probability of a molecule sticking upon collision is unity.

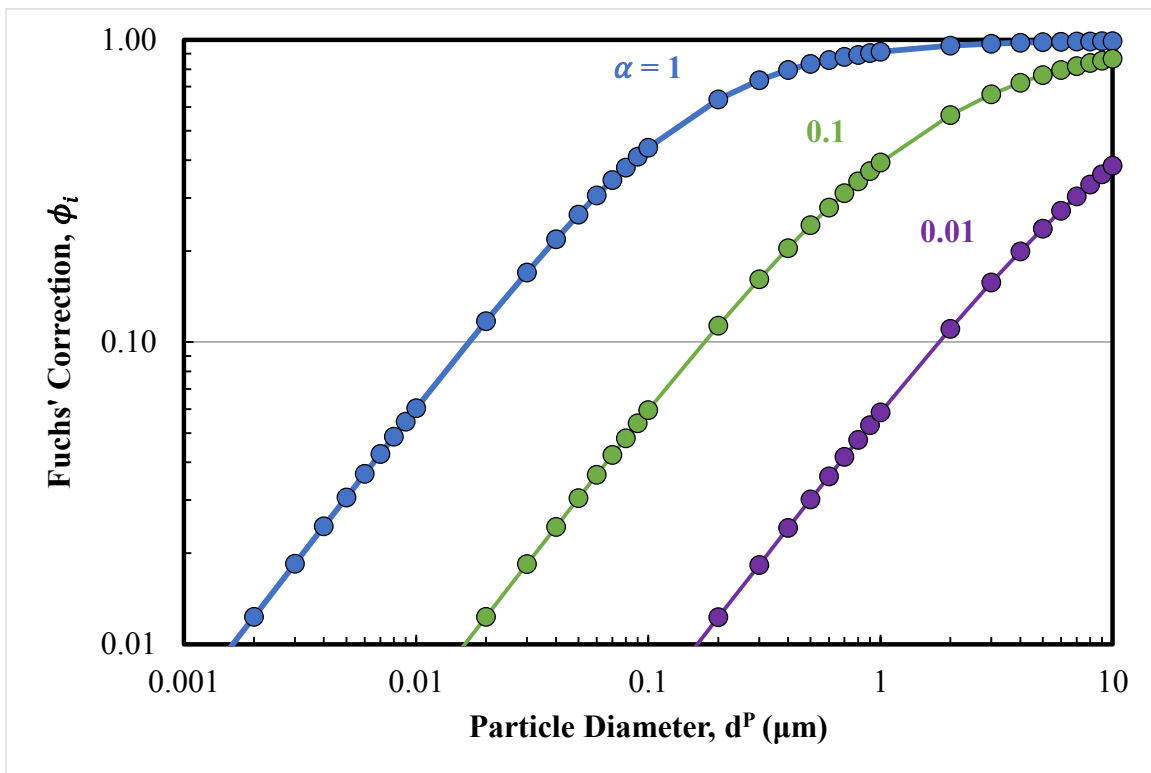


Figure 2.9: Fuchs' correction factor for mass transfer in the continuum limit for several accommodation coefficients and a mean free path at STP ($\lambda_{MFP} = 60.5 \text{ nm}$)

Gas-side limited mass transfer to and from single particles is calculated using mass transfer correlations developed for external flow around hard, perfect spheres. The classic formulation of mass transfer to a sphere for $Re < 100$ was developed by Frössling (1938). The analytical solution for the Sherwood number under low Reynold's number conditions is two, which reduces the mass transfer expression to the Maxwell equation in the continuum limit (Equation (2.29)). Frössling proposed simple convective corrections by including Reynold's and Schmidt terms in the Sherwood number as shown in Equation (2.31).

$$Sh_i^G = \frac{k_i^G d^P}{D_i^G} = 2 + 0.6(Re^G)^{1/2} (Sc_i^G)^{1/3} \quad (2.31)$$

$$Sc_i^G = \frac{\mu^G}{\rho^G D_i^G} \quad (2.32)$$

Where:

Sh_i^G = Gas-side Sherwood number for species i [--]

k_i^G = Gas-side mass transfer coefficient for species i [m/s]

Sc_i^G = Gas-side Schmidt number for species i [--]

Heat transfer to a single particle is developed by using the heat and mass transfer analogy with the constitutive equations. The relationship of heat and mass transfer is characterized using the Lewis number (Equation (2.33)), which is the ratio of the thermal and mass diffusivities. If the Lewis number approaches unity, then the thermal and mass boundary layer thicknesses are on the same order of magnitude: the equations for energy and mass transport are analogous.

$$Le = \frac{Sc}{Pr} = \frac{\kappa}{\rho C_p D} \quad (2.33)$$

where:

- Le = Lewis number [--]
- Sc = Schmidt number [--]
- Pr = Prandtl number [--]
- κ = Thermal conductivity [J/m·K·s]
- ρ = Mass density [kg/m³]
- C_p = Mass heat capacity [J/kg·K]
- D = Diffusion coefficient [m²/s]

Since aerosols meet many of these criteria, the Frössling correlation is used to calculate the Nusselt number (Equation (2.34)) which is used to calculate the heat transfer coefficient of the gas to the droplet. However, the Schmidt number, which is the ratio of momentum to mass diffusivity, is replaced by its thermal diffusivity counterpart, the Prandtl number, as detailed in Equation (2.35).

$$Nu^G = \frac{h^G d^P}{\kappa^G} = 2 + 0.6(Re^G)^{1/2}(Pr^G)^{1/3} \quad (2.34)$$

$$Pr^G = \frac{C_p^G \mu^G}{\kappa^G} \quad (2.35)$$

where:

- Nu^G = Gas-side Nusselt number [--]
- h^G = Gas-side heat transfer coefficient [J/m²·K·s]
- κ^G = Gas phase thermal conductivity [J/m·K·s]
- C_p^G = Gas phase mass heat capacity [J/kg·K]

The total heat transferred to and from the gas phase includes conduction due to the temperature difference between the bulk phases and convection due to mass transfer. When the conductive heat transfer is balanced with latent heat transfer (convection), the “wet bulb” temperature of the gas is reached. The temperature of the liquid droplet will approach the wet bulb temperature of the gas for nearly any condition since reaction rates are not considerable for transfer into droplets.

2.5 SAMPLING AND REMOVAL

Determining particle losses is important for characterizing sampling systems and removal devices. Changes to the particle size distribution during conveyance of the sampled field can result in inaccurate measurements of heat and mass transfer to the aerosol phase in unit operations and large errors in removal efficiency in particle capture devices.

Accounting for loss of sample fidelity requires consideration of many types of simultaneous mechanisms including impaction, interception, diffusion, turbulent diffusion, turbulent inertial deposition, gravitational settling, and phoretic deposition in finite changing geometries of sampling systems and transport lines. Properly characterizing a particle behavior in a suspending fluid moving past an obstacle is commonly accomplished using a set of non-scaled and dimensionless parameters.

The rate at which a particle adjusts to new flow conditions is given by the particle relaxation time (Equation (2.36)), which is $(1 - 1/e)$, or 63% of the total time required to reach the final velocity. The particle relaxation time is used to calculate the terminal settling velocity (Equation (2.37)), which accounts for gravitational settling, and the Stokes number (Equation (2.38)), which characterizes the ability of a particle to follow streamlines of the entraining fluid, to correlate removal mechanisms with changes in flow conditions and obstacle/duct geometry. The Reynolds number is another important

dimensionless quantity used to differentiate deposition mechanisms in different flow regimes.

$$\tau = \frac{\rho^P (d^P)^2 C_C}{18\mu^G} \quad (2.36)$$

where:

- τ = Particle relaxation time [--]
- ρ^P = Particle density [kg/m³]
- d^P = Particle diameter [m]
- C_C = Cunningham Slip Correction factor [--]
- μ^G = Gas-phase dynamic viscosity [Pa·s]

$$v_{TS} = \tau g \quad (2.37)$$

where:

- v_{TS} = Terminal settling velocity [m/s]
- g = Acceleration of gravity [m/s²]

$$Stk = \frac{\tau v}{d} \quad (2.38)$$

where:

- Stk = Stokes number [--]
- v = Fluid velocity [m/s]
- d = Obstacle characteristic length/diameter [m]

The following sections detail the equations used to calculate the sampling efficiency, or particle losses, across a particle size distribution as a function of the aerodynamic particle diameter. All defined parameters, dimensions, and relevant geometry are detailed in **Figure 2.10**. Development of the equations follows the

structure of the text by Kulkarni et al. (2011). References to individual works are provided where more detailed description is appropriate.

2.5.1 Total Sampling Efficiency

Particle losses during sampling occur in two distinct locations: (1) the sample inlet, where the aerosol is pulled into a fixed geometry at a specified flow rate, and (2) transfer lines, consisting of fittings, contractions, bends, and lengths of tubing. The total sampling efficiency is the product of the inlet and transfer efficiencies (Equation (2.39)). The inlet and transfer efficiencies are themselves the product of several loss mechanisms.

$$\eta_{Sample} = \eta_{Inlet}\eta_{Transf}. \quad (2.39)$$

where:

η_{Sample} = Total fraction of aerosol delivered to the sampling system through the sample probe inlet and including transfer lines[--]

η_{Inlet} = Total fraction of aerosol delivered to the transfer lines through the sample probe [--]

$\eta_{Transf.}$ = Total fraction of aerosol delivered to the analytical equipment through the transfer lines [--]

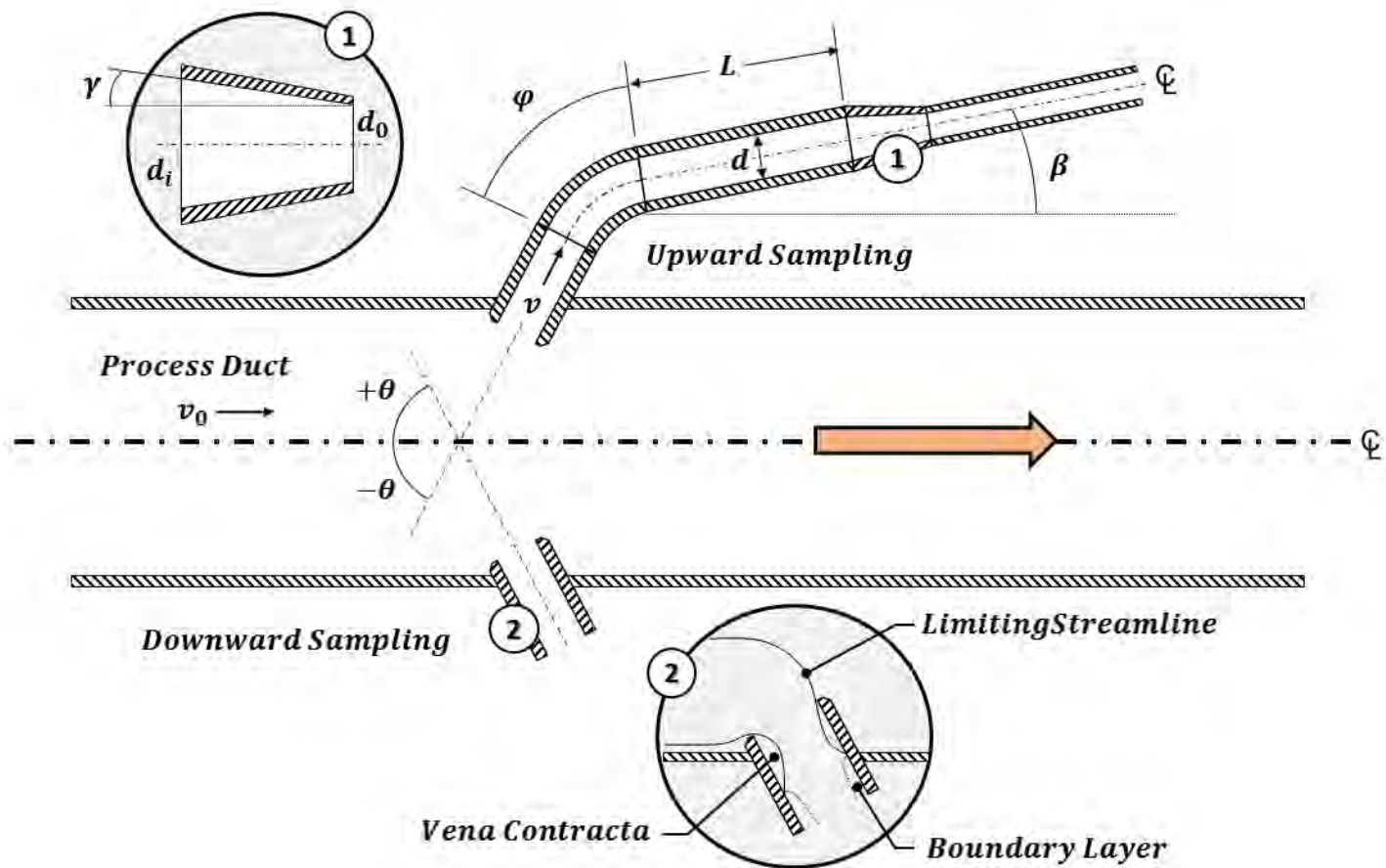


Figure 2.10: Parameter and geometric definitions for calculating particle losses are defined for sampling from a horizontal process duct.

2.5.2 Inlet losses

The inlet sampling efficiency is the product of three loss mechanisms: (1) aspiration, (2) entry losses, and (3) transmission (Equation (2.40)). In this study, perfect entry efficiency ($\eta_{Entry} = 1$) is assumed; the probe nozzle is assumed to be an infinitely thin walled tube.

$$\eta_{Inlet} = \eta_{Asp}\eta_{Entry}\eta_{Transm.} \quad (2.40)$$

where:

η_{Asp} = Ratio of particles of size i entering the sample probe relative to the undisturbed sample gas [--]

η_{Entry} = Ratio of particles of size i passing the sample probe inlet to those incident on the probe face [--]

$\eta_{Transm.}$ = Ratio of particles of size i exiting the inlet to those just past the inlet face [--]

Extracting an aerosol sample from quiescent or moving media often involves a change in flow direction and velocity as it passes through a probe nozzle. The loss of aerosols passing through the probe is dependent on the process velocity (v_0), the sampler geometry, sampler angle relative to the process flow direction (θ), gravitational acceleration, the sampler velocity (v) (or flow rate), and the particle's aerodynamic diameter (accounting for density and shape).

2.5.2.1 Anisoaxial Sampling Aspiration Efficiency

Under ideal sampling conditions, the inlet nozzle faces against the flow direction (isoaxial) and the sampler velocity exactly matches the process velocity (isokinetic). Anisoaxial sampling, or non-axis matched sampling, leads to interception and impaction losses due to directional changes required by the sampled gas. Anisokinetic sampling, or

non-velocity matched sampling, leads to size biasing since the inertia of large particles cause them to deviate from the sampler limiting streamlines. Sub-isokinetic ($v_0 > v$) sampling biases large particles because the limiting streamlines expand around the nozzle inlet; large particles continue straight into the nozzle while small particles follow the gas around the nozzle walls. Super-isokinetic ($v > v_0$) sampling biases small particles since the sampler streamlines pinch at the nozzle inlet; large particles continue straight past the nozzle walls while the smaller particles follow the streamlines into the nozzle. The aspiration efficiency strictly accounts for sampling biases due to inertial deviation from limiting streamlines.

Hangal and Willeke (1990) developed correlations for anisoaxial sampling efficiencies from horizontal duct flow for sampling angles from 0–90° with respect to the process flow direction. They found that a correlation developed by Durham and Lundgren (1980) fit their database for sampling angles from 0–60°, but angles in the range of 45–90° required an extension of the correlation developed by Laktionov (1973) to fit their data. Equations (2.41) and (2.42) present those correlations: (2.41) is valid for $0.02 \leq Stk \leq 4$, $0.5 \leq v_0/v \leq 2$, and 0–60° and (2.42) is valid for $0.02 \leq Stk \leq 0.2$, $0.5 \leq v_0/v \leq 2$, and 45–90°.

$$\eta_{Asp} = 1 + \left[\left(\frac{v_0}{v} \right) \cos\theta - 1 \right] \left\{ \frac{1 - [1 + (2 + 0.617[v_0/v])Stk']^{-1}}{1 - [1 + 2.617 Stk']^{-1}} \right\} \quad (2.41)$$

$$\times \{1 - [1 + 0.55 Stk' \exp(0.25S tk')]^{-1}\}$$

$$\eta_{Asp} = 1 + \left[\left(\frac{v_0}{v} \right) \cos\theta - 1 \right] \left[3 Stk \sqrt{\frac{v}{v_0}} \right] \quad (2.42)$$

$$Stk' = Stk \exp(0.022 \theta) \quad (2.43)$$

$$Stk = \frac{\tau v_0}{d} \quad (2.44)$$

where:

- v_0 = Free stream velocity (upstream velocity) [m/s]
- v = Sample stream velocity (sample probe velocity) [m/s]
- θ = Angle relative to the free stream velocity [deg]
- d = Probe nozzle inner diameter [m]

Once the aerosol is aspirated across the nozzle inlet, deposition can still occur by gravity settling and inertial losses in the transition of the nozzle body to the transfer lines.

2.5.2.2 *Transmission Efficiency: Gravitational Settling*

Hangal and Willeke (1990) modified the gravitational settling losses correlation developed by Okazaki, Wiener, and Willeke (1987) including the angle of inclination (θ) of the sample nozzle relative to the horizon (Equation (2.45)). For horizontal flow, the aspiration (sampling) angle and the inclination angle are the same. Horizontal sampling ($\theta = 0^\circ$) reduces Equation (2.45) to the isoaxial correlation developed by Okazaki and coworkers. Gravitational losses are zero in the limit of vertical sampling ($\theta = 90^\circ$). A fixed inlet length was used in the original correlation developed by Okazaki and colleagues. In this work, correlations developed by Bhatti and Shah (1987) were used to calculate the entry length as shown in Equation (2.48), below.

$$\eta_{Transm,grav} = \exp(-4.7K_\theta^{0.75}) \quad (2.45)$$

$$K_\theta = Z^{0.5} Stk^{0.5} Re^{-0.25} \cos\theta \quad (2.46)$$

$$Z = \frac{L v_{TS}}{d v} \quad (2.47)$$

$$\frac{L}{d} = \begin{cases} 0.05 Re, & Re \leq 4000 \\ 1.359 Re^{1/4}, & Re > 4000 \end{cases} \quad (2.48)$$

where:

$\eta_{Transm, Grav}$ = Gravitational settling efficiency in the sample probe inlet [--]

Z = Gravitational deposition parameter [--]

Re = Sample probe inlet Reynolds number [--]

L = Hydrodynamic entry region length [m]

2.5.2.3 Transmission Efficiency: Inertial Deposition

Inertial deposition in the nozzle inlet occurs by two mechanisms: (1) direct impaction on the nozzle wall and (2) turbulence losses in the *vena contracta* for super-isokinetic sampling. Hangel and Willeke (1990) included both deposition mechanisms in a single correlation, Equation (2.49). Equation (2.49) is valid for $0.02 \leq Stk \leq 4$, $0.25 \leq v_0/v \leq 4$. Since the *vena contracta* only exists during super-isokinetic sampling, the loss parameter, I_v , reduces to zero for $v_0/v > 1$.

$$\eta_{Transm, Inert} = \exp[-75(I_V + I_W)^2] \quad (2.49)$$

$$I_V = 0.09 \left[Stk \cos\theta \frac{v - v_0}{v_0} \right]^{0.3} \quad (2.50)$$

$$I_W = \begin{cases} Stk \sqrt{\frac{v_0}{v}} \sin(\theta - \alpha) \sin\left(\frac{\theta - \alpha}{2}\right), & \text{downward sampling} \\ Stk \sqrt{\frac{v_0}{v}} \sin(\theta + \alpha) \sin\left(\frac{\theta + \alpha}{2}\right), & \text{upward sampling} \end{cases} \quad (2.51)$$

$$\alpha = 12 \left[\left(1 - \frac{\theta}{90}\right) - \exp(-\theta) \right] \quad (2.52)$$

where:

$$\eta_{Transm,Inlet} = \text{Sampling efficiency including } vena \text{ contracta} \text{ and direct impaction loss [-]}$$

2.5.3 Transfer Efficiency

After an aerosol sample has passed through the entry region of a sample nozzle, a series of flow elements connects the sample nozzle to the analysis instrument. The components of the transfer section can lead to severe loss of sample integrity if the transit distance, time, and dimensional changes are not minimized. The correlations for deposition mechanisms used in this study were all developed for flow in circular cross-sections. Each deposition mechanism will be described in an independent subsection.

2.5.3.1 Transfer Efficiency: Gravitational Settling

A correlation (Equation (2.53)) for gravitational settling losses in inclined tubing under laminar flow conditions was developed by Heyder and Gebhart (1977), who modified the work of Thomas (1958) and Fuchs (1964). The angle of inclination is defined with respect to the horizon. A similar angular modification to the expression for gravitational losses in turbulent flow developed by Schwendiman et al. (1975) yields Equation (2.55).

$$\eta_{Grav,Lam} = 1 - \frac{2}{\pi} \left[2\kappa \sqrt{1 - \kappa^{2/3}} - \kappa^{1/3} \sqrt{1 - \kappa^{2/3}} + \arcsin(\kappa^{1/3}) \right] \quad (2.53)$$

$$\kappa = \frac{3}{4} Z \cos \beta \quad (2.54)$$

where:

$\eta_{Grav,Lam}$ = Transport efficiency in a circular tube including gravitational settling losses accounting for inclination angle in laminar flow [--]

β = Tube inclination angle [deg]

$$\eta_{Grav,Turb} = \left[-\frac{4Z\cos\beta}{\pi} \right] \quad (2.55)$$

where:

$\eta_{Grav,Turb}$ = Transport efficiency in a circular tube including gravitational settling losses accounting for inclination angle in turbulent flow [--]

2.5.3.2 Transfer Efficiency: Diffusional Deposition

Submicron particles undergoing Brownian Diffusion drift from high to low particle concentrations. The equations of motion can be solved, assuming a tube wall is a particle sink, to yield an expression for particle loss due to diffusional deposition. The result can be extended to include mass transfer enhancement by turbulence through definition of a mass transfer coefficient, which is a function of the flow conditions (Equation (2.56)). Integrating the transport equation across a finite length of tubing (L), allows for calculation of transfer efficiency. Sherwood number correlations for laminar (Holman, 1972) and turbulent (Friedlander, 1977) flow are presented in Equation (2.58).

$$\eta_{Diff} = \exp(-\xi Sh) \quad (2.56)$$

$$\xi = \frac{\pi D^P L}{Q} \quad (2.57)$$

$$Sh^P = \begin{cases} 3.66 + \frac{0.2672}{\xi + 0.10079 \xi^{1/3}}, & Re \leq 4000 \\ 0.0118 Re^{7/8} Sc^{1/3}, & Re > 4000 \end{cases} \quad (2.58)$$

$$Sc^P = \frac{\mu^G}{\rho^G D^P} \quad (2.59)$$

where:

η_{Diff} = Transport efficiency in a circular tube including diffusional losses [--]

d = Transfer tube inner diameter [m]

L = Tube length [m]

Q = Volumetric flow rate in the transfer tube [m³/s]

Sh^P = Sherwood number [--]

Sc^P = Schmidt number of the particle [--]

In the limit of laminar flow, the loss of particles is independent of the transfer tube diameter, but is inversely proportional to the sampler flow rate. Sampling efficiency is maximized at high flow rates and short tubing lengths. Sampling efficiency in turbulent flow is insensitive to the Reynolds number; decreasing the sample tubing length and increasing the tube diameter improves sampling efficiency.

2.5.3.3 Transfer Efficiency: Turbulent Inertial Deposition

Three deposition regimes are present in turbulent flow: (1) turbulent diffusion, which enhances central mixing in much the same manner as molecular transport, (2) turbulent diffusion-eddy impaction, which describes large particles being thrown by a turbulence intensity gradient to the laminar sub-layer next to the wall regardless of a concentration gradient, and (3) particle-inertia moderated regime, which captures the decrease in deposition rate for increasing particle size (Guha, 1997). The last two terms, called turbophoresis, describe the deposition rate caused by turbulence intensity gradients. Particles tend to follow fluid eddies and their depositional velocity essentially matches that of the fluid localized velocity. However, as particles increase in size, they deviate from the path of the fluid eddies due to their increasing inertia and the particle

trajectory becomes less sensitive to localized turbulence. The effect is that the deposition velocity decreases for much larger particles as defined by the particle-inertia moderated regime.

Equation (2.60), shown below, is taken from the work of Liu and Agarwal (1974), which contains a modification by Lee and Gieseke (1994). The presented correlation only accounts for turbulent diffusion-eddy impaction and is applicable for $\tau_+ < 12.9$.

$$\eta_{Turb,Inert} = \exp \left[-\frac{\pi d L v_t}{Q} \right] \quad (2.60)$$

$$v_+ = 5.03 \frac{v_t}{v} Re^{1/8} \quad (2.61)$$

$$\tau_+ = 0.0395 Stk Re^{3/4} \quad (2.62)$$

$$v_+ = 6 \cdot 10^{-4} \tau_+^2 + 2 \cdot 10^{-8} Re \quad (2.63)$$

where:

$\eta_{Turb,Inert}$ = Transport efficiency in a circular tube including turbulent-eddy impaction and inertial deposition losses [--]

v_t = Turbulent inertial deposition velocity [m/s]

v_+ = Dimensionless deposition velocity [--]

τ_+ = Dimensionless particle relaxation time [--]

2.5.3.4 Transfer Efficiency: Inertial Deposition in Bends

Particles collect on walls of tubing bends due to the changing flow path and particle inertia. Transport efficiency through tubing bends in laminar (Crane et al., 1977) and turbulent flow (Pui et al., 1987) is only a function of the bend angle and the Stokes number (Equation (2.64)). While Equation (2.64) does not include the curvature ratio, it

is recommended that it be above four due to the increase in deposition for sharper bends and because the data used in developing the correlations used curvature ratios above five. Additionally, the transfer efficiency approaches one as the Stokes number goes to zero. Gravitational settling losses in bends are calculated using an equivalent length of straight tubing.

$$\eta_{Bend,Inert} = \begin{cases} 1 - Stk \varphi, & Re \leq 4000 \\ \exp[-2.823 Stk \varphi], & Re > 4000 \end{cases} \quad (2.64)$$

where:

$\eta_{Bend,Inert}$ = Transport efficiency in a circular tube bend including inertial deposition losses [--]

φ = Bend angle [Rads]

2.5.3.5 Transfer Efficiency: Inertial Deposition in Contractions

Contractions and expansions should be avoided whenever possible due to the difficulty in accurately characterizing the turbulent flow patterns caused by sudden changes in flow geometry. It is recommended that the transfer efficiency through a contraction or expansion be calculated *in situ*. Muyschondt and co-authors (1996) correlated transfer efficiencies through varying contraction angles (γ), outer (d_o) and inner (d_i) diameter ratios, and flow regimes (Equation (2.65)). The definition of the Stokes number is provided for clarity in Equation (2.66); the Stokes number uses the gas velocity in the large diameter v_i and the characteristic length of the small diameter (d_o) tube.

$$\eta_{Cont,Inert} = 1 - \frac{1}{1 + \left\{ \frac{2 Stk \left[1 - \left(\frac{d_o}{d_i} \right)^2 \right]}{3.14 \exp(-0.0185\gamma)} \right\}^{-1.24}} \quad (2.65)$$

$$Stk = \frac{\rho^P (d^P)^2 C_C v_i}{18 \mu^G d_o} \quad (2.66)$$

where:

$\eta_{Cont,Inert}$ = Transport efficiency in a circular tube contraction including inertial deposition losses [--]

d_i = Inlet tube diameter [m]

d_o = Outlet tube diameter [m]

γ = Contraction angle [Deg]

v_i = Velocity of the gas in the large tube of a contraction [m/s]

Chapter 3: Analytical Methods and Supporting Equipment

This chapter describes the major analytical techniques and supporting equipment used in this study. The contents of each section include a theoretical basis of operation, statement of the major working equations, and a basic description of hardware specifications and setup. Further references are provided where appropriate. The methods outlined in this chapter were used at both the bench and pilot scale; specific experimental apparatuses and aerosol sources are described individually in Chapters 4 and 6, respectively.

3.1 FOURIER TRANSFORM INFRARED SPECTROSCOPY (FTIR)

Fourier Transform Infrared Spectroscopy is a widely used technique to rapidly quantify gas and vapor mixture compositions by measuring the absorption of infrared (600–4,200 cm^{-1}) radiation as it passes through a stream of sample gas moving in a fixed optical geometry. All polyatomic and hetero-nuclear diatomic molecules absorb infrared radiation which leads to excitation of molecular energy levels in the form of molecular rotation and vibration. Monatomic and homo-nuclear diatomic molecules do not absorb infrared radiation because they lack a net dipole moment which is required to have vibrational and rotational energy state transitions. The amount of energy that can be absorbed is dependent on the available transition states that a particular molecule can undergo and the energy contained in an incident photon, which is inversely proportional to the wavelength (proportional to the wavenumber). The number and position of active IR absorption bands located on an absorption spectrum is a function of the types of atoms present, bond angles, and bond strengths; the absorption of IR radiation is unique for each specie. These molecular “fingerprints” allow absorption spectrum to be parsed for each compound present in complicated, multicomponent sample matrices. Each identified

compound can then be quantified using a logarithmic absorption law and a set of reference spectra (calibration curves).

FTIR spectrophotometers collect absorbance/transmittance data across the IR frequency spectrum using variations of an interferometer, a black-body radiation source, and an IR detector. For illustrative purposes, **Figure 3.1**, will be used to discuss the basic principles of interferometry and to show the manipulation of optical data to produce IR spectra: a linear translating, Michelson-type interferometer is used for this example.

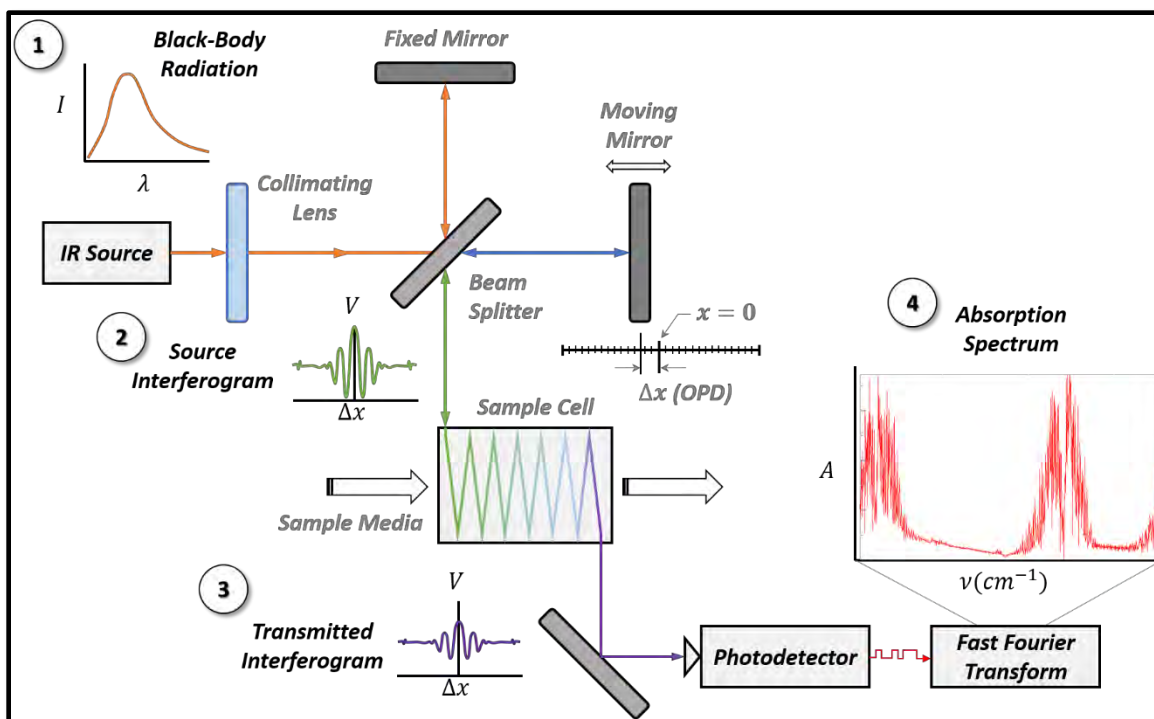


Figure 3.1: Flow chart of the operation sequence and optical information for FTIR using a Michelson-type interferometer.

The technique begins by creating a broad spectrum of IR frequencies by heating a black-body radiator (1). The radiation is collimated and sent to an angled beamsplitter located between two mirrors. Ideally, equal parts of the incident light will be reflected

and refracted to the two mirrors. Both mirrors reflect the light back to the beam splitter where it is recombined to form an interference pattern (2) which is dependent on the position of the mirrors relative to each other and the beam splitter. By fixing the position of one mirror and moving the other, the interference pattern can be changed very rapidly. The position of the moving mirror can be measured very accurately using a reference laser. The superposition of waves by variable path lengths forms the basic principles of an interferometer.

The recombined light is then directed to a sample cell with a fixed optical path length. Sample cells normally contain curved reflecting mirrors at opposite ends to cause the light beam to reflect multiple times prior to collection and quantification by an IR photodetector. The optical path is determined by the mirror spacing and by ray tracing the reflected beams from the entry to the exit of the sample cell body. The source light attenuates as it passes through the sample media flowing through the sample cell. After the light exits the sample cell, the intensity is measured as a function of time using a photodetector (3). The result is a plot of the measured intensity (usually as voltage) versus the difference in distance between the fixed and moving reflecting mirrors and the beamsplitter, commonly called the Optical Path Difference (OPD); this plot is called an interferogram. A fast Fourier Transform (FFT) translates the digitized information contained in the interferogram into the frequency domain. Data in the form of intensity versus frequency is called a transmittance plot. The absorbance of a sample can be made by comparing its transmittance spectrum to a blank, or background, spectrum.

Background spectra are measured in the presence of IR-inactive species (most commonly N_2), meaning transmittance is at its maximum value. As IR-active substances flow through the sample cell the transmittance spectrum is subtracted from the

background, producing an absorption spectrum (4). The raw data contained in the absorption spectrum is used for compositional analysis.

Component concentrations are related to the absorption spectra by the Beer-Lambert law (Beer-Lambert-Bouguer). The Beer-Lambert law states that the change in intensity of radiation as it passes through an absorbing media is directly proportional to the local intensity, the concentration of the absorber, and the transition probability (or molar attenuation coefficient). Equation (3.1) shows the differential form of the stated law.

$$-dI = \varepsilon(\lambda) C I dx \quad (3.1)$$

where:

- I = Intensity of radiation
- $\varepsilon(\lambda)$ = Molar attenuation coefficient
- C = Concentration of the absorber
- dx = Differential thickness of absorbing media

If the dependence of the molar attenuation coefficient on concentration is neglected, Equation (3.1) can be integrated to produce the more familiar form of the Beer-Lambert Law (Equation (3.2)).

$$A = \log\left(\frac{1}{T}\right) = \log\left(\frac{I_0}{I}\right) = \varepsilon(\lambda) C X \quad (3.2)$$

where:

- A = Absorbance
- T = Transmittance
- I_0 = Incident radiation intensity
- X = Total thickness of absorbing media

For multicomponent mixtures, the total attenuation of radiation is commonly assumed to be the sum of the individual component absorbance spectra as written in Equation (3.3).

$$A_{Tot} = \sum_{i=1}^{N_C} A_i = X \sum_{i=0}^{N_C} \varepsilon_i(\lambda) C_i \quad (3.3)$$

where:

A_{Tot} = Total absorbance of a mixture

A_i = Absorbance of component i

i = Component index

N_C = Number of IR absorbing components in the mixture

Therefore, if reference spectra are available for each compound present in a gas mixture, the total composition of the gas can be determined by the dot product of a scaling matrix and the multicomponent reference concentration absorbance matrix to reproduce the total absorbance spectrum. Theoretically, if the molar attenuation coefficient was independent of temperature, pressure, density, and composition, then one reference spectrum would be required for each component; the absorbance would scale exactly with the concentration.

However, in practice, many factors affect the shape and shift of spectral lines; and therefore, the molar attenuation coefficient across the entire IR bandwidth. Temperature affects absorbance through Thermal Doppler Broadening: due to the changing velocity distribution of molecules with temperature (and thereby the ratio of the absorber velocity to the speed of light), both red and blue Doppler shifts of the incident radiation frequency occur, resulting in a broadening of the observed absorption spectral lines. Changes in the sample pressure also have multiple effects on spectral line broadening. As the

concentration of the mixture increases, molecules will collide more frequently until the time between collisions is faster than the energy state transition. The result (called Collisional Broadening), is that there is more uncertainty in the energy difference between transitions, and therefore wider spectral features. Additionally, the proximity of molecules will induce intermolecular van der Waals forces which cause perturbations of the available transition states. This effect is called Quasistatic Broadening (Radziemski et al., 1987). Errors introduced by Pressure and Thermal broadening as well as non-linearities due to high concentrations can be greatly reduced by analyzing sample spectra at the same conditions as the reference spectra.

A second type of measurement error is a consequence of instrument limitations, specifically the spectral resolution and the IR detector sensitivity. Absorption lines of gases are roughly 0.2 cm^{-1} . However, most commercially available FTIRs have resolution bandwidths of $0.5\text{--}10 \text{ cm}^{-1}$. The result is that the “real” peak maxima get smoothed, or averaged, by the wider resolution band. The ratio of spectral feature peak heights are significantly affected for strong absorption peaks. Additionally, the peak maxima can saturate (or bottom out) the transmittance measurement. Therefore the analysis regions must avoid strong absorption bands due to the loss of concentration/absorption proportionality.

For the class of FTIR used in this work (Gasmeter™ DX4000 and CX4000), the reported noise level is about 2%, on an absorbance basis, meaning that if an absorbance of 1 is selected as the maximum absorbance criteria to minimize non-linearities in the analysis, then a spectrum containing an absorbance above 1.2 contains no useful information (Goff, 2005). At high concentrations (high absorbance) the molar attenuation coefficient becomes non-linear and several reference spectra are required to cover a large range of measureable concentrations.

In practice, the only compensation for temperature and pressure (total gas density) is made using the ideal gas law and on-board temperature and pressure measurements. The compensation pressure can be selected as either the ambient or sample cell pressure sensor. Path length compensation is made using the Beer-Lambert law, Equation (3.2). Corrections for each component are made relative to the scaled reference spectra; each reference spectrum has a recorded cell temperature, pressure, and path length.

3.1.1 Reference Spectra

Reference spectra for gases are generated in two ways: (1) purchasing gas cylinders with the desired composition for calibration, or (2) blending pure, IR-active gases with N₂ using calibrated mass flow controllers. Gas by either method is delivered at ambient pressure to the FTIR maintained at 180 °C. A three minute averaging scan is taken as the reference spectrum after the concentration reading on the FTIR has stabilized for at least five minutes.

Non-gaseous compounds require volatilization to create reference spectra. A Gasmeter™ Calibrator (**Figure 3.2**), supplied by Air Quality Analytical, Inc. was used to generate reference spectra for all liquid and solid species. The calibrator system consists of a needle valve and an Aalborg mass flow meter (Model No. GFM 17) to control the N₂ carrier rate, a Cole Parmer (Cat. No. 780100C) syringe pump to meter the calibration fluid, and two temperature controllers to maintain the vaporization zone (oven) and the heated outlet line at 180 °C. The syringe mates to the oven through a high temperature septum that is swaged to one side of the oven tee fitting. 25–500 µL Hamilton® gastight syringes are used.

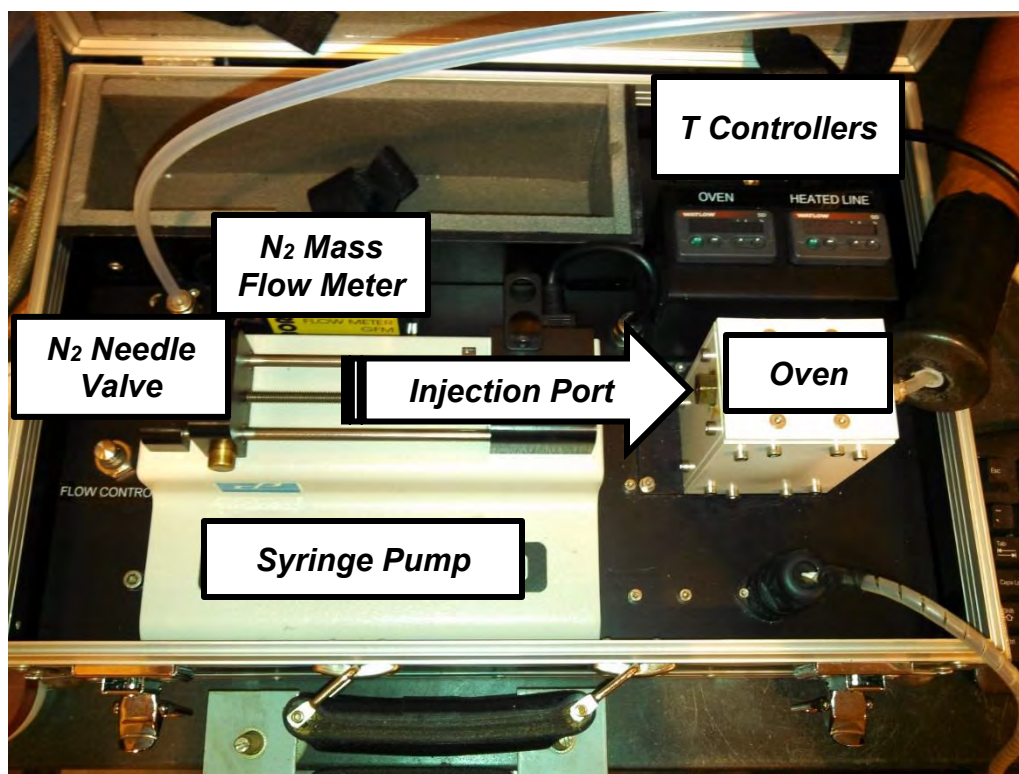


Figure 3.2: Gasmet™ Calibrator, supplied by Air Quality Analytical, Inc.

Liquids at room temperature are heated and mixed with a metered stream of N_2 carrier gas. Solids, however, must be dissolved in a solvent (usually H_2O) and the resulting solution is vaporized into the diluent gas. High accuracy reference spectra for the chosen solvent are required for solids calibrations. The spectra produced by the calibration solution will contain the absorbance signature of both the dissolved solid material as well as the solvent. After subtracting out the reference spectra for the solvent, the remaining residual signature is that of the solid compound. In Calcmet™, a three minute averaging scan is taken of the vaporized solution with the solvent calibration files active. The residual spectrum file is saved in Calcmet™ by selecting Options→Autosaving... and in the “Residuals” section, toggling the radio button labeled “All” next to the “Autosave Residual Spectra” selection. Residual files are named in the

following manner: “R_<Autosave Name>_<Residual Spectrum Index (starting at 00000)>.SPE.” Since the residual spectrum index is independent of the spectrum (.SPE) index, which is cumulative for the instrument, it is important to record the time in which the spectrum was recorded in the event that multiple residual files were mistakenly saved. The correct residual file can then be determined by identifying the correct time stamp. The residual spectrum file is renamed and saved with a reference file extension (.REF) in the same way as a spectrum file (.SPE) in the case of a pure liquid component.

Reference spectra generated on other FTIR are usually transferrable as long as the path length, temperature, and pressure are compensated and that the sample cell and windows are clean and free of IR absorbing material. After every major service and cleaning, new H₂O reference spectra are generated. This is required since H₂O is a very strong absorber across the entire IR band. At the Pickle Research Campus (PRC) pilot plant, calibration of CO₂ was cross-checked with online Vaisala CARBOCAP[®] Carbon Dioxide Transmitter Series GMT220 silicon-based NDIR sensors which are used to control the flow of CO₂ following major pilot campaigns.

3.1.2 Multicomponent Spectra Analysis

Accurate quantification of species during gas-phase analysis using FTIR requires proper adjustment of the baseline signal for deviations, analysis regions used for differentiating and quantifying molecules, and correct hardware setup. The following section briefly provides guidance on obtaining accurate analysis.

3.1.2.1 Baseline Corrections

The baseline of the sample spectra should read zero absorbance across the entire IR band when subtracting a background (N₂). However, the baseline slope and curvature is affected by changes to the operating conditions of the interferometer, specifically, the

interferometer temperature. Calcmet™ offers two corrections to adjust the baseline of a sample spectrum: slope correction and curve correction.

If the sample spectrum contains a region where no component is absorbing, the slope correction can be used. Slope correction applies a linear adjustment to the baseline. In some cases, the sample spectra will have molecular absorbance at all measured wavenumbers. The baseline curvature must be distinguished from true absorbance peaks; the curve correction is used under these conditions. The curve correction tool uses a second-order polynomial to perform the background correction. Curve correction should be used when there is no region free of absorbance signatures (Gasmet Technologies Oy, 2009). The default choice should always be to use the slope correction and pick an analysis region for each component containing only baseline. For typical amine-based CO₂ scrubber off-gas analysis, 2,500–2,700 cm⁻¹ contains no absorbing components and can be used for baseline analysis.

Reference spectra should not have background curvature within the noise level of the instrument. Baseline corrections are performed for the sample spectra only.

3.1.2.2 Analysis Regions

Analysis regions for components must include spectral information characteristic to that molecule without saturating the detector (absorbance above 1), or conversely, absorb strongly enough provide adequate signal-to-noise ratio. In multicomponent analysis, many spectral bandwidths of similar and disparate components can overlap. Calcmet™ software is able to resolve additive absorption of components provided the overlap is not too significant and the interference table is populated. Generally, the maximum absorption of a component should never exceed 1 during analysis as this is where the Beer-Lambert law begins to break down. Ideally, the absorption should be around 0.1 to prevent peak trimming (detector saturation) and to stay within the linear

calibration region. The analysis region must also be of a large enough bandwidth to provide curvature information. To define a curve, a minimum of 3x the wavenumber resolution is required. In this work, 24 cm⁻¹ is the minimum bandwidth for both the Gasmet™ DX4000 and CX4000 hardware.

Two analysis regions should be used for every component. Each species should include a unique spectral feature in the first analysis region and a clean baseline in the second region to adjust for baseline curvature. This work uses 2,500–2,700 cm⁻¹ to identify the baseline. **Table 3.1** shows the analysis regions used for multicomponent analysis in this study which were developed from Goff (2005), Sexton (2008), and Voice (2013).

Table 3.1: Analysis regions used for FTIR spectral analysis

Component	Conc. Units	Range 1 [cm ⁻¹]	Range 2 [cm ⁻¹]	Range 3 [cm ⁻¹]	# of References
H ₂ O	vol %	2475–2600	3000–3375	--	8
CO ₂	vol %	926–1150	2065–2245	2550–2700	10
PZ	ppmv	2500–3100	--	--	11
NH ₃	ppmv	895–1300	2475–2600	--	7
SO ₂	ppmv	1050–1450	2500–2600	--	7

Finally, the chemometrics package used by Calcmeter™ resolves the vectoral components of the spectra curves to fit the reference spectra used during quantification by modified classical least-squares fitting.

3.1.2.3 Pressure Compensation

The gas composition is calculated relative to the reference spectra concentrations. Therefore, if the sample conditions are different from the reference conditions, the total

molar concentration, or density, of the gas must be compensated. The only state property that changes during analysis is the sample cell pressure. Gasetm™ offers pressure compensation using a fixed value, ambient, or on-board cell pressure measurement to compensate the total concentration using ideal gas law. The concentration of the reference spectra are adjusted according to the reference/measured pressure ratio.

3.1.2.4 Voice Coil Pressure

The interferometer used to sweep the mid-infrared region is not hermetically sealed; therefore, the IR beam is passed through ambient gas unless an N₂ purge is applied. The N₂ purge is also necessary to prevent condensation of ambient H₂O on the interferometer mirrors caused by the multistage Peltier-cooled IR detector. The N₂ purge rate is controlled by a 0.0004” orifice placed downstream of a pressure regulator. The flowrate must be low enough that significant backpressure does not build in the interferometer cell because the interferometer mirrors are affixed to a carousel assembly which is translated using a voice coil. Excessive pressure will dampen the voice coil movement. The regulator and orifice should be checked periodically to maintain the correct flowrate. A set pressure of 10 psig is typically used.

3.1.3 FTIR Hardware

Two FTIR units were used in this work: (1) the portable Gasetm™ DX4000 and (2) the rackmount Gasetm™ CX4000. The only difference between the units is the casing mounts. **Table 3.2** show the specifications for the specific CX4000 unit used in this work.

Table 3.2: Temet Gaset™ CX4000 Analyzer Technical Specifications

Parameter	Value/Description
<i>General Parameters</i>	
Supplier/Model	Gaset Technologies, Inc. / CX4000
Serial Number	142840
Measurement principle	Fourier Transform Infrared (FTIR)
Performance	Simultaneous analysis of up to 50 compounds
Operating temperature	5-30°C, non-condensing
Storage temperature	-20-60°C, non-condensing
Power supply/consumption	115 V, 60 Hz/300 W maximum, 150 W continuous
Software	Calcmat™ V11.118, Windows 7 (64-bit)
<i>Spectrometer</i>	
Interferometer	Temet Carousel Interferometer (GICCOR)
Resolution	8 cm ⁻¹ (7.76 cm ⁻¹)
Scan Frequency	10 spectra/s
Detector	MCTP (Mercury, Cadmium, Tellurium, Pelletier Cooled)
IR source	SiC, 1550 K
Beamsplitter material	ZnSe
Window material	ZnSe (Spectrometer) /BaF ₂ (Sample Cell)
Wavenumber range	900-4,200 cm ⁻¹
<i>Sample Cell</i>	
Structure	Multi-pass, fixed path length 5.0 m
Material	Nickel, Rhodium, CVD Gold
Mirrors	Fixed, protected gold coating
Volume	0.4 L
Connectors	Imperial, 1/4" Compression
Gaskets	Kalrez®
Temperature	180 °C
Flow rate	1-5 L/min.
Response time	3 cell flushes
Required gas filtration	Filtration of particulates (2 µm)
<i>Measuring Parameters</i>	
Zero point calibration	Every 24 hours calibrate with N ₂
Zero point drift	< 2 % of measuring range per zero point calibration interval
Accuracy	2 % of measuring range
Temperature drift	< 2 % of measuring range per 10 K temperature change
Pressure influence	1 % change in measured value for 1 % sample pressure change
<i>Enclosure</i>	
Material/Weight	Aluminum/17 kg
Dimensions (mm)	482x196x450
<i>Input/Output</i>	
Digital Interface	9-pole D-connector for RS232 protocol

3.1.3.1 DX4000 Sample Pump

The DX4000 FTIR is a portable sampling unit. Sample is sent to the FTIR by a Gasetm™ Portable Sampling Unit (PSU) diaphragm pump. The heated pump is maintained at 180 °C at all times and has two onboard temperature controllers for mating heated sample lines. The pump also contains a heated filter to capture any particulate prior to sending the sample to the FTIR which could damage the sample cell mirrors.

Table 3.3 shows the specifications for the PSU.

Table 3.3: Gasetm™ Portable Sampling Unit (PSU) Technical Specifications

Parameter	Value/Description
<i>General Parameters</i>	
Operating Temperature	20 ± 20 °C
Voltage	115 VAC (50-60 Hz)
Power Draw	400-3600 W
<i>Heated Sample Pump</i>	
Material	316SS
Diaphragm material	Teflon®
Temperature	180 °C, Max.
Flow rate	4 LPM, constant
Enclosure	Explosion proof
<i>Heated Filter</i>	
Material	Bonded Microfiber (2 µm) or sintered steel (0.1 µm)
Temperature	180 °C
<i>Gas Connections</i>	
Sample In/Out	6 mm Swagelok®
Zero Gas In	6 mm Swagelok®
<i>Enclosure</i>	
Material	316SS
Dimensions	400 x 300 x 210 mm
Weight	12.3 kg

3.1.3.2 CX4000 Sample Pump

The CX4000 rackmount FTIR is fed with sample by an Air Dimensions, Inc.[®] Dia-Vac-R181[®] heated sample pump. A heated filter is located on the suction-side of the pump. A separate rackmount box with six temperature controllers is used to control the temperature of the mating heated lines, the heated pump, and filter. **Table 3.4–Table 3.5** show the specifications for the motor and sample pump head, respectively.

Table 3.4: Baldor[®] Super-E[®] VEM3538 FTIR Sample Pump Motor Technical Specifications

Parameter	Value/Description
Catalog number	0106826999-000010
Specification number	M35J302P862
Serial number	X1405M73896
Horsepower	0.5
Voltage	230/460 VAC (60 Hz)
Phase(s)	3
Full load amps	1.54/0.77 A
RPM	1735
NEMA nominal efficiency	82.5 %
Power factor	74 %
Service factor	1.25
Frame	56C
Enclosure	TEFC
Insulation class	F
KVA code	K
Design code	B

Table 3.5: Air Dimensions, Inc.[®] Dia-Vac-R181[®] FTIR Heated Sample Pump Head Technical Specifications

Parameter	Value/Description
Model number	R181
Heater power	150 W (2x 75 W)
Voltage	115 VAC (60 Hz)
Current Draw	1.3 A
Head material	316SS
Diaphragm material	Teflon [®]
Temperature range	30-400 °F
Max. ambient temperature	140 °F
Enclosure	Explosion proof
Port connectors	1/4" NPT

3.1.3.3 Heated Sampling Lines

Heated sampling lines were supplied by Gasmeter Technologies, Inc., Technical Heaters, Inc./Thermolab, and Clayborn Lab. While there are variations in Watt density, operating voltage, and style of electrical connections, the basic construction of the heated lines are all similar. The sample lines consist of exchangeable 1/4"–3/8" Teflon[®] tube cores wrapped in thermally insulated silicone and resistance heaters. The outer layer of the lines are either sheathed in polyamide braiding or corrugated plastic with stress relief loops.

Electrical connections for the lines include K-type (NiCrNi) thermocouples and three wires for power(live 1)/neutral(live 2)/ground. Connections to temperature controlling equipment are made by 7-pin cup-soldered Hirschmann[™] CM06E14S-61S connectors or by separate power and thermocouple breakout connections. 3-pin cup-soldered Amphenol[®] connectors and NEMA plugs were used for power while standard K-type thermocouple connectors were used for temperature measurement. **Figure 3.3** shows pinouts for the two common heated line connectors. Adaptors were fabricated by matching pins and soldering wires and thermocouple leads.

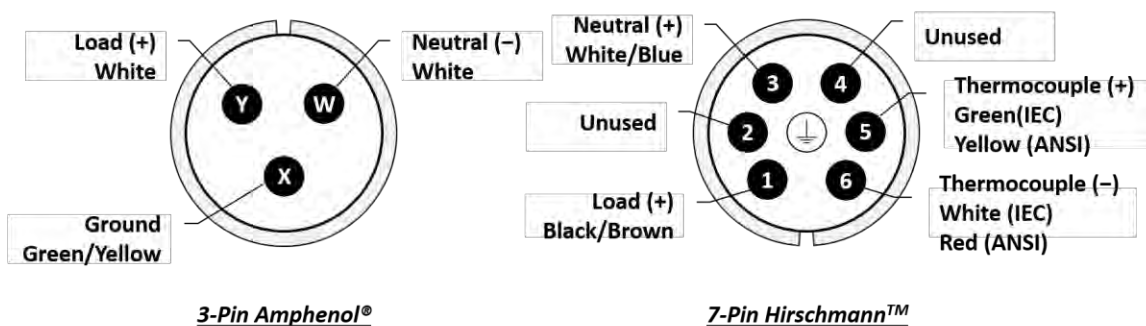


Figure 3.3: Pin assignments and standard wire colors for 120 VAC power/Thermocouple connectors as viewed from behind (soldered ends). A separate standard K-type thermocouple connector is used in combination with Amphenol® power connectors. Both connectors are keyed, as indicated by the outer notch.

3.1.3.4 Heated Connection Blankets

Connection points between heated equipment and FTIR sample lines must be insulated to prevent condensation. For lengths greater than a few inches, heated insulation pads are required, especially if the transition location is subject to ambient weather conditions. CleanAir® SKU 1233 heated/insulated electrical blankets with local PID temperature control were used in this work. **Table 3.6** provides the technical specifications for the heated blankets.

Table 3.6: CleanAir® SKU 1233 heated/insulated electrical blanket technical specifications.

Parameter	Value/Description
<i>Specification</i>	
Max. Operating Temperature	400 °F
Ambient Temperature	0 °F
Heat Output	42.7 W
Operating Voltage	120 VAC
Measured Resistance	337.1 Ω
Latch Mechanism	Velcro® Release
Dimensions (Open)	4" x 3" x 1" (L x W x H)
Dimensions (Closed)	4" x 6" x 1/2" (L x W x H)

3.1.3.5 Heated Sampling Probes (Stingers)

Universal Analyzers, Inc. Model 277S heated probes were used to pull sample gas from duct work at the pilot scale. **Table 3.7** shows the technical specifications for the heated sample probes. The probes contain a heated filter body which is used to knock out entrained liquid. Aerosol is vaporized in the probe. The gas sampled through the probes will contain the total (gas and aerosol phase) concentration of species moving through the ductwork.

Figure 3.4 details the heated probe electrical connections used to control the temperature of the probe. The manufacturer default thermomechanical switch, set at 350 °F, was used during the November, 2013 PRC pilot plant campaign. More precise temperature control was added following that campaign through the installation of locally mounted PID controllers in combination with solid-state relays (SSRs) to modulate the heater power.

The probes were installed at 135° relative to the flow direction to minimize sampling sheeting liquid from condensation and large entrained droplets. **Figure 3.5** shows a cross-sectional side-view of a mounted heated sample probe. The depth of the probe was set by a *post hoc* spacer built from all thread and a piece of angle cut to match the probe diameter. The spacing can be altered by adjusting the bracketing hex nuts.

Table 3.7: Universal Analyzers, Inc. Model 277S Heated Probe Technical Specifications

Parameter	Value/Description
<i>Operating Specifications</i>	
Sample flow rate	0-20 L/min. (0.7 CFM)
Calibration gas requirement	Sample flow rate plus 10 %
Operating pressure drop at 10 L/min.	12" water column (3.0 kPa)
Maximum stack gas temperature	700 °F (371 °C)
Oven and vaporizer temperature	350 °F (176 °C)
Dimensions	9" x 9" x 10" (230 mm x 230 mm x 250 mm)
Weight	20 lb. (9.1 kg)
Input power requirement	350 W (Custom)
Input voltage requirement	115 VAC, 50/60 Hz
<i>Material Specifications</i>	
Filter chamber heater type	Rod heaters in aluminum tube, PID controlled
Filter chamber material	316SS
Filter element type	Ceramic 2µm (Standard Option)
Chamber material	316SS

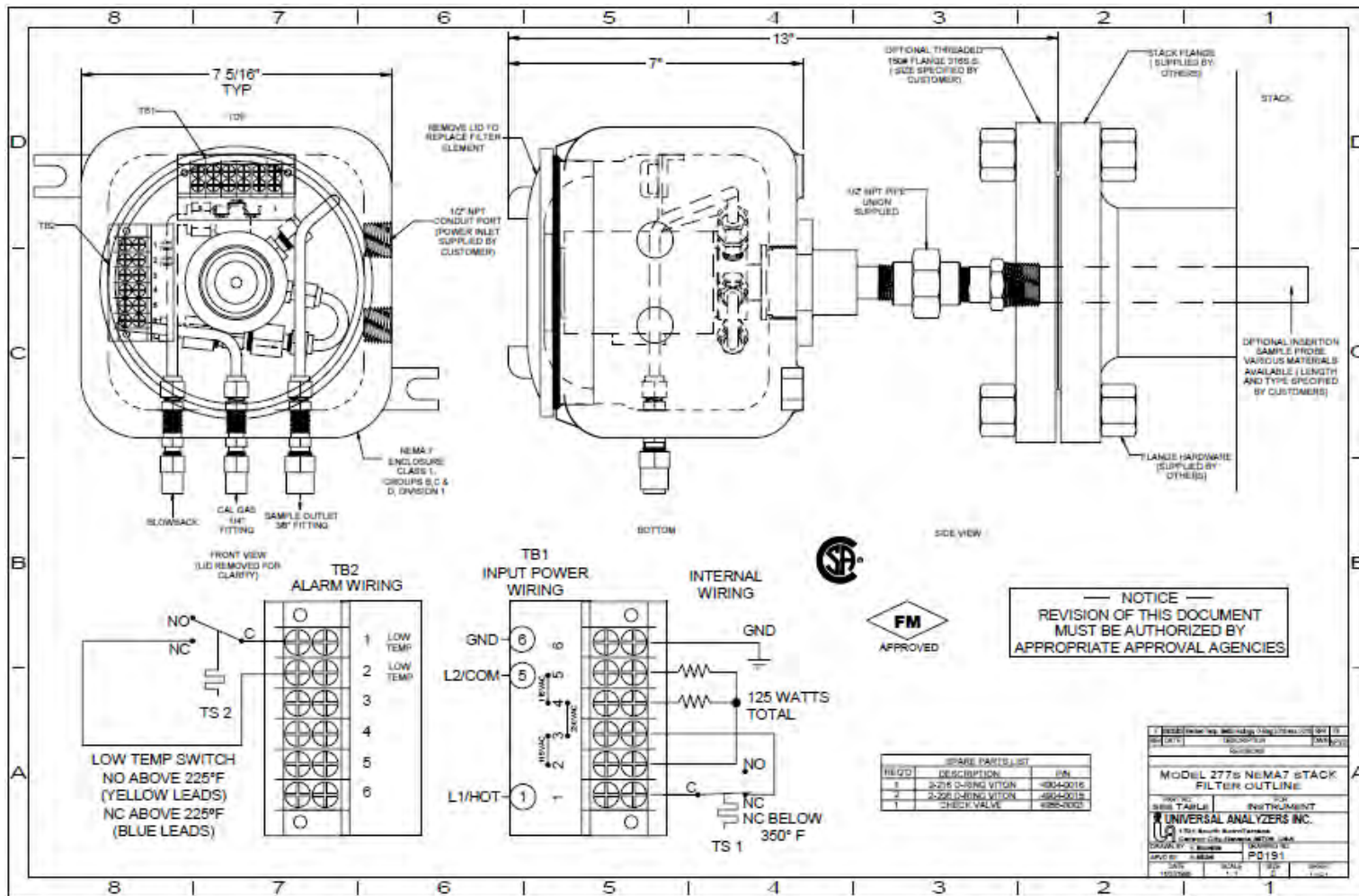


Figure 3.4: Mechanical and electrical drawing for the Universal Analyzers, Inc. Model 277S (no blowback) NEMA7 heated and filtered stack sampling “Stinger” probe. The high temperature (350 °F) thermomechanical switch was converted to PID control after the November 2013 SRP pilot campaign.

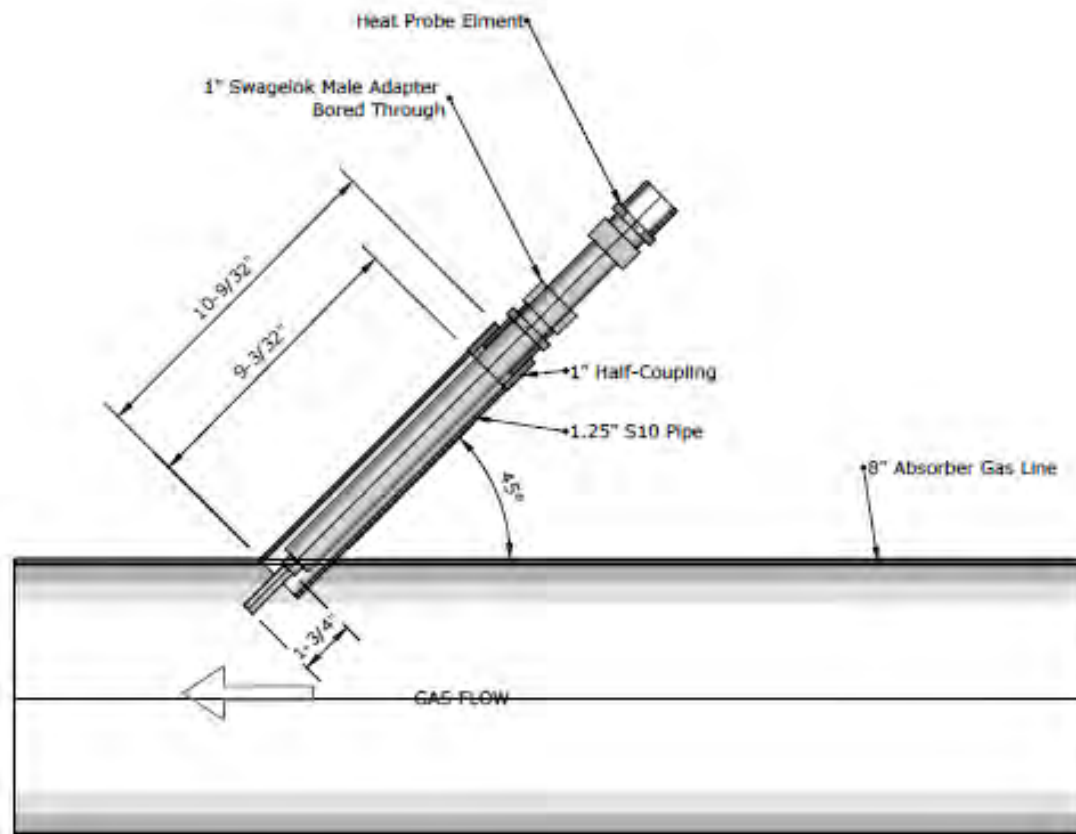


Figure 3.5: Heated sample probe side-view dimension diagram for connection of the stinger probe at the SRP pilot plant. The stinger probe depth into the process duct is set by a 1" Swagelok® to 1" MNPT adapter fitting using graphite ferrules. The tube adapter fitting connects to a 1" half-coupling welded to a short section of 1 ¼" S10 piping which is welded at approximately 135° with respect to the flow direction.

3.1.4 Multipoint Heated Stream Switcher (MSSH)

A multipoint, fast-switching system for FTIR measurements at the pilot scale was manufactured and delivered by Air Quality Analytical, Inc., D/B/A GASMET-USA™. The system was designed to switch between seven FTIR sampling points using a cascade solenoid/pneumatic control system (GASMET-USA, 2014).

The sampling portion of the MSSH is constructed using a double substrate channel with Swagelok® Modular Platform Components (MPC). The normally open (waste) common bypass manifold is flushed by an educator and sent to a vented location. The educator flush moves sample through all non-selected lines at all times to prevent liquid accumulation in stagnant lines and allows for much faster analytical response times. The normally closed (sample) common sample manifold is connected to the inlet of the FTIR sample pump and heated filter. If a valve is activated, the ducting is opened to the normally closed substrate channel and is sent for FTIR analysis. When the valve signal is turned off, an orifice bleeds off the pneumatic valve pressure and the ducting returns to the normally open (waste) substrate channel. The sample manifold and pneumatic switching valves are housed in an oven chamber which is temperature controlled to 180 °C to prevent condensation. **Figure 3.6** and **Table 3.8** show the MSSH PFD and the electrical terminal block assignments, respectively.

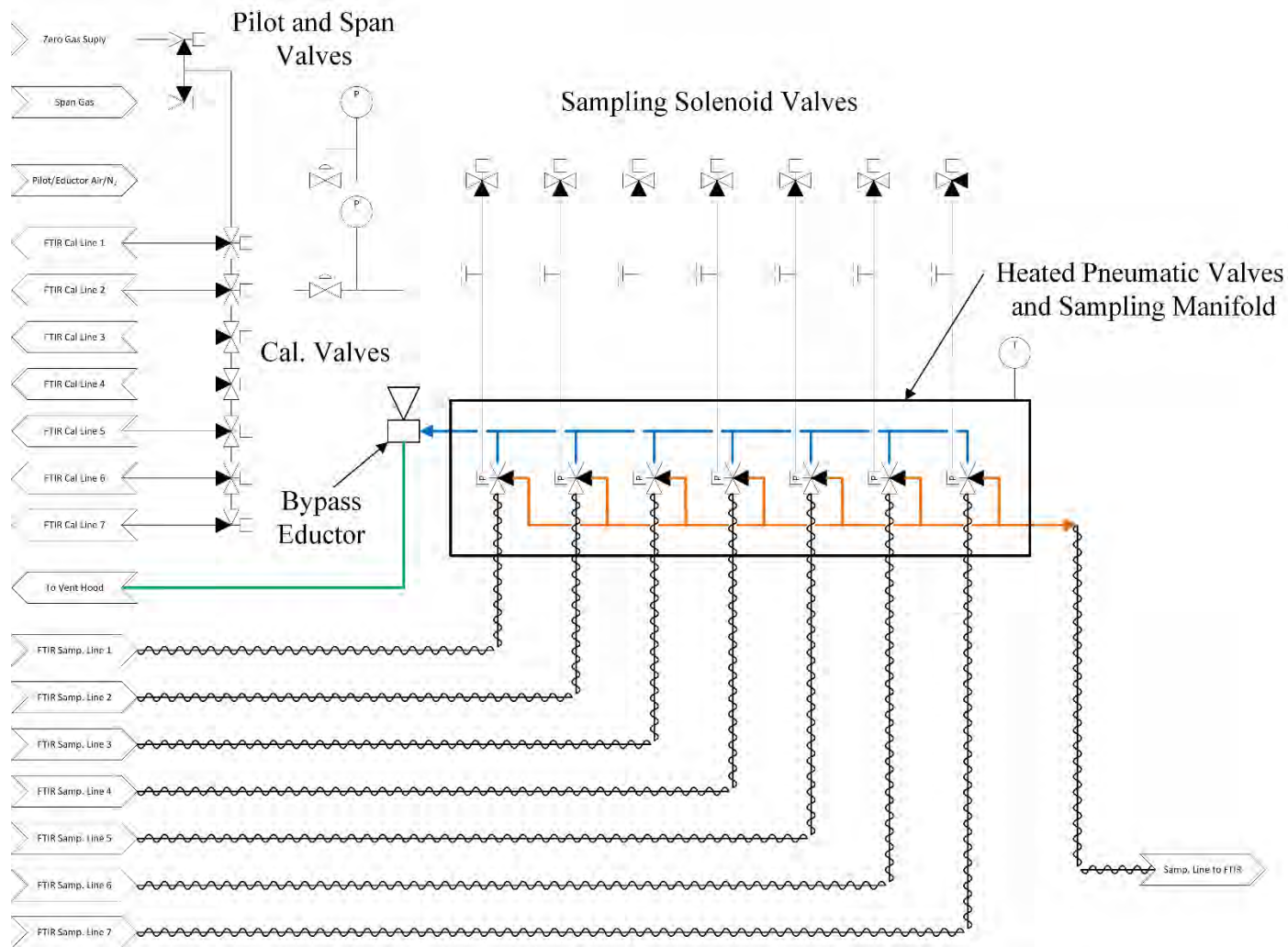


Figure 3.6: Process flow diagram of the MSSH. The common bypass manifold is sent to waste/vent. The common sample manifold is sent to the FTIR for analysis.

Table 3.8: MSSH-7 Stream Switcher Terminal Block Assignments

Terminal	Connection
<i>Load Bus</i>	
1	Solenoid valve 1 (120 VAC +)
2	Solenoid valve 2 (120 VAC +)
3	Solenoid valve 3 (120 VAC +)
4	Solenoid valve 4 (120 VAC +)
5	Solenoid valve 5 (120 VAC +)
6	Solenoid valve 6 (120 VAC +)
7	Solenoid valve 7 (120 VAC +)
8	Pilot valve 1 (120 VAC +)
9	Pilot valve 2 (120 VAC +)
10	Pilot valve 3 (120 VAC +)
11	Pilot valve 4 (120 VAC +)
12	Pilot valve 5 (120 VAC +)
13	Pilot valve 6 (120 VAC +)
14	Pilot valve 7 (120 VAC +)
15	Zero gas valve (120 VAC +)
16	Span gas valve(120 VAC +)
<i>Neutral Bus</i>	
18	Solenoid valve 1 (120 VAC -)
19	Solenoid valve 2 (120 VAC -)
20	Solenoid valve 3 (120 VAC -)
21	Solenoid valve 4 (120 VAC -)
22	Solenoid valve 5 (120 VAC -)
23	Solenoid valve 6 (120 VAC -)
24	Solenoid valve 7 (120 VAC -)
25	Pilot valve 1 (120 VAC -)
26	Pilot valve 2 (120 VAC -)
27	Pilot valve 3 (120 VAC -)
28	Pilot valve 4 (120 VAC -)
29	Pilot valve 5 (120 VAC -)
30	Pilot valve 6 (120 VAC -)
31	Pilot valve 7 (120 VAC -)
32	Zero gas valve (120 VAC -)
33	Span gas valve(120 VAC -)
<i>Oven Terminal</i>	
35	Oven heater (120 VAC +)
36	Oven heater (120 VAC -)
37	Oven thermocouple, K-type (-)
38	Oven thermocouple, K-type (+)
39/40	Ground

3.2 PHASE DOPPLER INTERFEROMETRY (PDI)

PDI is a non-interfering, laser-based technique for characterizing dynamic aerosol populations. PDI simultaneously measures the particle size distribution, the total particle density (or flux), and, in certain configurations, three dimensions of velocity.

PDI is a unique *in situ* aerosol analysis technique because the phase-shift between detectors, rather than the scattering intensity, is used for particle size determination. By using phase, rather than intensity, as the sizing principle, attenuation errors caused by multiple scattering and optical window fouling are mostly eliminated. The requirements for proper sizing are that the measured signal amplitude be greater than the background scattering noise and that particles pass along a trajectory that produces the favored scattering mode. Attenuation can reduce the signal amplitude to a point in which it cannot properly be detected; however, that issue is universally present in analysis systems using photodetectors. The mathematical basis for particle sizing by phase shift can be found in the works by Bachalo (1980) and Albrecht et al. (2003).

The following sections cover the general theoretical principles and equations used in PDI for particle sizing and velocity determination and follows the outline provided by the PDI-100 MD User's Manual (n.d.). Additionally, hardware description, cable connections, calibration and alignment procedures, and data processing are addressed.

3.2.1 Theory of Operation

The sampling principle of PDI is based on ideal scattering of light from a single, uniformly illuminated, spherical particle passing through the plane of an optical heterodyne created by the intersection of two laser beams. The intensity of refracted and reflected beams is given by the Fresnel equations and the temporal and spatial frequency of the scattered light interference pattern at any far-field point, relative to the position of the particle, can be calculated using the Lorenz-Mie equations and the particle diameter.

The temporal frequency, or the Doppler frequency, is used to calculate the particle velocity and the spatial frequency simultaneously measured at two locations, which gives a single measurement of the spatial wavelength (phase shift) of the Doppler signal, is linearly related to the particle diameter. Development of the working equations from vectorial two-point ray tracing is covered in considerable depth in the text by Albrecht et al. (2003). The fringe approximation is used in this description for simplification.

Figure 3.7 shows the layout of a basic forward-scattering PDI. The sample volume is created by the crossing of lasers of equal intensity. A single laser (1), of wavelength, λ , is split into two equal parts by a beam splitter and one ray is shifted in frequency by an acousto-optic modulator (Bragg cell) (2). The frequency shift is applied to distinguish particles with “negative” velocities; positive and negative frequency shifts are mathematically indistinguishable. The Bragg cell translates all Doppler shifts across the measureable velocity range into the positive frequency domain.

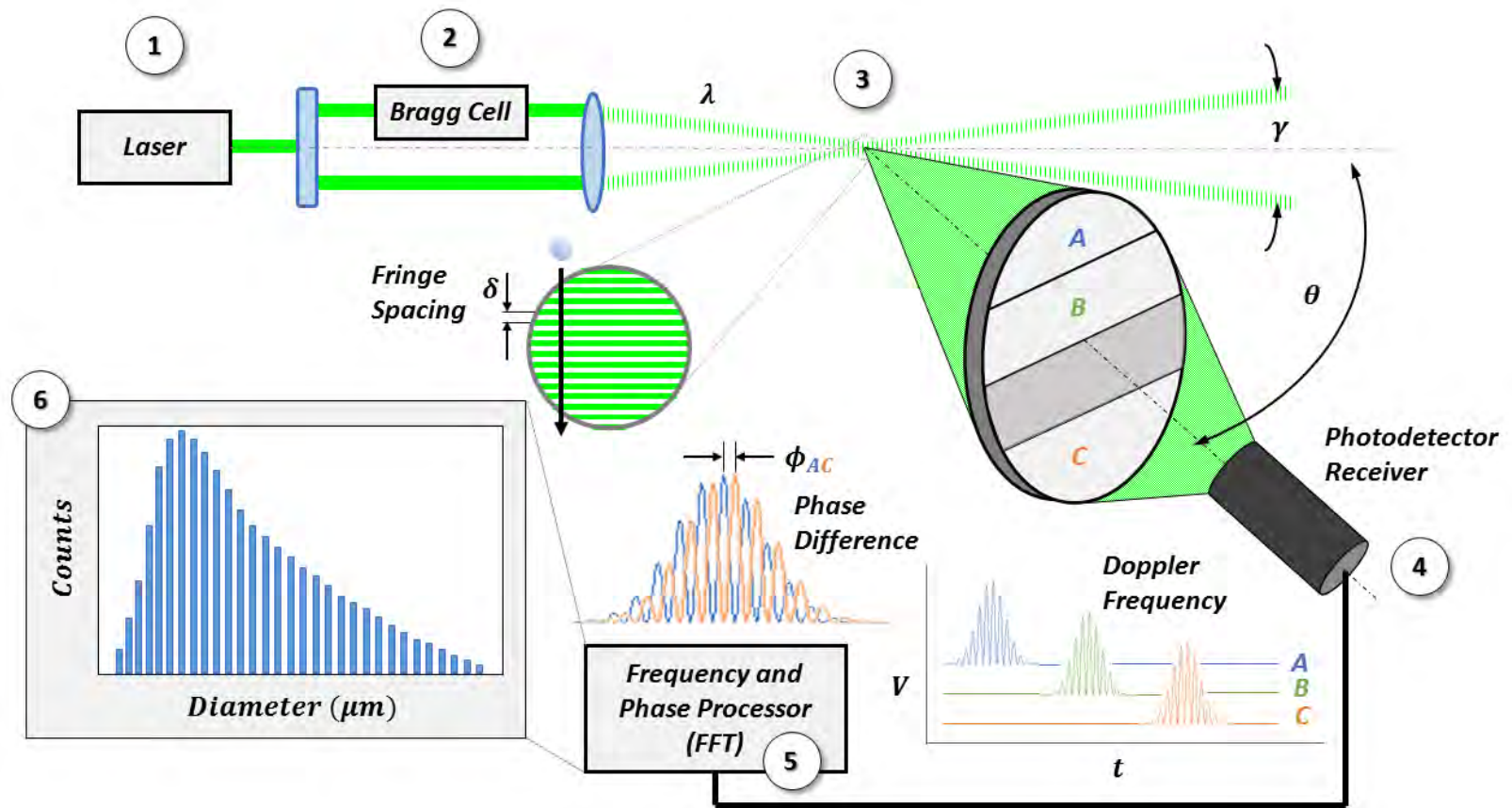


Figure 3.7: Schematic of geometric parameters, important measurement substeps, and data flow for a forward scattering PDI.

The sample volume (3) is created at the intersection of the two beams which are guided into the aerosol field by optics to cross at an angle, γ . The intersection of the two lasers creates a region of constructive and destructive interference bands called fringes. The spacing between the fringes, δ , is a function of the laser properties and the geometry of the crossing and can be calculated using Equation (3.4).

$$\delta = \frac{\lambda}{2 \sin\left(\frac{\gamma}{2}\right)} \quad (3.4)$$

where:

- δ = Fringe spacing [m]
- λ = Wavelength of the lasers [m]
- γ = Laser crossing angle [rad]

As a particle passes through the fringe pattern in the sample volume, the particle scatters coherent light in an alternating pattern of high and low intensity. The scattering intensity can be observed by placing one, or several, photodetectors (4) in a receiver optics housing at an elevation angle θ orthogonal to the laser crossing plane. The pattern of scattered light can be observed as a photomultiplier voltage oscillating in time. The pattern seen by the photodetectors is referred to as a Doppler burst. The time-spacing between the signal peaks, or the wavelength of the Doppler signal, is directly proportional to the particle velocity; the higher the particle velocity, the faster the scattering pattern moves across a fixed point in space.

When multiple photodetectors are spaced with a fixed geometry, the Doppler burst event arrives at each photodetector at a different time. The difference in arrival time, which is observed as a phase shift between the signals, is directly related to the detector spacing and also the particle diameter. Multiple photodetectors are used for

measurement redundancy and for phase wrap ambiguity. If the Doppler wavelength is smaller than the detector spacing, the phase shift will appear to be larger than 360° .

Spherical particles act as magnifying lenses for the interference pattern. Small particles have large curvature which leads to large magnification and consequently small phase shifts. Conversely, large particles have small curvature which leads to small magnifications and large phase shifts. **Figure 3.8** provides an illustration of the phase shift caused by diameter-curvature magnification.

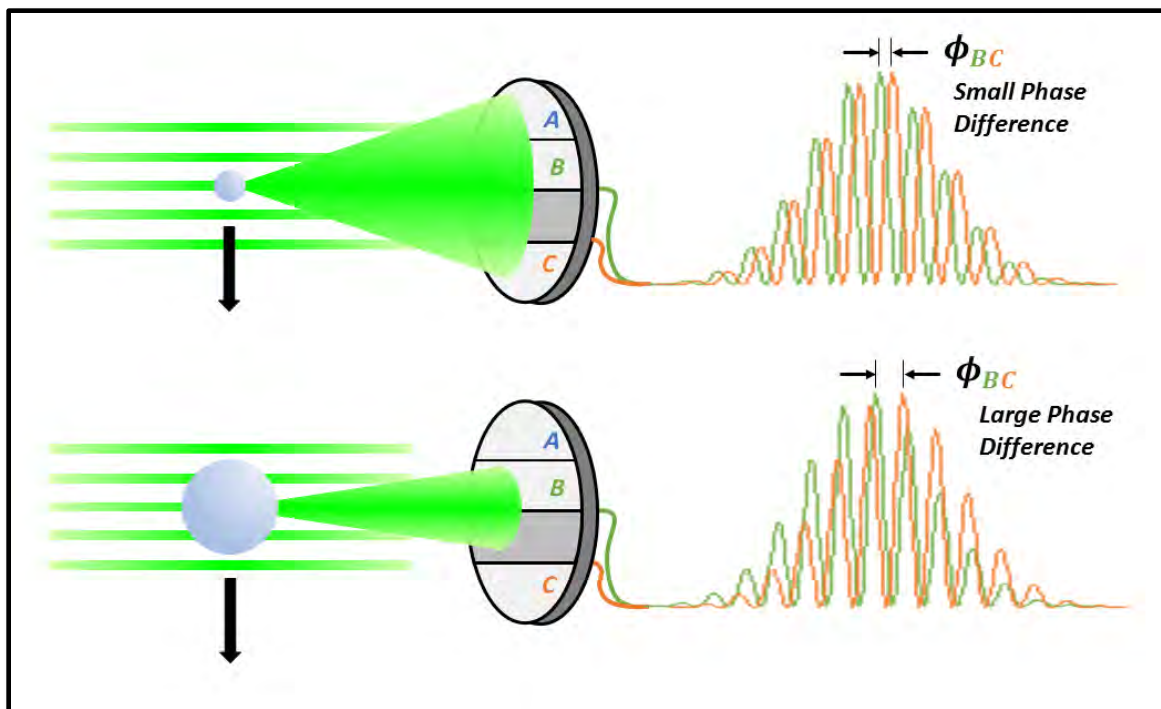


Figure 3.8: Phase shifts between photodetectors are caused by magnification of the interference fringe pattern due to the particle curvature.

The Doppler signals from each photodetector are passed to a signal analyzer where a Fast Fourier Transform (5) is performed to determine the Doppler frequency and the phase shift between each pair of photodetectors. Sampling and data processing

continues for each measured scattering event, also called a burst, until a sample set of sufficient statistical significance is collected and a particle size distribution is produced.

The total measurement time, dimensions of the measurement volume, and velocity distribution allow for the calculation of the particle flux. The particle flux can be integrated in time to give a total particle density.

3.2.2 Safety

The solid state lasers (532 nm) used in the PDI are Class 3B lasers. Even though the transmitter and receiver are flush mounted to the a custom test cell body, laser safety standards must still be followed in the event the instrument becomes unmounted while active or for specular reflections through the viewing window. Artium follows the class definition set by the Federal Register 21 CFR 1040.10 and the laser safety standards of the American National Standards Institute (ANSI Z136.1).

It is recommended that the end user not perform repair operations on the equipment due to the risk of laser radiation exposure. The instrument should be sent back to Artium for internal repairs. The safety interlocks on the laser should neither be bypassed nor compromised in any way.

When performing external alignment or when viewing the laser crossing, polarized protective glasses provided by Artium should be worn.

3.2.3 Hardware Setup and Connections

The PDI system is comprised of five major hardware components: (1) a power supply, (2) a signal processor, (3) transmitter optics, (4) receiver optics, and (5) a computer. In the case of the customized PDI developed for this work, the transmitter and receiver are contained in a single housing. Another crucial piece of hardware used in troubleshooting and calibration is an oscilloscope; a digital Tektronix® TDS2014C, 100

MHz, 4-Channel, 2GS/s oscilloscope was used in this work. The following sections detail the functions and electrical connections of the major hardware components. Connection labels are contained in parentheses.

3.2.3.1 Power Supply

The power supply enclosure provides interlocked power and instructions to the transmitter and the receiver. The customized PDI in this work uses a single, keyed multi-pin cable (POWER) and an Ethernet (COM) connections for the receiver and the transmitter. A USB type B cable (USB) connects to the computer to transmit the photomultiplier tube (PMT) gain, aperture settings, laser settings, and the phase calibration source information.

3.2.3.2 Advanced Signal Analyzer (ASA)

The ASA processes raw signals from the receiving optics and performs amplification, signal filtering, analog-to-digital conversion, and burst signal detection. A set of three BNC cables from the transmitter/receiver cable umbilical labeled RAW A, RAW B, and RAW C are connected to the INPUT SIGNALS bank of BNC receptacles. An Ethernet cable (COMPUTER) sends digitized information to the computer for software processing; the cable is connected to the Ethernet interface card on the back of the computer.

Several monitoring signals can be observed by connecting an oscilloscope by BNC connectors. The four channels used in this work are the RAW A, RAW B, RAW C, and GATE OUT signals. Raw signals (MONITOR SIGNALS) display unfiltered Doppler burst signals from each photodetector. The gate signal rises to 5 V when a burst is detected and falls to 0 V at the end of the signal. Signal observation with an

oscilloscope is crucial for aligning the lasers, performing phase calibration, and assessing signal quality in real-time.

3.2.3.3 Transmitter

The transmitter contains the laser source, the Bragg cell, and optical hardware used to split the laser source into two, equal intensity beams and reflectors to create the proper beam spacing and crossing angle. The laser is turned on by a keyed switch located on the back of the transmitter/receiver enclosure on the left-hand side of the heat sink. A laser alignment port was added for field adjustment and can be tuned using a long #2 hex driver supplied with the instrument. The port is capped by a small knurled fitting and is located on the right-hand side of the transmitter/receiver housing. The alignment port is not shown in **Figure 3.9**, but it is physically located on the long, lateral face of the housing midway between the desiccant holder and the cable umbilical.

3.2.3.4 Receiver

The receiver contains the photodetectors, aperture, and focusing lenses. The PDI in this work uses a fixed optical configuration; no additional lenses or apertures are available for selection. Geometry and parameters of the transmitter/receiver setup can be found in **Table 3.9** below.

Table 3.9: PDI transmitter and receiver optical parameters

Parameter	Value
<i>Transmitter Optics</i>	
Laser wavelength (nm)	532
Laser beam diameter (mm)	0.95
Laser beam waist (μm)	17.8
Focal length (mm)	25
Beam separation (mm)	17.46
Beam crossing angle ($^\circ$)	38.5
Fringe spacing (μm)	0.8
<i>Receiver Optics</i>	
Collection angle ($^\circ$)	65
Focal length (mm)	35
Slit aperture (μm)	10
<i>Transmitter/Receiver Angle</i>	
Forward scattering angle ($^\circ$)	40

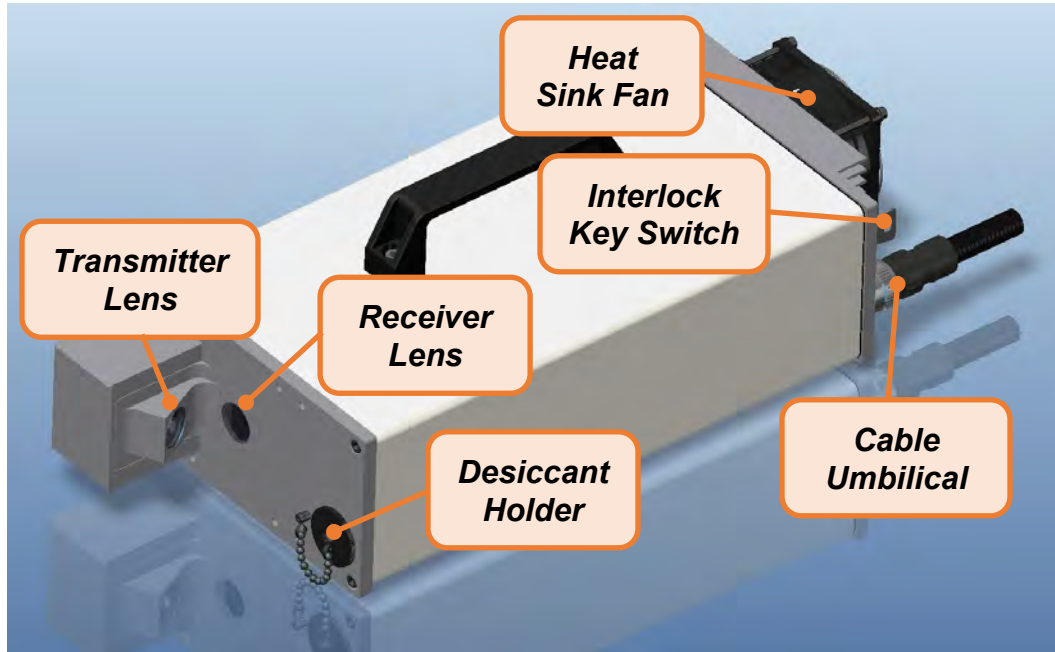


Figure 3.9: PDI Transmitter and Receiver housing without mounting brackets and laser alignment port.

3.2.3.5 Temperature and Humidity Control

The PDI housing requires climate control due to the sensitivity of the laser alignment to temperature changes and because the housing is not hermetically sealed. The transmitter/receiver umbilical breakout has an additional three pin connector which connects externally to a power supply that provides power to an onboard temperature controller, heater, Peltier cooler, and convection fan. The internal moisture content is suppressed by the use of disposable desiccant bags (McMaster-Carr 3492T15) located in a holding cage on the front end of the housing as shown in **Figure 3.9**. The knurled cap plug can be unscrewed and the desiccant bag is easily removed and replaced. It is very important that the temperature controller be plugged in and the desiccant be changed regularly to extend the life of the equipment and to ensure ideal laser alignment.

3.2.4 Test Cell

A customized, fixed-alignment PDI was developed for this study for the purpose of measuring high density ($>10^6$ part./cm³) aerosol over the size range 0.1–10 μm at the bench and pilot scale. Details of the most current design iteration are presented in this section. The development history will be covered in Chapter 6.

The PDI housing is mounted to a 1" Sch. 10 304SS pipe with three inlayed crown glass optical windows (transmitter, receiver, and observation). The pipe section has 1" #150 RFSO 304SS flanges welded at either end for mating. The PDI housing has aluminum guides and dowel pins for alignment on the test cell. Swivel arms hold the PDI housing on the test cell and are secured by wingnuts and all thread rod. **Figure 3.10–Figure 3.11** show details of the test cell mounting bracket and a cutaway of the analysis window section.

Several features designed to keep liquid sheeting and condensation from interfering with analysis were included. Protection cones for the receiver and transmitter

were added to keep the optical path free from high density aerosol up to the sample point to reduce laser attenuation. Engineering drawings for the cones can be seen in **Figure 3.12–Figure 3.13**. The cones were machined to fit into an inlaid channel such that the flow path was unobstructed. M1 fine thread screws with Teflon[®] washers seal the channel pieces and cones to the test cell. The cones also contain several microchannels for purge and vacuum flow. The intended design is to supply purge gas (clean N₂ at 5 SLPM) at one fitting and pull an identical flow rate out of the other (via an educator) to supply net zero flow in the hollow cone section as an additional preventative measure against liquid sheeting and fogging of the optical windows. Connections for the purge and vacuum lines are made by 1/8” push-to-connect fittings pushed through embedded o-rings in the test cell body. Silicone sealant was later added to improve the seal.

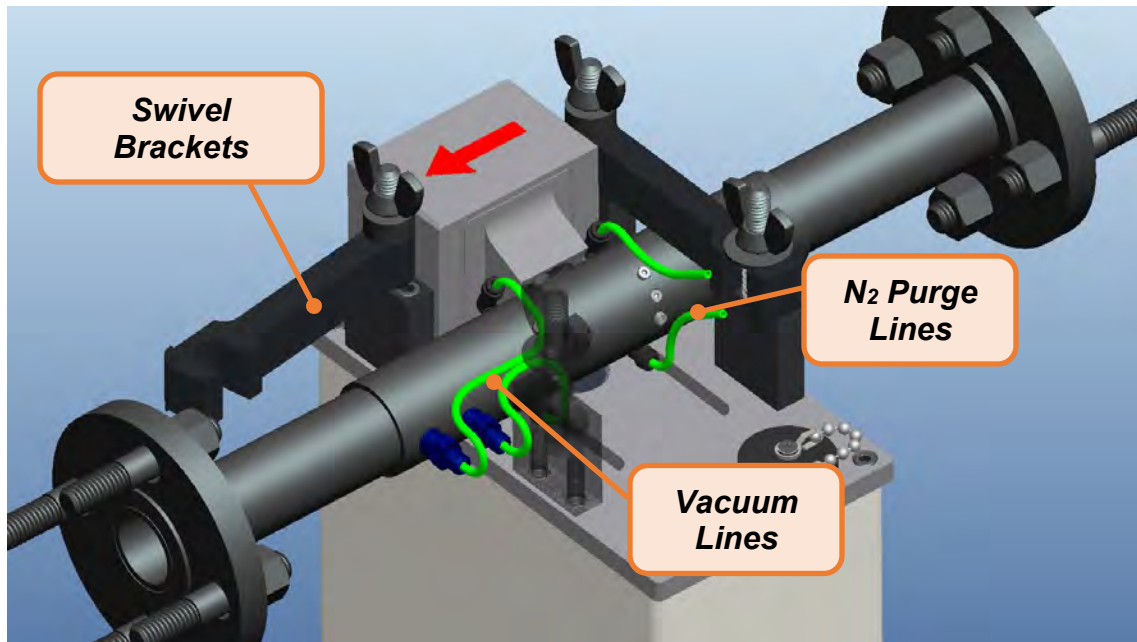


Figure 3.10: The PDI test cell mounts to the PDI housing using swivel brackets. Channels for the 1/8” vacuum and purge tubing are inlayed in the mounting face plate of the PDI enclosure.

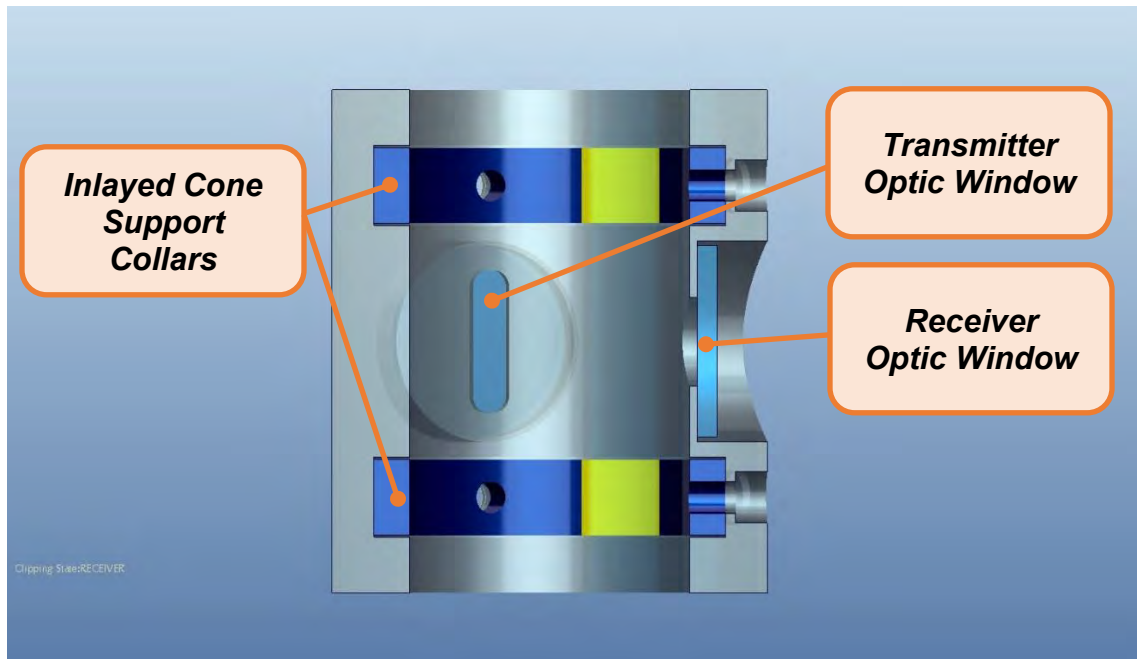


Figure 3.11: Cutaway view of the test cell window and protection cone collar body. The windows are fixed in place using Silicone sealant.

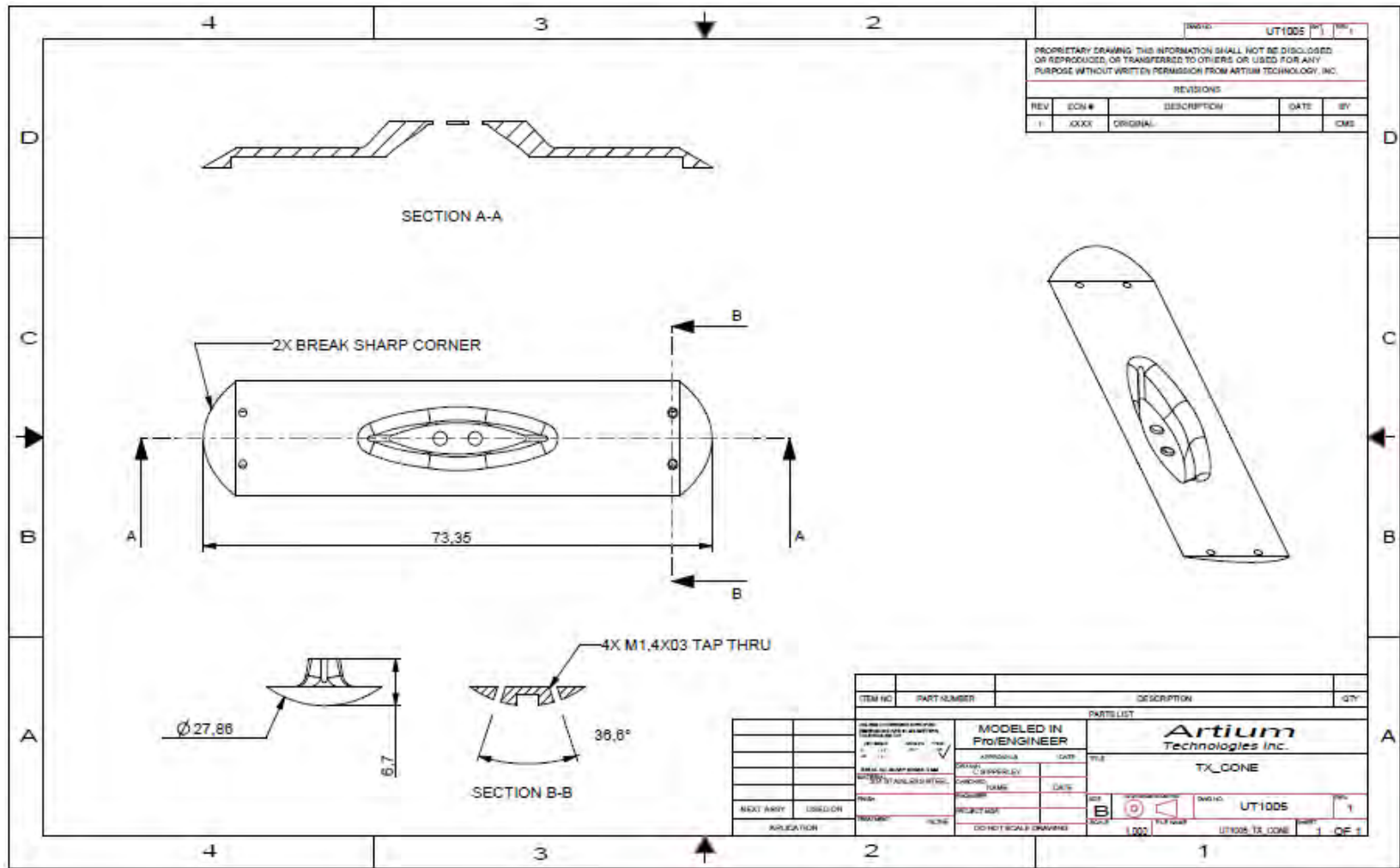


Figure 3.12: Engineering drawings for the PDI Transmitter laser protection cones.

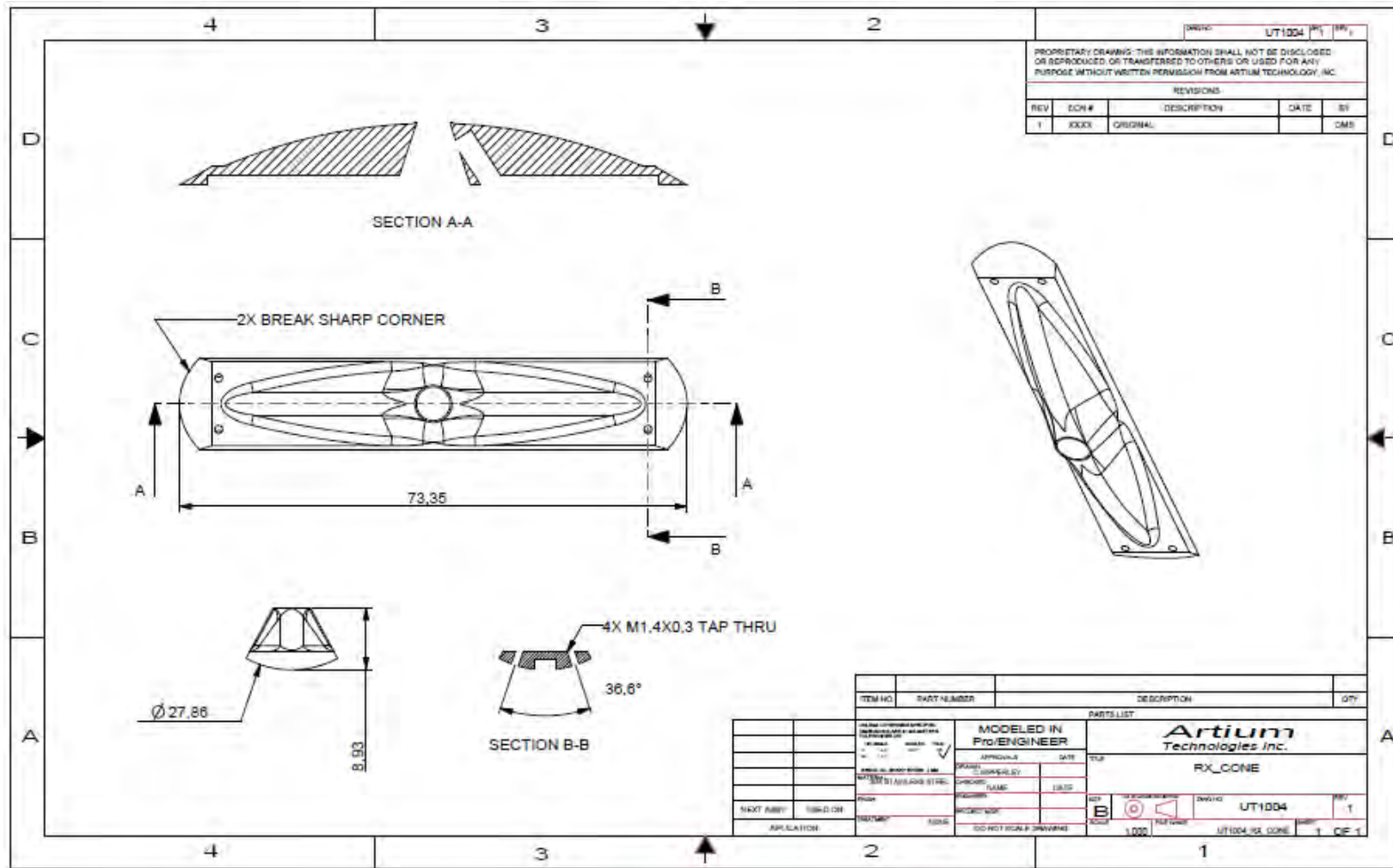


Figure 3.13: Engineering drawings for the PDI Receiver laser protection cones.

3.2.5 Software

The software used to control the PDI and to acquire and process data is Artium Integrated Management Software (AIMS). The following sections briefly describe important parameters and data criteria.

3.2.5.1 Acquisition Control

Three different stopping criteria for data collection can be chosen in AIMS under the Acquisition tab: (1) sampling time, (2) number of samples, or (3) free run (stop on user input). Good statistical representation requires many samples; a total threshold of 10,000 counts was selected for this work when data rates were feasible. Very low data rates required relaxation of that criteria. Typically, a sampling time of 5-10 minutes was chosen.

3.2.5.2 Auto-Setup

Processor settings can be automatically setup using the features found under the Auto-Setup tab in AIMS. The auto-setup algorithms collect a fixed number of signals made with aerosol flowing past the laser intersection to determine the optimum processor settings and PMT gain. Processor auto-setup is performed for every data set collected in this work. PMT gain was adjusted manually; however, this was done infrequently since the range of particle sizes and densities were fairly consistent for all measured applications.

3.2.5.3 Phase Calibration and Laser Alignment

The PDI used in this study was designed to be used at bench (laboratory) and pilot scale testing facilities under various atmospheric, electrical, and vibrational stress. After the PDI was moved and reinstalled in a new location, a phase calibration was performed and the laser alignment was adjusted.

Phase delays in PDI must be compensated due the sensitivity of particle size to phase and due to the high frequencies that occur within the instrument’s processors, signal cabling, and photodetector electronics. Phase delay is calibrated *in situ* using a calibration diode that produces “synthetic” Doppler signals at the expected frequency of the system to be measured. However, the Doppler frequency is proportional to the measured “real” particle velocity; a guess of the flow conditions must be made. The signal frequency input by the user is estimated using Equation (3.5, below).

$$f_r = f_D + f_s = \frac{v}{\delta} + f_s \quad (3.5)$$

Where:

- f_r = Expected signal frequency [MHz]
- f_D = Doppler frequency [MHz]
- f_s = Bragg cell shift frequency, 40 MHz
- v = Expected mean velocity of the process sample [m/s]
- δ = Fringe spacing, 0.8 μm [m]

With the lasers off, the phase calibration diode is enabled in AIMS under the “Phase Calibration” tab in the “Device Control” menu and the signal is observed with the oscilloscope. The “Amplitude” value is then adjusted until the observed signal on the oscilloscope is approximately 200 mV. The “Quick Phase Calibration” button is selected and the Phase offset of each photodetector pair is automatically updated in the software. The phase offset should only vary by a few degrees. It is important to record the phase offsets prior to recalibrating to ensure the instrument is calibrated correctly. The phase calibration diode will turn itself off at the end of the calibration algorithm.

The amplitude (and the phase delay) is a function of the PMT gain; it is often useful to sample the target aerosol with the uncalibrated PDI on the process sample to determine an approximate PMT gain setting prior to performing the phase calibration.

The custom PDI used in this work requires periodic realignment of the laser crossing to ensure a proper coherent sampling volume is created. The lasers and an aerosol source (airbrush at 100 psig air and H₂O) are turned on and the Doppler burst signals are viewed on the oscilloscope. A fine hex driver is used to turn an adjuster knob on the side of the PDI instrument to produce a clear Doppler signal with a well-defined high and low frequency. The Doppler burst signal should consist of a Gaussian pedestal component and have high amplitude, high frequency beat signal. The Doppler burst should be a symmetric, monomodal peak. A multimodal peak indicates that multiple particles are present in the sampling volume, or that the laser crossing is slightly misaligned. **Figure 3.14–Figure 3.15** show examples of Doppler burst signals as viewed on the oscilloscope.

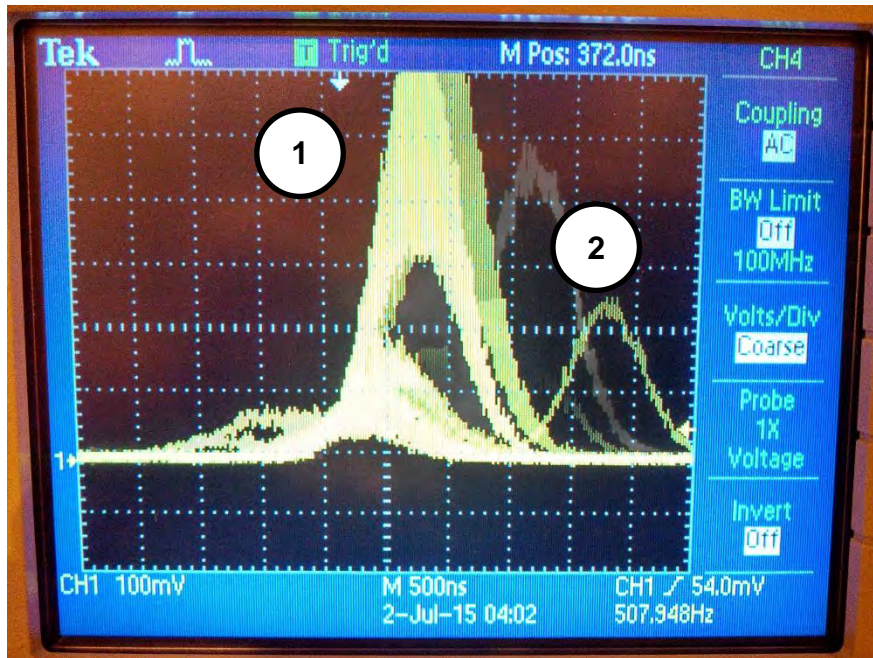


Figure 3.14: Doppler bursts for multiple particle trajectories. Particles passing through both beams in alignment produce a Gaussian pedestal with a thick, high frequency Doppler burst (1). Particles passing through a single beam will only contain a Gaussian pedestal and noise (2).

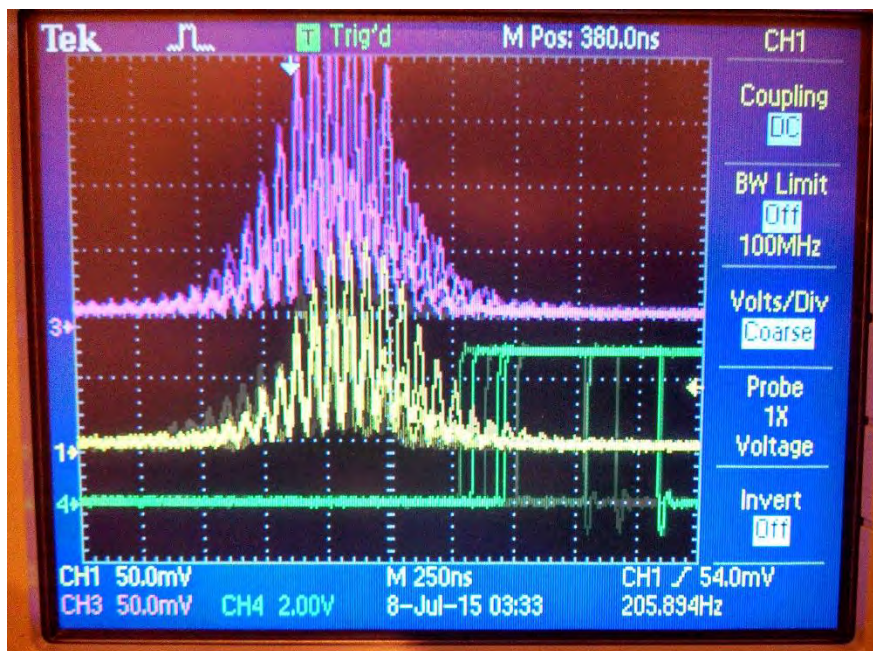


Figure 3.15: Properly aligned Doppler burst with gate signal detection.

3.2.5.4 Validation Criteria

Several criteria are used by AIMS to validate accurate measurements of particles. These validation criteria are used to discard samples which lead to sizing ambiguity or miscounting due to particle coincidence in the sample volume.

3.2.5.5 Velocity Filter

The velocity filter is used mostly to reject samples whose signal-to-noise ratio is very low. The velocity filter can also be used as a coarse truncation tool to specify “outlier” velocities which are not used for field averaging post processing. Generally, nearly all samples pass the velocity filter criteria.

3.2.5.6 Maximum Diameter Difference

PDI uses three photodetectors which size droplets using the phase difference between any two photodetectors. A three detector system provides two independent phase pair differences and one absolute phase difference, which result in redundant droplet size values for each sample (Sipperley et al., 2014). Since one pair of detectors can only detect phase shifts up to 360°, adding a third detector extends the size range considerably. The maximum diameter difference criteria takes advantage of the redundant phase measurements by excluding diameter measurements which are outside of a specified size band of the weighted mean value of the three measurements. If the criteria is not met for any of the three diameter determinations, the sample is completely rejected.

3.2.5.7 Maximum Phase Pair Difference

To a first approximation, the droplet size is a linear function of the phase difference for any two photodetectors; however, certain particle trajectories can lead to a mixture of refractive and reflective scattering. Setting an acceptance bandwidth over the

pure refractive phase difference line will reject particles experiencing mixed mode, or purely reflective scattering. **Figure 3.16** shows a phase difference plot for different photodetector pairs for raw data and for data with a $\pm 20^\circ$ maximum phase pair difference criteria. For non-integer spacing between photodetectors, phase difference lines for refraction and reflection are uniquely spaced such that no ambiguity between modes exists. Reflective signals move in the opposite direction of refractive signals; the phase pair relationship is uniquely valued for scattering modes. Particles that pass along the edge of the sample volume will produce mixed mode scattering which is a combination of reflection and refraction and the phase difference measured by photodetectors will lie in the region between the pure reflection and refraction lines as shown in **Figure 3.17**. The maximum phase pair difference criteria rejects particles scattering light by reflection or mixed mode. Additionally, increasing the value of the beam crossing angle, γ , increases the phase pair difference between refraction and reflection allowing for greater discrimination of scattering modes as well as the ability to measure smaller diameters.

3.2.5.8 Signal Processing

Signal processing takes place in the Advanced Signal Analyzer (ASA). The following section details important parameters which can be found under the “Processors” tab in the “Device Controls” menu.

3.2.5.9 Fast Fourier Transform (FFT) Bins

The measured frequency and phase is calculated using an FFT algorithm. The number of FFT bins is the maximum number of samples that can be collected through the duration of a signal. The resolution can be increased with more bins; however, 1,024 bins are commonly used.

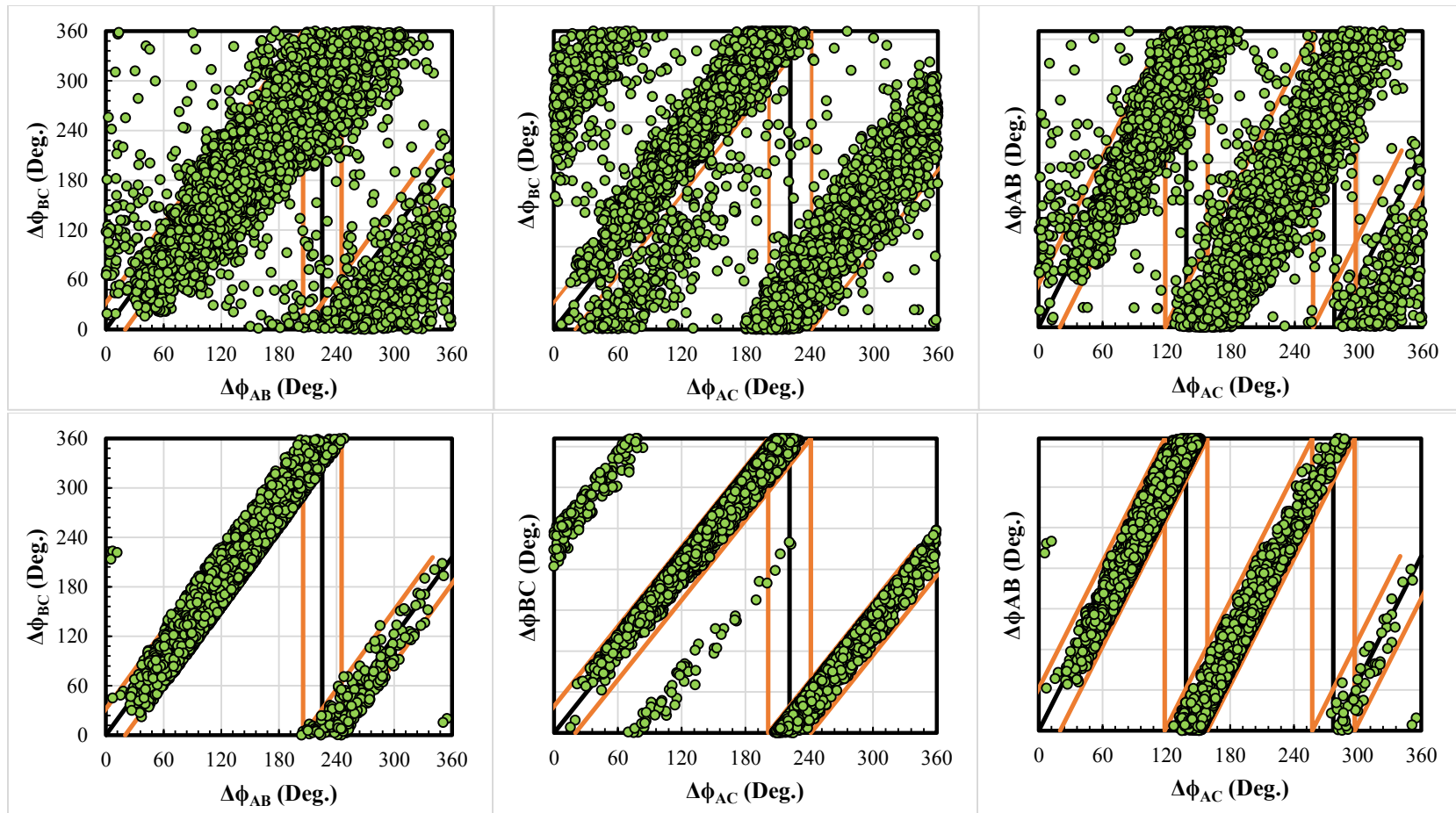


Figure 3.16: Phase difference plots for all three combinations of detectors A,B, and C. The black lines show the exact phase difference expected from an ideal refracting aerosol. The top plots show raw data with no applied validation criteria. The bottom plots show the data with a 20° phase difference criteria (orange lines).

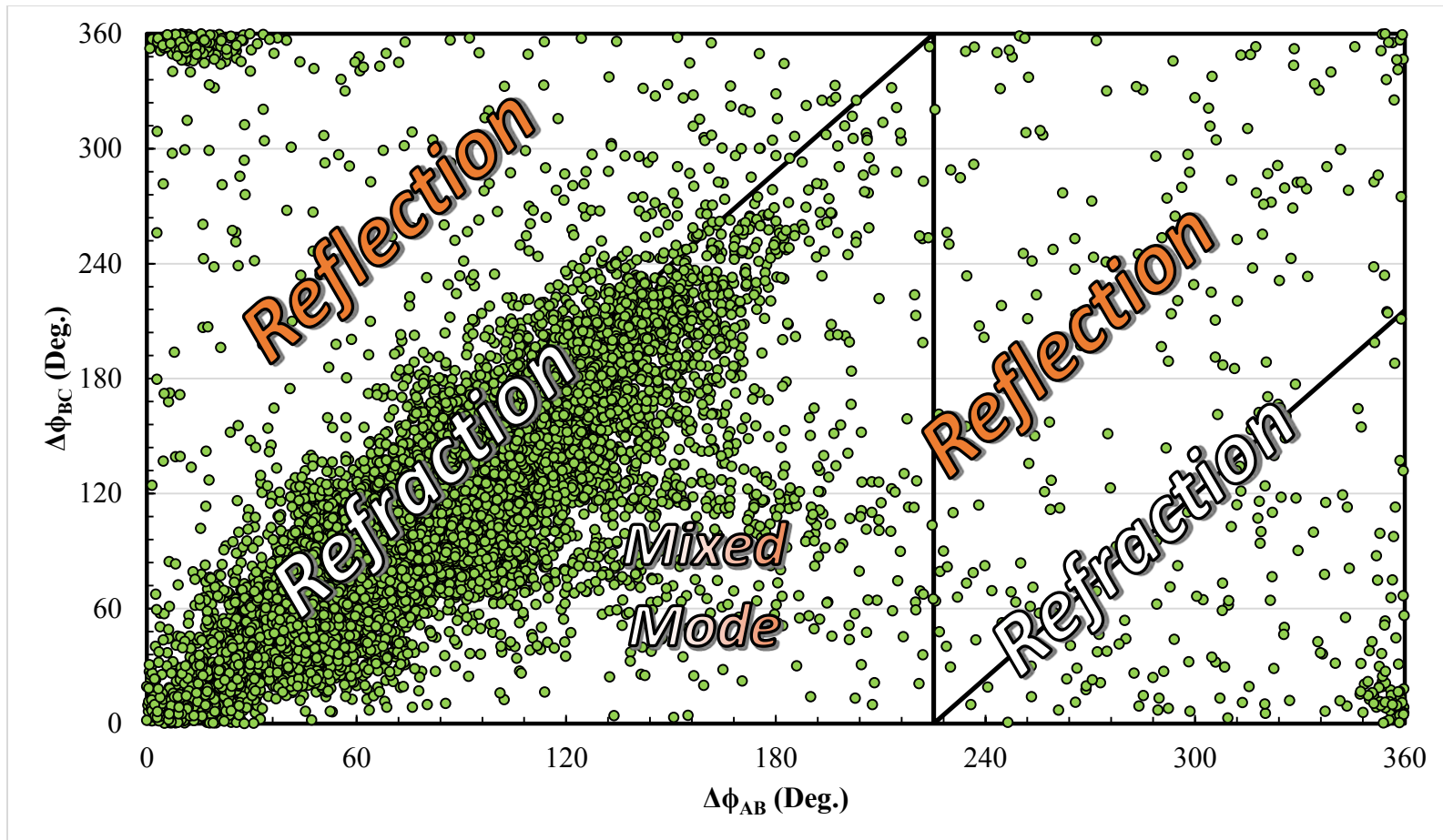


Figure 3.17: A raw phase difference plot for two photodetector pairs operating in refraction mode. The black line represents the exact phase difference for ideal refracting aerosol. Aerosols passing on trajectories which cause pure reflection or mixed mode scattering have phase shift differences which fall in the regions between refraction lines, as indicated in the figure above.

3.2.5.10 Analog Filter

The analog filter reduces high frequency noise as well as removes the sum frequency produced by the frequency mixer.

3.2.5.11 Mixer

The frequency that passes through the analog filter is the raw signal (Doppler plus Bragg Shift) minus the mixer frequency. This allows processed signal frequency to be lowered to a more manageable range. However, the mixer frequency should not be set to where the velocities of the measured particles produce a mixed signal of zero frequency.

3.2.5.12 Variable Mixer

The variable mixer field allows fine adjustment of the mixer frequency for values between 5–45 MHz. Mixer values are usually always set by the auto-setup algorithms.

The sampling rate is the frequency of the analog to digital converter. Since both the real and imaginary components of the signal are analyzed, the sampling rate is effectively double the value specified in AIMS. For high velocity applications, the sampling frequency must meet the Nyquist criterion for the highest sampled frequency. The auto-setup feature is used to set the sampling rate.

3.2.5.13 Burst Detection (BD) Decimation

Signals with low frequency noise can cause spurious particle detection. When higher sampling rates are used, BD decimation eliminates a set factor of the collected samples used by the burst detection system.

3.2.6 Optics

The following section details important optical parameters found under the “Optics” tab in the “Device Controls” menu in AIMS.

3.2.6.1 PMT Gain

Photomultiplier tubes amplify the current of incident photons by several orders of magnitude to produce electrical signals which are proportional to the intensity of the incident light. The “Gain” value adjusts the voltage of the PMT such that coherent light scattered from aerosol passing through the sample volume can be detected. The intensity of scattered light from refraction is proportional to the square of the aerosol diameter; smaller particles require higher PMT gain to be detected. However; as the PMT gain is increased, the noise also increases. Therefore a tradeoff between the minimum detectable size and an acceptable signal-to-noise ratio exists. The PMT gain is usually set manually by observing signal intensity versus diameter plots. The gain is set such that the largest particles just reach saturation of the detectors.

The intensity of scattered light from refraction is proportional to the square of the particle diameter and can be calculated using the analyzer geometry and ray tracing using the Lorenz-Mie solution to the Maxwell equation. Since the lasers are Gaussian beams, the intensity of the scattered light also depends on the trajectory of the particle through the sample volume. The scattered intensity by refraction can be calculated at the limiting trajectories of sampled particles: (1) the maximum intensity will occur for a particle passing through the center of the beams and (2) The minimum intensity will occur for a particle passing through the edge of the sample volume, which in most cases is defined as the laser beam waist, or $I_{Max}(1/e^2)$ (Shakal, 2008). An intensity versus diameter plot and the limiting scattering lines are shown in **Figure 3.18**.

The collection angle of the PDI ensures that refraction is the dominant scattering mechanism observed by the receiver and therefore particles below the minimum refraction intensity are those who scatter by mixed mode or by pure reflection. Assuming a uniformly illuminated sphere, Bachalo (1980) showed that a forward collection angle,

θ , of 30° ensures that light scattered by refraction is approximately 80 times as intense as that scattered by reflection. Intensities measured above the maximum line occur when two particles pass through the beam crossing concurrently.

3.2.6.2 Index of Refraction

Though particle sizing for the sampling angle and scattering mode in this work is insensitive to the index of refraction of the aerosol, the index of refraction can be set in AIMS. A value of 1.33 (H₂O) is the default value.

3.2.6.3 Scattering Mode

The scattering mode used in this study is refraction. The mode can be changed to reflection using the pulldown menu.

3.2.6.4 Data Exporting

Each piece of post processed data can be exported to a specified directory as individual .CSV files or as one collated .CSV file. Export templates can be created by right-clicking any graph of data value found in the “Results” menu, once a data set is loaded, and selecting “Add to Export Template”→“New Export Template”.

During the initial setup of the PDI, export templates were created for all important data. One master template was also created which collates all of the individual data export templates. All data is exported to the specified directory following a successful data acquisition.

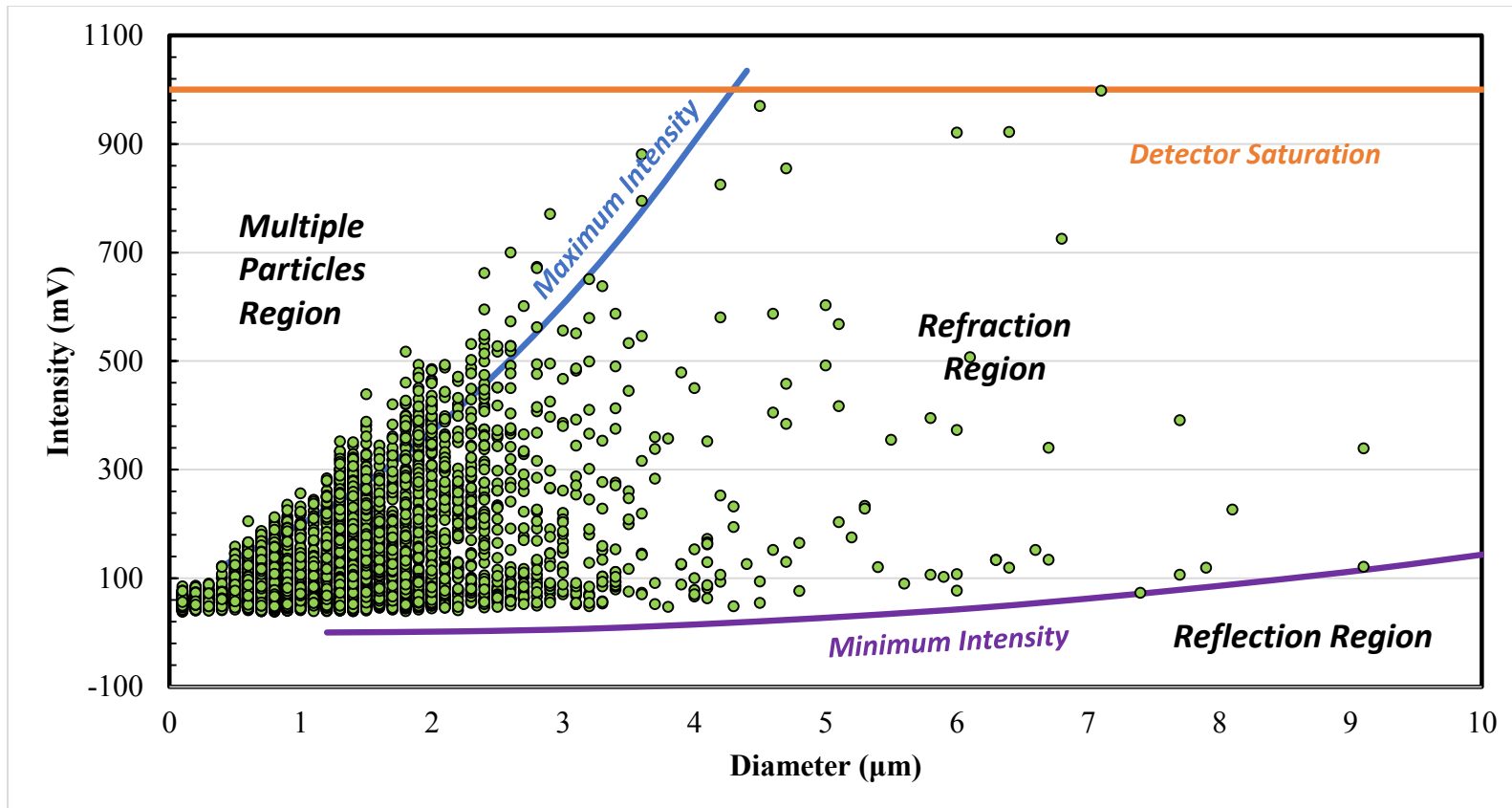


Figure 3.18: A plot of detector intensity versus particle diameter. The intensity of scattered light is assumed to occur by pure refraction and is proportional to the square of the particle diameter (Lorenz-Mie scattering). The **maximum intensity line** refers to a particle passing through the center of the beams. The **minimum intensity line** is for a particle crossing the minimum detection threshold (otherwise the edge of the sample volume).

3.2.7 PDI Calculations

The following section provides an overview of the general equations used to calculate particle size and velocity. The reader is referred to the text by Albrecht et al. (2003) for complete derivations.

3.2.7.1 Velocity

PDI is an extension of Laser Doppler Velocimetry (LDV), otherwise known as Laser Doppler Anemometry (LDA). LDV can be used to measure the velocity of individual particles in a polydisperse field.

A measurement volume is created at the intersection of two coherent beams of light, typically high intensity lasers with wavelengths in the visible portion of the electromagnetic spectrum. The intersection of the beams produces an interference pattern, otherwise called a fringe pattern, of alternating light and dark parallel bands. As particles pass through the probe volume, incident light reflects and refracts creating an observable far-field interference pattern. A photomultiplier tube, placed at an off-axis angle, measures the intensity of the scattered light. The resulting signal is a superposition of a high frequency Doppler (beat) signal and a low-frequency Gaussian pedestal. The Gaussian pedestal is a consequence of the Gaussian intensity profile of the lasers. The Doppler frequency is directly related to the velocity of the particle according to Equation (3.6.

$$v = f_D \delta \quad (3.6)$$

where:

- v = Particle velocity [m/s]
- f_D = Doppler frequency [Hz]

3.2.7.2 Size Determination

Particles passing through the beam intersection scatter refracted light in an interference pattern with a spatial frequency which is correlated to the particle diameter. Multiple detectors placed at known spacing allow measurement of the Doppler burst signal. The arrival of the Doppler burst signal is offset at each detector according to the far-field scattering pattern. The result is a phase shift between the detectors which is linearly correlated to the droplet diameter according to Equation (3.7 below (Van Den Moortel et al., 1997). The aerosol diameter limit of quantification (LOQ) of the custom PDI used in this work is 0.1 μm .

$$d^P = \frac{F \delta \Phi}{360 \Delta l} H \quad (3.7)$$

where:

- d^P = Particle diameter [m]
- F = Receiver focal length [m]
- Φ = Phase shift between any two detectors [deg]
- Δl = Distance between any two detectors [m]
- H = Optical constant [--]

Artium calculates the particle diameter using an average phase difference relationship as reported in Equations (3.8–(3.9 below. **Figure 3.19** shows a visual representation of the Doppler wavelength calculation from the phase shift and the detector geometry.

$$d^P = \frac{F\delta}{s\bar{\Lambda}} \quad (3.8)$$

$$\bar{\Lambda} = 360 \left[\frac{k_{12}S_{12}}{\Phi_{12}} + \frac{k_{13}S_{13}}{\Phi_{13}} + \frac{k_{23}S_{23}}{\Phi_{23}} \right] / [k_{12} + k_{13} + k_{23}] \quad (3.9)$$

where:

- s = Sizing slope factor [--]
- $\bar{\Lambda}$ = Weighted Doppler spatial wavelength [m]
- S_{ij} = Distance between detectors i and j [m]
- k_{ij} = Geometric constant for detectors i and j [m]
- Φ_{ij} = Phase shift between detectors i and k [deg]

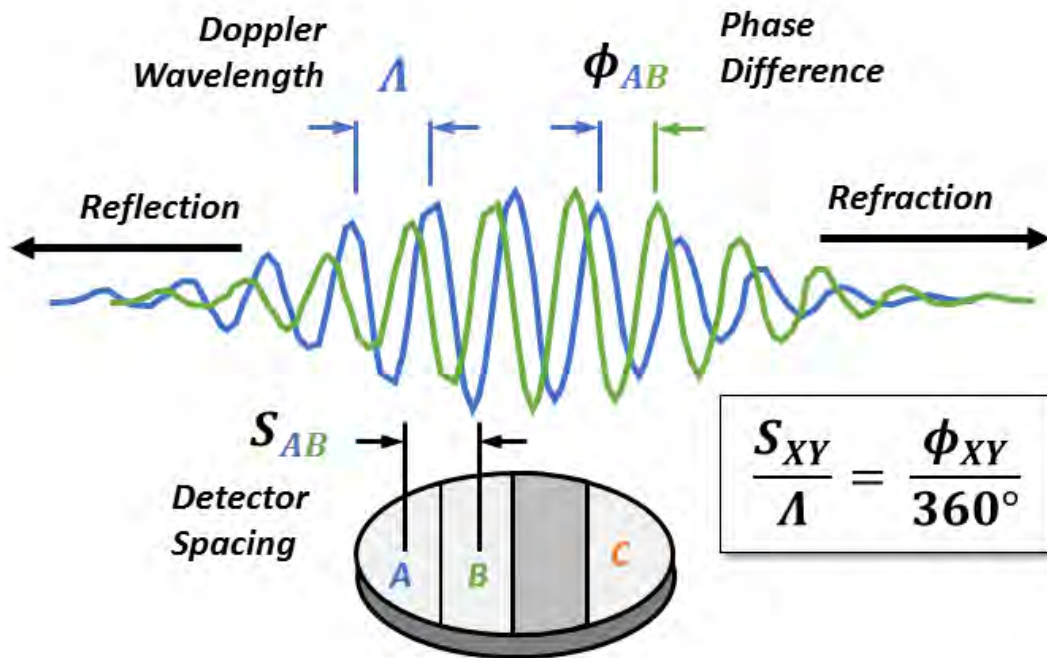


Figure 3.19: Doppler wavelength calculation schematic using the phase difference and the receiver geometry.

3.2.7.3 Probe Volume Correction

Calculating the probe volume, or area, is challenging for many reasons. Detecting a particle requires a minimum scattering intensity such that it can be distinguished from background noise. Particles scatter light in proportion to their surface area and the lasers have a Gaussian intensity profile. Therefore, smaller particles must be closer to the center of the beams to scatter an equivalent amount of light. The result is that the probe area is a function of particle diameter. The probe volume correction (PVC) accounts for the variation of the probe sampling volume with the particle diameter. **Figure 3.20** provides an illustration of the functional dependence of the probe volume width on the particle diameter.

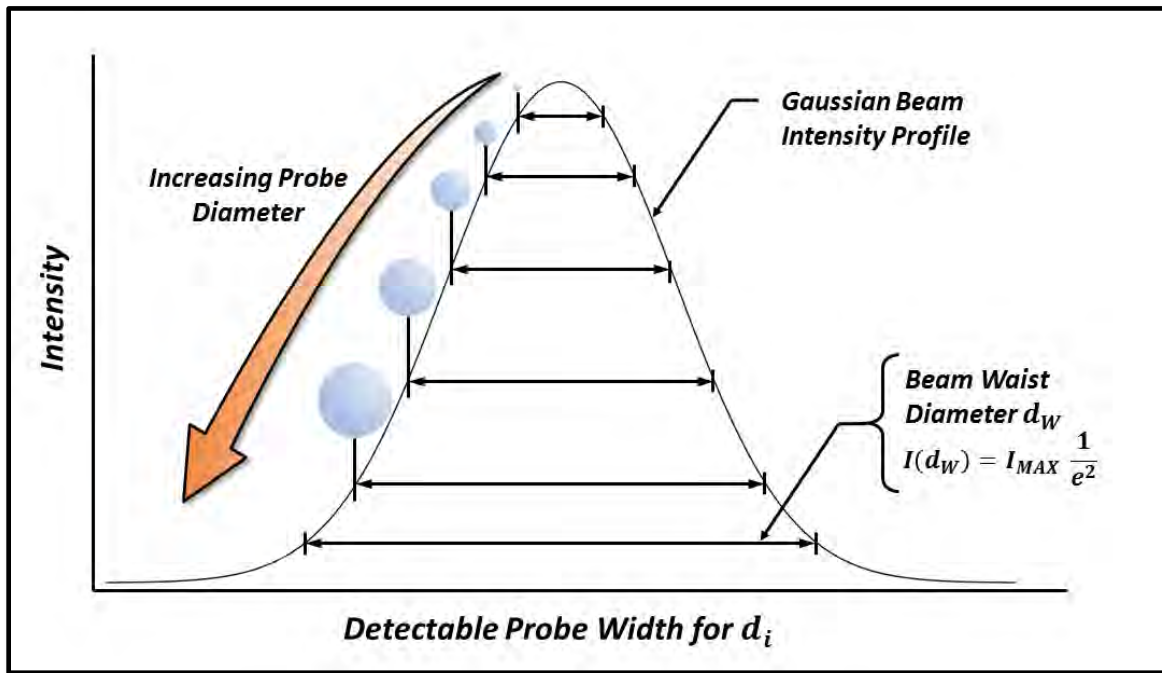


Figure 3.20: Probe volume is a function of particle diameter due to the Gaussian beam intensity profile and the scattering dependency on the square of the particle diameter. The detection volume, and probe width, decreases with decreasing particle diameter.

Correcting the particle flux for variable probe area is done by the transit method. For each detected particle, a total Doppler burst time and velocity are recorded. The traversed distance is then calculated by multiplying velocity by the measured crossing time. AIMS uses a proprietary method for calculating the maximum probe diameter from the collection of transit times. The number of particles in a size class are calculated using Equation (3.10 below).

$$n_c(d^P) = n(d^P)PVC(d^P) \quad (3.10)$$

where:

$n_c(d^P)$ = Corrected number of particles of diameter d^P [part./cm³]

$n(d^P)$ = Measured number of particles of diameter d^P [part./cm³]

$PVC(d^P)$ = Probe volume correction for particles of diameter d^P [--]

The probe volume correction is calculated using Equation (3.11).

$$PVC(d^P) = \frac{D_{max}}{\sqrt{D_{max}^2 - 4 r_w^2 \ln\left(\frac{d_{max}^P}{d^P}\right)}} \quad (3.11)$$

where:

D_{max} = Probe diameter of the largest detectable particle [m]

r_w = Laser beam radius (waist); $1/e^2$ [m]

d_{max}^P = Largest detectable particle diameter [m]

3.2.7.4 Number Density

The number density of the measured aerosol population is calculated using the perpendicular area of the probe volume, the velocity distribution of the particle cloud, and the flux of particles through the area in a given sampling time.

The total number density is given by the summation of the flux and the PVC area. Equation (3.12) shows the swept volume method for calculating the total particle density.

$$ND = \frac{1}{(PA)t_{tot}} \sum_i \frac{n_c(d_i^P)}{|\bar{v}_i|} \quad (3.12)$$

where:

- ND = Total particle density [part./cm³]
- PA = Probe area for the maximum detectable particle diameter [m²]
- t_{tot} = Total sampling time [s]
- $n_c(d_i^P)$ = Probe corrected particle count of diameter class i [part./cm³]
- $|\bar{v}_i|$ = Arithmetic absolute average velocity of diameter class i [m/s]

3.3 SUPPORTING EQUIPMENT

3.3.1 Pilot Plant Sample Blower

A regenerative blower was chosen to provide isokinetic sampling up for duct velocities up to 100 ft/s for PDI and FTIR analysis at pilot plants. The blower is mounted to a C channel skid and the flow rate is controlled manually by a variable speed drive (VSD) and a rotameter. The isokinetic volumetric flow rate was calculated for a 1" Sch. 10 pipe. Sampling bias for larger draw off ports are accounted for using the anisokinetic equations provided in Chapter 2. Specifications for the regenerative blower are shown below in **Table 3.10**.

Table 3.10: Ametek® Rotron® EN303AG58L Regenerative Blower Technical Specifications

Parameter	Value/Description
Motor enclosure - Shaft Mtl.	Explosion-proof - CS
Horsepower	0.5
Phase - Frequency	Single - 60 Hz
Voltage	115/230 VAC
Maximum flow rate	55 SCFM
Maximum pressure	55" H ₂ O
Maximum vacuum	45" H ₂ O
Motor nameplate amps	9.0/4.5 A
Max. blower amps	7.2/3.6 A
Inrush amps	38/19 A
Starter size	00/00
Service factor	1.0
Thermal protection	Not required
XP motor class - group	1-D
Shipping weight	52 lbs. (23.6 kg)
Connections	1-1/4" NPT

Chapter 4: Aerosol Growth Column (AGC) – Experimental Methods

This chapter describes the design and operation of the bench-scale laboratory research conducted on the Aerosol Growth Column (AGC) apparatus used throughout the course of this study. The AGC was designed as a multipurpose experiment; the apparatus was used to collect data (Chapter 5) for the purposes of aerosol growth modeling (Chapter 7) as well as to test pilot plant aerosol generation and analysis equipment (Chapter 6).

The primary data collected in an AGC experiment falls into three categories: (1) aerosol phase analysis by PDI, (2) inlet and outlet total (gas and aerosol) phase concentrations by FTIR, and (3) system operation data by LabVIEW™ data acquisition. Additionally, the solvent loading and amine concentration were characterized by cation chromatography and total inorganic carbon (TIC), respectively. For brevity, the reader is referred to Freeman (2011) for detailed descriptions of solvent analysis.

All data types are collated by (clock-synched) timestamp and post-processed by an algorithm written in Microsoft® Excel® Visual Basic® for Applications (VBA) and output into a summary table. Operating conditions, aerosol size distributions, total particle densities, and FTIR data are all tabulated and sorted by data collection time.

This chapter details the design basis, physical apparatus description, flow and wiring diagrams, operating procedures, and data interpretation for experimentation with the AGC. Tabulated results and conclusions can be found in Chapter 5.

4.1 NEED FOR AGC EXPERIMENTS

4.1.1 Aerosol Study Historical Development

At the beginning of this project, literature data concerning the impact of aerosols on the emission rate of amine from scrubbed flue gas was scarce. However, early pilot

plant studies experiencing very high amine carryover quickly recognized that high emissions rates were correlated with known nuclei sources, particularly fly ash/particulate matter (PM) and SO₃/H₂SO₄.

In 2011, Kamijo et al. presented pilot test results for both KS-1TM and monoethanolamine (MEA) which showed that emissions were proportional to inlet SO₃ concentration (Kamijo et al., 2013). Amine levels out of the wash section were 0.4–23.2 ppmv and 0.8–67.5 ppmv for KS-1TM and MEA, respectively, for 0–3 ppmv inlet SO₃. The outlet gas opacity provided visual confirmation of aerosol at the direct-contact cooler (DCC) and wash outlets.

Shortly thereafter, a joint study by the Netherlands Organisation for Applied Scientific Research (TNO) and The Foundation for Scientific and Industrial Research (SINTEF) at the Maasvlakte pilot plant provided one of the first data sets containing particle size, particle concentration, and online total phase measurements (van der Gijp et al., 2012; Kolderup et al., 2012). The presence of aerosol-bound amine emissions was confirmed by the addition of lithium and rubidium carbonate (Li₂CO₃, Rb₂CO₃) tracers in the absorber solvent and water wash loops; physical entrainment of the solvent and wash streams was found to be negligible.

Detailed characterization of the particle phase was attempted using a combination of light extinction measurements, an Aerodynamic Particle Sizer (APS), an Electrical Low-Pressure Impactor (ELPI), installation of a high efficiency droplet capture device called the Brownian Demister Unit (BDU), and mass balances using condensate collection (van der Gijp et al., 2012; Kolderup et al., 2012). The BDU was installed downstream of the water wash. The Sauter-mean droplet diameter (D₃₂) at top of the water wash tower prior to the BDU was reported to be 0.76–7.88 μm and decreased to 0.2–1.74 μm at the BDU outlet. The total particle density at the BDU inlet was 2.4x10⁵–

3.9×10^6 part./cm³ and 1.4×10^4 – 9.4×10^4 part./cm³ for the ELPI and APS, respectively, showing a large discrepancy between the two analytical techniques.

It was noted that the use of diluters, impaction pre-stages, vibrational sensitivity of the ELPI, and the well documented large particle bias of the APS led to quantification differences between the methods as well as increased absolute error of each individual measurement technique.

4.1.2 Early UT Aerosol Work

Around that time, work began at The University of Texas at Austin by studying the problem from a fundamental viewpoint through development of a simplified heat and mass transfer model for aerosols in CO₂ capture systems. It was theorized that by altering the operating conditions or physical design of the CO₂ capture plant, aerosol capture could be facilitated by condensational growth or evaporative shrinking; condensational growth is often used as a conditioning step for total particle density measurements by condensational particle counters (CPC). CPCs pass nanometer sized particles through a chamber saturated by a condensable vapor, usually H₂O or butanol, where the particles grow to sizes that can be detected using optical techniques.

Moreover, several aerosol researchers in literature have pointed to efficient removal of high density aerosols in packed columns by heterogeneous nucleation (condensation) (Heidenreich et al., 2000; Johannessen et al., 1997; Calvert et al., 1984). By effectively selecting operating conditions, they argue, and experimentally confirm, that high degrees of supersaturation can be achieved which can “activate” aerosol growth and subsequently increase their capture in randomly packed columns. The degree of supersaturation, and the influence of operating conditions is characterized by the ratio of heat and mass transfer rates, given by the Lewis number. In the work by Heidenreich and

co-authors, they demonstrated that high concentrations (10^6 particles/cm³) of submicron particles of variable starting composition can be efficiently collected using a two-stage cascade counter-current contactor by increasing the temperature difference between the inlet fluids (Heidenreich et al., 2000). Cascaded column designs to remove aerosols through growth conditioning would be readily incorporated into existing water wash and acid wash tower configurations.

To confirm the theorized influence of operating parameters on aerosol growth and capture, an experimental apparatus capable of generating and analyzing aerosols in relevant concentrations and size ranges was needed. The AGC was developed as a CO₂ absorber analog, the Liquid Vaporizer and Injector (LVI) was built to produce homogeneously nucleated submicron seed nuclei, and the PDI was selected to analyze particle fields *in situ* to reduce extractive sampling errors.

4.2 AEROSOL GROWTH COLUMN

The AGC design was determined by the several competing factors. Since a CO₂ stripper was omitted for operation and control simplification, the absorber column operates as a batch experiment. In order to minimize solvent inventory and consumables, the column dimensions were minimized. However, the packing density of small-scale, laboratory packings would be too high and unwanted particle capture would occur; additionally, the approximation of full-scale, randomly-packed CO₂ absorber performance using spray or fractal distribution would worsen considerably and manufacturing and maintenance of equipment would become more difficult as part sizes decrease. The result of the tradeoff was to select a column diameter of 1.5”.

The gas flowrate was chosen to match the superficial velocity of a larger-scale CO₂ absorber of approximately 1–6 ft/s. Selecting the range of inlet CO₂ between 0 and

20 vol %, assuming a mass transfer coefficient (k'_g) for CO₂ (implicitly defining the loading and amine concentration), setting a maximum column height, and setting the CO₂ removal rate at 90% determined the solvent flowrate. Additional solvent flow capacity was added such that the reaction enthalpy of CO₂ absorption capture could be pushed toward the bottom of the column: the temperature bulge would be minimized and the column could operate nearly isothermally. The total solvent inventory was set such that the loading change would be less than 5% for 8 m PZ and a capture rate of 90% for 12 vol % CO₂ inlet gas over a given experiment of approximately eight hours.

A current piping and instrumentation diagram (P&ID) of the AGC is shown in **Figure 4.1–Figure 4.3**. The P&ID is broken up into three sections: (**Figure 4.1**) gas distribution and mixing, including the LVI, (**Figure 4.2**) pre- and post-gas preparation including presaturation and condensation, and (**Figure 4.3**) the absorber section with local analysis.

4.2.1 Nitrogen (N₂)

N₂ is a distributed utility taken from a large, outdoor dewar. The supply is split following an isolation valve into four streams used for the absorber gas supply, the LVI gas supply, the PDI purge gas, and FTIR maintenance and calibration.

The flowrate to the absorber is controlled by an analog 100 SLPM Brooks 5851 I-Series mass-flow controller (MFC) (Tag FCV1301-1) connected to an NI 9265 4-ch, 20 mA current output module and an NI 9203 8-ch, 20 mA current input module. The inlet pressure to the MFC is regulated at 40 psig. Connection is made with a 15 pin D-Sub cable at the controller side and crimp pin connections at the NI module side. The NI modules are connected to a cDAQ-9174 USB chassis which is controlled by LabVIEW™ via a laptop and USB 2.0 connection.

The flowrate to the LVI is controlled by a pressure regulator.

The flowrate to the FTIR optical purge line is controlled by a pressure regulator with a Bird Precision critical orifice (0.004" ID). The regulator sets the pressure upstream of the orifice which allows very precise control of the small flowrate. The FTIR heated, manual multipoint switching box has two three-way valves and an SS-1RS4-SH needle valve which are used to control the flowrate of background (N₂) gas and air. The stream switcher is temperature-controlled to 180 °C and is connected to a temperature controller using a 4-pin Amphenol power line and a K-type thermocouple.

4.2.2 Carbon Dioxide (CO₂)

Bone dry, Gr. 3.0 CO₂ (Airgas[®] CDBD200) is stored in an adjacent lab and is sent through an overhead line into the AGC vent hood. The delivery pressure is regulated at 50 psig using a Y11-N245D320, CGA320 regulator attached to the tank. Alternatively, CO₂ is drawn from a large outdoor dewar. The delivery pressure is controlled by a large regulator located on the dewar tank pad and the CO₂ line is isolated by a ball valve located on the building exterior just upstream of the external wall pass through. The flowrate of CO₂ is controlled by a 15 SLPM Brooks 5850 I-Series MFC (Tag FCV1301-2) using the same NI modules and chassis as described for N₂.

At the end of experiments, the CO₂ line is isolated at the AGC wall isolation valve and the remaining CO₂ is bled to a vent hood to prevent leakage from the cylinder.

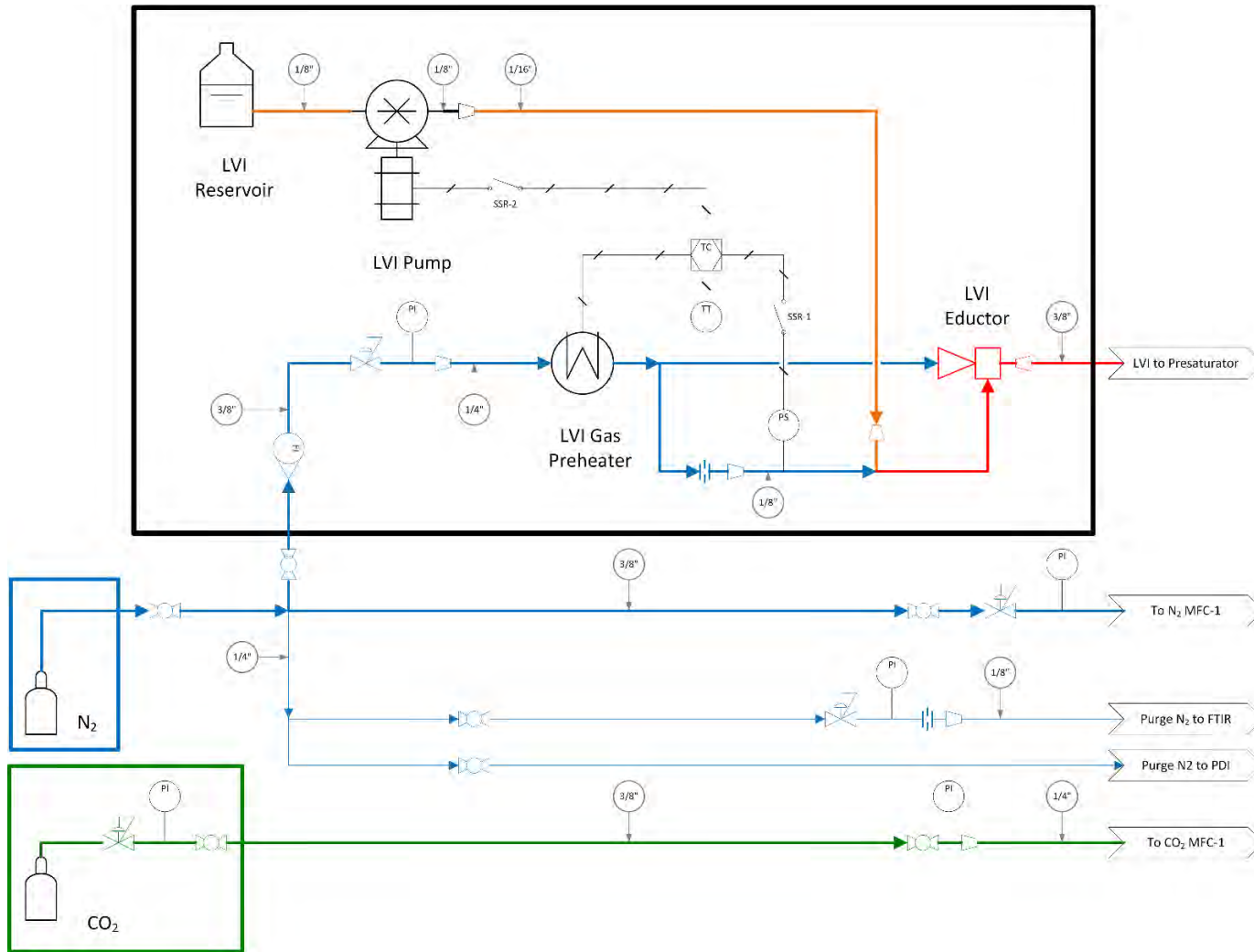


Figure 4.1: AGC P&ID #1. Gas distribution and LVI (bypass).

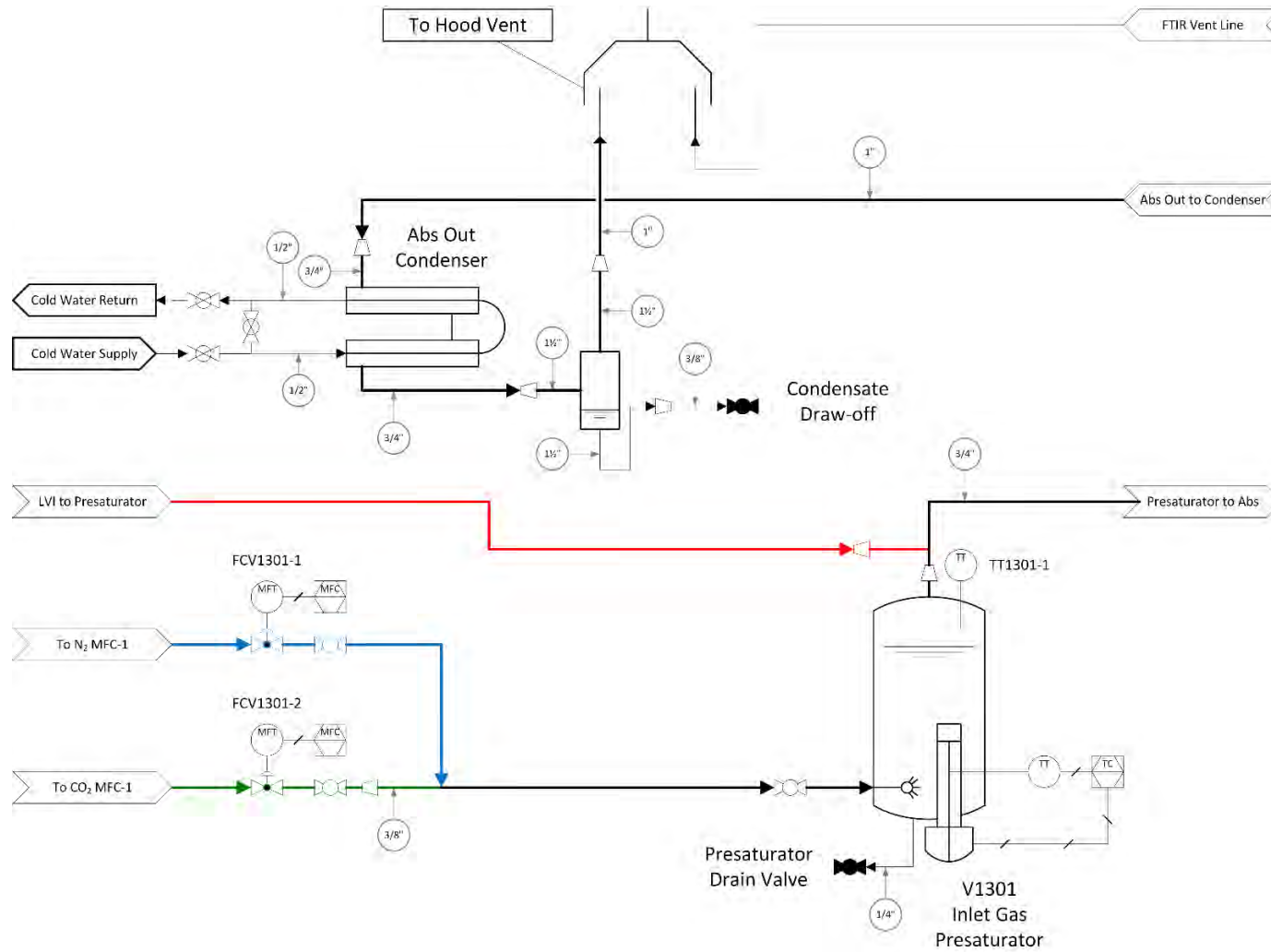


Figure 4.2: AGC P&ID #2. Inlet gas presaturation and mixing. Outlet gas condensation and vent.

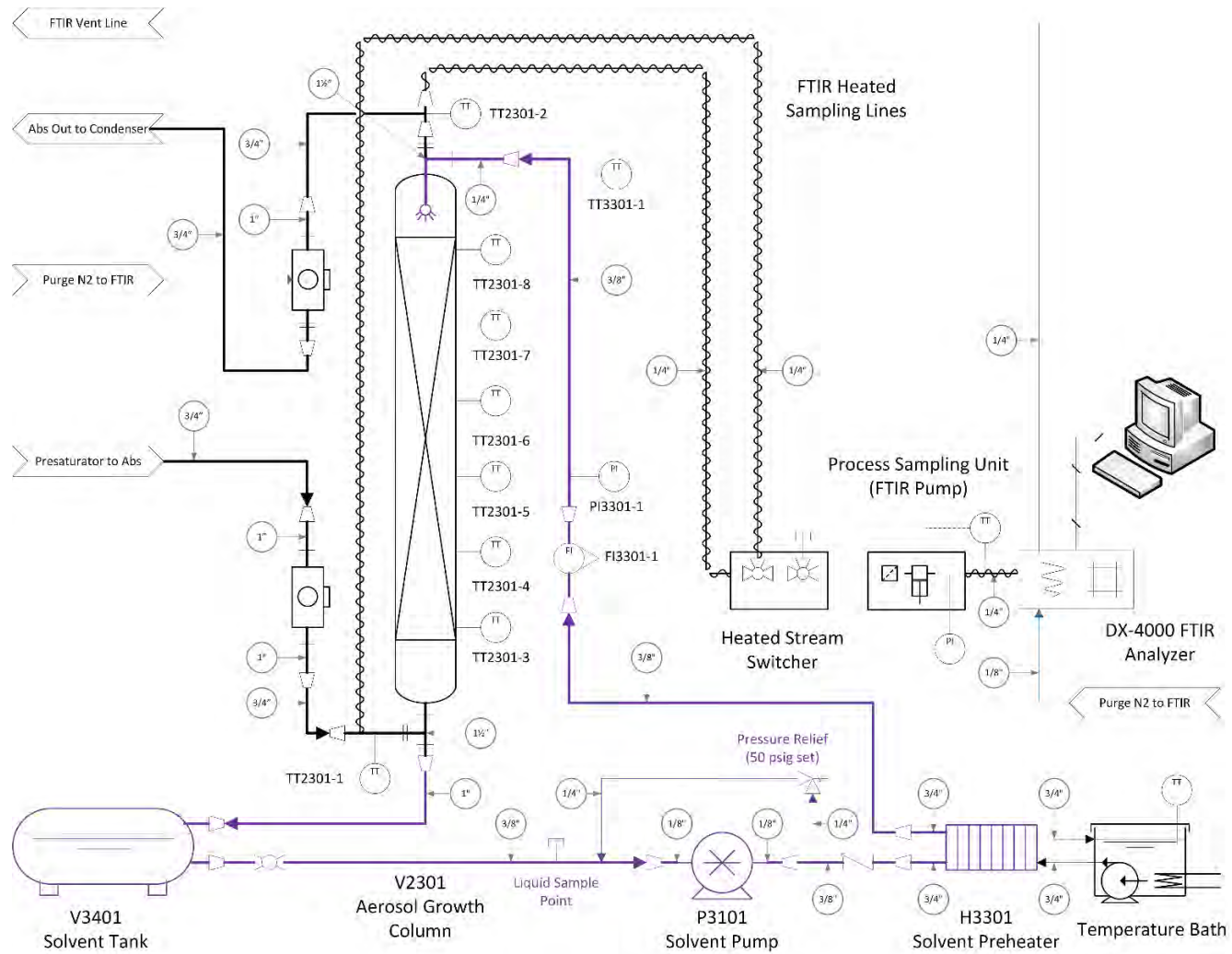


Figure 4.3: AGC P&ID #3. Absorber column, solvent loop, and analysis locations.

4.2.3 H₂O Presaturator

The N₂/CO₂ gas streams are mixed at a Swagelok tee and are bubbled through a presaturator tank (Tag V1301) to approximately maintain H₂O balance within the absorber column. The presaturator (**Figure 4.2**) for the AGC is constructed of 6" 304SS Sch. 10 pipe with #150 RFSO flanges. Temperature is controlled with a screw-plug immersion heater with a relayed temperature controller. The head-space temperature is logged with a separate K-type thermocouple (Tag TT1301-1) connected to a 4-ch ± 80 mV NI-9211 module.

The inlet gas is sparged into the presaturator through a 3/8" straight tube with several small drilled holes. The total liquid height in the saturator is maintained over 20".

The hot gas mixture from the LVI is mixed with the saturated process gas at the outlet of the presaturator in a 3/4" stainless steel threaded tee fitting.

4.2.4 Absorber Column

The absorption section of the AGC (**Figure 4.3**) is constructed out of a 1½" 304SS Sch. 10 pipe with #150 RFSO flanged end connections (Tag V2301). Gylon[®] 3500 gaskets were used for all flange connections. The packing is supported using removable lugs and a mesh screen support; the lugs are stainless steel rods whose length is set by welded Swagelok tube fittings. The mesh screen packing support rests on the lugs. The column can support up to 6' of packing. Six feet of packing was chosen for two reasons: (1) to get approximate CO₂ removal performance as a real, full-scale absorption column, and (2) to provide equivalent residence time for particle growth. At nominal conditions, the residence time in the packing is 2.5 seconds for the AGC, and about 5 seconds in the Pickle Research Center (PRC) pilot plant column. The packing used in this work was RSR 0.3 random packing.

Gas is introduced into a flanged tee at the bottom of the column. A gas temperature measurement (K-type thermocouple) (Tag TT2301-1) and an FTIR sample point constructed from a 3/4" threaded pipe tee reduced to a 1/4" tubing connections using a reducer bushings and a Swagelok® adapters are located just upstream of the flanged inlet tee. The gas outlet has a similar temperature/FTIR measurement point (Tag TT2301-2) configuration.

The temperature profile across the packed section is measured by six, K-type thermocouples (Tags TT2301-3 through TT2301-8) connected to an NI 9213 16-ch, ±78 mV thermocouple module. The column is wrapped in R6.3, aluminum-clad, elastomeric insulation.

Pressure drop across the packed section is measured using pressure taps located at the gas inlet and outlet tees and a manometer.

4.2.5 Solvent Loop

Solvent is drawn from a 16 gal SS tight-head drum (The Cary Company 26B6SS) (Tag V3401) by a Micropump® (Tag P3101) A-mount suction shoe pump head controlled by a Cole Parmer Console Drive. The flowrate is measured by a rotameter (Omega FL46302) (Tag FI3301-1). The flowrate is corrected for density using Equation (4.1).

$$Q_{Act}(GPM) = Q_{Read}(GPM) \sqrt{\frac{1.36 - [\rho^{Solv}(T^{Solv})/\rho^{H_2O}(T^{Ref})]}{0.36[\rho^{Solv}(T^{Solv})/\rho^{H_2O}(T^{Ref})]}} \quad (4.1)$$

where:

$Q_{Act}(GPM)$ = Volumetric flowrate of solvent at the actual solvent temperature (density) [GPM]

$Q_{Read}(GPM)$ = Volumetric flowrate of solvent at the reference conditions (H₂O at 70 °F) [GPM]

$\rho^{Solv}(T^{Solv})$ = Mass density of the solvent at the measured solvent temperature [kg/m³]

$\rho^{H_2O}(T^{Ref})$ = Mass density of the reference fluid (H₂O) at the reference temperature (70 °F) [kg/m³]

The density of the solvent was calculated using the measured solvent loading and amine concentration. The mass density correlation for PZ is taken from the Fawkes model user subroutine (vl2u2.f) Frailie et. al (2011) and is stated in Equation (4.2).

$$\rho^L = 1000[E + FT^L]\ln[Ax_{CO_2}^A + Bx_{PZ}^A + C\alpha + D] \quad (4.2)$$

where:

ρ^L = Mass density of loaded, aqueous PZ solution [kg/m³]

T^L = Liquid temperature [K]

x_i^A = Apparent mole fraction of component i [--]

α = CO₂ loading [mol CO₂/mol alkalinity]

A = 2.676

B = -3.0977 x 10⁻²

C = -7.26176 x 10⁻²

D = 2.102569

E = 1.5494

F = -5.728 x 10⁻⁴

Apparent mole fractions are calculated using the total molar quantity of a particular basic constituent molecule, regardless of speciation; all species containing a constituent component are summed together. Equations for PZ and CO₂ are shown in Equations (4.3)–(4.4), respectively.

$$x_{PZ}^A = \frac{C_{PZ}}{\left[\frac{1000}{MW_{H_2O}} + C_{PZ}(1 + 2\alpha) \right]} \quad (4.3)$$

$$x_{CO_2}^A = \frac{2\alpha C_{PZ}}{\left[\frac{1000}{MW_{H_2O}} + C_{PZ}(1 + 2\alpha) \right]} \quad (4.4)$$

where:

MW_{H_2O} = Molecular weight of H₂O [g/g-mol]

C_{PZ} = Concentration of PZ, molal [mol PZ/kg H₂O]

The solvent temperature is controlled by cross exchange with recirculated H₂O provided by a Lauda ECO E4G temperature bath. The cross exchanger is a Thermal Transfer Systems AN14-20H plate-and-frame heat exchanger (Tag H3301). The solvent is delivered into the top of the column using hollow-cone spray nozzles (Kyser and Associates 1/4A-316SS2 & 1/4A-316SS-5) connected to a blind flange. The solvent temperature is measured at the flange using a K-Type thermocouple (Tag TT3301-1). The CO₂-rich liquid drains through a 1" ID gravity line back into the solvent tank.

A pressure relief valve, set at 50 psig, is located at the pump discharge to protect against failure from flow blockage. The relief discharge is sent to the suction side of the pump.

4.2.6 Condenser

A countercurrent, shell-and-tube condenser (**Figure 4.2**) was designed and built to control condensation of the saturated gas exiting the absorber column. Gas passes through the shell-side and cooling H₂O on the tube-side. Graphite ferrules were used on the tubes so they can be removed so that all the shell and tube surfaces can be cleaned periodically. The condenser area was designed using a heat transfer coefficient of 400 W/m²·K and assuming a cooling water temperature of 10 °C.

The cooled gas exiting the exchanger is sent to a 2" threaded pipe tee to reduce the velocity such that condensate will drop out and drain to the condensate collection point located at the bottom of the column. The amount of condensate is observable in a clear tubing line with an isolation valve. The condensate is collected in a 5 gal plastic

carboy and is mixed back into the solvent inventory. Gas exits the knock-out tee at the top of the vent hood.

4.2.7 Liquid Sampling

A liquid sampling port was added on the suction side of the solvent pump. The sample port consists of a 3/8" Swagelok® tee with a 12.7 mm OD RESTEK® BTO Septa. Liquid samples are drawn using a 2 mL syringe and are transferred to 4 mL (1 dr.) amber vials for subsequent analysis.

Initially, the sample location was downstream of the solvent pump; however, as the pressure in the line increased, the septum would swell and the syringe plunger would be forced outward. Relocating the sample port upstream of the pump reduced swelling and possible leakage of the septum making sampling safer and easier.

4.2.7.1 AGC Thermocouple Calibration

All system thermocouples were calibrated using an Ametek® Jofra ETC-125 A calibrator. The calibrator contains three thermowells for variable thermocouple diameters. The thermowells sit inside a temperature controlled space capable of -10–125 °C and ±0.5 °C accuracy. Once the calibration set point was reached, the calibrator maintained stable operation for three minutes before a calibration data point was recorded. The thermocouple reading was recorded on LabVIEW™ and averaged over a minute. Overall, seven points were recorded for each thermocouple ranging from 20–80 °C in ten degree increments. **Table 4.1** shows the linear calibration parameters and raw data for the thermocouples used on the AGC.

Table 4.1: AGC thermocouple calibration raw data and linear fitting parameters.
All temperature are in °C.

Cal. (°C)	TT 1301-1	TT 2301-1	TT 2301-2	TT 2301-3	TT 2301-4	TT 2301-5	TT 2301-6	TT 2301-7	TT 2301-8	TT 3301-1
20.0	19.70	20.38	20.29	19.58	19.80	19.96	20.01	20.00	20.05	20.58
30.0	29.78	30.23	29.99	29.41	29.68	29.72	29.80	29.79	29.72	30.26
40.0	39.88	39.88	39.78	39.30	39.56	39.58	39.67	39.64	39.51	40.11
50.0	49.95	49.69	49.62	49.19	49.57	49.46	49.57	49.51	49.31	49.94
60.0	59.97	59.57	59.47	59.07	59.54	59.34	59.34	59.38	59.03	59.80
70.0	70.01	69.40	69.35	68.98	69.52	69.27	69.27	69.25	68.84	69.63
80.0	80.04	79.36	79.28	78.93	79.53	79.23	79.23	79.02	78.68	79.52
<i>Slope</i>	<i>0.994</i>	<i>1.018</i>	<i>1.017</i>	<i>1.011</i>	<i>1.004</i>	<i>1.012</i>	<i>1.014</i>	<i>1.016</i>	<i>1.023</i>	<i>1.017</i>
<i>Inter.</i>	<i>0.374</i>	<i>-0.697</i>	<i>-0.516</i>	<i>0.251</i>	<i>0.196</i>	<i>-0.104</i>	<i>-0.225</i>	<i>-0.281</i>	<i>-0.450</i>	<i>-0.839</i>

4.2.8 AGC Controls and Data Acquisition

The AGC is controlled using an application developed in LabVIEW™. The front panel display is used to control the N₂ and CO₂ set points, the data sampling rate, and provide visualization of the various temperature and flow readings. Data is written to an Excel spreadsheet whose name is prompted via window input at the first occurrence of data collection.

The back panel (block diagram) contains the function blocks, signal/flow conversion equations, and pin assignments for physical and virtual channels which are configured in the DAQ Assistant blocks.

Analog-to-digital conversion and internal marshalling occur at the chassis controller. The chassis connects to a laptop by a USB type B cable. The control enclosure and wiring is shown in **Figure 4.4**. All wiring colors match the current physical state of the AGC. Dashed lines are used to indicate wires with white striping.

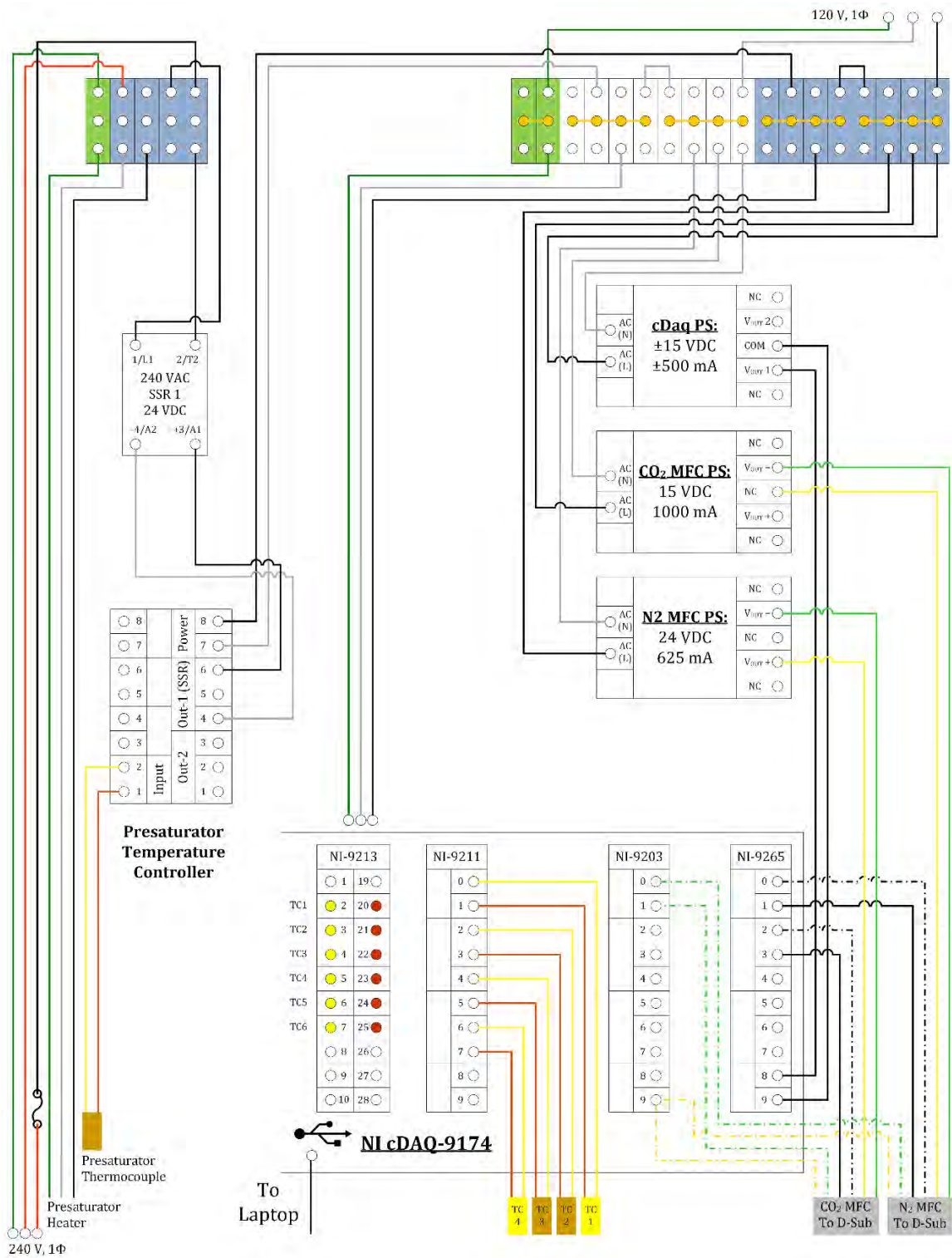


Figure 4.4: AGC control enclosure and wiring diagram.

4.3 AEROSOL LOSSES

A conservative estimate of the aerosol losses between the inlet and outlet PDI cell locations can be made using the loss equations in Chapter 2. The total efficiency includes six feet of 1.5" Sch. 10 pipe, six feet of 1/2" tubing, one 90° bend in 1/2" tubing, one 180° bend in 1/2" tubing, one 90° constriction from 1.5" Sch. 10 pipe to 1/2" tubing, and Brownian diffusion losses in the six foot packed section. Impaction and interception in the packing was assumed negligible. The total particle efficiency is shown in **Figure 4.5**, below.

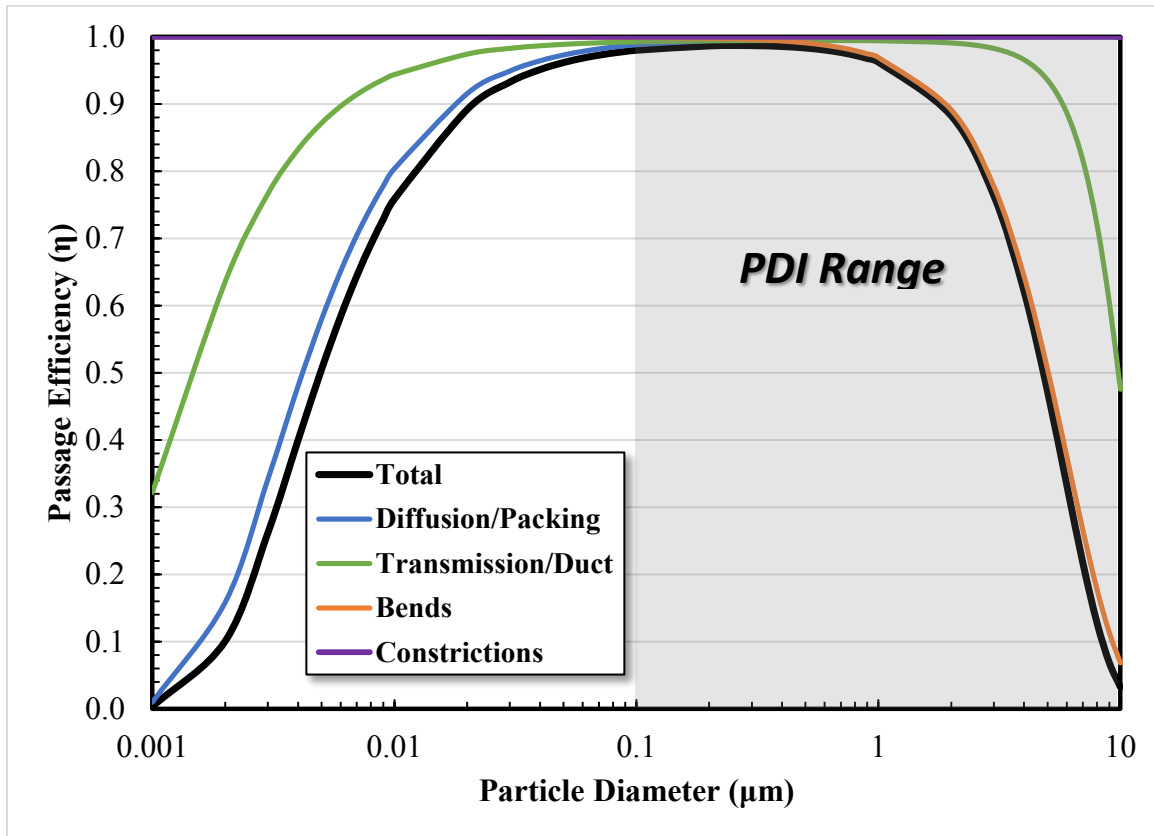


Figure 4.5: Calculated particle passage efficiency for the AGC assuming a total gas flowrate of 60 SLPM and a particle density of 1100 kg/m³. The total efficiency is the product of the individual efficiencies.

Brownian diffusion losses were calculated using a transfer unit (NTU) analogy with CO₂ to approximate turbulent effects captured by the molecular transfer coefficient which is a function of the fluid physical properties and flow dynamics. The number of gas-side mass transfer units is proportional to the diffusivity of the molecule raised to the two-thirds power (Equation (4.5)).

$$NTU_{CO_2}^G \propto D_{CO_2}^G{}^{2/3} \quad (4.5)$$

where:

$NTU_{CO_2}^G$ = Number of gas-side transfer units for CO₂ in structured packing [--]

$D_{CO_2}^G$ = Molecular diffusion coefficient of CO₂ [m/s²]

Assuming that aerosol motion by diffusion is analogous to molecular diffusion, which is exact at diminishing length scales, the number of transfer units for particle capture can be calculated by the ratio of the molecular and Brownian diffusion coefficients. Using a conservative estimate for the height of a transfer unit (HTU) of 0.2 m (taken from a brochure for absorption of NH₃ into H₂O), the number of gas-side transfer units for CO₂ in six feet of packing is between nine and ten (Cai et al., 2009). The number of particle transfer units, and therefore the removal, are calculated using Equations (4.6)–(4.7). The Brownian diffusion coefficient includes the Cunningham slip correction (Equation (2.22)).

$$NTU^P \cong NTU_{CO_2}^G \left[\frac{D^P}{D_{CO_2}^G} \right]^{2/3} \quad (4.6)$$

$$Rem(\%) = \left[1 - \frac{1}{\exp(NTU^P)} \right] \times 100\% \quad (4.7)$$

where:

Rem = Fraction of particles removed by Brownian Diffusion [%]

The main particle loss mechanisms in the AGC are Brownian diffusion below 0.1 μm and bend losses above 1 μm . However, in the measurement range of the PDI, only bend and transmission losses are significant. The losses in this region are a function of the gas velocity and the particle density. Due to the height restrictions of the vent hood, bends are unavoidable. Fortunately, the aerosols produced by the LVI and the airbrush used for PDI calibration reside below 4 μm where the total transmission efficiency is over 60% from the inlet to outlet PDI measurement points.

Increasing the duct diameter would decrease the bend deposition at the expense of increased deposition in the duct due to a transition to laminar flow.

4.4 LIQUID VAPORIZER AND INJECTOR (LVI)

The primary mechanism for creating aerosols at both the bench and pilot scale was to homogeneously nucleate vaporized sulfuric acid in the presence of water vapor. The piece of hardware designed and constructed for H_2SO_4 vaporization, called the Liquid Vaporizer and Injector (LVI), was supplied by Air Quality Analytical, Inc. and was delivered to The University of Texas at Austin (Air Quality Analytical, 2013).

Several changes and subsequent tests involving the LVI system were made throughout the course of this study and can be found cataloged in Appendix C. The purpose of this section is to provide an overview of the operating principles of the LVI and to describe the current hardware state.

4.4.1 Safety

The LVI system heats H_2SO_4 to 325 $^\circ\text{C}$; although, the actual temperature at the injection point is unknown and is a strong function of the mixing ratio between the process gas and the aerosol laden injection gas. The original gas lines were Tygon[®] 3350

tubing. The injection point is covered by ceramic insulation and an aluminum sheath to prevent skin contact burns.

Several safety interlocks are present in the LVI circuitry. Power to the temperature controller, air preheater, and liquid pump are relayed to a pressure switch, or Solid-state relay #1 (SSR-1) shown in **Figure 4.6**. If sufficient flowrate is not being sent to the eductor, the vacuum level will decrease and disconnect power to the remaining devices. The temperature controller has an alarm channel connected to SSR-2 which is relayed to the pump motor power supply. If the temperature alarm condition is not met, the pump cannot operate. SSR-3, as described in the LVI manual, provides a relay signal between the temperature controller and the air preheater (Air Quality Analytical, 2013).

4.4.2 Hardware and Operating Modes

The original design specification of the LVI was to produce 350–1,750 ppmv H₂SO₄ in 1 CFM of carrier gas. The concentrated H₂SO₄ vapor was to be injected into the pilot flue gas stream (350 CFM at 70 °F and 1.5 psig) producing a final H₂SO₄ concentration of 1–5 ppmv.

The LVI design operates by mixing Ricca Chemical, 50% (v/v) Sulfuric Acid, pumped by a Fluid Metering, Inc. H00CKCLF reciprocating-rotating ceramic head valveless metering pump with a FMI VS200 controller, into the suction side of an Air-VAC HAVR062HSS eductor operating under vacuum (10–20” Hg) with a motive fluid of preheated N₂, controlled to 325 °C, at 60–90 psig inlet pressure. **Figure 4.6–Figure 4.7** show P&IDs of the LVI system enclosures. The LVI controls and liquid reservoir (500 mL G45 amber bottle) are contained in a Hubbell-Wiegmann® NEMA 4 Single-Door Wall-MNT 30” x 24” x 8” steel enclosure. The eductor, heaters, and tubing are housed in a Hubbell-Wiegmann® 14" x 12" x 6" NEMA 4 JIC steel enclosure with a 3/8” 316SS

bulkhead outlet fitting. The injection enclosure is stuffed with several layers of Zircar[®] Ceramics ASB-2300, 6 PCF ceramic insulation. Additionally, all stainless steel fittings which could be exposed to high temperature H₂SO₄ are CVD coated with SilcoTek[®] Dursan[®] (amorphous silicon, oxygen, and carbon) protective coating (0.4–1.6 μm thick). The power, control, and liquid lines between the two enclosures are run through 3/4” liquid-tight tubing. The liquid H₂SO₄ concentration must be diluted by a factor of 500, from 50% v/v, to produce comparable gas-phase concentrations of condensed H₂SO₄ mist for AGC experiments.

The LVI can run in two modes: (1) bypass mode and (2) furnace mode. Bypass mode is the original LVI design in which all vaporization heat is supplied at the eductor body and is supplemented by radiant heat transfer to the carrier tubing. Furnace mode operates by providing supplemental heat through a Zircar[®] Ceramics model FIH-C, 1” x 3” x 6”, 200W, 60V Nichrome wire resistive tube furnace. The tubing in the furnace section was constructed of SGE[™] Analytical Science 1/2” x 9.5” x 60 cm GLT[™] borosilicate glass-lined tubing swaged with graphite ferrules. The tubing was packed with refractory ceramic fish-spine beads for added transfer area and capped on both ends with quartz glass wool.

The two operating modes are illustrated in **Figure 4.7** by the dashed red line labeled, “Furnace Bypass”.

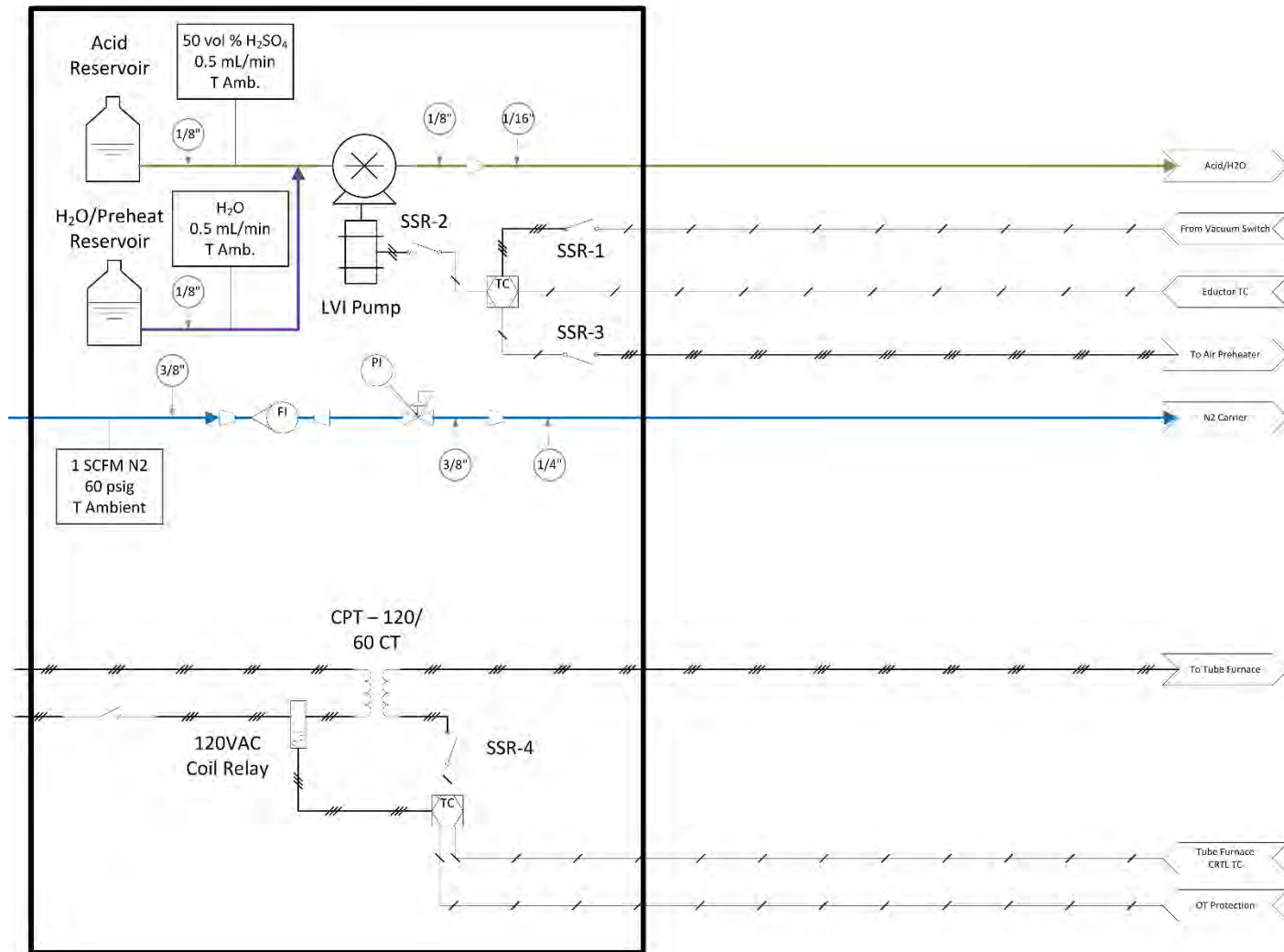


Figure 4.6: LVI control enclosure P&ID.

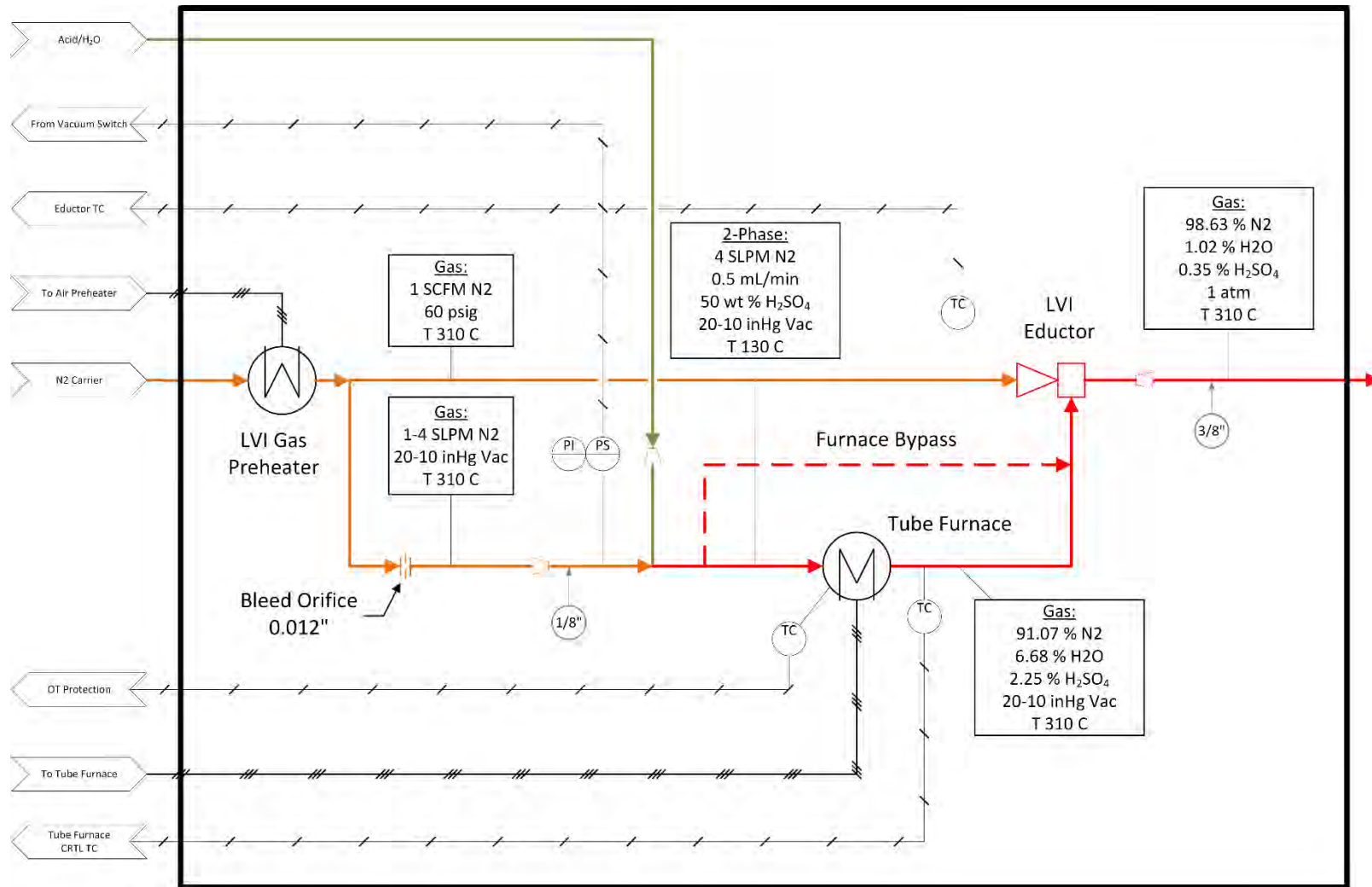


Figure 4.7: LVI injection enclosure P&ID.

The carrier gas (N₂) flowrate into the LVI system is measured by a direct-read Key Instruments MR3A06SVVT rotameter with Viton[®] O-ring seals and a glass float ($\rho_{\text{float}} = 2.53 \text{ g/mL}$). The rated accuracy is $\pm 5\%$ of full-scale (60 SCFM). The rotameter is installed upstream of the pressure regulator in the LVI enclosure and just downstream of an isolation valve on the N₂ supply line. The flowrate reading is compensated for gas density using the pressure and temperature at the outlet of the rotameter body using Equation (4.8) below. Equation (4.8) assumes that the gas density follows ideal gas law and that the density of both the reference gas and the process gas are negligible compared to the rotameter float. Conversion from standard conditions to actual conditions is done by dividing Equation (4.8) by the ratio of the process-to-standard gas density, yielding Equation (4.9). The supply pressure is 100 psig and the temperature is assumed to be ambient at 21 °C. Standard conditions for density correction are specified as 14.696 psia and 20 °C by Key Instruments.

$$Q_G(\text{ACFM}) = Q_{STD}(\text{SCFM}) \sqrt{\frac{P^{STD}}{P^G} \cdot \frac{T^G}{T^{STD}} \cdot \frac{MW_{STD}}{MW_G}} \quad (4.8)$$

$$Q_G(\text{SCFM}) = Q_{STD}(\text{SCFM}) \sqrt{\frac{P^G}{P^{STD}} \cdot \frac{T^{STD}}{T^G} \cdot \frac{MW_G}{MW_{STD}}} \quad (4.9)$$

where:

$Q_G(ACFM)$ = Volumetric flowrate of LVI N_2 at actual gas conditions [CFM]

$Q_G(SCFM)$ = Volumetric flowrate of LVI N_2 at standard gas conditions [CFM]

$Q_{STD}(SCFM)$ = Volumetric flowrate of the reference gas at standard conditions [CFM]

P^{STD} = Absolute standard pressure [Pa]

P^G = Absolute pressure of the actual gas [Pa]

T^{STD} = Absolute standard temperature [K]

T^G = Absolute temperature of the actual gas [K]

MW^{STD} = Molecular weight of the standard gas [g/gmol]

MW^G = Molecular weight of the actual gas [g/gmol]

The flowrate into the LVI system is choked because of the eductor nozzle diameter. Therefore, the flowrate through the eductor body should follow a linear relationship to the inlet set pressure controlled by the inlet pressure regulator. Equation (4.10) shows the calculation for the mass flowrate of an ideal compressible gas. The flowrate at different operating temperature can be calculated as shown in Equation (4.11).

$$\dot{m} = C_D A P_0 \sqrt{\frac{1}{RT_0} \gamma \left(\frac{2}{\gamma + 1} \right)^{\frac{\gamma+1}{\gamma-1}}} \quad (4.10)$$

$$\dot{m}(T_2) = \dot{m}(T_1) \sqrt{\frac{T_1}{T_2}} \quad (4.11)$$

where:

\dot{m} = Mass flowrate of LVI N₂ [kg/s]

C_D = Discharge coefficient [--]

A = Orifice throat cross-sectional area [m²]

P_0 = Absolute inlet pressure [Pa]

T_0 = Absolute inlet temperature [K]

γ = C_P/C_V [--]

C_P = Constant-pressure heat capacity of the gas [J/kg·K]

C_V = Constant-volume heat capacity of the gas [J/kg·K]

The flowrate of acid is calculated using a calibration curve for the pump, given in Equation (4.12), below. Additionally, the weight of the acid reservoir is weighed before and after experiments to validate the flowrate measurement through integration.

$$Q_{Act.} = 1.2017 Q_{Set} - 0.2465 \quad (4.12)$$

where:

$Q_{Act.}$ = Actual LVI H₂SO₄ pump rate [mL/min.]

Q_{Set} = LVI H₂SO₄ pump set point [mL/min.]

4.5 FTIR SAMPLING

The inlet and outlet total phase concentrations are measured by a multipoint FTIR sampling system. The AGC uses a heated, manual multipoint switching box to control the sampling location and the background (N₂) flowrate. A picture of the multipoint switching box is shown in **Figure 4.8**. The three way sample valves are capped on one exit port such that in the closed position, the gas in the lines are stagnant. The lines are flushed with N₂ before sampling by opening the three way valves with the FTIR pump off.

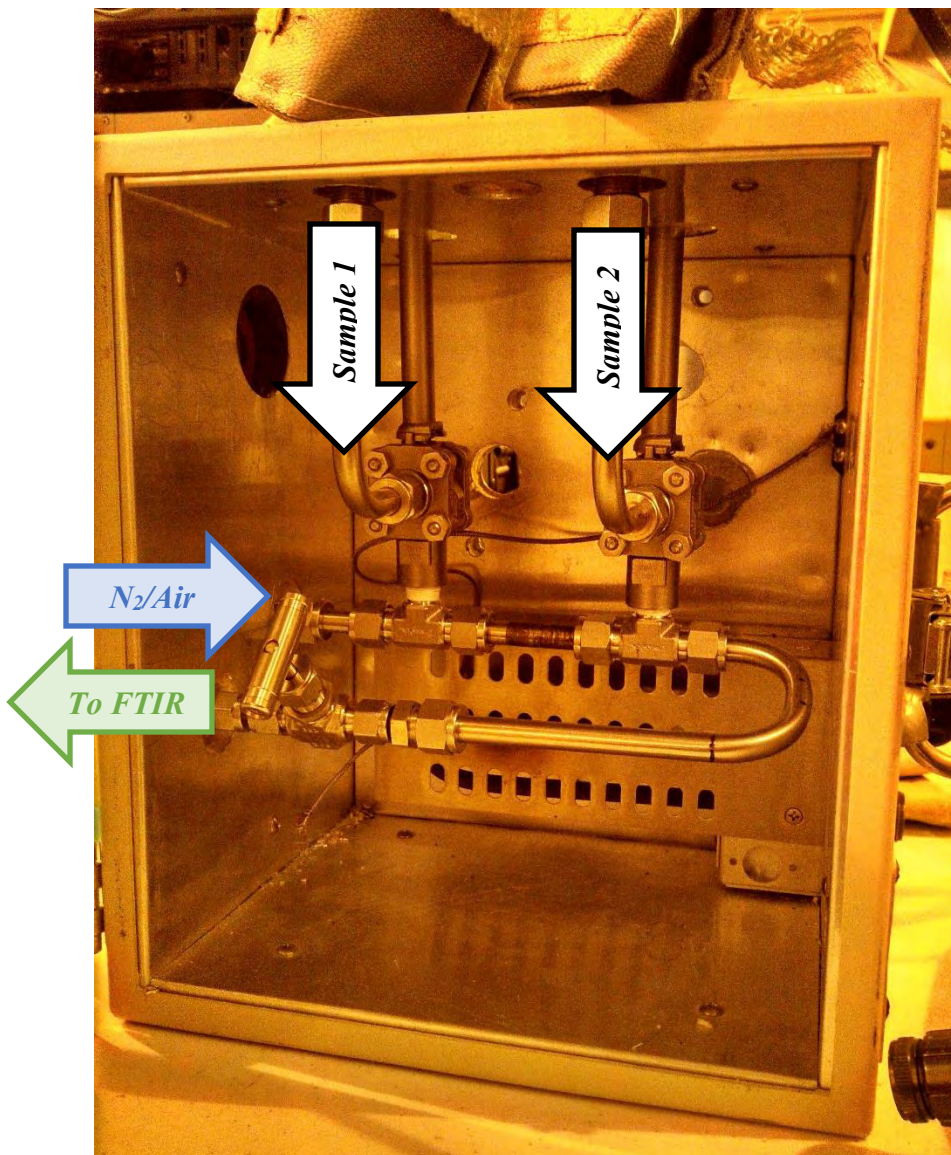


Figure 4.8: Heated manual multipoint switching box. An external manifold with an isolation valve controls N₂ and Air flow used to purge the system. Heated sample lines connect to the top of the box.

Background, air, or sample gas is sucked through a heated filter body and is pumped to the rackmount FTIR. The FTIR sampling PFD and a picture of the rackmount FTIR unit are shown in **Figure 4.10–Figure 4.11**. The rackmount FTIR is located

outside of the walk in hood. The heated FTIR lines pass overhead on a Unistrut® rack attached to the vent hood sloping beams using angled beam clamps.

All FTIR connections are covered by insulation blankets attached by Velcro® or tied using fiberglass woven insulation tape.

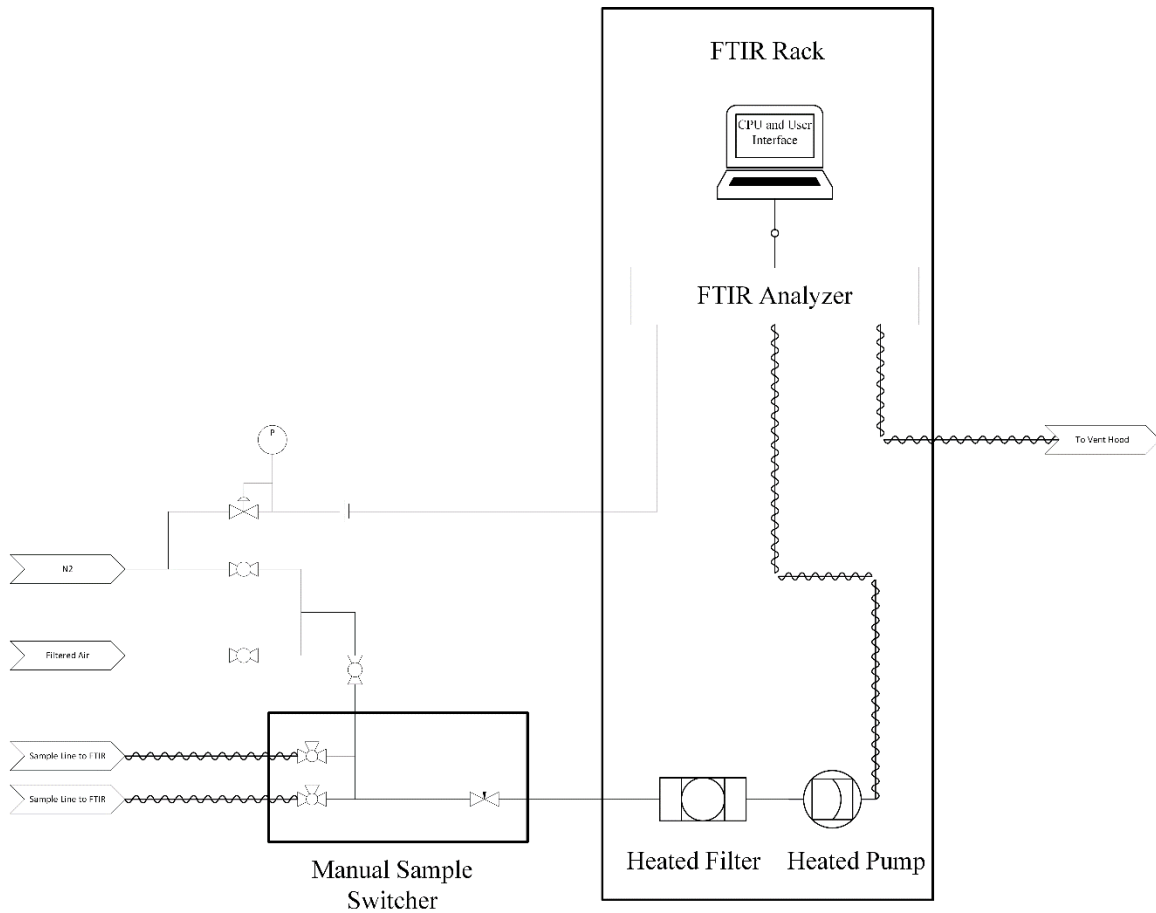


Figure 4.9: FTIR and multipoint sample switcher PFD for the AGC

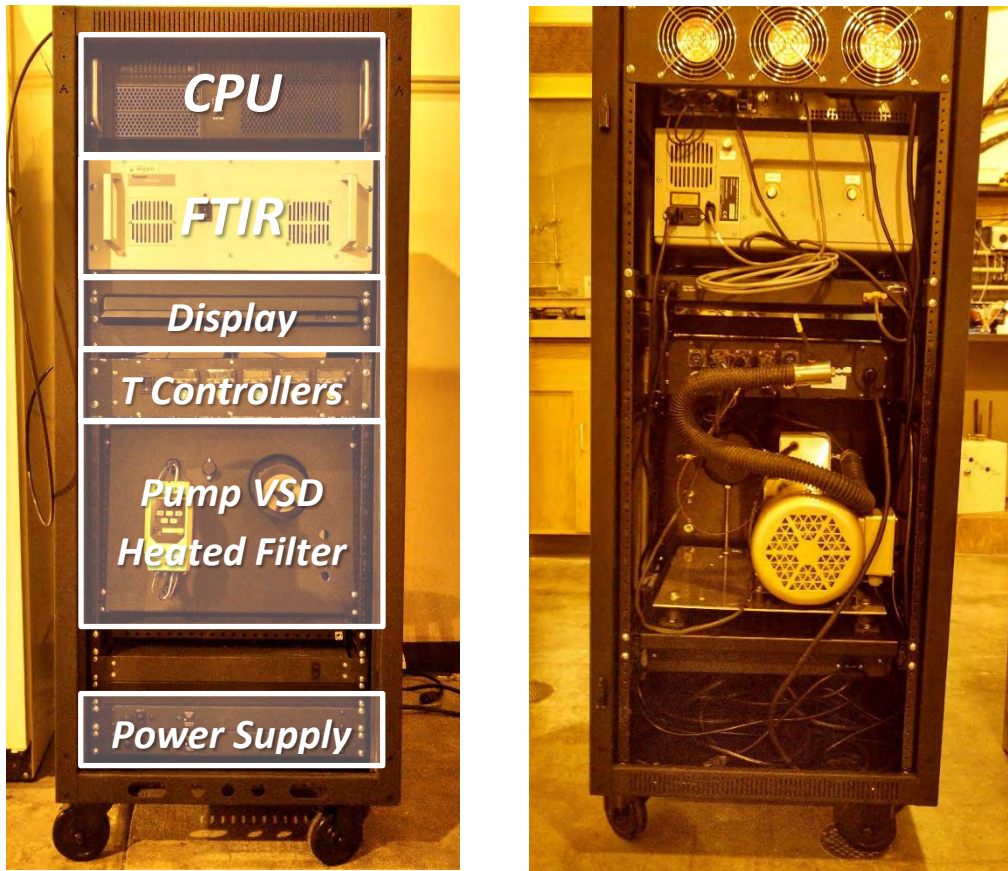


Figure 4.10: Front and back view of the rackmount FTIR and sampling system.

4.6 AEROSOL LOSSES

Aerosol sampling losses in the FTIR sampling system were calculated using the loss equations developed in Chapter 2. The aerosol is assumed to be vaporized upon entering the heated line and therefore no additional transmission losses are incurred. Isokinetic losses were calculated assuming a total process gas flowrate of 60 SLPM, a sampler flowrate of 5 SLPM, a duct inner diameter of 1.5" Sch. 10 piping, a sampler inner diameter of 1/4", and an aspiration angle of 90° relative to the process flow. Gravitational losses were included for both sample points; however, the inlet FTIR

sample point is oriented vertical while the outlet point is horizontal. **Figure 4.11** shows the sampling efficiency for the FTIR system on the AGC.

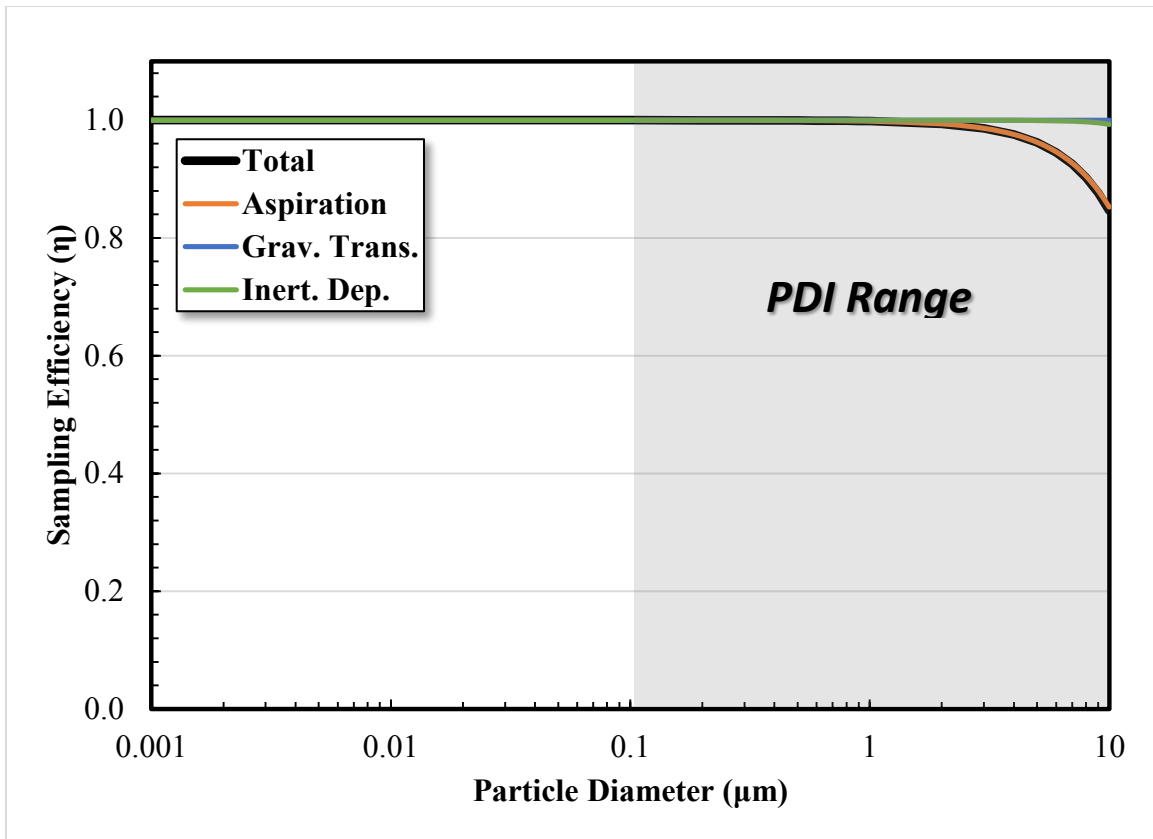


Figure 4.11: Aerosol sampling efficiency for FTIR analysis on the AGC. A particle density of $1,100 \text{ kg/m}^3$ was assumed.

Aerosol sampling efficiency with the FTIR system is only affected by aspiration loss due to anisoaxial, anisokinetic sampling. The FTIR has a maximum flowrate of approximately 10 SLPM to prevent significant backpressure on the analysis cell. A bypass stream could be used to match the process and sampler velocity, though the losses in the size range of interest are minimal.

4.7 PDI SAMPLING

The AGC has two insert locations for the PDI test cell which are both configured to operate in downward flow. The inlet measurement is located between the presaturator and the FTIR/gas inlet temperature measurement and the outlet measurement is located between the FTIR/gas outlet temperature measurement and the condenser inlet. Since only one PDI cell was supplied by Artium Technologies, a dummy cell is flanged in place at the cell location where PDI measurements are not taken to create equivalent flow conditions throughout the system.

The PDI sampling system was designed to take the full flowrate of the AGC column (125 SLPM). No sample pump is required since the inlet gas pressure and flowrate are compensated by the N₂/CO₂ MFCs and critical flow.

The N₂ push/purge condensation control system outlined in Chapter 3 introduces an additional stream of N₂ purge and eductor flush gas. The additional stream was returned just below the PDI analysis point prior to the inlet connection of the condenser.

Figure 4.12 shows the PDI in place at the outlet of the AGC.



Figure 4.12: Front and back view of PDI mounted on the AGC outlet.

4.8 OPERATING PROCEDURES

Proper PPE should be worn during AGC experiments; safety glasses and nitrile gloves should be worn at all times. Leather welding gloves should be worn when adjusting the heated manual multipoint switching box valves; even though the valves are outside of the heating zone, significant heat is conducted through the handles and they get very hot. Hard hats should always be worn outside when adjusting the CO₂ regulator or opening outside plug valves.

The PDI lasers should always be contained in the sample cell. If the lasers penetrate through cracks or are reflecting off of any surfaces, polarized safety glass must be worn while addressing the problem. The PDI **SHALL NOT** be operated if the lasers are not contained within the sample cell.

1. **FTIR Preheating and Background:** First, verify that the purge N₂ to the FTIR is set to 5 psig and that the FTIR outlet line is open to the hood. Ensure all connections are wrapped in insulation blankets. Next, preheat the FTIR, heated sampling lines, sample pump, filter, and manual switching box to 180 °C. The system takes approximately two hours to reach the set point temperature. Change the flush gas to N₂ to clear out adsorbed material the lines, open the sampling valves for the column inlet and outlet heated lines, and set the FTIR to five minute scans. Once the system reaches temperature, take a few spectrum and monitor the residual until it stops changing. Take a ten minute background scan. When the background is finished, take a short (30 second) scan to verify a clean baseline.
2. **Gas Preparation and Valve Positioning:** Verify that the N₂ and CO₂ sources are open to the system. Open the plug valves at the inlet and outlet of the N₂ and CO₂ MFCs. Open the sparging line valve at the inlet of the presaturator column. Open the

plug valve at the solvent tank outlet. Drain any condensate out of the collection line from the condenser into a carboy.

3. **Establishing Coolant Flow:** Open the bypass line on the cooling water supply and return. Open the supply and return gate valves and establish flow in the lines. Next, slowly open the supply and return ball valves and then shut the bypass line. Feel the cooling lines to ensure coolant flow.
4. **Electrical Connections:** Connect the USB 2.0 cable from the AGC control enclosure to the laptop outside of the vent hood. Plug the temperature bath and the immersion heater into the far wall at the 30A 240V receptacles. Turn on power to the AGC control enclosure, the LVI enclosure, and the solvent pump. Immediately put the presaturator temperature controller into standby by hitting the return key (far right button) twice until the reader flashes “stdby” in green. ***DO NOT*** turn on any heaters without flow established! Electrical heaters are designed to dissipate heat at very high temperature by convection and radiation; if flow is stagnant, the surface temperature of electrical heaters will get so high that they will melt. Open the LabVIEW™ visual interface “AGC PFD V2” in the “LabView VI” directory.
5. **Establishing Flows:** Run the VI and name the file as prompted; a CSV file will be created that can be open in Excel at the termination of the VI. Observe the temperature and flowrate readings to make sure there are not faulty connections or addressing problems. Set the N₂ flowrate around 25-35 SLPM to establish flow in the system. The presaturator temperature controller can now be turned on by hitting the return button twice. The default set point is 42 °C which creates a saturated gas at the presaturator outlet at 40 °C. Once the system adjusts to the set points, change the sampling rate in the VI to 10 seconds to reduce the data size.

6. **LVI Preheating:** Verify that the acid reservoir is full, or will not run dry during operation. Refill if necessary. Weigh the LVI solvent reservoir and record the starting mass. Establish flow by pulling the pressure regulator knob outward until it clicks and turn it clockwise until the pressure reads 75 psig. The vacuum gauge should read 16–20 inches Hg. A vacuum reading below that range indicates a plug; the LVI must be disassembled and the plug must be cleared. Flip the power switches to the “I” position on the terminal block. The temperature controllers should turn on. Hold down the Δ V buttons simultaneously on the temperature controller until the display reads “TUNE”. Then, hold the * Δ buttons until the display reads “OFF”. Hold down the Δ V buttons simultaneously until the display reads temperature. The default set point for the LVI heater is 325 °C. It takes approximately one hour to reach the set point. Remove the acid inlet line from the reservoir cap fitting and press it into the quick-disconnect fitting on the pump inlet. Set the acid flowrate using the stroke rate controller box. The pump is calibrated to a range of 0-10 mL/min. The control box sets the percentage of full-scale (10 mL/min) flow. Ensure the LVI pump controller is set to the off position.
7. **Establish CO₂ and Solvent Rate:** Once the presaturator holds steady at the set point, establish CO₂ flow using the LabVIEW™ VI and adjust the N₂ to reach the desired CO₂ concentration. Next, turn the pump switch on and adjust the speed dial until the solvent flow meter reads the desired flowrate. Next, turn the pump temperature bath on and plug in a set point. The temperature should reach steady state within a few minutes. The system should now be approaching the first steady state condition.
8. **PDI Preparation:** Establish purge and vacuum flow to the PDI test cell and use the rotameter to adjust the purge flow until it reads 5 SLPM. Turn on the PDI in the

following order: (1) power box, (2) computer, (3) ASA box, and (4) oscilloscope. Next, open AIMS on the computer and ensure that there are no error messages.

9. **LVI Injection and PDI Lasers:** Once the LVI reaches the set point temperature and maintains steady operation for about ten minutes, turn the LVI pump on. It will take about 25–30 minutes for the solvent to reach the injection point. Once the LVI pump has been turned on, turn the PDI laser key on the back of the PDI housing; the lasers should now be turned on.
10. **FTIR Inlet Sampling:** Close the valve for the AGC outlet heated line and flush the inlet line for one minute with N₂. Turn off N₂ by closing the plug valve on the inlet of the heated manual switching box. Turn on the FTIR pump by pressing the “start” key on the VSD. The default frequency is 50 Hz. Change the sampling time on the FTIR to one minute scans. Rename the spectrum and result files. Turn on continuous sampling on the FTIR. Establish steady state conditions on the FTIR readout and verify aerosol injection by observing consistent, rapid Doppler bursts on the oscilloscope.
11. **FTIR Outlet Sampling:** Open both the inlet and outlet sampling heated line valves and the N₂ valve at the heated switcher. Flush the lines for one minute. Close the inlet sampling and N₂ valves. The FTIR should now be sampling the AGC outlet gas.
12. **PDI Measurements and Data Logging:** Collect three PDI data sets for each steady state condition. Record LVI operating conditions. Take a solvent sample by transferring 3 mL from the lean sample point using a syringe. Place the sample into a labeled 3 mL amber vial for solvent analysis.
13. **Change the Set Point:** Change the operating conditions for the next steady state condition. The system takes approximately 5–10 minutes to reach the new condition.

Repeat step 12 for each steady state condition. Check the condensate collection line and drain as necessary.

14. **FTIR Inlet Sampling:** After all steady state conditions have been reached, change the FTIR sample point back to the inlet by first opening the N₂ and inlet sample valves, flush the lines with N₂ for one minute, and then closing the N₂ and outlet sample valves. Record data to compare the start and ending inlet conditions.
15. **Shutdown Preparation:** Turn the CO₂ flowrate to 0 SLPM. Remove the LVI liquid reservoir line from the LVI pump inlet. Allow the LVI pump to run an additional 20–30 minutes to blow down the liquid line. Turn off the LVI pump. Place the temperature controller in “PARK” by holding down the by holding down the \wedge V buttons simultaneously until the display reads “TUNE”. Then, hold the * \wedge buttons until the display reads “PARK”. Hold down the \wedge V buttons simultaneously until the display reads temperature and verify that the temperature is decreasing. Turn the PDI lasers off and then shutdown the computer, ASA, and power box. Put the presaturator heater in standby.
16. **FTIR Flushing:** Open the inlet, outlet, and N₂ valves on the heated switching box. Turn the FTIR pump off by hitting the “Stop” button. Flush the lines until the FTIR spectrum reads a clean baseline. Then, switch flush valve to air and turn the FTIR system heaters off. Watch the FTIR for about two minutes to ensure that the air flowrate is adjusted such that the cell pressure doesn’t exceed 1,100 mBar. Cease FTIR sampling.
17. **Shutdown:** Once the LVI temperature drops below 150 °C, power and N₂ can be shut off. Turn the LVI supply off at the wall manifold so the line completely blows down; the pressure will slowly bleed off until the gauge reads zero. Then turn the N₂ regulator knob all the way counter-clockwise and push it back inward until it clicks.

Turn the solvent pump off and then turn the solvent temperature heater off. Change the N₂ flowrate to zero SLPM on the LabVIEW™ VI. The VI can now be stopped. Finally, open the cooling water line bypass valve and then shut off the supply and return ball valves. Then close the 4" supply and return gate valves. Turn power off to the entire system.

4.9 DATA INTERPRETATION

4.9.1 Data Types

An AGC experiment produces several different data types: (1) aerosol data in individual PDI files, (2) gas phase analysis in one FTIR result file, (3) operating condition in one LabVIEW™ Excel file, (4) solvent analysis in one Excel file, and (5) LVI operating conditions in one Excel file.

4.9.1.1 PDI Data

A single PDI data set contains hundreds of pieces of information including the particle size distribution, the velocity distribution, total particle density, intensity and phase plots, and several calculations of sampling efficiency and statistics. The data of interest includes only the particle size distribution, the total particle density, and the timestamp.

A data algorithm, described in the following section, details the post processing steps to convert the size distribution into an equivalent total concentration for direct comparison to FTIR measurements. Additionally, the computer algorithm corrects flow measurements for temperature and density. The code for the algorithm "Analysis.xlsm" can be found in Appendix A.

4.9.2 Data Algorithm

Since multiple computers are used to collect data, timestamp variance must be compensated to match data on an absolute basis. A computer algorithm written by the author and Conlin Kang collates data by timestamp. The algorithm takes a single PDI data file and searches the FTIR result file and the LabVIEW™ file for the closest time match, with compensated clock offsets. The algorithm then records the outlet concentration numbers from the FTIR file and the temperature and flowrate readings from the LabVIEW™ file on one result line in a master Excel sheet. Statistics and correlations are used to post process the data for that data entry. The next PDI data file is selected and the operation proceeds until all of the PDI files have been matched to the FTIR and LabVIEW™ data files. **Figure 4.13** shows an illustration of the data manipulation steps.

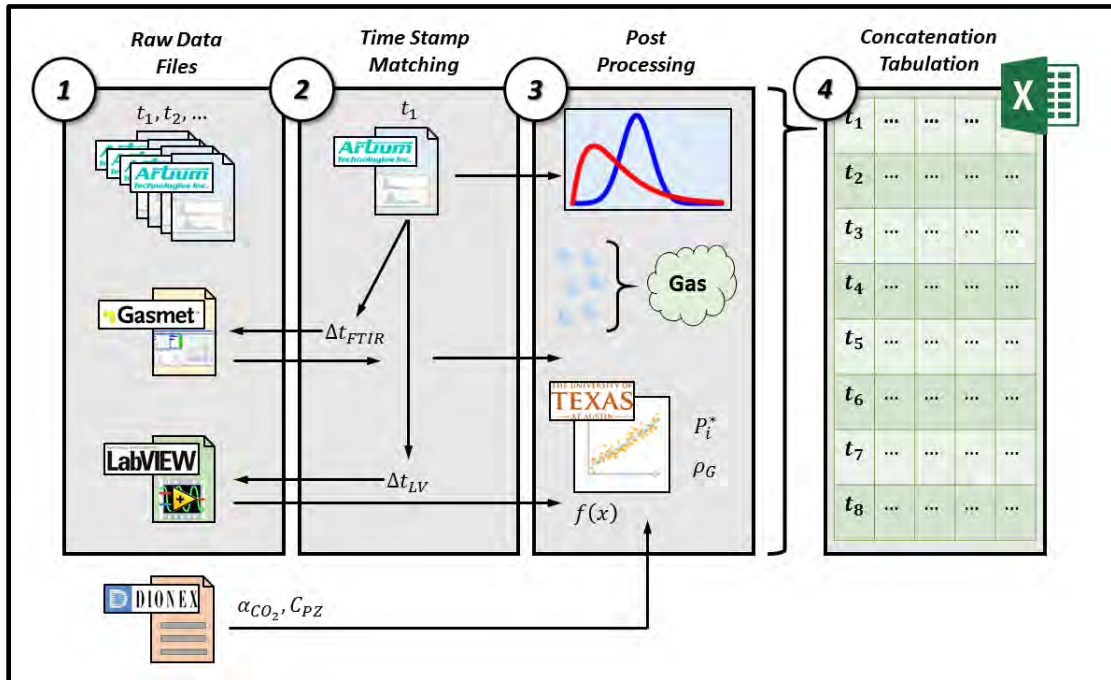


Figure 4.13: VBA Data processing algorithm for AGC experiments.

4.9.2.1 Aerosol Statistics

The data algorithm calculates several modes of the PSD using Equation (2.10). The modes are calculated for each PDI file and are also copied into the master Excel file.

4.9.2.2 Aerosol to Total Phase Conversion

The equilibrium partial pressures of H₂O, CO₂, and PZ are calculated using Equations (4.13)–(4.15). H₂O equilibrium is calculated using the DIPPR correlation for saturation pressure and using an approximate “true” mole fraction of H₂O (DIPPR, 1998). The true mole fraction normalizes the mole fractions by H₂O and PZ; CO₂ is assumed to be completely reacted with PZ. Correlations for CO₂ and PZ equilibrium partial pressures were taken from the work by Xu (2011).

$$P_{H_2O}^* = \frac{100}{101325} x_{H_2O}^T \exp \left[73.649 - \frac{7258.2}{T^L} - 7.3037 \ln(T^L) + 4.1653 \times 10^{-6} (T^L)^2 \right] \quad (4.13)$$

$$P_{CO_2}^* = \frac{100}{101325} \exp \left[35.3 - \frac{11054}{T^L} - 18.9\alpha^2 + \frac{4958\alpha}{T^L} + \frac{10163\alpha^2}{T^L} \right] \quad (4.14)$$

$$P_{PZ}^* = \frac{10^6}{101325} x_{PZ}^T \exp \left[-123 + 21.6 \ln(T^L) + 20.2\alpha - \frac{18174\alpha^2}{T^L} \right] \quad (4.15)$$

where:

- $P_{H_2O}^*, P_{CO_2}^*$ = Equilibrium partial pressures of H₂O and CO₂ [vol %]
 P_{PZ}^* = Equilibrium partial pressure of PZ [ppmv]
 T^L = Lean solvent temperature [K]
 x_i^T = “True” mole fraction of component i [--]
 α = CO₂ loading [mol CO₂/mol alkalinity]

The total volume of aerosol liquid is determined by integrating the normalized PSD multiplied by the total particle density (Equation (2.5)). An aerosol phase concentration (PZ molality and CO₂ loading) is set and multiplied by the calculated aerosol liquids volume. Since the total particle density is measured as particles per cubic centimeter of gas, the moles of aerosol per volume of gas is returned; the concentration in the gas phase is the product of the calculation. The total phase concentration of PZ is calculated using Equation (4.16).

$$y_{PZ} = P_{PZ}^* + 0.001 \frac{wt_{PZ} \rho^D}{MW_{PZ}} \frac{RT^G}{P} \left[\sum_i (d_i)^3 N_i \right] \quad (4.16)$$

where:

- y_{PZ} = Total phase concentration of PZ [ppmv]
 wt_{PZ} = Weight fraction of PZ [--]
 ρ^D = Mass density of the aerosol liquid phase [kg/m³]
 d_i = Particle diameter of size class i [μ m]
 N_i = Particle density of aerosols of diameter size i [part./cm³]

Equation (4.16) assumes that the gas at the PDI sample point is saturated to PZ. At high aerosol concentrations, the aerosol mass is likely to have absorbed all of the PZ by that point. However, at high aerosol concentrations, the error of that assumption will

be small compared to the total amount of amine absorbed into the aerosol phase. At low aerosol concentrations, the gas phase will remain close to saturation since the transfer rate to the aerosol phase will be small.

Physical properties of the aerosol liquid are calculated using the same equations as for the bulk solvent solution (see Chapter 7). The solvent PZ concentration and CO₂ loading are updated in the result file after laboratory analysis.

4.9.2.3 Aerosol Amine Concentration Optimization

The concentration in the aerosol phase of PZ is set by a minimization of the sum of the errors between the aerosol and FTIR measurements. As a first estimate, the PZ concentration is assumed to be constant across the entire experiment. CO₂ loading is assumed to be close to equilibrium to the outlet CO₂ concentration; however, since the aerosol physical properties are weak functions of loading, a constant value is assumed across an entire experiment.

4.10 ACKNOWLEDGEMENTS

Several people contributed to the work presented in this chapter. Conlin Kang wrote the starting section of code for the PDI/FTIR comparison which was modified by the author. Mark Nelson of Air Quality Analytical, Inc. designed and built the original LVI and provided assistance during the initial troubleshooting. Yong Kim assembled much of the rackmount FTIR and assisted during rewiring and modifications made by the author.

Chapter 5: Aerosol Growth Column (AGC) – Results

This chapter presents results obtained from AGC apparatus described in Chapter 4. The primary data collected in an AGC experiment falls into three categories: (1) aerosol phase analysis by PDI, (2) inlet and outlet total (gas and aerosol) phase concentrations by FTIR, and (3) system operation data by LabVIEW™ data acquisition. Additionally, the solvent loading and amine concentration were characterized by cation chromatography and total inorganic carbon (TIC), respectively.

All data types are collated by (clock-synched) timestamp and post-processed by an algorithm written in Microsoft® Excel® Visual Basic® for Applications (VBA) and output into a summary table. Operating conditions, aerosol size distributions, total particle densities, and FTIR data are all tabulated and sorted by data collection time.

This chapter details experimental results and procedural development of the AGC. Tabulated results and conclusions complete the chapter.

5.1 AGC EXPERIMENTS

The following section details experiments conducted on the AGC in chronological order. Instrumentation was added over the duration of this work; quantities not measured directly are labeled as assumed quantities.

5.1.1 Experiment Limitations

Due to the unstable operation of the LVI, back calculation of exact flowrates is futile. The eductor of the LVI plugged after nearly every experiment run with H₂SO₄ and even with H₂O on some occasions. In most cases, flow performance would change after each experiment due to severe corrosion and plugging. In the worst cases, eductors became so fouled and corroded that they were rendered unusable.

Even when corrosion was not an issue, the injection rate from the LVI was fairly unstable. The liquid and preheated gas mixing point was made in a tee fitting; if the liquid was not fully vaporized by the mixing point, liquid was sheared and the flow into the eductor suction was slug/plug flow. Further evidence of the shearing phenomenon was observed by the pulsation of the vacuum gauge and the bimodal distribution seen by the PDI PSDs. It is theorized that the bimodal distribution consists of a large fraction of submicron, homogeneous nuclei and partially atomized droplets that further break apart in partially evaporate in the turbulent section of the eductor. Troubleshooting and modifications to the LVI throughout this study are documented in Appendix C.

The PDI also had several problems that were addressed throughout the course of experimentation in addition to several delays and redesigns that cost over six months of experimental time. The major delays included replacing the original sapphire optical windows with crown glass due to beam steering due to birefringence, addition of a fine laser crossing adjustment tool, and a later stop modification for the laser adjuster when the screw drive was turned too far and fell out of its casing. Several of the delays required shipment back to Artium's facility in California.

Additionally, the original design of the N₂ purge/vacuum connections to control condensation on the PDI sample cell windows did not provide an adequate seal. Push-to-connect fittings with stub ends were pushed through a set of O-rings; however, the clearance between the PDI sample cell and the PDI housing was too small and the fittings would get pulled out very easily. Several sealants were tried but very few of them provided any rotational shear strength. As a result, once the fittings were twisted, they would immediately fall out. A low grade silicon sealant was ultimately found to be adequate.

Finally, the narrow clearance between the PDI test cell and the PDI housing caused several windows to crack when attaching the PDI cell to the housing, rendering the PDI inoperable.

In general, the LVI and the delays of the PDI system severely limited the progress of experimentation. Positively, most of the issues with the PDI have been addressed however instrument assembly remains a delicate process. The LVI, however, requires significant redesign to be operable. It is strongly recommended to use another aerosol generation source for future experimentation.

5.1.2 LVI Stability Tests

The first set of experiments encompasses measuring the performance of the LVI by introducing a tracer into the vaporized material which is observable by FTIR. A solution of 0.5 m PZ was gravimetrically mixed to create as the LVI trace solution. The LVI flowrate was then varied and the outlet PZ was measured. The solvent in the AGC was H₂O during these experiments and the LVI was operating in bypass mode.

Figure 5.1 shows the outlet H₂O measurement as the solvent temperature was varied for the first experiment. The black curve corresponds to the value that would be observed if Raoult's Law is assumed using the measured solvent inlet temperature and the vapor pressure correlation taken from the DIPPR database (DIPPR, 1998). The smoothness of the curves indicates that entrainment or condensation in the FTIR lines and connections is not present. The dashed lines enclose operating windows of the LVI; the injection rate was 1.0 and 1.5 mL/min. The H₂O curves clearly show the addition of H₂O into the gas as well as their proportional relationship with the LVI flowrate.

Figure 5.2 displays the PZ measurement during the second LVI injection timeframe. Assuming an eductor flowrate of 0.9 SCFM and 0.5 m PZ in the injection

liquid, the concentration of PZ should be 220 and 330 ppmv PZ for injection rates of 1.0 and 1.5 mL/min. Since the absorption solvent was H₂O, the absorber was acting as a water wash column. The levels measured by the FTIR correspond to 36–40% removal of PZ in the wash solution.

The LVI showed relatively stable operation during the 1.0 mL/min injection periods; however, the measured PZ was considerably less stable during an injection rate of 1.5 mL/min. It was discovered that while the pump was off, liquid was sucked through the lines, indicating that the pump sleeve was not sealing properly. At higher liquid flowrates, the air preheater was receiving too much liquid to vaporize, leading to intermittent condensation.

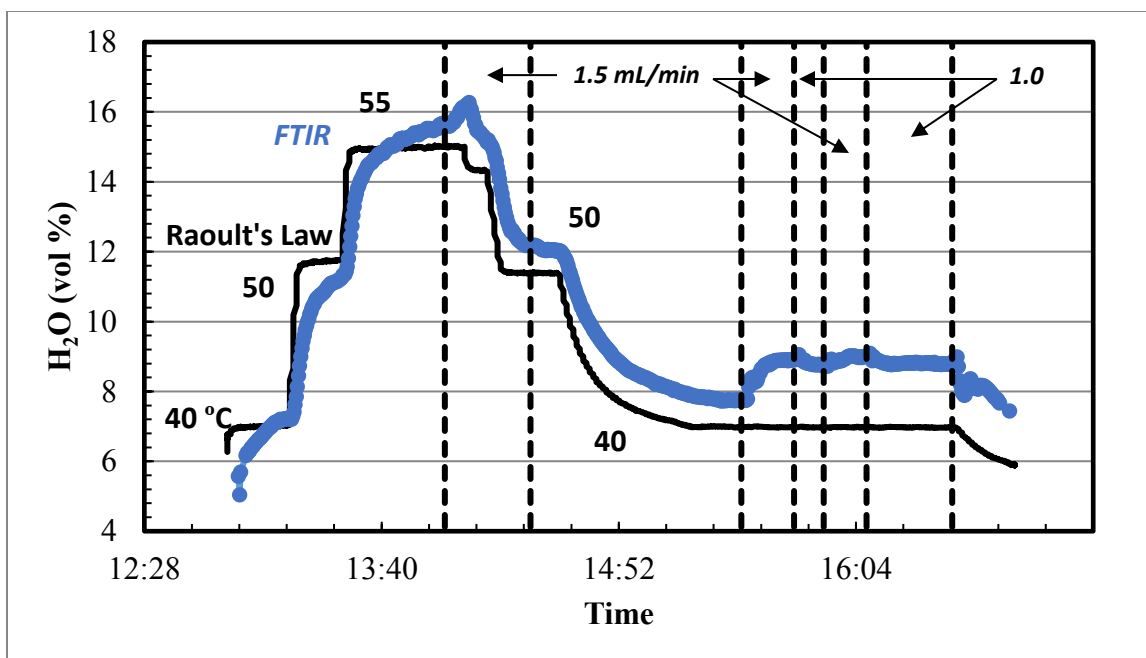


Figure 5.1: FTIR measurements of H₂O with varying solvent T and LVI flowrates. LVI Flowrates: 1.5 mL/min, 1.0 mL/min.

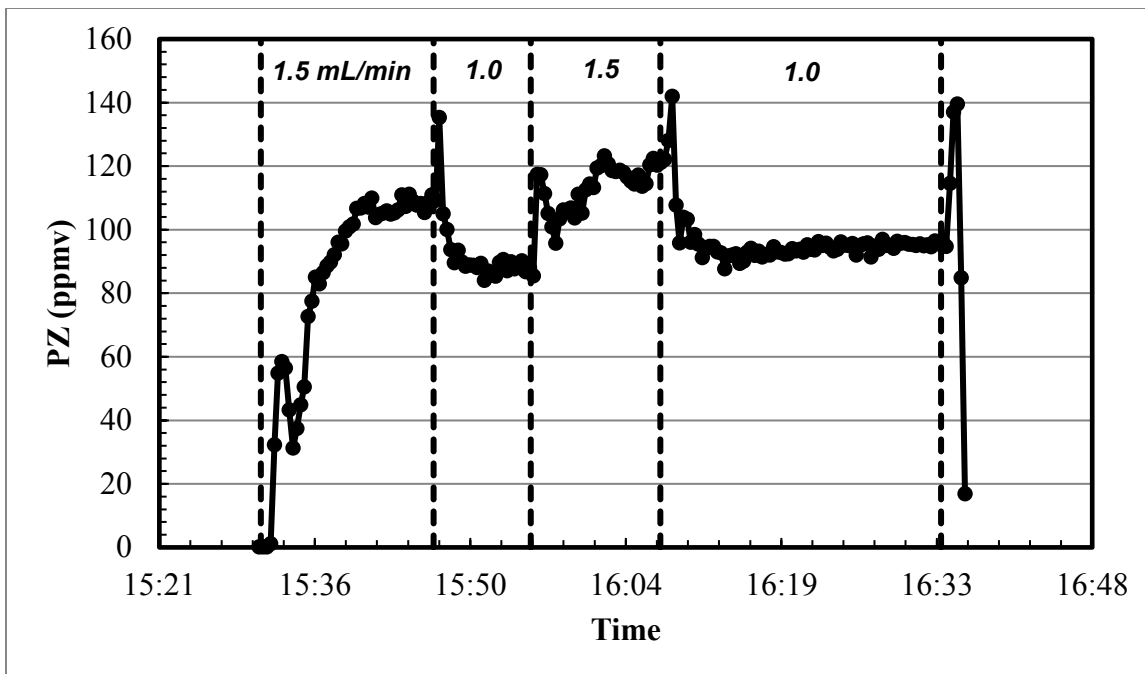


Figure 5.2: FTIR measurements of PZ with varying solvent T and LVI flowrates. LVI Flowrates: 1.5 mL/min, 1.0 mL/min.

Figure 5.3 shows a repeat experiment including the addition of CO₂ in the absorber inlet gas. The LVI flowrate was kept at a constant 1.0 mL/min. The LVI instability is prevalent throughout. A new pump sleeve was ordered and replaced during a solvent changeover and subsequent CO₂ capture tests were being conducted on the AGC.

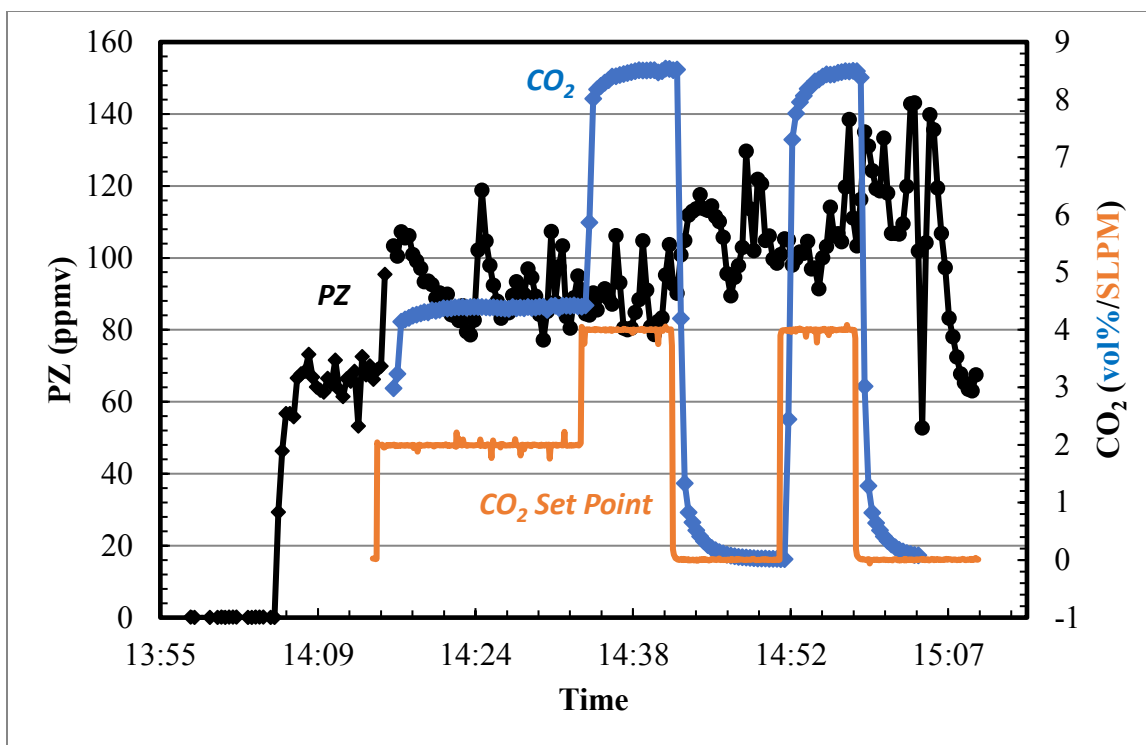


Figure 5.3: FTIR measurement of PZ with varying inlet CO₂ concentration. LVI: 0.5 m PZ at 1.0 mL/min. Absorber Solvent: H₂O at 40 °C.

5.2 CO₂ CAPTURE TESTS

After the LVI tests, the H₂O solvent was drained out of the solvent tank and 9 gallons of 0.3 m PZ was gravimetrically made using a freight scale and pumped into the solvent tank. The unloaded PZ solvent was used to measure CO₂ removal during variable operating conditions.

Figure 5.4 shows the CO₂ measurement at the outlet and the inlet CO₂ concentration assuming complete saturation at the measured presaturator head-space temperature. **Table 5.1** shows the operating conditions during the corresponding bracketed operating times.

The CO₂ capture rate varied from 32–65% and trended as expected; higher solvent flowrates and lower solvent temperatures produced higher removal rates. Since

the solvent capacity was very low, the loading increased rapidly during the experiment. The decreasing removal rates indicate the loading of the solution. No redistributors were used; therefore, liquid maldistribution may lead to less effective area than expected, and consequently the lower observed capture rates. This is further exacerbated by the hollow-cone spray geometry which would introduce the liquid at the walls or edge of the packing.

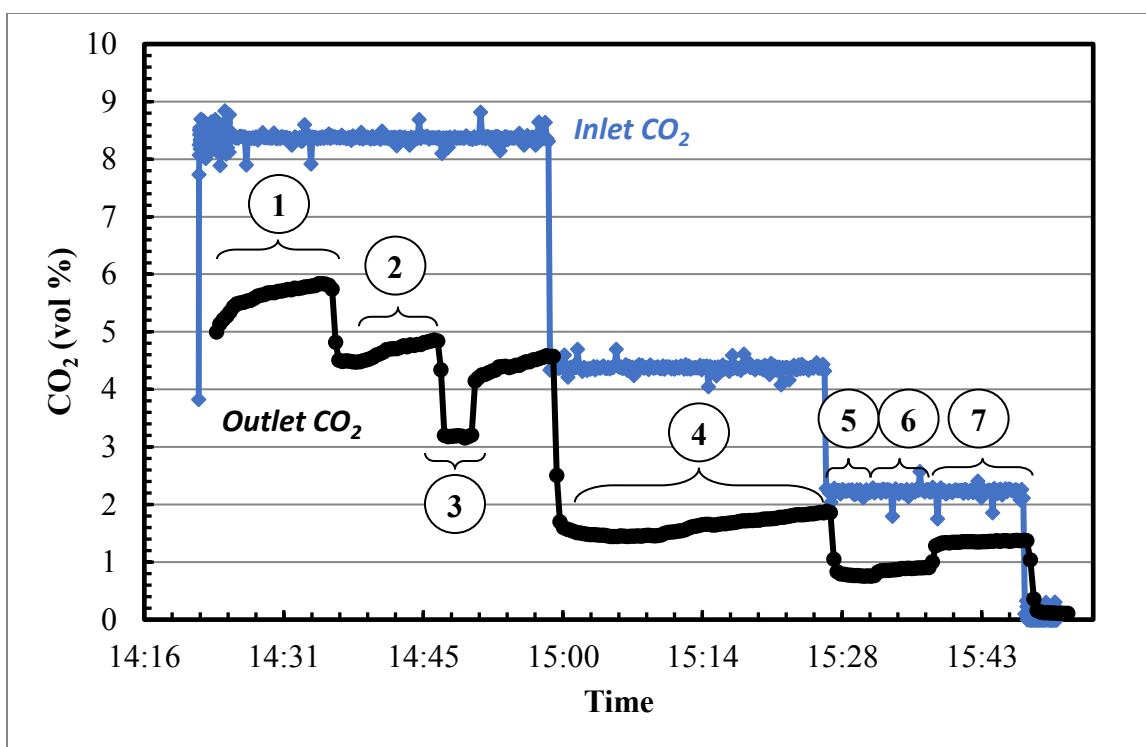


Figure 5.4: 06/24/14 CO₂ Capture test. Inlet and outlet CO₂ concentrations. Solvent: 0.3 m PZ.

Table 5.1: 06/24/14 AGC operation data

Case	Gas Rate (SLPM)	Solvent Rate (GPM)	Solv. Inlet T (°C)	CO ₂ In (vol %)	CO ₂ Out (vol %)	CO ₂ Cap. (%)
1	44.19	0.1	40.01	8.35	5.62	32.69
2	44.20	0.2	40.35	8.35	4.66	44.19
3	44.27	0.3	40.39	8.35	3.20	61.68
4	42.23	0.3	37.00	4.38	1.65	62.33
5	41.31	0.3	34.68	2.24	0.79	64.73
6	41.26	0.2	34.44	2.24	0.86	61.61
7	41.19	0.1	33.89	2.24	1.35	39.73

Assuming that the solvent loading is constant across ranges 1–3, the average k'_g for CO₂ transfer can be calculated by matching the column height using the log-mean driving force and the height of a transfer unit (HTU) of the packing. The inlet solvent loading was assumed to be 0.01 mol CO₂/mol alkalinity and the solvent concentration was taken as 0.3 m PZ. The effective and physical area of the packing was assumed to be equivalent. **Table 5.2** shows the calculated k'_g and rich loadings that correspond to the measured inlet and outlet CO₂ concentrations and the solvent flowrates.

Table 5.2: Calculated k'_g values for cases 1–3 assuming constant inlet loading and an effective mass transfer area of 315 m²/m³. The k'_g value was adjusted to match the packing height by calculating the HTU and NTU of the AGC. The rich loading was calculated by mass balance.

Case	Solv. Rate [GPM]	L/G [mol/mol]	Rich LDG [mol/mol]	k'_g [mol/Pa·m ² ·s]
1	0.1	10.58	0.26	1.60E-07
2	0.2	21.15	0.14	1.58E-07
3	0.3	31.73	0.09	1.58E-07

Figure 5.5 shows a CO₂ capture test the following day using the same solvent inventory however the orifice on the spray nozzle was removed to introduce the solvent by a single drip point to investigate liquid distribution effects on the CO₂ capture rate. The corresponding operating conditions can be found in **Table 5.3**.

The measured capture rates are much lower than those observed on 06/24/14; the spray nozzle is critical for liquid distribution in the AGC.

Following the 06/25/14 CO₂ capture experiment, the inlet CO₂ turned off and the solvent temperature was increased to mimic stripping operation. The results from this test are shown in **Figure 5.6** with the corresponding operation parameters found in **Table 5.4**. It is clear from the developed CO₂ partial pressures that the solvent was nearly saturated with CO₂.

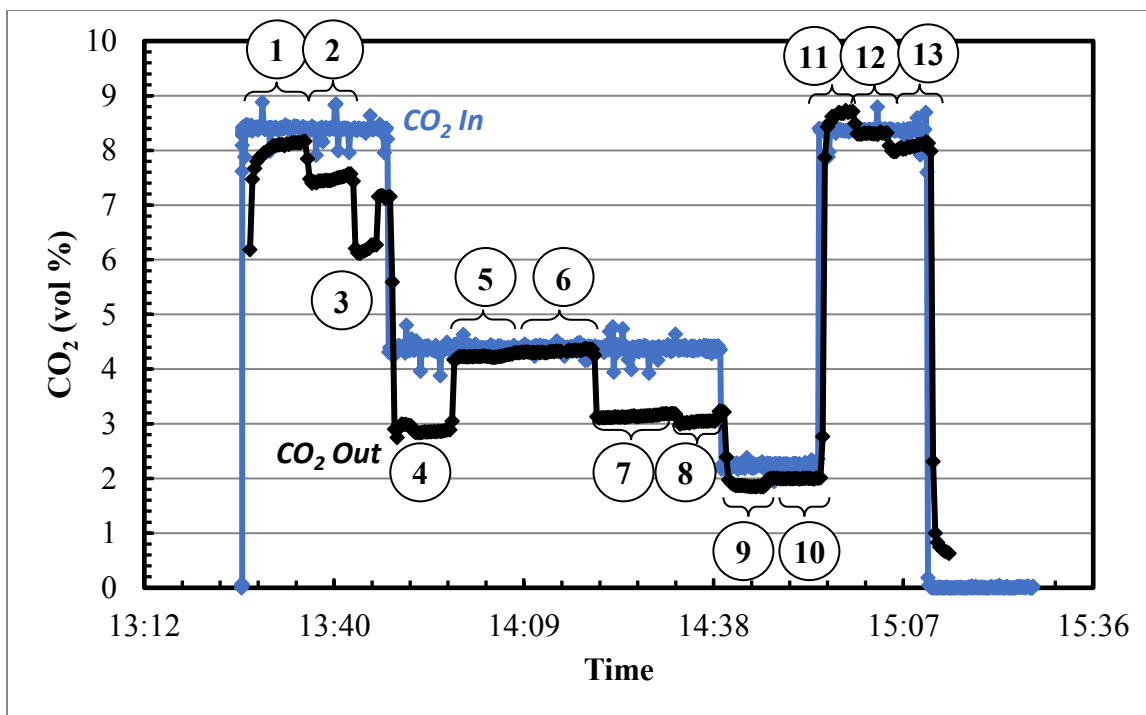


Figure 5.5: 06/25/14 CO₂ Capture test. Inlet and outlet CO₂ concentrations. Solvent: 0.3 m PZ.

Table 5.3: 06/25/14 AGC operation data

Meas. Range	Gas Rate (SLPM)	Solvent Rate (GPM)	Solv. In T (°C)	CO ₂ In (vol %)	CO ₂ Out (vol %)	CO ₂ Cap. (%)
1	44.21	0.1	25.69	8.38	8.07	3.70
2	44.26	0.2	25.75	8.39	7.45	11.20
3	44.21	0.3	25.78	8.38	6.22	25.76
4	42.17	0.2	25.86	4.35	2.87	34.02
5	42.21	0.1	26.92	4.40	4.21	4.32
6	42.17	0.1	40.04	4.38	4.32	1.37
7	42.21	0.2	40.42	4.37	3.14	28.15
8	42.21	0.3	40.46	4.38	3.08	29.68
9	41.26	0.2	40.46	2.25	1.88	16.44
10	41.28	0.1	40.16	2.23	2.39	-7.17
11	44.23	0.1	40.18	8.37	8.60	-2.75
12	44.22	0.2	40.51	8.39	8.30	1.07
13	44.19	0.3	40.57	8.35	8.06	3.47

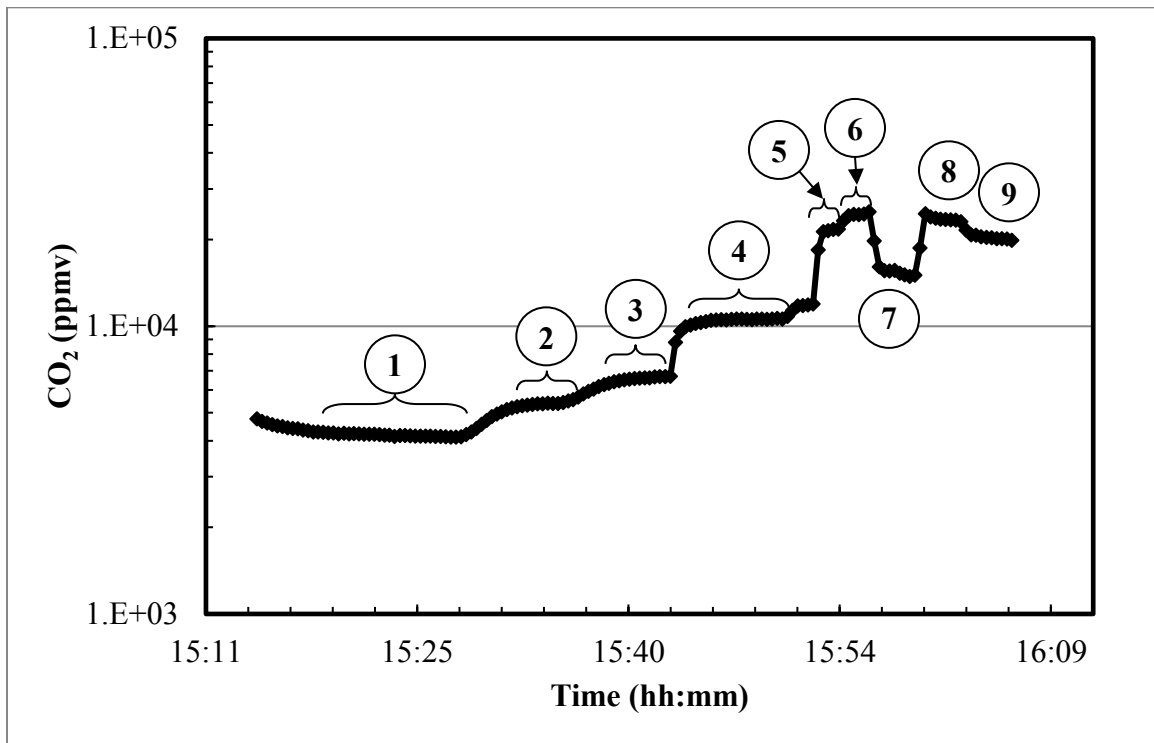


Figure 5.6: 06/25/2014 CO₂ stripping operation outlet CO₂ FTIR measurements

Table 5.4: 06/25/2014 CO₂ Stripping operation data

Meas. Range	N ₂ Flow (SLPM)	Liquid Rate (GPM)	Solvent T (°C)
1	40.23	0.1	40.35
2	40.20	0.1	48.73
3	40.22	0.1	58.56
4	40.24	0.2	59.85
5	10.02	0.3	59.99
6	5.13	0.3	60.01
7	1.15	0.3	60.03
8	5.21	0.3	60.03
9	10.14	0.3	60.06

5.2.1 Operating Conditions Tests

The solvent used in the following studies was gravimetrically prepared by mixing 3 kg of PZ with 10 gallons of tap H₂O to produce a roughly 0.9–1.0 m PZ solution. The initial solvent PZ concentration and CO₂ loading produced an initial P*_{CO₂} of 110.4 ppmv and P*_{PZ} of 2.8 ppmv at 40 °C as measured by FTIR.

Two different LVI solutions were used to create inlet aerosol: (1) 0.5 m PZ and (2) 0.05 vol % H₂SO₄. The LVI N₂ flowrate for all experiments was 1.035 SCFM produced by an eductor inlet pressure of 60 psig which produced a vacuum level of 20 in. Hg at the eductor suction. The LVI liquid flowrate was set to 1.0 mL/min for all cases. **Table 5.5** shows the calculated composition produced for both the PZ and H₂SO₄ aerosol cases. These streams were mixed with a constant process gas flowrate of 20 SLPM that was saturated to H₂O at 40 ± 1 °C. The presaturator temperature was set to 40 °C throughout all experiments, even when the solvent temperature was increased.

Table 5.5: LVI compositions produced using 0.5 m PZ and 0.05 vol % H₂SO₄, respectively. The LVI product gas is mixed with the process gas (20 SLPM) which is saturated to H₂O at 40 °C.

Component	Unit	PZ Aerosol	H ₂ SO ₄ Aerosol
N ₂	vol %	95.7	95.6
H ₂ O	vol %	4.3	4.4
PZ	ppmv	383	--
H ₂ SO ₄	ppmv	--	7.5

Reported inlet CO₂ concentrations were calculated using the output of the N₂ and CO₂ MFCs, adjusted for H₂O assuming saturation at the measured presaturator head-space temperature using DIPPR correlations, and renormalized to the total flowrate produced by mixing the LVI and saturated process gas (DIPPR, 1998). No condensation between the LVI/process gas mixing point and the inlet of the absorber was assumed because no appreciable liquid was ever observed in that line experimentally.

5.2.1.1 Effect of Inlet CO₂

The inlet CO₂ concentration was varied between 0 and 8 vol % during both the PZ and H₂SO₄ aerosol experiments. **Figure 5.7** and **Figure 5.10** show inlet CO₂, outlet CO₂, outlet H₂O, outlet PZ, and the solvent flowrate. The steady state PZ concentration for the PZ and H₂SO₄ aerosol case was 50–75 and 5–7 ppmv, respectively. The dashed gray lines indicate when the LVI pump was either connected (LVI On) or disconnected (LVI Off). The dead volume in the LVI liquid line for this test caused a response lag of about 3 minutes.

At a solvent rate of 12 GPH and 4 vol % inlet CO₂, PZ jumped from 50 to 100 ppmv for the PZ aerosol case. Further increases in CO₂ concentration appear to cause very small relative differences in outlet PZ measured during PZ aerosol injection. The large concentration independent change in CO₂ may be attributable to changes in the nucleation environment where an acid (CO₂) and a base (PZ) can fully react and

condense in a humid environment. Alternatively, the low concentration of PZ in the solvent may not be supplying sufficient vapor pressure to cause large enough saturation changes to cause observable aerosol growth even when exothermic absorption of CO₂ yields an increase in the bulk solvent temperature. The high solvent rates of 6–18 GPH, corresponding to a liquid-to-gas ratio (L/G) of 9.5–28.4 mol/mol, would also dampen any temperature bulging, and consequently saturation changes in the column.

Under identical conditions, but with H₂SO₄ injection, PZ shows less clear behavior. Though PZ initially increases by about 17% as CO₂ is increased from 0 to 4 vol%, an additional doubling of CO₂ to 8 vol % causes a 17 % decrease in PZ. Once the solvent flowrate and CO₂ concentrations are lowered from 12 to 6 GPH and 8 to 4 vol %, respectively, outlet PZ increased from 3.5 to 5.5 ppm. When the inlet CO₂ is turned off, PZ returns to the baseline of 6 ppmv.

Amine emissions respond to the inlet CO₂ concentration depending on the nuclei composition. FTIR measurements showed a nearly doubling of the outlet PZ when CO₂ was introduced into the AGC for PZ seed nuclei; aerosols produced from H₂SO₄ did not exhibit this behavior. However, emissions do appear to be inversely proportional to CO₂, though the absolute change was quite small in these tests. The predicted effect of CO₂ on aerosol growth is likely dampened under these conditions, i.e. high solvent rates and low solvent concentrations.

5.2.1.2 Effect of L/G

L/G was varied in this study between 9.5–57.0 mol/mol. **Figure 5.8** and **Figure 5.10** show the effect of L/G changes independent of inlet CO₂ concentrations for the PZ and H₂SO₄ aerosol cases, respectively.

Stepwise decrease in solvent rate significantly reduces the outlet PZ measured during PZ aerosol injection experiments; **Figure 5.8** shows that PZ decreases in a proportional fashion. Though this behavior was seen during the variable CO₂ experiments, the degree of reduction in PZ is not nearly as high. A mass balance using the LVI and process gas compositions leads to a total (gas and aerosol) PZ concentration of 383 ppmv. Since the baseline PZ measured at the AGC outlet is 50-75 ppmv, the AGC column is absorbing PZ, as well as possibly capturing PZ-containing aerosol with an efficiency of 80.4-86.9 %. It is therefore possible that increasing the solvent rate provides more absorption capacity and greater collection of PZ. In the case of the CO₂ experiment (**Figure 5.7**), PZ is not scrubbed with such high efficiencies when the solvent rate is increased. CO₂ may be serving to sequester PZ inside of the aerosols through reaction. Modeling work has shown that for even conservative CO₂ absorption rates, the absorption rate of CO₂ into amine-containing aerosols is very fast and that the aerosol phase is at a much higher CO₂ loading than the solvent, and therefore has a much lower P^*_{PZ} than the solvent. Fast reaction of CO₂, be it during nucleation or upon entering into the absorber would prevent favorable partitioning of PZ towards the solvent. The CO₂ rich aerosol would then only respond to very large changes in driving forces created by CO₂ absorption at very low liquid rates, or large temperature differences between the inlet gas and liquid.

Figure 5.10 shows that H₂SO₄ has opposite behavior compared to PZ aerosols upon varying the inlet solvent rate, though the measurement differences are less distinguishable clean. Creation of supersaturation might explain the inverse relationship between solvent rate and PZ emissions. The inlet gas is about a 1.5:1 mixture of gases at 310 and 40 °C that cools further due to heat loss in the system prior to entering the absorber; therefore, it is expected that the inlet gas temperature is higher than the inlet

solvent at 40 °C. If the solvent temperature is raised, then the temperature difference across the column is minimized. Conversely, if the colder solvent's flowrate is increased, the temperature gradient would be steeper, and cause higher degrees of supersaturation, and consequently more aerosol growth.

L/G affects outlet PZ emissions to a much higher degree than CO₂ for both aerosol cases investigated. Without size distribution measurements of the aerosols, differentiation of absorption and aerosol behavior is nearly impossible, though comparing the H₂O curves to that of PZ does provide some perspective. The outlet FTIR measurement, in the absence of aerosol generation, closely approximates saturated solvent conditions. The variability in these measurements is atypical of system control and heater oscillations. Further, the near parallel behavior of H₂O and PZ indicates that the majority of the measured PZ is in the aerosol phase.

5.2.1.3 Effect of Temperature

The final operation variable explored in this study was the inlet solvent temperature. The temperature was increased from 40 to 50 °C without changing the solvent flowrate and in the absence of CO₂.

Figure 5.9 and **Figure 5.10** show the change in outlet PZ for the PZ and H₂SO₄ aerosol cases, respectively. PZ emissions dropped by 20% for the PZ aerosol case; distinct trends for the H₂SO₄ aerosols are indistinguishable. Increasing the solvent temperature decrease PZ absorption in the solvent as well as reduce the temperature gradient across the AGC. The PZ absorption or solvent washing and the supersaturation or aerosol growth mechanisms should influence the outlet PZ in opposing directions. Looking back at **Figure 5.8**, the H₂O curve increases with solvent flowrate, which would be consistent with aerosol growth mechanism, but then decreases at higher flowrates,

which is consistent with the absorption mechanism. It is possible that both mechanisms are occurring simultaneously, or in the best case, are starting to be captured in the packing.

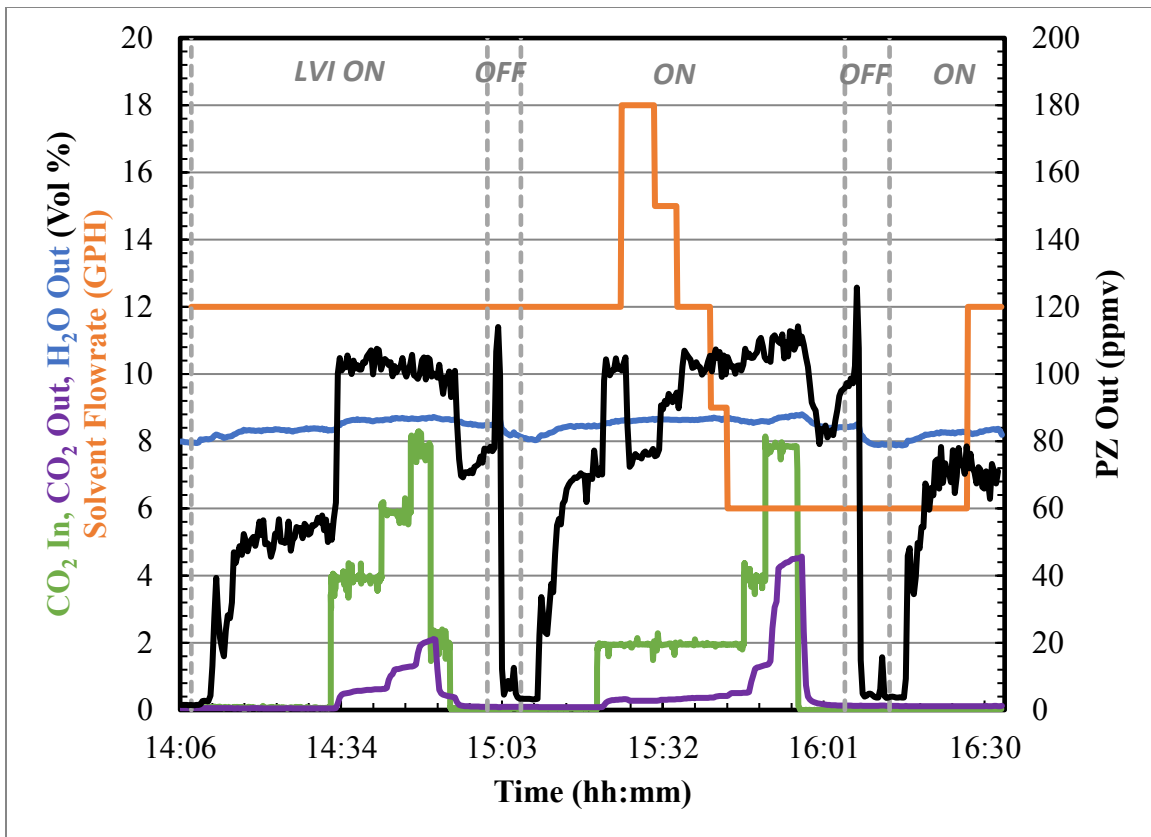


Figure 5.7: Outlet PZ measurements for variable AGC operating conditions with injection of 0.5 m PZ by the LVI operating in bypass mode. Outlet PZ increases sharply with CO₂, but is not correlated to the concentration. PZ is inversely related to solvent rate. Inlet solvent T is 40 °C and nominally 1 m PZ at 0.18 CO₂ loading. (08/14/14)

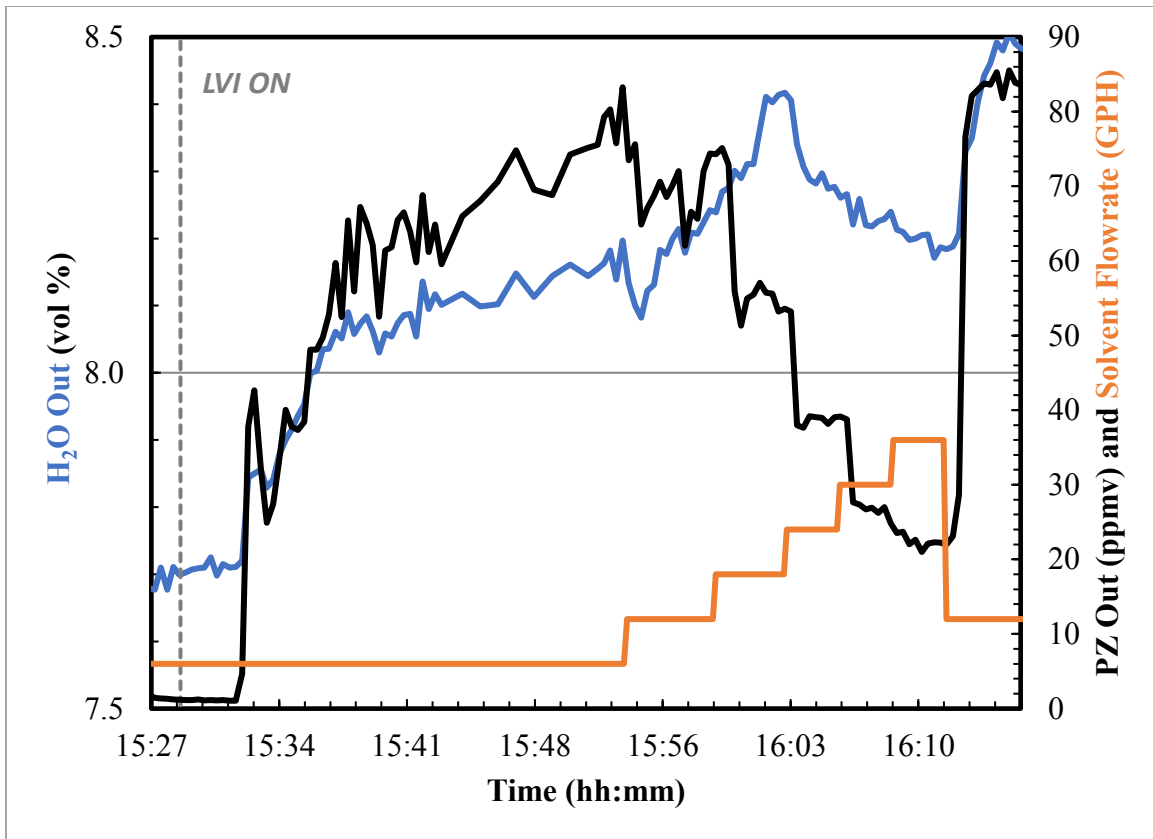


Figure 5.8: Absorber outlet emissions under PZ aerosol load in response to changing solvent flowrate; CO₂ flow is zero. Outlet PZ is inversely proportional to the solvent rate. L/G varies from 9.5-57.0 mol/mol. Inlet solvent T is 40 °C and nominally 1 m PZ at 0.3 CO₂ loading. (08/15/14).

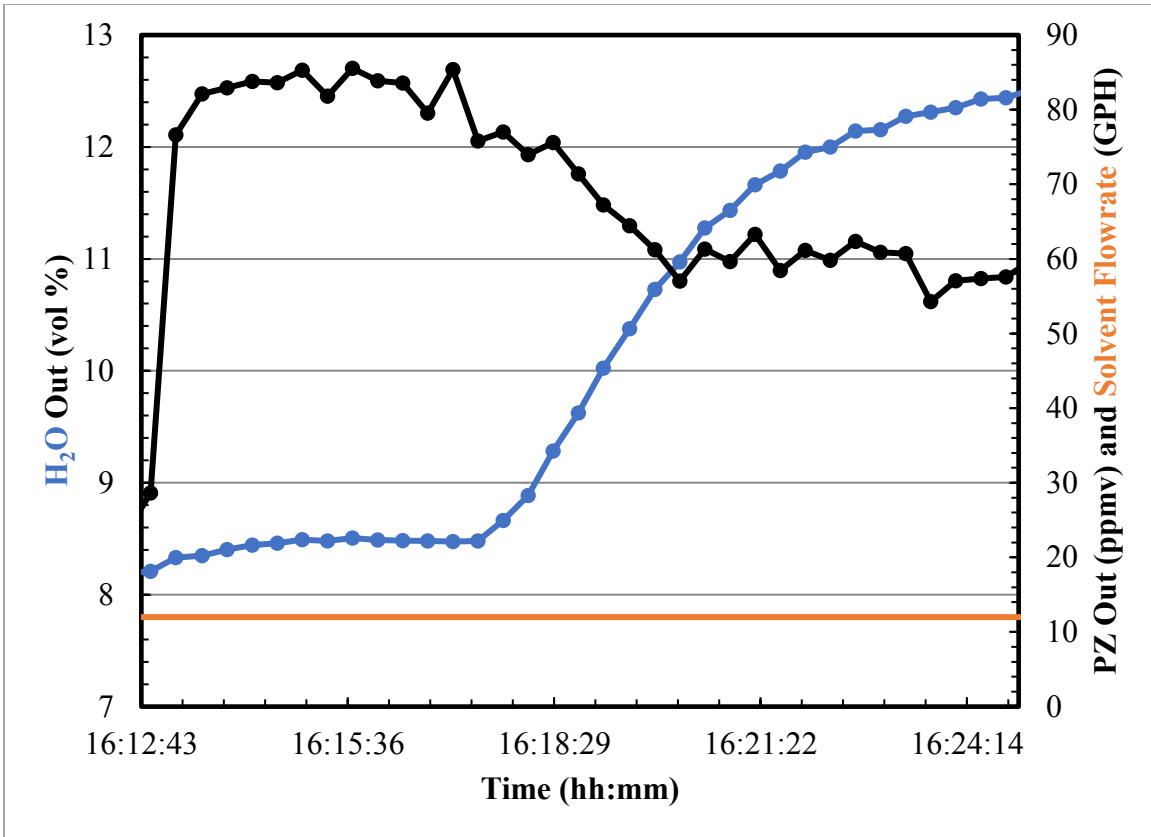


Figure 5.9: Absorber outlet emissions under PZ aerosol load in response to changing the solvent inlet temperature from 40 to 50 °C. The solvent is nominally 1 m PZ at 0.3 CO₂ loading. Outlet PZ is inversely proportional to the solvent temperature. (08/15/14).

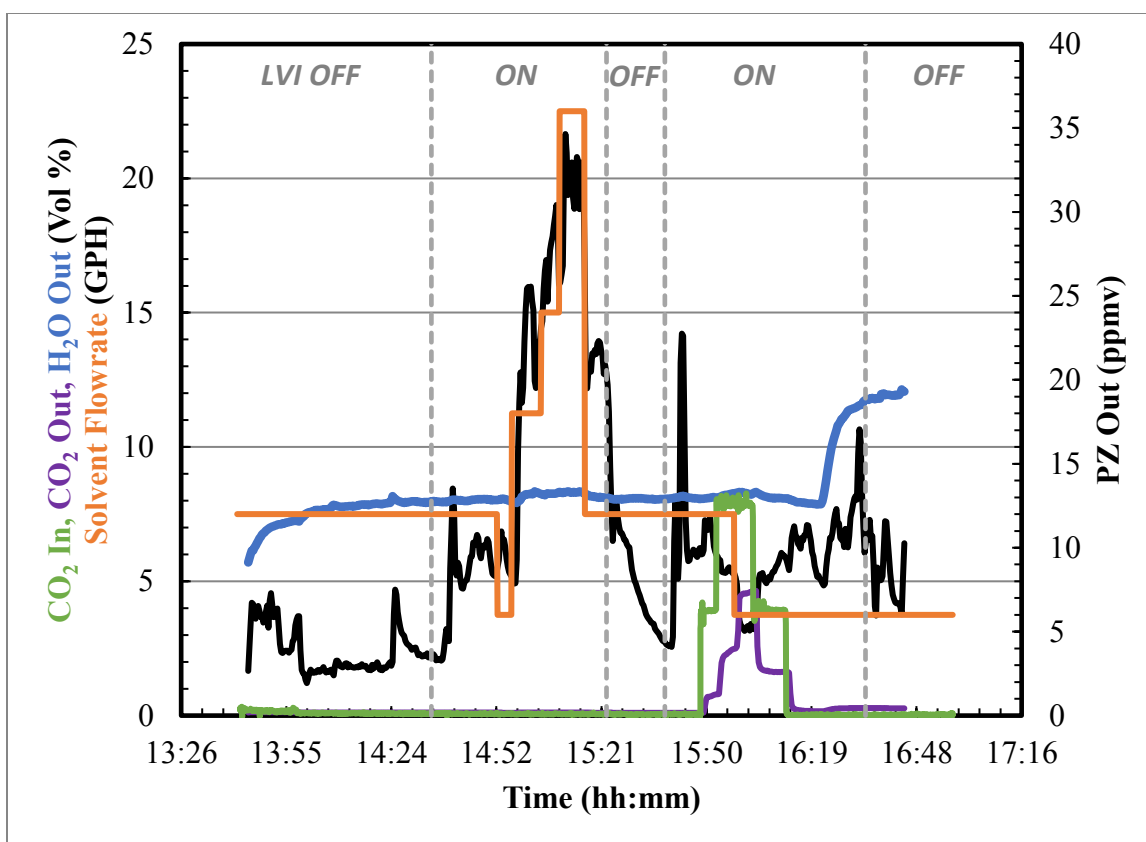


Figure 5.10: Outlet PZ measurements for variable AGC operating conditions with injection of 0.05 vol/vol H₂SO₄ by the LVI operating in bypass mode. Outlet PZ shows a weak, inverse correlation to CO₂ concentration and is positively correlated to solvent flowrate. Inlet solvent T is 40 °C and nominally 1 m PZ at 0.3 CO₂ loading. (08/19/14).

5.3 PDI TESTS

5.3.1 PDI Gen. 2

A modular PDI (Gen. 2) with a lower detection limit of 0.5 μm was tested on the AGC during the November, 2013 pilot campaign (Chapter 5). The LVI was operated at 2 mL/min of 10 vol % H₂SO₄. The AGC solvent was DI H₂O at 40 and 50 °C. The PSD statistics are tabulated below (Table 5.6). Figure 5.11 shows the PSDs measured during that experiment. In the range of 0.5–10 μm , the PSD appears to be a monomodal,

lognormal distribution though the spread of the peak might indicate two closely matched modes.

Table 5.6: PSD statistics for H₂SO₄ aerosols on the AGC. LVI flowrate: 2.0 mL/min of 10 vol % H₂SO₄. AGC solvent is H₂O.

Solv. T [°C]	Total Dens. [Part./cm ³]	D ₁₀ [μm]	D ₃₂ [μm]
40	6.0E+03	1.42	1.99
40	2.0E+04	1.29	1.85
40	6.2E+03	1.20	1.68
50	1.3E+04	1.33	1.83
50	1.2E+04	1.35	1.84

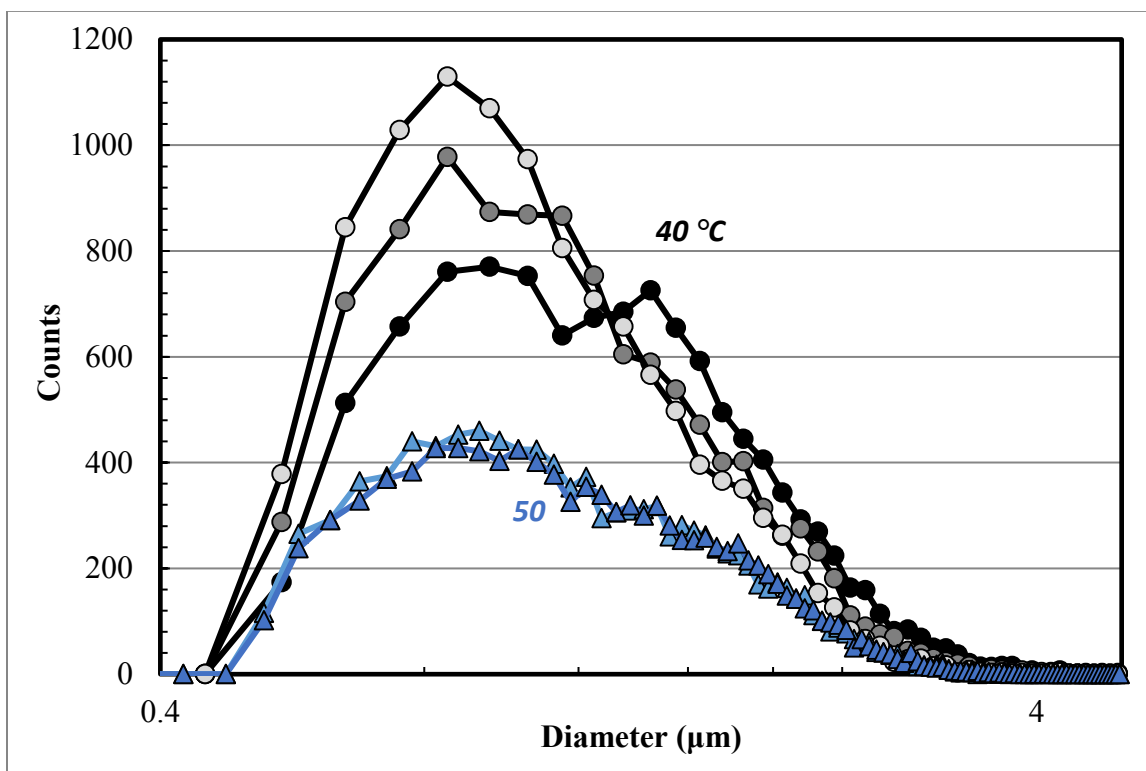


Figure 5.11: Consecutive PDI analyses taken on the AGC outlet at an H₂SO₄ injection rate of 2 mL/min. and a solvent temperature of 40 and 50 °C. The solvent is DDI H₂O.

Though the measurements made on the AGC was the first successful use of the PDI, the high variability in particle density demonstrated the instability of the LVI operation. Additionally, the particle density was far below what was calculated using the LVI injection rate. It is very clear that the LVI was partially vaporizing the injection H_2SO_4 and/or significant capture of the seed nuclei was occurring at the injection mixing point.

The simultaneous failure of the LVI during the November, 2013 campaign lead to significant redesign over the course of a year as the custom (Gen. 3) PDI was being designed and built in parallel.

5.3.2 PDI Gen. 3

The solvent used during the reported experiment was collected on March 25, 2015; the PRC data logs show a solvent composition of 30 wt % (5 m PZ) and a lean solvent loading of 0.2 moles CO_2 /mol alkalinity. The LVI flowrate was set to 0.42 mL/min of H_2O mixed with 18 SLPM of N_2 at 325 °C. Flowrates measured by rotameter (solvent rate and LVI N_2 rate) are corrected for temperature and pressure. The LVI liquid flowrate is corrected by a calibration curve (Appendix C).

Raw experimental data is given below in **Table 5.7–Table 5.11**.

Figure 5.12 shows the outlet PZ as the inlet CO_2 , solvent rate, and inlet solvent temperature change. PZ emissions show a clear increase as CO_2 is added to the system. However, changes to the amount of CO_2 have a less significant effect on PZ and show an inverse relationship. This same behavior was observed in the work by Khakharia (2015).

Table 5.7: PDI data imported and calculated from raw PDI file output. The integrated volume is the total volume of liquids in the aerosol phase.

Particle Conc. [part./cm³]	D₁₀ [μm]	D₂₁ [μm]	D₃₂ [μm]	D₄₃ [μm]	Integrated Vol. [μm³/cm³]
7.00E+05	0.286	0.406	0.726	1.194	3.088E+04
8.51E+05	0.287	0.434	0.966	2.212	5.370E+04
2.60E+05	0.291	0.496	1.228	2.312	2.409E+04
2.08E+05	0.294	0.516	1.340	2.548	2.218E+04
7.06E+06	0.703	0.924	1.077	1.191	2.587E+06
2.75E+06	0.565	0.784	0.947	1.063	6.039E+05
2.71E+06	0.571	0.789	0.952	1.070	6.081E+05
2.59E+06	0.563	0.782	0.948	1.070	5.668E+05
6.06E+06	0.679	0.902	1.063	1.189	2.065E+06
6.71E+06	0.732	0.965	1.135	1.278	2.814E+06
6.61E+06	0.745	0.976	1.144	1.281	2.878E+06
6.60E+06	0.740	0.975	1.149	1.297	2.864E+06
6.69E+06	0.702	0.919	1.073	1.193	2.429E+06
7.03E+06	0.701	0.921	1.073	1.186	2.552E+06
6.12E+06	0.687	0.909	1.063	1.174	2.125E+06
1.37E+06	0.351	0.580	1.131	1.995	1.650E+05
1.20E+06	0.343	0.537	0.916	1.412	1.062E+05
8.78E+06	0.905	1.150	1.344	1.522	6.432E+06
8.80E+06	0.904	1.150	1.342	1.511	6.430E+06
9.31E+06	0.781	1.014	1.189	1.348	4.596E+06
8.88E+06	0.782	1.016	1.201	1.400	4.439E+06
5.92E+05	0.317	0.708	2.253	4.039	1.569E+05
5.44E+05	0.321	0.764	2.480	4.255	1.733E+05
3.11E+05	0.503	1.712	3.706	5.010	5.195E+05
2.57E+05	0.561	1.771	3.405	4.541	4.556E+05
6.60E+05	0.473	1.526	3.475	4.926	8.670E+05
6.72E+05	0.460	1.384	3.041	4.244	6.812E+05
1.42E+07	0.977	1.176	1.330	1.467	1.139E+07
1.48E+07	0.978	1.186	1.358	1.540	1.224E+07
1.49E+07	0.985	1.196	1.367	1.539	1.258E+07
1.70E+07	0.937	1.120	1.264	1.411	1.180E+07
1.68E+07	0.926	1.112	1.254	1.383	1.134E+07
1.70E+07	0.936	1.117	1.262	1.409	1.172E+07
9.04E+06	0.785	1.009	1.173	1.315	4.397E+06

Table 5.8: Upstream gas mixing and presaturator temperature data.

N₂ MFC (FCV1301-1) [SLPM]	CO₂ MFC (FCV1301-2) [SLPM]	T_{Presat.} (TT1301-1) [°C]	LVI N₂ [SLPM]	LVI H₂SO₄ [mL/min]
25.2	0.0	39.9	18.07	0.41
25.2	0.1	39.9	18.07	0.41
25.2	0.0	40.1	18.07	0.41
26.4	0.0	40.2	18.07	0.41
25.1	5.0	40.3	18.07	0.41
25.2	10.0	40.4	18.07	0.41
25.2	10.0	40.4	18.07	0.41
25.2	10.0	40.4	18.07	0.41
24.6	5.0	40.4	18.07	0.41
25.3	3.0	40.3	18.07	0.41
25.1	3.0	40.3	18.07	0.41
25.1	3.0	40.3	18.07	0.41
25.2	5.0	40.2	18.07	0.41
25.2	5.0	40.3	18.07	0.41
24.6	5.0	40.4	18.07	0.41
25.3	0.0	40.2	18.07	0.41
25.2	0.0	40.2	18.07	0.41
25.2	5.0	40.3	18.07	0.41
25.1	5.0	40.2	18.07	0.41
26.4	8.0	40.2	18.07	0.41
25.2	8.0	40.3	18.07	0.41
25.2	0.0	39.9	18.07	0.41
25.2	0.0	40.0	18.07	0.41
25.1	0.0	39.9	18.07	0.41
25.2	0.0	40.0	18.07	0.41
25.2	0.0	40.2	18.07	0.41
25.2	0.0	40.1	18.07	0.41
25.2	5.0	40.1	18.07	0.41
25.2	5.0	40.2	18.07	0.41
25.2	5.0	40.2	18.07	0.41
25.2	8.0	40.3	18.07	0.41
25.2	8.0	40.3	18.07	0.41
25.2	8.0	40.3	18.07	0.41
25.2	8.0	40.2	18.07	0.41

Table 5.9: AGC inlet and outlet flowrate, temperatures, and solvent concentration.

T_{Gas In} (TT2301-1) [°C]	T_{Solv. In} (TT3301-1) [°C]	T_{Gas Out} (TT2301-1) [°C]	Solv. Flow (FI3301-1) [GPM]	Solv. Conc. [molal]	Solv. Lean Ldg. [mol/mol]
42.2	38.5	34.9	0.172	5	0.25
42.3	38.5	34.8	0.172	5	0.25
44.5	41.8	40.1	0.173	5	0.25
44.5	41.4	39.7	0.173	5	0.25
45.1	40.9	39.5	0.173	5	0.25
45.6	40.9	40.5	0.173	5	0.25
45.6	40.9	40.6	0.173	5	0.25
45.6	40.9	40.6	0.173	5	0.25
45.3	41.1	39.7	0.173	5	0.25
45.1	41.1	39.4	0.173	5	0.25
45.1	41.1	39.4	0.173	5	0.25
45.1	41.1	39.4	0.173	5	0.25
45.2	40.9	39.5	0.173	5	0.25
45.2	40.9	39.6	0.173	5	0.25
45.3	41.1	39.7	0.173	5	0.25
44.2	48.9	45.7	0.174	5	0.25
44.1	48.9	45.7	0.174	5	0.25
44.6	48.9	46.1	0.174	5	0.25
44.6	48.9	46.1	0.174	5	0.25
44.7	48.8	46.1	0.174	5	0.25
44.7	48.7	46.1	0.174	5	0.25
42.5	37.9	34.9	0.301	5	0.25
42.7	38.0	35.1	0.301	5	0.25
42.9	37.2	35.1	0.430	5	0.25
43.1	37.5	35.3	0.430	5	0.25
43.7	46.5	42.3	0.434	5	0.25
43.7	46.8	42.9	0.434	5	0.25
44.3	46.9	43.7	0.434	5	0.25
44.5	47.3	44.4	0.434	5	0.25
44.5	47.3	44.4	0.434	5	0.25
44.6	47.8	45.3	0.435	5	0.25
44.6	47.8	45.3	0.435	5	0.25
44.6	47.8	45.3	0.435	5	0.25
44.7	48.8	46.0	0.174	5	0.25

Table 5.10: Calculated inlet and measured (FTIR) outlet gas concentrations.

H₂O In [vol %]	CO₂ In [vol %]	PZ In [ppmv]	H₂O Out [vol %]	CO₂ Out [vol %]	PZ Out [ppmv]
4.38	0.10	0.00	5.10	0.05	10.53
4.38	0.12	0.00	5.44	0.06	11.42
4.38	0.06	0.00	7.99	0.11	8.14
4.46	0.06	0.00	7.78	0.11	7.84
4.69	9.88	0.00	7.77	1.85	31.30
4.94	17.89	0.00	7.84	8.37	15.94
4.94	17.87	0.00	7.90	8.78	12.38
4.94	17.87	0.00	7.92	8.86	11.96
4.65	10.00	0.00	7.90	2.40	21.59
4.58	6.16	0.00	7.74	0.97	28.74
4.57	6.22	0.00	7.71	0.96	28.59
4.57	6.22	0.00	7.74	0.96	28.44
4.69	9.88	0.00	7.78	1.90	30.46
4.69	9.87	0.00	7.78	1.97	29.13
4.65	10.00	0.00	7.87	2.33	22.52
4.39	0.02	0.00	10.89	0.31	21.14
4.38	-0.07	0.00	10.89	0.26	16.93
4.69	9.87	0.00	11.27	1.84	66.52
4.69	9.89	0.00	11.32	1.84	64.98
4.90	14.51	0.00	10.83	3.45	62.11
4.85	14.86	0.00	11.06	3.58	58.93
4.38	0.07	0.00	5.78	0.06	11.99
4.38	0.09	0.00	5.98	0.06	12.03
4.38	0.08	0.00	6.05	0.06	13.03
4.38	0.08	0.00	5.92	0.06	15.07
4.38	0.11	0.00	8.47	0.12	28.67
4.38	0.08	0.00	8.89	0.12	33.96
4.69	9.88	0.00	9.52	0.27	147.63
4.69	9.86	0.00	9.72	0.28	161.70
4.69	9.86	0.00	9.80	0.28	164.31
4.85	14.88	0.00	10.36	0.51	176.00
4.85	14.88	0.00	10.37	0.55	201.55
4.85	14.88	0.00	9.92	0.56	179.86
4.85	14.85	0.00	10.66	3.29	69.62

Table 5.11: Calculated PZ volatility, integrated aerosol PZ content, and the absolute relative error between the integrated PDI PSD and the measurement made by FTIR.

P*PZ [ppmv]	Droplet Ldg. [mol/mol]	PZ in Droplet [ppmv]	Total PZ [ppmv]	Error (PDI/FTIR) [%]
9.24	0.235	0.24	9.48	10.0
9.29	0.241	0.41	9.70	15.0
12.08	0.246	0.19	12.26	50.7
11.67	0.246	0.17	11.84	51.0
11.21	0.365	20.09	31.30	0.0
11.25	0.419	4.69	15.94	0.0
11.26	0.420	4.72	15.98	29.1
11.26	0.421	4.40	15.66	31.0
11.38	0.374	16.03	27.41	27.0
11.40	0.339	21.87	33.26	15.7
11.44	0.339	22.37	33.81	18.3
11.44	0.339	22.26	33.70	18.5
11.23	0.365	18.86	30.09	1.2
11.24	0.367	19.81	31.05	6.6
11.38	0.373	16.50	27.88	23.8
21.24	0.268	1.31	22.55	6.7
21.21	0.261	0.84	22.05	30.2
21.17	0.343	50.91	72.08	8.4
21.16	0.343	50.89	72.05	10.9
20.98	0.369	36.33	57.31	7.7
20.92	0.370	35.08	56.00	5.0
8.82	0.242	1.21	10.03	16.3
8.88	0.240	1.34	10.22	15.1
8.36	0.241	4.01	12.37	5.1
8.52	0.237	3.52	12.04	20.1
17.48	0.239	6.83	24.31	15.2
17.90	0.238	5.38	23.28	31.5
18.17	0.270	89.92	108.08	26.8
18.68	0.270	96.84	115.52	28.6
18.68	0.270	99.53	118.21	28.1
19.43	0.292	93.44	112.87	35.9
19.43	0.295	89.80	109.23	45.8
19.43	0.296	92.84	112.27	37.6
20.99	0.367	34.75	55.74	19.9

The solvent rate seems to have the most significant effect on the total outlet PZ. Solvent rate has a stronger effect on the enthalpy distribution in an absorber than the CO₂ content of the flue gas owing to its large heat capacity. Therefore, significantly changing the solvent rate will change the temperature profile in the absorber which alters CO₂ removal, and more importantly the saturation/supersaturation conditions throughout the column.

The lean solvent temperature has a marginal effect, which is mostly explained by volatility changes with temperature, though the inverse relationship in this work is the opposite of that found in Khakharia (2015).

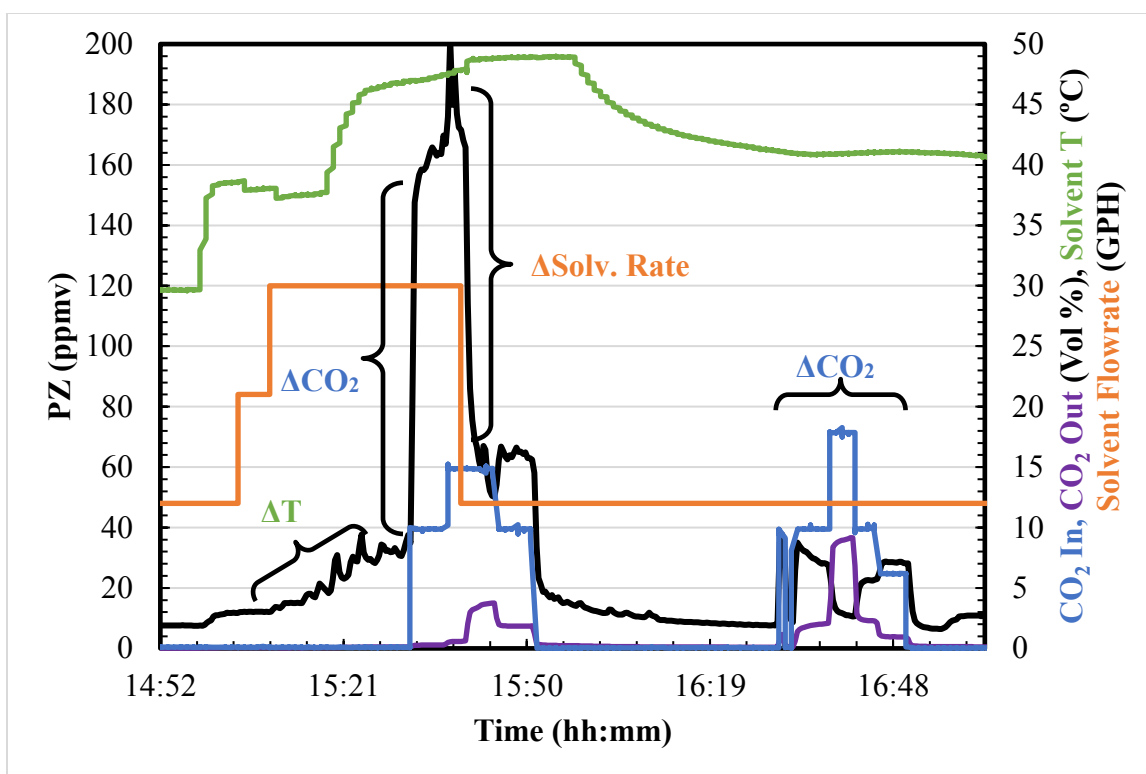


Figure 5.12: The measured outlet PZ is correlated with the inlet CO₂, the lean solvent rate, and the lean solvent temperature. The solvent was nominally 5 m PZ and 0.2 CO₂ loading. The LVI flowrate was set to 0.42 mL/min of H₂O. The inlet gas temperature ranged between 42 and 45 °C.

5.3.2.1 *The Effect of CO₂*

The influence of CO₂ on the measured particle size distribution at the AGC outlet is shown below in **Figure 5.13**. When no CO₂ is present in the flue gas, the particle distribution mean lies below the detectability of the PDI (0.1 μm). When CO₂ is added to the inlet gas, the PSD shifts to the right indicating growth out of the submicron region, or alternatively that CO₂ is a critical component required for nucleation. **Figure 5.13** shows one example at equivalent operating conditions; however, the large change in the PSD was consistent for all other observations of CO₂/no-CO₂ cases. The only measured differences were the total particle density and the mean of the CO₂ PSD distributions.

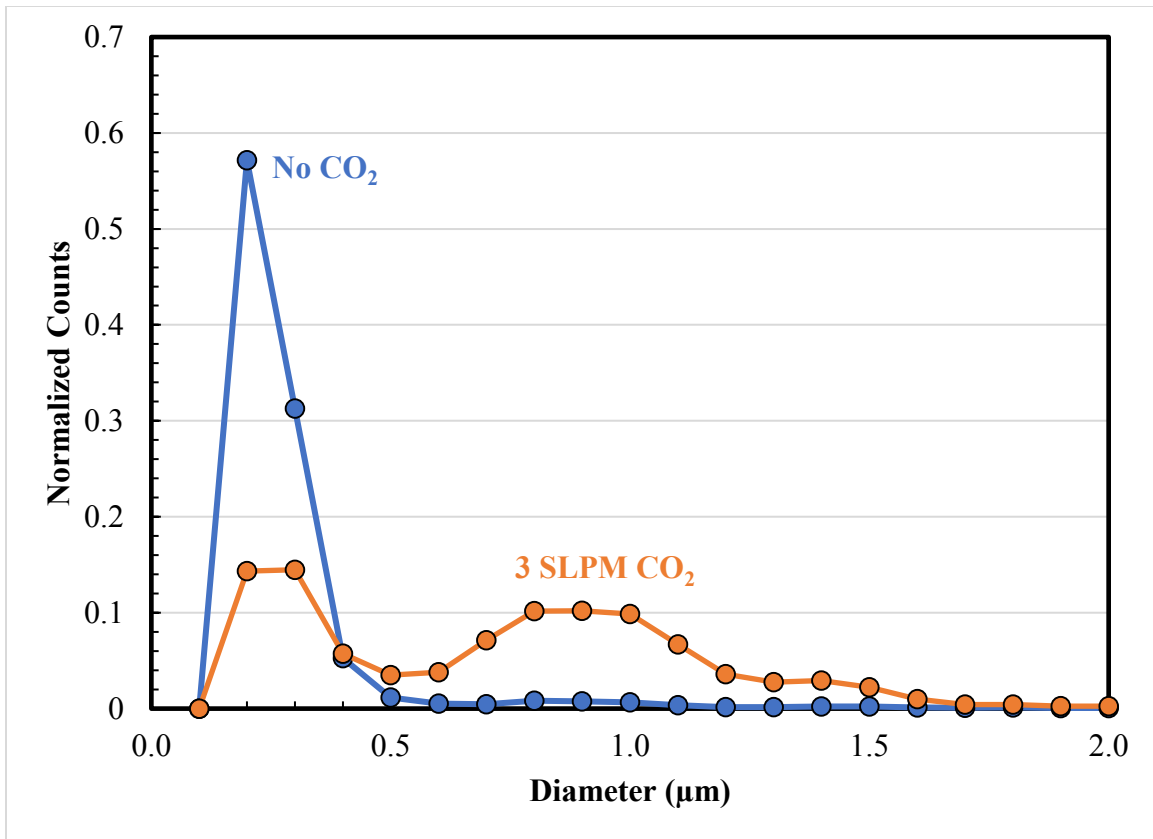


Figure 5.13: The aerosol particle size distribution shifts to the right (growth by condensation) with the addition of CO₂. Lean Solvent: 40 °C, 0.2 GPM. Inlet CO₂: 0 and 3 SLPM.

The count-average particle diameter (D_{10}) and total particle density for all measured PSDs is plotted against the inlet CO₂ content in **Figure 5.14**. **Figure 5.14** does not control for other varying process conditions. **Figure 5.15** replots the data with constant operating conditions (but changing inlet CO₂) and shows that the total particle density and the average particle diameter are strongly correlated and that a maximum particle diameter and density exists somewhere between 0 and 10 vol %, most likely around or below 6 vol %. When the measured outlet PZ is plotted against the inlet CO₂ concentration, the location of the maximum is less obvious due to the scatter in the 10 vol % data. Khakharia (2015) measured the outlet amine concentration by FTIR, for a mixed

PZ and 2-Amino-2-methyl-1-propanol (AMP) solvent system, and found that the outlet concentration showed a maximum value for an inlet CO₂ concentration of 6 vol %.

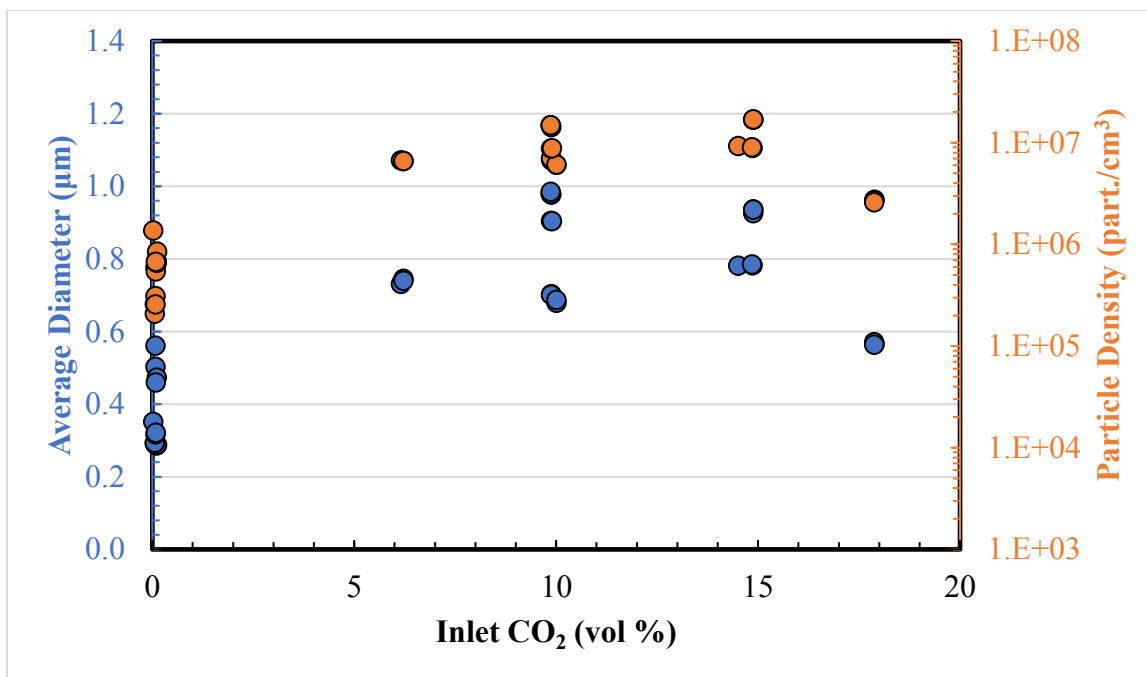


Figure 5.14: The measured count-average particle diameter (●) and total particle density changes (●) with inlet CO₂ content. No control for operating conditions other than inlet CO₂ was made.

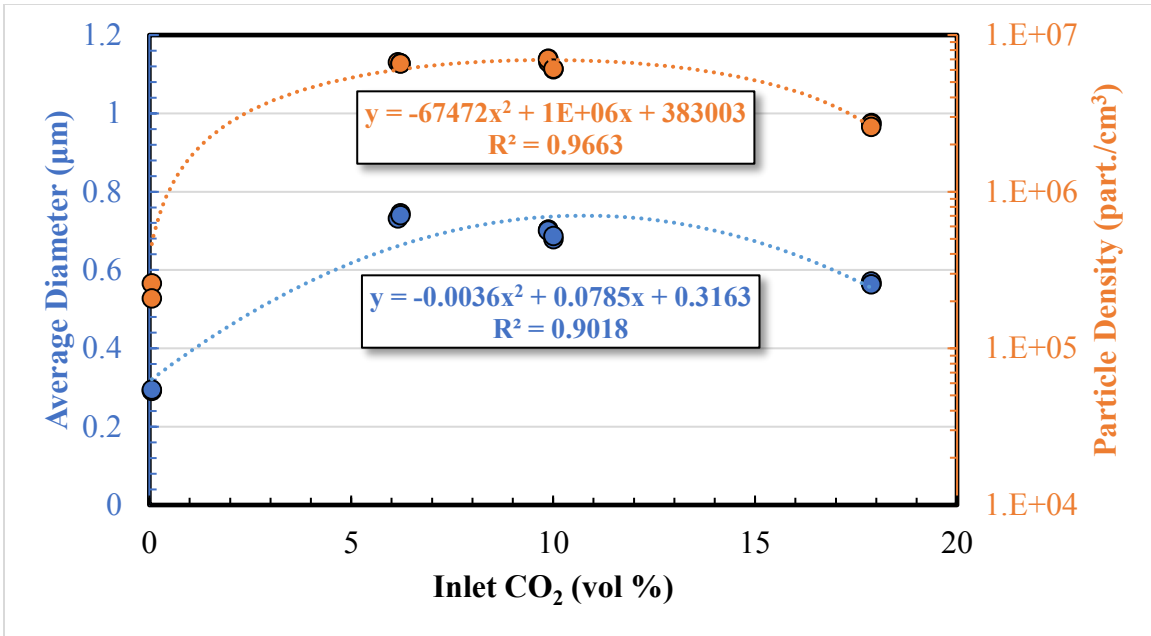


Figure 5.15: The measured count-average particle diameter (●) and total particle density (●) changes with inlet CO₂ content. All other process conditions kept constant. The spread in data for constant inlet CO₂ content indicates repeatability of the measurement.

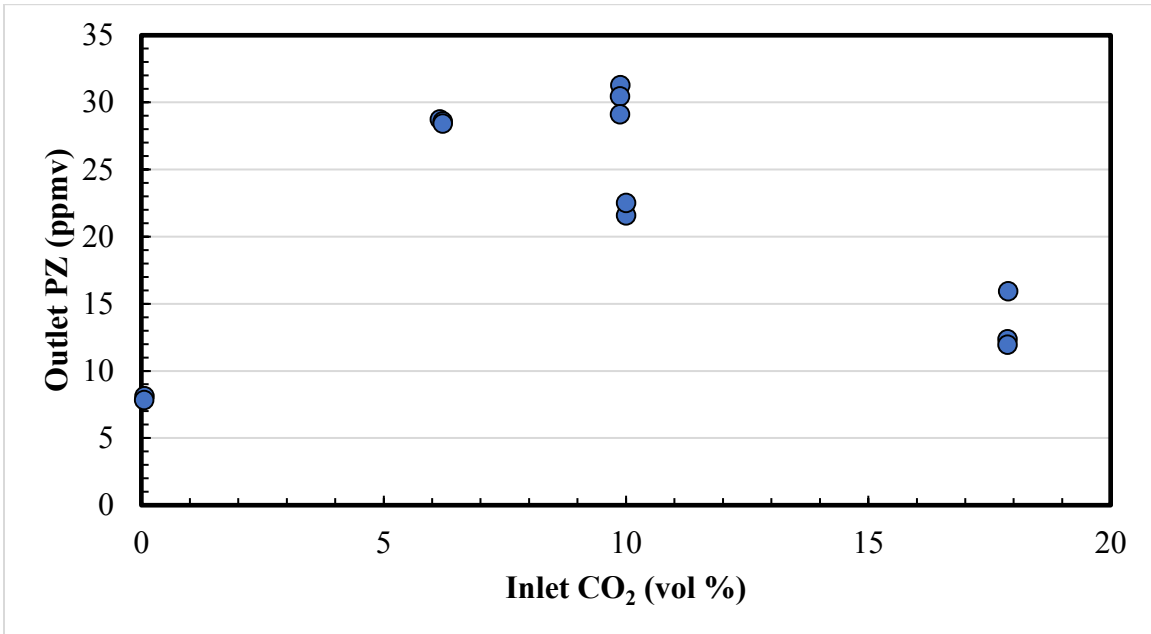


Figure 5.16: Outlet PZ measured by FTIR shows a maximum as the inlet CO₂ content is increased. All other process conditions are kept constant.

Comparison with the work of Khakharia (2015) shows a very similar relationship of the outlet amine concentration with the inlet value of CO₂. The mixed solvent system used by Khakharia was 2.6 M (mol/L) AMP and 0.9 M PZ. The values of emitted AMP and PZ were normalized to account for differences in particle concentrations as well as the solvent concentration's impact on the absolute emission level. Each amine was normalized independently. The average outlet concentrations were read off of Figure 5.9 from Khakharia's dissertation.

Figure 5.17 shows the normalized outlet amine concentrations from this work and that of Khakharia as the inlet CO₂ content varies. The lines indicate the amines used in the work of Khakharia and the solid orange points are the measurements taken in this study. Though there is scatter in the data around 10 vol % inlet CO₂, the same maximum behavior is observed when only PZ is used by itself. However, the location of the maximum is unclear in the data set collected in this work.

Khakharia's hypothesized that two competing mechanisms cause the emissions maximum to occur for varying inlet CO₂: (1) the effect of CO₂ on loading (speciation effect) and (2) reaction enthalpy (temperature effect). As the inlet CO₂ content decreases, the CO₂ loading is leaner across the column and more free amine exists in the bulk solution which increases volatility. However, a smaller absolute quantity of CO₂ is captured, which means less reaction enthalpy and therefore smaller temperature changes in the bulk solvent which ultimately reduces the volatility.

The changes in volatility impact the degree of saturation throughout the column. As pointed out by Khakharia, areas of supersaturation in the column will lead to heterogeneous nucleation. However, because the aerosol nuclei is generated from SO₂/SO₃/Fly ash, they contain solute not present in the bulk solvent. Additionally, because aerosol liquid is close to equilibrium in CO₂, the a larger fraction of the amine

contained in the aerosol is bound to CO₂ as reacted products and therefore the activity of amine in the aerosol phase is much lower than the bulk solvent. The solute effect, attributed to the work of Köhler (1921, 1926), greatly reduces the required saturation required for heterogeneous condensation (Seinfeld et al., 1998). The Köhler effect is especially important for smaller aerosols, typically under one micron. The calculation of supersaturation must be relative to the existing nuclei composition. Supersaturation relative to insoluble nuclei can be calculated using the dew point of the gas and must be adjusted for the contact angle; no additional considerations for the solute effect are required.

The location of the maximum will depend on the thermodynamics of the amine/CO₂/H₂O system and the operation of the absorber column, particularly the solvent flow rate and the gas/solvent temperatures. Flow rate and temperature have the greatest effect on enthalpy in the column. The amine or amine system will influence the aerosol growth rate by liquid chemistry (pK_a effect), CO₂ solubility (solvent rate effect), heat of absorption (temperature effect), and volatility (vapor pressure effect).

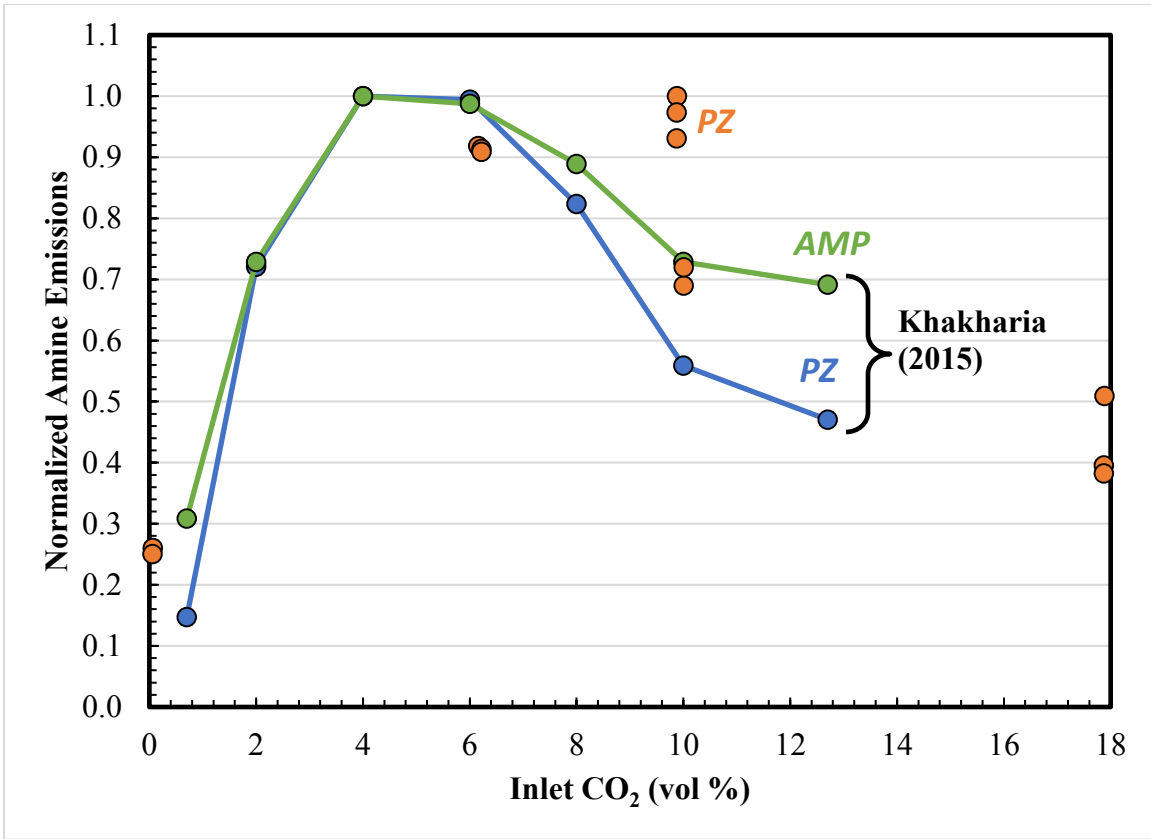


Figure 5.17: Normalized amine emissions for varying inlet CO₂ concentrations from this study (●) and the work of Khakharia (2015). This study used 5 m PZ. Khakharia used a mixed solvent system composed of 2.6 M AMP (●) and 0.9 M PZ (●).

The maximum behavior may also be related to growth and capture of a bimodal aerosol distribution. The addition of CO₂ causes the entire aerosol population to grow, and as CO₂ is increased further, losses in the packing and bends will increase and the total particle density will start to decrease. If a single mode is present, the average particle diameter should reach a plateau as the right-hand side of the PSD starts to be captured and eventually the average diameter becomes the overall cut diameter of the process. If a second, smaller mode is present, as the larger mode is captured the average

particle diameter and the total particle density will decrease; the smaller mode will become more significant to the count-averaging procedure.

Figure 5.18 shows the relationship between the average particle diameter and the total particle density for variable inlet CO₂ with all other process conditions held constant. The average diameter and the logarithm of the total particle density are linearly related.

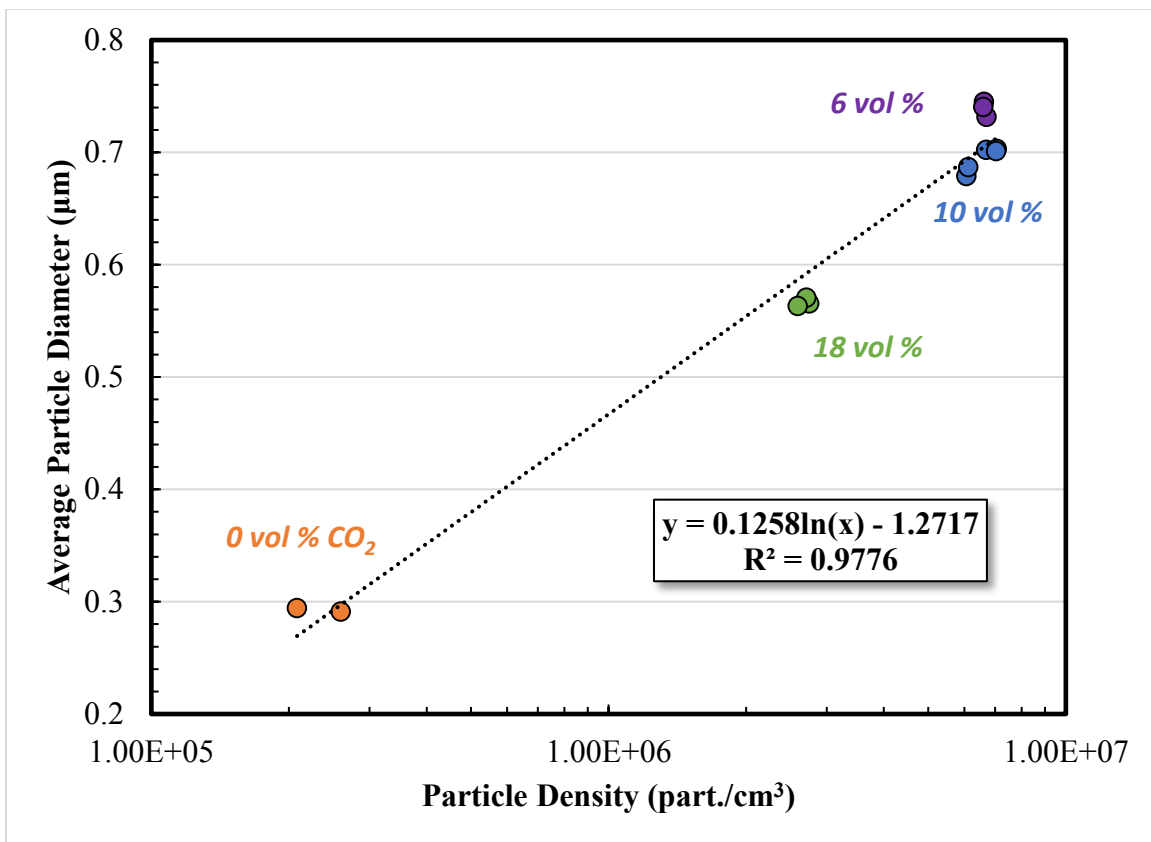


Figure 5.18: The average particle diameter and the logarithm of particle density are correlated linearly for variable inlet CO₂. All other process conditions kept constant.

5.3.2.2 The Effect of L/G

The average diameter and the total particle density for changing lean solvent rate is shown in **Figure 5.19**. For all other process conditions held constant, the average diameter and total particle density are positively correlated with the lean solvent rate. Similarly to the inlet CO₂ concentration, the average droplet diameter and the total density track each other for variations in solvent rate (**Figure 5.20**).

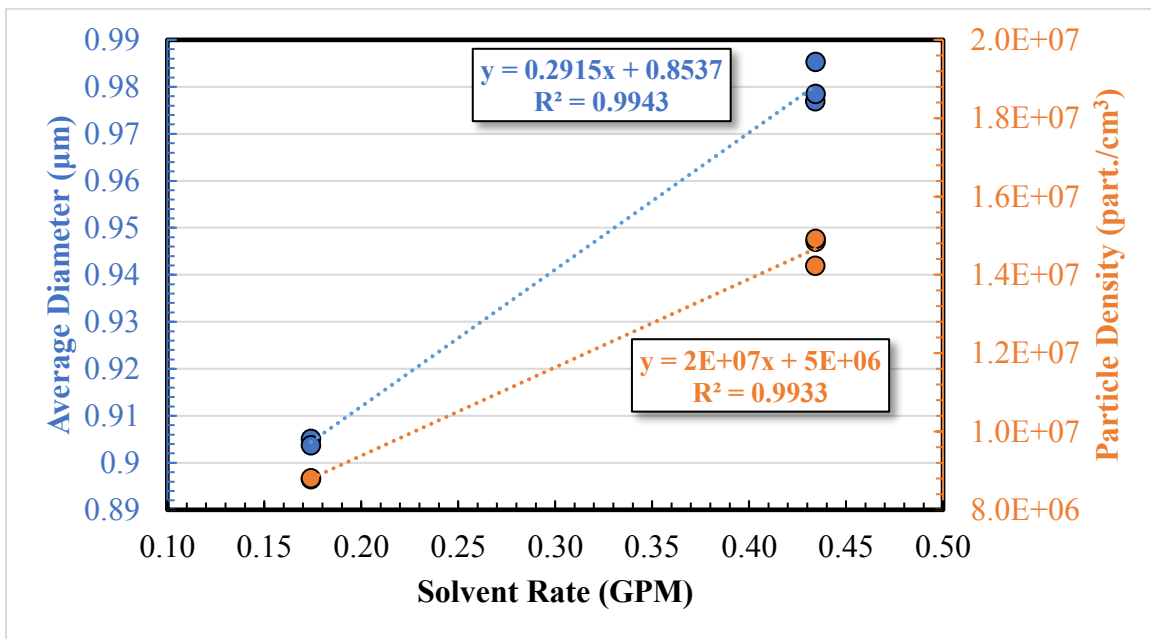


Figure 5.19: The measured count-average particle diameter (●) and total particle density increases (●) with the solvent rate. All other process conditions kept constant (inlet CO₂ is 10 vol %).

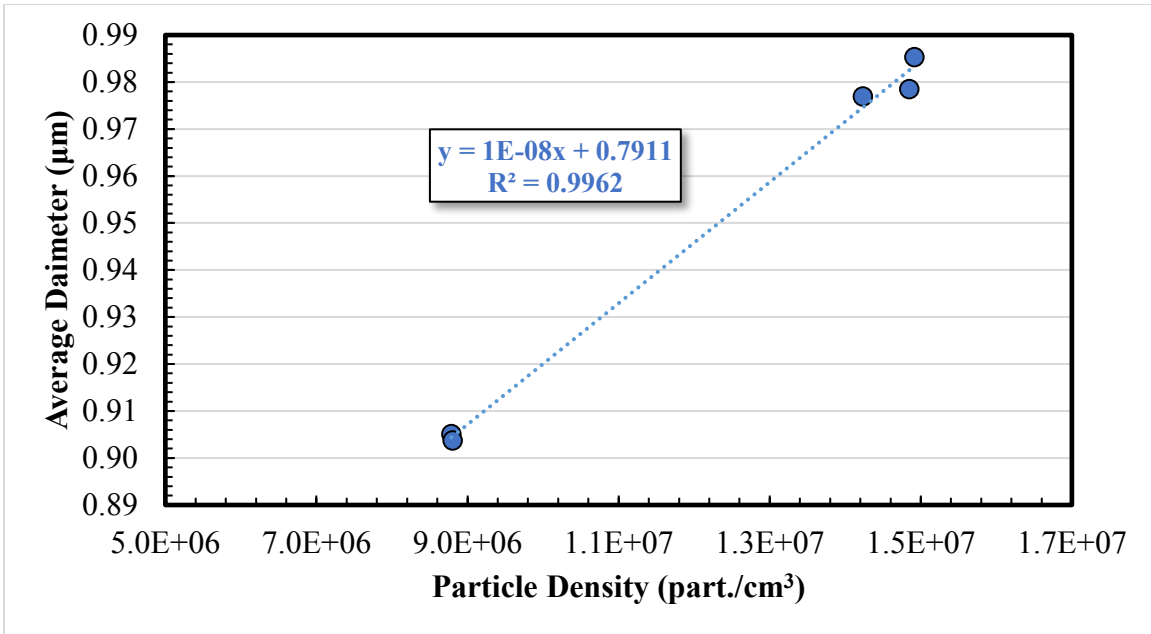


Figure 5.20: The average particle diameter and the particle density are positively correlated for variable lean solvent rate. All other process conditions kept constant.

5.3.2.3 Particle Density Comparison

A comparison to the outlet amine concentration versus the measured particle density data collected by Khakharia (2015) can be seen in **Figure 5.21**. Even though the solvent systems (MEA by Khakharia and PZ in this work) and aerosol sources are different, the qualitative shape of the concentration response is quite similar. A common transition appears for very dense aerosols; the concentration/density dependence becomes linear. The transition point may be related to the particle diameter. The larger the average particle size, the larger the contribution of the aerosol phase is to the outlet amine concentration. Without size information from Khakharia, that conclusion cannot be confirmed.

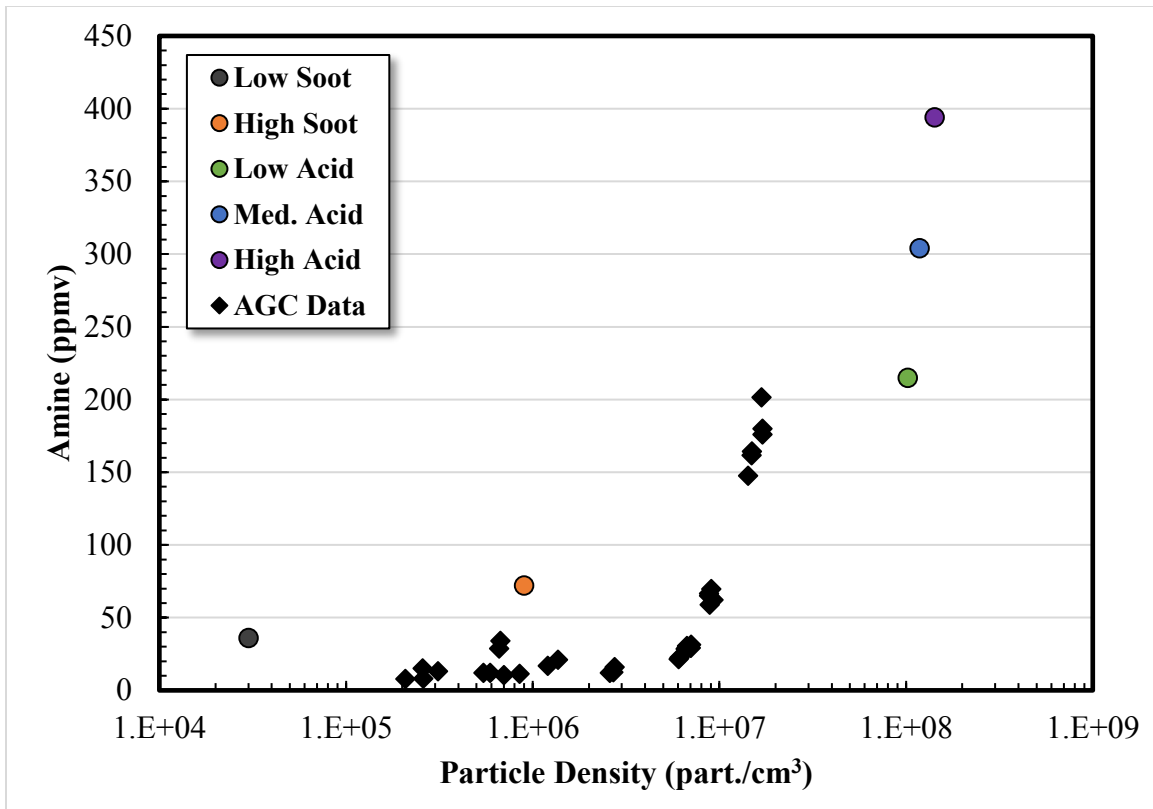


Figure 5.21: Measured outlet amine concentration data for the AGC (PZ solvent, \blacklozenge) plotted against data collected by Khakharia (2015) (MEA solvent, \bullet) as a function of the measured particle density.

5.3.2.4 PDI/FTIR Fitting

Figure 5.22 shows the calculated total concentration of PZ which includes the solvent vapor pressure and the integrated particle size distribution. The CO_2 loading in the droplet phase was assumed to be in equilibrium with the outlet gas; the loading was calculated using the empirical correlation developed in the work of Xu (2011a). The relationship between loading and the equilibrium partial pressure is quadratic and can be solved using the Quadratic Formula (Equations (5.1)–(5.4)). The positive root is always positive and the negative root always produces negative (non-real) loadings.

$$\ln(P_{CO_2}^*) = A + \left(\frac{B}{T}\right) + C\alpha + D\alpha^2 + E\left(\frac{\alpha}{T}\right) + F\left(\frac{\alpha^2}{T}\right) \quad (5.1)$$

$$0 = \left[A + \left(\frac{B}{T}\right) - \ln(P_{CO_2}^*)\right] + \left[C + \left(\frac{E}{T}\right)\right]\alpha + \left[D + \left(\frac{F}{T}\right)\right]\alpha^2 \quad (5.2)$$

$$0 = \varphi_C + \varphi_B\alpha + \varphi_C\alpha^2 \quad (5.3)$$

$$\alpha^* = \frac{-\varphi_B + \sqrt{(\varphi_B)^2 - 4\varphi_A\varphi_C}}{2\varphi_A} \quad (5.4)$$

where:

α^* = Equilibrium loading [mol CO₂/mol alk.]

The concentration of PZ in the aerosol phase was set by minimizing the absolute relative error between the FTIR measurement and the calculated total concentration of PZ. For this experiment, the PZ concentration in the aerosol was 0.31 m and the average error was 20 %. **Figure 5.22** shows the comparison between the calculated and measured outlet PZ. The open orange circles are the equilibrium partial pressure of PZ at the measured lean solvent temperature and nominal solvent concentration. Generally, the volatility estimation matches the baseline FTIR emissions well; the assumed solvent composition of 5 m PZ and 0.25 lean loading is approximately correct across the entire experiment.

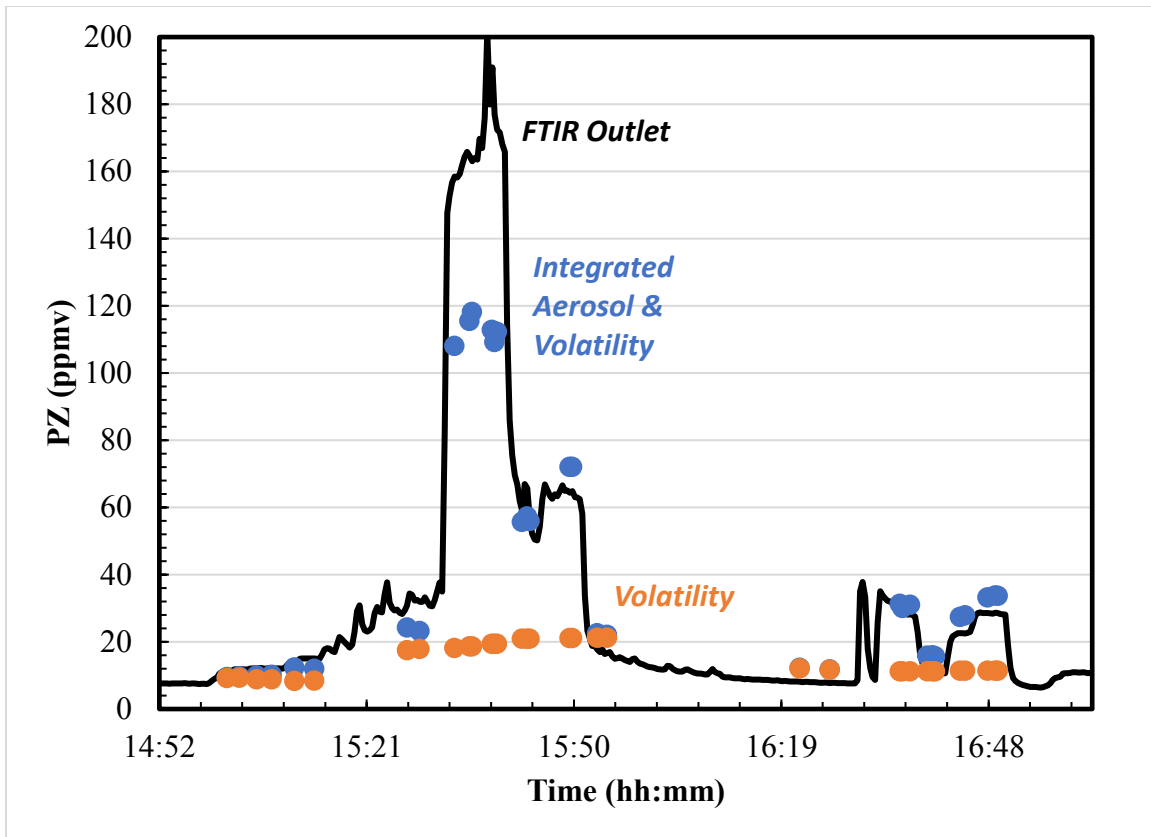


Figure 5.22: Calculated volatility (●), integrated aerosol volumetric PZ concentration (●), and outlet PZ measured by FTIR (black line). The solvent concentration was assumed to be 5 m at 0.25 lean loading.

The assumption of a constant aerosol concentration fits the data well over most of the experiment; however, the absolute relative error increases with increasing measured outlet PZ. Error is not clearly correlated to particle density or average particle diameter, which are both direct measurements from the PDI; however, the PDI should systematically under predict the density and PSD relative to what is volatilized in the FTIR since particle loss will occur between the measurement points. The FTIR measures directly at the AGC outlet whereas the PDI is downstream by a few feet.

In addition to possible measurement error, the concentration inside the aerosol droplet is likely to change with differing operating conditions which impact the gas-phase

composition. In the region of highest measured outlet PZ, significant changes are occurring to the operation of the AGC; the solvent rate was dropped by more than half and the inlet lean temperature was decreased by 10 °C.

5.3.2.5 Density, Diameter, and Emissions

The contribution of aerosols to the total emission of PZ becomes significant at a particle density of 2×10^6 part./cm³, as shown in **Figure 5.23**. Additionally, the total outlet PZ increases with increasing average particle diameter, as seen in **Figure 5.24**.

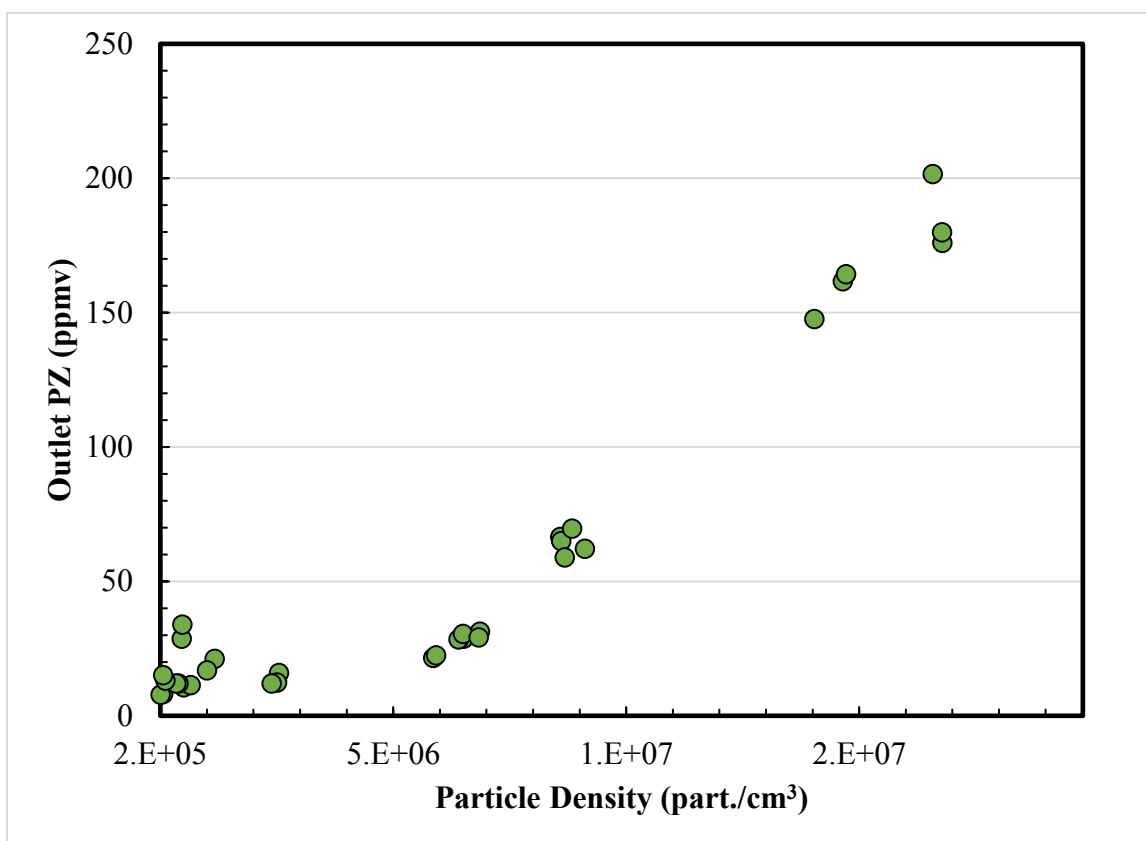


Figure 5.23: Outlet PZ is linearly correlated to particle density above 2×10^6 part./cm³. Below 2×10^6 part./cm³, the PZ contained in the aerosol is an insignificant contributor to the total outlet PZ content.

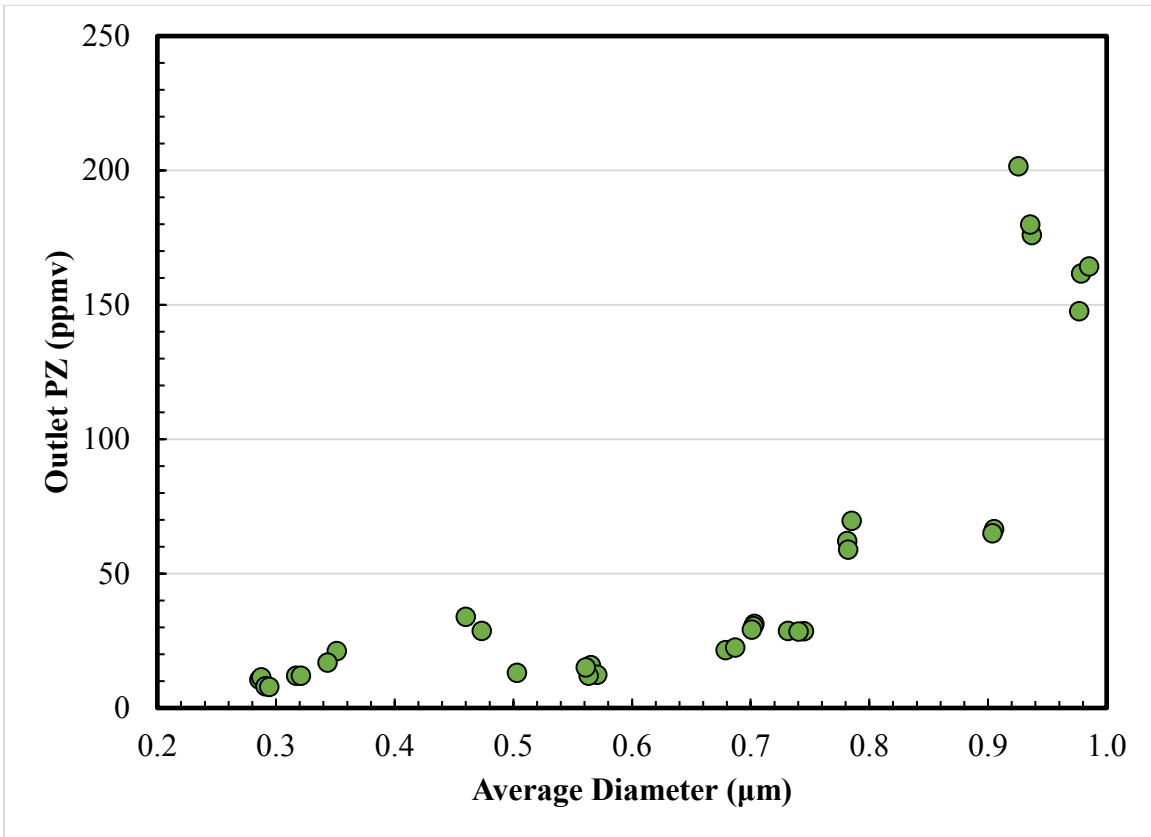


Figure 5.24: Outlet PZ is correlated to the count-average particle diameter.

Plotting the two correlating variables (diameter and density) against one another yields **Figure 5.25**; the count-average diameter and the total particle density are positively correlated across the experiment. The positive correlation runs counter to a mass balance argument which says that the amount of condensable material is relatively constant, meaning that if the particle density is higher, the total condensed material is spread amongst more singular condensation points and therefore each aerosol grows less and the resulting average diameter is smaller.

However, the mass balance argument does not account for measurement capture biases. The LOD of the PDI is 0.1 µm; anything below that diameter is not measured.

As particles grow out of the submicron region, they become detectable and are included in the measured total density. As the field continues to shift into the measureable region, the average diameter increases along with the number of detectable particles.

A diffusional capture mechanism, though very unlikely in this process, would also cause the observed correlation. As the particle distribution shifts downward into the submicron region, diffusional capture becomes more significant and the total particle density would decrease.

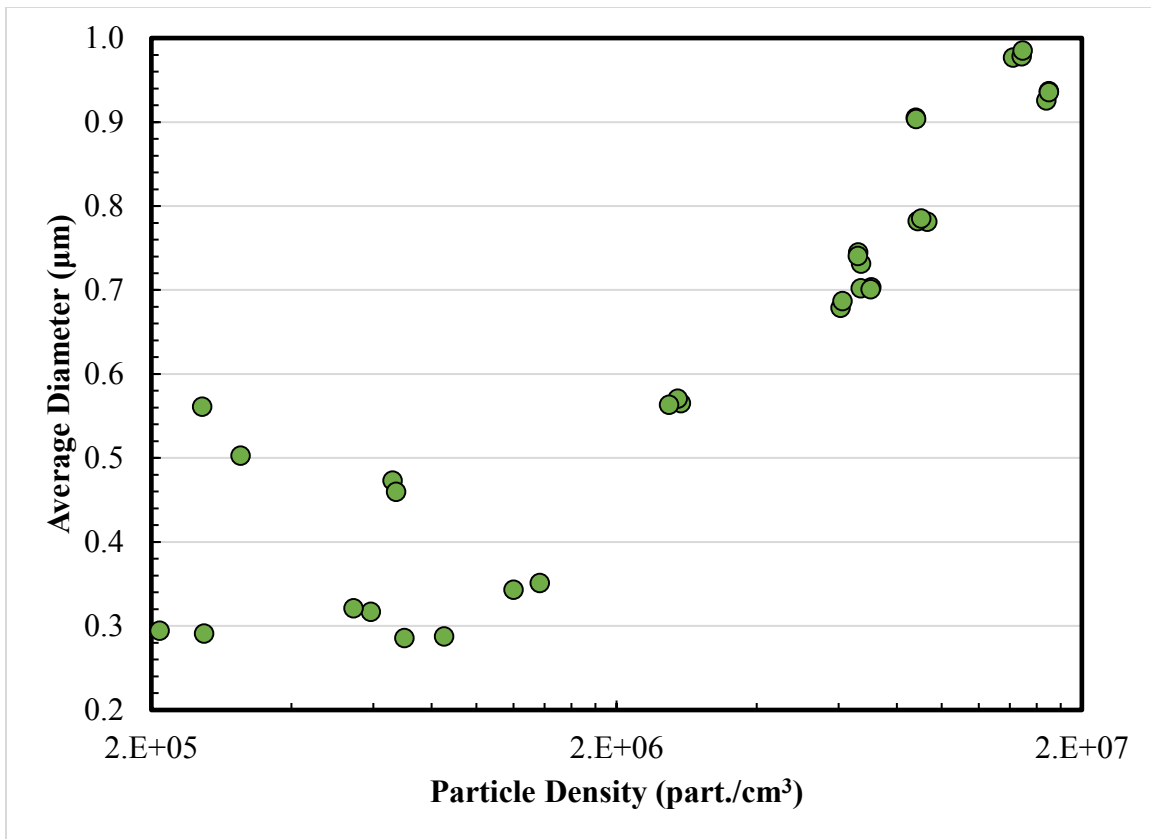


Figure 5.25: The count-average diameter and the total particle density are positively correlated across the experiment.

5.4 SUMMARY/CONTRIBUTION

The work presented in this chapter represents significant progress in development of hardware, experimental procedure, and data analysis in the effort to meet the stated goals of this work. The major areas of contribution are listed as follows:

- Development of an experimental apparatus capable of testing the effects of variable operating conditions on the amine slippage rate with phase discrimination – AGC column (Multipoint FTIR and PDI)
 - Created Standard Operating Procedures
- Development of analytical equipment to measure high density aerosols *in situ* in fully saturated process streams – PDI
- Development of a data post-processing algorithm to collate disparate data sources yielding directly comparable phase analyses – AGC data algorithm (coupled FTIR, PDI, and LabVIEW™ data)
- Test and troubleshoot an aerosol source – LVI

AGC performance tests showed that the AGC is capable of achieving over 90% CO₂ removal; although, the mass transfer rate is lower than expected and requires a significant solvent rate to reach the designed CO₂ removal mark. The effective area is a small fraction of the physical area. Liquid distribution might be limiting the overall removal rate; the hollow cone spray nozzle distributor is crucial in achieving good CO₂ removal.

A control and data logging system was designed, constructed, and implemented. A LabVIEW™ VI was coded to collect data and control AGC instrumentation. A data file output was created for post-processing.

Although the LVI was plagued with problems (see Appendix C), some results concerning the LVI operability were achieved. The level of emitted amine was found to

follow the LVI injection rate as expected. This result was confirmed by multicomponent analysis with PZ and H₂O which both showed proportional response to the LVI flow rate.

Several generations of the PDI were tested on the AGC. The iterative design process of the PDI yielded an instrument that has since been successfully tested on the AGC and two separate pilot plants with measurement capabilities of 0.1–12 μm and up to 1x10⁸ part./cm³.

Although this work was fraught with equipment failure (LVI) and lengthy delays (PDI), a small data set illustrating the impact of process conditions on the outlet amine emissions and phase-specific correlations was collected. Unfortunately, many experiments where solvent was collected for analysis were aborted due to LVI failure and therefore the usable data sets have many missing pieces.

5.4.1 The Effect of CO₂

CO₂ has a very large impact on the measured PSD; a small addition of CO₂ causes submicron aerosols to grow into the micron size range. A maximum for the average particle diameter and the total particle density exists somewhere between 0–10 vol % inlet CO₂; this finding is consistent with Khakharia (2015), but expands that study by providing a direct measurement of aerosol growth rather than relying entirely on FTIR analysis. The average particle diameter and the total particle density had a nearly linear relationship. Additionally, this work showed that PZ alone can lead to appreciable aerosol emissions. Aerosol formation has now been confirmed for MEA, AMP/PZ, and PZ systems.

The inlet CO₂ is crucial in creating supersaturation which leads to condensation/heterogeneous nucleation. The imbalance in CO₂ transfer rate between the aerosol and bulk-solvent phases creates large amine activity differences (caused by

speciation and enthalpy) which lead to significant driving forces for condensational growth.

In this work, the large solvent rates used during experimentation suppressed the enthalpy effects experienced by the bulk solvent. Therefore, small additions of CO₂ create the driving force for growth, but additional increases have a relatively minor effect. Consequently, changing the solvent rate had the largest impact on the growth of the aerosol as it is the most significant parameter effecting enthalpy in the column.

5.4.2 The Effect of Solvent Rate

A 2.5x increase in solvent rate yielded a 10% increase in the average particle diameter and a 69% increase in the total particle density. The solvent temperature was about 5 °C hotter than the inlet gas across the solvent rate change.

The average particle diameter and the total particle density were found to be positively correlated. The functional dependence cannot be determined since only two discrete points were measured (in triplicate).

5.4.3 FTIR and Integrated PDI Comparison

Generally, the calculated emissions (aerosol plus volatility) match the qualitative behavior of the FTIR measurements quite well even with the weakness of an assumed, constant aerosol composition. The developed data algorithm and the PDI measurements show great promise in providing accurate emissions measurements and data post-processing. Given a more reliable aerosol source, large amounts of data can be collected in very short time periods and several steady state conditions can be tested in a single day of experimentation.

Below 2×10^6 part./cm³, the main contributor to the outlet PZ is solvent volatility. Above that value, the outlet PZ is linear with respect to the total particle density. A

similar dependence of the outlet PZ and the count-average particle diameter was observed. The emissions/total particle density dependence is quite similar to the observations of Khakharia (2015) even though different nuclei and solvent were used.

5.4.4 Diameter/Total Density Relationship

The AGC experiment showed a positive relationship between the count-average diameter and the total particle density. It is theorized that this effect is caused by the detection limit of the PDI. Aerosols produced by the LVI are believed to be submicron. Droplets smaller than 0.1 μm are below the detection limit of the PDI. As aerosols grow and move out of the submicron region, they become visible to the PDI and count towards the measured particle density.

5.5 ACKNOWLEDGEMENTS

Several people contributed to the work presented in this chapter. Conlin Kang wrote the starting section of code for the PDI/FTIR comparison which was modified by the author. Mark Nelson of Air Quality Analytical, Inc. designed and built the original LVI and provided assistance during the initial troubleshooting. Yong Kim assembled much of the rackmount FTIR and assisted during rewiring and modifications made by the author. Matthew Beaudry provided assistance during the AGC experiments.

Chapter 6: Pilot Plant Measurements

This chapter describes aerosol and total phase measurements taken at two CO₂ capture pilot plant locations using variations on a custom-built sampling system employing simultaneous PDI and FTIR analysis: (1) the Post-Combustion Carbon Capture Center (PC4) on the Pilot Solvent Test Unit (PSTU) at the National Carbon Capture Center (NCCC) in Wilsonville, Alabama, and (2) the Pickle Research Center (PRC) pilot plant in Austin, Texas. Hardware components and site-specific modifications not described in Chapter 3, or when additional detail is required, will be described in this chapter.

Data collected during pilot plant measurements falls into three categories: (1) aerosol phase analysis by PDI, (2) total (gas and aerosol) phase concentrations by FTIR, and (3) system operation data, if available. The data algorithm described in Chapter 4 (raw code in Appendix A) was modified for pilot plant measurements by exclusion of the LabVIEW™ search function and correcting an error in time stamp matching.

Results are presented chronologically for the purpose of delineating generational improvements to PDI analysis, which was the prime driver of performing pilot plant measurements.

6.1 NCCC – JUNE 5, 2013 - PDI GENERATION 1 TEST

Due to the high cost of a modular PDI system, a cooperative purchasing agreement was made between UT and Southern Company to procure a PDI system that would work at both the pilot scale (8" duct) and bench scale (1.5" duct). Pending a successful test at both facilities, the PDI system would be cost-shared and utilized at both locations. The first PDI performance test was scheduled at NCCC to be held in late May or early July of 2013.

NCCC is a United States Department of Energy (DOE) sponsored testing facility built to accelerate the development of cost-effective pre and post-combustion cost-effective carbon abatement processes by supplying real, industrially relevant coal-fired flue gas and syngas over a wide range of quality and flowrates.

6.1.1 Pilot Plant Setup

NCCC is located at the Gaston Steam Plant in Wilsonville, Alabama next to the Coosa River. The Gaston Steam Plant consists of 5 units; primary power production is done in Unit #5 (880 MWe, 12,000 tpd CO₂, supercritical pulverized coal boiler) and the older Units #1–4 are used during peaking times and scheduled/unscheduled outages of Unit #5. Flue gas from the boilers is treated with SCR, ESP, and a Chiyoda Jet Bubbler Reactor FGD unit prior to being sent up the stack. The PC4 test facility takes a slip stream (3 MWe, 60 tpd CO₂) of flue gas off the duct connecting the Chiyoda scrubber to the Unit #5 stack. A pipe rack runs across the coal delivery conveyor into an SO₂ polisher before reaching the header for the PC4 facility. A fraction of this test gas (0.5 MWe, 10 tpd CO₂) is used to run the PSTU pilot plant. The PSTU is a traditional amine scrubbing unit with up to 3 beds of packing and two intercooler sections and has a separate water wash column located at the absorber outlet. **Figure 6.1** shows the stack of Unit #5, the Chiyoda FGD unit, and the draw-off pipe sent across the facility to the PSTU.

The CO₂ capture system was testing a proprietary Chiyoda solvent which had been in service for approximately 1,000 hours in the PSTU. The absorber was operating without intercooling and a single stage water wash was in use. Additional details of the test including amine emission levels, CO₂ capture rates, and operating conditions were held as proprietary. Unfortunately, it is unknown how much amine was removed across

the demisters in the wash tower and absorber. Emissions data using an extractive sampling system with an impinger train was taken on the day of the PDI test, but results are currently unreported.



Figure 6.1: Flue gas from Unit #5 (880 MWe) is drawn off after the Chiyoda SO₂ scrubber (shown in the left picture) and is piped into the PSTU (shown on the right) and other smaller pilot plants, test skids, and bench-top apparatuses located at PC4. The feed rate to PSTU is equivalent to a 0.5 MWe scrubbing system (10 tpd CO₂ captured).

6.1.2 Sample Location

Aerosol size distributions were measured by a modular PDI system immediately downstream of the water wash located on the 8th floor platform. Sampling occurred in a duct with downward flow approximately 10 feet from the water wash outlet. The PDI beams entered into the 12” duct by two optical access windows set 140° apart. **Figure 6.2** shows the optical access windows and table setup provided by NCCC. The windows are equipped with N₂ flush lines entering the top of the flanged connection to prevent condensation on the windows. In the event of condensation, liquid was drained through a small line at the bottom of the flanged piece. Stainless steel cones were welded onto each flanged piece to protect the windows from excess condensation and to prevent laser intensity degradation prior to sampling the gas. These precautionary designs anticipated very dense aerosol plumes. **Figure 6.3** shows the dimensions of the optical access windows at NCCC.

Southern Research Institute (SRI) provided optical access windows and physical support was overseen and coordinated by Carl Landham.

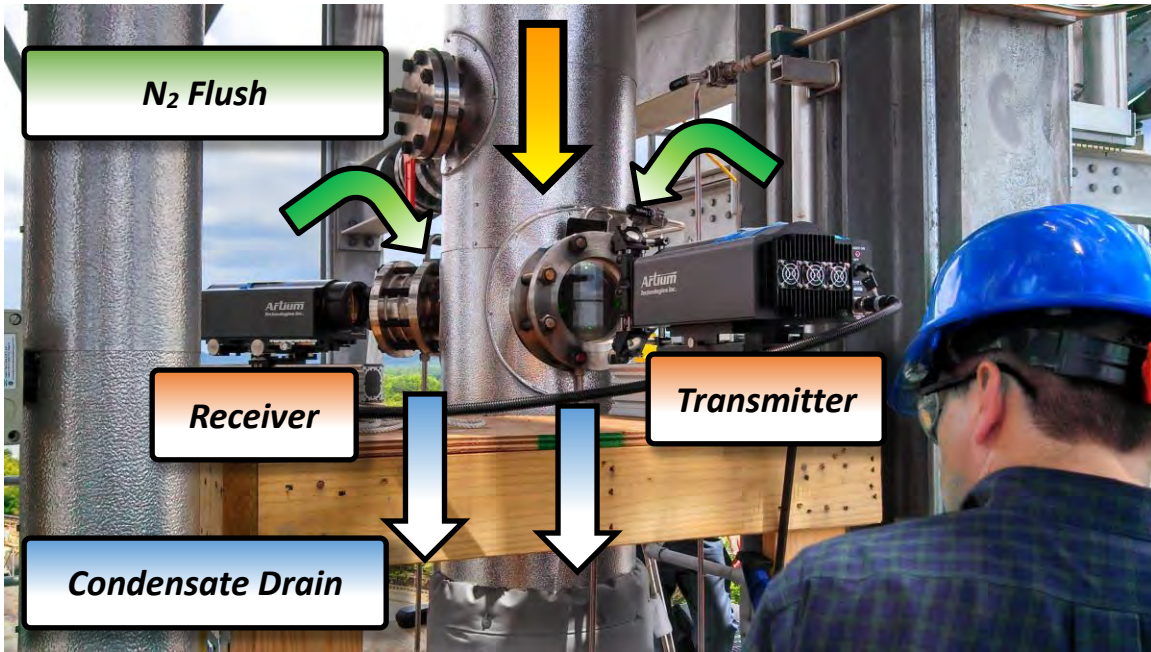


Figure 6.2: Equipment and optical setup of the Generation 1 PDI test on the water wash outlet duct of the PSTU at NCCC. The PDI transmitter and receiver are 140 ° apart on a 12” duct. The gas flow is oriented downward.

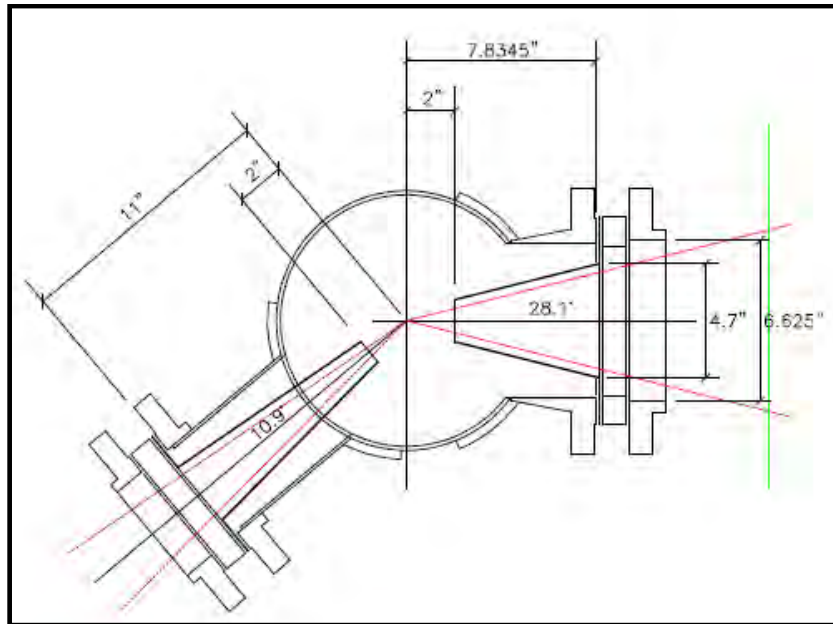


Figure 6.3: Dimensions of the optical access windows on the PSTU. The viewing cones are designed to accommodate the crossing angles of the transmitter and receiver.

6.1.3 Equipment

Equipment and technical support of the PDI analyzer was provided by William Bachalo and Chad Sipperley from Artium Technologies, Inc.

The modular PDI system provided by Artium for the PDI generation 1 test had an additional beam expander for the transmitter to increase the beam crossing angle to 28.1° in the vertical plane. The custom-built beam expander was constructed of adjustable lenses attached to a mounting rail. Prior to testing on the PSTU, the beams from the transmitter and the receiver had to be aligned to the designed focal lengths of 350 and 500 mm for the transmitter and receiver, respectively. **Table 6.1** shows the general parameters of the generation 1 PDI.

Table 6.1: Generation 1 PDI optical and geometric parameters.

PDI Gen.	Duct Size [in]	Laser Waist [μm]	Cross Angle [$^\circ$]	Rec. Focal Length [mm]	Trans. Focal Length [mm]	Lower Det. Size [μm]
1	12	50	28.1	500	375	0.5

A small, pocket-sized nebulizer was used to demonstrate the efficacy of the transmitter/receiver system with an *ad hoc* beam expander for a dense particle cloud containing 0.1–20 μm droplets. The PDI analyzer measured a well-behaved, log-mean particle distribution with a count-mean diameter of around 5 μm . The nebulizer fog was shown to be well within the measuring capabilities of the PDI.

The analyzer and peripherals were then repacked and lifted by crane to the 6th floor landing of the PSTU and hand-carried the rest of the way to the 8th floor where the water wash and duct work are located. The equipment was secured on the support with C-clamps and quickly realigned. The support beam and PDI optical heads are shown in

Figure 6.2. The transmitter and beam expander are located in the foreground and the receiver is in the background.

Figure 6.4 shows a view of the beam crossing at the center of the duct and the detector output displayed on an oscilloscope. A closer view of the beam crossing can be seen in **Figure 6.5**. The significant haze surrounding the beams indicates a high concentration of particles scattering light.



Figure 6.4: Receiver output to an oscilloscope. The oscilloscope display shows a noisy baseline for both detectors with no discrete Doppler bursts, indicating a high concentration of particles $\leq 1 \mu\text{m}$.



Figure 6.5: Close-up view of the transmitted beam crossing. The intersection of the laser beams is where the gas is sampled for moving particles. 50 μm diameter beams were used in this test.

6.1.4 Results

In the early afternoon (1 to 3 PM) of July 5, 2013, a thick white fog was visibly present at various viewports along the absorber column and at the inlet of the water wash. The plume at the sample location appeared thinner (less opaque) compared to the wash inlet. Even though aerosols were visually present, the PDI analyzer was unable to measure a particle size distribution due to the high concentration of particles less than 1 μm .

Droplets and larger aerosols were visibly present but were not measured by the instrument. The operability of the analyzer was reconfirmed by measuring the particle size distribution of the nebulizer on the wooden support structure built around the water wash duct. The test confirmed the same result as previously measured during laser alignment.

The change in opacity between the absorber and water wash outlets may be indicative of growth and capture in demister packing; however, without concentration measurements, that observation remains unconfirmed.

6.1.5 PDI Improvements

Following the generation 1 PDI test, Artium proposed that focusing the transmitted lasers to 2–5 μm in diameter (50 μm was used in this test) would increase signal response at higher particle concentrations; however, the optical path length would need to be reduced. The PDI analyzer would remain a true *in situ* analytical tool for PSD determination on smaller bench scale systems, but the shorter optical path length requirement would necessitate pulling a sample stream out of the process duct which would introduce particle loss errors.

6.2 PRC – NOVEMBER, 2013 CAMPAIGN – PDI GENERATION 2 TEST

Following the PDI generation 1 test, the second-half of the PDI demonstration/purchasing test was carried out at the PRC pilot plant in November, 2013. Aerosol generation and analysis were included as a part of a larger testing matrix under the Carbon Capture Pilot Plant Project (C2P3) activity at the PRC pilot plant. This project was funded by the Department of Energy under Award Number DE-FE0005654

6.2.1 Pilot Plant Setup

The PRC pilot plant absorber column is 16.8 in (0.43 m) ID and used 20 ft (6.1 m) of Raschig RSP-250 packing. The packed section is broken up into two beds with an intermediate chimney tray collection and redistribution point that can be used to cool the amine solvent. The collected solvent can be distributed to the packed bed below or returned to the bottom of the top bed of packing by an upward-facing spray nozzle.

The inlet gas is a combination of ambient air and pure CO₂ mixed in proportions to produce synthetic flue gas. The inlet gas rate varies from 300–750 CFM which corresponds to an equivalent CO₂ input rate of 0.1 MW. Relative humidity is set by ambient conditions and the ratio of air to makeup CO₂. The CO₂ rich synthetic flue gas is counter-currently contacted with amine solvent, reducing the CO₂ content while adding H₂O, amine, and degradation products to the lean gas exiting the top of the absorber. The processed flue gas enters an air cooler to condense H₂O and semi-volatiles. The cooled gas is then sent to a knockout drum containing a coarse mesh entrainment pad and a submicron fiber filter to knock out any entrained material prior to exiting the riser vent.

CO₂-rich solvent from the absorber is sent to a stripping section where the exothermic absorption reactions are reversed by the input of heat. The hot, lean solvent is cross-exchanged with the rich solvent stream to reduce the sensible and latent heat requirement. The stripped CO₂ gas is passed through a condenser to remove condensable species and sent to an accumulator tank. The accumulator tank and makeup CO₂ are combined and mixed with ambient air to makeup the absorber inlet gas.

The PRC pilot plant with labeled equipment is shown in **Figure 6.6**. Prior to 2010, the stripping section consisted of a simple stripper, which is a packed (or trayed) column whose geometry is identical to the absorber. Variations on multistage flashing with heat and material bypass (reflux) replaced the simple stripper; a flash skid was erected on concrete piers located in front of the simple stripper. The current configuration is called the Advanced Flash Stripper (AFS) and is labeled in the foreground of **Figure 6.6**.



Figure 6.6: Front view of the PRC pilot plant. PDI and FTIR sample points and the LVI injection point are shown as well.

6.2.2 Sample Locations

FTIR sampling occurred at two out of three total locations during the November, 2013 campaign: (1) the absorber inlet and (2) the absorber outlet. **Figure 6.7** shows a side view of the PRC pilot plant and provides a detail view of an FTIR sampling point with stinger probe.



Figure 6.7: Side view of the PRC pilot plant detailing the locations of the inlet and outlet FTIR sampling points. The picture on the right shows a detail view of an FTIR sampling location stinger probe (absorber inlet).

PDI measurements and manual impinger sampling for condensable amine and H₂O (performed by URS corporation, now AECOM) were taken just upstream of the absorber outlet FTIR sampling point. Their locations and proximity at the absorber outlet are shown in **Figure 6.8**.

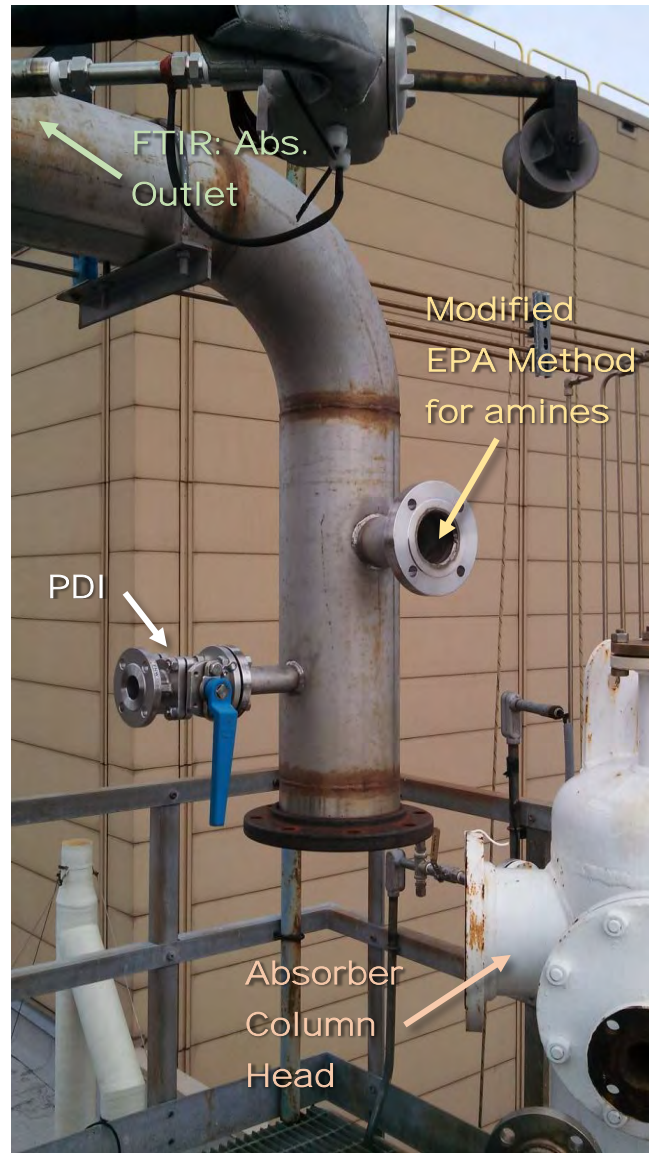


Figure 6.8: Absorber outlet sampling location proximity for FTIR, PDI, and manual impinger sampling for amines (and H₂O).

SO_x (gaseous SO₂ and SO₃/H₂SO₄ mist) measurements were also conducted at the absorber inlet using EPA Method 8 (performed by URS corporation, now AECOM). The sample was drawn through isokinetic stack samplers located on a nozzle welded to the absorber column shell, just above the gas inlet duct location offset by 90°.

The overall locations of all sampling and aerosol injection points are shown the following process flow diagram (Figure 6.9).

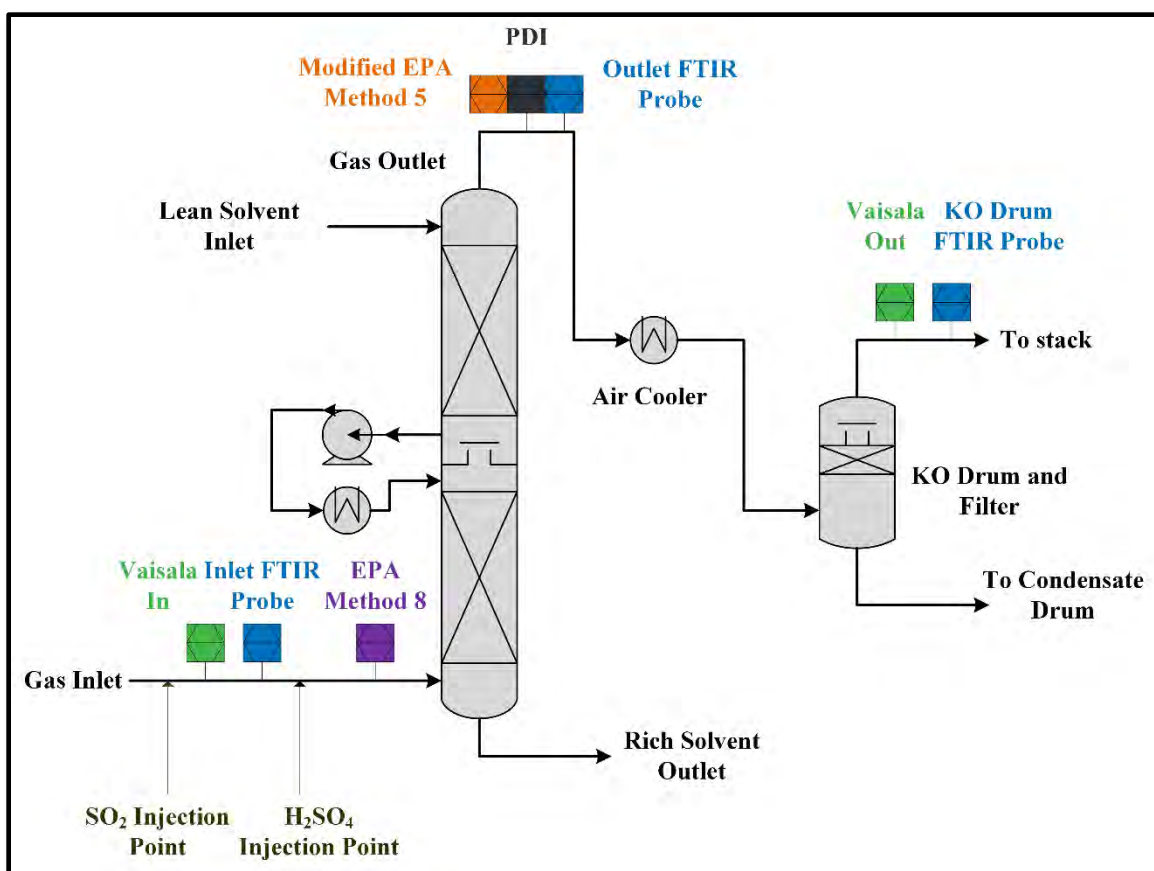


Figure 6.9: Locations of sampling and aerosol injection points at the PRC pilot plant. The knockout location was not sampled during the November, 2013 campaign. Vaisala probes measure CO₂ content by IR.

6.2.3 Equipment

6.2.3.1 FTIR Sampling

The portable DX4000 FTIR analyzer (Section 3.1.3), the portable sampling unit (Section 3.1.3.1), and the heated, manual multipoint switcher box (Section 4.5) were used in the November, 2013 campaign. The sampling locations outside used the heated stinger probes (Section 3.1.3.5) without temperature controlled heated insulation pads (Section 3.1.3.4). The FTIR connection points in the pilot plant were wrapped in heating tape and were controlled by a variac at a constant voltage.

6.2.3.2 PDI Sampling

Following Artium's recommendations, a new PDI sampling system was developed to reduce the optical path in which the lasers had to traverse in the process stream. The parameters for the second generation PDI, and the first generation PDI for reference, are shown in **Table 6.2**. The sampling system was designed to pull a moderate slipstream of the process gas into a 1½" Sch. 10 sample cell with optical windows. The sample cell diameter was optimized based on two competing requirements. Smaller diameters would improve instrument sensitivity and allow for higher total particle densities as well as minimize the size of sampling equipment; whereas, larger diameters would reduce particle losses and prevent steep temperature gradients in the sample cell caused by the very large length-to-diameter (L/D) ratio with normal sample tubing at smaller flowrates.

A prototype cell was designed and built with flanged sight-glass windows. Flanges for the optical windows were cut from a 1/16" thick Teflon® sheet. 1/8" NPT fittings were milled into the side of the back flanges on the optical windows and 1/8" tubing was passed through bored-thru fittings to provide flush gas on the process-exposed

surface of the windows. **Figure 6.10** shows the modular PDI transmitter and receiver in operation at the PRC pilot plant absorber outlet sampling point and the vertically oriented PDI sampling cell. The PDI sample port was oriented horizontally, but due to the weight and size of the modular PDI pieces and support bar, the sample was run through a 90° elbow, then passed through the sampling cell. The computer, ASA, and power box were set on a table supporting the PDI optical apparatus.

Table 6.2: Generation 1 and 2 PDI optical and geometric parameters.

PDI Gen.	Duct Size [in]	Laser Waist [μm]	Cross Angle [$^\circ$]	Rec. Focal Length [mm]	Trans. Focal Length [mm]	Lower Det. Size [μm]
1	12	50	28.1	500	375	0.5
2	1½	50	28.1	481	126	0.5

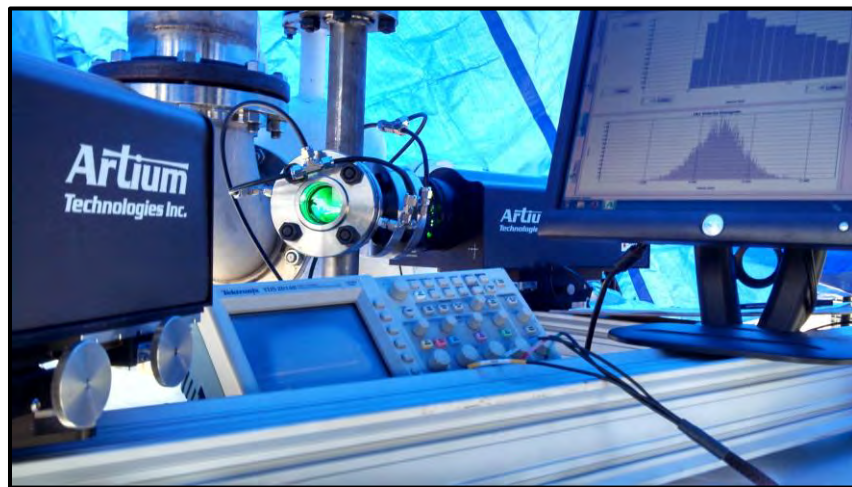


Figure 6.10: The second generation PDI was oriented vertically to accommodate the modular PDI setup. An airbrush operated with H₂O was used to generate test aerosol for this picture. The PSD and velocity histogram are shown on the computer monitor.

The sampling configuration is shown in **Figure 6.11**. A 1½” sample port was located on the 8” process gas line and was isolated by a full-port ball valve. The sample cell was flanged to the ball valve with a 90° elbow. The sample rate was controlled by a blower (described in Section 3.3.1) with a variable speed drive and was monitored using a large rotameter. The sample was returned to a port located a few feet downstream.

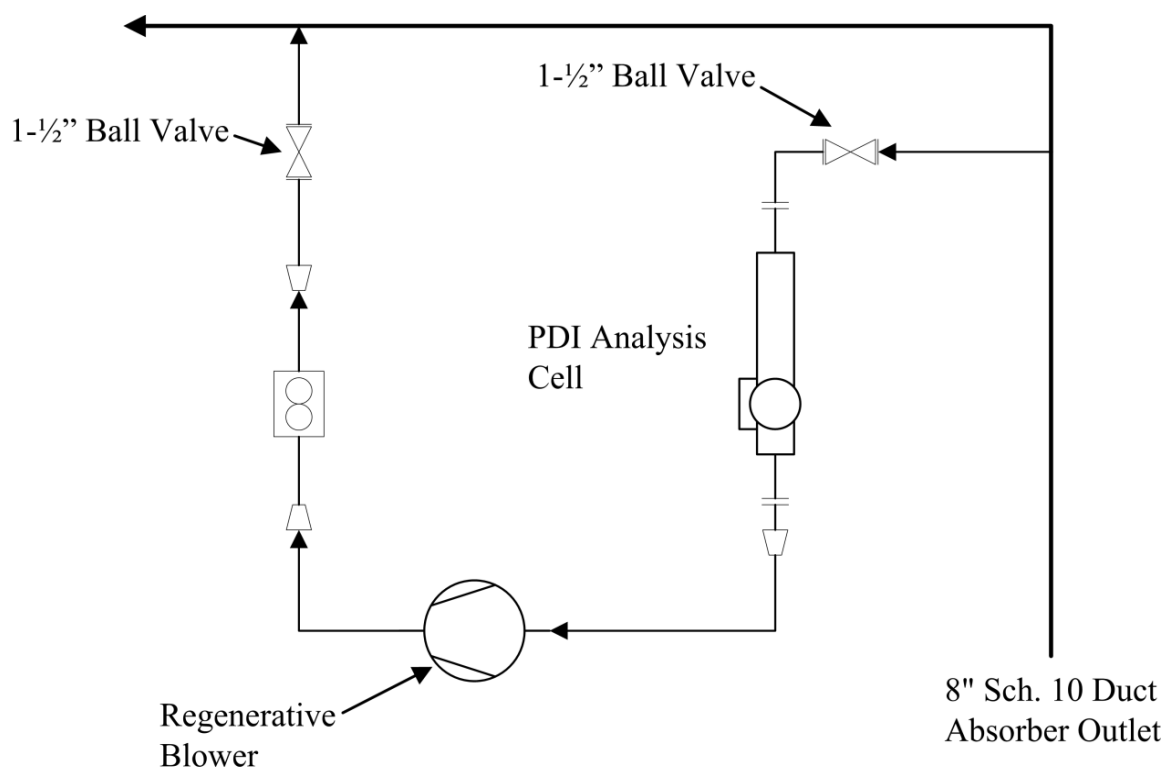


Figure 6.11: PDI sampling and return PFD for the second generation PDI test.

6.2.3.3 Aerosol Sources

Aerosol nuclei were generated by two methods: metering SO₂ from compressed gas cylinders and by vaporized H₂SO₄ using the LVI.

SO₂ was introduced into the inlet gas stream through a 1/4” penetration just downstream of the absorber blower. The flow rate of SO₂ was controlled to a set point by

adjusting a large needle valve. The concentration of SO₂ was verified by FTIR measurements made at the absorber inlet. The compressed gas cylinders contained 2 vol % SO₂ and were regulated to 30 psig. **Figure 6.12** shows the physical location of the SO₂ injection point relative to the absorber blower and the LVI injection location just before the absorber inlet.

Aerosol formation by nucleation with SO₂ is a serious concern for CO₂ capture plants operating with coal-fired flue gas. Since SO₂ reacts quickly with amine solvents, SO₂ in the form of sulfates has to be removed on a consistent basis by reclaiming or by a polishing column upstream of the absorber. If reclaiming is chosen in lieu of upstream polishing, unexpected amine loss in the aerosol would occur and be very difficult to suppress. In countries with higher SO_x permitting, a polishing column may seem economically unattractive, especially when reclaiming costs are very small relative to capture plant expenses. However, SO₂ removal might be required to prevent aerosol formation, rather than solvent contamination.

A detailed description of aerosol generation by LVI can be found in Chapter 4 and Appendix C.

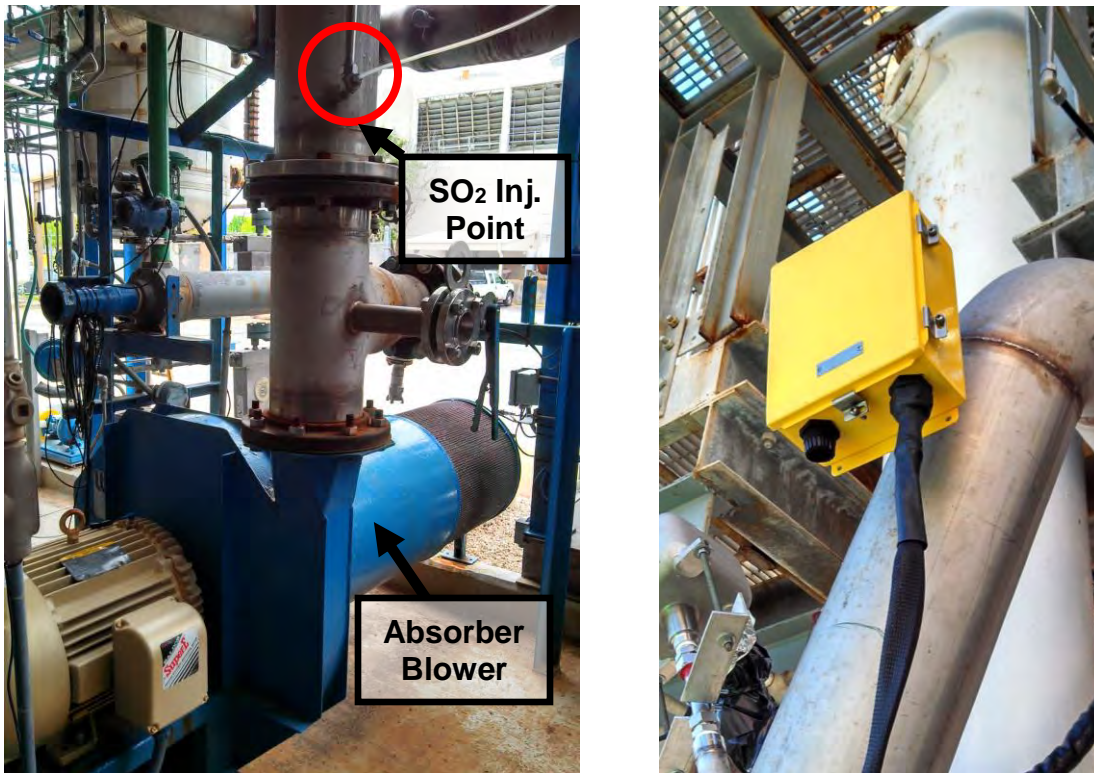


Figure 6.12: SO₂ injection location (left picture) downstream of the absorber blower. The LVI injection enclosure (right picture) was located upstream of the absorber inlet port, the inlet FTIR sampling point, and the SO_x manual sampling point.

6.2.4 Results

6.2.4.1 *Steady State Conditions*

In total, 4 steady state conditions were achieved over the duration of the campaign. The absorber conditions are summarized in **Table 6.3**. The steady state reported values are averaged over a period of 30 minutes. CO₂ concentrations reported in **Table 6.3** are the values from the Vaisala CO₂ probes.

Table 6.3: Absorber steady state conditions during the November, 2013 PRC pilot plant campaign.

Run	Date/ End Time	Solvent Rate [GPM]	Gas Rate [ACFM]	PZ Conc. (CO₂ Free) [wt %]	Lean Loading [mol/mol]	CO₂ In [vol %]	CO₂ Out [vol %]	Intercooling [Y/N]	Spray Nozzle [Y/N]
1A	11/21/2013 12:30	12.00	350.08	23.80	0.220	12.01	1.57	Y	Y
1B	11/21/2013 16:00	12.00	349.86	24.49	0.218	12.00	1.32	Y	Y
2A	11/22/2013 10:00	12.00	349.94	24.15	0.216	12.00	2.37	Y	N
2B	11/22/2013 14:00	12.00	350.04	24.43	0.218	11.99	2.38	Y	N

6.2.4.2 Manual Sampling

Table 6.4 shows the data collected by URS (now AECOM) across the campaign. The dry basis data was converted to a wet basis using the reported flue gas moisture content measured simultaneously by URS. The basis conversion was performed so direct comparison with the FTIR could be made.

Table 6.4: Manual sampling data provided by AECOM (formerly URS Corp.)

Run	1	2	4	5	7	8
Date	11/21	11/21	11/22	11/22	11/22	11/22
Time	14:22- 14:52	16:04- 16:34	10:08- 10:38	11:05- 11:35	13:46- 14:16	14:59- 15:29
<i>Absorber Inlet:</i>						
Flue gas moisture (%)	5.09	6.22	--	--	3.63	--
SO _x (mg/dscf) [as SO ₄ ²⁻]	<0.03	<0.03	--	--	1.16	--
SO _x (ppm, dry)	<0.26	<0.27	--	--	10.23	--
<i>Absorber Outlet:</i>						
Flue gas moisture (%)	--	7.25	7.93	6.34	6.53	5.21
PZ (mg/dscf)	--	2.01	1.69	2.07	4.58	1.94
PZ (ppm, dry)	--	19.8	16.7	20.4	45.2	19.1

6.2.4.3 FTIR

FTIR and the manual sampling comparisons are shown in **Figure 6.13** and **Figure 6.14** below. PZ concentrations are reported on a wet basis; URS measurements are adjusted for the reported H₂O content reported in **Table 6.4**.

Generally, the PZ and H₂O concentrations measured by the manual sampling method were higher than those reported by the FTIR. However, based on the solvent concentration measured by titration and the reported outlet temperature measured at the

absorber outlet elbow (TT-400), a Raoult's law calculation resulted in H₂O content closer to the manual method than the FTIR measurements. The source of the mismatch was determined to be an out of date calibration on the FTIR. Mark Nelson of Air Quality Analytical confirmed that the high residuals seen during analysis were due to H₂O calibrations not being representative of the current physical state and operating conditions (lamp intensity, gain setting, etc.) of the FTIR.

After recalibration, the H₂O measurements agreed very closely. The mole fraction of H₂O used in Raoult's Law is an approximate "true" mole fraction, assuming all CO₂ is bound by reaction to amine. The absorber outlet pressure was used as the total pressure in the calculation. The CO₂ measurement by the FTIR and reported pilot plant data agree closely.

In addition to the error associated with H₂O calibrations, quantification limits of the FTIR further increase the deviations between analysis methods. Specifically, the measurement period containing URS runs 4 and 5 show the lowest measured concentrations. The quantification limit of PZ is around 1–2 ppm, meaning the aforementioned measurement envelope contains the most error.

On Nov. 21 (**Figure 6.13**), an intermittent burst of aerosols generated by the LVI produced an increase in PZ emissions measured by the FTIR. The manual measurement (URS-2) matched the FTIR measurement; however, an absolute comparison to a baseline concentration cannot be made due to inconsistent LVI operation.

Nov. 22 (**Figure 6.14**) measurements showed initial inconsistencies with respect to PZ measurements. Consistency between manual sampling and FTIR methods was reproduced during SO₂ injection. Spray intercooling was turned on prior to the URS-8 measurement, in which the PZ concentration decreased on both the FTIR and manual sampling methods.

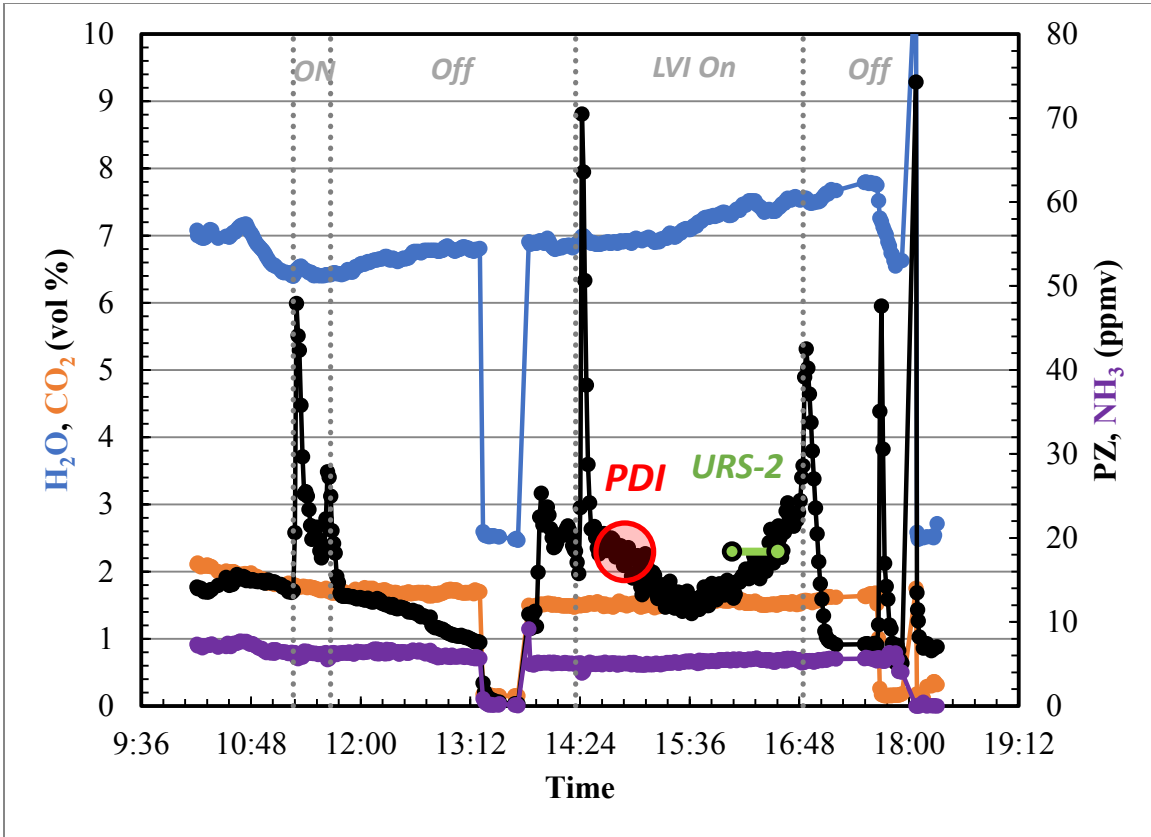


Figure 6.13: FTIR (UT/SRP) and manual sampling (URS) data taken 11.21.2013. Dashed lines with circle points are manual sampling PZ concentrations averaged over a 30-minute interval adjusted for moisture content. The LVI was in operation between the dotted gray lines. PDI sampling occurred inside the red circle.

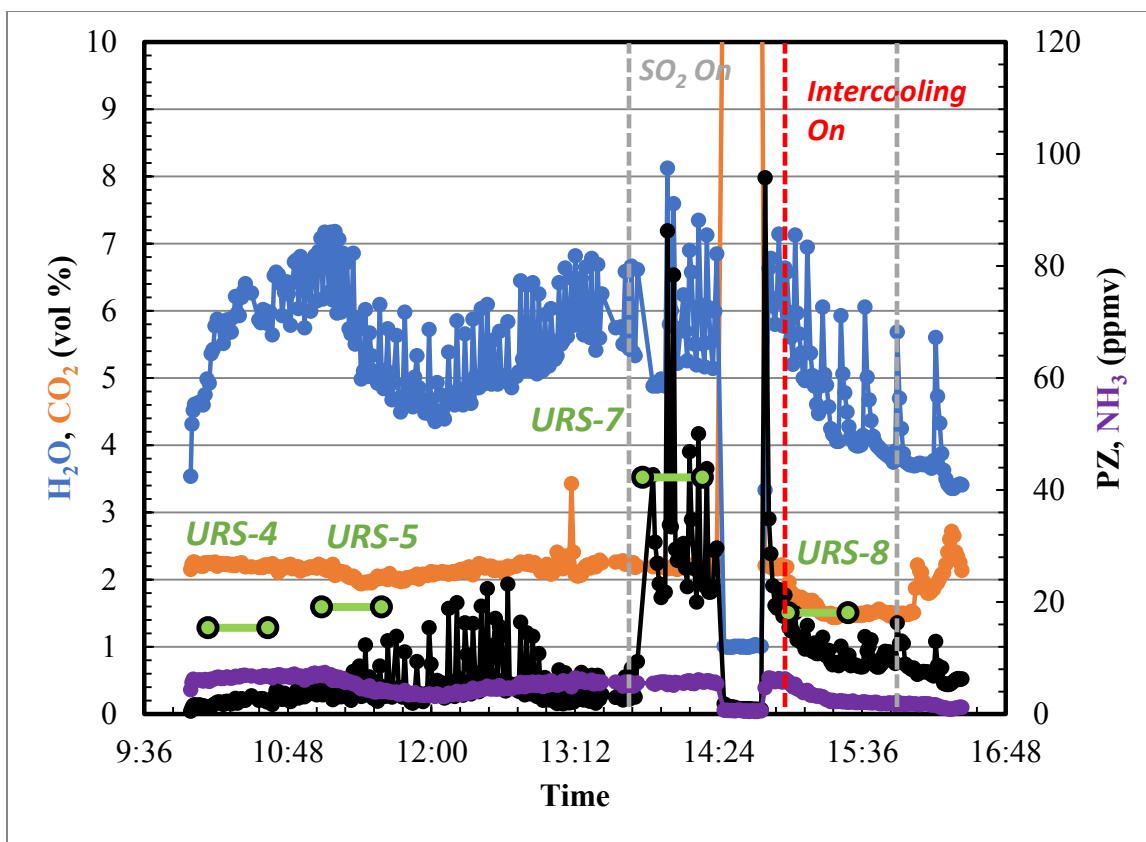


Figure 6.14: FTIR (UT/SRP) and manual sampling (URS) data taken 11/22/2013. Dashed lines with circle points are manual sampling PZ concentrations averaged over a 30-minute interval adjusted for moisture content. SO₂ was injected during the period containing URS-7 and URS-8. Spray intercooling was turned on in between URS-7 and URS-8.

The SO_x/SO₄ analysis is inconsistent between the manual sampling and FTIR methods. Due to the operation issues of the LVI, comparison of the Nov. 21 data are difficult to make since the actual injection rate of H₂SO₄ is below the detection limit of the manual sampling method. In addition, the particle distributions provided by the PDI analyses would only correspond to about 1–5 ppm increase in PZ emissions, assuming the composition of the aerosol is the same as the lean solvent; that assumption has been found to be a large overestimation as reported in the concentration optimizations from Chapter 5 and in pilot plant data later in this chapter.

Despite the limitations of the LVI tests, the SO₂ content measurements on Nov. 22 were also inconsistent even when the SO₂ injection rate was easily measureable. The targeted injection rate was 25 ppm controlled by a rotameter. The FTIR results (**Figure 6.15**) were close to the targeted concentration at 22.5 ppm; however, the manual sampling method showed significantly less at 10 ppm. Since the manual sampling point is located just above the absorber gas inlet point above the sump section, humidification of the inlet gas in the entrance section may cause the underreporting of SO₂ and SO_x levels. This finding is also consistent with the high levels of H₂O reported in the inlet gas, even though the majority of the source gas is taken from ambient conditions where the H₂O content is usually less than 2 vol %. The freezing temperatures during the campaign would further exacerbate the measured difference.

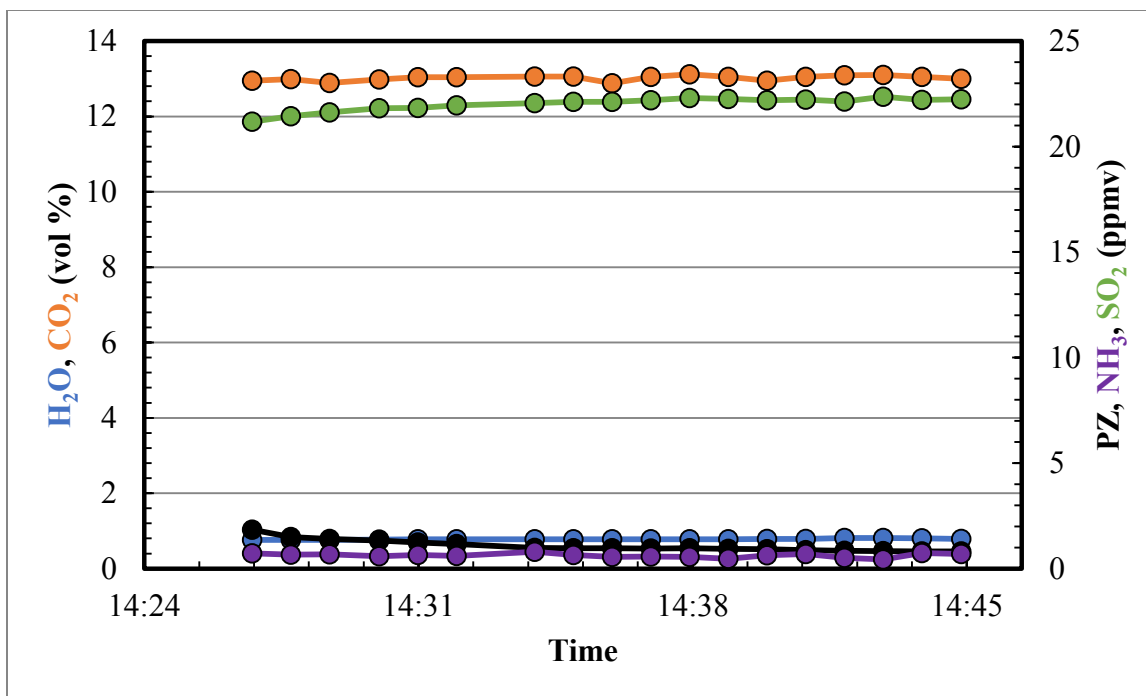


Figure 6.15: FTIR analysis of SO₂ at the absorber inlet heated probe. SO₂ was injected at a targeted concentration of 25 ppmv.

The increase of outlet PZ emissions were found to be close to stoichiometric with input of SO₂. The baseline and high level of PZ was 4.2 and 32.5 ppmv, respectively with the addition of 22.5 ppmv of SO₂. The ratio of increase in PZ to inlet SO₂, on a molar basis, was 1.26. The basis for aerosol formation might be analogous to the formation of ammonium sulfite/bisulfite aerosol in ammonia scrubbers in the absence of photolytic oxidation. Several studies have suggested the following reaction scheme for the interaction of SO₂ and NH₃ in the presence of a humid gas (Shale, 1973; Bai et al., 1994):

Table 6.5: Possible NH₃-SO₂-H₂O vapor-phase reactions and solubility product constants (Bai et al., 1994). Partial pressures used in K_{sp} expressions are atm.

Reaction Equilibrium	Equilibrium Constant	T [°C]
$(NH_4)_2S_2O_2(s) \leftrightarrow 2NH_3(g) + 2SO_2(g) + H_2O(g)$	$K_{sp} = \begin{cases} \exp[94.6 - (39144/T)] \\ \exp[96.5 - (40767/T)] \end{cases}$	$\begin{cases} 60 - 110 \\ 0 - 23 \end{cases}$ (1)
$(NH_4)_2SO_3(s) \leftrightarrow 2NH_3(g) + SO_2(g) + H_2O(g)$	$K_{sp} = \begin{cases} \exp[73.8 - (30601/T)] \\ \exp[76.6 - (32630/T)] \end{cases}$	$\begin{cases} 60 - 110 \\ 0 - 23 \end{cases}$ (2)
$(NH_4)_2SO_3H_2O(s) \leftrightarrow 2NH_3(g) + SO_2(g) + 2H_2O(g)$	$K_{sp} = \begin{cases} \exp[93.8 - (39144/T)] \\ \exp[96.7 - (40090/T)] \end{cases}$	$\begin{cases} 60 - 110 \\ 0 - 23 \end{cases}$ (3)
$NH_4HSO_3(s) \leftrightarrow NH_3(g) + SO_2(g) + H_2O(g)$	$K_{sp} = \begin{cases} \exp[53.8 - (22116/T)] \\ \exp[54.7 - (22928/T)] \end{cases}$	$\begin{cases} 60 - 110 \\ 0 - 23 \end{cases}$ (4)

Analogously, amine can participate in the nucleation of SO₂. Reactions 1–4 could also serve as a heterogeneous nucleation site for amine inside the absorber process. Equally probable is the homogenous nucleation of amine/SO₂/H₂O solution aerosols. Since the absorption of SO₂ in amine absorbers is very fast, nucleation and absorption occur simultaneously. The conversion efficiency of SO₂ to aerosol should increase with moisture content and decreasing temperature. In the work by Bai et al. (1994), they note that the moisture content and temperature dictate the NH₃ utilization rate and dominant

reaction. For constant moisture content, lower temperatures favor the formation of bisulfite (NH_4HSO_3) and higher temperatures favor sulfite ($[\text{NH}_4]_2\text{SO}_3$). However, an ideal mixture of the two is the most likely product mix. The moles of NH_3 to SO_2 should then lie between one and two, assuming no competing absorption and no additional condensation on the seed nuclei.

When spray intercooling was turned on, outlet PZ decreased from 32.5 to 11.3 ppmv. Since the baseline PZ emissions with intercooling were not measured, the PZ to SO_2 ratio cannot be calculated. Intercooling should suppress temperature gradients in the column and reduce areas of supersaturation. Lower supersaturation would reduce the driving forces for heterogeneous nucleation/condensation onto the seed nuclei. Even though nucleation is favored at lower temperatures, the saturation pressure decreases with temperature lowering the quantity of NH_3 /amine reactant.

Though reactions 1–4 are for solid formation, the formation of an aqueous phase is also thermodynamically favorable due to the solution equilibrium between the strong acid (SO_2) and base (NH_3 /Amine). Additional amine/ H_2O / CO_2 would condense onto the aerosol and the droplets would grow inside the absorber column. The apparent stoichiometry might be a coincidence since absorption, nucleation, and condensation are all likely competing mechanisms.

6.2.4.4 PDI

During startup of the campaign, the LVI was tested for a brief period of time to establish operation of the PDI using the generation 2 configuration. **Figure 6.16** shows three consecutive measurements using the PDI. The total passed samples was set to 10,000 counts for each data set.

Most notably, the concentration was much lower than expected. Assuming an inlet gas containing 3 ppmv H₂SO₄, a monomodal distribution ($d_g = 0.2 \mu\text{m}$, $\sigma_g = 2$), and a nuclei acid concentration of 0.5 molar (mol H₂SO₄/L), the total particle density calculated by mass balance should be $3.3 \times 10^6 \text{ part./cm}^3$. Confirmation of the low particle count was observable by FTIR (**Figure 6.13**); initially, the LVI would produce higher aerosol densities until the injected liquid would cool the eductor mixing point and the vaporization heat would diminish. When the acid injection was turned off, the LVI lines would blow down and clear out the accumulated liquid. This was observed during both acid injection periods in **Figure 6.13**.

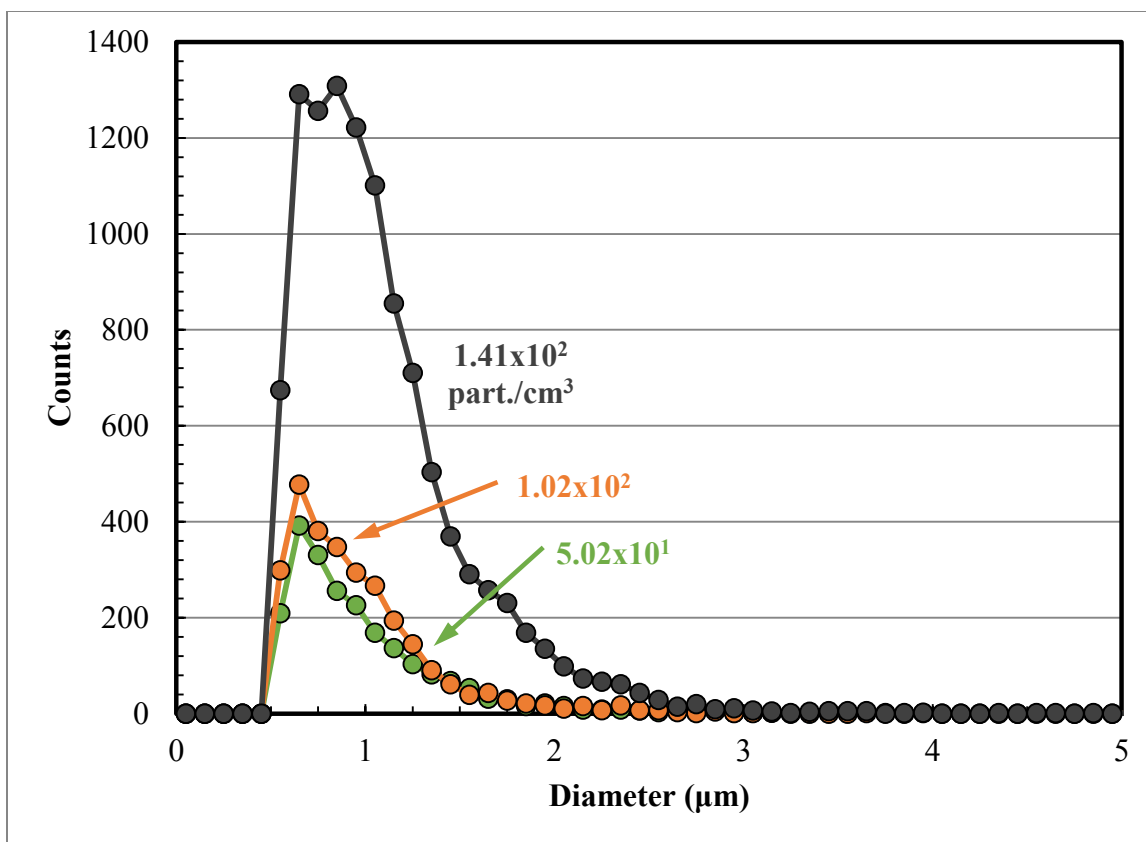


Figure 6.16: Consecutive PDI analyses taken on 11/19/2013 starting at 08:27 at an H₂SO₄ injection rate of 1.5 mL/min. All data sets are 10,000 total counts.

During steady state operation, the PDI was tested with aerosol generated by the LVI. The PDI sampling window is indicated by the red circle in **Figure 6.13**. The measured PSDs are plotted below in **Figure 6.17** and the average diameter, Sauter-mean diameter, and total particle densities are reported in **Table 6.6**. The diameter statistics are reproducible ($\sigma = 0.06 \mu\text{m}$), whereas the total particle density varied significantly ($\sigma = 2,250 \text{ part./cm}^3$). The low and highly variable particle densities were indicative of the corrosion and unstable operability of the LVI.

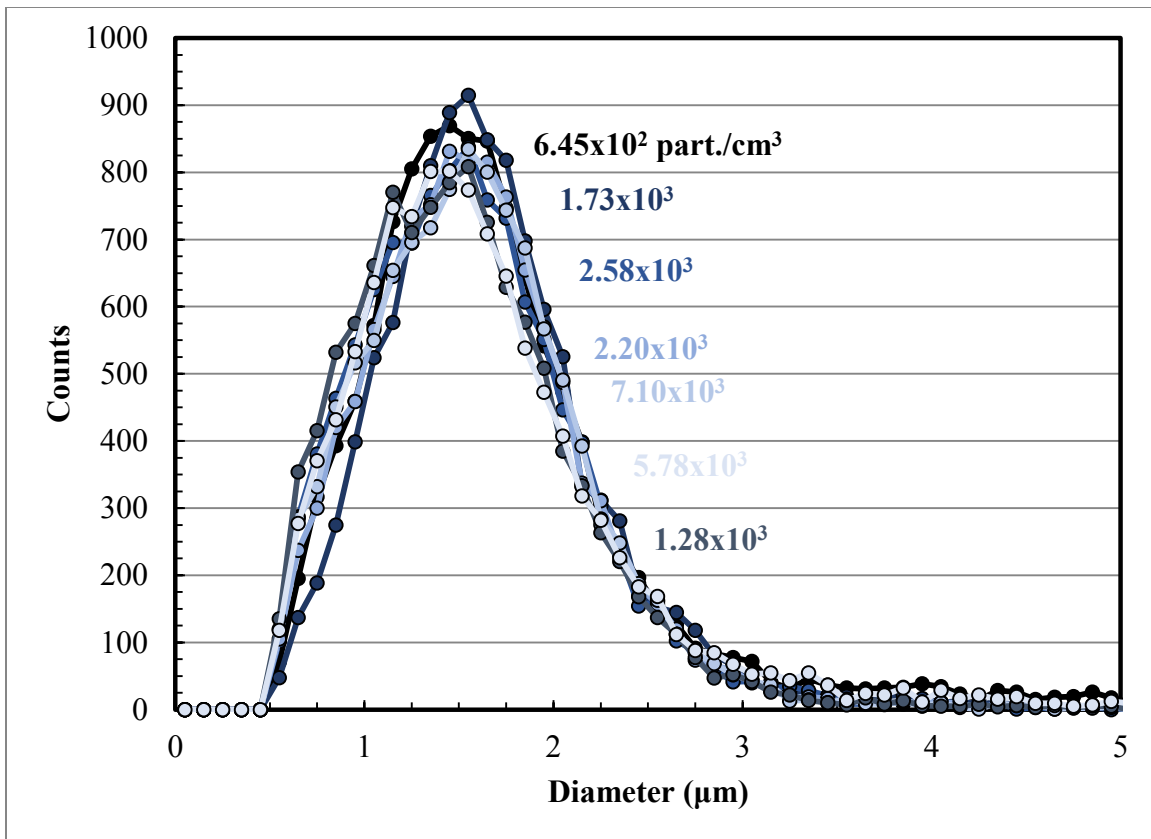


Figure 6.17: Consecutive PDI analyses taken on 11/21/2013 starting at 14:30 at an H_2SO_4 injection rate of 2 mL/min. All data sets are 10,000 total counts.

Table 6.6: PDI data for Figure 6.17. Subscript definitions are in Table 2.1.

Run #	D₁₀ [μm]	D₃₂ [μm]	Density [part./cm³]
1	1.67	2.92	6.45E+02
2	1.63	2.15	1.73E+03
3	1.53	2.05	2.58E+03
4	1.56	2.09	2.20E+03
5	1.55	2.04	7.10E+03
6	1.49	2.05	5.78E+03
7	1.59	2.37	1.28E+03

6.2.5 PDI Improvements

Following the successful demonstration of the generation 2 PDI test on the PRC pilot plant and the AGC, Artium began designing a customized PDI and analysis cell capable of measuring down to 0.1 μm. A complete description of the generation 3 PDI can be found in Chapter 3.

Design and construction of a weatherproof enclosure for the PDI electronics was pursued in parallel with the new PDI design.

6.3 PRC – MARCH, 2015 CAMPAIGN – PDI GENERATION 3 TEST

The generation 3 PDI and upgraded LVI were tested at the PRC pilot plant in March, 2015. The purpose of the campaign was to evaluate the performance of variable solvent concentration (5 and 8 m PZ), the AFS thermal efficiency, and aerosol generation and analysis using multipoint FTIR, PDI, and manual sampling. Reducing the solvent concentration broadens the solubility window, allowing for lower lean CO₂ loading which permits for greater optimization of the heat duty without the risk of precipitation.

6.3.1 Equipment

6.3.1.1 FTIR Sampling

The rackmount FTIR analyzer (CX4000) (Section 3.1.3) and the MSSH (Section 3.1.4) were used for total-phase analysis. The sampling points were the same as those described in the November, 2013 campaign. The variac and insulated wrap were replaced with temperature controlled heating pads (Section 3.1.3.4). The FTIR was integrated into DeltaV™ midway through the campaign. Appendix D contains details of the physical connections, data configuration, and computer code required to output the FTIR results to DeltaV™.

The MSSH control was not integrated into DeltaV™ prior to the March, 2015 campaign. A manual switchbox was made out of two three-position switches and Wago terminal crimp connectors. **Figure 6.18** shows the wiring diagram of the control box and the connection points on the MSSH terminal bus.

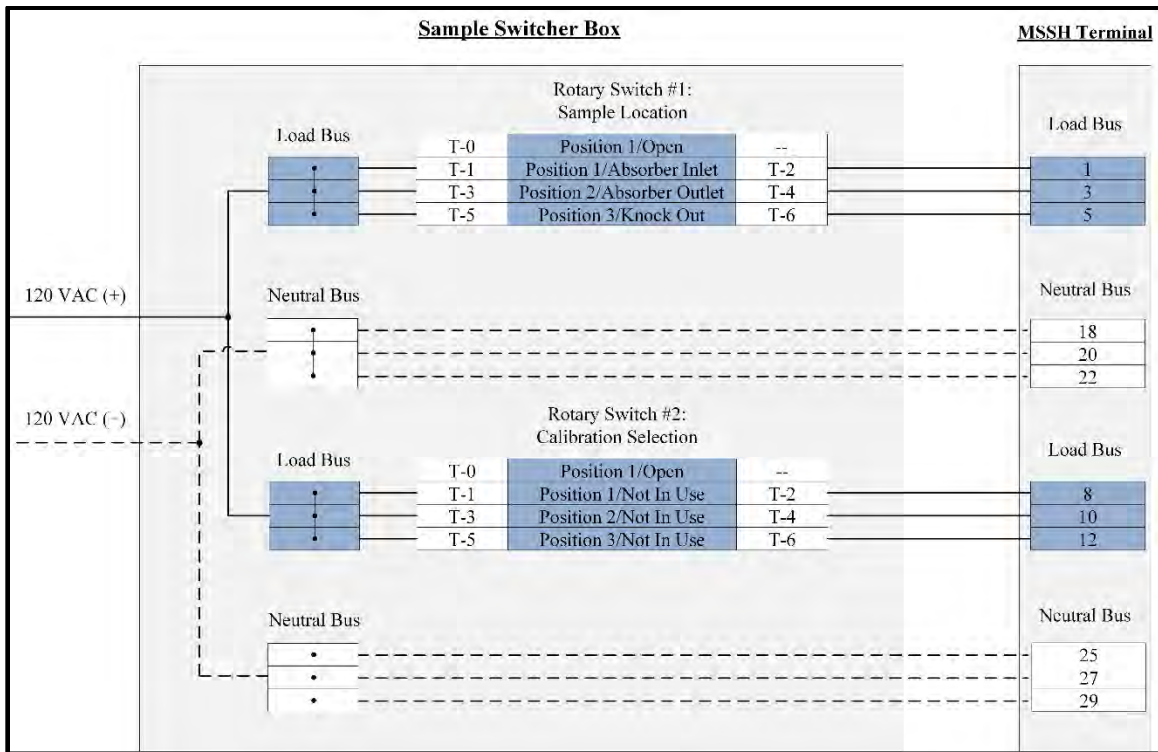


Figure 6.18: MSSH manual sampling switcher box. The switcher box selects the sample solenoid which then activates the heated pneumatic valve.

6.3.1.2 PDI Sampling

The sampling system of the PDI was modified from **Figure 6.11** by removing the 90° elbow in between the extraction port and the PDI analysis cell to prevent large particle loss before PDI analysis.

A weatherproof enclosure for the PDI electronics was purchased and modified for the campaign. **Figure 6.19** shows the enclosure with the PDI electronics fixed in place. The enclosure has a shelf above the electronics to store the PDI housing during inclement weather and for spare part storage.



Figure 6.19: PDI weatherproof enclosure. The PDI power box, ASA, and computer are contained in the enclosure on rackmount railing. The oscilloscope can be set on the shelf for signal observation during calibration and analysis.

The parameters for the first, second, and third generation PDI are shown in **Table 6.7**. N₂ purge and flush was attempted during sampling; however, the sample cell was not delivered sealed.

Table 6.7: Generation 1, 2, and 3 PDI optical and geometric parameters.

PDI Gen.	Duct Size [in]	Laser Waist [μm]	Cross Angle [°]	Rec. Focal Length [mm]	Trans. Focal Length [mm]	Lower Det. Size [μm]
1	12	50	28.1	500	375	0.5
2	1½	50	28.1	481	126	0.5
3	1	17.8	38.5	35	25	0.1

6.3.1.3 Aerosol Sources

Two sources of aerosols were used in the March, 2015 campaign: (1) SO₂ injection by MFC and manual rotameter, and (2) H₂SO₄ injection by the LVI operated in furnace mode. The injection point locations were the same as the November, 2013

The SO₂ MFC, which was controlled in DeltaV™, was operated for a short period of time before the controller became stuck and inoperable. The majority of SO₂ injection periods were controlled by the manual rotameter. Since the SO₂ tanks empty quickly, the pressure regulator and rotameter were monitored every 5–10 minutes to ensure a constant SO₂ concentration.

6.3.2 Results

6.3.2.1 Steady State Conditions

In total, 21 steady state conditions were achieved over the duration of the campaign. The absorber conditions are summarized in **Table 6.8**. The steady state reported values are averaged over a period of 30 minutes. CO₂ concentrations reported in **Table 6.8** are the values from the Vaisala CO₂ probes.

Table 6.8: Absorber steady state conditions during the March, 2015 PRC pilot plant campaign.

Run	Date/ End Time	Solvent Rate [GPM]	Gas Rate [ACFM]	PZ Conc. (CO ₂ Free) [wt %]	Lean Loading [mol/mol]	CO ₂ In [vol %]	CO ₂ Out [vol %]	Intercooling [Y/N]	Spray Nozzle [Y/N]
1	3/11/2015 16:00	9.3	350	29.0	0.221	12.01	1.20	Y	Y
2	3/12/2015 11:30	10.2	350	29.8	0.226	11.94	0.33	Y	Y
3	3/12/2015 16:00	10.2	350	29.7	0.229	11.96	0.20	Y	Y
4	3/13/2015 06:30	10.2	350	29.7	0.232	11.99	0.29	Y	N
5	3/13/2015 10:00	10.2	350	30.0	0.224	12.03	0.56	Y	N
6	3/13/2015 14:00	12.0	350	30.0	0.265	12.09	1.19	Y	Y
7	3/16/2015 13:00	14.0	350	31.4	0.245	12.01	2.51	N	N
8	3/17/2015 13:30	14.0	350	30.7	0.236	11.99	0.33	Y	Y
9	3/17/2015 16:30	14.0	500	30.5	0.235	12.03	1.95	Y	Y
10	3/19/2015 12:00	14.0	500	30.3	0.204	12.04	1.55	Y	Y
11	3/20/2015 06:30	9.3	350	30.0	0.201	11.99	1.01	Y	Y
12	3/20/2015 10:30	14.0	350	29.8	0.237	12.00	0.14	Y	Y
13	3/23/2015 14:30	14.0	500	38.8	0.242	11.55	3.72	N	Y
14	3/23/2015 18:00	14.0	500	40.8	0.241	11.97	3.10	Y	Y
15	3/24/2015 15:30	14.0	350	40.2	0.242	11.94	0.37	Y	Y
16	3/25/2015 06:30	10.2	350	40.7	0.231	11.98	0.64	Y	Y
17	3/25/2015 14:45	10.2	350	29.9	0.200	11.94	0.25	Y	Y
18	3/25/2015 16:15	10.2	350	--	--	11.94	0.25	Y	Y
19	3/26/2015 06:30	7.0	350	30.1	0.235	6.00	0.16	Y	Y
20	3/26/2015 14:00	8.6	350	29.7	0.184	11.96	1.42	N	N
21	3/27/2015 08:00	10.2	350	29.4	0.235	11.98	2.66	Y	Y

6.3.2.2 *Physical Observations*

During aerosol injection, a clear plume was visible at the vent stack outlet; however, the opacity was very different for SO₂ and H₂SO₄ injection. The SO₂ plume was very thin and brown/blue in color whereas the H₂SO₄ plume was thick and white.



Figure 6.20: SO₂ (left) and H₂SO₄ (right) plumes at the absorber outlet vent stack.

A practical observation from aerosol injection was the plugging of the knockout filter with collected H₂O/PZ/CO₂. After SO₂ injection, the pressure drop across the filter began slowly increasing (**Figure 6.21**). As a result, the blower speed increased. When the pressure drop was deemed too high by the operators, the filter was rinsed with hot water and the gaskets were soaked in a drum of water to clean out collected material. The filter was then dried overnight by running the blower at a high speed with the air

chiller operating at a higher temperature to prevent fog formation. **Figure 6.22** shows the filter and wire mesh pad in the knockout filter tank. The gas flows upwards through the mesh pad into the inner portion of the filter body and then passes through the element, finally exiting out of a nozzle on the side of the knockout tank.

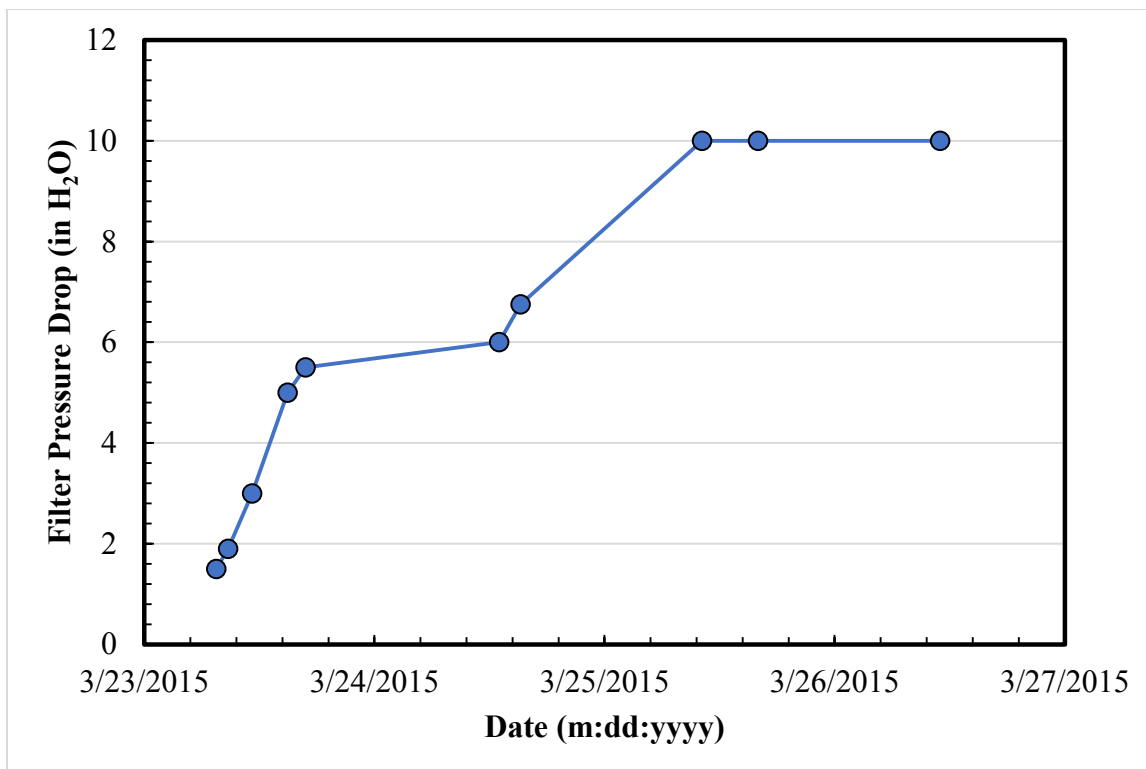


Figure 6.21: The knockout filter pressure drop increased across the campaign following SO₂ injections due to accumulation of H₂O/PZ/CO₂ liquid and solids.

Amines which have rich solubility limitations will lead to solids problems since the collected liquid will eventually reach equilibrium to the gas at that point. Collection devices which are not self-draining or rinsed frequently will encounter this problem even if the solvent loading is carefully chosen to avoid precipitation limits. Condensate tanks, dead legs, control valves, and relief lines are subject to this problem and should be

routinely checked, especially in the case of relief lines which may have very small leaks, which overtime can lead to plugging. Steam injection points would be effective at clearing blockages.



Figure 6.22: The knockout tank consists of an upstream coarse wire mesh pad (left) and a 0.3 μm filter (right). The filter and mesh were periodically rinsed with warm water to re-dissolve collected material.

6.3.2.3 Manual Sampling

Manual sampling data provided by AECOM is shown below (**Table 6.9**). Measurements of H_2O and PZ followed similar deviations to that measured in the November, 2013 campaign. H_2O at the absorber inlet was higher than that measured by the FTIR. $\text{SO}_x/\text{H}_2\text{SO}_4$ was lower than that measured by the FTIR for both the SO_2 and

H₂SO₄ injections; manual sampling SO₂ and H₂SO₄ values were 8.5 ppmv (34%) and 8.4 ppmv (80%) lower than the FTIR and calculated set point, respectively.

The PZ measurements at the absorber outlet matched the FTIR measurements within 10–20% for most tests, including the H₂SO₄ injection (Run 6). The values measured on March 24 were the only data outlier; however, a wire in the heated probe was slowly melting through and it is unclear if the probe was fully operational that day.

Table 6.9: Manual sampling data provided by AECOM (formerly URS Corp.)

Run	1	3	4	5	6	7
Date	3/13	3/24	3/25	3/25	3/26	3/26
Time	14:04- 14:37	15:45- 16:15	13:50- 14:20	15:25- 15:55	11:35- 12:05	13:25- 13:55
<i>Absorber Inlet:</i>						
Flue gas moisture (%)	3.80	4.98	4.17	4.24	2.88	2.84
SO _x (mg/dscf) [as SO ₄ ²⁻]	1.80	1.75	1.78	1.60	0.178	2.39
SO _x (ppm, dry)	15.9	15.4	15.7	14.1	1.58	21.1
<i>Absorber Outlet:</i>						
Flue gas moisture (%)	6.36	5.33	5.13	5.74	12.7	13.1
PZ (mg/dscf)	3.76	5.72	4.59	4.79	13.6	6.30
PZ (ppm, dry)	37.0	56.4	45.2	47.2	134	62.1

6.3.2.4 FTIR

The MSSH allows for rapid switching of sample location to the FTIR. The continuous bypass keeps sample gas in the lines at all times; therefore, the response lag of the individual sample lines is eliminated from the system. The response lag is thereby reduced to the common sampling line which connects the MSSH to the FTIR system.

Figure 6.23 shows an example of the FTIR system response when switching through the

three sampling locations along the absorber. The lag time to steady state is on the order of 5 minutes, though it is often dependent on the change in PZ concentration across sampling locations. The sample points are abbreviated as: absorber inlet (In), absorber outlet (Out), and downstream of the knockout tank (KO).

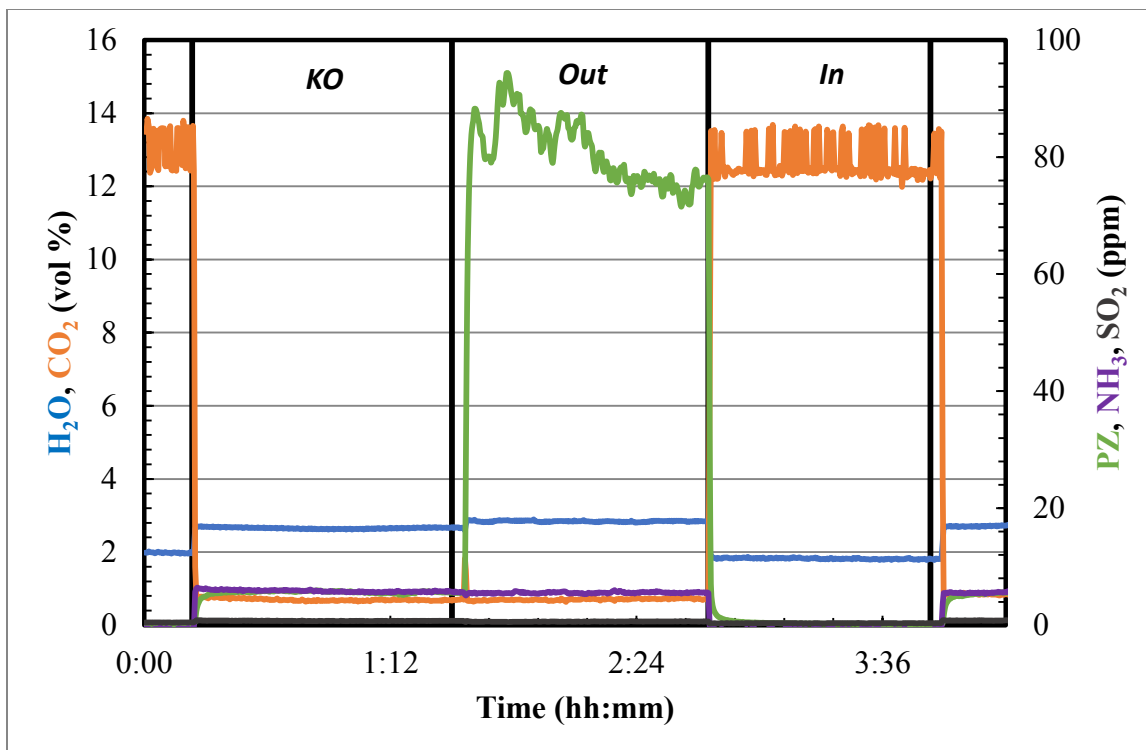


Figure 6.23: FTIR response to MSSH sample switching (03/25/2015). The FTIR reaches steady state after five minutes between sample point switches.

The accuracy of the new FTIR and sampling system was evaluated by comparing CO₂ measurements to the PRC pilot plant Vaisala CO₂ probes and the H₂O concentration calculated by Raoult's Law using the titrated solvent composition and the absorber outlet temperature probe (TT-400). Direct comparison of H₂O to Raoult's law assumes equilibrium at the temperature probe as well as negligible condensation between the absorber temperature probes and the FTIR sampling point.

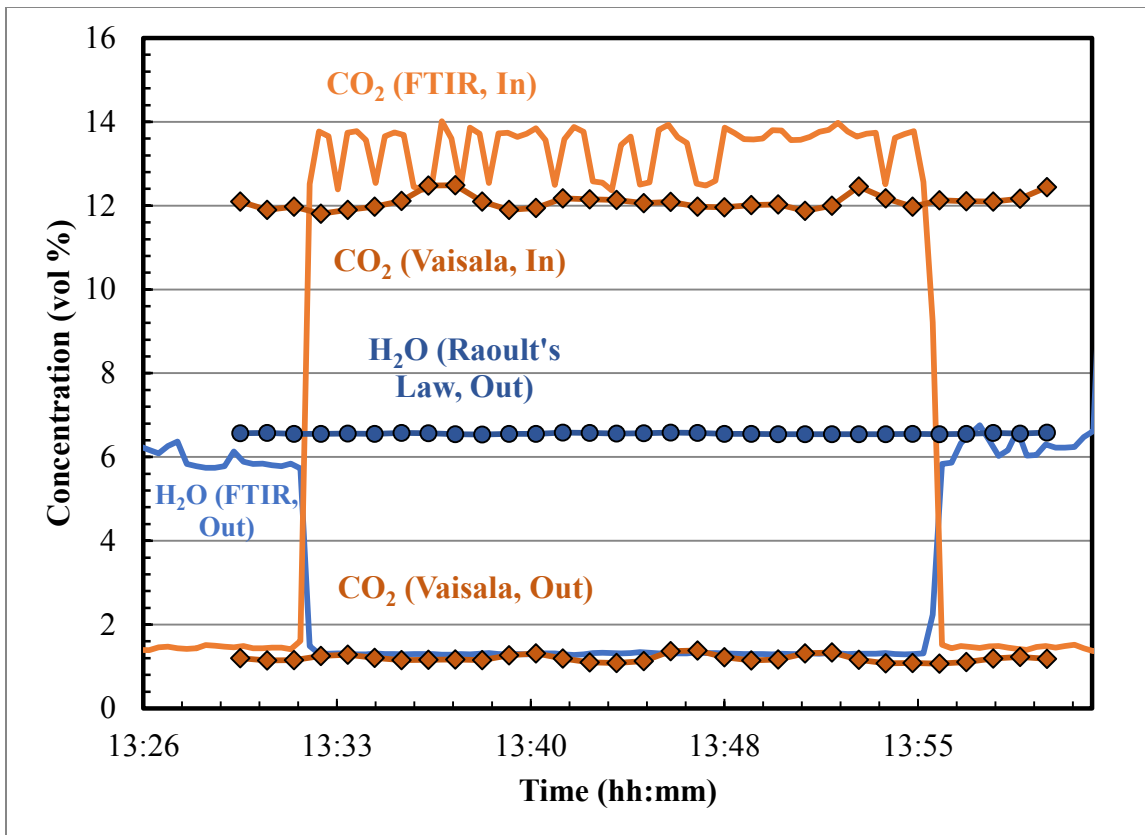


Figure 6.24: FTIR measurements compared to CO₂ inlet and outlet measurements using Vaisala CO₂ probes and H₂O by Raoult's Law

The CO₂ measurement by FTIR was lower for both the inlet and outlet measurements relative to the Vaisala probes. On average, the measurements deviated by about 5–10% across the campaign. However, the CO₂ removal measured by the FTIR was higher by an absolute average deviation of 3.4% on a comparable dry basis across the campaign. For H₂O, the FTIR and Raoult's Law comparison were nearly identical; however, in other cases, the deviation was more than 10%. The combination of errors in the solvent analysis, condensation in the gas duct, and mass-transfer effects could create such large deviations.

Following the campaign, the CO₂ measurements were compared using a simultaneous calibration procedure. The results of that comparison are plotted below in **Figure 6.25**. The FTIR measurements were

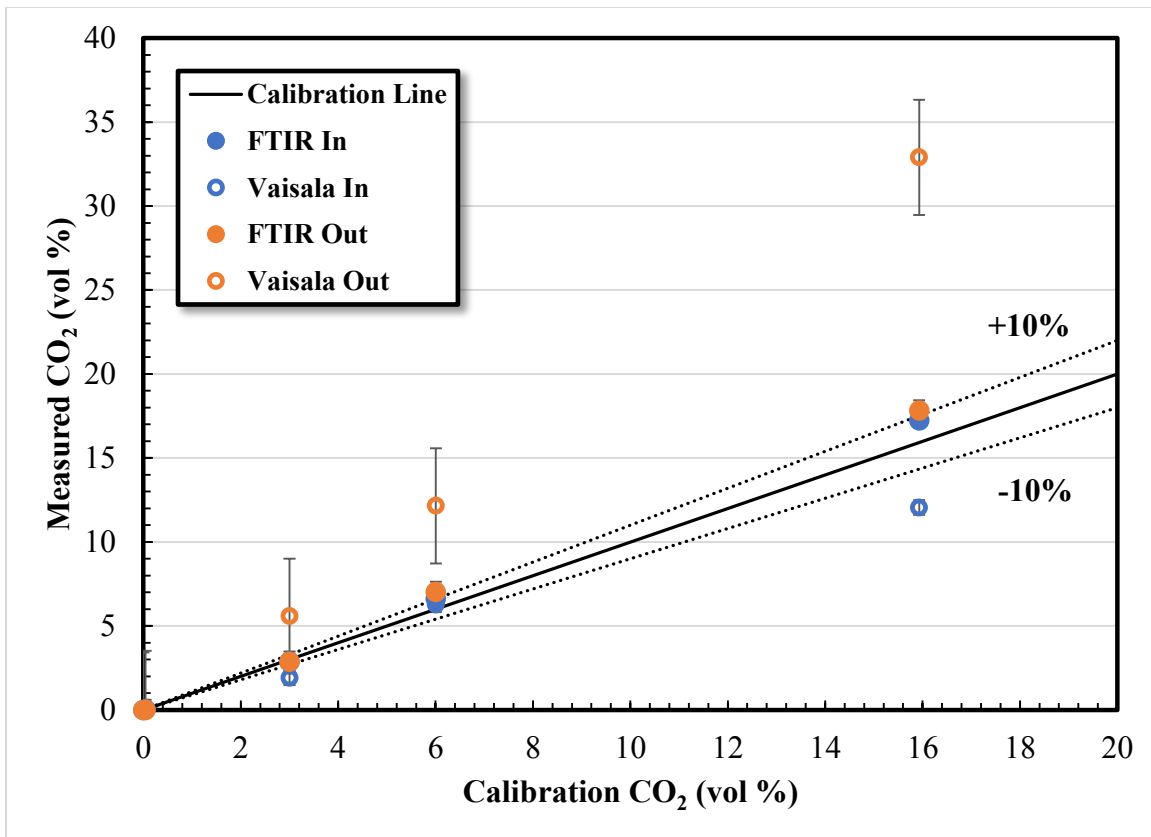


Figure 6.25: Vaisala and FTIR CO₂ calibration comparison. Error bars are the maximum standard deviation for each data set.

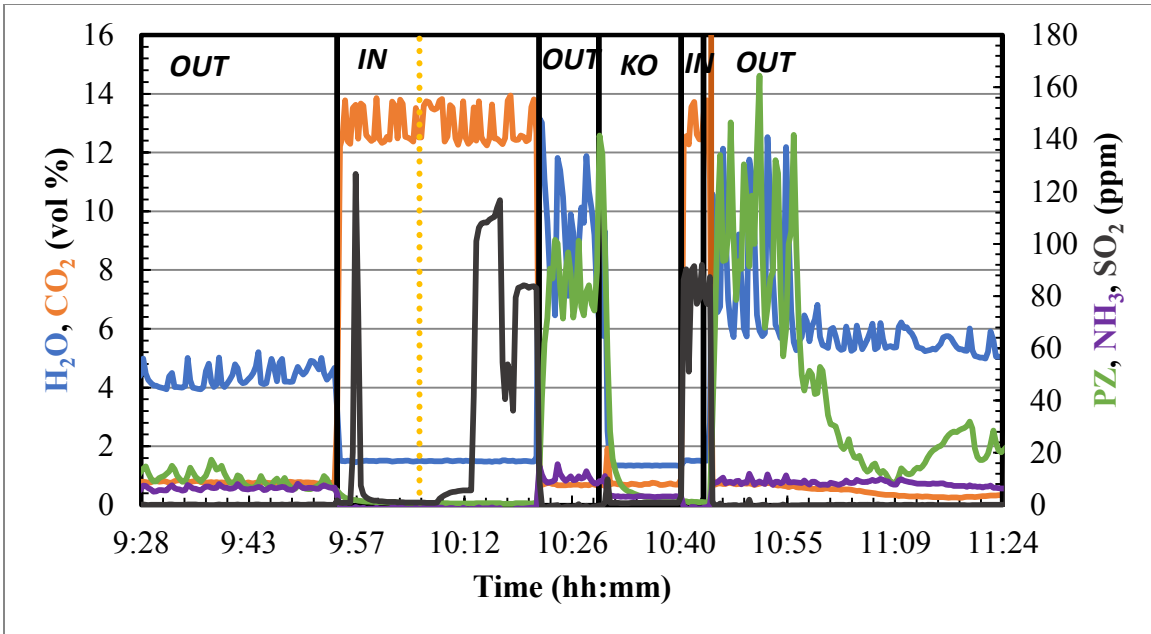


Figure 6.26: Response of outlet PZ to SO₂ injection #1 using a mass flow controller (03/13/15)

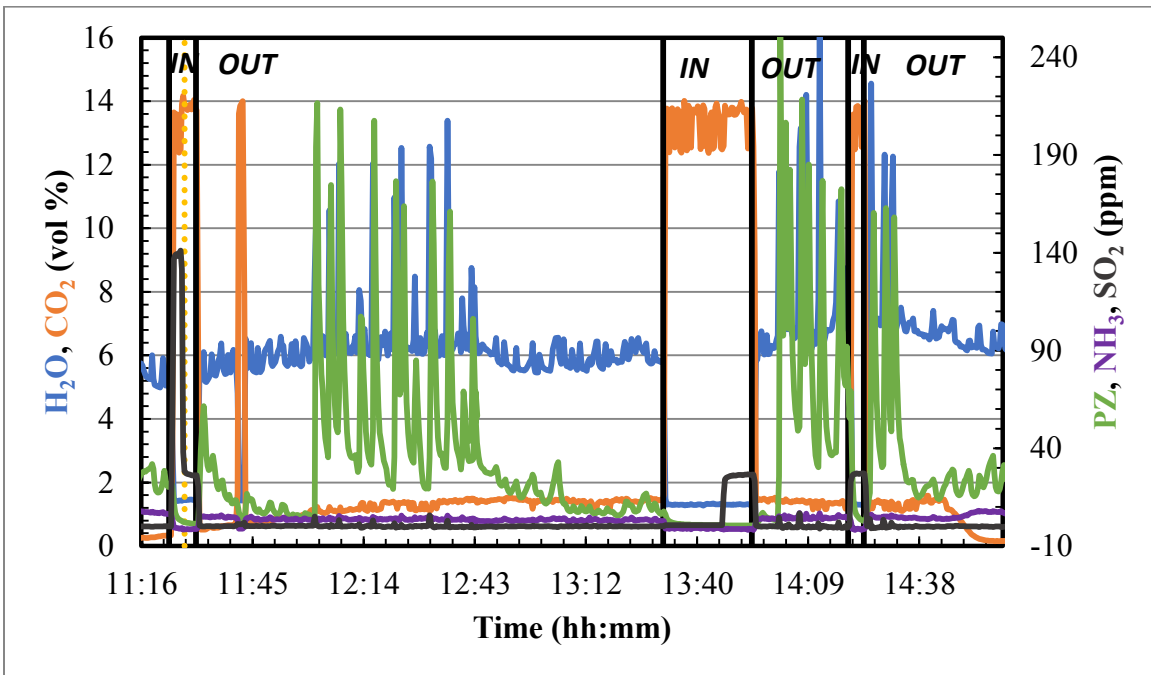


Figure 6.27: Response of outlet PZ to SO₂ injection #2-3 using a rotameter (03/13/15)

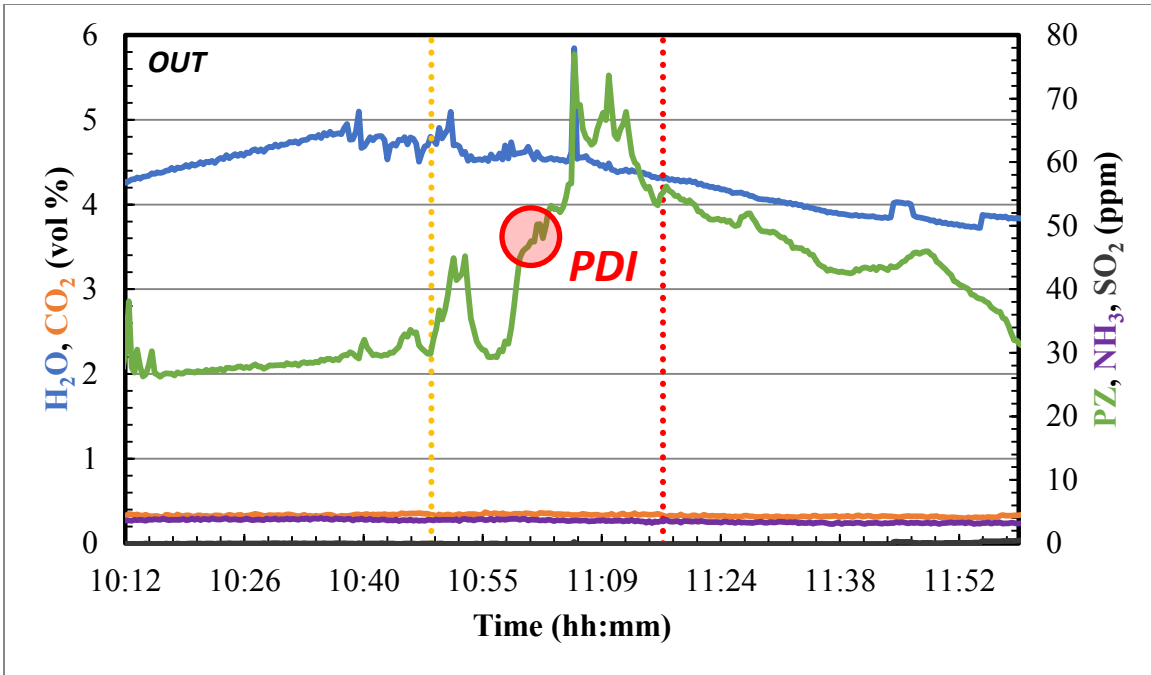


Figure 6.28: Response of outlet PZ to H₂SO₄ injection #2 (03/20/15)

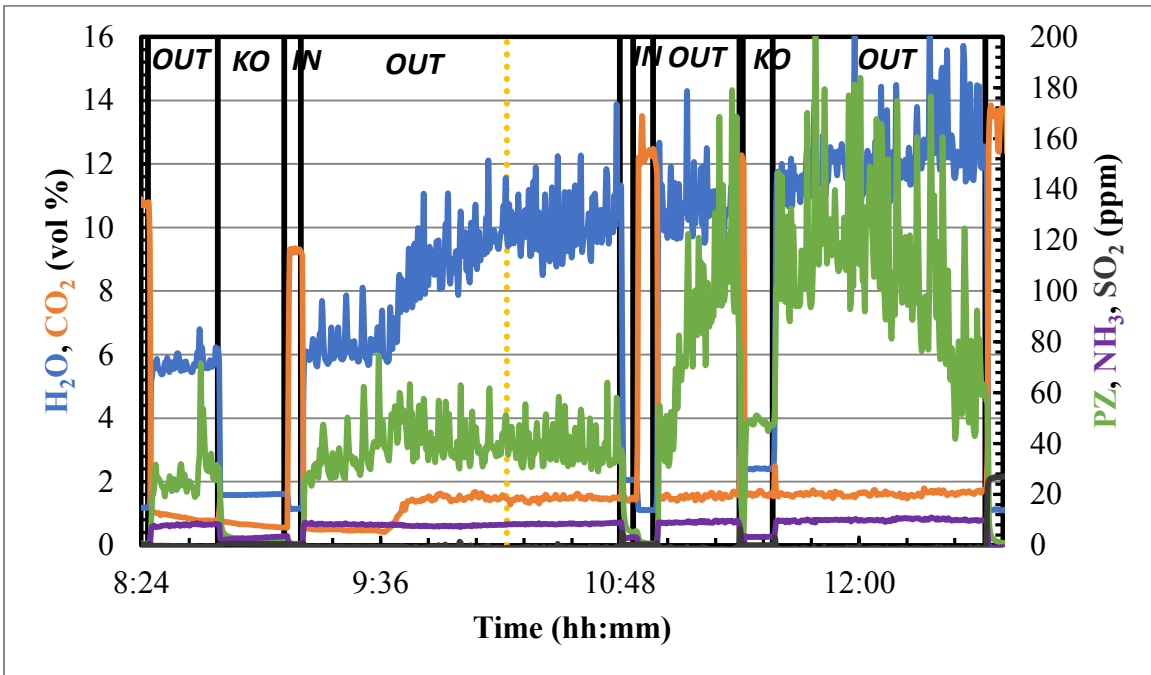


Figure 6.29: Response of outlet PZ to H₂SO₄ injection #3 (03/20/15)

The injection data, steady state run numbers, and PZ response measured by FTIR are shown in **Table 6.10**. Concentrations were averaged over a period of 30 minutes. Similar to the November, 2013 campaign, the response of the outlet amine to SO₂ was in the range of 0–2 mol amine/mol SO₂. However, the ratio does not appear to be simply a result of the simultaneous reactions listed in **Table 6.5**. The ratio does not show any strong correlation with the nucleating environment, which would be approximated by the inlet gas temperature and moisture content. The ratio is likely the result of multiple competing mechanisms, including nucleation, condensation, and bulk gas absorption.

In order to determine the relative rates of nucleation and absorption, an approximate absorption fraction was calculated using the total injection time and rate of SO₂ coupled with a solvent mass balance using analyzed sulfate concentrations and the total solvent inventory. Based on back-calculation of FeSO₄ additions, the average solvent inventory was taken to be 1,400 kg. The absorbed fraction was then calculated by minimizing the error between the total moles of injected SO₂ and the measured sulfate concentration. H₂SO₄ (by LVI) was assumed to be completely in the aerosol phase and uncollected. **Figure 6.30** shows the calculated and measured sulfate accumulation curves; the result of the error minimization yielded an absorption percent of 34.9%. The SO₂ absorption percent for the maximum (1,500 kg) and minimum (1,300 kg) solvent inventory is 38.0 and 31.8%, respectively.

The peak between runs 11 and 17 is due to concentration and dilution of the solvent between 5 and 8 m PZ. The solvent is concentrated by removing H₂O out of condensate tanks until the desired concentration is reached. The solvent is diluted by adding the stored condensate back into the system.

Table 6.10: Aerosol injection and outlet PZ response data for the March, 2015 PRC pilot plant campaign. DeltaV™ run numbers are the closest matching steady state points to the injection time periods. The last column recalculates the PZ/SO₂ ratio using an absorption fraction of 34.9% (65.1% SO₂ is nucleated).

<i>SO₂ Injections</i>								
Inj. #	Time (hh:mm)	Date	DeltaV™ Run #	SO ₂ /H ₂ SO ₄ In (ppmv)	PZ Base (ppmv)	PZ High (ppmv)	PZ/(SO ₂ /H ₂ SO ₄) (mol/mol)	Adj. PZ/SO ₂ (mol/mol)
1	10:22-10:58	03/13/2015	5	82.5	9.4	95.4	1.04	1.60
2	12:02-12:46	03/13/2015	6	26.4	19.7	58.1	1.45	2.23
3	14:02-14:33	03/13/2015	6	26.0	8.9	76.4	2.59	3.99
4	13:49-16:30	03/24/2015	15	28.0	17.2	17.7	0.02	0.03
5	13:22-16:06	03/25/2015	17	27.7	40.3	63.2	0.83	1.27
6	12:42-14:02	03/26/2015	20	27.0	67.0	70.2	0.12	0.18

<i>H₂SO₄ Injections</i>							
Inj. #	Time (hh:mm)	Date	DeltaV™ Run #	SO ₂ /H ₂ SO ₄ In (ppmv)	PZ Base (ppmv)	PZ High (ppmv)	PZ/(SO ₂ /H ₂ SO ₄) (mol/mol)
1A	15:44-16:13	03/16/2015	7	10.0	28.4	37.7	0.93
1B	16:13-16:24	03/16/2015	7	13.7	28.4	55.3	1.97
2	10:50-11:24	03/20/2016	12	10.0	26.7	49.3	2.26
3	10:18-12:38	03/26/2015	20	10.0	38.9	106.2	6.73

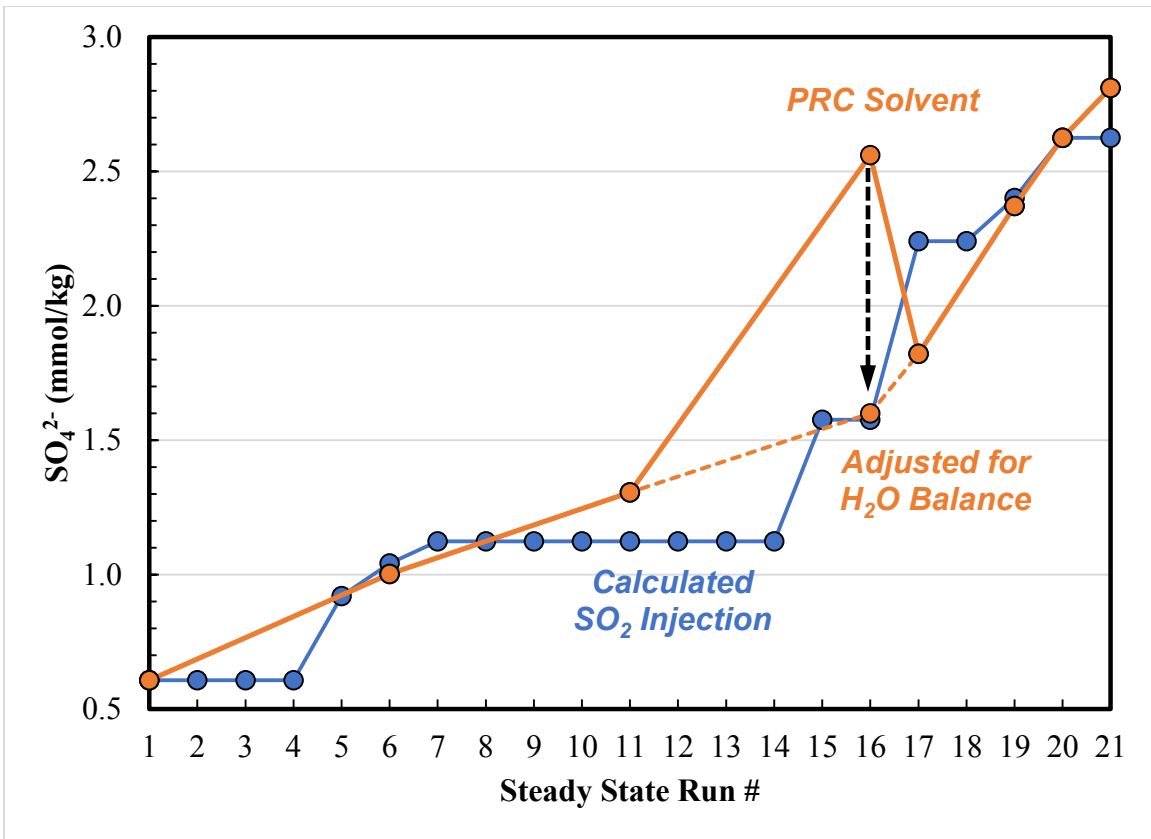


Figure 6.30: Sulfate accumulates in the PRC pilot plant solvent proportionally to the SO₂ injection rate and time. The calculated SO₂ absorption percent is 34.9% assuming a total solvent inventory is 1,400 kg over the duration of the campaign.

In both the H₂SO₄ and SO₂ aerosol cases, no single variable is indicative of the amine reaction or condensation relative to the aerosol phase.

6.3.2.5 PDI

The custom-built PDI arrived at UT a few days prior to the campaign. During the first assembly, the transmitter window cracked and rendered the PDI inoperable. Replacement windows were ordered and reapplied using silicone sealant cured over 24 hours. After testing the PDI with the airbrush, the system was craned up to the top deck of the PRC pilot plant and flanged into position.

When the sample isolation valve was opened, it was discovered that the retaining collar pieces which hold the PDI purge and flush cones had not been screwed into place; the process gas leaked out of the screw holes and eventually condensate drained out onto the outside surface of the analysis cell windows. The holes were covered with electrical tape as a short term fix.

Next, the PDI laser crossing was adjusted using the airbrush. During the adjustment procedure, the drive screw that adjusts the laser focus fell out of its casing. No stop mechanism was included in the original design. Unfortunately, the system had to be shipped back to Artium's facility in California and was returned later the next day.

Once the PDI was returned, a single measurement was made during H₂SO₄ Injection #2, as indicated in the red circle in **Figure 6.28**. Following that measurement, the system became overwhelmed with condensate and had to be removed and cleaned.

Figure 6.31 shows the measured velocity distribution in the analysis cell during injection of H₂SO₄ using the LVI. The curve is a Gaussian distribution centered about 1.32 m/s (4.33 ft/s). The negative velocities indicate back mixing caused by turbulence. The average velocity from this curve is used to adjust the blower speed to match the duct velocity.

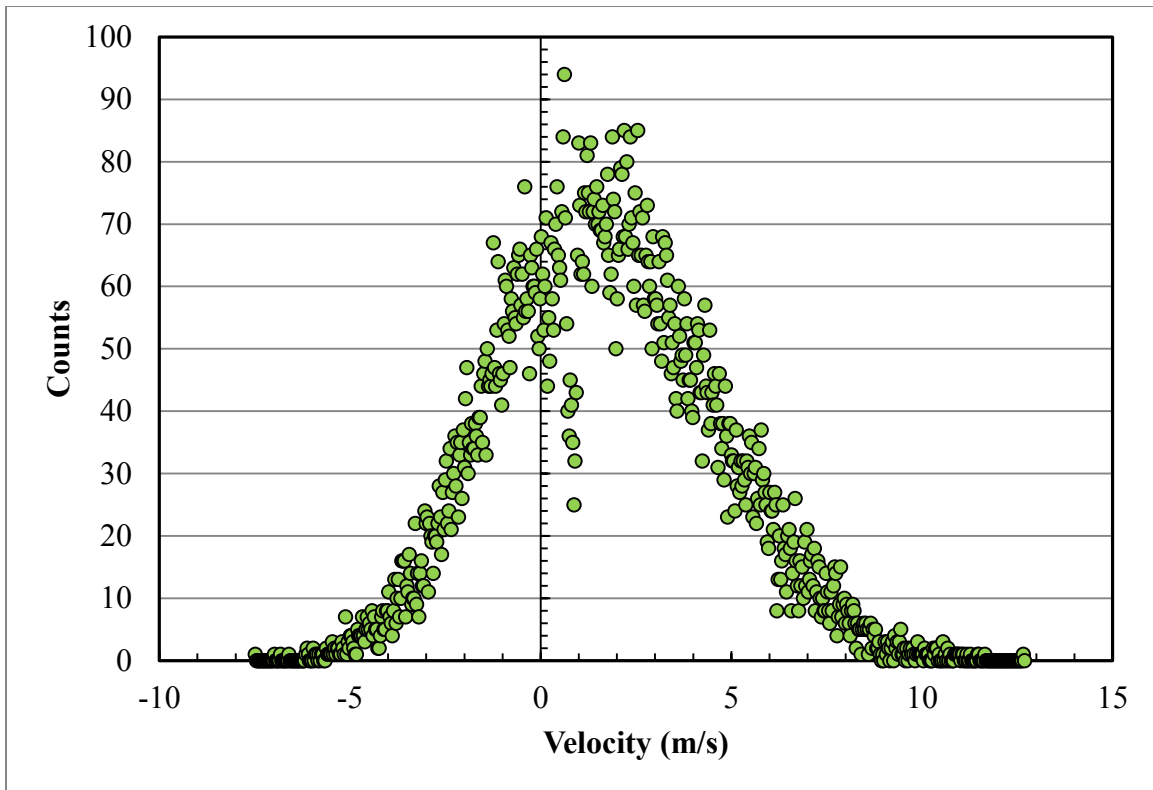


Figure 6.31: Velocity distribution measured in the PDI analysis cell with purge and flush gas. The total data set is 15,802 counts. Negative velocities indicate back-mixing and turbulence in the cell.

The PSD is shown in **Figure 6.32**; the total sample set is 15,802 counts and the bin size is 0.01 μm . The two dashed lines indicate the limits of quantification for the second and third generation PDI analyzers. The curves clearly show that the second generation PDI was not observing a finer mode in the PSD, which necessitated the *ex situ* modification to the PDI analyzer.

Furthermore, the total particle density was several orders of magnitude higher than was observed in the November, 2013 campaign. This finding cannot be explained by the omission of the finer mode. A bimodal-lognormal curve was optimized to approximate the measured PSD with the total particle density constraint (**Figure 6.33**).

The approximating curve is compared to the measured data in **Figure 6.34**. The “fine” and “coarse” modes account for 70.7 and 29.3% of the particle density, respectively. Even if the coarse mode was observed independently, the total particle density was still three to four orders of magnitude higher than that measured in the November, 2013 campaign. This finding can only be attributable to the modifications and significant improvement made to the LVI.

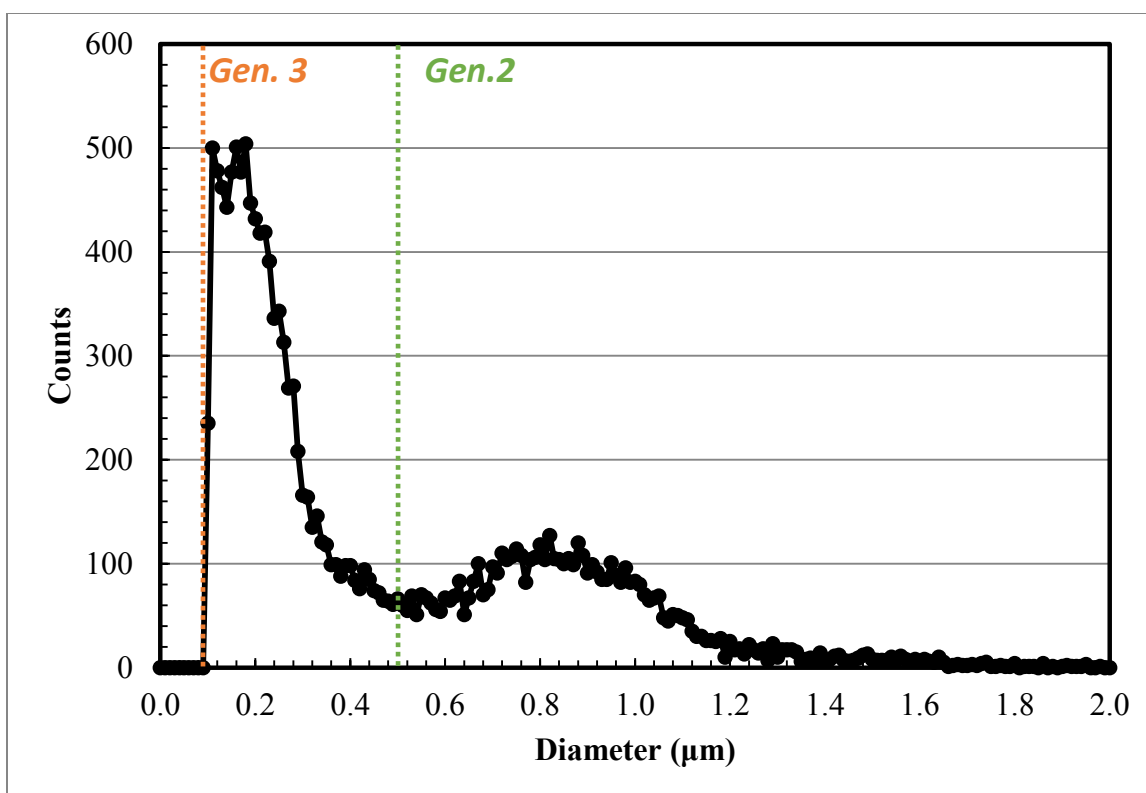


Figure 6.32: PSD measured during H₂SO₄ injection at the PRC pilot plant. The total particle density is 9.9×10^5 part./cm³. The total data set is 15,802 counts. The dashed lines indicate the quantification limits for the **generation #2 and **generation #3** PDI showing the marked improvement.**

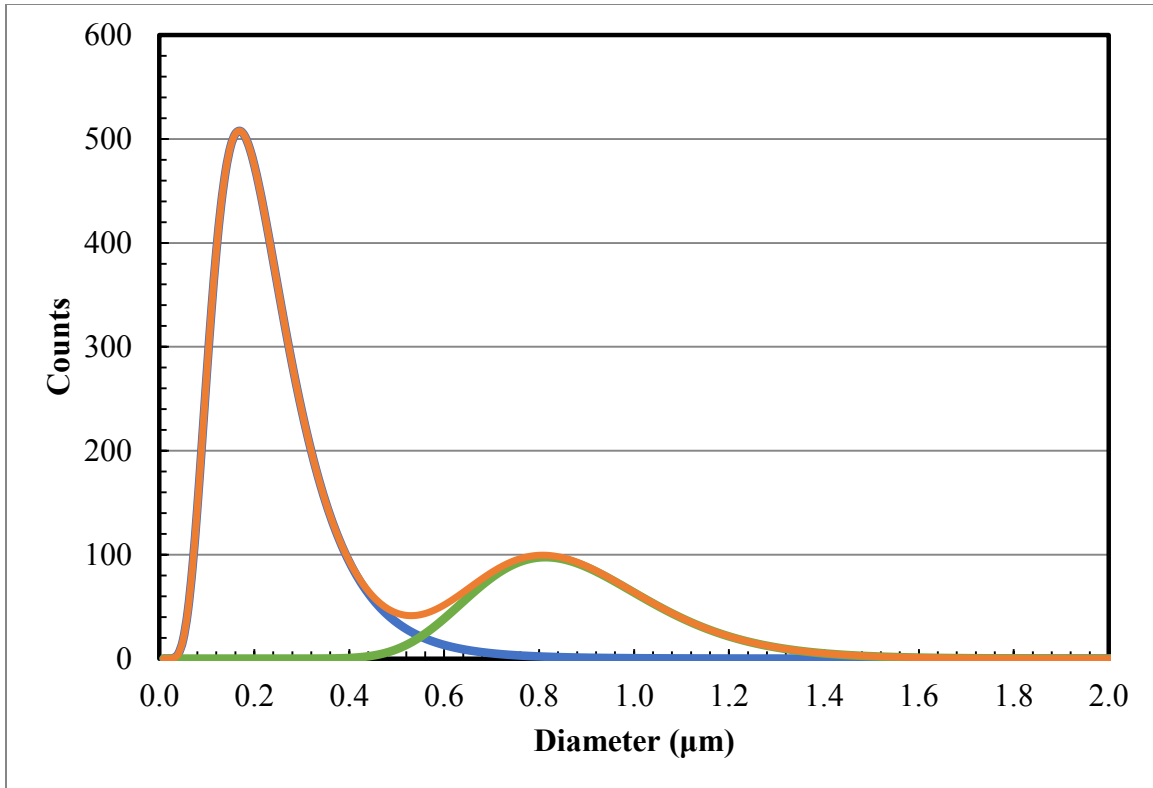


Figure 6.33: A bimodal-lognormal distribution constrained to a total particle density of 9.9×10^5 part./cm³. The individual distribution mode parameters were optimized to match the measured PSD in Figure 6.32. **Fine Mode parameters: $\sigma_G = 1.60 \mu\text{m}$, $d_G = 0.21 \mu\text{m}$, 7.0×10^5 part./cm³. **Coarse Mode** parameters: $\sigma_G = 1.25 \mu\text{m}$, $d_G = 0.86 \mu\text{m}$, 2.9×10^5 part./cm³.**

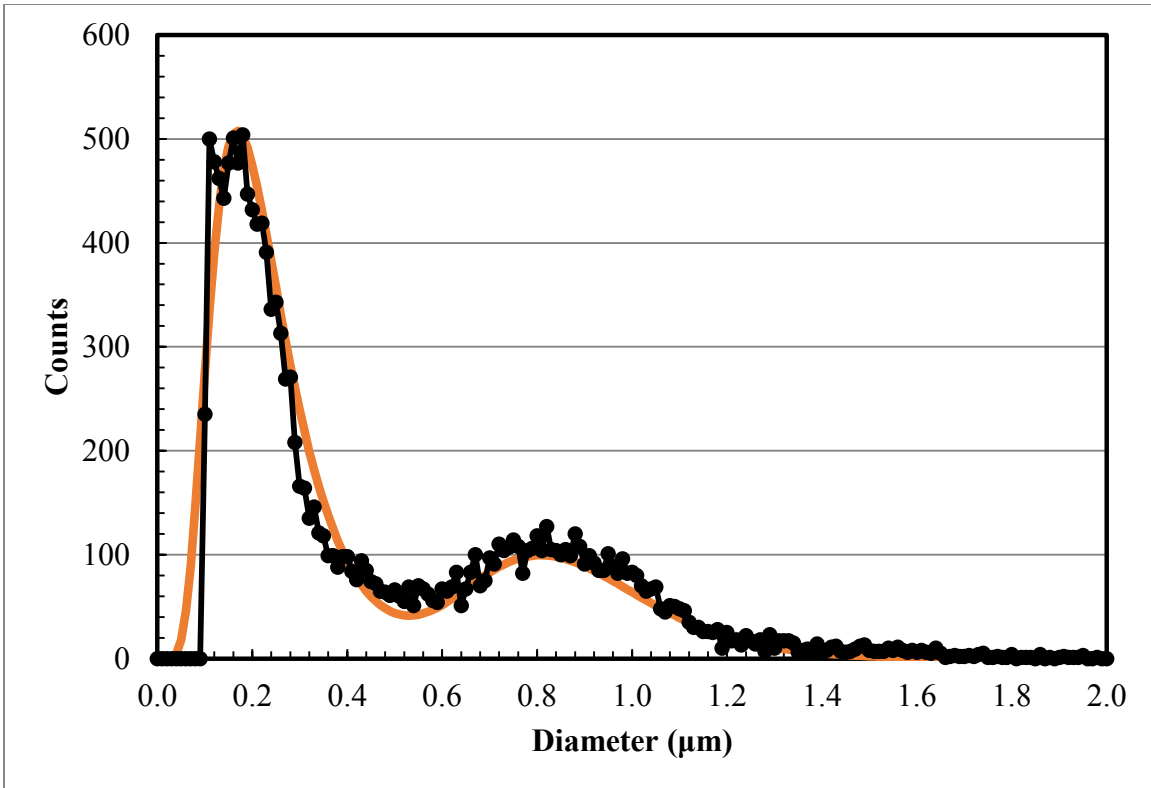


Figure 6.34: Measured and approximated PSD at the PRC pilot plant.

The cumulative distributions for the measured and calculated PSDs are shown in **Figure 6.35**. The distribution averages are listed below in **Table 6.11**. The cumulative distribution illustrates the large differences between the diameter and volume averages as it relates to emissions of amine. 50% of the diameter distribution lies below 0.28 μm; whereas 50% of the volume, or mass, distribution lies below 1.02 μm. This effect is also noticeable by the lack of the inflection point in the cumulative volume distribution, which means that the volume, or emissions, are contained almost entirely in the coarse mode. In terms of PDI measurement, the second generation PDI was only capable of measuring the coarse mode. The coarse mode could be integrated to match the emissions measured by FTIR with fair accuracy. Even if the PDI is missing nucleation or Aitken modes, their

contribution to the mass, or emissions, is likely negligible assuming they are not many orders of magnitude higher in total particle density.

Table 6.11: Distribution statistics for the PSD measured at the PRC pilot plant with H₂SO₄ aerosol. The “Fine” and “Coarse” modes are approximating curves of the Total (Measured) distribution.

Mode	Total Density [part./cm ³]	d _G [μm]	σ _G
Fine	7.0x10 ⁵	0.21	1.60
Coarse	2.9x10 ⁵	0.86	1.25
Total	9.9x10⁵	0.28	--

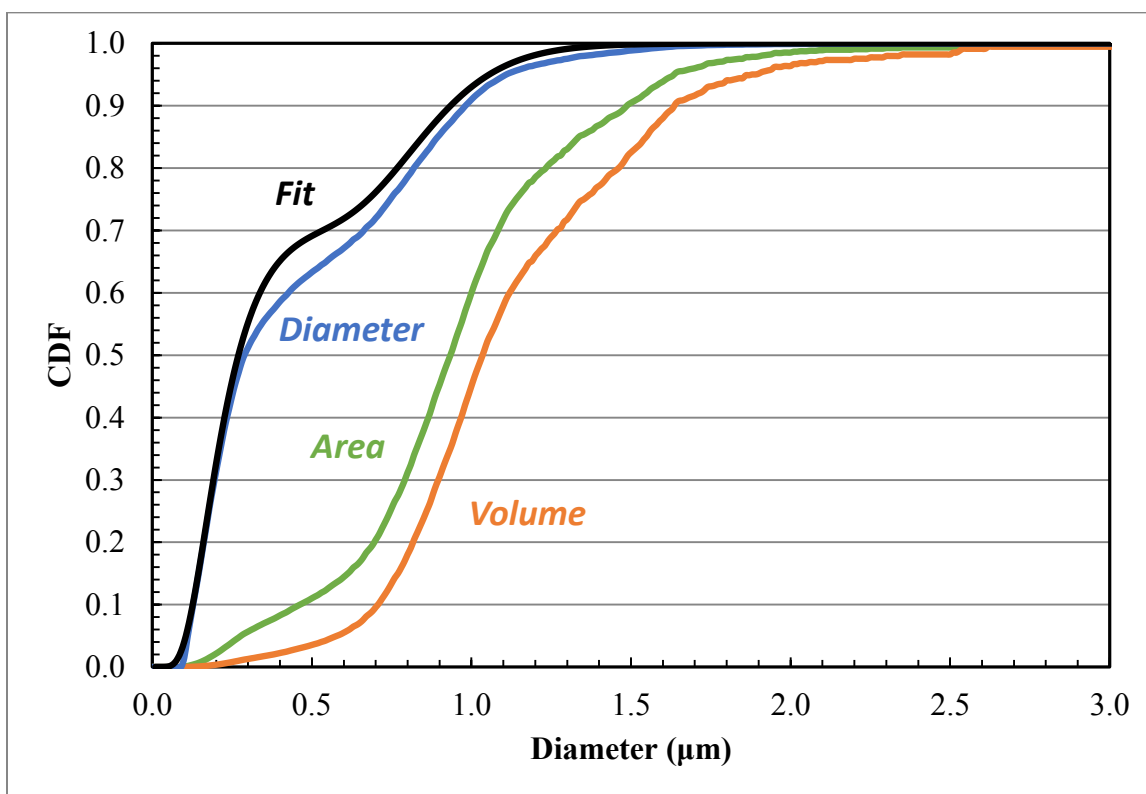


Figure 6.35: Cumulative distributions for the diameter, surface area, and volume of the measured PSD. The black line is the diameter cumulative distribution using the fitting curve from Figure 6.33.

The measured PSD was used to calculate the exact PZ concentration in the aerosol that would match the FTIR concentration (48.01 ppmv). The calculated aerosol amine concentration was nearly 50 wt %, which is much higher than observed in AGC experiments and those at other pilot plants presented later in this chapter. This finding can be partially explained by the lack of other data points; only one PSD was recorded and could be in significant error. Additionally, the PSD was mostly composed of a submicron mode and the aerosol integration is very insensitive to the aerosol amine concentration. Therefore, a relatively modest error in the particle density number (factor of 2) can produce several orders of magnitude difference in the calculated amine concentration.

The low calculated amine concentration also does not match the finding of low PZ:SO₂/H₂SO₄ which would suggest very dilute aerosols.

6.3.3 PDI Improvements

Following the successful demonstration of the generation 3 PDI test on the PRC pilot plant and the AGC, the purge and flush system was modified and the analysis cell was sealed using Teflon washers, machine screws, and silicone sealant.

6.4 NCCC – DECEMBER, 2015 – PDI GENERATION 3.1 TEST

Early in 2015, Southern Company acquired the Slipstream Solvent Test Unit (SSTU) from Shell Cansolv and began commissioning work to test MEA solvent at the end of the year. As a part of the initial testing and troubleshooting work, UT was invited to take FTIR and PDI measurements at the outlet of the SSTU after passing through an added water wash column to observe the effects of process conditions on the outlet emissions levels and aerosol growth/shrinkage. Additionally, ELPI measurements,

performed by Southern Research Institute, would occur simultaneously for direct method comparison.

FTIR and PDI data were collected over seven days. Some of that data will be omitted because unique aerosol control devices were tested during those periods and the data is currently deemed sensitive for publication. The conclusions from that data are no different than was found during the rest of the testing period; the PDI shows the effect of process changes on the aerosol PSD in both size and total particle density. Also, the integrated PSD matches the FTIR with reasonable accuracy.

6.4.1 Equipment

The configuration of the absorber and wash section of the SSTU is shown below in **Figure 6.36**. Due to expansion of the testing facility at NCCC, an upgraded blower was added to simultaneously feed the PSTU and SSTU. The two blowers will be referred to as the upstream blower (PSTU blower) and the blower located between the absorber and water wash (SSTU blower). When the SSTU blower is used, the absorber operates under a slight vacuum. In either case, bypass valves are located on each blower so they can be tested independently. The bypass valves are in close proximity to each blower, the bypass piping does not add significant distance or residence time to the process. The sampling location for PDI/FTIR was 55 feet downstream of the water wash tower just in front of a BDU filter. The return port was located downstream of the BDU.

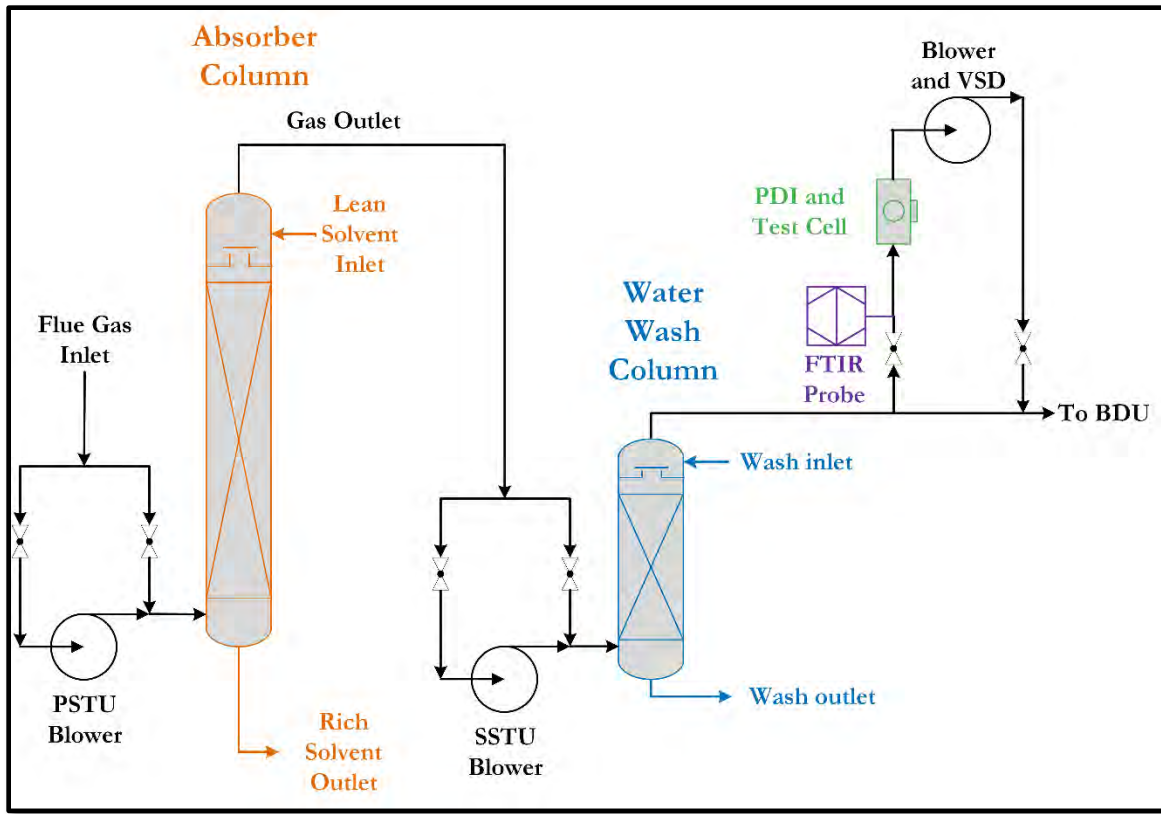


Figure 6.36: SSTU process flow diagram with FTIR/PDI sample/return loop. The physical piping distance between the top of the water wash column and the sample port is 55 feet.

One sample location was provided for both PDI and FTIR sampling; therefore, a simultaneous unit was designed. The FTIR was sampled through a tee fitting using the heated “stinger” probes used at the PRC pilot plant and drawn into the DX4000 portable FTIR using the PSU pump. The PDI analysis cell was flanged to the FTIR sampling tee. **Figure 6.37** shows the sampling system in place at NCCC. The sampler piping was wrapped in fiberglass insulation to prevent condensation.



Figure 6.37: Simultaneous FTIR/PDI sampling unit located at the outlet of the SSTU water wash operating at NCCC.

The simultaneous sampling system was designed to minimize particle losses in sampling and transmission to the analysis section. **Figure 6.38** shows the calculated transmission efficiency using the physical dimensions of the sampling system. The flow rate was assumed to be 125 SLPM which gives a PDI cell velocity of 12 ft/s. The valve

length from the process duct was taken to be 12 inches at 90° relative to the process duct and horizontal with respect to the ground. The constriction from the 4" duct to the 1½" sampler was 90° since the connection was a tapped flange with a threaded pipe nipple. The 1½" section length was 16", 8¼" for the PDI cell and 7¾" for the FTIR draw-off tee and connecting pipe nipples and flanges. The main contributions towards particle loss was gravity settling and turbulent deposition during aspiration. Because the duct velocity is very low, particle losses will be very minimal; the sampling efficiency for 10 µm particles is still about 80%.

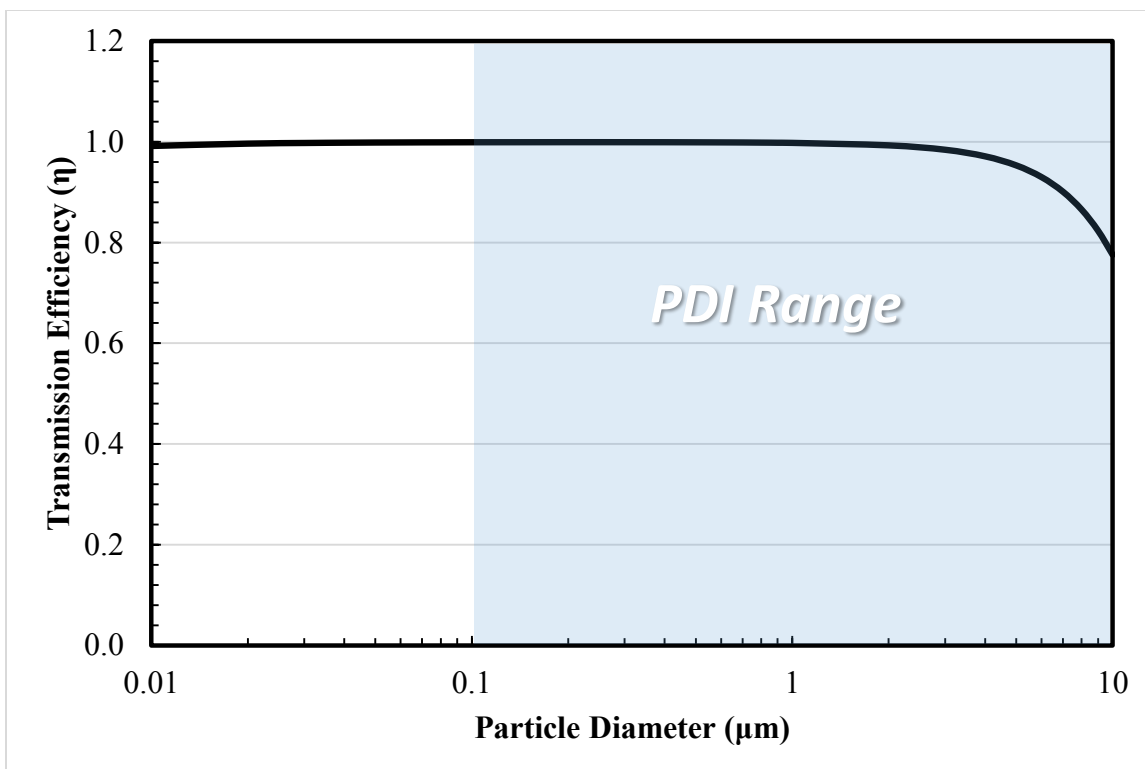


Figure 6.38: Calculated transmission efficiency (see Section 2.5 for equations) for the PDI/FTIR simultaneous sampling system assuming a flow rate of 125 SLPM. The aerosol density was 1,000 kg/m³ and the gas properties were calculated at 40 °C and 1 psig.

6.4.2 Results

The data presented in this section provides direct comparisons between the FTIR and PDI using only one adjustable parameter: the aerosol amine concentration. The aerosol amine concentration was assumed to be constant across a day of sampling. Calculations and the algorithms used to manipulate the raw data are described in Chapter 4 and Appendix A.

Figure 6.39–Figure 6.45 display the FTIR/PDI comparison data collected from December 5–12, 2015. The optimized aerosol MEA content is listed in each figure caption and the overall measured ranges and fitting error for each sampling day is tabulated below (Table 6.12).

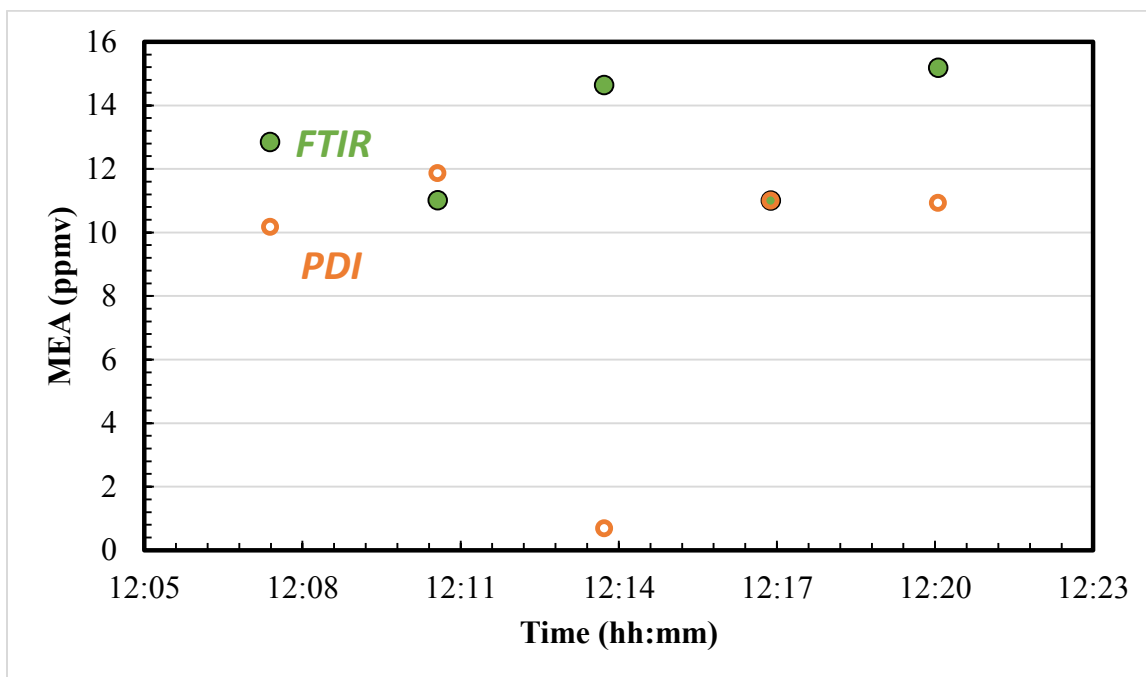


Figure 6.39: PDI/FTIR comparison data for December 5, 2015 measured at the water wash outlet of the SSTU at NCCC. $C_{MEA} = 0.084$ m MEA

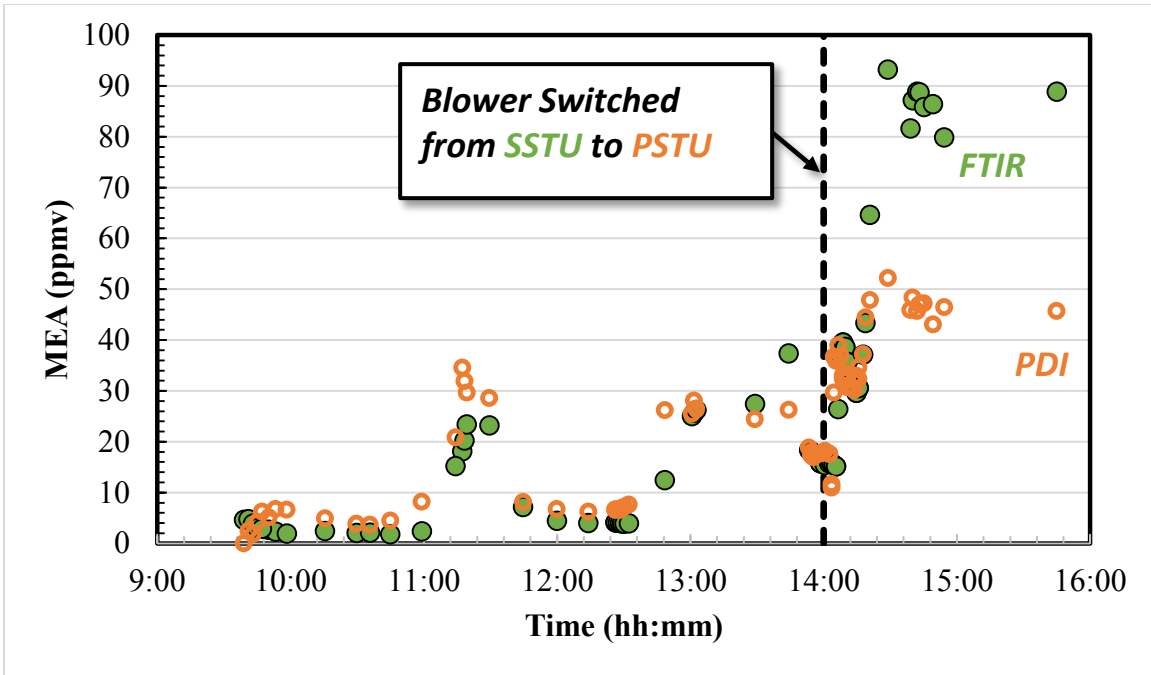


Figure 6.40: **PDI/FTIR** comparison data for December 7, 2015 measured at the water wash outlet of the SSTU at NCCC. $C_{MEA} = 0.023$ m MEA

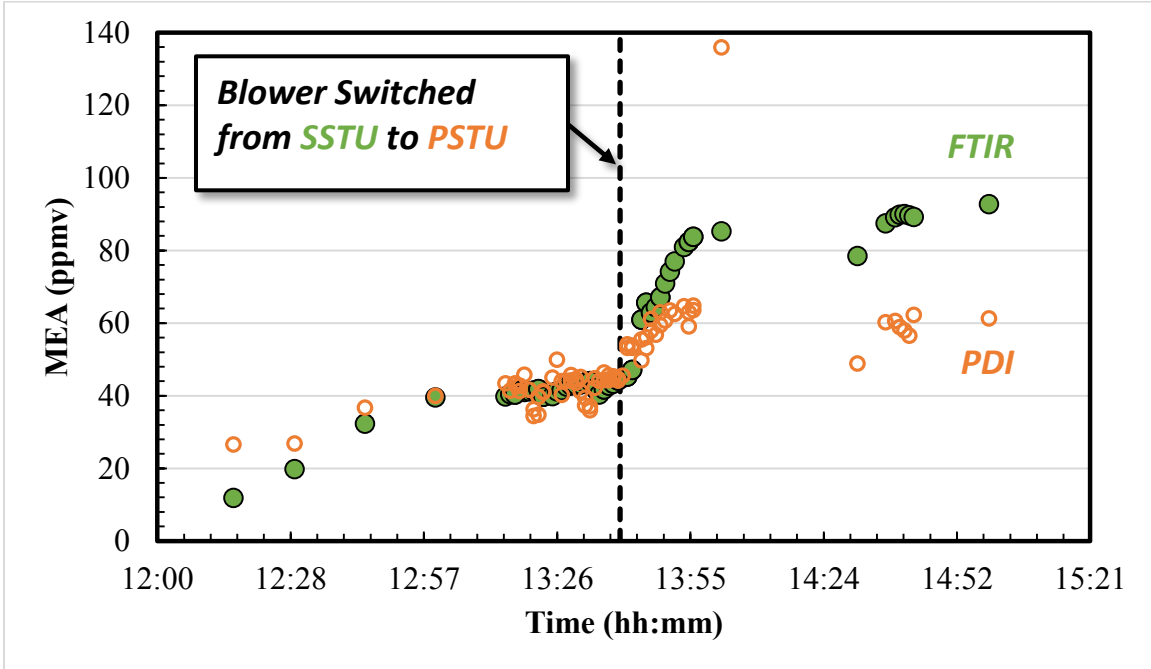


Figure 6.41: **PDI/FTIR** comparison data for December 8, 2015 measured at the water wash outlet of the SSTU at NCCC. $C_{MEA} = 0.035$ m MEA

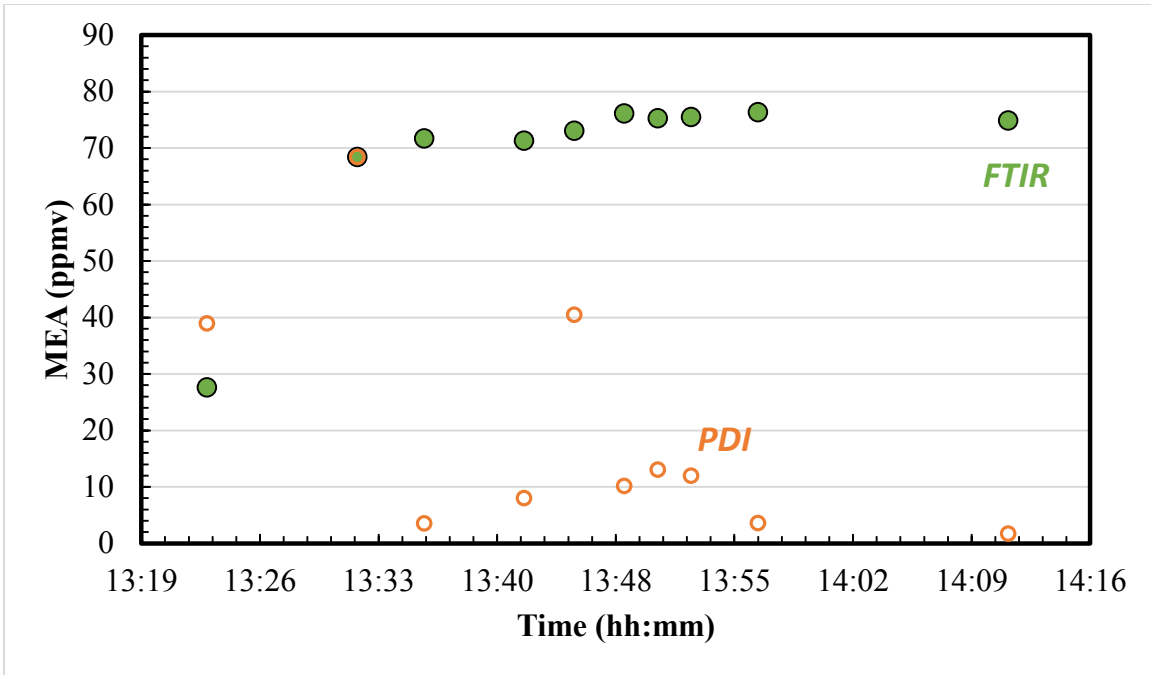


Figure 6.42: **PDI/FTIR** comparison data for December 9, 2015 measured at the water wash outlet of the SSTU at NCCC. $C_{MEA} = 0.036$ m MEA

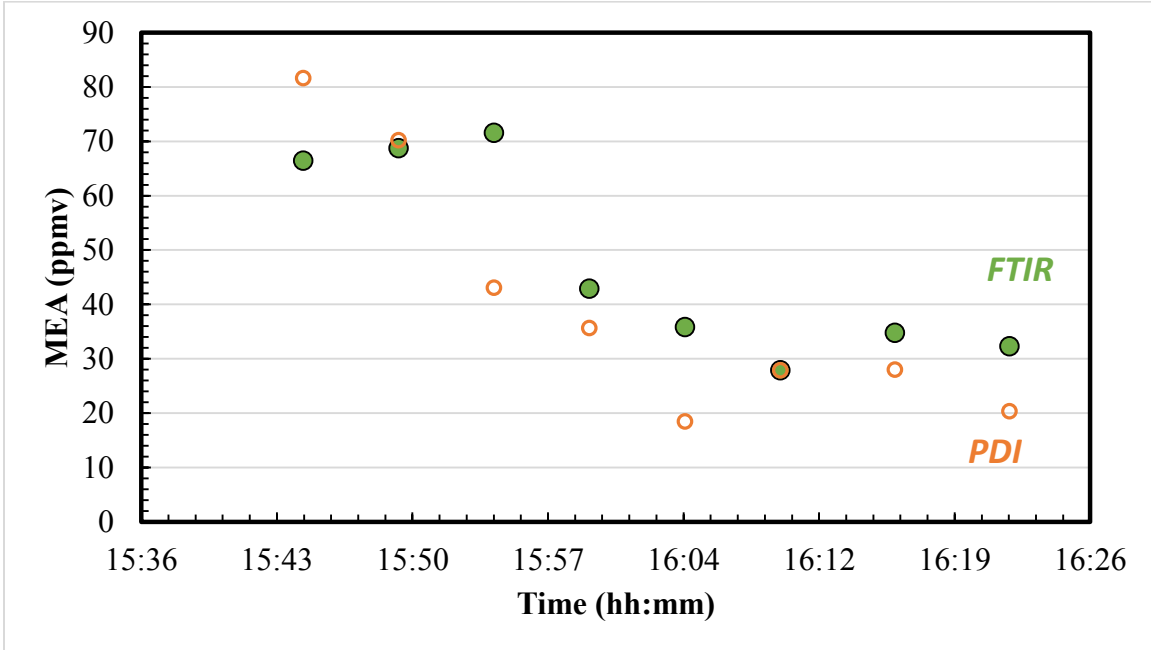


Figure 6.43: **PDI/FTIR** comparison data for December 10, 2015 measured at the water wash outlet of the SSTU at NCCC. $C_{MEA} = 0.260$ m MEA

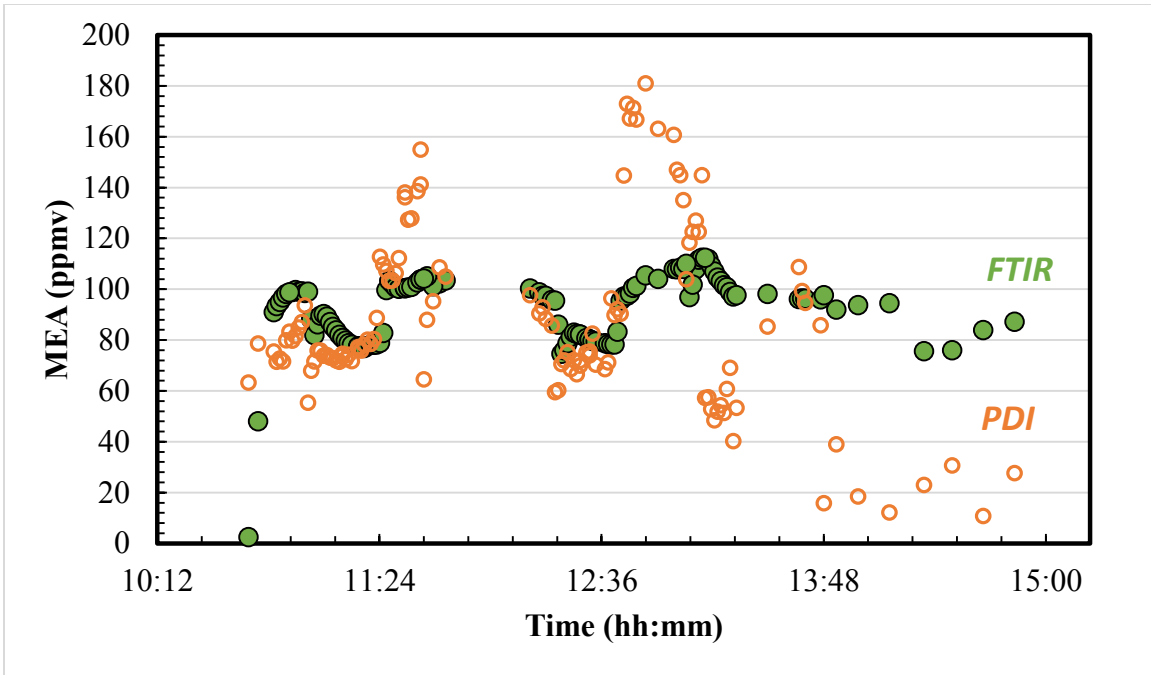


Figure 6.44: PDI/FTIR comparison data for December 11, 2015 measured at the water wash outlet of the SSTU at NCCC. $C_{MEA} = 0.081$ m MEA

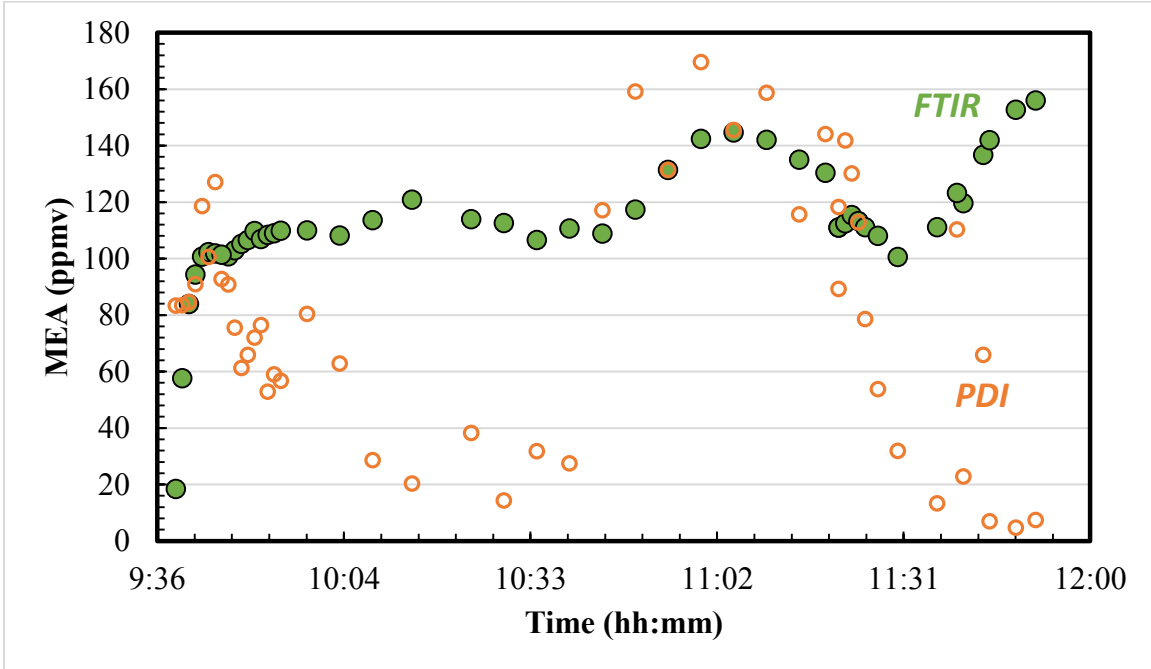


Figure 6.45: PDI/FTIR comparison data for December 12, 2015 measured at the water wash outlet of the SSTU at NCCC. $C_{MEA} = 0.120$ m MEA

Table 6.12: PSD statistics for each sampling day at the SSTU at NCCC. PDI/FTIR error is the average absolute relative error.

Day	Average Diam. Range [μm]	Density Range [part./ cm^3]	Calc. Aerosol MEA (C_{MEA}) [mol/kg]	PDI/FTIR Error [%]
12/05/2015	1.21–2.25	8.78×10^4 – 5.50×10^5	8.4×10^{-2}	30.39
12/07/2015	2.13–2.76	6.18×10^5 – 4.66×10^6	2.3×10^{-2}	49.09
12/08/2015	2.16–2.59	2.82×10^6 – 9.37×10^6	3.5×10^{-2}	14.81
12/09/2015	3.48–4.52	3.33×10^4 – 2.54×10^6	3.6×10^{-2}	71.57
12/10/2015	3.90–4.34	5.83×10^4 – 3.17×10^5	2.6×10^{-1}	23.32
12/11/2015	2.46–4.12	1.22×10^5 – 4.67×10^6	8.1×10^{-2}	44.91
12/12/2015	2.73–5.83	1.36×10^4 – 2.58×10^6	1.2×10^{-1}	44.53

The calculated aerosol amine concentration is much less than the absorber solvent. This is partially expected given that the aerosol passes through a water wash column where condensation will take place. The average particle diameter is significantly beyond one micron and the particle density is on the order of 10^4 – 10^6 part./ cm^3 . This finding is quite different than the work of Mertens and coworkers (2014) who measured mostly submicron aerosols at very high concentrations ($\sim 10^8$ part./ cm^3), but similar to that of Kolderup et al. (2012) where the reported average Sauter-mean diameter was 4.3 μm and the total particle density measured by ELPI was 1.32×10^6 part./ cm^3 .

This difference illustrates a few points: (1) upstream conditioning and downstream water wash columns greatly impact the size distribution and total density of the aerosol phase, and (2) the sampling location relative to the vent stack impacts the PSD. In the work by Mertens et al., nucleation occurs in a quench column just before the absorber and no water wash column was employed after the absorber. Therefore coagulation is still occurring in the absorber due to the high particle density. In the study by Kolderup et al., which used real coal-fired flue gas, nucleation took place upstream in

an FGD scrubber and was run through ductwork before going into a second SO₂ scrubber upstream of the absorber column. The combination of multiple gas saturation changes and significantly more residence time should allow for coagulation to reach completion and the particle concentration should be significantly lower; the aerosol at the absorber inlet is likely large as well. Additionally, the aerosol field out of the absorber goes through an additional change in saturation in the water wash, which causes additional growth by condensation. The combinations of these process variances result in order of magnitude differences in PSD statistics.

By extension, the aerosol leaving the absorber or water wash is not in equilibrium with the gas and will continue to grow as it passes through ductwork and cools. Therefore, the PSD will be affected by the length of piping in between the process and the sampling point. For measurements taken at pilot plants, that distance and the relevant flow rate should be reported.

Measurement and process variations in the aerosols can also be quantified by calculating the MEA content in the aerosol required to perfectly fit the FTIR data. **Figure 6.46–Figure 6.52** show the calculated MEA concentration in the aerosol for each measurement point required to match the FTIR data. Even though there is significant scattering in the calculated values, the aerosol concentration is always much lower than the absorber solvent.

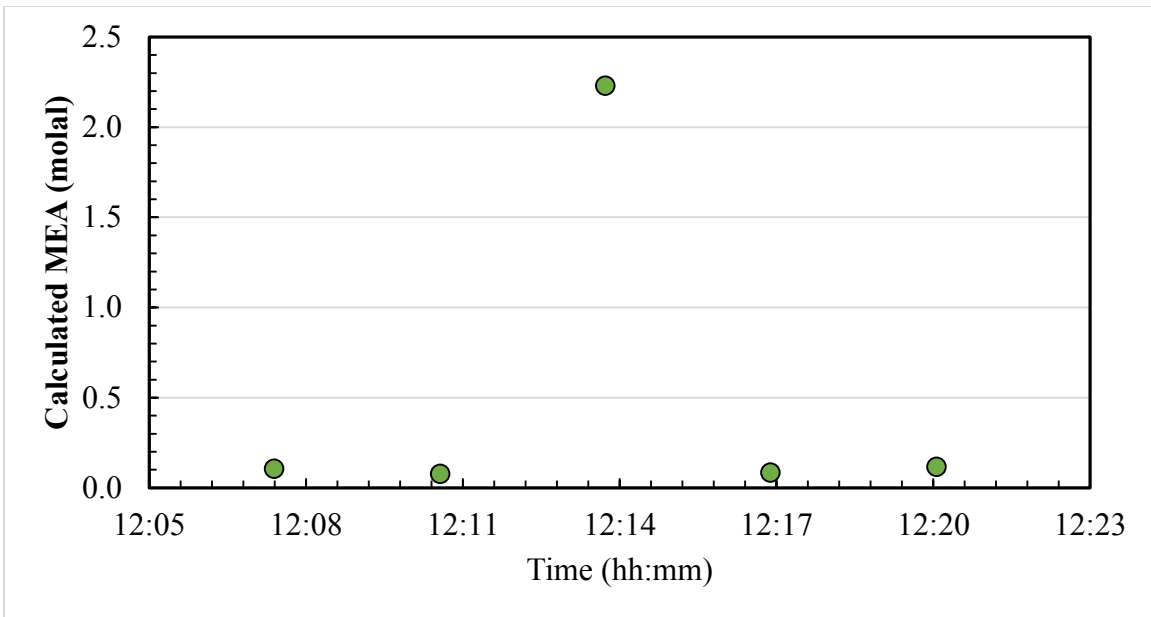


Figure 6.46: Calculated MEA concentration in the aerosol required to perfectly fit the FTIR data for December 5, 2015 measured at the water wash outlet of the SSTU at NCCC.

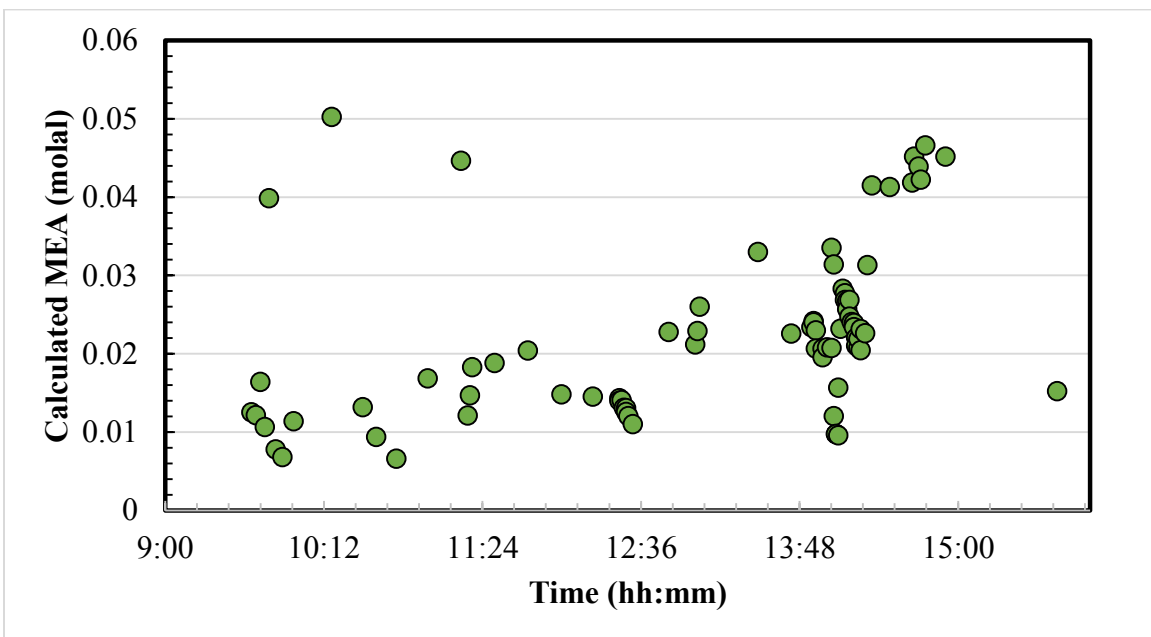


Figure 6.47: Calculated MEA concentration in the aerosol required to perfectly fit the FTIR data for December 7, 2015 measured at the water wash outlet of the SSTU at NCCC.

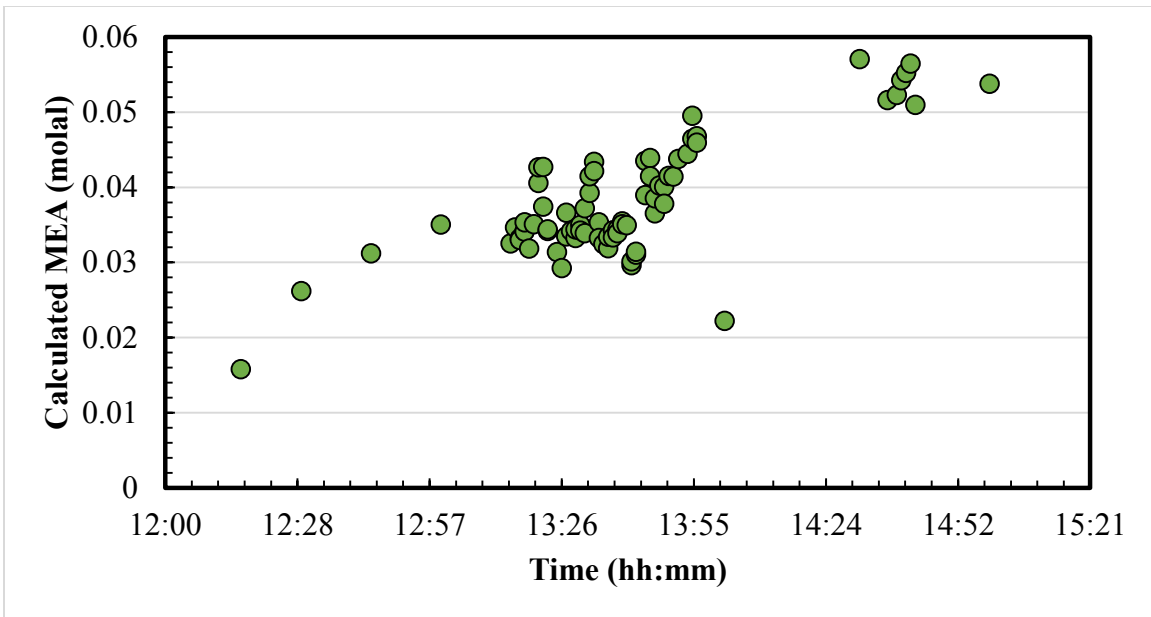


Figure 6.48: Calculated MEA concentration in the aerosol required to perfectly fit the FTIR data for December 8, 2015 measured at the water wash outlet of the SSTU at NCCC.

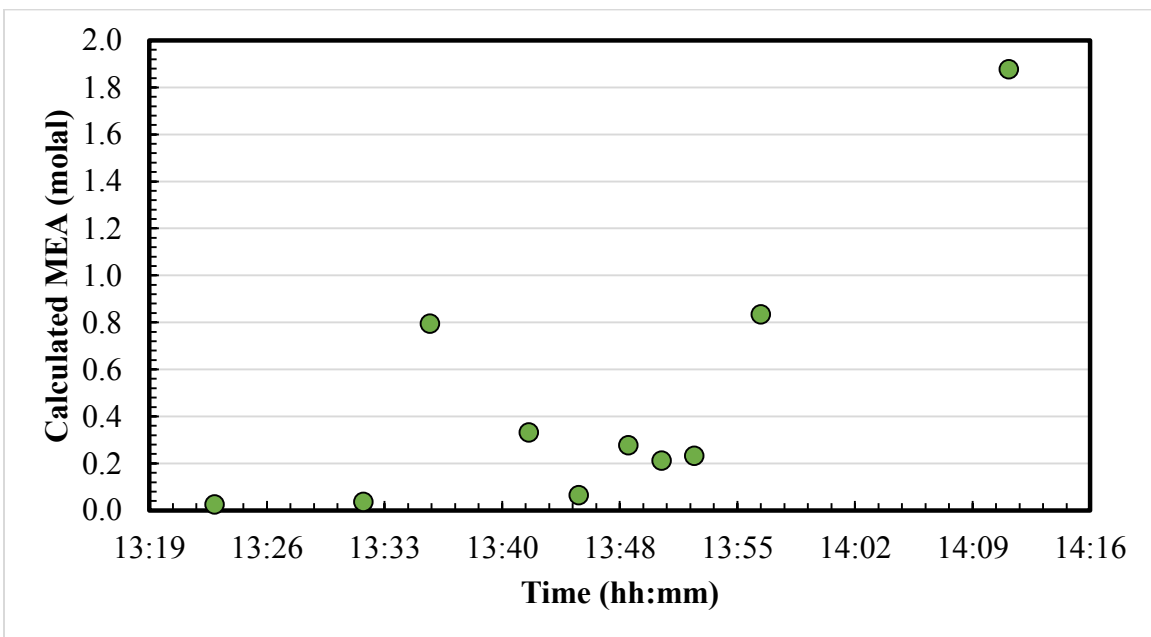


Figure 6.49: Calculated MEA concentration in the aerosol required to perfectly fit the FTIR data for December 9, 2015 measured at the water wash outlet of the SSTU at NCCC.

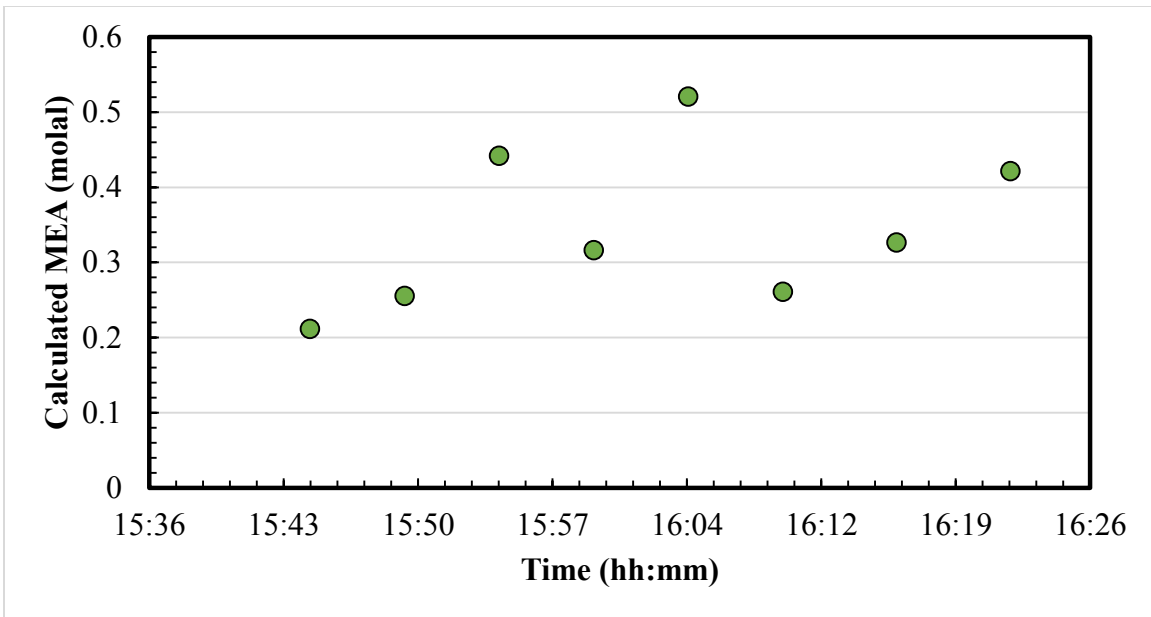


Figure 6.50: Calculated MEA concentration in the aerosol required to perfectly fit the FTIR data for December 10, 2015 measured at the water wash outlet of the SSTU at NCCC.

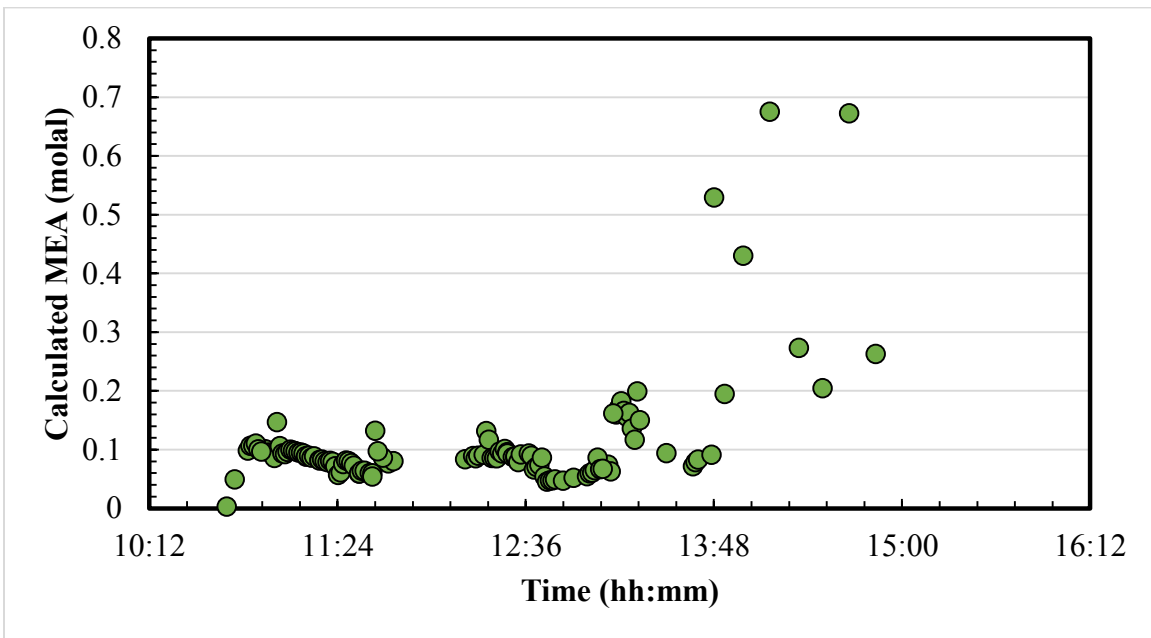


Figure 6.51: Calculated MEA concentration in the aerosol required to perfectly fit the FTIR data for December 11, 2015 measured at the water wash outlet of the SSTU at NCCC.

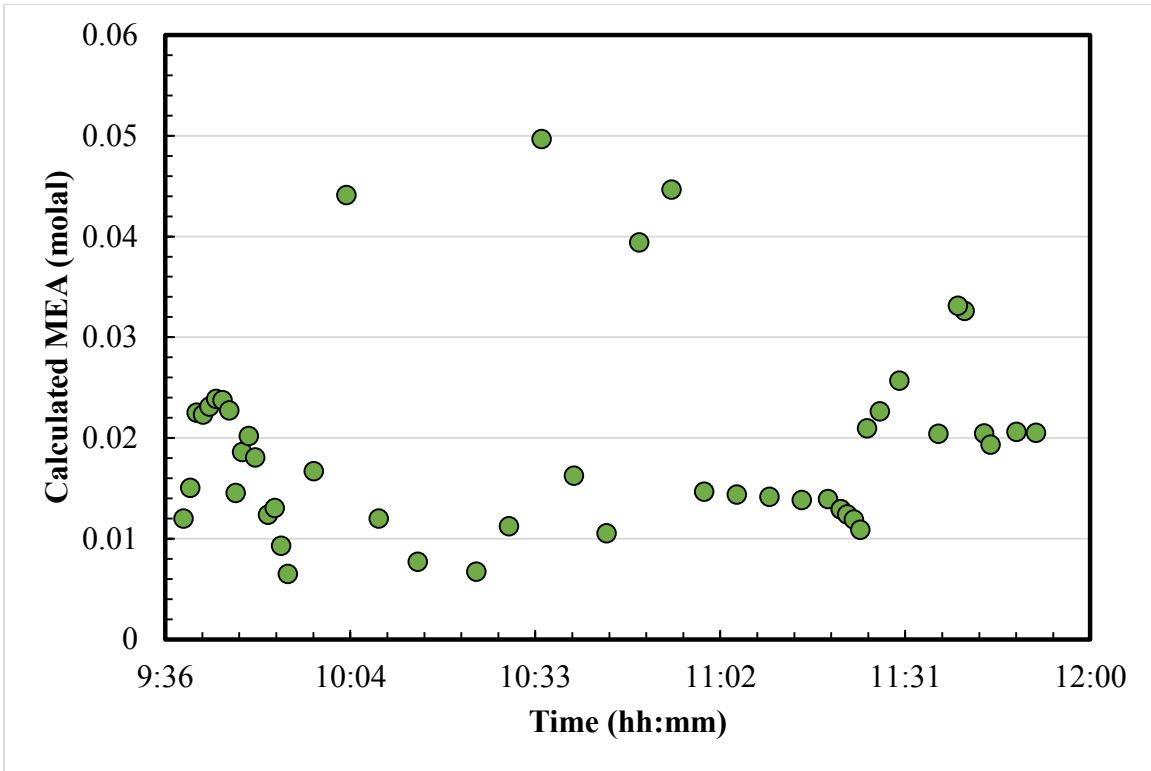


Figure 6.52: Calculated MEA concentration in the aerosol required to perfectly fit the FTIR data for December 12, 2015 measured at the water wash outlet of the SSTU at NCCC.

A noticeable change in the concentration fit occurs when the blower position is swapped from upstream the intermediate blower (SSTU) to the upstream blower (PSTU) as seen on the 7th and 8th. The concentration fit is influenced by the total particle density and the PSD, approximated here by the count average diameter.

The count-average diameter changes from about 2.3 μm to 2.6 μm , or a 13% increase, after switching the blowers on both days; however, the particle density does not behave in the same way going from the 7th to the 8th. **Figure 6.53** indicates that the switch from the SSTU to the PSTU blower allows larger, and more particles into the system, possibly indicating that the location of the intermediate blower (SSTU) provides some measure of aerosol collection. If the aerosol field entering the absorber is

submicron, they likely pass through the first blower (PSTU) and grow inside the absorber and water wash. When the PSTU blower is bypassed, the aerosol field has traveled through the supersaturated environment of the absorber prior to entering the SSTU blower. The turbulence of the blower would provide some degree of capture efficiency. However, the change in the particle concentration is not nearly as apparent during sampling on the 8th. The particle concentration changes from 3.5×10^6 part./cm³ to 4.4×10^6 part./cm³, or a 26% increase, during the blower switch on the 7th. The concentration on the 8th appears to slowly increase approaching the blower switch, but no step-wise increase occurs after the change.

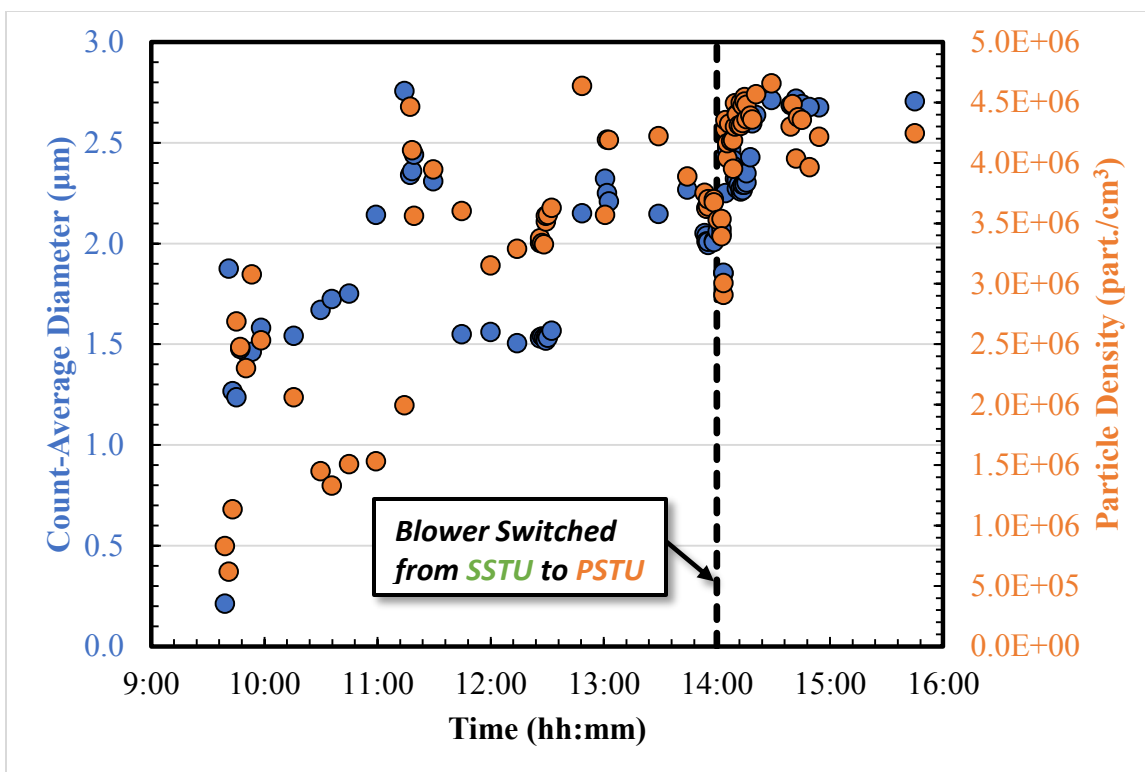


Figure 6.53: Count-average diameter and total particle density on December 7, 2015. Both the diameter and density increase after switching from the PSTU to the SSTU blower.

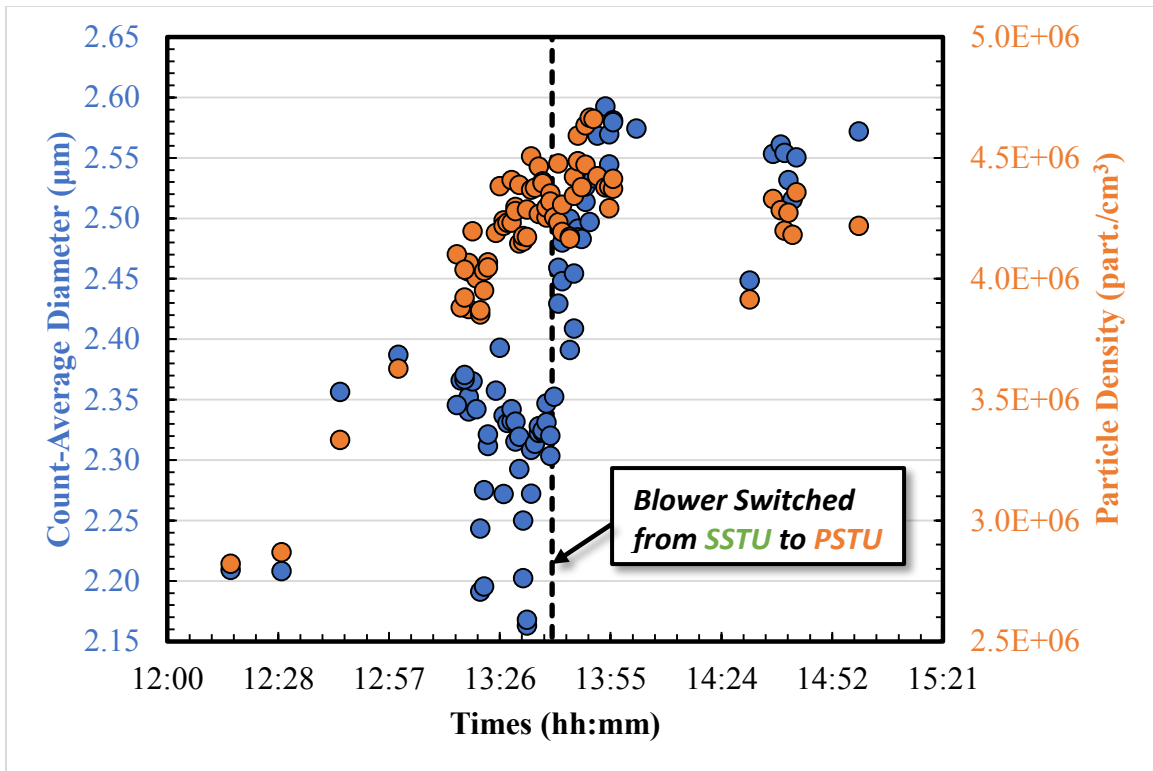


Figure 6.54: Count-average diameter and total particle density on December 8, 2015. The diameter increase after switching from the PSTU to the SSTU blower; however, the density is not affected by the blower change.

Another noticeable feature is the concentration mismatch on the 11th through the 12th. During those days, NCCC was testing a proprietary aerosol removal device in the periods indicated by the dashed black lines in **Figure 6.54–Figure 6.55**. The inverse relationship between the average particle diameter and the total particle density is particularly evident during operation and bypassing of the aerosol suppression device. This finding is consistent with a mass balance argument that the total condensable material is relatively constant, and at higher particle densities, it is spread amongst more condensation sites resulting in more, smaller particles. As the density decreases, the number of condensation sites reduces, and accumulation per condensation site increases, resulting in fewer, larger particles.

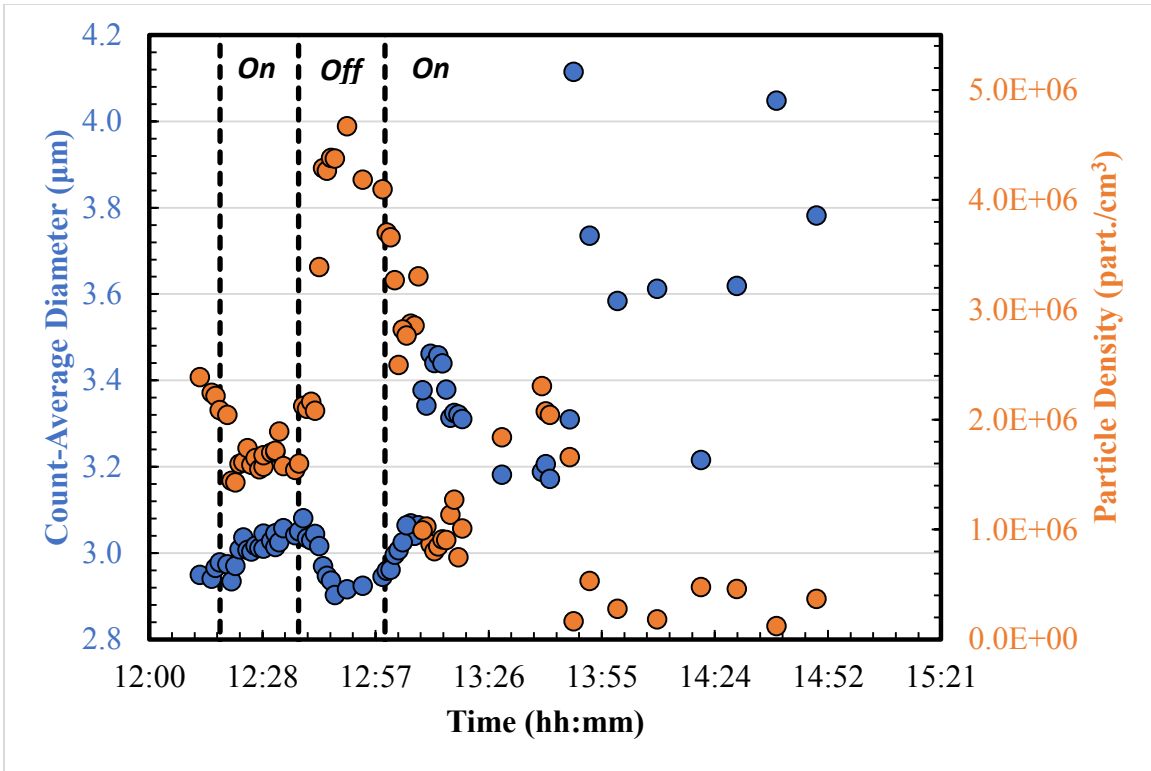


Figure 6.55: Count-average diameter and total particle density on December 11, 2015 at NCCC. The aerosol removal device is in operation as indicated by the dashed black lines.

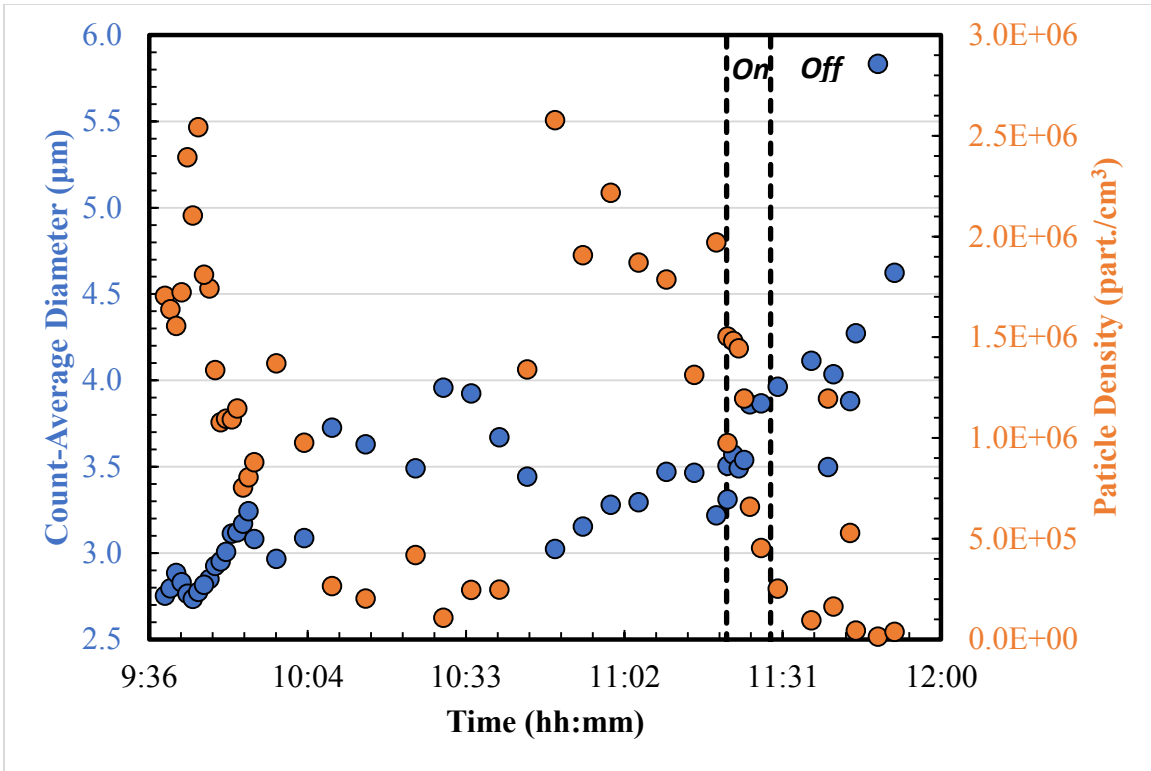


Figure 6.56: Count-average diameter and total particle density on December 12, 2015 at NCCC. The aerosol removal device is in operation as indicated by the dashed black lines.

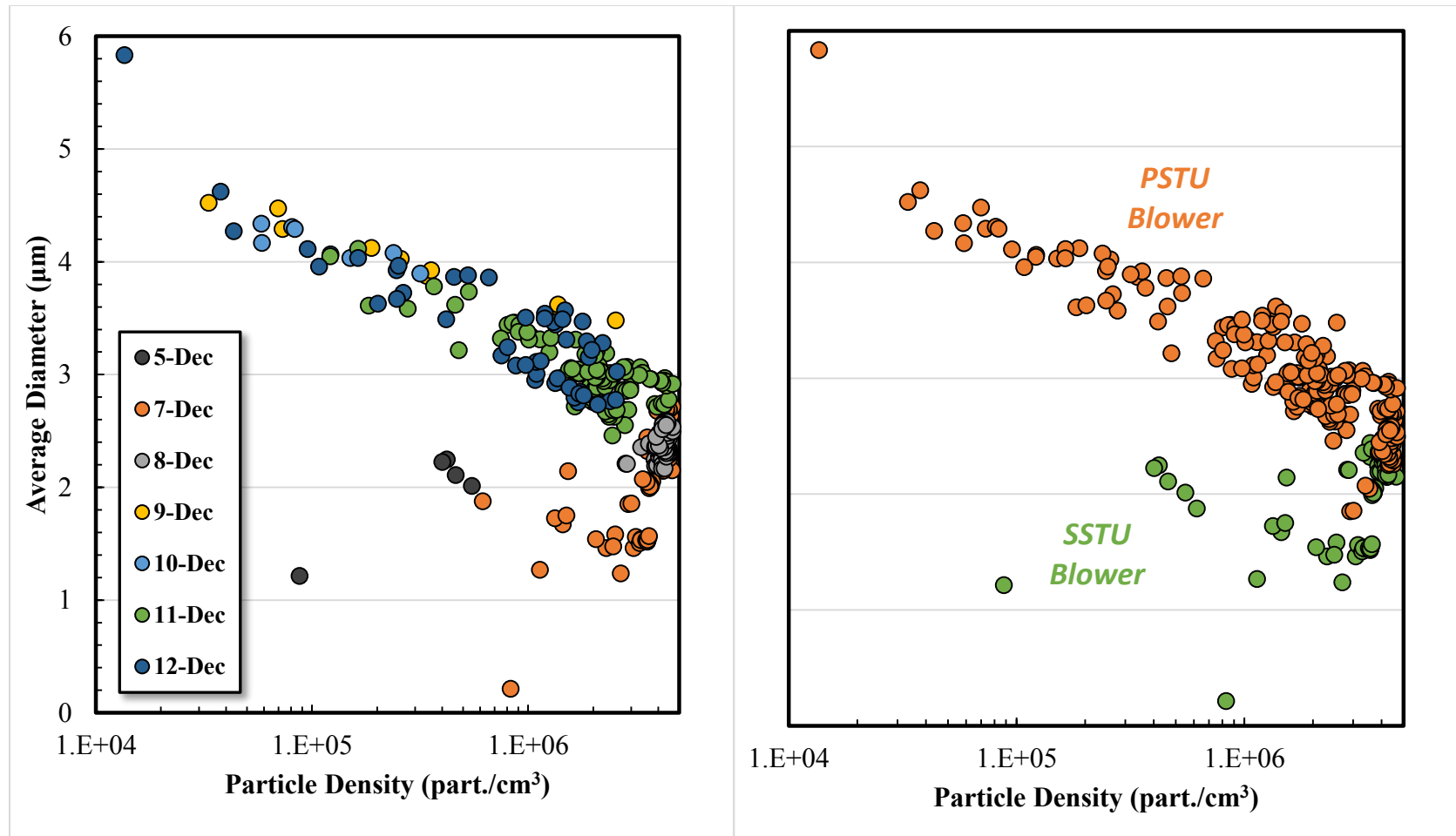


Figure 6.57: The average diameter and particle density relationship depends on sampling day (left) and the location of the blower (right). The **PSTU** blower shows an inverse relationship. The **SSTU** blower shows a positive correlation between the average diameter and the total particle density.

6.4.2.1 Sampling Error

The enclosed analysis cell constructed for the custom-built PDI introduces unique errors during sample analysis. Specifically, condensation or entrained liquid on the windows can lead to signal attenuation. For constant signal gain, attenuation of the signal increases the minimum detectable particle diameter since the incident light is reduced prior to the measurement point. Since condensate accumulation is a dynamic process, measurement error will gradually increase, leading to two effects: (1) the average particle diameter will increase, and (2) the total particle density will decrease in time because smaller particles will become invisible in the measurement noise. **Figure 6.58** shows a pictorial representation of the effect of condensate on the detectable probe volume with reduction of the Gaussian beam intensity.

To quantify the condensation error, the average diameter to total particle density ratio was plotted against the absolute sampling time and normalized to the maximum ratio by day (**Figure 6.59**). The normalization scheme should increase towards unity over the total sampling period.

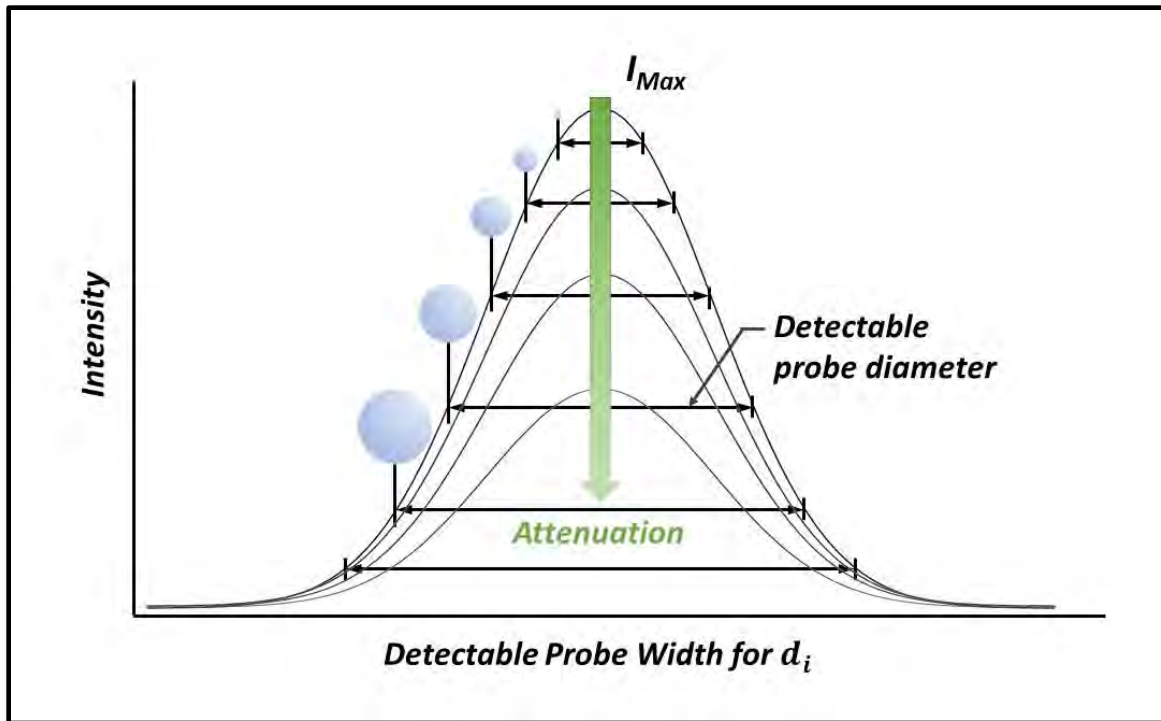


Figure 6.58: As window attenuation increases due to condensation, the maximum intensity of the initial laser beams decreases. As a result, the minimum detectable particle diameter (and the probe volume) as well as the total particle density decreases.

Some evidence of this error exists, particularly on the 10th through the 12th. The sampling logs recorded that the purge/vacuum system was slowly losing suction across the 10th to the 12th, so the condensation issue is expected to be more pronounced on those days. However, during the first few days of sampling, the average diameter to total density ratio appears independent of sampling time. The trend in the beginning section of the 8th may be due to condensate accumulation at the sampling valve blowing through at the initiation of sampling. Over time, the condensate got flushed away by the purge/vacuum system.

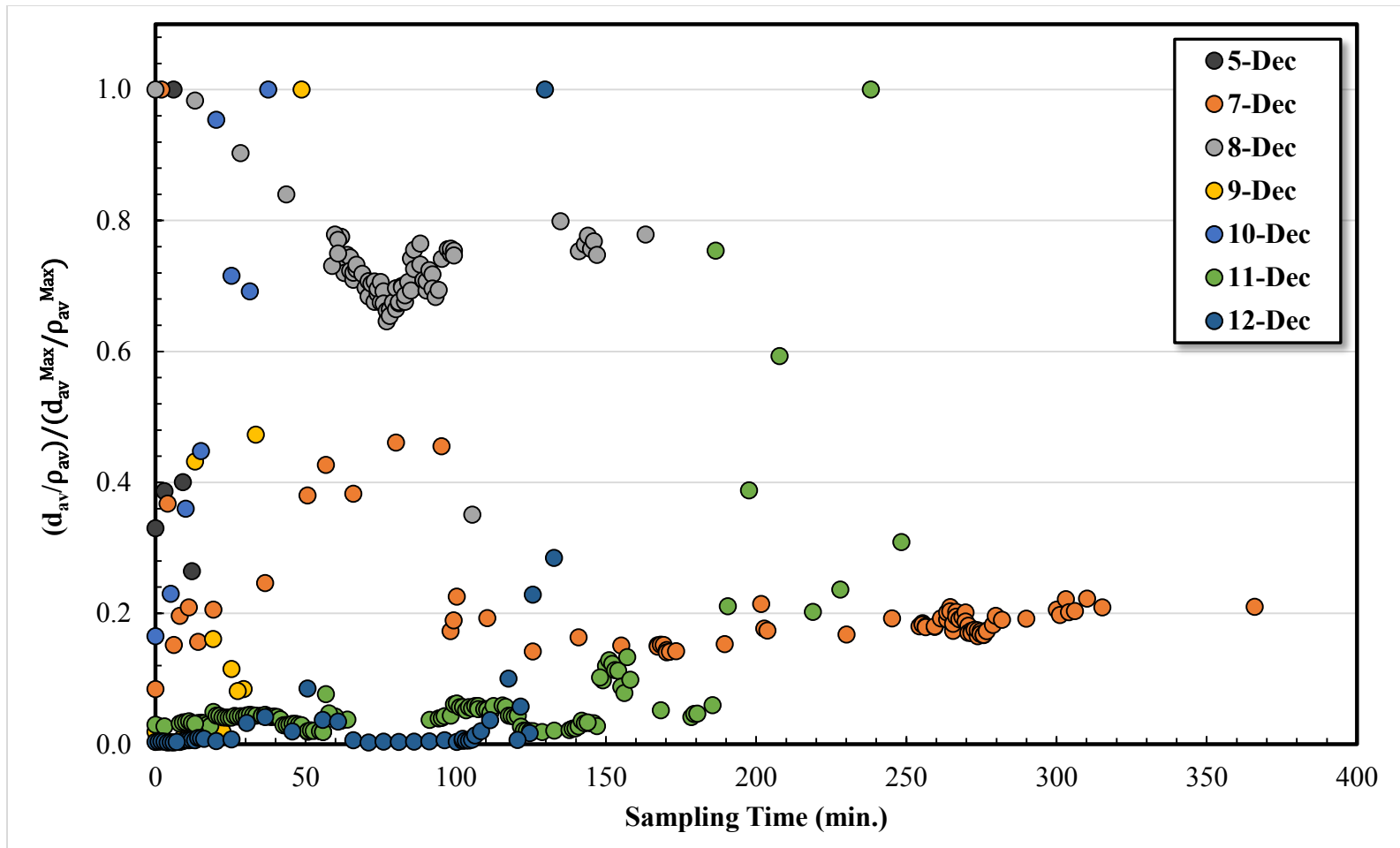


Figure 6.59: The normalized average diameter to total particle density ratio plotted against the absolute sampling time. If condensation attenuated the signals from the smaller droplets and was systematic in time, the curves would trend upwards. No such correlation is apparent.

6.5 CONCLUSIONS

The work presented in this chapter represents significant progress in development of hardware, experimental procedure, and data analysis in the effort to meet the stated goals of this work. The major conclusions are enumerated below and more detailed descriptions close out the chapter:

- PDI measured total particle densities up to 1.7×10^7 part./cm³ between 0.1 to 12 μm at pilot scale CO₂ absorbers
- PZ will form aerosols at pilot plant conditions
- SO₂ in the absorber feed gas will nucleate to make aerosol and increase amine emissions
- Aerosols grow by condensing H₂O both in, and after the water wash. Sample locations should be immediately after absorber or water wash

6.5.1 PDI and FTIR Measurement

In this chapter, aerosol and total phase measurement was performed at multiple pilot plants using custom-built equipment. PDI as an analytical tool for analyzing high density aerosols in fully saturated gas streams was developed concurrent with pilot plant activities. The optical path length and sampling configuration were modified leading to successful measurements up to 10^7 part./cm³ between 0.1–12 μm .

Condensation and liquid sheeting on the PDI cell window seem to cause a systematic error in the correlation between the average particle diameter and the total particle density. As liquid accumulates, the beam intensity entering the PDI is attenuated which obscures small particles. The loss of small particles reduces the total particle density and shifts the average particle diameter to larger sizes. A better purge and

vacuum system should be designed to more effectively block or remove condensate away from the analysis windows.

A multipoint, fast-switching FTIR system was built and implemented at the PRC pilot plant and comparison was made with manual sampling and pure gas calibration. FTIR and manual sampling measurements closely match H₂O vapor pressure predictions made by Raoult's Law at the absorber outlet. Inlet H₂O content does not match between methods; the manual sampling probe is above the absorber sump and the gas sampled at that location is expected to be closer to saturation than the inlet FTIR sample probe which is sampling upstream of the absorber inlet. CO₂ measurements were validated against calibration cylinders and SO₂ was confirmed against a calibrated rotameter.

6.5.2 Aerosol Characteristics

Aerosols were characterized at two pilot plants operating with two different amine solvents (MEA and PZ), and two different source gases (coal-fired flue gas and synthetic flue gas with SO₂/H₂SO₄ injection). At both locations, the aerosol field was very dense, on the order of 10⁵–10⁷ part./cm³ with average particle diameters between 1–6 μm. Those findings are consistent with the pilot plant work of Kolderup and co-authors (2012) but inconsistent with the findings of Mertens et. al (2014).

The bench scale testing done by Mertens measured aerosol densities close to 10⁹ part./cm³ and the PSD resided mostly under one micron even after passing through the absorber column. That result is similar to the work presented in Chapter 5 of this dissertation, though the particle density in those tests were several orders of magnitude smaller as the LVI did not function properly. The higher densities and smaller particle sizes are a result of the absence of pretreatment columns and significantly longer residence times found in pilot scale plants. At the bench scale, nucleation is occurring

just upstream of the absorber so the particle density is very high and nucleation/coagulation/condensation are occurring simultaneously. Whereas in pilot and commercial scale units, nucleation takes place in the FGD scrubber, and the gas passes through several other unit operations in which the saturation of the gas changes multiple times and travels through many feet of ductwork. The additional residence time allows for coagulation to nearly reach completion and condensation to become the dominant aerosol dynamic.

The average particle diameter and the total particle density were found to be inversely related in the pilot plant measurements. This finding is counter to that presented in Chapter 5. The inverse relationship may be due to the mass balance of condensables and the quantity of nuclei; more nuclei means more condensable sites and therefore the amount of available condensate is spread amongst more condensable surfaces. The result is smaller average particle diameters. The converse behavior is larger particle diameters at lower particle densities. This assumes that aerosols are free to grow in the ductwork without collection, which would cause the opposite behavior. In the case of the bench scale work presented in Chapter 5, the direct correlation between the diameter and density is believed to be caused by the limit of detection of the PDI, especially when a significant portion of the aerosol field is contained in the submicron region and the PSD is bimodal, lognormally distributed.

At the PRC pilot plant, the third generation PDI measured a bimodal, lognormal distribution during H₂SO₄ injection. The Fine Mode parameters were: $\sigma_G = 1.60 \mu\text{m}$, $d_G = 0.21 \mu\text{m}$, $7.0 \times 10^5 \text{ part./cm}^3$. The Coarse Mode parameters were: $\sigma_G = 1.25 \mu\text{m}$, $d_G = 0.86 \mu\text{m}$, $2.9 \times 10^5 \text{ part./cm}^3$. It was confirmed that the PDI measurements taken during the November, 2013 campaign missed a significant distribution mode in the submicron region, but that the LVI was not operating properly and the total particle density was very

low in the earlier campaign. The bimodal distribution was also found during bench scale testing in Chapter 5.

Compared to the PRC campaign, the PSDs taken during NCCC testing in December, 2015 were mostly monomodal, lognormal distributions. However, the average particle size was much larger (on the order of several microns) even though the particle density closely matched that found in the testing at PRC.

6.5.3 PDI/FTIR Fitting

The PDI integration algorithm outlined in Chapter 4 was augmented to post-process FTIR and PDI data taken during pilot plant sampling. Since the operating conditions and inlet gas changes over time and even throughout the day, the aerosol amine content fitting parameter was optimized over a single, 24 hour sampling period.

Using the data set collected during sampling at NCCC during December, 2015, the absolute average relative error between the FTIR concentration reading and the integrated PSD with an optimized aerosol amine (MEA) concentration was 41%. Most of the fitting error is a result of large process changes during a sampling period.

Changing the location of the blower from an intermediate location (between the absorber and wash tower) to upstream of the absorber caused a 13% increase in the average diameter (2.3 to 2.6 μm). A 13% increase in diameter should cause a 44% increase in the outlet amine emission assuming the aerosol amine concentration remains constant. However, the re-optimized concentration after the process change was found to increase by 23.3% and 15.4% after the blower change on the 7th and 8th, respectively.

The effect on the total particle density was not as apparent. The total particle density appeared to increase from 3.5×10^6 part./cm³ to 4.4×10^6 part./cm³, or a 26% increase on December 7; however, the particle concentration does not appear to go

through a distinct step change on December 8, even though the blower change was identical.

The increase in diameter and density do not completely account for the change in the total phase analysis data from the FTIR. The blower change causes a change in the PSD as well as the aerosol concentration. The upstream blower (PSTU) handles the inlet aerosol, which are predominantly submicron. Therefore, collection in the PSTU blower is assumed to be quite small and any heat added to the gas stream would evaporate a small amount of water from the aerosol. The intermediate blower (SSTU) handles aerosol that has passed through the absorber where condensation and growth has taken place. The larger inlet aerosols are expected to be collected with non-negligible efficiency in the impeller and turbulence of the blower. The findings are consistent with this hypothesis outside of the particle density response on the 8th.

The calculated aerosol amine content was much lower than the solvent. The difference is likely caused by two things: (1) the aerosol passing through a water wash tower and condensing H₂O, and (2) the proximity of the sampling location to that of the process. Since aerosol continue to condense material and become collected in the outlet ductwork, the measured PSD is dependent on the sampling location. It is expected that the average diameter would increase and the total particle density would decrease as the sampling point is moved further downstream of the absorber/wash column.

Finally, the PDI confirmed the operation of a proprietary aerosol abatement technology tested at NCCC at the end of 2015. The particle density decreased as the technology was in operation.

6.5.4 SO₂/H₂SO₄ Nucleation

Two nuclei sources were tested during the campaigns at PRC: pure SO₂ and vaporized H₂SO₄. It was theorized that SO₂ would either homogeneously nucleate with amine to create an aqueous aerosol or that condensation of the amine would occur following primary nucleation of NH₃/SO₂ as outlined in literature. The former is more likely given that amine and NH₃ partial pressures are similar in the gas phase and that the large difference in volatility between amines and NH₃ would create a significantly larger driving force for homogeneous nucleation, assuming similar reaction free energies with SO₂.

PZ was found to increase with injection of SO₂. A mass balance was performed on SO₂ absorption using the known injection concentrations and time periods to determine the split between SO₂ absorbing into the absorber solvent and that found in the aerosol phase. The total solvent inventory was estimated using a FeSO₄ tracer and the absorbed SO₂ was quantified as SO₄²⁻ using IC. 34.9% of the incoming SO₂ is absorbed in the solvent.

Using that absorption fraction, the ratio of outlet PZ to inlet SO₂ was calculated during each injection period. The average PZ/SO₂ ratio was 1.53 (on a mole basis) and ranged from 0.03–3.99. If nucleation occurred following the mechanisms outline in NH₃ scrubbing literature, the ratio would be between 1 and 2, since the proposed reaction mechanism is composed of two solubility product equations forming NH₄HSO₃(s) and (NH₄)₂SO₃. A combination of absorption and nucleation/condensation occur simultaneously with the absorber solvent and SO₂.

Because SO₂ partitions into two phases, removal of SO₂ through thermal reclaiming is likely not an option since emission rates due to aerosols will be far too high. An SO₂ polisher is a critical part of aerosol abatement.

H₂SO₄ injection produces aerosols in PZ absorbers. The ratio of PZ/H₂SO₄ averaged 2.97 (on a mole basis) and ranged from 0.93–6.73. Since nucleation occurs far upstream of the absorber in the FGD scrubber, simple polishing units will be ineffective at removing the aerosol source. Aerosol removal devices, solvent selection, and growth and capture techniques are the recommended abatement strategies.

For both nucleation sources, the absorbed content of PZ is much lower than expected given the growth predictions detailed in Chapter 7. However, the aerosol density was very high (9.9×10^5 part./cm³) which would cause significant prediction error because the model does not include the aerosol phase in the total mass balance. Therefore the gas phase saturation is strongly impacted by the aerosol phase and the overall condensable mass is distributed over a larger amount of condensation sites, meaning less growth and a lower amine to H₂SO₄ ratio. In that case, the growth rate is limited by the mass transfer rate of amine out of the bulk solvent. Since the H₂O concentration in the gas phase is very high, the aerosol accumulates H₂O very quickly and transfer of amine and CO₂ is significantly slower, leading to smaller, more dilute aerosols. Similarly, the high concentration of SO₂ (25–85 ppmv) would create a very high density of condensation nuclei, thereby limiting the growth rate by depletion of condensable species.

6.5.5 Pilot Plant Observations

During aerosol injection testing, the outlet knockout filter plugged rapidly from accumulating liquid and solid material resulting in an increase in pressure drop across the filter element from one to ten inches of H₂O. The filter was rinsed using hot water and the gaskets were soaked and dried overnight.

When the air chiller temperature was increased, the pressure drop rose more slowly. It is possible that fog formation in the air chiller hydrates the filter element faster and decreases the available interstitial flow paths for the gas.

Also, the accumulation of solid precipitates indicates that solidified $\text{PZ}\cdot 6\text{H}_2\text{O}$ or the rich-end precipitate leads to filter plugging. Aerosols carrying PZ would be captured on the filter and the trapped liquid would reach saturation to CO_2 with the outlet gas. The result is a rich liquid that, in the case of PZ, would concentrate to the point of the solubility limit. The use of an aerosol collection device must include measures for cleaning or periodically removing collected liquid and solids. This also limits the practical solutions for aerosol collection for amines with solubility limitations.

6.6 ACKNOWLEDGEMENTS

The author would like to give special thanks to Matt Beaudry who collected PDI and FTIR data during the December, 2015 NCCC campaign. That data was critical to the development of this chapter.

Several other people contributed to the work in this chapter. Mark Nelson of Air Quality Analytical, Inc. designed and built the original LVI and provided consulting during the location and installation of the FTIR stinger probes at the PRC pilot plant. William Bachalo and Chad Sipperley of Artium Technologies, Inc. performed the first PDI test at NCCC and designed and constructed the custom-built PDI used throughout this work. Southern Research Institute (SRI) provided optical access windows and physical support was overseen and coordinated by Carl Landham during the first generation PDI testing at NCCC. Testing at PRC was overseen and operated in conjunction with the Separations Research Program at The University of Texas at Austin and by Dr. Eric Chen who leads design, fabrication, and operation of the pilot testing

program for the Rochelle Research group at PRC. AECOM performed manual sampling during the November, 2013 and March, 2015 campaigns at PRC. Paul Nielsen provided SO_4^{2-} analysis for the March, 2015 campaign at PRC. Justin Anthony of Southern Company Services, Inc. oversaw the December, 2015 sampling at NCCC.

Chapter 7: Aerosol Growth Modeling

Conventional water wash (WW) design has proven ineffective at eliminating volatile emissions in several pilot-scale carbon dioxide (CO₂) capture plants employing aqueous alkanolamine absorption/stripping. Condensation of species into aerosols suspended within the flue gas, not physical entrainment, has been identified as the main discharge pathway from amine scrubbers. Removing small particles (0.1-10 μm) by diffusion or impaction requires significant pressure drop, which can nearly double the blower work required by the absorber unit. If aerosols are to be removed, any additional pressure drop must be utilized effectively for mass transfer in the bulk CO₂ removal process to minimize additional incurred costs of emission reduction equipment. Alternatively, aerosols could be conditioned in a way to improve removal efficiency by altering the size distribution such that their capture becomes more energetically favorable, as detailed in the work by Heidenreich et al. (2000). Understanding the interconnectivity of bulk-phase processes and aerosol dynamics will lead to more cost-effective and environmentally conscious design of amine-based CO₂ capture units.

This chapter describes model development, parameter sensitivity, and concept analysis of aqueous aerosols passing through CO₂ capture systems. A system of equations was developed to model heat and mass transfer to a single aerosol droplet in order to determine the effect of operating conditions and process configurations on the rate of aerosol growth or shrinkage by condensation and evaporation for the purpose of developing techniques or processes to suppress amine emissions in the aerosol phase leaving the CO₂ absorption system. The accumulated amine in the aerosol and an assumed particle size distribution allows for a direct estimate of the emissions rate out of an absorber.

The first sections of this chapter will detail the mathematical concepts and correlations used to calculate thermodynamic, physical, and kinetic properties used in the overall system of coupled differential equations. Ideally, an emission model would be capable of describing the many macro and molecular processes involved in aerosol formation, growth, and interaction with the bulk phases, the particle ensemble, and the geometry of the process equipment. Solving the complete set of transport equations for either a continuous or discretized particle distribution is a time-intensive task. In most models, simplifications are made to source or sink terms to make computations tractable without sacrificing accuracy. Simplifications or assumptions will be highlighted throughout. Since the model is a sequential calculation procedure involving steady state unit operation simulations in Aspen Plus® and aerosol growth calculations in MATLAB®, the linking procedure will be described in detail. Finally, case studies will be provided to develop theoretical concepts linking observed aerosol behavior and basic mass and energy transfer equations.

The main script and subroutine code can be found in Appendix E.

7.1 BASIC PHASE MODELING CONCEPTS

In the simulated application, aerosols are passing through a packed gas-liquid contactor undergoing exothermic reactive absorption. The droplets travel through variable gas-phase concentrations and temperature gradients which alter the particle ensemble. Conversely, as the aerosols condense or vaporize, their collective mass will add or subtract from the bulk vapor. The complete interacting system involves three phases: a bulk gas, bulk liquid, and discrete packets of fluid of variable size. A schematic of the three phase transfer system is shown below in **Figure 7.1**. Mass and energy fluxes occur to and from the bulk gas into the two liquid phases; however, the aerosol and bulk

liquid have no direct linkage. The bulk gas acts as a buffer. Additionally, interfacial area between the bulk gas and liquid is defined by the hydraulic equipment and physical parameters whereas the interfacial area of the aerosol is a function of the particle size distribution.

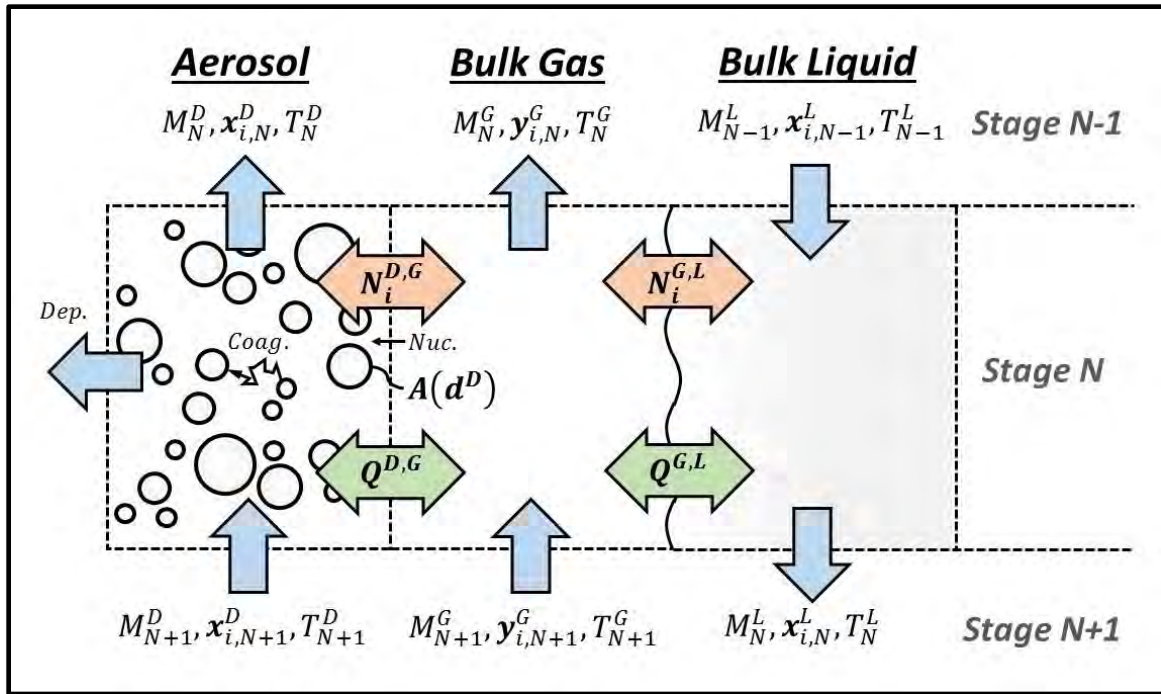


Figure 7.1: Three phase mass and heat transfer schematic for a single calculation stage.

This effort will start by simplifying the problem by neglecting the aggregate enthalpy and mass of the droplets (one-way coupling) relative to the bulk absorption process. Further, coagulation and deposition were neglected in the first stage of model development. The resulting formulation is a single homogeneous (well-mixed) droplet passing through a varying, quiescent gas. **Figure 7.2** shows the simplified three phase transfer system. Heat and mass transfer to and from the aerosol, but are not accounted for

in the bulk gas balances; the aerosol is assumed as a negligible perturbation of the steady state gas-liquid process.

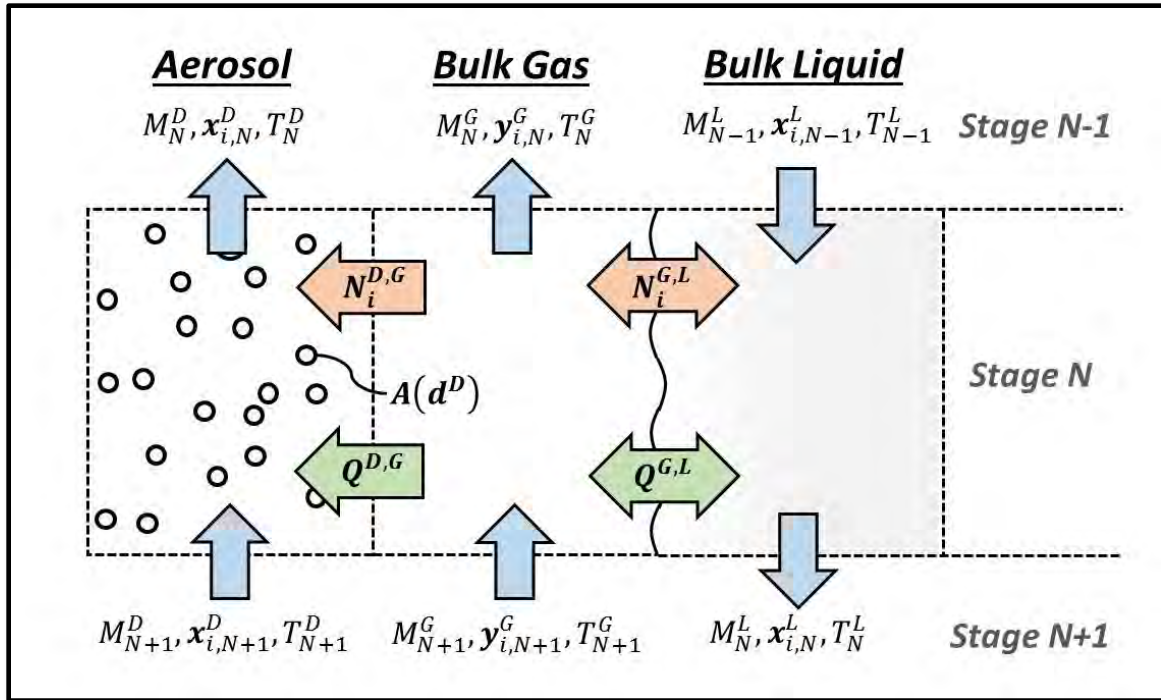


Figure 7.2: Simplified three phase mass and heat transfer schematic for a single calculation stage. The mass and energy balance between the aerosol and gas phase is neglected. The aerosol is assumed to contribute negligibly towards the total material and energy balance. A monomodal distribution is assumed and the calculation is performed for a single droplet.

The main reason for not coupling the aerosol and gas-phase balances was due to the choice to use Aspen Plus[®] for the absorber model and a *post hoc* MATLAB[®] model for the aerosol integration. MATLAB[®] was used for several reasons: (1) the number of discretization stages in Aspen Plus[®] would be computationally prohibitive for the aerosol calculations, (2) the Kelvin effect could not be readily included in Aspen Plus[®]

thermodynamic calculations, and (3) deposition and coagulation calculations could be added to later formulations of the model.

Aspen Plus[®] was chosen to perform the absorber calculation due to the large experience base in model development and implementation in the Rochelle research laboratory as well as the extensive experimental database used to regress thermodynamic and kinetic parameters. Additionally, coding the absorber and water wash unit operations into MATLAB[®] is not a trivial exercise. The result is that aerosol mass and heat integration, calculated by MATLAB[®] scripts, are performed using the gas-phase profiles generated in Aspen Plus[®].

The following sections provide a brief overview of the momentum, material, and heat transport differential equations, written in a Lagrangian reference frame, which represent the core of the aerosol model. Gas-phase compositions and physical properties at each calculation node from absorber/water wash simulations in Aspen Plus[®] are required to calculate mass and heat transfer coefficients and the force balance on an individual aerosol. Piece-wise spline interpolation is used to calculate properties between each absorber node for use at each aerosol calculation node. Packed height, column diameter, liquid holdup, and packing void fraction are used to arrive at the effective gas velocity which defines the residence time in a calculation node according to the aerosol momentum balance. **Figure 7.3** shows a schematic of the multi-level discretization scheme and the reference frame linkage made by the momentum balance equations.

Figure 7.2–Figure 7.3 visualize the stage balance equations and computational sequencing used in this work. Thermodynamics, physical properties, and transfer equations, cast in the balance and sequencing framework allow for computation of the final state of an aerosol passing through a CO₂ absorption column.

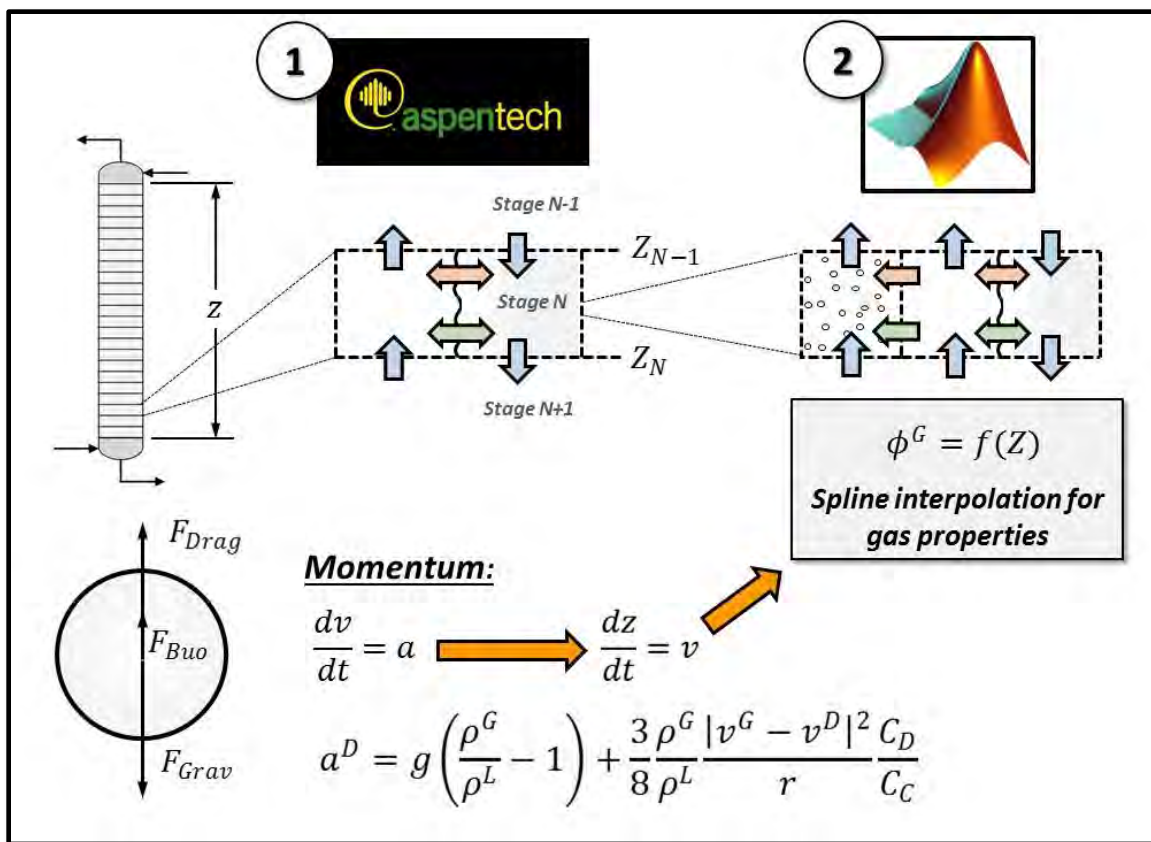


Figure 7.3: The absorber (Eulerian) and aerosol (Lagrangian) reference states are linked by the momentum balance. Absorber calculations are performed in Aspen Plus® and the aerosol integration and interpolation are performed in MATLAB®.

7.2 THERMODYNAMICS

The solvent system studied in this work is aqueous PZ. PZ can react with CO₂ and H₂O to form several reaction products: PZ carbamate (PZCOO⁻), PZ dicarbamate (PZ(COO)₂²⁻), protonated PZ carbamate (H⁺PZCOO⁻), protonated PZ (H⁺PZ), and diprotonated PZ (H²⁺PZ). Bicarbonate (HCO₃³⁻) and carbonate (CO₃²⁻) salts are also formed by acid/base reactions of amine/H₂O/CO₂. Representing chemical equilibrium in a reactive solution involves regressing a large amount of experimental data to determine the thermodynamic parameters affecting activity coefficients and chemical speciation. A

review of the Aspen Plus® thermodynamic framework can be found in Frailie (2014). Formation energies, enthalpies, heat capacities, and electrolyte-NRTL parameters are all presented there with confirmation of fidelity compared to collected data.

Since this work integrates heat and mass transfer to the aerosol in MATLAB®, the approximations of the complex thermodynamic routines in Aspen Plus® were made using correlations developed in the Rochelle research laboratory. The correlations are semi-empirical, and represent the complex chemical equilibrium using “total” concentration values like CO₂ loading and apparent mole fractions. In Aspen Plus® a change to a thermodynamic parameter impacts the others; therefore, all parameters have to be re-regressed if the model changes. Apparent concentration correlations do not require re-regressing if speciation changes are made.

7.2.1 Universal and Component Constants

Universal constant values (with units) are tabulated below (**Table 7.1**). The Boltzmann constant (k_B), Avogadro’s number (N_{Av}), and the universal gas constant (R) are internally consistent. The acceleration of gravity is denoted by g .

Table 7.1: Universal constant parameters

Constant	Units	Value
N_{Av}	molec./mol	6.022×10^{23}
k_B	$\text{m}^2 \cdot \text{kg} / \text{s}^2 \cdot \text{K} \cdot \text{molec.}$	1.381×10^{-23}
R	$\text{Pa} \cdot \text{m}^3 / \text{mol} \cdot \text{K}$	8.314
g	m / s^2	9.807

Component constants are used to calculate the average molecular weight, convert mole fractions to mass fractions, calculate mole-weighted average properties, and to calculate corresponding state values like the reduced temperature. Values and units are shown in **Table 7.2**, below and are taken from the DIPPR database (1998).

Table 7.2: Component-specific constants

Property	Units	N ₂	H ₂ O	CO ₂	PZ
MW_i	g/gmol	28.0134	18.0153	44.0095	86.1356
$T_{C,i}$	K	126.2	647.096	304.2	638.0

7.2.2 Equilibrium Partial Pressures

The equilibrium partial pressures of H₂O, CO₂, and PZ are calculated using Equations (7.1)–(7.3). H₂O equilibrium is calculated using the DIPPR correlation for saturation pressure and using an approximate “true” mole fraction of H₂O (DIPPR, 1998). The activity of H₂O is assumed to be unity. The true mole fraction normalizes the mole fractions by H₂O and PZ; CO₂ is assumed to be completely reacted with PZ. Correlations for CO₂ and PZ equilibrium partial pressures were taken from the work by Xu (2011).

$$P_{H_2O}^* = \frac{100}{101325} x_{H_2O}^T \exp \left[73.649 - \frac{7258.2}{T^L} - 7.3037 \ln(T^L) + 4.1653 \times 10^{-6} (T^L)^2 \right] \quad (7.1)$$

$$P_{CO_2}^* = \frac{100}{101325} \exp \left[35.3 - \frac{11054}{T^L} - 18.9\alpha^2 + \frac{4958\alpha}{T^L} + \frac{10163\alpha^2}{T^L} \right] \quad (7.2)$$

$$P_{PZ}^* = \frac{10^6}{101325} x_{PZ}^T \exp \left[-123 + 21.6 \ln(T^L) + 20.2\alpha - \frac{18174\alpha^2}{T^L} \right] \quad (7.3)$$

where:

$P_{H_2O}^*, P_{CO_2}^*$ = Equilibrium partial pressures of H₂O and CO₂ [vol %]

P_{PZ}^* = Equilibrium partial pressure of PZ [ppmv]

T^L = Lean solvent temperature [K]

x_i^T = “True” mole fraction of component i [--]

α = CO₂ loading [mol CO₂/mol alkalinity]

Comparisons between correlations and Aspen Plus® predictions are shown below in **Figure 7.4–Figure 7.6**.

Due to the large driving forces, deviations between $P_{H_2O}^*$ predictions in Aspen Plus® and the MATLAB® approximate model will impact the growth rate predictions most significantly. As expected, as the solution salt species (CO₂ reaction products and amine concentration) increase, the activity coefficient of H₂O deviates further from unity. Consequently, calculations involving more dilute solvent concentrations will be more accurate.

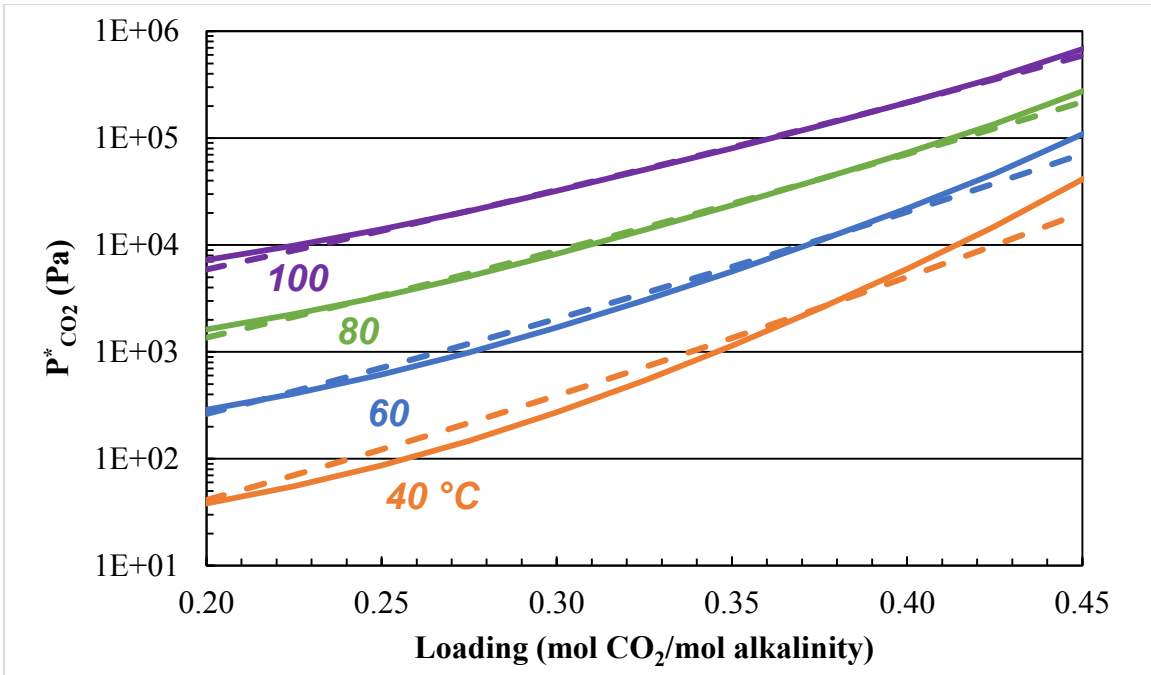


Figure 7.4: CO₂ solubility comparison between Aspen Plus[®] (solid lines) and the empirical correlation (dashed lines).

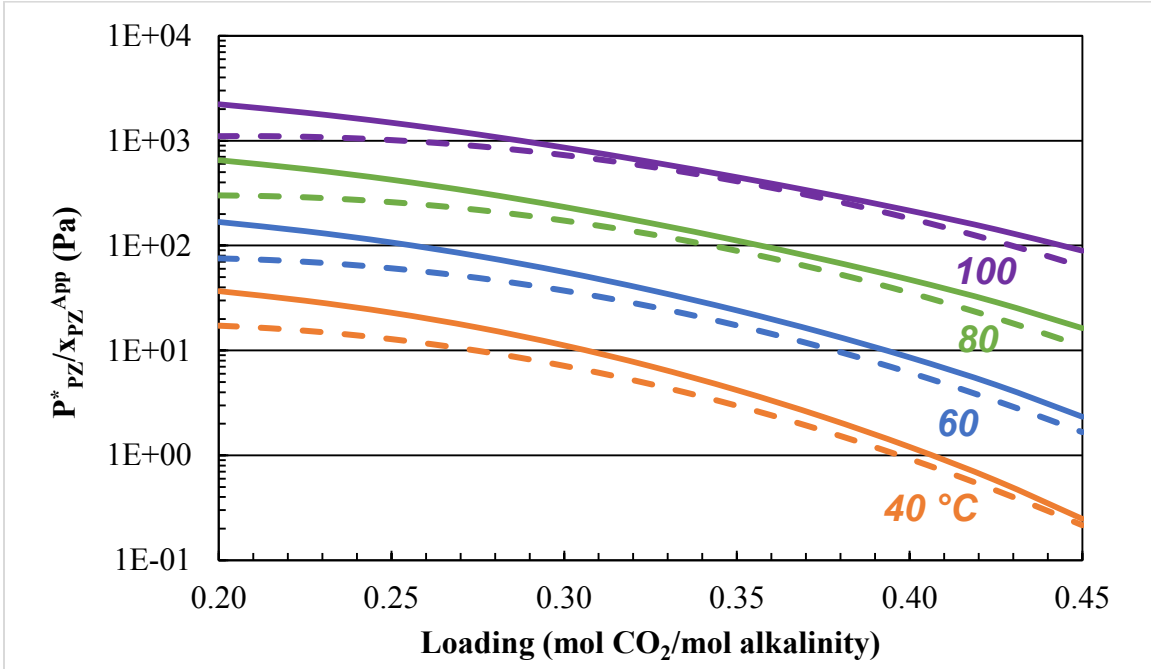


Figure 7.5: PZ volatility comparison between Aspen Plus[®] (solid lines) and the empirical correlation (dashed lines).

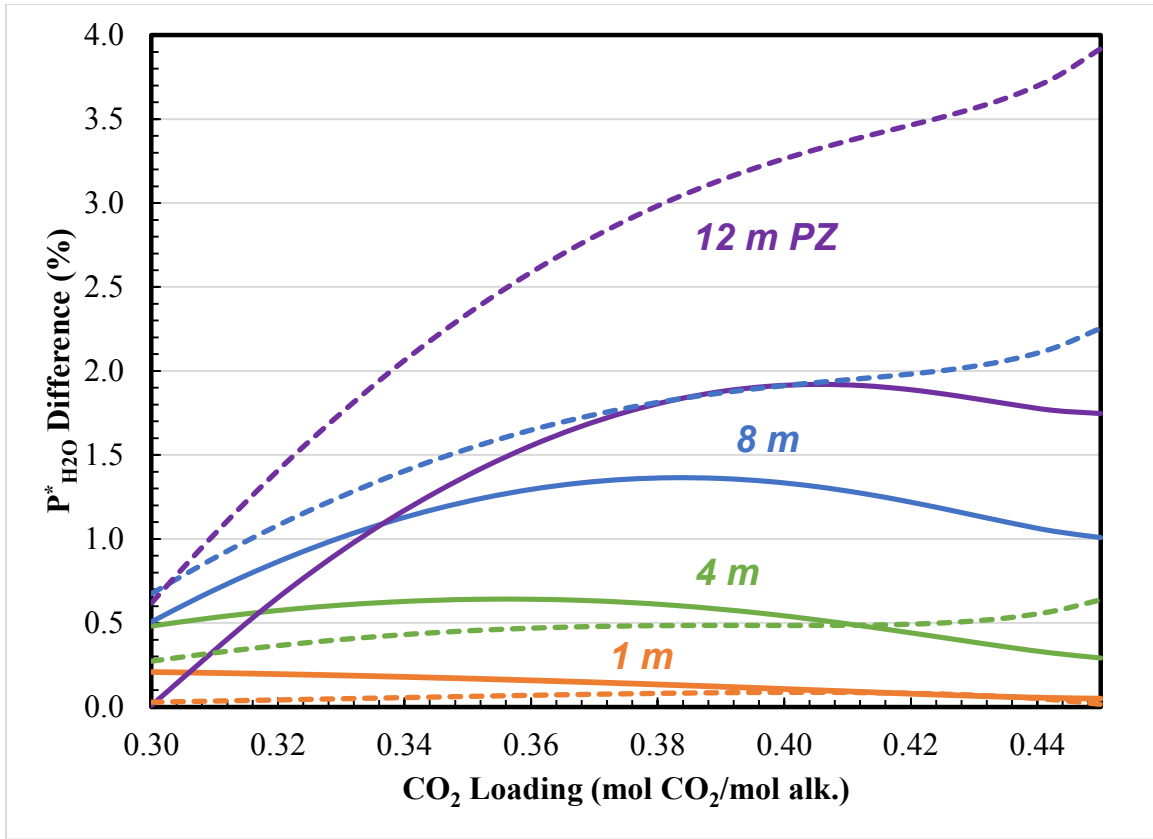


Figure 7.6: Percent difference in $P^*_{\text{H}_2\text{O}}$ between Aspen Plus® and Raoult's Law for 1–12 m PZ at 40 (solid lines) and 60 °C (dashed lines) and 0.30–0.45 CO_2 loading.

Correction for the effect of surface curvature (Kelvin correction) on equilibrium partial pressure is made for every component using Equation (2.26), repeated below (Equation (7.4)). Physical property correlations are given in Section 7.3.

$$P_i^{*,C} = P_i^{*,F} \exp\left(\frac{4\sigma v_i^L}{d^P k_B T G}\right) \quad (7.4)$$

7.2.3 Heats of Absorption and Vaporization

The heat of vaporization of H_2O (Equation (7.5)) is taken from the DIPPR database and follows equation form 106 (DIPPR, 1998). The heat of absorption for CO_2 (Equation (7.6)) and PZ (Equation (7.7)) are calculated by taking the differential of their

respective solubility curves with respect to inverse temperature (Gibbs-Helmholtz relationship).

$$\Delta H_{H_2O} = \frac{1}{1000} (5.6 \times 10^7) (1 - T_{H_2O}^R)^{(0.61204 - 0.6257 T_{H_2O}^R + 0.3988 [T_{H_2O}^R]^2)} \quad (7.5)$$

$$\Delta H_{CO_2} = -R[-11054 - 18.9\alpha + 10163\alpha^2] \quad (7.6)$$

$$\Delta H_{PZ} = -R[21.6 T^L + 18174\alpha^2] \quad (7.7)$$

where:

ΔH_i = Heat of absorption/vaporization of component, i [J/mol]

T_i^R = Reduced temperature for component i [--]

T^L = Liquid temperature [K]

α = CO₂ loading [mol CO₂/mol alkalinity]

7.2.4 Liquid Heat Capacity

The heat capacity of the PZ/H₂O/CO₂ system was calculated using pure component heat capacities of H₂O (Equation (7.8)) and PZ (Equation (7.9)); CO₂ was assumed to have negligible heat capacity.

$$Cp_{H_2O} = 2.7637 \times 10^5 - 2.0901 \times 10^3 T^L + 8.125 T^{L^2} - 1.4116 \times 10^{-2} T^{L^3} + 9.3701 \times 10^{-6} T^{L^4} \quad (7.8)$$

$$Cp_{PZ} = 4.2470 \times 10^4 + 4.7214 \times 10^2 T^L \quad (7.9)$$

where:

Cp_i = Heat capacity of component, i [J/kmol·K]

The mixture heat capacity (Equations (7.10)–(7.12)) is calculated using an ideal mixing rule with an excess property correction with fitting parameters taken from data regression of 183 data points for 2–12 m PZ between 0.157 and 0.400 CO₂ loading and 40–150 °C. The AARD of the regression was 1.58 %.

$$Cp_{Ex,1} = x_{PZ}^A x_{CO_2}^A (-8,722 + 36.22 T^L) + (x_{PZ}^A - x_{CO_2}^A)(40,762 - 173.38 T^L) \quad (7.10)$$

$$Cp_{Ex,2} = x_{H_2O}^A x_{CO_2}^A (4,604 - 17.76 T^L) + (x_{H_2O}^A - x_{CO_2}^A)(-5,368 + 20.38 T^L) \quad (7.11)$$

$$Cp_{MIX}^L = x_{H_2O}^A Cp_{H_2O} + x_{PZ}^A Cp_{PZ} + \frac{1}{1000} (Cp_{Ex,1} + Cp_{Ex,2}) \quad (7.12)$$

where:

- Cp_{Ex} = Excess heat capacity [kJ/mol·K]
- x_i^A = Apparent mole fraction of component, i [--]
- Cp_{MIX}^L = Mixture liquid heat capacity [J/kmol·K]

7.3 PHYSICAL PROPERTIES

Physical properties used in the model are taken from Aspen Plus® subroutines when applicable. All other property calculations are done using equations and parameters from the DIPPR database (DIPPR, 1998).

7.3.1 Molecular Volume

The liquid molecular volume is used to calculate the Kelvin correction for each component. The correlations (Equations (7.13)–(7.15)) presented here are taken from the DIPPR database and follow equation form 100 and 105.

$$v_{H_2O} = \frac{1}{1000 N_{Av}} \left[-0.13851 + 0.64038 T^L - 1.9124 \times 10^{-3} T^{L^2} + 1.8211 \times 10^{-6} T^{L^3} \right]^{-1} \quad (7.13)$$

$$v_{CO_2} = \frac{1}{1000 N_{Av}} \left[\frac{2.768}{0.2612} \right]^{-1} \quad (7.14)$$

$$v_{PZ} = \frac{1}{1000 N_{Av}} \left\{ \frac{1.0425}{0.3223 \left[1 + \left(1 - \frac{T^L}{638} \right)^{0.28571} \right]} \right\}^{-1} \quad (7.15)$$

where:

$$v_i = \text{Pure component molecular volume for component } i \text{ [m}^3\text{/molec.]}$$

7.3.2 Density

The liquid mixture density (Equation (7.16)) is calculated using the “vl2.u2” subroutine in the Fawkes model in Aspen Plus®.

$$\rho_{MIX}^L = 1000 \left[1.5494 - 5.728 \times 10^{-4} T^L \right] \ln \left[2.676 x_{CO_2}^A - 3.097710^{-2} x_{PZ}^A - 7.26176 \times 10^{-2} \alpha + 2.102569 \right] \quad (7.16)$$

where:

$$\rho_{MIX}^L = \text{Liquid mass density [kg/m}^3\text{]}$$

7.3.3 Surface Tension

The surface tension is calculated (Equations (7.17)–(7.19)) using the same mixing rule used in Aspen Plus®; however, the contribution of CO₂ is neglected and the mole fractions of H₂O and PZ are renormalized excluding CO₂.

$$\sigma_{H_2O} = 0.17766(1 - T_{H_2O}^R)^{(2.567 - 3.3377 T_{H_2O}^R + 1.9699 T_{H_2O}^R{}^2)} \quad (7.17)$$

$$\sigma_{PZ} = 0.024853(1 - T_{PZ}^R)^{(1.1667)} \quad (7.18)$$

$$\sigma_{MIX} = x_{H_2O}^T \sigma_{H_2O} + x_{PZ}^T \sigma_{PZ} \quad (7.19)$$

where:

σ_i = Pure component surface tension for component i [N/m]

σ_{MIX} = Mixture surface tension [N/m]

7.4 MASS TRANSFER/KINETICS

7.4.1.1 Gas Film Limited Components

Chemical species whose mass transfer rate is assumed to be limited by the gas film (H₂O and PZ) are modeled using the equations developed in Section 2.4.2. The physical properties of the gas are taken directly from the steady state profiles generated in Aspen Plus®; therefore, no additional property calculations are required. The mass transfer rate for all gas-film limited components is adjusted for length-scale effects using the Fuchs-Sutugin correction (Equation (2.30)).

7.4.1.2 Reaction/Liquid Film Limited Components

CO₂ is the only chemical specie whose mass transfer rate is assumed to be limited by the combination of reaction kinetics and diffusion in the liquid film of the aerosol. For packed absorber calculations, the mass transfer coefficient for CO₂ into a flat liquid film is calculated using the Pseudo-First Order expression for the mass transfer coefficient, k'_g . Plaza derives the analytical expression for k'_g (2012). Generally, k'_g is a mass transfer coefficient whose driving force is defined as the difference in CO₂ partial

pressure between the interface and the bulk solvent (Equation (7.20)). If the gas-side mass transfer resistance is assumed negligible, then the interface CO₂ partial can be replaced with the bulk gas CO₂ partial pressure.

$$N_{CO_2} = k'_g(P_{CO_2}^{*I} - P_{CO_2}^{*L}) \quad (7.20)$$

where:

- N_{CO_2} = Flux of CO₂ [mol/m²·s]
- k'_g = Liquid-side mass transfer coefficient [mol/m²·Pa·s]
- $P_{CO_2}^{*I}$ = Equilibrium partial pressure of CO₂ at the gas-liquid interface composition and temperature [Pa]
- $P_{CO_2}^{*L}$ = Equilibrium partial pressure of CO₂ at the bulk liquid composition and temperature [Pa]

Experimentally measured values of k'_g , measured by Dugas (2009b), are shown below in **Figure 7.7** for 2–12 m PZ at 40 and 60 °C and variable loading. k'_g is relatively independent of the amine concentration; the mass transfer rate functional relationship with respect to the amine concentration and diffusivity (implicitly viscosity) tend to oppose each other equivalently.

At typical lean and rich loadings ($P^*_{CO_2} = 500$ and $5,000$ Pa), k'_g is approximately 1×10^{-6} to 1×10^{-7} mol/m²·Pa·s. $P^*_{CO_2}$ is chosen at the lean and rich ends to provide a nominal driving force for CO₂ absorption such that the physical size of the absorber is minimized while and the irreversibility is kept small to reduce stripping energy consumption. However, CO₂ accumulation in the aerosol phase is much faster than the bulk solvent, and therefore the loading of the aerosol is much higher than the solvent. The result is that $P^*_{CO_2}$ for the aerosol is much higher and k'_g will be lower relative to the solvent. In this work, k'_g is not used in the traditional film theory sense, but is treated as

an adjustable parameter with approximate bounds dictated by experimental k'_g measurements. That assumption is discussed in Section 7.11.1 as a part of sensitivity analysis.

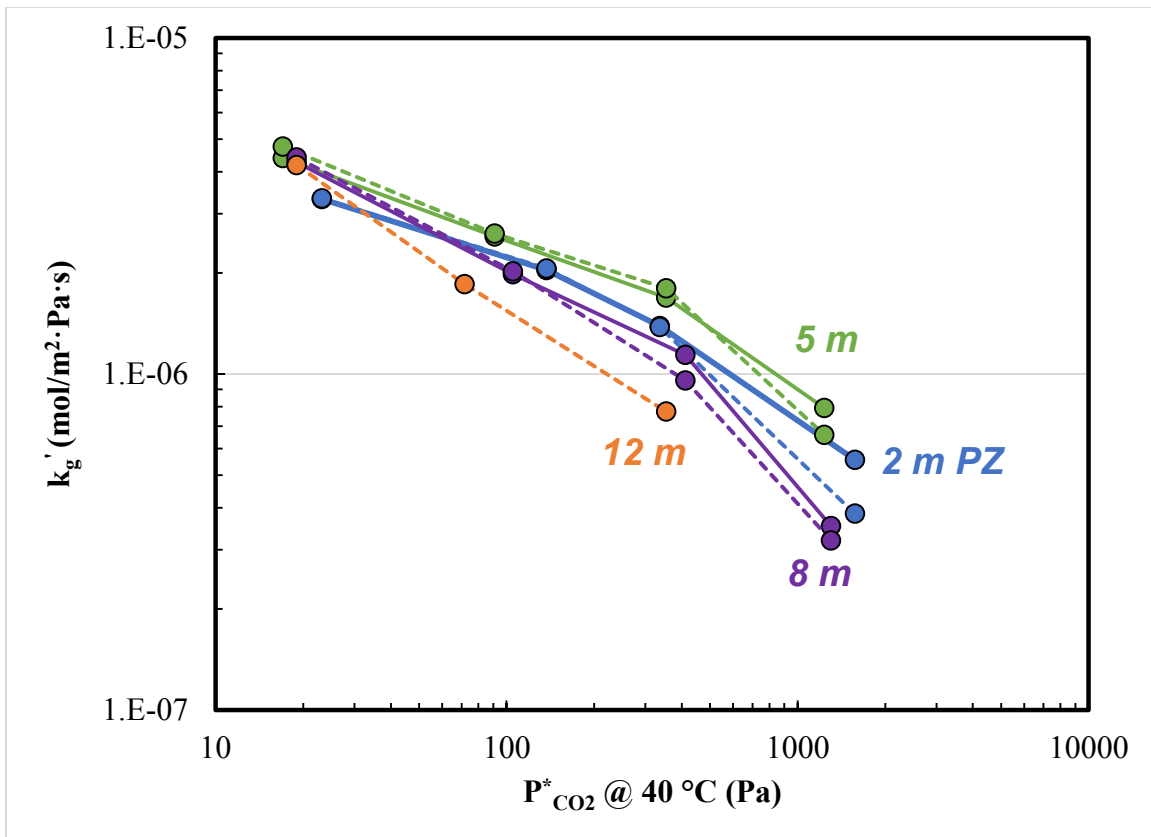


Figure 7.7: k'_g experimental data taken from Dugas (2009b) for 2–12 m PZ at 40 (solid lines) and 60 °C (dashed lines).

7.5 AEROSOL DIMENSIONS

In this study, aerosols are assumed to be perfect spheres. Their physical dimensions are calculated using the total moles and mixture molar volume (Equation (7.21)). The surface area (Equation (7.23)) and the diameter (Equation (7.22)) are determined by spherical geometry equations.

$$V^D = \sum_i^{N_c} n_i MW_{Mix}^D / (1000 \times \rho_{Mix}^D) \quad (7.21)$$

$$d^D = \left(\frac{6V^D}{\pi} \right)^{1/3} \quad (7.22)$$

$$A^D = \pi(d^D)^2 \quad (7.23)$$

where:

- V^D = Volume of the aerosol [m³]
- n_i = Number of moles of component i [mol]
- MW_{Mix}^D = Average molecular weight of the droplet phase [g/gmol]
- d^D = Diameter of the aerosol [m]
- A^D = Surface area of the aerosol [m²]

7.6 ABSORBER INPUT PROFILES, PARAMETERS, AND CALCULATIONS

7.6.1 Input Parameters

Column sizing and hydraulic condition input parameters from Aspen Plus[®] simulations are required to perform the particle tracking calculations in the MATLAB[®] model. **Table 7.3** shows the required input parameters and their units.

Table 7.3: Aerosol model input parameters from Aspen Plus[®]

Parameter	Units	Description
h_{col}	[m]	Column height
d_{col}	[m]	Column inside diameter
v_{frac}	[--]	Packing void fraction (fraction of free volume not occupied by packing)
L_{hold}	[--]	Liquid holdup (fraction of free volume occupied by the liquid)

7.6.2 Input Profiles

Profiles generated by Aspen Plus® simulations are saved in external MATLAB® .Mat files. Those exported profiles contain all of the gas-side physical and transport properties required to calculate mass and heat transfer rates to the aerosol phase. A custom property set in Aspen Plus® is used to export column profiles. An example absorber profile dataset and the parameter definitions are given in **Table 7.5–Table 7.6** and **Table 7.4**, respectively. **Table 7.5–Table 7.6** show only the top 20 stages of the absorber; the stage numbering convention in Aspen Plus® is to start from the top of the column with stage one.

Table 7.4: Aspen Plus® parameter definitions and units

Aspen Plus® Parameter	Symbol	Description
TEMP	T^G	Bulk gas temperature [K]
MOLEFRAC	y_i	Mole fraction of component i [--]
PPMX	P_i^G	Bulk gas partial pressure of component i [Pa]
MWMX	MW^G	Average molecular weight of the gas phase mixture [g/gmol]
RHOMX	ρ^G	Mass density of the gas phase [kg/m ³]
KMX	κ^G	Thermal conductivity of the gas phase [W/m·K]
CPMX	Cp^G	Molar heat capacity of the gas phase [J/kmol·K]
MUMX	μ^G	Viscosity of the gas phase [N·s/m ²]
DMX	D_i^G	Gas phase effective diffusion coefficient of component i [m ² /s]
VOLFLMX	Q^G	Volumetric flow rate of the bulk gas [m ³ /s]

Table 7.5: Reformatted sample absorber profile input data taken from a custom Aspen Plus® property set.

Stage	VAPOR TEMP	VAPOR MOLEFRAC N ₂	VAPOR MOLEFRAC H ₂ O	VAPOR MOLEFRAC CO ₂	VAPOR MOLEFRAC PZ	VAPOR PPMX N ₂	VAPOR PPMX H ₂ O	VAPOR PPMX CO ₂	VAPOR PPMX PZ
[--]	[K]	[--]	[--]	[--]	[--]	[N/m ²]	[N/m ²]	[N/m ²]	[N/m ²]
1	314.22	9.127E-01	7.081E-02	1.651E-02	7.706E-06	9.248E+04	7.175E+03	1.673E+03	0.781
2	314.74	9.079E-01	7.299E-02	1.912E-02	7.501E-06	9.199E+04	7.396E+03	1.937E+03	0.760
3	315.30	9.026E-01	7.540E-02	2.202E-02	7.356E-06	9.145E+04	7.640E+03	2.231E+03	0.745
4	315.90	8.968E-01	7.804E-02	2.519E-02	7.275E-06	9.087E+04	7.907E+03	2.552E+03	0.737
5	316.55	8.905E-01	8.089E-02	2.860E-02	7.257E-06	9.023E+04	8.197E+03	2.898E+03	0.735
6	317.23	8.838E-01	8.397E-02	3.222E-02	7.303E-06	8.955E+04	8.509E+03	3.264E+03	0.740
7	317.94	8.767E-01	8.727E-02	3.601E-02	7.411E-06	8.883E+04	8.843E+03	3.649E+03	0.751
8	318.68	8.693E-01	9.077E-02	3.993E-02	7.578E-06	8.808E+04	9.197E+03	4.046E+03	0.768
9	319.45	8.616E-01	9.446E-02	4.395E-02	7.800E-06	8.730E+04	9.572E+03	4.453E+03	0.790
10	320.22	8.537E-01	9.833E-02	4.800E-02	8.073E-06	8.650E+04	9.963E+03	4.864E+03	0.818
11	321.01	8.456E-01	1.023E-01	5.207E-02	8.394E-06	8.568E+04	1.037E+04	5.276E+03	0.850
12	321.81	8.374E-01	1.065E-01	5.610E-02	8.756E-06	8.485E+04	1.079E+04	5.684E+03	0.887
13	322.60	8.292E-01	1.107E-01	6.007E-02	9.154E-06	8.402E+04	1.122E+04	6.087E+03	0.927
14	323.38	8.211E-01	1.150E-01	6.395E-02	9.581E-06	8.319E+04	1.165E+04	6.480E+03	0.971
15	324.15	8.130E-01	1.193E-01	6.772E-02	1.003E-05	8.238E+04	1.208E+04	6.862E+03	1.016
16	324.90	8.051E-01	1.235E-01	7.135E-02	1.049E-05	8.158E+04	1.252E+04	7.230E+03	1.063
17	325.62	7.974E-01	1.277E-01	7.484E-02	1.096E-05	8.080E+04	1.294E+04	7.583E+03	1.110
18	326.30	7.900E-01	1.318E-01	7.817E-02	1.142E-05	8.005E+04	1.335E+04	7.921E+03	1.157
19	326.95	7.830E-01	1.357E-01	8.134E-02	1.187E-05	7.933E+04	1.375E+04	8.242E+03	1.202
20	327.56	7.762E-01	1.394E-01	8.436E-02	1.228E-05	7.865E+04	1.412E+04	8.548E+03	1.245

Table 7.6: Reformatted sample absorber profile input data taken from a custom Aspen Plus® property set (cont'd.)

Stage	VAPOR MWMX	VAPOR RHOMX	VAPOR KMX	VAPOR CPMX	VAPOR MUMX	VAPOR DMX N ₂	VAPOR DMX H ₂ O	VAPOR DMX CO ₂	VAPOR DMX PZ	VAPOR VOLFLMX
[--]	[g/gmol]	[kg/m ³]	[W/m·K]	[J/kmol·K]	[N·s/m ²]	[m ² /s]	[m ² /s]	[m ² /s]	[m ² /s]	[m ³ /s]
1	27.570	1.068	2.593E-02	2.970E+04	1.829E-05	2.471E-05	2.659E-05	1.868E-05	9.879E-06	22.209
2	27.590	1.067	2.592E-02	2.973E+04	1.830E-05	2.462E-05	2.665E-05	1.875E-05	9.900E-06	22.367
3	27.612	1.066	2.592E-02	2.977E+04	1.831E-05	2.453E-05	2.672E-05	1.882E-05	9.922E-06	22.541
4	27.637	1.064	2.591E-02	2.981E+04	1.832E-05	2.445E-05	2.680E-05	1.889E-05	9.945E-06	22.733
5	27.663	1.063	2.590E-02	2.985E+04	1.833E-05	2.439E-05	2.688E-05	1.897E-05	9.969E-06	22.943
6	27.690	1.062	2.589E-02	2.990E+04	1.835E-05	2.434E-05	2.696E-05	1.905E-05	9.994E-06	23.168
7	27.717	1.060	2.587E-02	2.995E+04	1.836E-05	2.431E-05	2.704E-05	1.914E-05	1.002E-05	23.410
8	27.745	1.059	2.586E-02	3.001E+04	1.837E-05	2.429E-05	2.712E-05	1.923E-05	1.005E-05	23.665
9	27.772	1.057	2.585E-02	3.006E+04	1.838E-05	2.430E-05	2.721E-05	1.932E-05	1.007E-05	23.935
10	27.799	1.056	2.583E-02	3.012E+04	1.839E-05	2.431E-05	2.729E-05	1.941E-05	1.010E-05	24.215
11	27.824	1.054	2.582E-02	3.018E+04	1.840E-05	2.434E-05	2.738E-05	1.951E-05	1.013E-05	24.506
12	27.847	1.052	2.580E-02	3.024E+04	1.841E-05	2.438E-05	2.746E-05	1.960E-05	1.015E-05	24.805
13	27.868	1.051	2.578E-02	3.029E+04	1.842E-05	2.443E-05	2.755E-05	1.969E-05	1.018E-05	25.110
14	27.887	1.049	2.577E-02	3.035E+04	1.843E-05	2.449E-05	2.763E-05	1.978E-05	1.020E-05	25.418
15	27.905	1.047	2.575E-02	3.041E+04	1.844E-05	2.455E-05	2.771E-05	1.987E-05	1.023E-05	25.727
16	27.920	1.046	2.573E-02	3.047E+04	1.845E-05	2.461E-05	2.778E-05	1.996E-05	1.025E-05	26.035
17	27.934	1.044	2.572E-02	3.052E+04	1.845E-05	2.468E-05	2.785E-05	2.004E-05	1.027E-05	26.340
18	27.947	1.043	2.570E-02	3.058E+04	1.845E-05	2.475E-05	2.792E-05	2.012E-05	1.030E-05	26.638
19	27.959	1.041	2.569E-02	3.063E+04	1.846E-05	2.481E-05	2.798E-05	2.019E-05	1.032E-05	26.927
20	27.970	1.040	2.567E-02	3.068E+04	1.846E-05	2.487E-05	2.803E-05	2.026E-05	1.033E-05	27.205

7.6.3 Calculations

The absolute vapor velocity, which is used to calculate the relative velocity of the droplet, includes corrections for the volume occupied by the packing and liquid. Equation (7.24) shows the vapor velocity calculation.

$$v^G = \frac{4Q^G}{[(1 - L_{hol})v_{frac}\pi(d_{col})^2]} \quad (7.24)$$

where:

$$v^G = \text{Actual gas phase velocity in the absorber [m/s]}$$

7.7 DIFFERENTIAL EQUATIONS

A set of seven coupled, non-linear ordinary differential equations are used to describe the dynamic growth process of a single aerosol drop as it passes through gas-liquid contactors. The equations are composed of component mole (4), energy (1), and momentum (2) balances. The momentum balance is split into two equations (velocity and position) since MATLAB[®] integrators only deal with first-order differential equations.

7.7.1 Component Mole Balances

N₂ is assumed to be a non-transferring component. Gas-side limited components (H₂O and PZ) follow the Maxwell equation for mass transfer with the Fuchs-Sutugin correction (Equations (7.26)–(7.27)). CO₂ is assumed to be reaction and diffusion limited; k'_g is used as an adjustable parameter for modeling the rate of CO₂ absorption (Equation (7.28)). The use of k'_g is equivalent to assuming a surface area limited reaction rate.

$$\frac{dn_{N_2}}{dt} = 0 \quad (7.25)$$

$$\frac{dn_{H_2O}}{dt} = 2\pi D_{H_2O, Mix}^G d^D \frac{(P_{H_2O}^G - P_{H_2O}^{*,C})}{RT^G} \phi(Kn) \quad (7.26)$$

$$\frac{dn_{PZ}}{dt} = 2\pi D_{PZ, Mix}^G d^D \frac{(P_{PZ}^G - P_{PZ}^{*,C})}{RT^G} \phi(Kn) \quad (7.27)$$

$$\frac{dn_{CO_2}}{dt} = \pi (d^D)^2 k'_g (P_{CO_2}^G - P_{CO_2}^{*,C}) \quad (7.28)$$

where:

- n_i = Number of moles of component i [mol]
- $D_{i, Mix}^G$ = Effective, gas phase diffusion coefficient of component i [m^2/s]
- d^D = Diameter of the aerosol [m]
- P_i^G = Partial pressure of component i in the bulk gas [Pa]
- $P_i^{*,C}$ = Equilibrium partial pressure of component i over the aerosol surface including the Kelvin effect correction [Pa]
- $\phi(Kn)$ = Fuchs-Sutugin correction for gas side mass transfer [--]

7.7.2 Enthalpy Balance

The droplet temperature changes due to the exchange of enthalpy associated with mass transfer and convection caused by the temperature difference between the phases (Equation (7.29)). Because only the droplet enthalpy balance is considered, no reference state is required since only a relative balance is being performed. Implicitly, the reference state for each component is taken at the droplet temperature and the corresponding phase defined by the vaporization or absorption enthalpy definition.

Absorption is defined as a phase transition from the gas into a liquid; vaporization is defined as a phase transition from a liquid into a gas.

$$\frac{dT^D}{dt} = \frac{1000 \left[\left(\sum_i^{N_c} \frac{dn_i}{dt} \Delta H_i \right) + h^G A^D (T^G - T^D) \right]}{Cp_{Mix}^D \sum_i^{N_c} n_i} \quad (7.29)$$

where:

- T^D = Droplet temperature [K]
- ΔH_i = Heat of vaporization/absorption of component i [J/mol]
- h^G = Heat transfer coefficient of the gas to the drop [$J/m^2 \cdot s \cdot K$]
- A^D = Surface area of the drop [m^2]
- T^G = Temperature of the bulk gas [K]
- Cp_{Mix}^D = Heat capacity of the drop [$J/kmol \cdot K$]

7.7.3 Momentum Balance

The momentum balance is composed of two, coupled differential equations: velocity and position. Acceleration is calculated using a force balance as described in Section 2.3.2.

$$\frac{dv^D}{dt} = a^D \quad (7.30)$$

$$\frac{dh^D}{dt} = v^D \quad (7.31)$$

where:

- v^D = Drop absolute velocity [m/s]
- a^D = Drop acceleration [m/s^2]
- h^D = Height of drop in the column [m]

7.8 INITIAL CONDITIONS

The initial conditions supplied to the simulation are the droplet size, composition (CO₂ loading and PZ molality), and temperature. H₂O, CO₂, and droplet temperature are assumed to be in equilibrium to the inlet gas. The starting position is at the first section of packing ($h^D = 0$) at the bottom of the absorber and the initial velocity is calculated assuming Stokes flow with no slip correction and assuming no acceleration. The relative velocity equation is closed-form and is shown in Equation (7.32). The initial conditions are processed using a subroutine controlled by the main script.

$$v^{Rel} = \frac{(d^D)^2(\rho^D - \rho^G)g}{18\mu^G} \quad (7.32)$$

where:

- v^{Rel} = Relative velocity of the drop with respect to the gas [m/s]
- ρ^D = Drop mass density [kg/m³]
- ρ^G = Gas mass density [kg/m³]
- μ^G = Viscosity of the gas [Nm]

7.9 INTEGRATION ALGORITHM

A set of 5 ordinary differential equations are solved using a semi-explicit, stiff-system Rosenbrock ODE solver algorithm (ODE23s) internal to the MATLAB[®] function suite. The set of equations are written in nested differential-algebraic (DAE) form. The system of differential equations is highly non-linear due to the complex thermodynamic relationships and mixing rules required to calculate driving forces and physical properties. A numerical Jacobian is used in the ODE23s algorithm. Other ODE solvers (Runge-Kutta) were investigated but were found to be computationally inefficient and provided little improvement in accuracy.

7.10 PROGRAM STRUCTURE

The aerosol growth program is controlled by a main script and a set of subroutines and a completion condition (or event). A flow chart illustrating information management and calculation procedure is shown in **Figure 7.8** below.

Three matrices (.mat files) containing correlation parameters (correl.mat), component-specific constants (comcons.mat), and the absorber profile (abspro.mat) calculated in Aspen Plus[®] are taken as inputs. Additionally, column information and the aerosol initial conditions must be specified as part of the main script.

A separate subroutine (“initialize_x.m”) converts intuitive initial conditions (CO₂ loading and PZ molality, drop diameter, temperature) into mole and mass fractions and total moles and calculates the terminal velocity. The initial condition matrix is taken as an input into the integration algorithm (ODE23s). A subroutine (“diffeql_x.m”) containing algebraic and differential equations is integrated by the ODE23s algorithm. A stopping conditions, or event (“event_x.m”), is checked after each integration step to determine if the aerosol has reached the top of the column and is passing upwards with the gas. Once the stopping condition is reached, a set of composition, temperature, and size profiles are calculated in the main script.

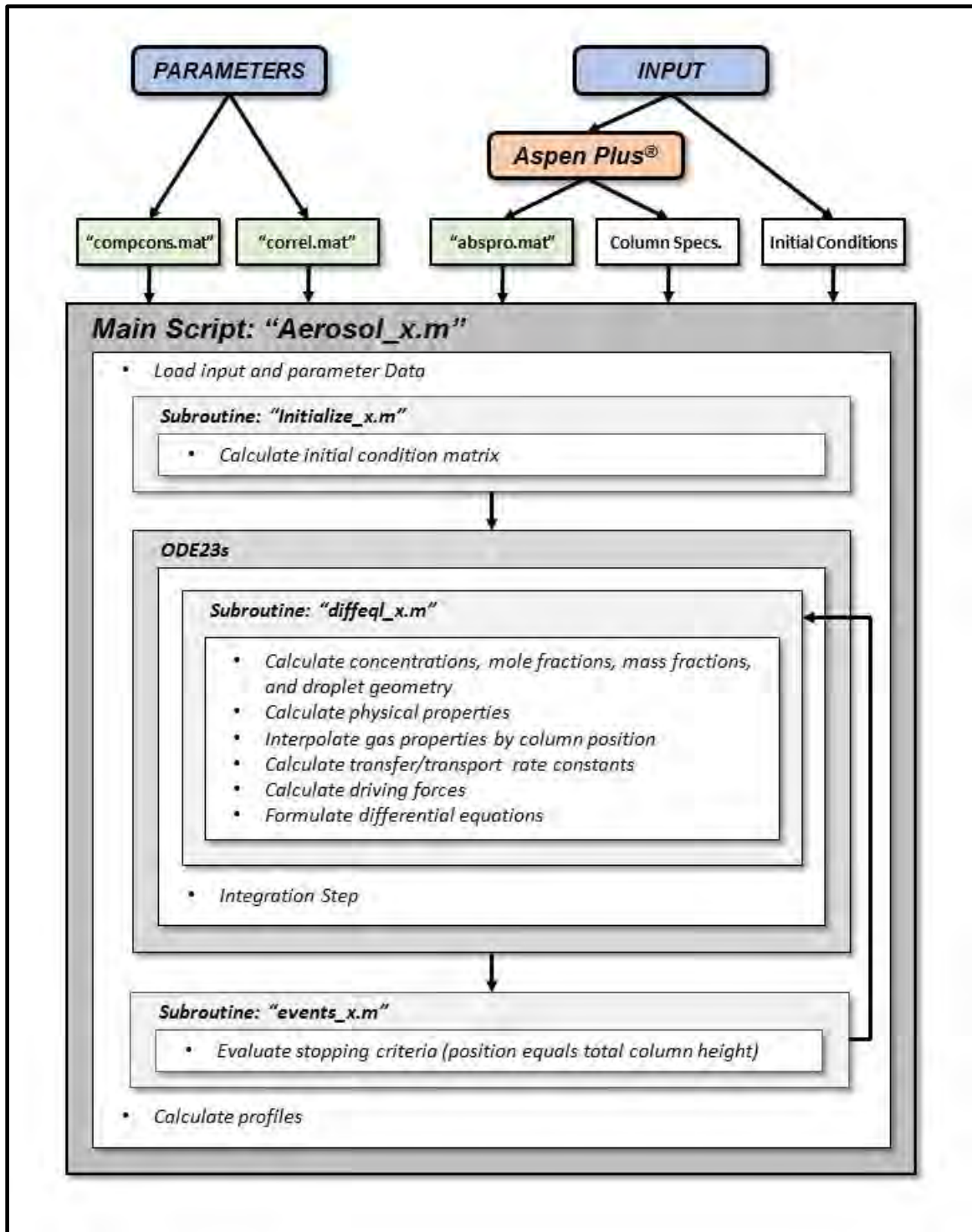


Figure 7.8: Aerosol integration program flow chart

7.11 RESULTS

7.11.1 Sensitivity Analysis: k'_g

The sensitivity of the aerosol integration model to the mass transfer coefficient of CO_2 was analyzed using a generic absorber model converged in Aspen Plus[®]. A $3 \mu\text{m}$ particle entering the absorber was assumed to be in thermal equilibrium with the gas, and in equilibrium to H_2O and CO_2 . The starting PZ concentration was calculated by constraining the summation of the mole fractions to unity. The initial aerosol conditions and the absorber boundary parameters are shown in **Figure 7.9**. The CO_2 mass transfer coefficient, k'_g , was varied between 1×10^{-6} – 1×10^{-8} $\text{mol}/\text{Pa} \cdot \text{m}^2 \cdot \text{s}$. Since the aerosol is much richer than the solvent, the k'_g is assumed to be at the lower end of the data given by Dugas (2009). All other absorber and aerosol parameters were kept constant.

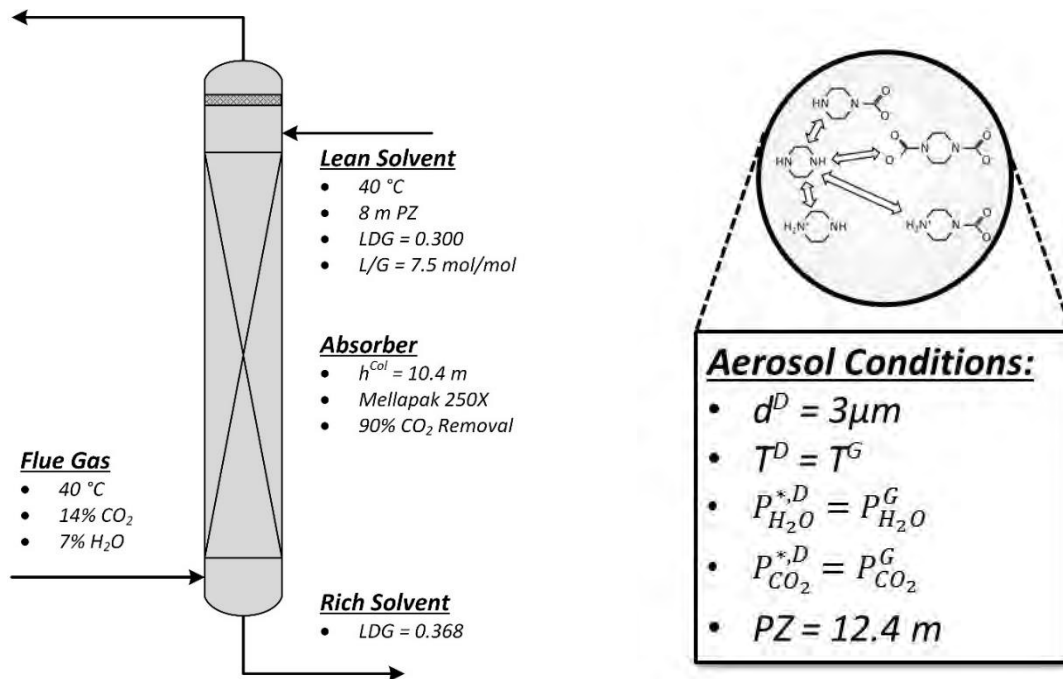


Figure 7.9: Absorber and initial aerosol conditions for the sensitivity case study. The PZ concentration in the aerosol is not independent since H_2O and CO_2 are set by the bulk gas concentration.

Figure 7.10 shows the diameter of the particle as it passes through the absorber. The particle grows more slowly with decreasing k'_g , as expected. Growth of the aerosol requires a driving force for species movement into the aerosol phase from the bulk gas and the growth rate depends on the driving force as well as the transfer coefficient.

Aerosols will continue to grow in the absorber because of the presence of condensable acid (CO_2) and base (amine/PZ) species which absorb into the aqueous aerosol and decrease the activity of H_2O . H_2O then condenses to reach equilibrium with the bulk gas, which is approximately in equilibrium with the bulk solvent. The acid-base reacted salts decrease in activity due to dilution by H_2O , and further driving force for absorption is created.

The aerosol model includes an energy balance which can affect the mass transfer rates by lowering the liquid temperature during evaporation or raising the temperature during condensation proportional to the heat of absorption/vaporization of the transferred species. The temperature difference corresponding to mass transfer should be the wet-bulb temperature, or the temperature where convective heat transfer and the latent heat of component mass transfer are equal. Since the particle is close to saturated conditions to H_2O , which is the fastest transferring component, the temperature difference should be negligible for small mass transfer rates. Since the driving force for mass transfer is small in the absorber, the temperature difference between the gas and the aerosol will be very small, but non-negligible. **Figure 7.11** shows that the model captures this behavior, though the small length scales show simulation instability.

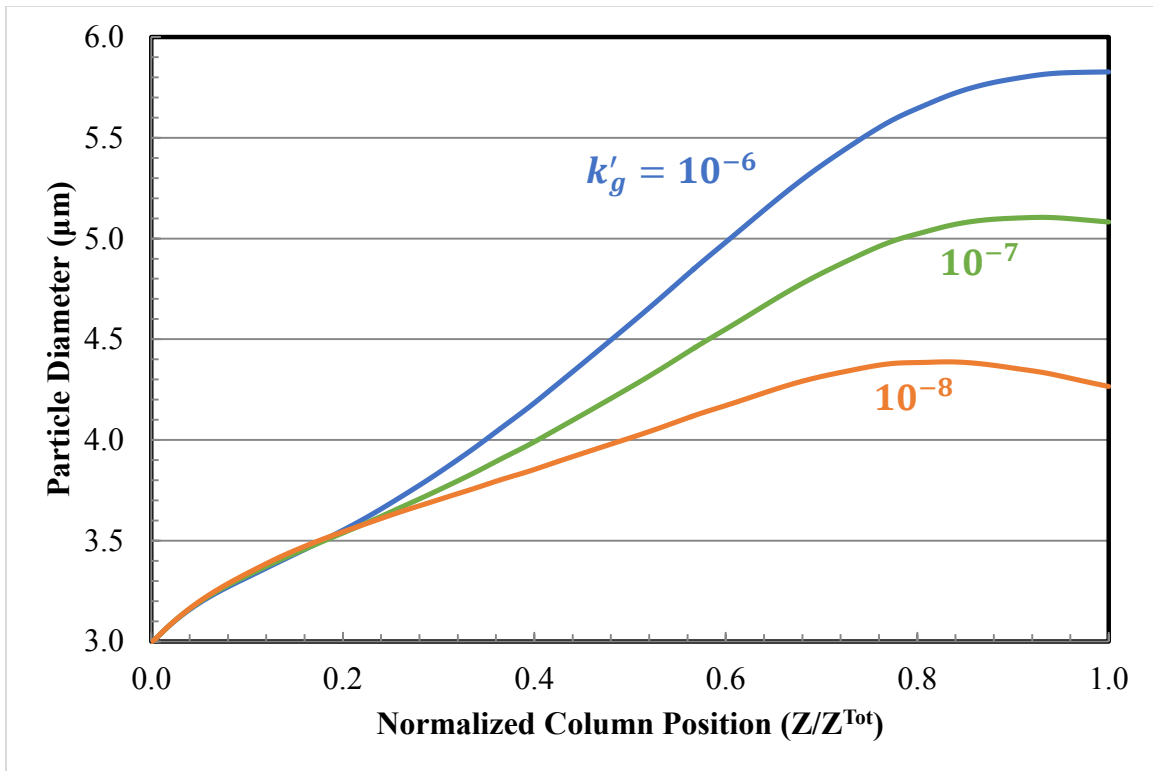


Figure 7.10: Particle growth curves as a function of normalized column position for $k'_g = 10^{-6}$, 10^{-7} , and 10^{-8} mol/Pa·m²·s. Column input and aerosol initial conditions are given in Figure 7.9.

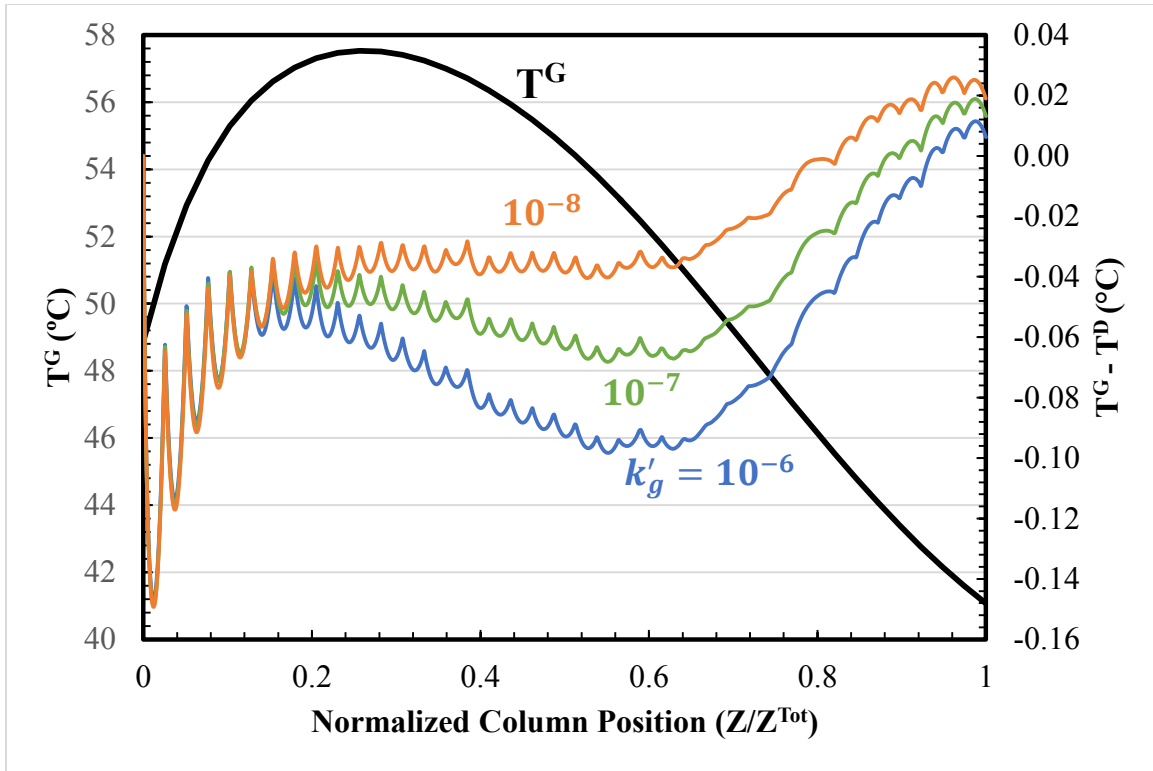


Figure 7.11: Bulk gas temperature profile and the temperature difference between the gas and aerosol for $k'_g = 10^{-6}$, 10^{-7} , and 10^{-8} mol/Pa·m²·s.

Figure 7.12 and **Figure 7.13** show the driving force for CO₂ and PZ mass transfer for three k'_g cases. As k'_g decreases, the transfer rate of CO₂ relative to PZ decreases, resulting in slower changes of loading. As loading decreases, the partial pressure of amine increases, thereby decreasing amine transfer. As amine transfer slows, the aerosol becomes dilute and reaches equilibrium to H₂O and the particle ceases to grow. The transfer of CO₂ is therefore important to the growth rate of the aerosol due to the effect on amine transfer rates. For higher values of k'_g , CO₂ transfer is faster; and therefore, the CO₂ loading is higher. Since PZ partial pressure is inversely related to loading, higher values of k'_g will produce lower equilibrium partial pressure of PZ, as shown in **Figure 7.13**.

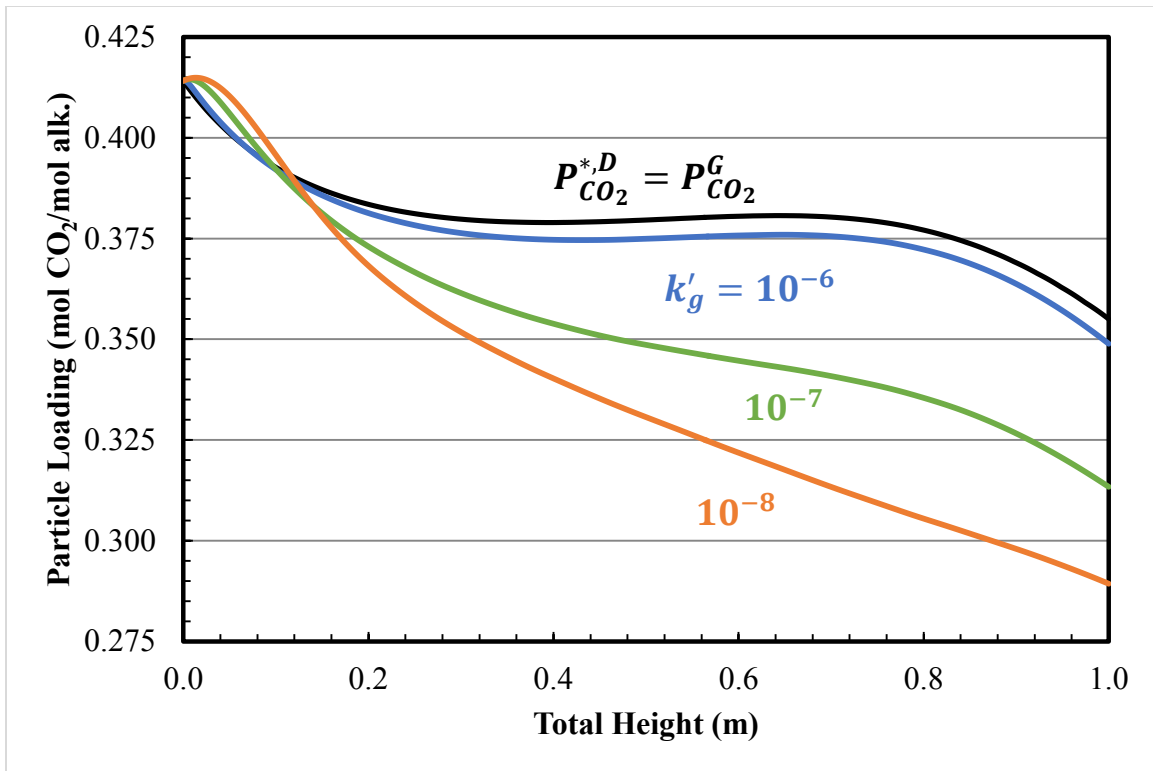


Figure 7.12: Aerosol CO₂ loading as it passes through the absorber for $k'_g = 10^{-6}$, 10^{-7} , and 10^{-8} mol/Pa·m²·s. The initial aerosol diameter is 3 μm. The black curve represents the CO₂ loading which produces an equilibrium partial pressure equivalent to the bulk gas CO₂ concentration.

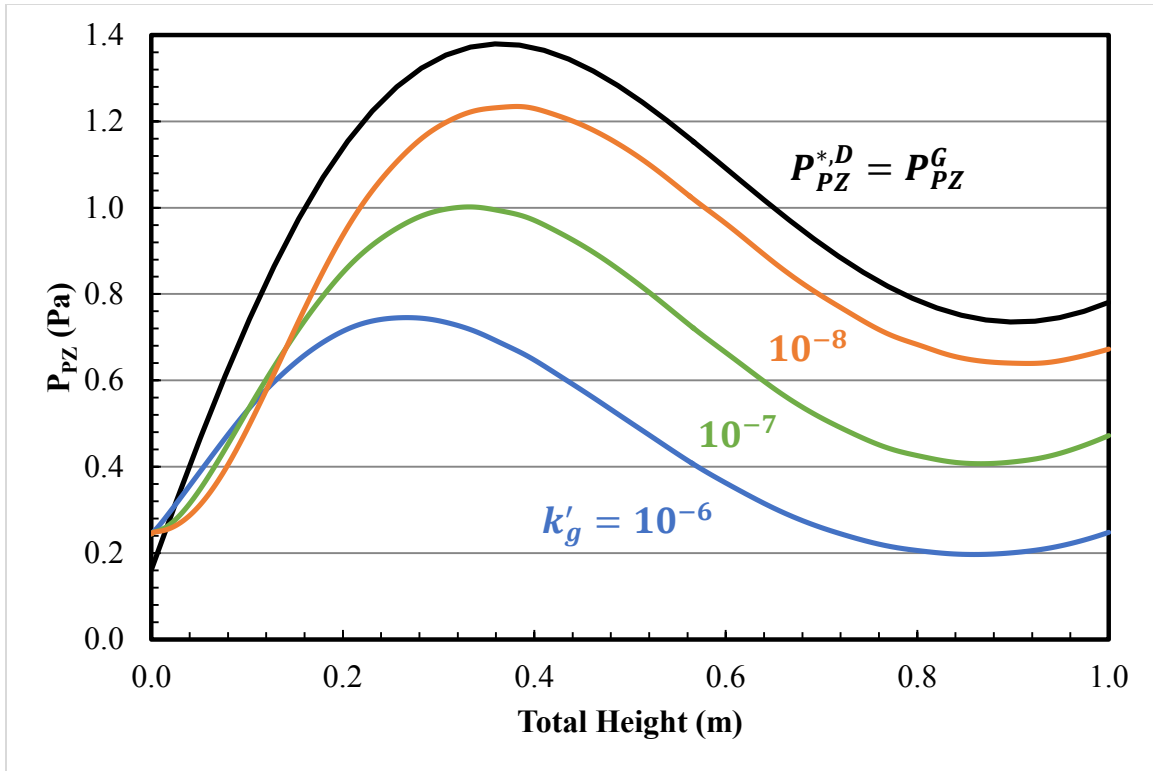


Figure 7.13: Aerosol PZ equilibrium partial pressure as it passes through the absorber for $k'_g = 10^{-6}$, 10^{-7} , and 10^{-8} mol/Pa·m²·s. The black curve is the bulk gas PZ partial pressure.

The ratio of the transfer rate of CO₂ to PZ affects the overall growth rate due to the complicated relationship between loading and the amine partial pressure. For a given k'_g and diffusion coefficient of PZ, the driving forces such that the aerosol loading stays constant can be determined using Equations (7.33)–(7.35). Since loading is defined as the number of moles of CO₂ per alkalinity site, PZ has a factor of 2 accounting for both reactive nitrogen groups. The flux of CO₂ must be twice that of PZ.

$$2 \frac{dn_{CO_2}}{dt} = \frac{dn_{PZ}}{dt} \quad (7.33)$$

$$2\pi(d^D)^2 k'_g (P_{CO_2}^G - P_{CO_2}^{*,D}) = 2\pi D_{PZ,Mix}^G d^D \frac{(P_{PZ}^G - P_{PZ}^{*,D})}{RT^G} \phi(Kn) \quad (7.34)$$

$$\frac{\Delta P_{CO_2}}{\Delta P_{PZ}} = \frac{D_{PZ,Mix}^G \phi(Kn)}{k'_g RT^G d^D} \quad (7.35)$$

where:

- v^D = Drop absolute velocity [m/s]
- a^D = Drop acceleration [m/s²]
- h^D = Height of drop in the column [m]

Figure 7.14 shows the calculated driving force ratio for a constant PZ diffusion coefficient $D_{PZ,Mix}^G = 10^{-5}$ m²/s. Noticeable features include the length scale transition (accounted for by the Fuchs-Sutugin correction) occurring at roughly 0.1 μm. For very small particles, the ratio of the CO₂ to PZ mass transfer rate is constant, irrespective of the droplet diameter. Furthermore, the required driving force for CO₂ is several orders of magnitude higher than for the amine. CO₂ transfer will be limiting to amine systems whose volatility is a very strong function of CO₂; the larger the loading difference between the bulk solvent and the aerosol, the greater the suppression in volatility, which creates larger amine driving forces. The CO₂ driving force can only compensate up to the absolute partial pressure in the bulk gas (on the order of 10⁵ Pa). This further illustrates the complex relationship between the growth rate of the aerosol and the equilibrium (CO₂ solubility and amine volatility) and the mass transfer rate (k'_g). The amine impact on thermodynamic equilibrium and the reaction/diffusion rate causes differentiation in growth behavior for variable amine systems.

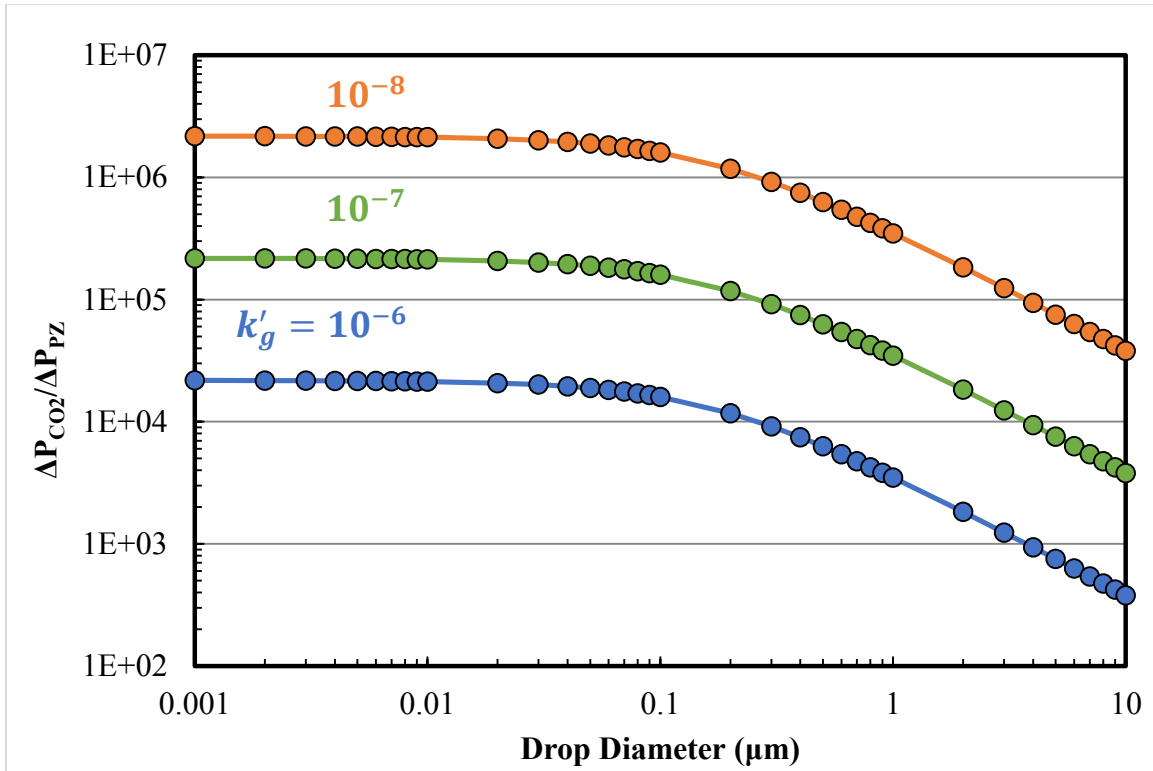


Figure 7.14: Driving forces to maintain aerosol loading: $D_{PZ,Mix}^G = 10^{-5} \text{ m}^2/\text{s}$, $T^G = 40 \text{ }^\circ\text{C}$, $\lambda_{MFP} = 66 \text{ nm}$, and $k'_g = 10^{-6}$, 10^{-7} , and $10^{-8} \text{ mol/Pa}\cdot\text{m}^2\cdot\text{s}$.

Figure 7.14 shows that for submicron particles, the driving force to maintain loading is constant. This is a result of the diameter dependence of PZ mass transfer in the kinetic regime. As particles increase in size, the diameter dependence changes for PZ and the ratio of the CO₂ to PZ driving force drops since the mass transfer rate of CO₂ increases relative to PZ.

The curves for k'_g illustrate the required driving force to maintain CO₂ equilibrium. For example, a 1 Pa driving force for PZ requires a 10⁴ Pa driving force for CO₂ transfer for a submicron drop given a k'_g of 10⁶ mol/s·Pa·m². The effect of the driving force is evident in **Figure 7.12**, where the loading in the aerosol moves further away from equilibrium as it passes through the absorber. A k'_g of 10⁶ mol/s·Pa·m² is

nearly fast enough to maintain equilibrium with bulk gas for a droplet larger than 3 μm . Larger particles will require smaller CO_2 driving forces relative to PZ driving forces to maintain CO_2 equilibrium.

7.11.2 Growth in the Water Wash

Growth in the water wash column is expected to occur by the rapid condensation of H_2O onto the amine/ CO_2 concentrated aerosol leaving the absorber. The main driving force for condensational growth in the water wash is caused by the very dilute amine concentration used in the scrubbing liquid. Traditional water wash columns are designed to remove amine down to low ppm levels for environmental purposes as well as maintaining the overall amine inventory, and thereby lowering makeup rates. Additional driving force for condensation will occur if the water wash is maintained at a different temperature than the absorber to maintain H_2O balance in the amine scrubbing system.

Growth in the water wash was simulated using the same absorber and initial conditions from the sensitivity analysis. A short section of packing with a dilute scrubbing liquid was added above the absorber section. The design specification was to reduce the bulk gas PZ concentration to 1 ppm by varying the packing height.

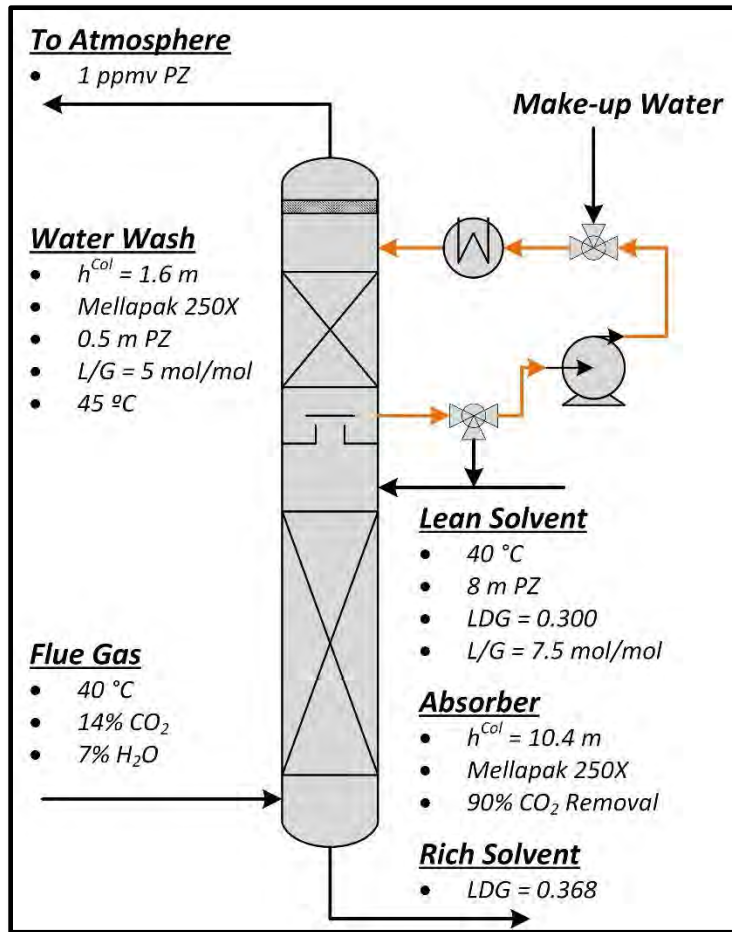


Figure 7.15: Absorber and water wash conditions for growth analysis between the two unit operations. The column heights were set by 90 % CO_2 removal (absorber) and 1 ppm PZ in the outlet gas (water wash).

Figure 7.16 shows the particle diameter as it passes through the absorber and the water wash for variable k'_g . The column position is normalized to the total packed column height. The simulation does not include empty column sections used for column supports, redistributors, or gas-liquid disengagement. The gradients between those sections are also unaccounted for; instant concentration and temperature changes exist at the inlet and outlet of packed sections.

Another limitation of this analysis is that the aerosol is assumed to be uniformly mixed; radial temperature and concentration gradients are assumed negligible in the aerosol phase. The mass transfer resistance is assumed to be entirely in the gas film. If the liquid does provide mass transfer resistance by diffusion and reaction, then the growth rates will be overpredicted. The growth rates presented here represent maximum expected growth rates.

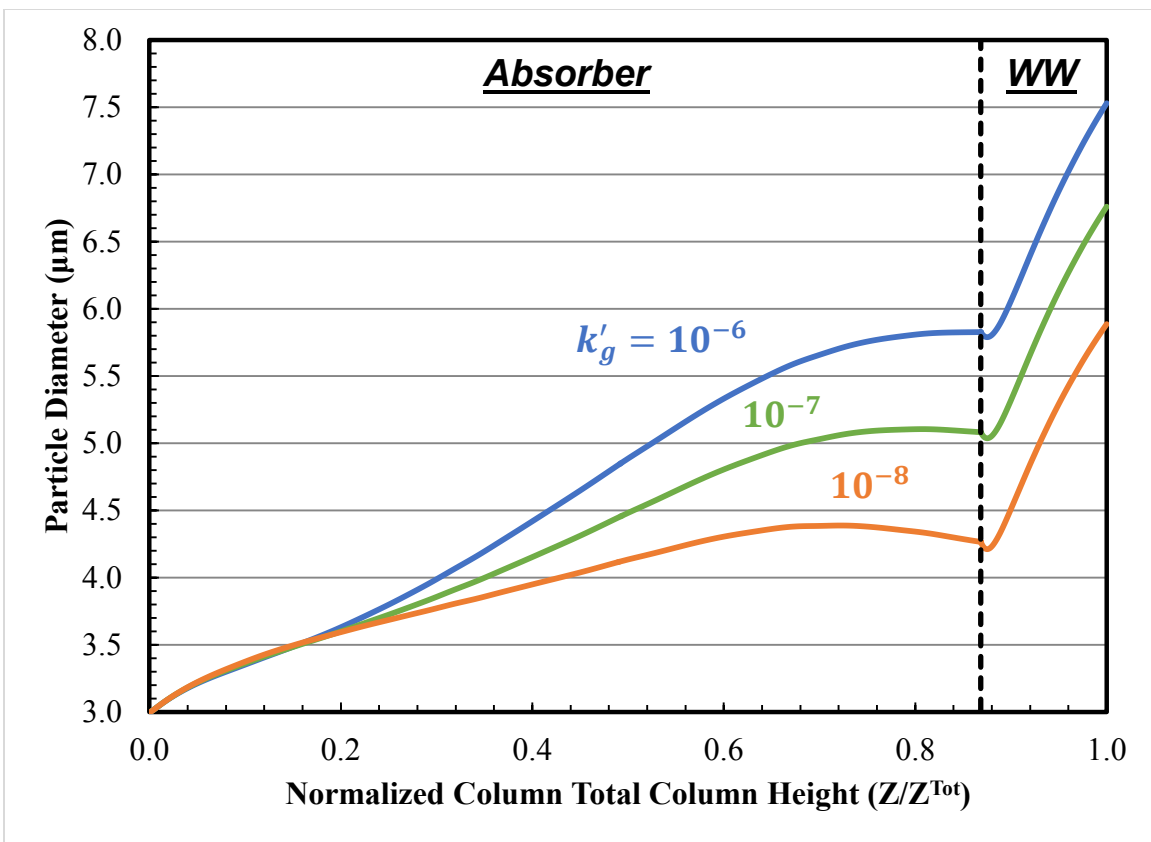


Figure 7.16: Particle growth curves as a function of normalized column position (normalized to the total column height) for $k'_g = 10^{-6}$, 10^{-7} , and 10^{-8} mol/Pa·m²·s.

The growth rate in the water wash is significantly faster than the absorber. The relative and per packed height growth rates are shown below in **Table 7.7**. k'_g plays a

large role in growth inside the absorber; the relative growth varies from 142% to 194 % for k'_g between 10^{-8} and 10^{-6} mol/s·Pa·m². The growth per packed height in the water wash is relatively constant for variable k'_g . However, the condensed volume is still a function of k'_g , or a combination of the different initial PZ concentration and surface area. The major finding is that the growth rate out of the water wash is significantly greater than that in the absorber, nearly an order of magnitude per packed height.

Table 7.7: Final diameter, growth ratio, and growth per packed height for aerosols passing through an absorber and water wash for $k'_g = 10^{-8}$, 10^{-7} , and 10^{-6} mol/s·Pa·m². The initial diameter d_i^D into the absorber was 3 μm.

k'_g	Absorber			Water Wash		
	d_f^D	d_f^D/d_i^D	$\left(\frac{d_f^D - d_i^D}{h^{Col}}\right)$	d_f^D	d_f^D/d_i^D	$\left(\frac{d_f^D - d_i^D}{h^{Col}}\right)$
[mol/s·Pa·m ²]	[--]	[μm]	[μm/m]	[--]	[μm]	[μm/m]
10^{-8}	4.266	1.422	0.122	5.886	1.379	1.027
10^{-7}	5.082	1.694	0.200	6.760	1.330	1.067
10^{-6}	5.827	1.942	0.272	7.530	1.292	1.083

Another consequence of faster condensation is a larger temperature difference between the aerosol and the bulk gas. **Figure 7.17** shows the bulk gas temperature profile as well as the temperature difference between the aerosol and the bulk gas. The ΔT is very small in the absorber since the rate of condensation/evaporation is slow. As the aerosol passes into the water wash, the immediate change in saturation causes a very sharp jump in the ΔT curves followed by a region where significant mass transfer is occurring. In that region, the ΔT is nearly 0.65 °C for the maximum condensation rate.

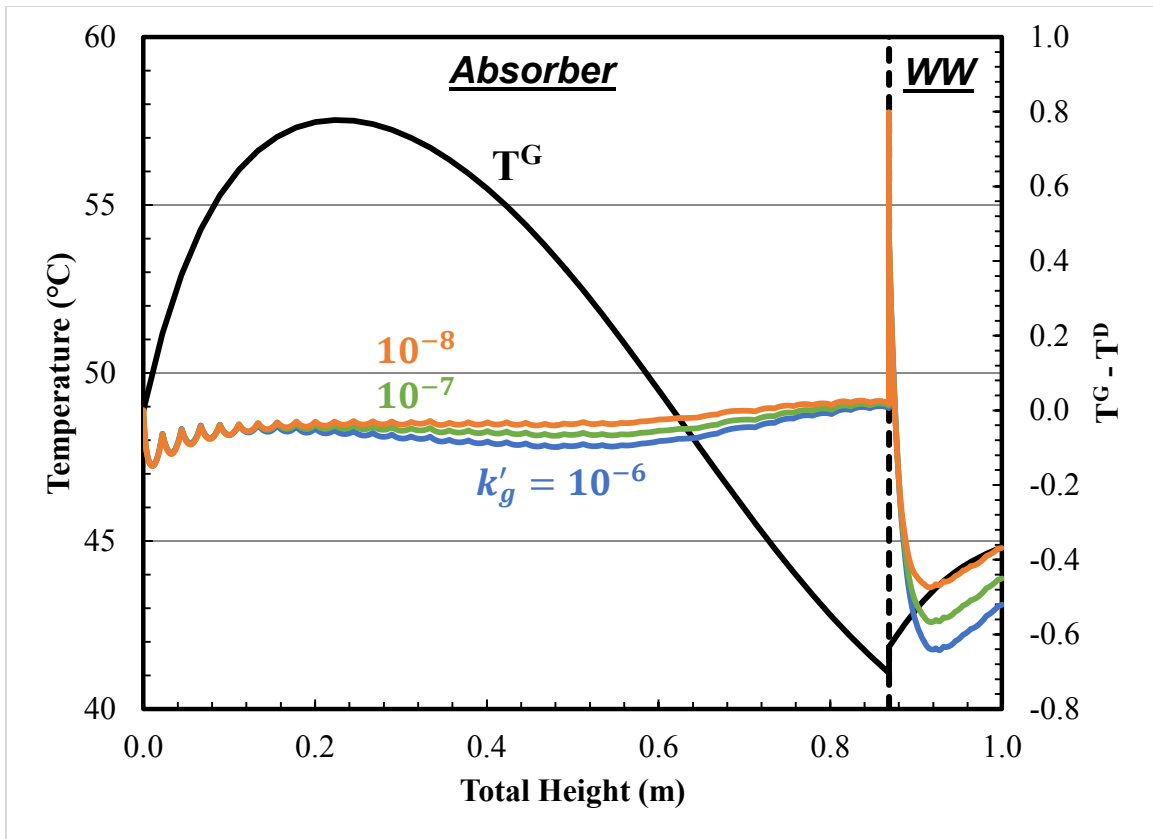


Figure 7.17: Bulk gas temperature profile and the temperature difference between the gas and aerosol for $k'_g = 10^{-6}$, 10^{-7} , and 10^{-8} mol/Pa·m²·s.

Figure 7.18 and Figure 7.19 show the expected trends in the water wash; the CO₂ loading approaches equilibrium and the equilibrium partial pressure of PZ drops in the water wash, approaching the 1 ppmv design specification. The sharp change in the equilibrium curves are due to the absence of gradients between the absorber and water wash packed sections.

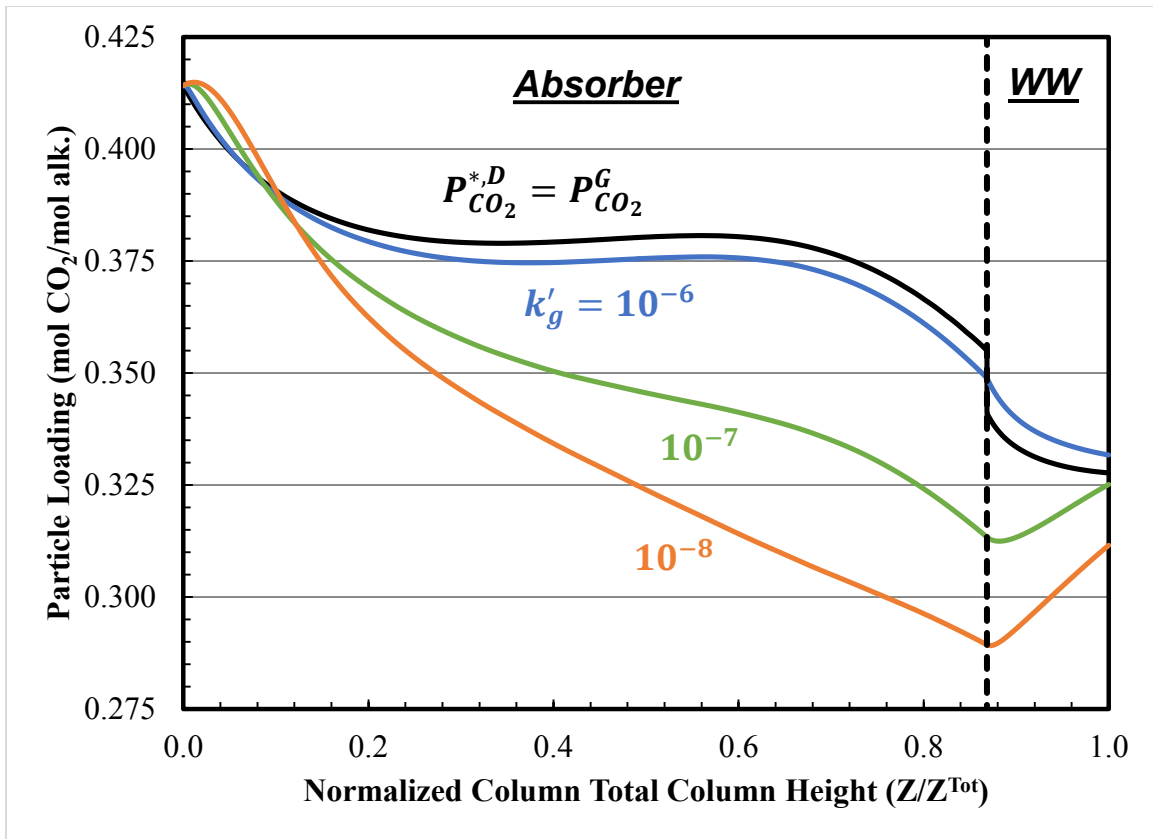


Figure 7.18: Aerosol CO₂ loading as it passes through the absorber and water wash for $k'_g = 10^{-6}$, 10^{-7} , and 10^{-8} mol/Pa·m²·s. The black curve represents the CO₂ loading which produces an equilibrium partial pressure equivalent to the bulk gas CO₂ concentration.

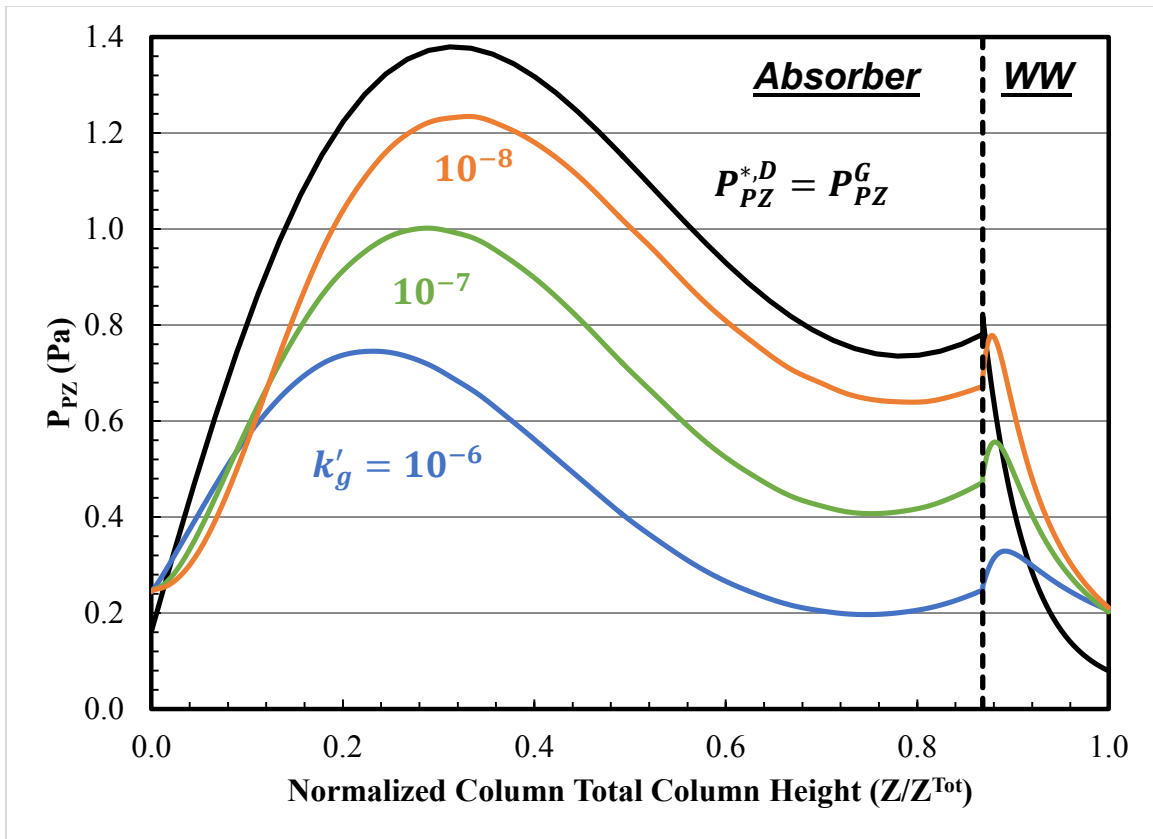


Figure 7.19: Aerosol PZ equilibrium partial pressure as it passes through the absorber and water wash for $k'_g = 10^{-6}$, 10^{-7} , and 10^{-8} mol/Pa·m²·s. The black curve is the bulk gas PZ partial pressure.

7.11.3 Water Wash Design Effects

The growth rate in the water wash is significantly faster than in the absorber. By diluting the solvent (increased H₂O saturation) and by increasing the packed column height (increased residence time), the aerosol should continue to grow.

7.11.3.1 Increasing Packed Height

Using the same sensitivity analysis case as before, assuming a constant $k'_g = 10^{-6}$ mol/s·Pa·m², the water wash height was approximately doubled to 3 m. Increasing the packing height from 1.6 to 3.0 m resulted in additional aerosol growth of 13.69%, as

shown in **Figure 7.20**. The initial diameter into the water wash was 5.890 μm ; at 1.6 m the diameter was 7.694 μm and at 3.0 m the diameter was 8.739. The change in diameter per unit of packed height was 1.125 $\mu\text{m}/\text{m}$ in the bottom section and slowed to 0.855 $\mu\text{m}/\text{m}$ in the additional 1.4 m of packed height, indicating that the growth rate slows as equilibrium is approached towards the top of the column. The addition of packed height shows diminishing returns; however, the trade-off judgement would require a more stringent economic and emissions analysis.

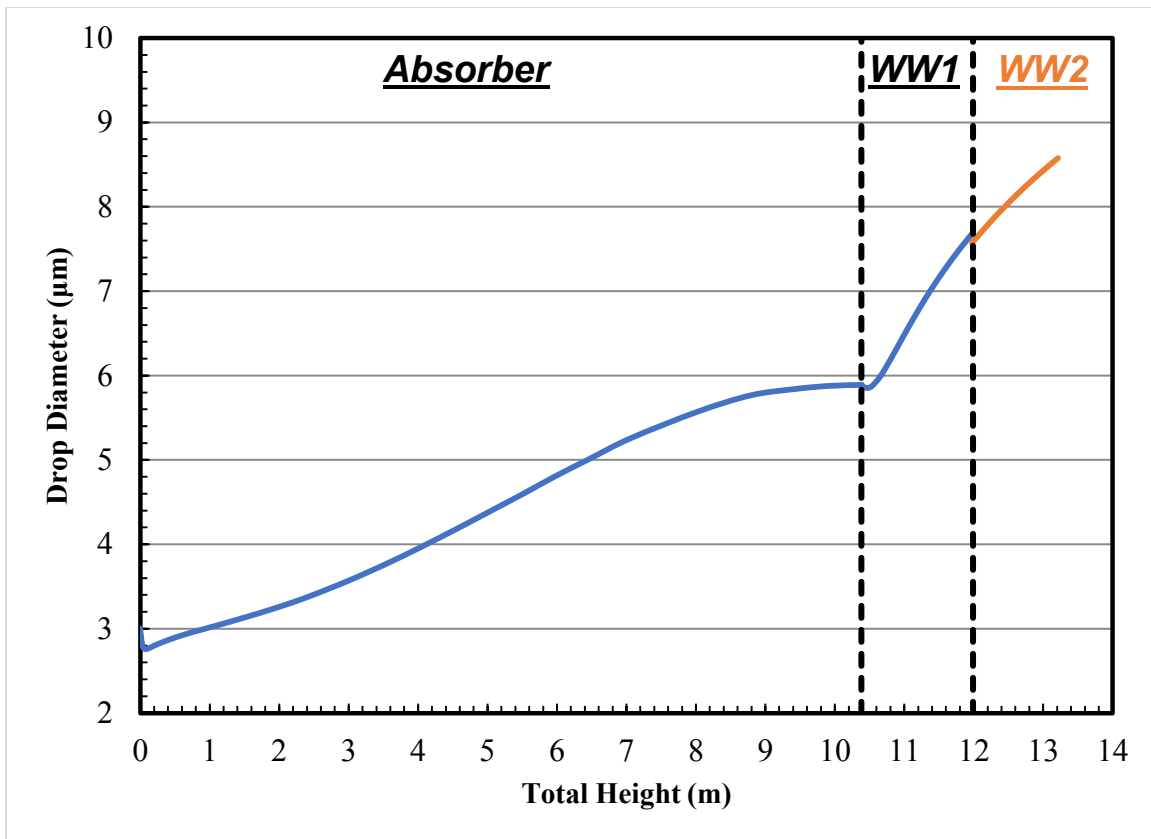


Figure 7.20: The addition of more packing height in the water wash can significantly increase the final diameter of aerosols leaving the amine scrubbing system. Condensation of H_2O continues with increased residence time.

7.11.3.2 Changing Water Wash Solvent Concentration

The water wash solvent concentration was varied to explore the effect of changing H₂O saturation in the gas. The amine concentration in the wash was doubled to 0.5 m PZ from the initial sensitivity case (0.25 m PZ) and the column height was adjusted to match the outlet drop diameter. **Figure 7.21** shows the aerosol droplet diameter passing through the water wash with two different inlet PZ concentrations; the column height is absolute, not normalized.

An additional 0.5 m of packing (31.25%) was required to match the outlet diameter when the PZ concentration in the wash was doubled. Increasing the solvent concentration in the water wash lowers the activity of H₂O in the solvent and therefore the fugacity in the gas phase. The driving force for condensation onto the aerosol decreases and the growth rate slows.

If the water wash is designed for growth and capture of aerosols, the solvent concentration should be kept as low as possible and the column height should be increased.

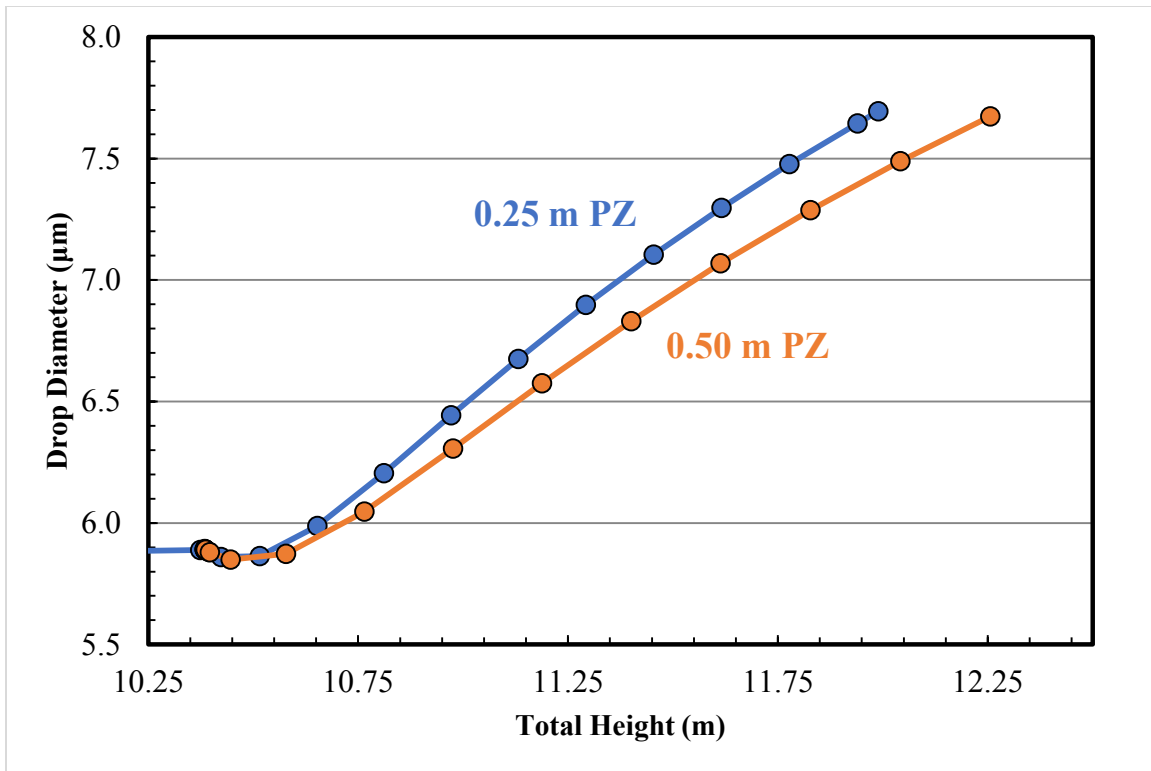


Figure 7.21: Variations in the water wash solvent concentration alter the aerosol growth rate. Dilution of the solvent increases the activity of H₂O and therefore the driving force for condensation onto the amine/CO₂ concentrated aerosol. $k'_g = 10^{-6}$ mol/s·Pa·m².

7.11.4 Growth Rate Extrapolation

The growth model was tested using different initial diameters to verify that the growth rate extrapolated correctly according to the mass transfer limitation. Growth curves are also very useful for estimating the total emissions from an absorber with an assumed initial PSD and total density; that calculation will be explored at the end of this chapter.

Several possible cases exist: (1) continuum approximated, gas-side mass transfer for larger drops ($> 1 \mu\text{m}$), (2) kinetic approximated, gas-side mass transfer for small drops ($< 1 \mu\text{m}$), and (3) reaction/diffusion approximated mass transfer modeled using k'_g .

7.11.4.1 Maxwell Solution – Continuum Approximation ($Kn \rightarrow 0$)

The continuum approximation for mass transfer follows the Maxwell solution. Equations (7.36) and (7.37) show an abridged derivation of the final growth expression given by Equation (7.38). A Sherwood number of 2 is assumed and substituted for the mass transfer coefficient. The square of the initial and final diameter are linearly related. This mechanism would be consistent with a limiting rate determined by the gas film diffusion of piperazine.

$$\frac{d(\rho^D V^D)}{dt} = \frac{A^D k_{g,i}}{RT^G} (P_i^G - P_i^*) \quad (7.36)$$

$$\frac{d(d^D)}{dt} = \frac{4D_{i,Mix}^G}{d^D \rho^D RT^G} (P_i^G - P_i^*) \quad (7.37)$$

$$(d_f^D)^2 = (d_i^D)^2 + \int_{t_i}^{t_f} \frac{8D_{i,Mix}^G}{\rho^D RT^G} (P_i^G - P_i^*) \quad (7.38)$$

where:

$$d_f^D = \text{Final droplet diameter } [\mu\text{m}]$$

$$d_i^D = \text{Initial droplet diameter } [\mu\text{m}]$$

7.11.4.2 Maxwell Solution – Kinetic Approximation ($Kn \rightarrow \infty$)

Kinetic theory of mass transfer can be modeled using continuum fluid theory adjusted by a length scale factor as shown in Equation (7.39) (Fuchs-Sutugin correction). Taking the limit of the Knudsen number as it approaches infinity, the final growth expression is obtained below (Equation (7.41)). The initial and final diameter are linearly related.

$$\frac{d(\rho^D V^D)}{dt} = \frac{A^D k_{g,i}}{RT^G} (P_i^G - P_i^*) \phi(Kn) \quad (7.39)$$

$$\frac{d(d^D)}{dt} = \frac{2D_{i,Mix}^G}{\rho^D RT^G \lambda_{MFP}} (P_i^G - P_i^*) \quad (7.40)$$

$$d_f^D = d_i^D + \int_{t_i}^{t_f} \frac{2D_{i,Mix}^G}{\rho^D RT^G \lambda_{MFP}} (P_i^G - P_i^*) \quad (7.41)$$

7.11.4.3 CO₂ Reaction/Diffusion Limited (k'_g)

The final mass transfer limitation case is an approximation used to model CO₂ transfer which is limited by a combination of reaction and diffusion. In this work, a constant parameter (k'_g) was used to approximate the total mass transfer resistance. The final growth expression is shown in Equation (7.44). The initial and final diameters are linearly related.

$$\frac{d(\rho^D V^D)}{dt} = \frac{A^D k'_g}{RT^G} (P_i^G - P_i^*) \quad (7.42)$$

$$\frac{d(d^D)}{dt} = \frac{2k'_g}{\rho^D RT^G} (P_i^G - P_i^*) \quad (7.43)$$

$$d_f^D = d_i^D + \int_{t_i}^{t_f} \frac{2k'_g}{\rho^D RT^G} (P_i^G - P_i^*) \quad (7.44)$$

7.11.4.4 Extrapolation Case Study

Using the same conditions from the sensitivity analysis (including the water wash), the initial diameter was varied and plotted against the final diameter. A constant k'_g of 10^{-7} mol/s·Pa·m² was assumed. **Figure 7.22** shows the plot of the initial and final diameters. The growth expression for the modeled sensitivity case follows the integral growth laws for kinetic theory or CO₂ (k'_g) limited transfer. The growth constant, which is a function of the specific driving forces throughout the column, is 22.78.

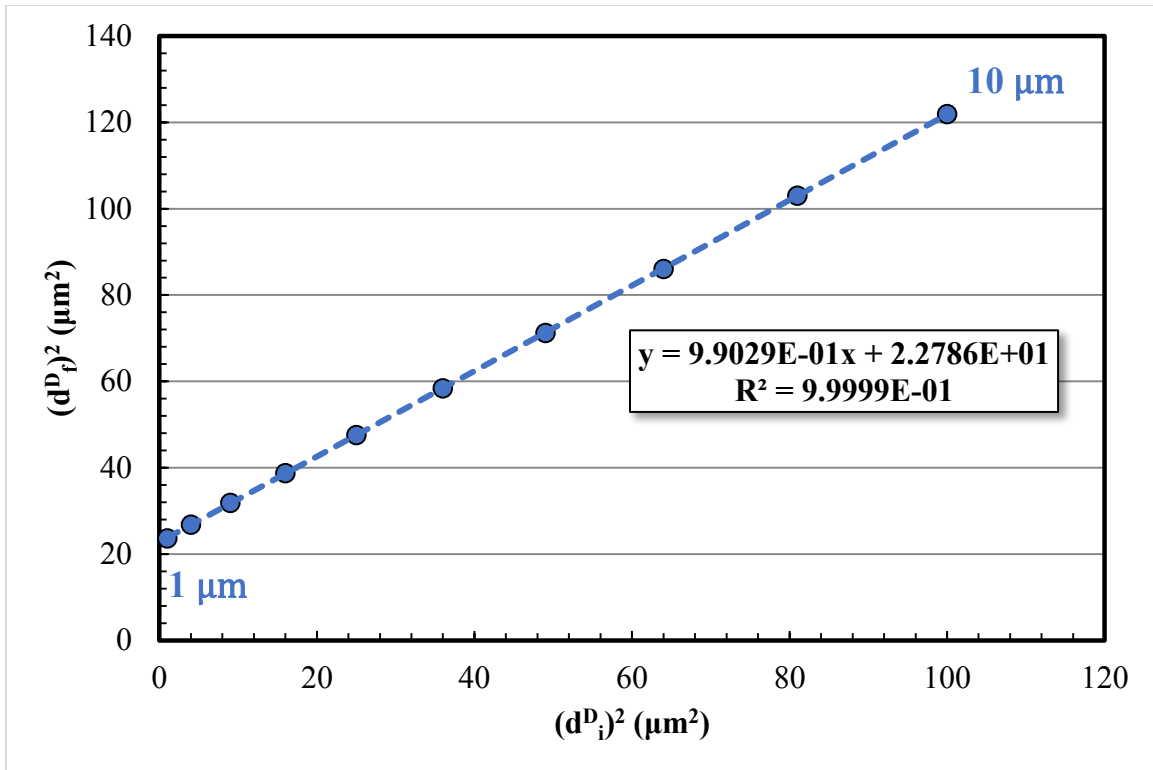


Figure 7.22: The square of the final and initial aerosol diameters are linearly related for the sensitivity case study with the included water wash tower. The squared relationship indicates a gas-side component transfer limitation in the growth rate.

7.11.5 Growth Rate Theory – Absorber Driving Forces

Aerosol growth is hypothesized to be dependent on the condensation driving force between the gas and the aerosol, which is a function of the bulk gas and liquid contacting process and the specific amine system used, particularly the dependence of the amine volatility with loading.

CO₂ solubility of the amine affects the solvent flow rate, which in turn affects the enthalpy transfer (and temperature bulge) in the column. Additionally, the heat of absorption affects the amplitude of the temperature bulge and the reaction kinetics and solvent rate affect the location of the temperature bulge. The interrelationship between

temperature, loading, and amine volatility determine the equilibrium partial pressure above the bulk solvent; the gas temperature and CO₂ composition determine the equilibrium partial pressure above the aerosol. Three case studies will be presented here to develop the hypothesis: (1) a generic non-intercooled absorber with water wash (sensitivity case), (2) a non-intercooled absorber (SRP pilot plant), and (3) the SRP pilot plant with intercooling at the middle of the column. These three cases will illustrate the aerosol growth dependence on the availability of CO₂ and PZ in the gas phase in relation to the temperature profile resulting from operating conditions, or in the specific case, the addition of solvent intercooling.

7.11.5.1 Case 1 – Generic Absorber

The generic absorber used in Case 1 is the same absorber described in the sensitivity analysis (**Figure 7.9**).

To begin, it is useful to consider the bulk transfer process before looking at specific aerosol results. A higher L/G ratio moves the temperature bulge down the column towards the rich end (**Figure 7.23**). Given that CO₂ loading, temperature, and liquid PZ concentration do not change significantly in the water wash, those profiles will be excluded.

P_{PZ}^* above the solvent is a strong function of loading and temperature. **Figure 7.24** shows those effects where the temperature bulge is directly visible near the bottom half of the column and the increase in P_{PZ}^* near the top of the column is a direct result of the solution loading.

In order to replenish the driving force for H₂O concentration, salt species must continually accumulate in the aerosol liquid. Acid-base reactions of PZ and CO₂ form the required salt species. It is predicted that areas of highest PZ and CO₂ availability will

grow fastest. **Figure 7.25** shows the P_{PZ} and P_{CO_2} profiles in the column and regions of expected growth rates.

Plotting the diameter as it passes through those predicted growth regions shows reasonably accurate predictions. At the top of the column, the sharp decrease in P_{CO_2} actually seems to cause aerosol shrinkage. This is due to the loading decrease in the aerosol liquid which would reduce the driving force for amine condensation. Additionally, the gas temperature is above the liquid temperature at the top of the column; since the aerosol temperature is approximately equal to the gas, P_{H_2O} above the aerosol is increased relative to the solvent due to the temperature difference. Therefore, as the amine driving force decreases with loading, the salt accumulation rate decreases and P_{H_2O} increase relative to the solvent. Those two effects lead to a slowing of the growth rate, or in this particular case, evaporation back towards the bulk solvent.

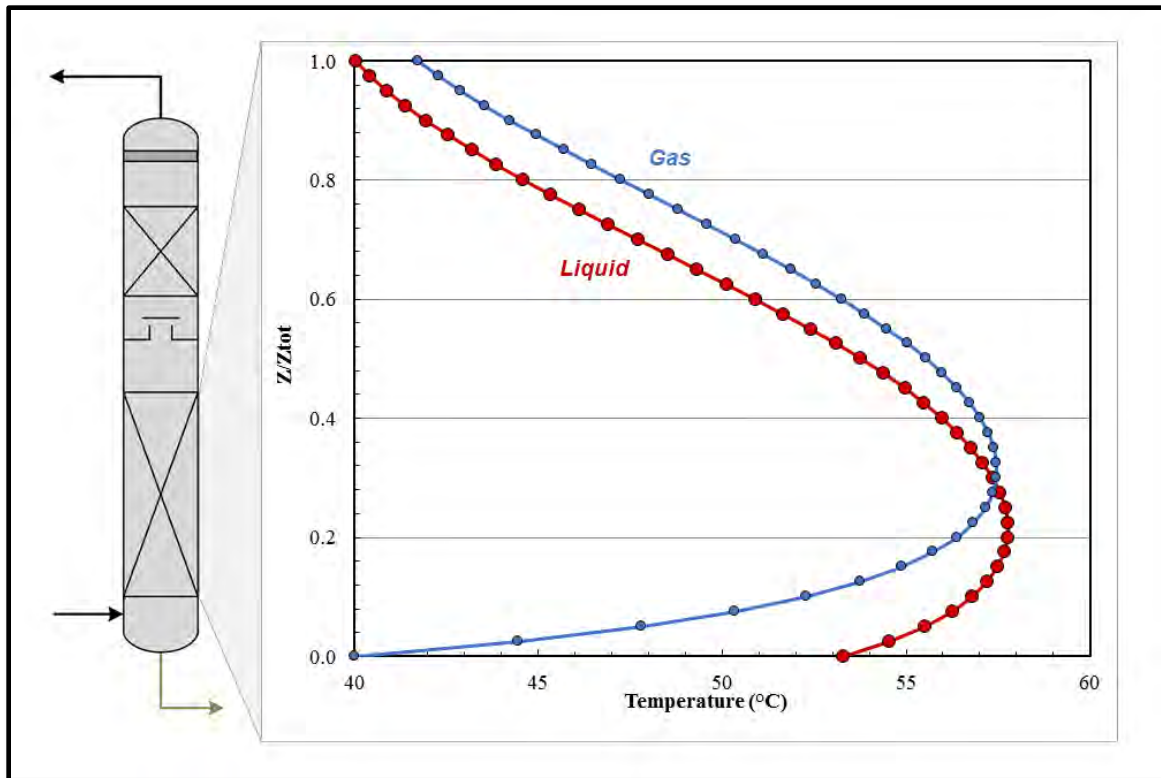


Figure 7.23: The temperature bulge location is a function of L/G, phase heat capacities, inlet temperatures, and the reaction rate and enthalpy. A large L/G (8 mol/mol) moves the temperature bulge towards the bottom of the column.

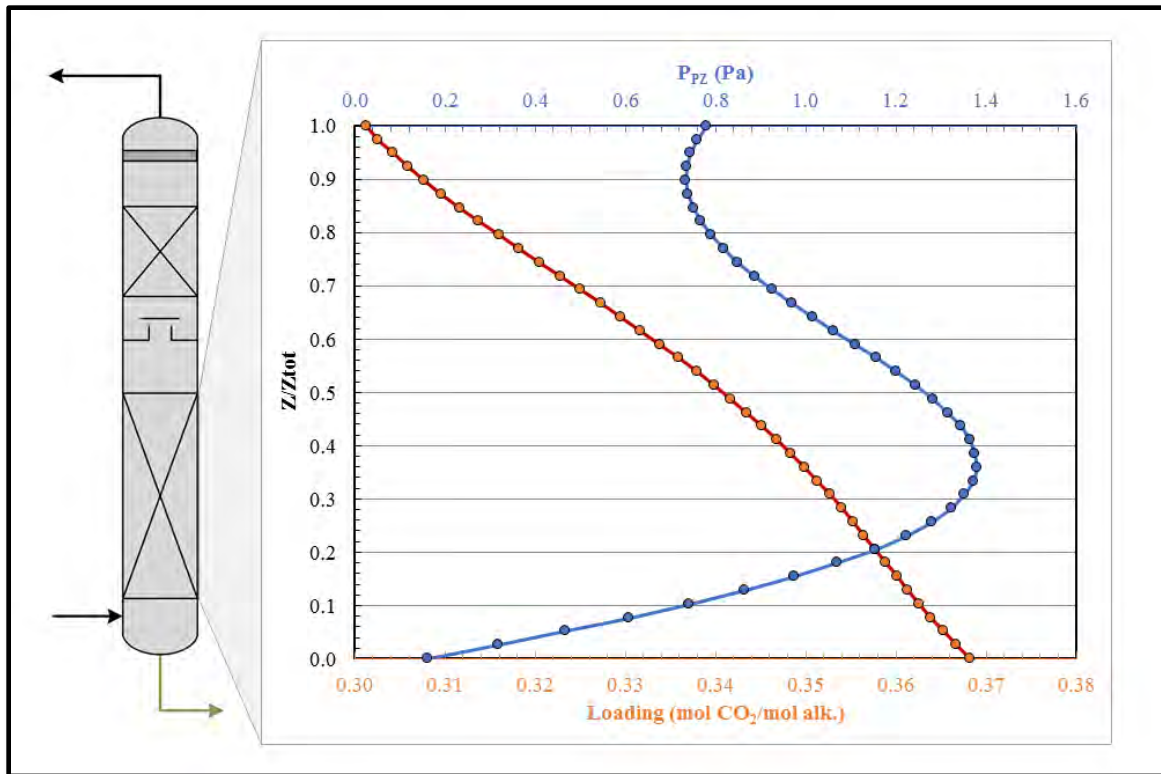


Figure 7.24: The partial pressure of PZ is a strong function of the liquid loading and temperature. The temperature bulge is directly reflected in the P_{PZ} curve. The inflection at the top of the column is caused by the rapid decrease in loading.

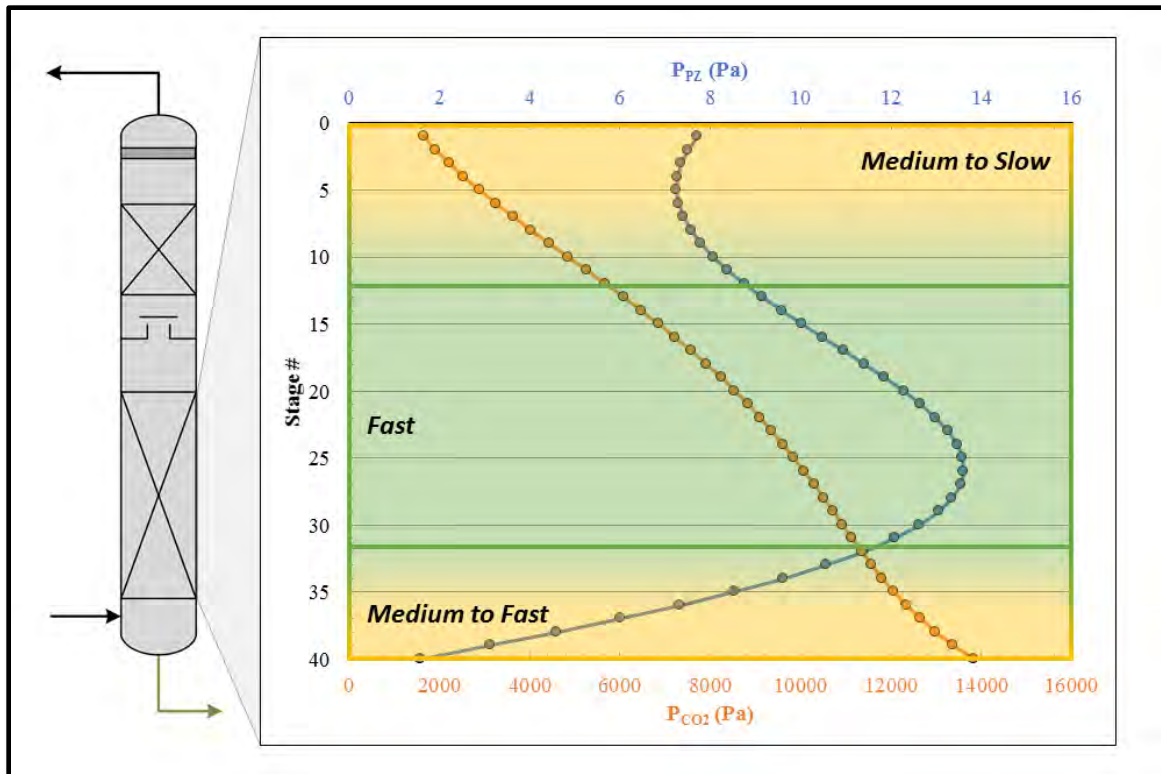


Figure 7.25: Condensation onto aerosols requires a continuous driving force. Accumulation of salts (CO_2 and PZ) increases the driving force for H_2O condensation. Areas in the column with the highest CO_2 and PZ content will grow the fastest.

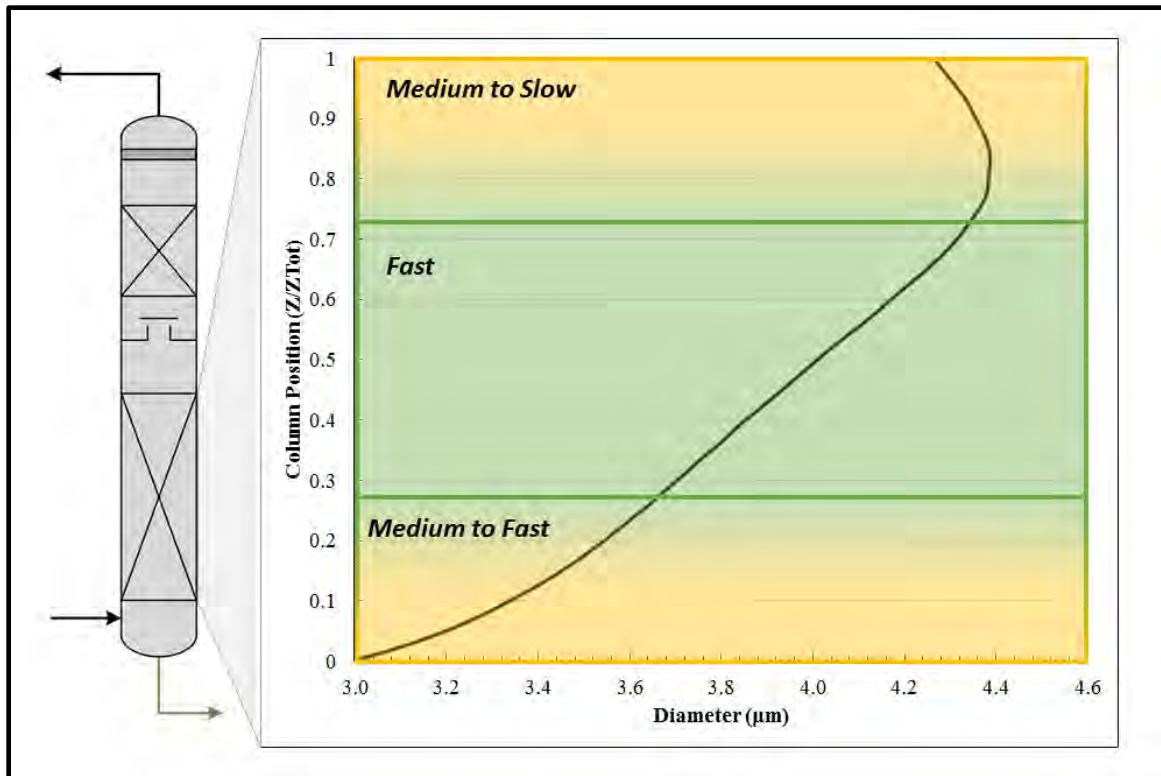


Figure 7.26: The gradient blocks indicate regions of high concentration of CO₂ and PZ which is theorized to cause aerosol growth. The aerosol actually shrinks at the top of the absorber where P_{CO₂} is lowest, even though P_{PZ} is still relatively high.

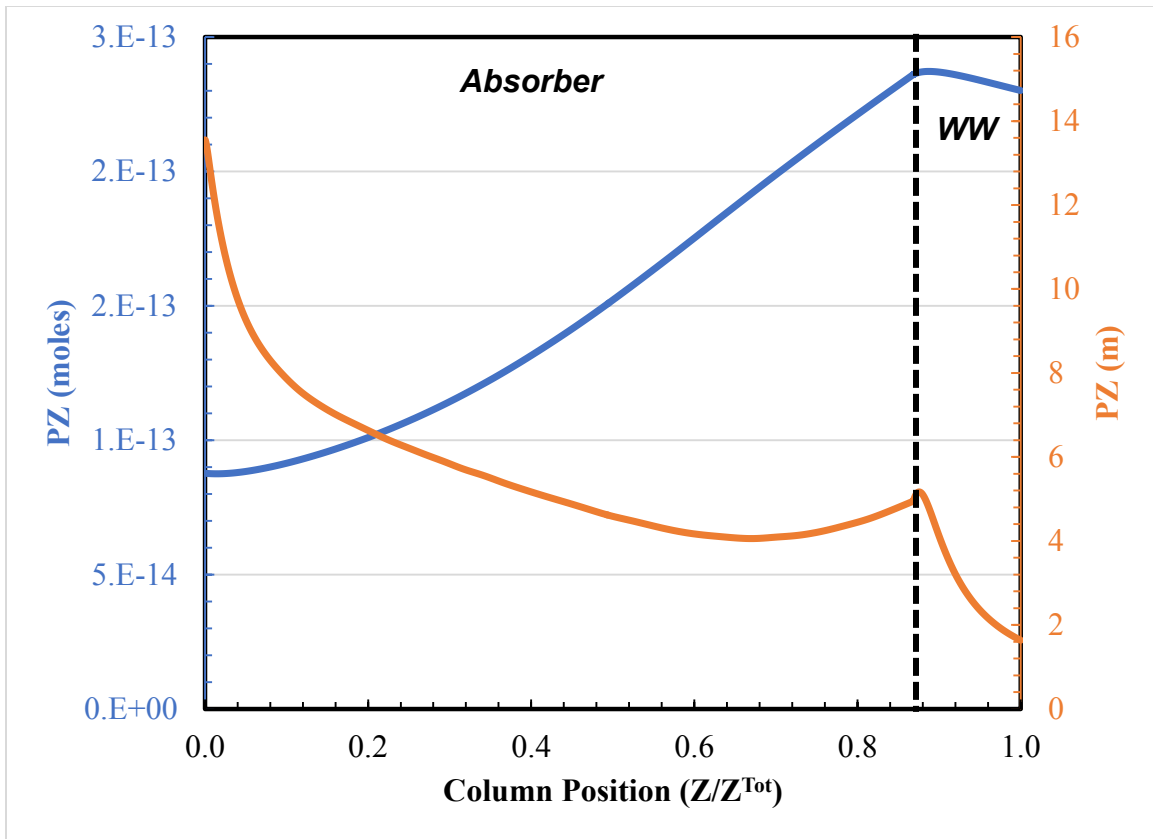


Figure 7.27: The PZ concentration in the aerosol droplet changes as it moves through areas of changing saturation in the absorber. In the water wash, accumulation of H₂O occurs very rapidly which is reflected in the molality curve. The dilution suppresses PZ volatility such that PZ does not transfer readily out of the aerosol. The total moles of PZ remains relatively constant in the water wash.

7.11.5.2 Case 2 and 3 – The Effect of Intercooling

Cases 2 and 3 illustrate the effect of intercooling on the aerosol growth rate. As a concrete example, and to show the model is capable simulating real-life absorber profiles, the absorber column at the SRP pilot plant was modeled in Aspen Plus[®] and validated against pilot plant data. The SRP model was used to investigate the influence of intercooling on the diameter change inside the packed section. Case 2 refers to the steady state condition employing no intercooling, referred to as NIC (non-intercooled), and Case 3 refers to the same conditions but with full intercooling, referred to as IC (intercooled).

Traditional, full-draw, in-and-out intercooling was used in the IC case with no other parameters changed. As a consequence of intercooling, the CO₂ removal rate increases because the mass transfer pinch caused by the temperature bulge is suppressed by the cooling of the solvent back to 40 °C at the middle of the column.

Figure 7.28 shows the input conditions for the NIC/IC cases along with the simulated rich loading and CO₂ removal for either case.

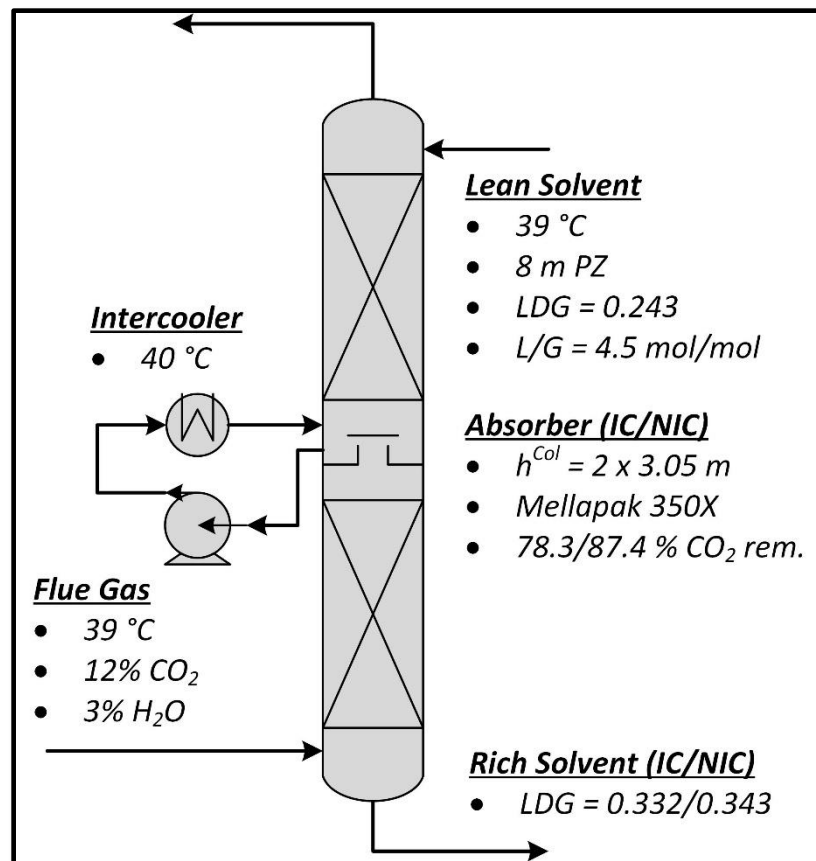


Figure 7.28: IC/NIC input conditions and simulated rich loading and CO₂ removal percentages. In-and-out intercooling was added to the NIC case without any parameter changes to yield the IC case.

As described in Case 1, aerosol growth is dependent on continual absorption of H₂O, which can be accomplished in two ways: (1) decreasing the droplet temperature relative to the gas, or (2) accumulating other species (CO₂ and amine), thereby lowering H₂O activity.

The temperature effect is usually dampened by conductive heat transfer. The heat transfer coefficient for aerosols is quite large. Even for moderate rates of evaporation/condensation, the droplet temperature is nearly equivalent to the gas, and therefore that situation rarely exists for moderate driving forces.

$P_{\text{H}_2\text{O}}^*$ over the aerosol is suppressed as other components lower the mole fraction, or activity, of H₂O. Absorption of CO₂/PZ accomplishes this task. Referring back to Case 1, it was shown that PZ volatility is a strong function of CO₂ loading. In areas of high loading, or otherwise fast CO₂ absorption, PZ volatility is minimized. Since aerosols are assumed to transfer CO₂ at appreciable rates, P_{PZ}^* over the droplet will be significantly reduced relative to the bulk gas, which is in equilibrium to the nominal solvent loading. Solvent loadings are chosen such that $P_{\text{CO}_2}^*$ above the liquid is always under-saturated relative to the gas; absorption of CO₂ takes place over the length of the column.

Tying together all of the above discussion, the loading in the aerosol will always be higher than the bulk solvent because of the relative CO₂ mass transfer rate-to-fluid volume ratio. Consequently, P_{PZ}^* over the aerosol will be much smaller than that relative to the bulk liquid. It follows then, that the aerosol will have a continuous driving force for PZ absorption given that (1) P_{CO_2} in the gas remains high and (2) the ratio of CO₂ and PZ mass transfer rates is always greater than the stoichiometric ratio (1:2 for PZ).

Temperature profiles for the NIC and IC cases are shown in **Figure 7.29**, below. The use of intercooling suppresses temperature bulging in the entire column since heat is taken out at the middle draw-off point.

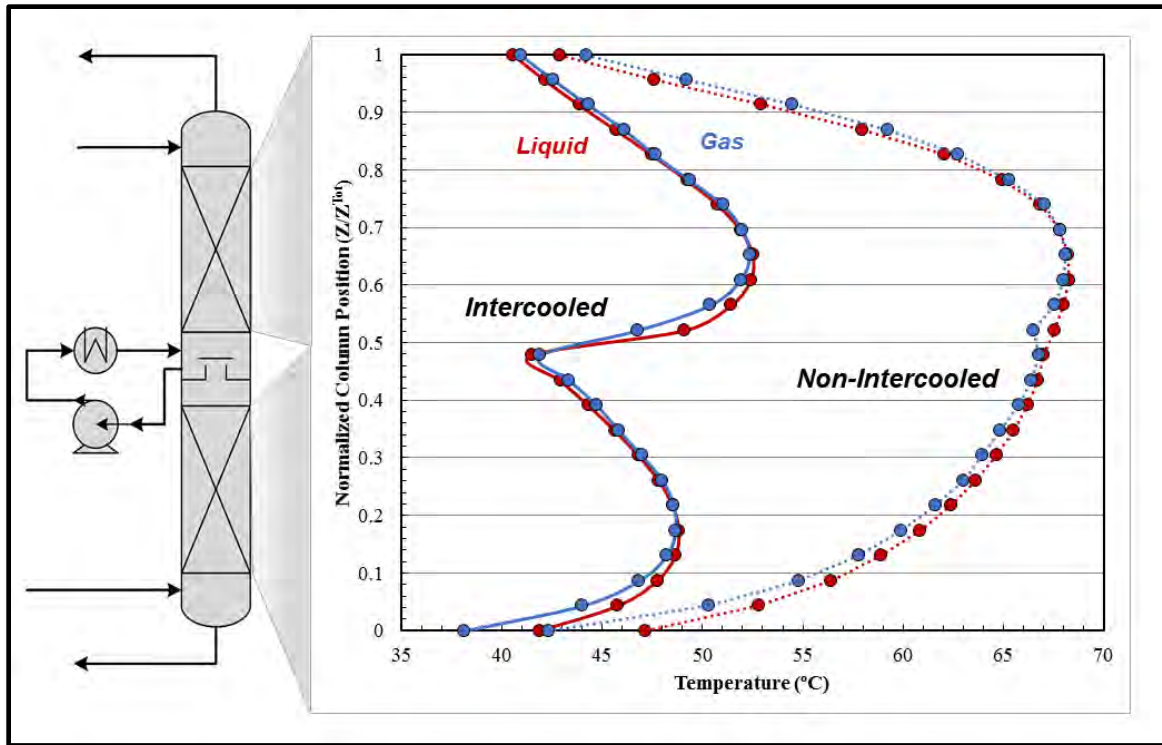


Figure 7.29: Temperature profiles for the NIC and IC SRP absorber cases. Intercooling suppresses temperature bulging throughout the entire column.

Removing heat also removes the mass transfer pinch for CO₂ absorption caused by the relationship between CO₂ solubility and temperature. The gas phase concentration of CO₂ and PZ are thus both affected by intercooling. The profiles for those two component are shown in **Figure 7.30** for both the NIC and IC cases. Intercooling reduces P_{PZ} throughout the column even though P_{CO₂} remains similar to the NIC case.

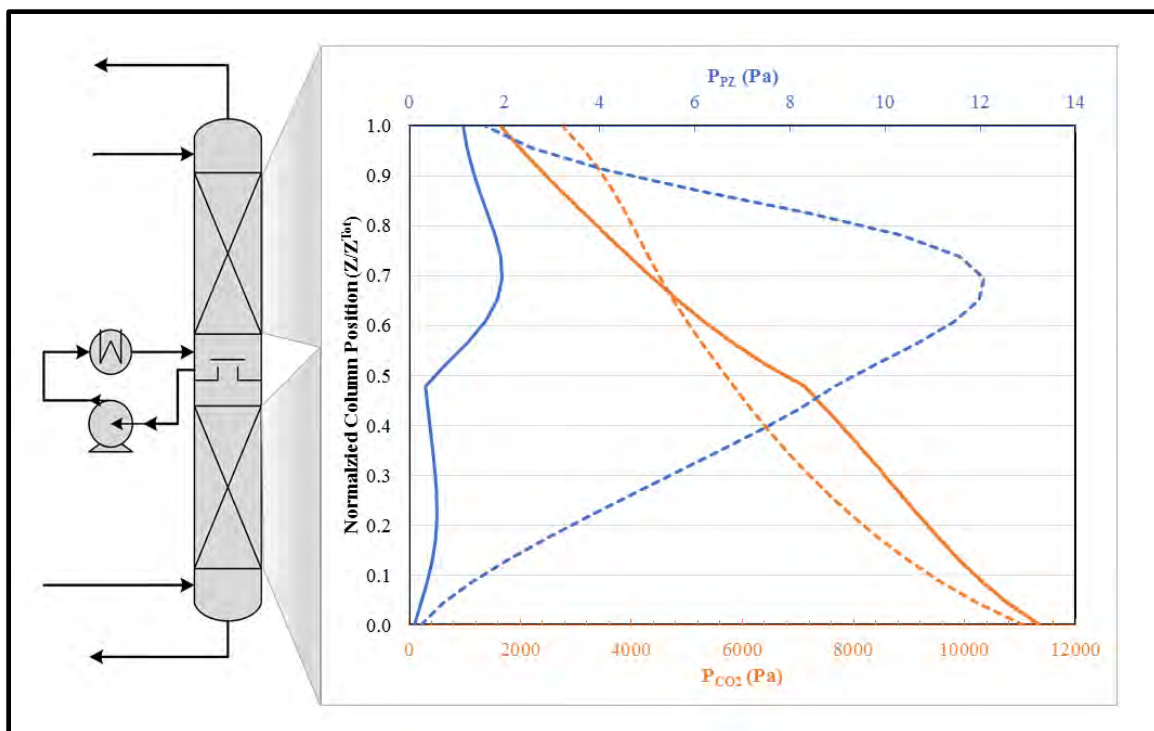


Figure 7.30: P_{PZ} and P_{CO_2} curves for the NIC (solid lines) and IC (dashed lines) cases. Intercooling suppresses PZ volatility over the solvent due to the increased loading (faster absorption) and reduced temperatures.

Integration using the aerosol growth model for a $3 \mu\text{m}$ initial drop produces the diameter curves in **Figure 7.31**. The NIC case grows an additional $0.62 \mu\text{m}$ compared to the IC case. The difference in growth is most notable near the middle of the column where the temperature bulge is located in the NIC case. There, both P_{CO_2} and P_{PZ} are high and condensation driving forces are largest.

Figure 7.33 shows relatively little difference in growth rate for small droplets. Recall from the modeling Equations (7.41) and (7.44) that the transfer rate of gas-film controlled components is first-order in diameter, while CO_2 transfer is proportional to the area, or square of the diameter. As particles shrink, the ratio of CO_2 to PZ transfer decreases. In order to maintain equilibrium to CO_2 , the driving force for transfer must

increase. Using the assumption of a fixed k'_g of 10^{-7} mol/s Pa m², the aerosol growth rate for small particles is controlled by CO₂ transfer, not amine absorption.

Aerosols grow faster in non-intercooled columns due to differences in solvent composition and temperature. Non-intercooled columns have much larger absolute temperature differences and are less efficient at removing CO₂. The resulting rich loading is less for a non-intercooled absorber while holding all other variables constant. PZ available in the gas phase is higher across the absorber caused by loading/temperature effects. Aerosols passing through a non-intercooled column experience larger driving forces for PZ absorption and therefore H₂O transfer.

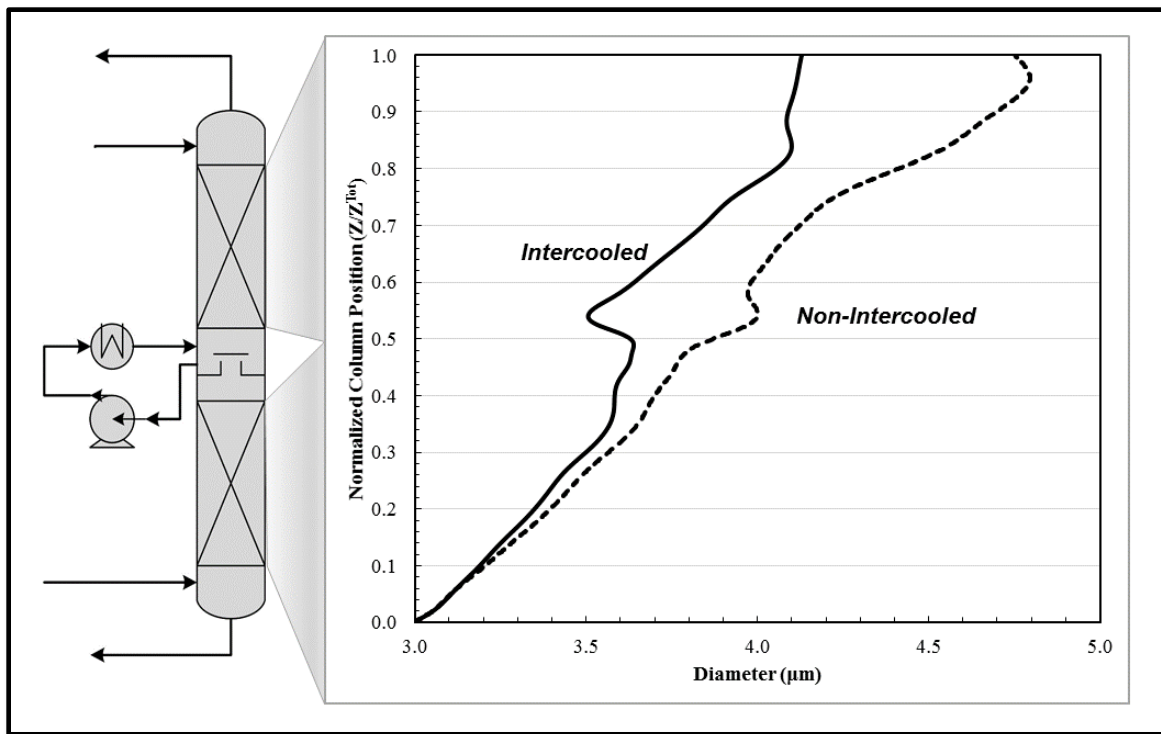


Figure 7.31: Droplets in non-intercooled columns grow larger due to the increased availability of condensable amine. The lower CO₂ capture rate also supplies more CO₂ for acid-base reaction with the amine.

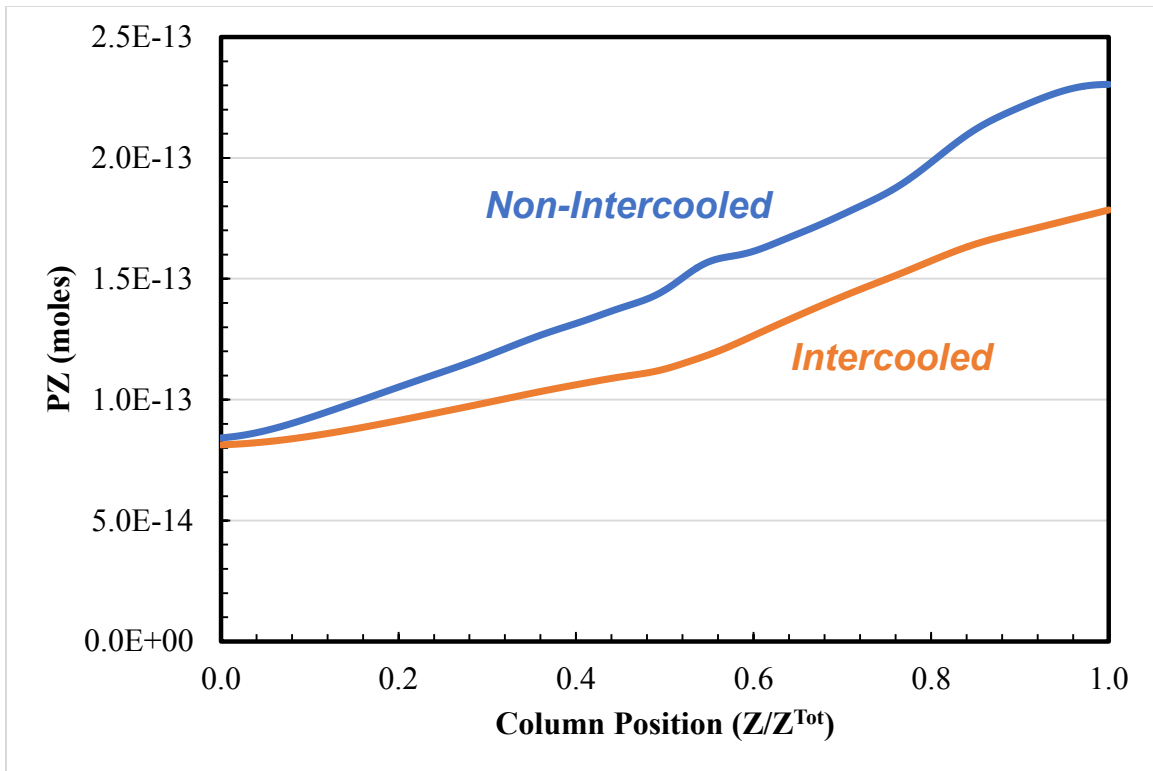


Figure 7.32: More PZ accumulates in the non-intercooled case. However, PZ accumulates for both absorber cases due to the PZ driving force created by the loading difference between the aerosol and the bulk liquid.

The integration procedure can be carried out for a range of diameters to produce the growth curves shown in **Figure 7.33**. These curves can be used to estimate the emissions from the column assuming a PSD and a total particle density.

Figure 7.34 shows the total moles of PZ and the PZ molality in the final droplet as a function of the initial droplet diameter. The total moles of PZ increases as expected, since the initial droplet increases and grows linearly with the initial diameter. The molality in the final droplet remains constant, but uniformly different for the NIC and IC cases. The average final molality for the NIC case was 6.4 m PZ versus 8.3 m PZ for the IC case. Because the total mole curves are very similar between the NIC and IC cases, the difference in molality is caused by less H_2O condensation in the IC case.

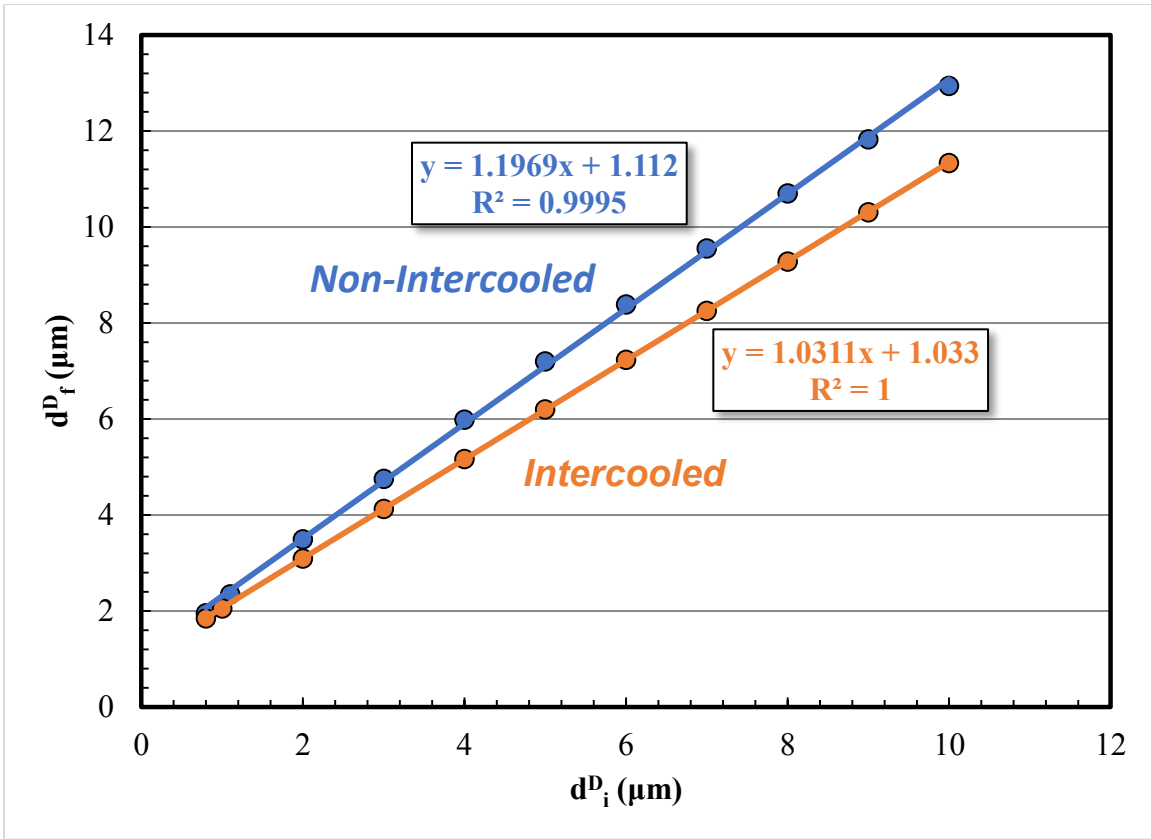


Figure 7.33: Growth curves for the NIC and IC cases show that the NIC cases grow at a faster rate. The availability of more condensable species (CO_2 and PZ) increases the driving forces throughout the column.

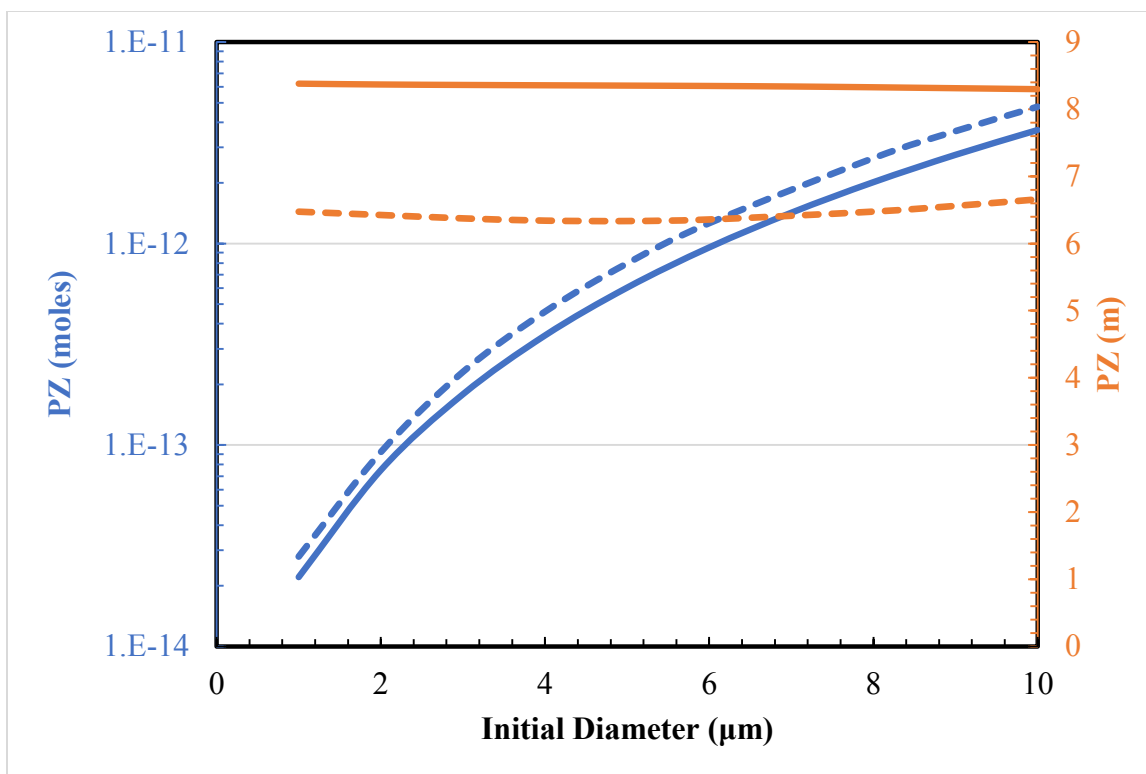


Figure 7.34: The final total moles of PZ depends on the initial diameter for both the NIC and IC cases. The molality is constant for a given initial diameter, but is higher for the IC case: NIC = 6.4 m PZ, IC = 8.3 m PZ. The dashed lines are for the NIC case, the solid lines are for the IC case.

7.12 AEROSOL GROWTH HYPOTHESIS

Aerosol growth is hypothesized to be dependent on the condensation driving force between the gas and the aerosol, which is a function of the bulk gas and liquid contacting process and the specific amine system used, particularly the dependence of the amine volatility with loading.

CO₂ solubility of the amine affects the solvent flow rate, which in turn affects the enthalpy transfer (and temperature bulging) in the column. Additionally, the heat of absorption affects the amplitude of the temperature bulge and the reaction kinetics and solvent rate affect the location of the temperature bulge. The interrelationship between

temperature, loading, and amine volatility determine the equilibrium partial pressure above the bulk solvent; the gas temperature and CO₂ composition determine the equilibrium partial pressure above the aerosol.

Figure 7.35 shows calculated driving forces for aerosol growth at the lean and rich end of the absorber for 8 m PZ, 9 m MEA, and 4.8 m AMP at 40 °C. The partial pressures of MEA and PZ are calculated using the correlations found in Xu (2011). Partial pressures for AMP are calculated from an Aspen Plus[®] model developed in the Rochelle research group. The dashed lines indicate equilibrium to the gas ($P_{\text{CO}_2,\text{Rich}} = 12,000 \text{ Pa}$, $P_{\text{CO}_2,\text{Lean}} = 1,200 \text{ Pa}$) and the equilibrium partial pressure of CO₂ above the solvent ($P^*_{\text{CO}_2,\text{Rich}} = 5,000 \text{ Pa}$, $P^*_{\text{CO}_2,\text{Lean}} = 500 \text{ Pa}$). The inequity of partial pressures between the bulk solvent and aerosol due to the accumulation rate of CO₂ causes preferential transfer of amine into the aerosol and subsequent transfer of H₂O to dilute the salt species reacting in the aerosol liquid.

Under isothermal conditions, the driving force for aerosol growth is a strong function of the loaded solvent volatility. The slope of the volatility curve influences the dependence of the CO₂ composition on aerosol growth. The ratio of the lean-to-rich driving force for PZ, MEA, and AMP are 5.17, 2.05, and 0.92, respectively. In the absence of temperature bulging and solvent capacity effects, aerosols growing by PZ accumulation would be more sensitive to changes in CO₂.

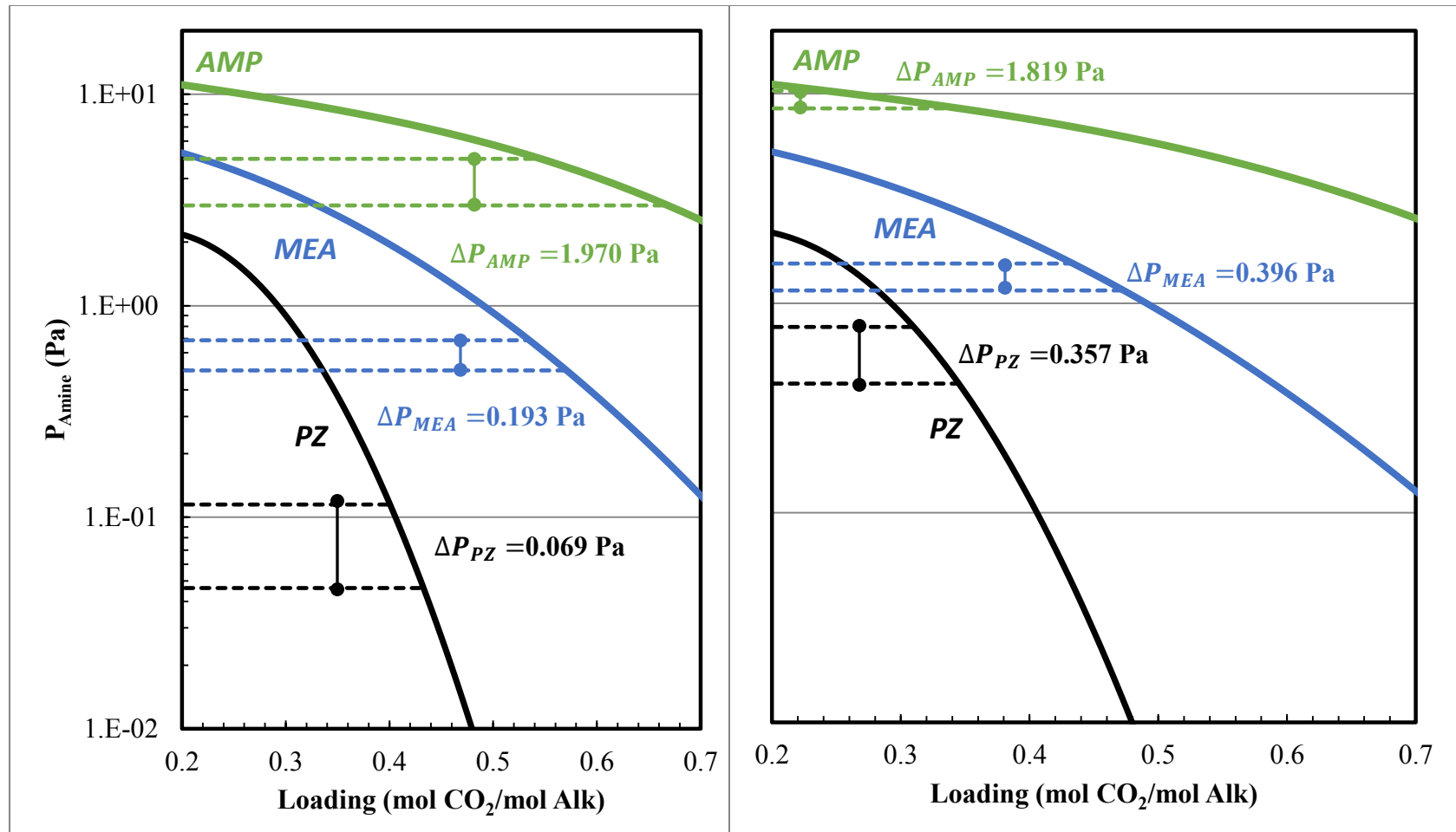


Figure 7.35: Amine driving forces between the gas and aerosol at the absorber rich (left) and lean (right) ends for 8 m PZ, 9 m MEA, and 4.8 m AMP at 40 °C. ($P_{\text{CO}_2,\text{Rich}} = 12,000$ Pa, $P_{\text{CO}_2,\text{Lean}} = 1,200$ Pa, $P^*_{\text{CO}_2,\text{Rich}} = 5,000$ Pa, $P^*_{\text{CO}_2,\text{Lean}} = 500$ Pa).

For amines whose volatility decreases with CO₂ loading, such as PZ, MEA, and AMP, the aerosol phase amine activity will be significantly less than the bulk solvent since the CO₂ accumulation in the aerosol drop is very fast relative to absorption in the bulk solvent. The difference in amine activity between the aerosol and bulk liquids creates a driving force for amine transfer into the aerosol phase which is buffered by the gas phase, since the aerosol will be in thermal equilibrium to the gas. As the aerosol accumulates reacted CO₂/amine species, the H₂O activity decreases relative to the bulk solvent, which creates a driving force for H₂O transfer into the aerosol. The bulk solvent partial pressures are a function of the gas-liquid process; specifically, the inlet temperatures, flow rates, and compositions.

For amines whose volatility increases with CO₂ loading, the aerosol phase amine activity will be higher than the bulk solvent due to the imbalance in CO₂ accumulation rates between the aerosol and the bulk solvent. In that case, any amine picked up by the aerosol will quickly reach equilibrium to CO₂ and a driving force for amine evaporation out of the aerosol, back to the solvent, will be created. The result is an aerosol that is more dilute in amine than the bulk solvent. Because the aerosol is less concentrated in amine than the bulk solvent, the H₂O activity will be higher than the solvent and H₂O will transfer out of the aerosol. The imbalance in H₂O activity will lead to shrinkage of the aerosol by evaporation.

H₂O imbalance can also be caused by the addition of salt/amino acids promoters; the H₂O activity of the bulk solvent would be depressed by additional diluents. In the case of the AMP/potassium taurate system measured by Khakharia (2015), the activity of AMP in the aerosol would have to match the activity of both the AMP and potassium taurate in the bulk solvent such that the H₂O activity would be equal across both phases. Therefore, AMP in the aerosol would have to be significantly more concentrated in the aerosol than the bulk solvent. The higher concentration in the aerosol would offset the loading difference leading to a driving force for amine transfer back into the bulk solvent. As amine transfers out of the aerosol, the activity of H₂O would increase and cause mass transfer out of the aerosol towards the bulk solvent which would preclude growth of the aerosol.

Blended amine systems should grow aerosols if any of the substituent amines have inverse loading/volatility dependence. The subsystem of the inversely volatile amine provides a continuous driving force for H₂O transfer. The accumulation of amine/CO₂/H₂O creates a driving force for other components to transfer.

Driving forces between the three phases are important to consider. The bulk gas serves as a buffer between the aerosol and bulk liquid. **Figure 7.36** illustrates a scenario for condensation onto an aerosol. Three phase film profiles are useful for understanding how CO₂ and temperature affect the driving force for amine accumulation. The gradient for CO₂ transfer from the aerosol into the gas is assumed to be negligible; CO₂ equilibrium is assumed. In the illustrated scenario, CO₂ is transferring into the bulk liquid while transferring at a stoichiometric rate into the aerosol. The loading and temperature difference create a driving force for amine accumulation; and therefore, H₂O accumulation as the aerosol becomes concentrated in PZ-CO₂ salt species.

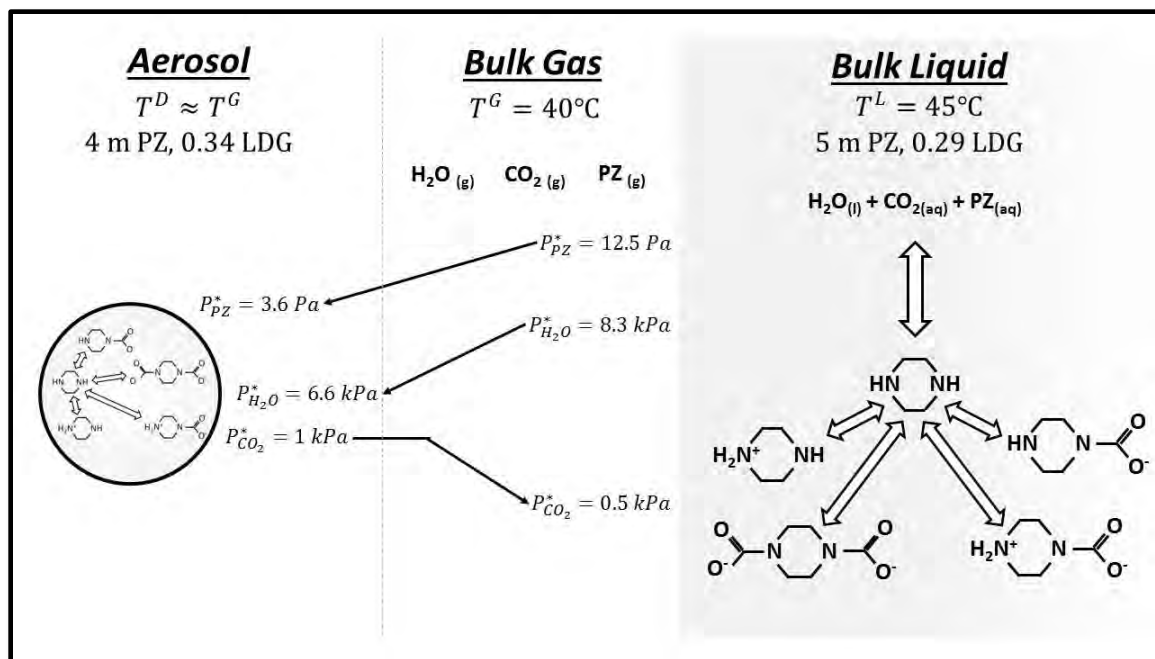


Figure 7.36: Three phase film diagram for mass transfer between an aerosol, gas, and bulk liquid. Temperature and CO₂ loading affects the transport between the liquid phases and the gas acts as a temperature and mass buffer.

7.13 EMISSIONS MODELING

The growth curves produced from the aerosol integration model can be used with assumptions of the initial total particle density and PSD to estimate the final emissions out of the top of the absorber. The study presented here approximates the growth of H₂SO₄ aerosols passing through the absorber outlined in the sensitivity case.

The initial distribution is modeled assuming an initial SO₃ concentration (3 ppmv) and starting PSD composed of a bimodal-lognormal distribution. The total particle density is set by assuming an H₂SO₄ concentration (0.1 mol/L) and the bimodal distribution parameters (Coarse Mode: $d_G = 1 \mu\text{m}$, $\sigma_G = 1.2 \mu\text{m}$; Fine Mode: $d_G = 0.4 \mu\text{m}$, $\sigma_G = 1.5 \mu\text{m}$) as well as the weighting of the PSD modes (Fine Mode = 0.9, Coarse Mode = 0.1). **Figure 7.37** shows the PSD for using the assumed conditions.

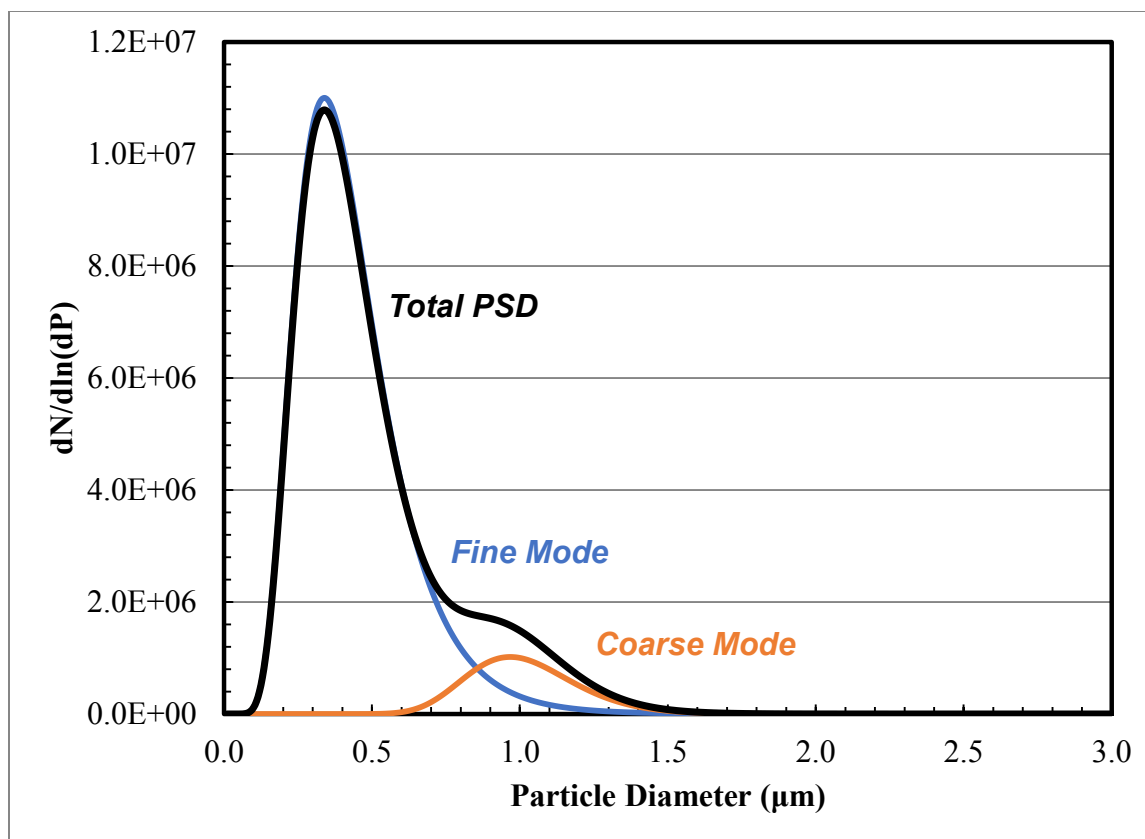


Figure 7.37: Bimodal-lognormal PSD composed of two individual (Coarse and Fine Modes) lognormal distributions weighted 0.1:0.9 (Coarse:Fine). The total particle density calculated by mass balance of 3 ppmv SO₃ assuming a liquid H₂SO₄ concentration of 0.1 mol/L is 4.58x10⁶ part./cm³.

Using the growth curves from Case 2 and 3 (NIC/IC) described earlier, an estimation in the difference in emission rate can be made. The change in the initial PSD using the growth curves (**Figure 7.37**) is shown in **Figure 7.38**. Assuming a concentration of PZ (0.5 m), based on the measurements taken from pilot plants and the AGC, the final emitted PZ can be calculated by integrating the PSD. The IC and NIC emission levels are calculated to be 121.32 and 165.13 ppmv, respectively. In either case, the emissions levels are far above what would be allowed in a normal plant.

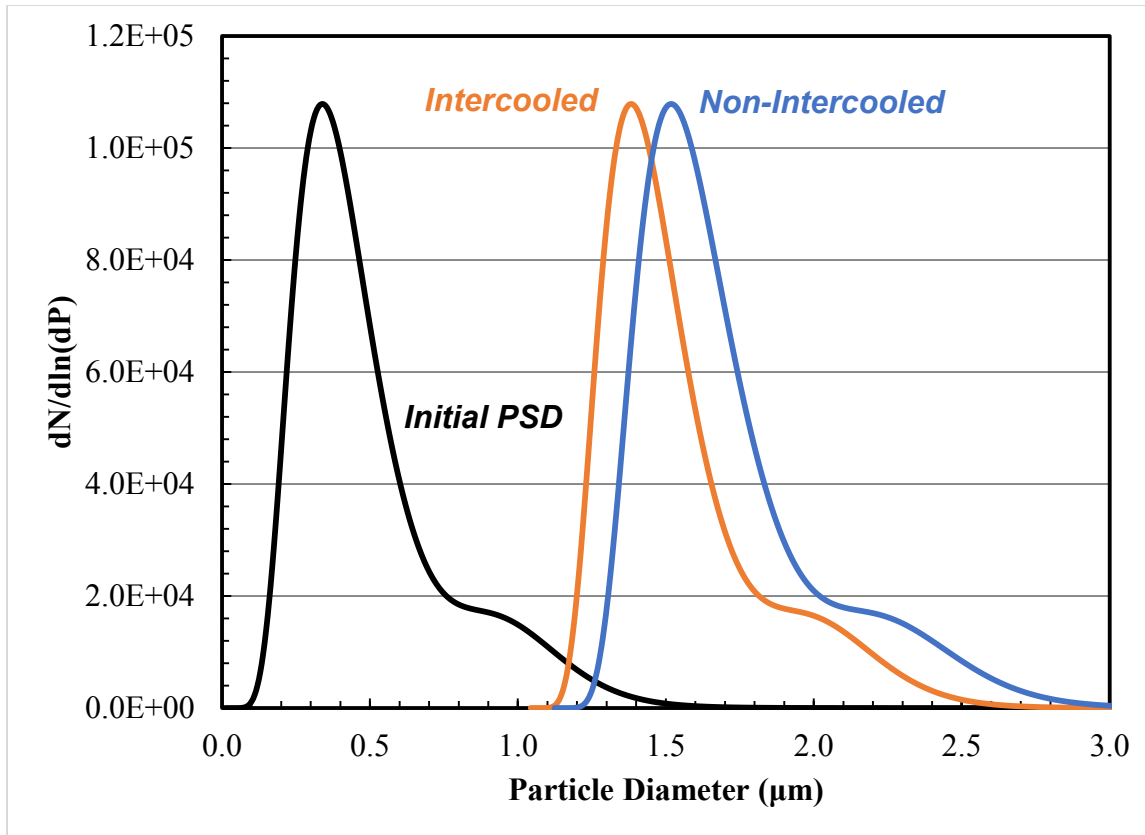


Figure 7.38: Initial and final PSDs using growth curves for the IC and NIC case studies.

Emissions estimates using the aerosol integration model represent maximum expected emissions. The weakest assumption made during equation development was the omission of the component mass balances with the bulk gas, especially when the total particle density exceeds about 10^5 part./ cm^3 . If the aerosol concentration is very high, the growth rate will be limited by mass transfer of amine out of the bulk liquid; the driving force for condensation in the gas will be quickly diminished by the very large surface area contained in the aerosol phase.

The calculated outlet diameter is also very similar to that measured in pilot plants, specifically the SRP pilot plant absorber. Submicron inlet aerosols grow about an order of magnitude in the absorber column but are still too small to be collected efficiently by traditional demister pads. This finding is consistent with the measurements at SRP (Chapter 6) and measurements at the miniature pilot plant detailed in the work of Mertens et al. (2014). Water

wash towers can provide additional saturation for growth of aerosols to a size that can be efficiently collected by physical means.

7.14 CONCLUSIONS

This chapter contains the fundamental equations, calculation hierarchy, and case studies for heat and mass transfer modeling to a single aqueous aerosol passing through an amine scrubbing CO₂ capture plant, including a single-stage water wash column. The model developed in this study allows for development of theoretical explanations for observations at pilot plants, design calculations for bench scale approximations, and a means of future development necessary to match pilot plant and bench scale PSDs. The major areas of contribution are listed as follows:

- Development of modeling equations, subroutines, and integration algorithms to simulate aerosol growth using Aspen Plus[®] steady state cases
- Determine parameter sensitivity for modeling cases: k'_g
- Determine the effect of process variables and unit operations on the aerosol diameter and composition: water wash towers, intercooling, P_{CO_2}/P_{PZ}
- Estimate emissions from initial PSD assumptions matching H₂SO₄ cases
- Provide theoretical explanation for aerosol growth: CO₂ loading and amine volatility

7.14.1 Parameter Sensitivity: k'_g

In this study, the CO₂ mass transfer coefficient (k'_g) was left as an adjustable parameter. k'_g , was varied between 1×10^{-6} – 1×10^{-8} mol/Pa·m²·s for identical initial conditions in an exploratory case study involving only the absorber column. The outlet diameter grew from 3 μm initially to a range of 4.266 to 5.827 μm for k'_g varying from 10^{-8} to 10^{-6} mol/s·Pa·m², respectively.

In order to maintain CO₂ loading in equilibrium to the bulk gas, which is the cause of the driving force for amine condensation, the CO₂ driving force is on the order of 10^4 to 10^6 Pa for

k'_g varying from 10^{-6} to 10^{-8} mol/s·Pa·m², respectively. $D_{PZ,Mix}^G$ was assumed to be 10^{-5} m²/s in that study.

7.14.2 Growth in the Water Wash

Mechanistically, aerosols grow in the water wash because the bulk gas H₂O is higher than in the absorber section. H₂O in the gas is relative to the amine content of the contacted liquid; absorber solvent is typically 30–40 wt % amine, whereas water wash solvents contain 5 wt % or less amine. Growth rate for an aerosol depends on the inlet droplet composition into the wash section as well as the amine content in the water wash liquid. High salt content (PZ/CO₂ species) increases the H₂O driving force and subsequently the particle growth rate.

7.14.2.1 Packing Height

Increasing the packing height from 1.6 to 3.0 m resulted in additional aerosol growth of 13.7% (for k'_g equaling 10^{-8} mol/s·Pa·m², and a water wash solvent concentration of 0.25 m PZ). Increasing the residence time allows for further growth of the aerosol but at the expense of capital cost. Incorporation of a capture efficiency curve for standard mesh pad demister would allow for a fully detailed design to determine the optimal water wash height for aerosol abatement.

7.14.2.2 Water Wash Concentration

The amine concentration in the wash was doubled to 0.5 m PZ from the initial sensitivity case (0.25 m PZ) and the column height was adjusted to match the outlet drop diameter.

An additional 0.5 m of packing (31.25%) was required to match the outlet diameter (7.673 μm). when the PZ concentration in the wash was doubled. Increasing the solvent concentration in the water wash lowers the activity of H₂O in the solvent and therefore the fugacity in the gas phase. The driving force for condensation onto the aerosol decreases and the growth rate slows.

In a single stage wash, the water wash concentration should be kept as low as possible to increase the H₂O activity in the gas relative to the concentrated aerosol. Alternatively, a

cascaded water wash (varying concentration and temperature) could be used to provide a gradient of H₂O activity throughout the washing section. Since the concentration of aerosols measured in pilot plants tends to be very high (10⁶–10⁸ part./cm³), a cascaded wash might be required to provide growth due to the mass balance limitation as detailed in the study by Heidenreich et al. (2000).

7.14.3 Growth Rate Theory

Aerosol growth is hypothesized to be dependent on the condensation driving force between the gas and the aerosol, which is a function of the bulk gas and liquid contacting process and the specific amine system used, particularly the dependence of the amine volatility with loading. In the absorber, continual absorption of amine and CO₂ from the bulk gas creates a driving force for H₂O uptake. PZ and CO₂ in the gas are related to the bulk CO₂ transfer process; PZ in the gas is a strong function of temperature and loading.

The interrelationship of thermodynamics (CO₂ solubility, heat of absorption), kinetics (reaction rates and amine/product diffusivity), and operating conditions (solvent flow rate) create an intricate design network for choosing the proper system design for aerosol abatement without negatively impacting the CO₂ capture process.

Additionally, the heat of absorption affects the amplitude of the temperature bulge and the reaction kinetics and solvent rate affect the location of the temperature bulge. The interrelationship between temperature, loading, and amine volatility determine the equilibrium partial pressure above the bulk solvent; the gas temperature and CO₂ composition determine the equilibrium partial pressure above the aerosol.

It is theorized that amines with high volatility and very strong vapor pressure depression with CO₂ content will produce the greatest driving forces for amine accumulation into the aerosol. Additionally, solvent systems with non-volatile salt species (K₂CO₃/PZ or AMP/KTau) will increase the amine content in the aerosol phase to balance the depressed H₂O activity of the bulk solvent. Because the amine concentration will be higher in the aerosol relative to that of the

bulk solvent, the effect of CO₂ loading on the amine vapor pressure will be offset by the concentration, and in some cases, the amine will transfer back to the gas phase towards the bulk solvent. Therefore a driving force argument would explain the observations made by Khakharia (2015), not a kinetics argument.

7.14.3.1 The Effect of Intercooling

Aerosols grow faster in non-intercooled columns due to differences in solvent composition (CO₂ loading) and temperature. Non-intercooled columns have much larger absolute temperature differences and are less efficient at removing CO₂, meaning that throughout the column, the amine vapor pressure is nearly always higher than that of intercooled columns. Since P_{CO_2} and P_{PZ} are higher for non-intercooled columns, larger driving forces exist for condensation (growth).

7.14.4 Emissions Modeling

A simple model to predict emissions from an absorber was developed using the growth curves created from varying the initial aerosol diameter in the aerosol model. The growth curves, whose functionality is determined by the largest source of mass transfer resistance, are applied to an assumed PSD. The amine content in the final PSD is integrated and multiplied by an assumed total particle density to calculate an equivalent ppm concentration leaving with the scrubbed gas.

The initial distribution is modeled assuming an initial SO₃ concentration (3 ppmv) and starting PSD composed of a bimodal-lognormal distribution. The total particle density is set by assuming an H₂SO₄ concentration (0.1 mol/L) and the bimodal distribution parameters (Coarse Mode: $d_G = 1 \mu\text{m}$, $\sigma_G = 1.2 \mu\text{m}$; Fine Mode: $d_G = 0.4 \mu\text{m}$, $\sigma_G = 1.5 \mu\text{m}$) as well as the weighting of the PSD modes (Fine Mode = 0.9, Coarse Mode = 0.1). The total particle density is calculated from a mass balance and was $4.58 \times 10^6 \text{ part./cm}^3$.

Using a steady state, validated case from a pilot plant campaign at SRP, the outlet PZ emissions from the aerosol phase were calculated to be 121 and 165 ppmv for the intercooled

and non-intercooled cases, respectively. Either value is far above what would be allowed from an industrial scale plant, not only for environmental reasons, but also the loss rate of solvent amine.

The results of the emission study represent a worst-case scenario since the component mass balances were assumed to be negligible in the first formulation of the aerosol integration model. As Heidenreich and co-workers (2000) showed, as the total particle density exceeds 10^5 part./cm³, the bulk-side mass balance becomes impacted to the point where the saturation in the gas phase is significantly diminished and the growth rates calculated using the aerosol model in this work would become too high.

7.14.5 Recommendations

The cases detailed in this chapter illustrated that aerosols grow by two mechanisms in an absorber/wash column. In the absorber, continual absorption of amine and CO₂ from the bulk gas creates a driving force for H₂O uptake. PZ and CO₂ in the gas are related to the bulk CO₂ transfer process; PZ in the gas is a strong function of temperature and loading. Aerosols grow in the water wash because the H₂O content in the gas is increased due to the dilute contacting solvent.

Leveraging absorber and water wash design and operating conditions show promising results for aerosol abatement even at very high particle concentrations. The absorber serves as a concentrating mechanism for aerosol growth; inlet aerosols are usually dilute in H₂SO₄ since they nucleate in the FGD scrubber and pass through dilute solvent preconditioning towers prior to entering the absorber bottom. Altering the temperature, loading, and amine volatility impact the driving force for salt accumulation in the absorber. Although aerosols will grow in the absorber, their diameters are still likely too small to be captured efficiently by traditional demister pads.

Significant growth occurs in the water wash section. Maximizing the H₂O activity is the key parameter affecting aerosol growth; the water wash concentration should be kept low. The

water wash should also be designed with significant residence time to allow for growth to occur, or, a knockout with traditional demister can be placed significantly downstream for additional growth. The modeling work in this study also points to the conclusions outline in Heidenreich et al. (2000), that a cascaded wash section with alternating temperature (H_2O activity) can be utilized for further aerosol growth.

Controlling aerosol growth rate by changing operating conditions in the absorber and water wash must be weighed against capital and operating expenses. Collecting droplets by impaction or diffusion requires significant ΔP . Designing a water wash column with significant residence time to grow aerosols will increase removal efficiency while lowering ΔP .

7.15 ACKNOWLEDGEMENTS

Several people contributed to the work in this chapter. The authors would like to acknowledge the Luminant Carbon Management Program for funding this work. The authors would also like to thank Darshan Sachde and Peter Frailie for providing Aspen Plus[®] pilot plant simulations and thermodynamic/kinetic models.

Chapter 8: Conclusions and Recommendations

This dissertation presents contributions made in three major areas: (1) bench scale aerosol testing, (2) pilot plant aerosol analysis, and (3) aerosol modeling in CO₂ absorber systems. In addition, a state-of-the-art *in situ* particle analysis technique (PDI) was developed and applied to aerosol characterization in CO₂ absorption/stripping systems at variable process scales. Particle size distributions (PSDs) and total particle densities were directly related to total phase (aerosol and gas) concentrations, measured by FTIR, for the first time. Changes in the aerosol distribution parameters were correlated against operating conditions. Those parameters and practical design considerations for aerosol abatement were simulated using a heat and mass transfer integration program. The simplified model represents the first application of aerosol modeling equations to predict aerosol growth and total amine emissions in amine-based CO₂ capture systems. This chapter summarizes the conclusions developed from the preceding content chapters and provides recommendations for future work.

8.1 AEROSOL GROWTH THEORY

Aerosol growth is hypothesized to be dependent on the condensation driving force between the gas and the aerosol, which is a function of the bulk gas and liquid contacting process and the specific amine system used, particularly the dependence of the amine volatility with loading. Because CO₂ transfer is faster to the aerosol phase than the bulk liquid, the CO₂ loading in the aerosol is higher relative to the solvent. Since most amines experience strong vapor pressure depression by reaction with CO₂, the amine volatility above the aerosol is less than the bulk liquid; a driving force for moving amine to the aerosol exists because of the thermodynamic relationship between CO₂ and amine partial pressure.

As amine/CO₂ reaction products accumulate, H₂O must transfer from the gas to rebalance the H₂O equilibrium. This cycle of salt accumulation and H₂O dilution causes perpetuating aerosol growth.

The growth phenomenon will occur for any amine or amine blend whose volatility decreases with CO₂ loading. Amines that salt out with CO₂ or amine blends with non-volatile promoters will not significantly grow seed nuclei. Because non-volatile promoters cannot partition into the aerosol phase, the activity of H₂O will always be lower above the solvent relative to the aerosol. H₂O will evaporate from the aerosol and the amine activity will increase to the point that amine will transport back towards the solvent.

8.1.1 Necessity of CO₂

CO₂ is a necessary component for aerosol growth with amines and H₂O. CO₂ lowers amine volatility and induces amine concentration gradients across the bulk gas, between the aerosol and bulk liquid. The impact of CO₂ was both simulated and observed experimentally.

Data collected on the Aerosol Growth Column (AGC) with piperazine (PZ) solvent showed that submicron particles grew into the micron diameter range when CO₂ was added to the inlet gas. The average particle diameter increased with CO₂ until a maximum was reached, similar to that found in Khakharia (2015).

Simulation of aerosol growth showed that areas of high gas phase CO₂ and amine content lead to the fastest growth rates. CO₂ solubility of the amine affects the solvent flow rate, which in turn affects the enthalpy transfer (and temperature bulging) in the column. Additionally, the heat of absorption affects the amplitude of the temperature bulge and the reaction kinetics and solvent rate affect the location of the temperature bulge. The influence of the CO₂ loading/temperature effect was captured by the case studies of intercooled and non-intercooled columns. Intercooling suppresses temperature bulging and increases loading; amine volatility is reduced throughout the column. Aerosol growth in intercooled columns is expected to be less than for non-intercooled absorbers.

8.1.2 Water Wash Growth

Aerosols grow predominantly by H₂O condensation in the water wash column. The H₂O activity is lowered significantly in the absorber due to the accumulation of amine/CO₂ salts. As

aerosols pass from the absorber into the water wash, the gas phase saturation changes proportionally to the thermodynamic condition of the water wash liquid, which is very dilute H₂O.

Simulation results showed that lowering the steady state water wash amine content and increasing the packing height would increase the final aerosol diameter. This is expected based on the H₂O condensation driving force and the increased residence time. Doubling the water wash height lead to an additional 50 % growth for the described case study.

Numerical modeling also showed that aerosols grow significantly more in the water wash than in the absorber. This was found in pilot plant measurements where the average diameters at the absorber outlet were between 0.5–2 μm and the average diameters after the water wash were greater than 2 μm.

8.1.3 PZ Makes Aerosol

Measurements taken at both the bench and pilot scale showed that absorbers using aqueous PZ solvent experience elevated emissions caused by inlet aerosol nuclei. PZ emissions were found to increase very rapidly with the inlet particle density. PZ, or any amine with vapor pressure reduction by CO₂ is expected to grow aerosols by heterogeneous nucleation. Elevated amine emissions by aerosols have been measured for MEA, PZ, and AMP/PZ.

8.2 PILOT PLANT OBSERVATIONS

8.2.1 Amine Concentration in the Aerosol

The amine concentration in the aerosol was estimated by comparing PSD and total particle density measured by PDI against FTIR measurements. The amine concentration in the aerosol was calculated to be at least an order of magnitude lower than the CO₂ capture solvent.

During pilot plant measurements, the sampling locations were far downstream from the absorber or water wash. It is expected that aerosols continue to condense H₂O out of the gas until they reach a pseudo equilibrium. However; simulation showed the final amine concentration in the aerosol liquid to be slightly more dilute than the capture solvent and strongly

dependent on the use of intercooling. It is hypothesized that the amine concentration is strongly affected by water transfer. Intercooling suppresses temperature bulging in the column and thereby reduces the H₂O partial pressure. Less driving force for H₂O condensation is expected. Columns with very low L/G ratios and no intercooling will have the largest temperature bulges and therefore the most driving force for H₂O condensation. Since the AGC has a very high L/G ratio compared to pilot plants, the estimated amine content in the aerosols was higher than that found in pilot plant measurements.

8.2.2 SO₂ and H₂SO₄ Cause Aerosols

During pilot plant testing, injections of SO₂ were found to increase PZ emissions. On average, 34.9% of the incoming SO₂ was absorbed in the solvent while the remainder formed PZ/SO₂ aerosols. The average PZ/SO₂ ratio was 1.53 (on a mole basis) and ranged from 0.03–3.99. A combination of absorption, nucleation/condensation occur simultaneously with the absorber solvent and SO₂.

Because SO₂ partitions into two phases, removal of SO₂ through thermal reclaiming is likely not an option since emission rates due to aerosols will be far too high. An SO₂ polisher is a critical part of aerosol abatement.

H₂SO₄ injection produces aerosols in PZ absorbers. The ratio of PZ/H₂SO₄ averaged 2.97 (on a mole basis) and ranged from 0.93–6.73. Since nucleation occurs far upstream of the absorber in the FGD scrubber, simple polishing units will be ineffective at removing the aerosol source. Aerosol removal devices, solvent selection, and growth and capture techniques are the recommended abatement strategies.

8.2.3 Aerosols Plug Filter Devices

During aerosol injection testing, the outlet knockout filter plugged rapidly from accumulating liquid and solid material resulting in an increase in pressure drop across the filter element from one to ten inches of H₂O.

When the air chiller temperature was increased, the pressure drop rose more slowly. It is possible that fog formation in the air chiller hydrates the filter element faster and decreases the available interstitial flow paths for the gas.

Accumulation of solid precipitates indicates that solidified $\text{PZ}\cdot 6\text{H}_2\text{O}$ or the rich-end precipitate leads to filter plugging. Aerosols carrying PZ would be captured on the filter and the trapped liquid would reach saturation to CO_2 with the outlet gas. The result is a rich liquid that, in the case of PZ, would concentrate to the point of the solubility limit. Amines with solid solubility problems limit the practical solutions for aerosol collection.

8.3 PHASE DOPPLER INTERFEROMETRY

8.3.1 Field Demonstration

A transportable, custom-built PDI was used to measure aerosol PSDs and total particle densities at variable process scales. The PDI performed successful measurements up to total particle densities of 1.7×10^7 part./ cm^3 in the size range of 0.1–12 μm .

8.3.2 Density and Size Measurements

PDI is a unique aerosol analytical tool because it provides both the total particle density and high resolution PSD information in real-time. Both pieces of information are crucial for discriminating the impact of the seed nuclei count and growth by condensation on the emission rate of amine out of the CO_2 capture unit.

8.3.2.1 Density and Size Correlation

The particle density and average diameter were found to be correlated at both the bench and pilot scale. However, the two variables were positively correlated on the AGC and inversely correlated at the pilot scale.

Aerosols produced by the Liquid Vaporizer and Injector (LVI) are believed to be submicron. Droplets smaller than 0.1 μm are below the detection limit of the PDI. As aerosols

grow and move out of the submicron region, they become visible to the PDI and count towards the measured particle density.

It is theorized that the inverse relationship is due to the mass balance of condensables and the quantity of nuclei; more nuclei means more condensable sites and therefore the amount of available condensate is spread amongst more condensable surfaces. The result is smaller average particle diameters.

8.3.2.2 *Aerosol Concentration Estimation*

The information provided by the PDI allows for phase discrimination between the aerosol and gas. Total phase measurements (FTIR) can be compared directly to PDI measurements to estimate the concentration of amine in the aerosol by post-processing algorithms.

8.3.2.3 *Aerosol Abatement Testing*

The PSD and total particle density data showed the impact of process changes and operating conditions on the aerosol phase using both the raw data and the aerosol amine concentration calculation algorithm.

In the pilot plant measurements at the National Carbon Capture Center (NCCC), the fan location was switched from upstream (PSTU blower) of the absorber to an intermediate (SSTU blower) location between the absorber and the water wash. The average diameter was shown to increase 13 % by switching from the SSTU to the PSTU blower; however, the particle density did not uniformly change. Without both the total density and average diameter information, such a change might be mistaken for aerosol collection rather than by condensation or evaporation.

8.4 RECOMMENDATIONS

8.4.1 *Aerosol Generation*

The biggest outstanding issue in this study is the aerosol generator used on the AGC and at the PRC pilot plant. Random and unpredictable plugging of the LVI in multiple locations significantly hindered experimentation over the course of several years.

A new aerosol generation source should be used in future experiments. Creating supersaturation by vaporization of H_2SO_4 is very difficult; H_2SO_4 is extremely corrosive and easily condensable, even when significant effort is given to eliminate cold spots.

The preferred H_2SO_4 aerosol generation pathway is to catalytically oxidize SO_2 to SO_3 and provide the H_2O vapor in the diluent stream like that found in the works of Kamijo et al. (2013), Mertens et al. (2014), Wall (1982), and Roesler (2010). However, material hazards control becomes more complicated because leaks of aerosol source material would be gaseous rather than a containable liquid. It may be preferable to separate the bench and pilot scale aerosol generation activities since the safety requirements for transporting gas from outdoor cylinders across considerable distance into the lab is likely prohibitive.

Alternatively, the LVI could be fixed using the current vaporization principle, but all stainless steel tubing would need to be replaced with glass tubing with proper support apparatus for use outdoors. An eductor should be avoided to prevent corrosion of sensitive openings and to prevent upstream plugging.

8.4.2 Aerosol Growth Column

Liquid samples should be taken for analysis during experimentation. Leaks and uncertainty in the solvent inventory makes back-calculation of the CO_2 loading difficult. Direct measurements of CO_2 loading would also make simulation and reconciliation much easier.

The solvent inventory tank should incorporate a level gauge such that an approximate volume can be determined. Additionally, level indication would make filling and draining easier.

Block valves should be added to isolate the absorber column, heat exchanger, and presaturator. Isolation would allow for safer draining and installation of new meters and equipment.

The condensate collection line should be plumbed back to the solvent tank to ensure that condensate is always returned and that water balance is maintained in the system. A liquid seal would be required to ensure no gas flows in the condensate line.

A rich solvent liquid sample and thermocouple should be added to the gravity drain line. The rich solvent loading and temperature would greatly help simulation and data reconciliation.

8.4.3 Phase Doppler Interferometer

8.4.3.1 Installation Improvements

The clearance between the PDI housing and the analysis cell windows is very small. During installation, it is very easy to hit the optical windows on the alignment fascia while trying to clear the window purge line fittings. Aluminum wear strips should be applied to the alignment fascia surfaces to provide passive protection against cracking the optical windows.

The purge/vacuum fitting design should be revisited. The push-to-connect fittings wear out the internal O-rings which are very difficult to replace. Currently, silicone sealant is used to affix the fittings, but eventually they will leak if not properly addressed.

8.4.3.2 Portability

The PDI CPU, ASA, and power supply should be repackaged to create a more easily transportable sampling system. The current enclosure requires a crane to move and some pilot plants have very little clearance, especially at higher locations where sampling occurs. Multiple weatherproof cases should be considered.

8.4.3.3 Condensate Control

Practical improvements to the PDI also include adding a liquid trap in the analysis cell suction line to prevent liquid backflow into the rotameter.

The removal of condensate upstream of the analysis cell should be given consideration. The quality of process gas varies greatly in pilot plants. In some cases, ducts are not insulated at all and significant liquid sheeting and entrainment occurs. Liquid collects at sample penetrations

and flushes out when the isolation valves are opened. If equipment is flanged in place, the liquid blows through the lines and can accumulate on optical surfaces. Either a blow down bypass or a more creative method for removing sheeting liquid is required to increase the duration of PDI sampling.

The analysis cell has removable insulation to prevent heat loss in the cell. Heating tape would be a good addition for temperature control, especially when sampling is occurring during winter months.

8.4.3.4 Data Analysis

The quantity of data produced by the PDI is very large for each sample run. A consistent exporting methodology should be implemented to pull the minimum amount of data for post processing. Currently, the time stamp, total particle density, and the PSD are exported as individual pieces of data and concatenated manually. The PDI/FTIR processing algorithm is statically defined by the concatenation template location. This process can be automated by exporting the time stamp, total particle density, and the PSD (in that order). The time stamp and the total particle density are static arrays, whereas the PSD is dynamic, dependent on the number of size bins and entries. Putting the PSD at the end of the file would allow for dynamic processing in VBA.

AIMS also does not offer logarithmic size bins. The raw data (recorded sizes) can be exported as a separate piece of data. An algorithm can be easily coded to sort particle sizes based on user-defined bins.

More thought should be given to adjustment of the total particle density and the passed sample fraction. Smaller PSDs will tend to have more failed sizing attempts and therefore the error during PDI/FTIR concentration matching will be larger since significant portions of the total particle density are excluded. Artium suggested a first-order approximation of dividing the reported total particle density by the passed fraction. However, this applies a uniform correction, whereas the sizing exclusions will be biased towards smaller particles. The probe volume

correction curve might serve as a better basis for renormalization since that correction is related to the sizing exclusion criteria.

8.4.4 Aerosol Modeling

8.4.4.1 Mass Balance Incorporation

The biggest assumption made in the modeling work was neglecting the aerosol mass from the overall balance equations. This was done intentionally since the steady-state calculations were done in Aspen Plus[®] and the integration was done in MATLAB[®]. However, the absolute growth of the particles and the aerosol liquid concentration were found to be affected by saturation depletion caused by dense aerosol clouds.

The mass balance can be incorporated in a few ways: (1) code an absorber into MATLAB[®] and perform the integration simultaneously, or (2) back-calculate the steady-state conditions in the absorber profiles by subtracting the mass absorbed into the aerosols using the fine integration discretization.

8.4.4.2 CO₂ Mass Transfer Rate

CO₂ was found to have a significant impact on the growth rate of the aerosol in the absorber. Currently, a fitting parameter is used to approximate the parallel mass transfer resistance of reaction and diffusion. Discretizing the aerosol liquid film and incorporating a moving boundary would provide insight into the assumption of the magnitudes of diffusion versus reaction. If diffusion is negligible, a purely volumetric reaction rate should be used. The aerosol would be approximated by a well-mixed, semi-batch reactor.

8.4.4.3 Thermodynamics

Thermodynamic representation in the aerosol model is done using semi-empirical equations and activity coefficient assumptions. While the deviations between rigorous Aspen Plus[®] calculations are minor (a few percent), they can have large impacts on the driving forces, especially H₂O in the water wash. Coding an absorber model using the same semi-empirical

thermodynamic formulations would remedy the offset. Alternatively, a more rigorous subroutine for full speciation and electrolyte interaction could be employed to minimize the offset.

8.4.4.4 Emissions Predictions

The above recommendations would significantly improve emissions predictions. Specifically, incorporation of the mass balance would greatly impact the growth rate which is a crucial part of predicting amine emissions. The total particle density should be added to improve saturation depletion calculations.

Aerosol removal curves could be added onto the final calculation stage to simulate the effect of mesh demister pads or duct runs to the stack. Efficiency curves would also allow for testing of aerosol collection devices like cyclones and swirl tubes.

Appendix A: AGC and PDI/FTIR Data Algorithm

A.1 AGC EXPERIMENT DATA ALGORITHM

The AGC data algorithm searches the FTIR result file and the LabVIEW™ log for the closest matching timestamp extracted from individual PDI data files. The script prompts for selection of column headings used to identify the offset of the desired data column to that of the searched time column.

A.1.1 Analysis.xlsm

'Declare global FTIR variables

Global FTIRtimeAddress As String
Global FTIRPDITimeOffset As Integer
Global FTIRPZOffset As Integer
Global FTIRCO2Offset As Integer
Global FTIRH2OOffset As Integer

'Declare global LabView variables

Global LVtimeAddress As String
Global LVN2FlowOffset As Integer
Global LVCO2FlowOffset As Integer
Global LVTSatOffset As Integer
Global LVGasInTOffset As Integer
Global LVSolvInTOffset As Integer
Global LVSolvRateOffset As Integer
Global LVGasOutTOffset As Integer
Global LVAbsTProOffset As Integer

Sub PDI_Path_Select()

'Select the folder containing the PDI files

```
With Application.FileDialog(msoFileDialogFolderPicker)
```

```
.AllowMultiSelect = True
```

```
.Show
```

```
'Output the file pathway
```

```
Cells(1, 2) = .SelectedItems(1)
```

```
End With
```

```
'Declare variable
```

```
Dim folderspec As String
```

```
'Clear file list from previous analysis
```

```
Range("A7:D1000").Select
```

```
Selection.ClearContents
```

```
'Write label text
```

```
Cells(7, 1).Value = "Number of PDI Files"
```

```
'Select cell to place "X" and row/column offsetting
```

```
Range("A8").Select
```

```
'Set folderspec variable string to the file pathway
```

```
folderspec = Cells(1, 2).Value
```

```
'Create a file system object and count the files present in the folder
```

```
Set fs = CreateObject("Scripting.FileSystemObject")
```

```
Set f = fs.getfolder(folderspec)
```

```
Set fc = f.Files
```

```
PDI_Files_Num = fc.Count  
Cells(7, 2).Value = PDI_Files_Num
```

'For each file in the file collection fc, output the file name and place and "X" in the next row down

```
For Each fl In fc  
    With ActiveCell  
        .Value = "X"  
        .Offset(0, 1).Value = fl.Name  
        .Offset(1, 0).Select  
    End With  
Next fl  
End Sub
```

Sub FTIR_Path_Select()

```
'Select FTIR file for analysis  
With Application.FileDialog(msoFileDialogOpen)  
    .AllowMultiSelect = True  
    .Show  
    'Output the FTIR file pathway  
    Cells(2, 2) = .SelectedItems(1)  
End With  
Set FTIR_Pathway = Cells(2, 2)  
  
'Open the FTIR file
```

```
Workbooks.Open Filename:=FTIR_Pathway
```

```
'Declare variables and set variables as objects
```

```
Set WB1 = ActiveWorkbook
```

```
Dim sCell As Range
```

```
Dim timeColOffset As Integer
```

```
Dim FTIRPDIClockOffsetMin As Integer
```

```
Dim PZColOffset As Integer
```

```
Dim CO2ColOffset As Integer
```

```
Dim H2OColOffset As Integer
```

```
'Prompt for selection of the time heading cell
```

```
Set sCell = Application.InputBox("Select Time Heading Cell", Type:=8)
```

```
'Count the number of data entries
```

```
Range(sCell.Address).Select
```

```
Count_Num = Range(Selection, Selection.End(xlDown)).Count - 1
```

```
'Prompt for the clock offset between the PDI and FTIR in minutes
```

```
FTIRPDIClockOffsetMin = InputBox("Enter the clock offset between the PDI and FTIR in minutes [FTIR-PDI]", "Clock Offset", 1)
```

```
Cells(1, 5) = "Clock Offset"
```

```
Cells(2, 5) = FTIRPDIClockOffsetMin
```

```
'Calculate the actual time using the clock offset
```

```
Range(sCell.Address).Offset(1, 2).FormulaR1C1 = "=RC[-2]+Time(0,R2C5,0)"
```

```
Range(sCell.Address).Offset(1, 2).Select
```

Selection.AutoFill Destination:=Range(Selection, Selection.Offset(Count_Num - 1))

'Set the timeColOffset variable to the column index of the time heading cell

timeColOffset = sCell.Offset(0, 2).Column

'Set the FTIRtimeAddress variable to the address of the time heading cell

Range(sCell.Address).Offset(0, 2).Select

FTIRtimeAddress = ActiveCell.Address

'Prompt for selection of the PZ concentration heading cell

Set sCell = Application.InputBox("Select PZ Heading Cell", Type:=8)

'Set the concColOffset variable to the column index of the PZ concentration heading cell

PZColOffset = sCell.Column

'Calculate the offset between the PZ concentration and timestamp column

FTIRPZOffset = PZColOffset - timeColOffset

'Prompt for selection of the CO2 concentration heading cell

Set sCell = Application.InputBox("Select CO2 Heading Cell", Type:=8)

'Set the concColOffset variable to the column index of the CO2 concentration heading cell

CO2ColOffset = sCell.Column

'Calculate the offset between the PZ concentration and timestamp column

FTIRCO2Offset = CO2ColOffset - timeColOffset

'Prompt for selection of the H2O concentration heading cell

Set sCell = Application.InputBox("Select H2O Heading Cell", Type:=8)

'Set the concColOffset variable to the column index of the H2O concentration heading cell

H2OColOffset = sCell.Column

'Calculate the offset between the PZ concentration and timestamp column

FTIRH2OOffset = H2OColOffset - timeColOffset

'Close the FTIR workbook

WB1.Close

End Sub

Sub LabView_Path_Select()

'Select LabView data file for analysis

With Application.FileDialog(msoFileDialogOpen)

.AllowMultiSelect = True

.Show

'Output Labview data file pathway

Cells(3, 2) = .SelectedItems(1)

End With

Set LabView_Pathway = Cells(3, 2)

'Open the LabView data file

Workbooks.Open Filename:=LabView_Pathway

'Declare variables and set variables as objects

Set WB1 = ActiveWorkbook

Dim sCell As Range

Dim timeColOffset As Integer

Dim LVPDIclockOffsetMin As Integer

Dim N2FlowColOffset As Integer

Dim CO2FlowColOffset As Integer

Dim TSatColOffset As Integer

Dim gasInTColOffset As Integer

Dim solvInTColOffset As Integer

Dim solvRateColOffset As Integer

Dim gasOutTColOffset As Integer

Dim absTProColOffset As Integer

'Prompt for selection of the time heading cell

Set sCell = Application.InputBox("Select Time Heading Cell", Type:=8)

'Set the timeColOffset variable to the column index of the time heading cell

timeColOffset = sCell.Offset(0, 2).Column

'Offset the LabView time to the next column that separates the time value from the date

Range(sCell.Address).Offset(0, 2).Select

LVtimeAddress = ActiveCell.Address

'Count the number of data entries

Range(sCell.Address).Select

Count_Num = Range(Selection, Selection.End(xlDown)).Count - 1

'Create an adjacent column for the time value

```
Range(sCell.Address).Offset(0, 1) = "Time"
```

'Separate the time value from the date/time field

```
Range(sCell.Address).Offset(1, 1).FormulaR1C1 = "=Time(hour(RC[-1]),minute(RC[-1]),second(RC[-1]))"
```

'Select the new column and autofill the conversion formula

```
Range(sCell.Address).Offset(1, 1).Select
```

```
Selection.AutoFill Destination:=Range(Selection, Selection.Offset(Count_Num - 1))
```

'Create an adjacent column for the corrected time value

```
Range(sCell.Address).Offset(0, 2) = "Corrected Time"
```

'Prompt for the clock offset between the PDI and LV in minutes

```
LVPDIclockOffsetMin = InputBox("Enter the clock offset between the PDI and LV in minutes [LV-PDI]", "Clock Offset", 1)
```

```
Cells(1, 5) = "Clock Offset"
```

```
Cells(2, 5) = LVPDIclockOffsetMin
```

'Calculate the actual time using the clock offset

```
Range(sCell.Address).Offset(1, 2).FormulaR1C1 = "=RC[-1]+Time(0,R2C5,0)"
```

```
Range(sCell.Address).Offset(1, 2).Select
```

```
Selection.AutoFill Destination:=Range(Selection, Selection.Offset(Count_Num - 1))
```

'Prompt for selection of the N2 Flow rate heading cell

```
Set sCell = Application.InputBox("Select N2 Flow Rate Heading Cell", Type:=8)
```

'Set the N2FlowColOffset variable to the column index of the solvent temperature heading cell

N2FlowColOffset = sCell.Column

'Calculate the offset of the N2 Flow Rate and time column indices

LVN2FlowOffset = N2FlowColOffset - timeColOffset

'Prompt for selection of the CO2 Flow rate heading cell

Set sCell = Application.InputBox("Select CO2 Flow Rate Heading Cell", Type:=8)

'Set the N2FlowColOffset variable to the column index of the solvent temperature heading cell

CO2FlowColOffset = sCell.Column

'Calculate the offset of the CO2 Flow Rate and time column indices

LVCO2FlowOffset = CO2FlowColOffset - timeColOffset

'Prompt for selection of the Presaturator T heading cell

Set sCell = Application.InputBox("Select Presaturator T Heading Cell", Type:=8)

'Set the TSatColOffset variable to the column index of the solvent temperature heading cell

TSatColOffset = sCell.Column

'Calculate the offset of the Presaturator T and time column indices

LVTSatOffset = TSatColOffset - timeColOffset

'Prompt for selection of the Gas In T heading cell

Set sCell = Application.InputBox("Select Gas In T Heading Cell", Type:=8)

'Set the gasInTColOffset variable to the column index of the solvent temperature heading cell

gasInTColOffset = sCell.Column

'Calculate the offset of the Gas In T and time column indices

LVGasInTOffset = gasInTColOffset - timeColOffset

'Prompt for selection of the Solv In T heading cell

Set sCell = Application.InputBox("Select Solvent In T Heading Cell", Type:=8)

'Set the solvInTColOffset variable to the column index of the solvent temperature heading cell

solvInTColOffset = sCell.Column

'Calculate the offset of the Solvent In T and time column indices

LVSolvInTOffset = solvInTColOffset - timeColOffset

'Prompt for selection of the Solv Rate heading cell

Set sCell = Application.InputBox("Select Solvent Rate Heading Cell", Type:=8)

'Set the solvInTColOffset variable to the column index of the solvent temperature heading cell

solvRateColOffset = sCell.Column

'Calculate the offset of the Solvent Rate and time column indices

LVSolvRateOffset = solvRateColOffset - timeColOffset

'Prompt for selection of the Gas Out T heading cell

Set sCell = Application.InputBox("Select Gas Out T Heading Cell", Type:=8)

'Set the gasOutTColOffset variable to the column index of the solvent temperature heading cell

gasOutTColOffset = sCell.Column

'Calculate the offset of the Gas Out T and time column indices

LVGasOutTOffset = gasOutTColOffset - timeColOffset

'Prompt for selection of the Absorber T Profile heading cell

Set sCell = Application.InputBox("Select Absorber T Profile Heading Cell", Type:=8)

'Set the solvInTColOffset variable to the column index of the solvent temperature heading cell

absTProColOffset = sCell.Column

'Calculate the offset of the Absorber T Profile and time column indices

LVAbsTProOffset = absTProColOffset - timeColOffset

'Save and close the LabView data file

WB1.Save

WB1.Close

End Sub

Sub Analyze()

Set PDI_Pathway = Cells(1, 2)

Set FTIR_Pathway = Cells(2, 2)

Set LabView_Pathway = Cells(3, 2)

Set PDI_Files_Num = Cells(7, 2)

For Each s In Sheets

If s.Name = "Analysis_Table" Then

Application.DisplayAlerts = False

s.Delete

Exit For

End If

Next

Sheets.Add

ActiveSheet.Name = "Analysis_Table"

Cells(1, 1) = "MW of PZ (g/mol)"

Cells(1, 2) = 86.136

Cells(2, 1) = "MW of CO2 (g/mol)"

Cells(2, 2) = 44.0095

Cells(8, 1) = "PDI Pathway"

Cells(8, 2) = "PDI File Name"

Cells(8, 3) = "PDI Time"

Cells(8, 4) = "Particle Concentration (part./cm3)"

Cells(8, 5) = "Count Mean"

Cells(8, 6) = "Diameter Mean"

Cells(8, 7) = "Area Mean"

Cells(8, 8) = "Volume Mean"

Cells(8, 9) = "Integral Droplet Volume (um3/cm3)"

Cells(8, 10) = "LabView Time"

Cells(8, 11) = "N2 Flow Rate (SLPM) [FCV1301-1]"

Cells(8, 12) = "CO2 Flow Rate (SLPM) [FCV1301-2]"
Cells(8, 13) = "Presaturator T (C) [TTXXXX-X]"
Cells(8, 14) = "LVI N2 Flow Rate (CFH)"
Cells(8, 15) = "Corrected LVI N2 Flow Rate (SLPM)"
Cells(8, 16) = "LVI H2O Flow Rate (mL/min)"
Cells(8, 17) = "Corrected LVI H2O Flow Rate (mL/min)"
Cells(8, 18) = "LVI T (C)"
Cells(8, 19) = "Gas In T (C) [TTXXXX-X]"
Cells(8, 20) = "Solvent In T (C) [TTXXXX-X]"
Cells(8, 21) = "Solvent Conc. of PZ (mol/kg)"
Cells(8, 22) = "Solvent Lean LDG (mol/mol alk.)"
Cells(8, 23) = "Apparent xPZ (--)"
Cells(8, 24) = "Apparent xCO2(--)"
Cells(8, 25) = "Solvent Density (kg/m3)"
Cells(8, 26) = "Solvent Flow Rate (GPM) [FI3301-1]"
Cells(8, 27) = "Corrected Solvent Flow Rate (GPM) [FI3301-1]"
Cells(8, 28) = "Gas Out T (C) [TTXXXX-X]"
Cells(8, 29) = "Eq. H2O Partial Pressure (vol %)"
Cells(8, 30) = "Lean CO2 Solubility (vol %)"
Cells(8, 31) = "PZ Volatility (ppmV)"
Cells(8, 32) = "FTIR Time"
Cells(8, 33) = "H2O In (vol %)"
Cells(8, 34) = "CO2 In (vol %)"
Cells(8, 35) = "PZ In (ppmV)"
Cells(8, 36) = "H2O Out (vol %)"
Cells(8, 37) = "CO2 Out (vol %)"
Cells(8, 38) = "PZ Out (ppmV)"

```

Cells(8, 39) = "Conc. of PZ in Drop (mol/kg)"
Cells(8, 40) = "CO2 LDG in Drop (mol/mol alk.)"
Cells(8, 41) = "Apparent xPZ in Drop (--)"
Cells(8, 42) = "Apparent xCO2 in Drop (--)"
Cells(8, 43) = "Drop Density (kg/m3)"
Cells(8, 44) = "Aerosol Conc.Of PZ (ppmV)"
Cells(8, 45) = "Total Conc. of PZ (ppmV)"
Cells(8, 46) = "Error between PDI and FTIR (%)"
Cells(8, 47) = "Absorber T1 (C) [TTXXXX-X]"
Cells(8, 48) = "Absorber T2 (C) [TTXXXX-X]"
Cells(8, 49) = "Absorber T3 (C) [TTXXXX-X]"
Cells(8, 50) = "Absorber T4 (C) [TTXXXX-X]"
Cells(8, 51) = "Absorber T5 (C) [TTXXXX-X]"
Cells(8, 52) = "Absorber T6 (C) [TTXXXX-X]"

```

```
Columns("A:AZ").AutoFit
```

```
Range("A8:AZ8").Select
```

```
Selection.Borders(xlDiagonalDown).LineStyle = xlNone
```

```
Selection.Borders(xlDiagonalUp).LineStyle = xlNone
```

```
Selection.Borders(xlEdgeLeft).LineStyle = xlNone
```

```
Selection.Borders(xlEdgeTop).LineStyle = xlNone
```

```
With Selection.Borders(xlEdgeBottom)
```

```
    .LineStyle = xlContinuous
```

```
    .ColorIndex = 0
```

```
    .TintAndShade = 0
```

```
    .Weight = xlMedium
```

```
End With
```

```

Sheets("File_List").Select
Range("A8").Select
With Range("A8")
    Count_Num = 1
    For i = 0 To PDI_Files_Num - 1
        If .Offset(i, 0) = "X" Or .Offset(i, 0) = "x" Then
            .Offset(i, 1).Copy
            Sheets("Analysis_Table").Select
            Range("A8").Offset(Count_Num, 0) = PDI_Pathway
            Range("A8").Offset(Count_Num, 1).Select
            ActiveSheet.Paste
            File_Num = File_Num + 1
            File_Name = Range("A8").Offset(Count_Num, 1)
            Dim WB1 As Workbook
            FullFilename = PDI_Pathway & "\" & File_Name
            Workbooks.Open Filename:=FullFilename
            Set WB1 = ActiveWorkbook
            PDI_Analyze
            WB1.Save

'Copy and paste the PDI timestamp
WB1.Activate
Range("C1").Copy
Workbooks("Analysis").Activate
Range("A8").Offset(Count_Num, 2).PasteSpecial (xlPasteValues)

```

'Copy and paste the total particle concentration

WB1.Activate

Range("C2").Copy

Workbooks("Analysis").Activate

Range("A8").Offset(Count_Num, 3).PasteSpecial (xlPasteValues)

'Copy and paste the calculated particle size distribution statistics

WB1.Activate

Range("J6:M6").Copy

Workbooks("Analysis").Activate

Range("A8").Offset(Count_Num, 4).PasteSpecial (xlPasteValues)

'Copy and paste the integrated particle volume

WB1.Activate

Range("E6").Select

Selection.End(xlDown).Copy

Workbooks("Analysis").Activate

Range("A8").Offset(Count_Num, 8).PasteSpecial (xlPasteValues)

'Close PDI file workbook

WB1.Close

Dim str() As String

str = Split(Range("A8").Offset(Count_Num, 2).Value)

PDI_Time = TimeValue(str(2) & " PM")

'LabView Lookup Loop

```

FullFilename = LabView_Pathway
Workbooks.Open Filename:=FullFilename
Set WB1 = ActiveWorkbook
Range(LVtimeAddress).Select
Looping_Num = 1

Do
    LabView_Time = CDate(Range(LVtimeAddress).Offset(Looping_Num, 0))
    If LabView_Time = PDI_Time Then

        N2FlowRate = Range(LVtimeAddress).Offset(Looping_Num, LVN2FlowOffset)
        CO2FlowRate = Range(LVtimeAddress).Offset(Looping_Num,
LVCO2FlowOffset)

        TSat = Range(LVtimeAddress).Offset(Looping_Num, LVTSatOffset)
        gasInT = Range(LVtimeAddress).Offset(Looping_Num, LVGasInTOffset)
        solvInT = Range(LVtimeAddress).Offset(Looping_Num, LVsolvInTOffset)
        solvRate = Range(LVtimeAddress).Offset(Looping_Num, LVsolvRateOffset)
        gasOutT = Range(LVtimeAddress).Offset(Looping_Num, LVGasOutTOffset)
        absProT1 = Range(LVtimeAddress).Offset(Looping_Num, LVAbsTProOffset)
        absProT2 = Range(LVtimeAddress).Offset(Looping_Num, LVAbsTProOffset + 1)
        absProT3 = Range(LVtimeAddress).Offset(Looping_Num, LVAbsTProOffset + 2)
        absProT4 = Range(LVtimeAddress).Offset(Looping_Num, LVAbsTProOffset + 3)
        absProT5 = Range(LVtimeAddress).Offset(Looping_Num, LVAbsTProOffset + 4)
        absProT6 = Range(LVtimeAddress).Offset(Looping_Num, LVAbsTProOffset + 5)

        Workbooks("Analysis").Activate
        Range("A8").Offset(Count_Num, 9) = LabView_Time

```

```

Range("A8").Offset(Count_Num, 10) = N2FlowRate
Range("A8").Offset(Count_Num, 11) = CO2FlowRate
Range("A8").Offset(Count_Num, 12) = TSat
Range("A8").Offset(Count_Num, 18) = gasInT
Range("A8").Offset(Count_Num, 19) = solvInT
Range("A8").Offset(Count_Num, 25) = solvRate
Range("A8").Offset(Count_Num, 27) = gasOutT
Range("A8").Offset(Count_Num, 46) = absProT1
Range("A8").Offset(Count_Num, 47) = absProT2
Range("A8").Offset(Count_Num, 48) = absProT3
Range("A8").Offset(Count_Num, 49) = absProT4
Range("A8").Offset(Count_Num, 50) = absProT5
Range("A8").Offset(Count_Num, 51) = absProT6

```

Exit Do

ElseIf LabView_Time > PDI_Time Then

```

time_privous = DateDiff("s", CDate(Range(LVtimeAddress).Offset(Looping_Num -
1, 0)), PDI_Time)

```

```

time_next = DateDiff("s", LabView_Time, PDI_Time)

```

If Abs(time_privous) < Abs(time_next) Then

```

LabView_Time = CDate(Range(LVtimeAddress).Offset(Looping_Num - 1, 0))

```

```

N2FlowRate = Range(LVtimeAddress).Offset(Looping_Num - 1,
LVN2FlowOffset)

```

```

CO2FlowRate = Range(LVtimeAddress).Offset(Looping_Num - 1,
LVCO2FlowOffset)

```

```

TSat = Range(LVtimeAddress).Offset(Looping_Num - 1, LVTSatOffset)

```

```

gasInT = Range(LVtimeAddress).Offset(Looping_Num - 1, LVGasInTOffset)
solvInT = Range(LVtimeAddress).Offset(Looping_Num - 1, LVSolvInTOffset)
solvRate = Range(LVtimeAddress).Offset(Looping_Num - 1, LVSolvRateOffset)
gasOutT = Range(LVtimeAddress).Offset(Looping_Num - 1, LVGasOutTOffset)
absProT1 = Range(LVtimeAddress).Offset(Looping_Num - 1,
LVAbsTProOffset)
absProT2 = Range(LVtimeAddress).Offset(Looping_Num - 1, LVAbsTProOffset
+ 1)
absProT3 = Range(LVtimeAddress).Offset(Looping_Num - 1, LVAbsTProOffset
+ 2)
absProT4 = Range(LVtimeAddress).Offset(Looping_Num - 1, LVAbsTProOffset
+ 3)
absProT5 = Range(LVtimeAddress).Offset(Looping_Num - 1, LVAbsTProOffset
+ 4)
absProT6 = Range(LVtimeAddress).Offset(Looping_Num - 1, LVAbsTProOffset
+ 5)

ElseIf Abs(time_priovus) >= Abs(time_next) Then
  LabView_Time = CDate(Range(LVtimeAddress).Offset(Looping_Num, 0))

  N2FlowRate = Range(LVtimeAddress).Offset(Looping_Num - 1,
LVN2FlowOffset)
  CO2FlowRate = Range(LVtimeAddress).Offset(Looping_Num - 1,
LVCO2FlowOffset)
  TSat = Range(LVtimeAddress).Offset(Looping_Num - 1, LVTSatOffset)
  gasInT = Range(LVtimeAddress).Offset(Looping_Num - 1, LVGasInTOffset)
  solvInT = Range(LVtimeAddress).Offset(Looping_Num - 1, LVSolvInTOffset)

```

```

    solvRate = Range(LVtimeAddress).Offset(Looping_Num - 1, LVSolvRateOffset)
    gasOutT = Range(LVtimeAddress).Offset(Looping_Num - 1, LVGasOutTOffset)
    absProT1 = Range(LVtimeAddress).Offset(Looping_Num - 1,
LVAbsTProOffset)
    absProT2 = Range(LVtimeAddress).Offset(Looping_Num - 1, LVAbsTProOffset
+ 1)
    absProT3 = Range(LVtimeAddress).Offset(Looping_Num - 1, LVAbsTProOffset
+ 2)
    absProT4 = Range(LVtimeAddress).Offset(Looping_Num - 1, LVAbsTProOffset
+ 3)
    absProT5 = Range(LVtimeAddress).Offset(Looping_Num - 1, LVAbsTProOffset
+ 4)
    absProT6 = Range(LVtimeAddress).Offset(Looping_Num - 1, LVAbsTProOffset
+ 5)

```

End If

Workbooks("Analysis").Activate

```

Range("A8").Offset(Count_Num, 9) = LabView_Time
Range("A8").Offset(Count_Num, 10) = N2FlowRate
Range("A8").Offset(Count_Num, 11) = CO2FlowRate
Range("A8").Offset(Count_Num, 12) = TSat
Range("A8").Offset(Count_Num, 18) = gasInT
Range("A8").Offset(Count_Num, 19) = solvInT
Range("A8").Offset(Count_Num, 25) = solvRate
Range("A8").Offset(Count_Num, 27) = gasOutT
Range("A8").Offset(Count_Num, 46) = absProT1

```

Range("A8").Offset(Count_Num, 47) = absProT2

Range("A8").Offset(Count_Num, 48) = absProT3

Range("A8").Offset(Count_Num, 49) = absProT4

Range("A8").Offset(Count_Num, 50) = absProT5

Range("A8").Offset(Count_Num, 51) = absProT6

Exit Do

End If

If Loop_Num > 10000 Then

Exit Do

End If

Looping_Num = Looping_Num + 1

Loop

WB1.Close

'Write the read LVI N2 Flow Rate

Range("A8").Offset(Count_Num, 13) = 19

'Correct the LVI flow rate for T & P

Range("A8").Offset(Count_Num, 14).FormulaR1C1 = "= 28.316847/60*RC[-1]*((28.96*790801.1*293.15)/(28.01*101325*294.15))^(1/2)"

'Write the read LVI H2O Flow Rate

Range("A8").Offset(Count_Num, 15) = 0.5

'Correct the read LVI H2O Flow Rate

Range("A8").Offset(Count_Num, 16).FormulaR1C1 = "=1.2017*RC[-1]-0.2465"

'Write the read LVI T

Range("A8").Offset(Count_Num, 17) = 325

'Write the solvent concentration and loading

Range("A8").Offset(Count_Num, 20) = 5

Range("A8").Offset(Count_Num, 21) = 0.25

'Calculate solvent apparent mole fractions of PZ and CO2

Range("A8").Offset(Count_Num, 22).FormulaR1C1 = "=RC[-2]/((1000/18.01528)+RC[-2]*(1+2*RC[-1]))"

Range("A8").Offset(Count_Num, 23).FormulaR1C1 = "=2*RC[-2]*RC[-3]/((1000/18.01528)+RC[-3]*(1+2*RC[-2]))"

'Calculate the solvent mass density

Range("A8").Offset(Count_Num, 24).FormulaR1C1 = "=1000*(1.5494-0.0005728*(RC[-5]+273.15))*ln(2.676*RC[-1]-0.030977*RC[-2]-0.0726176*RC[-3]+2.102569)"

'Correct the solvent flow rate

Range("A8").Offset(Count_Num, 26).FormulaR1C1 = "=RC[-1]*((1.36-(RC[-2]/1000))/(0.36*(RC[-2]/1000)))^(1/2)"

'Calculate equilibrium H2O partial pressure, CO2 solubility, PZ volatility

```
Range("A8").Offset(Count_Num, 28).FormulaR1C1 =  
"=(100/101325)*((1000/18.01528)/((1000/18.01528)+RC[-8]))*exp(73.649-(7258.2/(RC[-  
9]+273.15))-7.3037*ln(RC[-9]+273.15)+0.0000041653*(RC[-9]+273.15)^2)"
```

```
Range("A8").Offset(Count_Num, 29).FormulaR1C1 = "(100/101325)*exp(35.3-  
(11054/(RC[-10]+273.15))-18.9*RC[-8]^2+4958*(RC[-8]/(RC[-10]+273.15))+10163*(RC[-  
8]^2/(RC[-10]+273.15)))"
```

```
Range("A8").Offset(Count_Num, 30).FormulaR1C1 = "(1000000/101325)*(RC[-  
10]/(RC[-10]+(1000/18.01528)))*exp(-123+21.6*ln(RC[-11]+273.15)+20.2*RC[-9]-  
18174*(RC[-9]^2/(RC[-11]+273.15)))"
```

'Write the inlet gas concentration

```
Range("A8").Offset(Count_Num, 32) = 7
```

```
Range("A8").Offset(Count_Num, 33) = 12
```

```
Range("A8").Offset(Count_Num, 34) = 10
```

```
FullFilename = FTIR_Pathway
```

```
Workbooks.Open Filename:=FullFilename
```

```
Set WB1 = ActiveWorkbook
```

```
Range(FTIRtimeAddress).Select
```

```
Looping_Num = 1
```

```
Do
```

```
FTIR_Time = CDate(Range(FTIRtimeAddress).Offset(Looping_Num, 0))
```

```
If FTIR_Time = PDI_Time Then
```

```
PZConc = Range(FTIRtimeAddress).Offset(Looping_Num, FTIRPZOffset)
```

```
CO2Conc = Range(FTIRtimeAddress).Offset(Looping_Num, FTIRCO2Offset)
```

```
H2OConc = Range(FTIRtimeAddress).Offset(Looping_Num, FTIRH2OOffset)
```

```

Workbooks("Analysis").Activate
Range("A8").Offset(Count_Num, 31) = FTIR_Time
Range("A8").Offset(Count_Num, 35) = H2OConc
Range("A8").Offset(Count_Num, 36) = CO2Conc
Range("A8").Offset(Count_Num, 37) = PZConc
Exit Do

ElseIf FTIR_Time > PDI_Time Then
    time_privous = DateDiff("s",
CDate(Range(FTIRtimeAddress).Offset(Looping_Num - 1, 0)), PDI_Time)
    time_next = DateDiff("s", FTIR_Time, PDI_Time)
    If Abs(time_privous) < Abs(time_next) Then
        FTIR_Time = CDate(Range(FTIRtimeAddress).Offset(Looping_Num - 1, 0))
        PZConc = Range(FTIRtimeAddress).Offset(Looping_Num - 1, FTIRPZOffset)
        CO2Conc = Range(FTIRtimeAddress).Offset(Looping_Num - 1,
FTIRCO2Offset)
        H2OConc = Range(FTIRtimeAddress).Offset(Looping_Num - 1,
FTIRH2OOffset)
    ElseIf Abs(time_privous) >= Abs(time_next) Then
        FTIR_Time = CDate(Range(FTIRtimeAddress).Offset(Looping_Num, 0))
        PZConc = Range(FTIRtimeAddress).Offset(Looping_Num, FTIRPZOffset)
        CO2Conc = Range(FTIRtimeAddress).Offset(Looping_Num, FTIRCO2Offset)
        H2OConc = Range(FTIRtimeAddress).Offset(Looping_Num, FTIRH2OOffset)
    End If
Workbooks("Analysis").Activate
Range("A8").Offset(Count_Num, 31) = FTIR_Time
Range("A8").Offset(Count_Num, 35) = H2OConc
Range("A8").Offset(Count_Num, 36) = CO2Conc

```

```

Range("A8").Offset(Count_Num, 37) = PZConc
Exit Do
End If
If Loop_Num > 10000 Then
Exit Do
End If
Looping_Num = Looping_Num + 1
Loop
WB1.Close

```

'Write the droplet concentration and loading

```

Range("A8").Offset(Count_Num, 38) = 0.6
Range("A8").Offset(Count_Num, 39) = 0.3

```

'Calculate droplet apparent mole fractions of CO2 and PZ

```

Range("A8").Offset(Count_Num, 40).FormulaR1C1 = "=RC[-2]/((1000/18.01528)+RC[-2]*(1+2*RC[-1]))"
Range("A8").Offset(Count_Num, 41).FormulaR1C1 = "=2*RC[-2]*RC[-3]/((1000/18.01528)+RC[-3]*(1+2*RC[-2]))"

```

'Calculate the droplet mass density

```

Range("A8").Offset(Count_Num, 42).FormulaR1C1 = "=1000*(1.5494-0.0005728*(RC[-15]+273.15))*ln(2.676*RC[-1]-0.030977*RC[-2]-0.0726176*RC[-3]+2.102569)"

```

'Calculate the concentration of PZ found in the aerosol phase

```
Range("A8").Offset(Count_Num, 43).FormulaR1C1 = "=RC[-35]*(RC[-5]*86.136/1000)/(1+RC[-5]*(86.136+2*RC[-4]*44.0095)/1000)/86.136*RC[-1]*8.3144621*(273+RC[-16])*1/101325*0.001"
```

'Calculate total PZ concentration

```
Range("A8").Offset(Count_Num, 44).FormulaR1C1 = "=RC[-1]+RC[-14]"
```

'Calculate the absolute difference in the PZ concentration

```
Range("A8").Offset(Count_Num, 45).FormulaR1C1 = "=abs((RC[-8]-RC[-1])/RC[-8])*100"
```

```
Count_Num = Count_Num + 1
```

```
End If
```

```
Next
```

```
End With
```

```
Columns("A:AZ").AutoFit
```

```
End Sub
```

Sub PDI_Analyze()

```
Cells(4, 3) = "Normalized Counts"
```

```
Cells(4, 4) = "Normalized Volume"
```

```
Cells(4, 5) = "Concentration of Droplet"
```

```
Cells(4, 6) = "Diameter Counts"
```

```
Cells(4, 7) = "Area Counts"
```

Cells(4, 8) = "Volume Counts"

Cells(4, 9) = "d4 Counts"

Cells(4, 10) = "Count Mean"

Cells(4, 11) = "Diameter Mean"

Cells(4, 12) = "Area Mean"

Cells(4, 13) = "Volume Mean"

Cells(5, 3) = "--"

Cells(5, 4) = "(μ^3 /Part.)"

Cells(5, 5) = "(μ^3 /cm³)"

Cells(5, 6) = "(μ)"

Cells(5, 7) = "(μ^2)"

Cells(5, 8) = "(μ^3)"

Cells(5, 9) = "(μ^4)"

Cells(5, 10) = "--"

Cells(5, 11) = "(μ)"

Cells(5, 12) = "(μ^2)"

Cells(5, 13) = "(μ^3)"

Columns("A:M").AutoFit

Cells(6, 1) = 0.1

Cells(7, 1) = 0.2

Range("A6:A7").Select

Selection.AutoFill Destination:=Range(Selection, Selection.End(xlDown))

Range("A6").Select

Count_Num = Range(Selection, Selection.End(xlDown)).Count

Range("B6").Select

Range("B" & CStr(Count_Num + 6)).FormulaR1C1 = "=SUM(R[-" & CStr(Count_Num) & "]C:R[-1]C)"

Range("C6").FormulaR1C1 = "=RC[-1]/R" & CStr(Count_Num + 6) & "C[-1]"

Range("D6").FormulaR1C1 = "=4/3*PI()*(RC[-3]/2)^3*RC[-1]"

Range("E6").FormulaR1C1 = "=RC[-1]*R2C3"

Range("F6").FormulaR1C1 = "=RC[-5]*RC[-4]"

Range("G6").FormulaR1C1 = "=RC[-6]^2*RC[-5]"

Range("H6").FormulaR1C1 = "=RC[-7]^3*RC[-6]"

Range("I6").FormulaR1C1 = "=RC[-8]^4*RC[-7]"

Range("C6:I6").Select

Selection.AutoFill Destination:=Range("C6:I" & CStr(Count_Num + 6 - 1))

Range("B6").Select

Selection.End(xlDown).Select

Selection.AutoFill Destination:=Range("B" & CStr(Count_Num + 6) & ":I" & CStr(Count_Num + 6)), Type:=xlFillDefault

Range("J6").FormulaR1C1 = "=R[" & CStr(Count_Num) & "]C[-4]/R[" & CStr(Count_Num) & "]C[-8]"

Range("K6").FormulaR1C1 = "=R[" & CStr(Count_Num) & "]C[-4]/R[" & CStr(Count_Num) & "]C[-5]"

Range("L6").FormulaR1C1 = "=R[" & CStr(Count_Num) & "]C[-4]/R[" & CStr(Count_Num) & "]C[-5]"

```
Range("M6").FormulaR1C1 = "=R[" & CStr(Count_Num) & "]C[-4]/R[" & CStr(Count_Num) & "]C[-5]"
```

End Sub

A.2 FTIR/PDI PILOT EXPERIMENT DATA ALGORITHM FOR PM DATA SETS

The AGC data algorithm was modified to create an algorithm for campaign measurements using the PDI and FTIR. Since the PDI outputs timestamps with AM and PM tags, two codes were generated; one uses a string search with an AM tag and the other uses a PM tag. For brevity, the PM code is given here. The AM code is identical with the exception of all instances of PM being replaced by AM which are highlighted in orange.

A.2.1 PM_PDI_FTIR_Analysis.xlsm

'Declare global FTIR variables

Global FTIRtimeAddress As String

Global FTIRPDItimeOffset As Integer

Global FTIRPZOffset As Integer

Global FTIRCO2Offset As Integer

Global FTIRH2OOffset As Integer

Sub PDI_Path_Select()

'Select the folder containing the PDI files

With Application.FileDialog(msoFileDialogFolderPicker)

.AllowMultiSelect = True

.Show

'Output the file pathway

Cells(1, 2) = .SelectedItems(1)

End With

'Declare variable

Dim folderspec As String

'Clear file list from previous analysis

Range("A7:D1000").Select

Selection.ClearContents

'Write label text

Cells(7, 1).Value = "Number of PDI Files"

'Select cell to place "X" and row/column offsetting

Range("A8").Select

'Set folderspec variable string to the file pathway

folderspec = Cells(1, 2).Value

'Create a file system object and count the files present in the folder

Set fs = CreateObject("Scripting.FileSystemObject")

Set f = fs.getfolder(folderspec)

Set fc = f.Files

PDI_Files_Num = fc.Count

Cells(7, 2).Value = PDI_Files_Num

'For each file in the file collection fc, output the file name and place and "X" in the next row
down

```
For Each fl In fc
    With ActiveCell
        .Value = "X"
        .Offset(0, 1).Value = fl.Name
        .Offset(1, 0).Select
    End With
Next fl
End Sub
```

Sub FTIR_Path_Select()

```
'Select FTIR file for analysis
With Application.FileDialog(msoFileDialogOpen)
    .AllowMultiSelect = True
    .Show
    'Output the FTIR file pathway
    Cells(2, 2) = .SelectedItems(1)
End With
Set FTIR_Pathway = Cells(2, 2)

'Open the FTIR file
Workbooks.Open Filename:=FTIR_Pathway

'Declare variables and set variables as objects
Set WB1 = ActiveWorkbook
Dim sCell As Range
```

Dim timeColOffset As Integer

Dim FTIRPDIClockOffsetMin As Integer

Dim PZColOffset As Integer

Dim CO2ColOffset As Integer

Dim H2OColOffset As Integer

'Prompt for selection of the time heading cell

Set sCell = Application.InputBox("Select Time Heading Cell", Type:=8)

'Count the number of data entries

Range(sCell.Address).Select

Count_Num = Range(Selection, Selection.End(xlDown)).Count - 1

'Prompt for the clock offset between the PDI and FTIR in minutes

FTIRPDIClockOffsetMin = InputBox("Enter the clock offset between the PDI and FTIR in minutes [FTIR-PDI]", "Clock Offset", 1)

Cells(1, 1) = "Clock Offset"

Cells(2, 1) = FTIRPDIClockOffsetMin

'Calculate the actual time using the clock offset

Range(sCell.Address).Offset(1, 2).FormulaR1C1 = "=RC[-2]+Time(0,R2C1,0)"

Range(sCell.Address).Offset(1, 2).Select

Selection.AutoFill Destination:=Range(Selection, Selection.Offset(Count_Num - 1))

'Set the timeColOffset variable to the column index of the time heading cell

timeColOffset = sCell.Offset(0, 2).Column

'Set the FTIRtimeAddress variable to the address of the time heading cell

```
Range(sCell.Address).Offset(0, 2).Select
```

```
FTIRtimeAddress = ActiveCell.Address
```

'Prompt for selection of the PZ concentration heading cell

```
Set sCell = Application.InputBox("Select PZ Heading Cell", Type:=8)
```

'Set the concColOffset variable to the column index of the PZ concentration heading cell

```
PZColOffset = sCell.Column
```

'Calculate the offset between the PZ concentration and timestamp column

```
FTIRPZOffset = PZColOffset - timeColOffset
```

'Prompt for selection of the CO2 concentration heading cell

```
Set sCell = Application.InputBox("Select CO2 Heading Cell", Type:=8)
```

'Set the concColOffset variable to the column index of the CO2 concentration heading cell

```
CO2ColOffset = sCell.Column
```

'Calculate the offset between the PZ concentration and timestamp column

```
FTIRCO2Offset = CO2ColOffset - timeColOffset
```

'Prompt for selection of the H2O concentration heading cell

```
Set sCell = Application.InputBox("Select H2O Heading Cell", Type:=8)
```

'Set the concColOffset variable to the column index of the H2O concentration heading cell

```
H2OColOffset = sCell.Column
```

'Calculate the offset between the PZ concentration and timestamp column

```
FTIRH2OOffset = H2OColOffset - timeColOffset
```

'Close the FTIR workbook

WB1.Close

End Sub

Sub Analyze()

Set PDI_Pathway = Cells(1, 2)

Set FTIR_Pathway = Cells(2, 2)

Set PDI_Files_Num = Cells(7, 2)

For Each s In Sheets

 If s.Name = "Analysis" Then

 Application.DisplayAlerts = False

 s.Delete

 Exit For

End If

Next

Sheets.Add

ActiveSheet.Name = "Analysis"

Cells(1, 1) = "PDI & FTIR Analysis Table"

Cells(3, 1) = "PDI Pathway"

Cells(3, 2) = "PDI File Name"

Cells(3, 3) = "PDI Time"
 Cells(3, 4) = "Particle Concentration (part./cm3)"
 Cells(3, 5) = "Count Mean"
 Cells(3, 6) = "Diameter Mean"
 Cells(3, 7) = "Area Mean"
 Cells(3, 8) = "Volume Mean"
 Cells(3, 9) = "Integral Droplet Volume (um3/cm3)"
 Cells(3, 10) = "FTIR Time"
 Cells(3, 11) = "H2O (vol %)"
 Cells(3, 12) = "CO2 (vol %)"
 Cells(3, 13) = "PZ/MEA (ppmV)"
 Cells(3, 14) = "Conc. of PZ/MEA in Drop (mol/kg)"
 Cells(3, 15) = "CO2 LDG in Drop (mol/mol alk.)"
 Cells(3, 16) = "Apparent xMEA in Drop (--)"
 Cells(3, 17) = "Apparent xCO2 in Drop (--)"
 Cells(3, 18) = "Drop Density (kg/m3)"
 Cells(3, 19) = "Aerosol Conc.Of PZ/MEA (ppmV)"
 Cells(3, 20) = "Total Conc. of PZ/MEA (ppmV)"

Columns("A:T").AutoFit

Range("A3:T3").Select

Selection.Borders(xlDiagonalDown).LineStyle = xlNone

Selection.Borders(xlDiagonalUp).LineStyle = xlNone

Selection.Borders(xlEdgeLeft).LineStyle = xlNone

Selection.Borders(xlEdgeTop).LineStyle = xlNone

With Selection.Borders(xlEdgeBottom)

.LineStyle = xlContinuous

```

.ColorIndex = 0

.TintAndShade = 0

.Weight = xlMedium

End With

Sheets("File_List").Select
Range("A8").Select
With Range("A8")
    Count_Num = 1
    For i = 0 To PDI_Files_Num - 1
        If .Offset(i, 0) = "X" Or .Offset(i, 0) = "x" Then
            .Offset(i, 1).Copy
            Sheets("Analysis").Select
            Range("A3").Offset(Count_Num, 0) = PDI_Pathway
            Range("A3").Offset(Count_Num, 1).Select
            ActiveSheet.Paste
            File_Num = File_Num + 1
            File_Name = Range("A3").Offset(Count_Num, 1)
            Dim WB1 As Workbook
            FullFilename = PDI_Pathway & "\" & File_Name
            Workbooks.Open Filename:=FullFilename
            Set WB1 = ActiveWorkbook
            PDI_Analyze
            WB1.Save

            'Copy and paste the PDI timestamp

            WB1.Activate

```

```
Range("C1").Copy
```

```
Workbooks("PM_PDI_FTIR_Analysis").Activate
```

```
Range("A3").Offset(Count_Num, 2).PasteSpecial (xlPasteValues)
```

```
'Copy and paste the total particle concentration
```

```
WB1.Activate
```

```
Range("C2").Copy
```

```
Workbooks("PM_PDI_FTIR_Analysis").Activate
```

```
Range("A3").Offset(Count_Num, 3).PasteSpecial (xlPasteValues)
```

```
'Copy and paste the calculated particle size distribution statistics
```

```
WB1.Activate
```

```
Range("J6:M6").Copy
```

```
Workbooks("PM_PDI_FTIR_Analysis").Activate
```

```
Range("A3").Offset(Count_Num, 4).PasteSpecial (xlPasteValues)
```

```
'Copy and paste the integrated particle volume
```

```
WB1.Activate
```

```
Range("E6").Select
```

```
Selection.End(xlDown).Copy
```

```
Workbooks("PM_PDI_FTIR_Analysis").Activate
```

```
Range("A3").Offset(Count_Num, 8).PasteSpecial (xlPasteValues)
```

```
'Close PDI file workbook
```

```
WB1.Close
```

```
Dim str() As String
```

```

str = Split(Range("A3").Offset(Count_Num, 2).Value)
PDI_Time = TimeValue(str(2) & " PM")

FullFilename = FTIR_Pathway
Workbooks.Open Filename:=FullFilename
Set WB1 = ActiveWorkbook
Range(FTIRtimeAddress).Select
Looping_Num = 1

Do
    FTIR_Time = CDate(Range(FTIRtimeAddress).Offset(Looping_Num, 0))
    If FTIR_Time = PDI_Time Then
        PZConc = Range(FTIRtimeAddress).Offset(Looping_Num, FTIRPZOffset)
        CO2Conc = Range(FTIRtimeAddress).Offset(Looping_Num, FTIRCO2Offset)
        H2OConc = Range(FTIRtimeAddress).Offset(Looping_Num, FTIRH2OOffset)
        Workbooks("PM_PDI_FTIR_Analysis").Activate
        Range("A3").Offset(Count_Num, 9) = FTIR_Time
        Range("A3").Offset(Count_Num, 10) = H2OConc
        Range("A3").Offset(Count_Num, 11) = CO2Conc
        Range("A3").Offset(Count_Num, 12) = PZConc
        Exit Do
    ElseIf FTIR_Time > PDI_Time Then
        time_privous = DateDiff("s",
CDate(Range(FTIRtimeAddress).Offset(Looping_Num - 1, 0)), PDI_Time)
        time_next = DateDiff("s", FTIR_Time, PDI_Time)
        If Abs(time_privous) < Abs(time_next) Then
            FTIR_Time = CDate(Range(FTIRtimeAddress).Offset(Looping_Num - 1, 0))

```

```

PZConc = Range(FTIRtimeAddress).Offset(Looping_Num - 1, FTIRPZOffset)
CO2Conc = Range(FTIRtimeAddress).Offset(Looping_Num - 1,
FTIRCO2Offset)
H2OConc = Range(FTIRtimeAddress).Offset(Looping_Num - 1,
FTIRH2OOffset)

ElseIf Abs(time_priovus) >= Abs(time_next) Then
    FTIR_Time = CDate(Range(FTIRtimeAddress).Offset(Looping_Num, 0))
    PZConc = Range(FTIRtimeAddress).Offset(Looping_Num, FTIRPZOffset)
    CO2Conc = Range(FTIRtimeAddress).Offset(Looping_Num, FTIRCO2Offset)
    H2OConc = Range(FTIRtimeAddress).Offset(Looping_Num, FTIRH2OOffset)
End If

Workbooks("PM_PDI_FTIR_Analysis").Activate
Range("A3").Offset(Count_Num, 9) = FTIR_Time
Range("A3").Offset(Count_Num, 10) = H2OConc
Range("A3").Offset(Count_Num, 11) = CO2Conc
Range("A3").Offset(Count_Num, 12) = PZConc

Exit Do

End If

If Loop_Num > 10000 Then
    Exit Do
End If

Looping_Num = Looping_Num + 1

Loop

WB1.Close

'Write the droplet concentration and loading
Range("A3").Offset(Count_Num, 13) = 0.6

```

Range("A3").Offset(Count_Num, 14) = 0.3

'Calculate droplet apparent mole fractions of CO2 and PZ

Range("A3").Offset(Count_Num, 15).FormulaR1C1 = "=RC[-2]/((1000/18.01528)+RC[-2]*(1+2*RC[-1]))"

Range("A3").Offset(Count_Num, 16).FormulaR1C1 = "=2*RC[-2]*RC[-3]/((1000/18.01528)+RC[-3]*(1+2*RC[-2]))"

'Calculate the droplet mass density

Range("A3").Offset(Count_Num, 17).FormulaR1C1 = "=1000*(1.5494-0.0005728*(RC[-15]+273.15))*ln(2.676*RC[-1]-0.030977*RC[-2]-0.0726176*RC[-3]+2.102569)"

Range("A3").Offset(Count_Num, 17).FormulaR1C1 = "=1000"

'Calculate the concentration of PZ found in the aerosol phase

Range("A3").Offset(Count_Num, 18).FormulaR1C1 = "=RC[-10]*(RC[-5]*86.136/1000)/(1+RC[-5]*(86.136+2*RC[-4]*44.0095)/1000)/86.136*RC[-1]*8.3144621*(273+40)*1/101325*0.001"

'Calculate total PZ concentration

Range("A3").Offset(Count_Num, 19).FormulaR1C1 = "=RC[-1]"

Count_Num = Count_Num + 1

End If

Next

End With

Columns("A:T").AutoFit

End Sub

Sub PDI_Analyze()

Cells(4, 3) = "Normalized Counts"

Cells(4, 4) = "Normalized Volume"

Cells(4, 5) = "Concentration of Droplet"

Cells(4, 6) = "Diameter Counts"

Cells(4, 7) = "Area Counts"

Cells(4, 8) = "Volume Counts"

Cells(4, 9) = "d4 Counts"

Cells(4, 10) = "Count Mean"

Cells(4, 11) = "Diameter Mean"

Cells(4, 12) = "Area Mean"

Cells(4, 13) = "Volume Mean"

Cells(5, 3) = "--"

Cells(5, 4) = "(μ^3 /Part.)"

Cells(5, 5) = "(μ^3 /cm³)"

Cells(5, 6) = "(μ)"

Cells(5, 7) = "(μ^2)"

Cells(5, 8) = "(μ^3)"

Cells(5, 9) = "(μ^4)"

Cells(5, 10) = "--"

Cells(5, 11) = "(um)"

Cells(5, 12) = "(um2)"

Cells(5, 13) = "(um3)"

Columns("A:M").AutoFit

Cells(6, 1) = 0.1

Cells(7, 1) = 0.2

Range("A6:A7").Select

Selection.AutoFill Destination:=Range(Selection, Selection.End(xlDown))

Range("A6").Select

Count_Num = Range(Selection, Selection.End(xlDown)).Count

Range("B6").Select

Range("B" & CStr(Count_Num + 6)).FormulaR1C1 = "=SUM(R[-" & CStr(Count_Num) & "]C:R[-1]C)"

Range("C6").FormulaR1C1 = "=RC[-1]/R" & CStr(Count_Num + 6) & "C[-1]"

Range("D6").FormulaR1C1 = "=4/3*PI()*(RC[-3]/2)^3*RC[-1]"

Range("E6").FormulaR1C1 = "=RC[-1]*R2C3"

Range("F6").FormulaR1C1 = "=RC[-5]*RC[-4]"

Range("G6").FormulaR1C1 = "=RC[-6]^2*RC[-5]"

Range("H6").FormulaR1C1 = "=RC[-7]^3*RC[-6]"

Range("I6").FormulaR1C1 = "=RC[-8]^4*RC[-7]"

Range("C6:I6").Select

Selection.AutoFill Destination:=Range("C6:I" & CStr(Count_Num + 6 - 1))

```

Range("B6").Select
Selection.End(xlDown).Select
Selection.AutoFill Destination:=Range("B" & CStr(Count_Num + 6) & ":I" & CStr(Count_Num
+ 6)), Type:=xlFillDefault

Range("J6").FormulaR1C1 = "=R[" & CStr(Count_Num) & "]C[-4]/R[" & CStr(Count_Num) &
"]C[-8]"
Range("K6").FormulaR1C1 = "=R[" & CStr(Count_Num) & "]C[-4]/R[" & CStr(Count_Num)
& "]C[-5]"
Range("L6").FormulaR1C1 = "=R[" & CStr(Count_Num) & "]C[-4]/R[" & CStr(Count_Num) &
"]C[-5]"
Range("M6").FormulaR1C1 = "=R[" & CStr(Count_Num) & "]C[-4]/R[" & CStr(Count_Num)
& "]C[-5]"

End Sub

```

Appendix B: PDI Supporting Documentation

B.1 AEROSOL ANALYZER SELECTION

One of the major parts of this study was to select an aerosol analyzer capable of measuring PSDs and total particle densities from fully saturated process streams at both the bench and pilot scale. Generally, aerosol analyzers fall into two categories: *in situ* and *ex situ*.

In situ analyzers are broadly defined as those measurement types that do not destructively interfere with the sampled media; however, many “*in situ*” techniques use preconditioners such as temperature controllers, denuders, and diluters when sampling from very harsh environments or when particle densities are high enough to cause significant sizing errors. Therefore, this work defines *in situ* measurements as those, under perfect conditions and without geometric restrictions, that could measure PSDs and total particle density in the process gas directly. A true *in situ* measurement would capture the true properties of the process aerosols and measurement error would be limited to only the instrument error.

Ex Situ measurements involve selective partitioning of the aerosol field by mobility mechanisms to yield sizing and density measurements. In nearly every case, they require pulling a small fraction of the process stream for external analysis. *Ex situ* measurements therefore rely on the ability to sample particles without biasing their *in situ* properties.

Neither *ex situ* nor *in situ* analyzers can provide perfect measurements. Spatial non-uniformities, high particle densities, broad concentration ranges, velocity distributions, evaporation, coalescence, deposition, fogging of optical surfaces, large variation in particle diameter (up to several orders of magnitude), inlet efficiencies, and wall losses can cause limitations for each instrument class (Kulkarni et al., 2011b). Most instruments fail under harsh conditions: extremes in temperature and pressure, reactions, and corrosive environments must all be considered when selecting a particle analyzer.

B.1.1 Aerosol Analyzer Selection

Selecting an aerosol analyzer requires some *a priori* estimation of the expected particle field information including the total particle density, the approximate size distribution range, and process conditions; specifically, the relative humidity.

Figure B.1 shows the aerosol specific information available at the time of analyzer selection and subsequent data collected at UT after the selection of the PDI. The reported ranges are color-coded by the aerosol source; orange bars indicate real flue gas generated from coal-fired boilers (Kolderup et al., 2012; Fujita et al., 2013) whereas the blue bars indicate synthetic flue gas made by either natural gas combustion and subsequent addition of flyash and SO₃ (Khakharia, 2015; Brachert et al., 2014; Mertens et al., 2014) or by the addition of vaporized H₂SO₄ into air and makeup CO₂ (UT). The dark blue bar at the top of the chart indicates the entire envelope of aerosol size data.

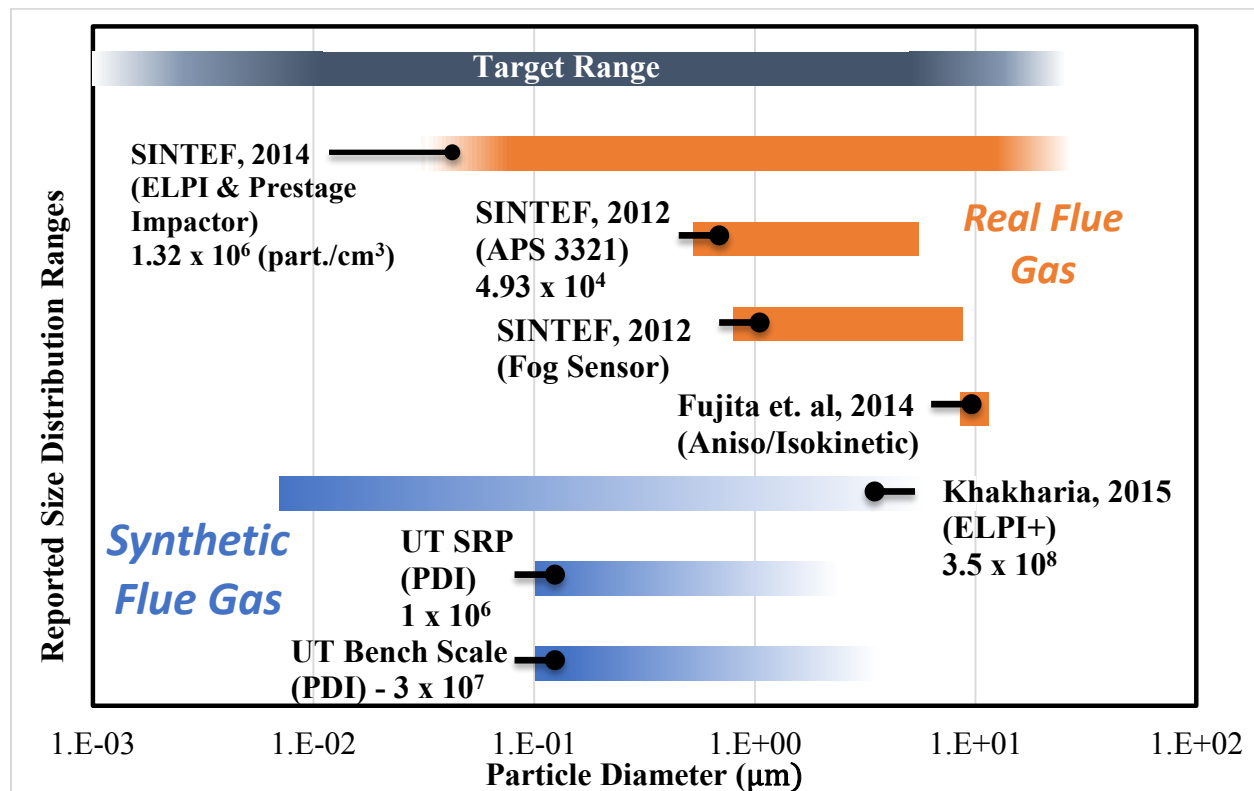


Figure B.1: Reported size ranges and total particle densities in CO₂ capture pilot plants and bench scale units. Size determination method is contained in parentheses.

Generally, the real flue gas data showed larger average particle sizes and lower total particle densities. That relationship is expected given the longer residence times in real systems for nucleation and coagulation to proceed nearly to completion and condensation to start dominating dynamic processes.

The target size range was then plotted against a literature search of aerosol analyzers irrespective of density limitations (**Figure B.2**). *Ex situ* and *in situ* techniques are indicated by color.

No single instrument was capable of spanning the four orders of magnitude in particle size as indicated by the target range; therefore, the “possible” range of aerosol sizes was reduced to a subset of “significant” aerosols. The purpose of this work is to reduce amine emissions caused by aerosols, which are proportional to the total liquids volume of the integrated aerosol field and the aerosol amine concentration. Because the volume of a droplet is proportional to the cube of the diameter, the emission rate is proportional to the cube of particle diameter. Similarly, emissions scale linearly with particle density. Therefore, the target range was weighted by the cube of diameter and linearly to concentration. The applied “mass” bias meant that the upper part of the target range, or the supermicron range, is most significant to aerosol emissions due to the cubic response in diameter. However, the submicron range tends to contain very high densities and is more critical when nucleation and coagulation are the dominant aerosol mechanisms. Ultimately, a target range of 0.1–10 μm was chosen as the basis for the size measurement range.

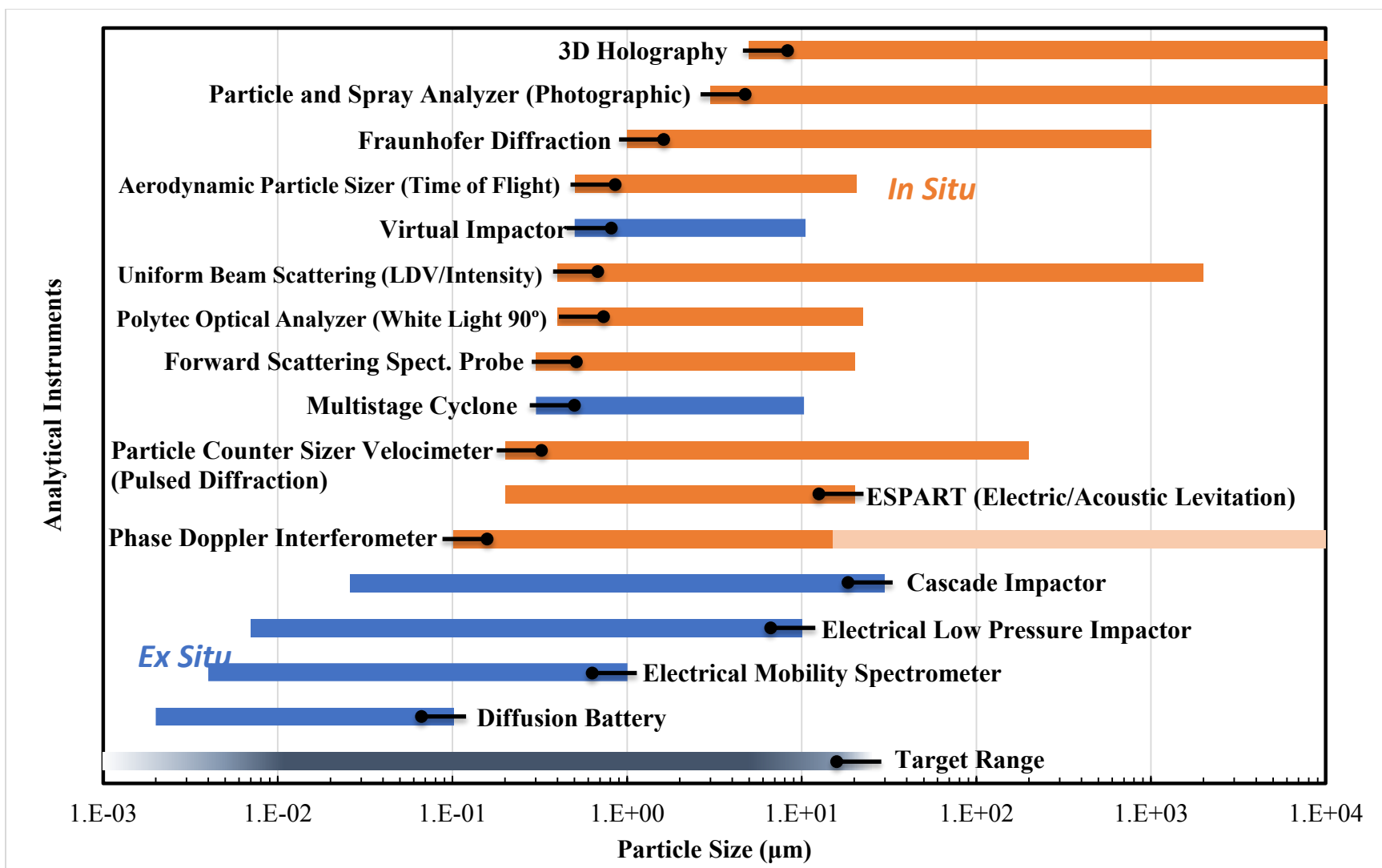


Figure B.2: Operating windows for aerosol size analysis instruments. *In situ* instruments are defined as non-interfering although a sample often requires extraction from a measurement point.

B.1.2 Instrument Review and Known Limitations

After comparing instrument sizing envelopes with the biased target range, further literature review was conducted to screen analyzers by particle density limitations, measurement errors, experimental limitations, and measured properties. The results of the literature review are tabulated in **Table B.1–Table B.3**.

It was clear from literature that the instruments most closely matching the target aerosols were the ELPI (now ELPI+) and the PDI which are the best *ex situ* and *in situ* instruments, respectively. A trade off was quickly identified between the instruments; the PDI (*in situ*) will provide more accurate measurements for larger aerosols while the ELPI (*ex situ*) can measure an order of magnitude smaller in particle diameter using four discrete stages.

B.1.2.1 ELPI Errors and Limitations

Several sources of error are known for cascade impactors and corona chargers which are sub pieces of the ELPI: (1) particle bounce off of impaction stages leads to multiple counting, (2) critical orifices on latter stages lead to condensation and evaporation due to temperature and pressure fluctuations which bias collection, (3) the imparted charge to an aerosol is a function of the particle properties and the diameter, and (4) diffusion and electrophoretic collection on the walls of the impaction column further bias sizing measurements. Additionally, the ELPI sizes based on the aerodynamic diameter; the actual particle density is required to determine the mass concentration. The ELPI also requires *ex situ* sampling which can lead to significant changes in the PSD as outlined in Chapter 2.

Some of the known biases are addressed using empirically fit kernel functions which calculate the charging efficiency of the preconditioning corona charger and the cut efficiency of each individual impactor stage.

Table B.1: Review of Analytical Instruments Capable of Measuring Particle Size Distributions. ^[1](Kulkarni et al., 2011b); ^[2](Biswas, 1985); ^[3](Dekati Ltd., 2014); ^[4](O’Hern et al., 1993); ^[5](Artium Technologies, 2015); ^[6](Stark et al., 2008); ^[7](Mazumder et al., 2007); ^[8](Malvern Instruments, 2007).

Instrument	Operating Principle	Measured Properties	Size Range (µm)	Conc. Limit (part./cm ³)	Sources of Error / Limitations	Ref(s).
Diffusion Battery	Diffusion	Size, Count	0.001 – 0.1	Volume	Assumes 100% collection. Complex inversion for polydisperse aerosol. <i>Ex Situ</i> losses.	[1]
Electrical Mobility Spectrometer	Electrostatic Attraction	Size, Count	0.003 – 1	> 10 ⁵ (sub µ)	Charging bias with size. Diffusion and electrophoretic losses. Mobility-equivalent particles (mass/charge). <i>Ex Situ</i> losses.	[1]
Electrostatic Low Pressure Impactor	Impaction and Interception - Charged	Size, Count, Composition	0.006 – 10	1.7x10 ⁴ – 7.9x10 ⁷	Diffusion and electrophoretic losses. Requires <i>a priori</i> density. Particle bounce/multi-counting. T/P changes due to critical flow - condensation/evaporation. <i>Ex Situ</i> losses.	[1][2][3]
Cascade Impactor	Impaction & Interception	Size, Count, Composition	0.025 – 30	Volume	Requires post processing. Requires <i>a priori</i> density. Particle bounce/multi-counting. T/P changes due to critical flow - condensation/evaporation. <i>Ex Situ</i> losses.	[1][2]
Phase Doppler Interferometer	LDV & LM Scattering (Phase)	Size, Count, Velocity	0.1 – 8,000+	> 10 ⁶	Trajectory ambiguity. Particle opacity. PMT sensitive concentration. Coincidence errors. Assumes spherical particles.	[1][4][5]

Table B.2: Review of Analytical Instruments Capable of Measuring Particle Size Distributions. ^[1](Kulkarni et al., 2011b); ^[2](Biswas, 1985); ^[3](Dekati Ltd., 2014); ^[4](O’Hern et al., 1993); ^[5](Artium Technologies, 2015); ^[6](Stark et al., 2008); ^[7](Mazumder et al., 2007); ^[8](Malvern Instruments, 2007).

Instrument	Operating Principle	Measured Properties	Size Range (µm)	Conc. Limit (part./cm ³)	Sources of Error / Limitations	Ref(s).
Particle Counter Sizer Velocimeter	Diffraction - Pulsed	Size, Count, Velocity	0.2 – 200	10 ⁷ (sub µ) 100 ppm (+µ)	Intensity attenuation from sheeting and high particle density. Coincidence errors.	[1][4]
Electrical Single Particle Aerodynamic Relaxation Time (ESPART)	Electric / Acoustic Levitation – Aerodynamic Phase Lag (LDV)	Size, Count, Charge	0.2 – 20	~10 ⁶ (Based on LDV limitations)	Uncertainty in density, charge, and shape – measures aerodynamic distribution. Coincidence errors. Measurement depends on sample viscosity (T/P).	[1][6][7]
Multistage Cyclone	Impaction and Interception	Size, Count, Composition	0.3 – 10	Volume	Requires post processing. Requires <i>a priori</i> density. Particle re-entrainment. T/P changes due to critical flow - condensation/evaporation. <i>Ex Situ</i> losses.	[1]
Forward Scattering Spectrometer Probe	LM Scattering (Intensity)	Size, Count, Velocity	0.3 – 20	Not Listed	Intensity attenuation from sheeting and high particle density. Coincidence errors. Trajectory errors.	[1][4]
Polytec Optical Analyzer	White Light Scattering at 90°	Size, Count	0.4 – 22	10 ⁶ (sub µ) 10 ³ (+µ)	Coincidence errors. Trajectory errors. Stronger index of refraction dependence. Intensity attenuation from sheeting and high particle density.	[1][4]

Table B.3: Review of Analytical Instruments Capable of Measuring Particle Size Distributions. ^[1](Kulkarni et al., 2011b); ^[2](Biswas, 1985); ^[3](Dekati Ltd., 2014); ^[4](O’Hern et al., 1993); ^[5](Artium Technologies, 2015); ^[6](Stark et al., 2008); ^[7](Mazumder et al., 2007); ^[8](Malvern Instruments, 2007).

Instrument	Operating Principle	Measured Properties	Size Range (µm)	Conc. Limit (part./cm ³)	Sources of Error / Limitations	Ref(s).
Virtual Impactor	Impaction & Interception	Size, Count, Composition	0.5 – 10	Volume	Requires post processing. Requires <i>a priori</i> density. T/P changes due to critical flow - condensation/evaporation. <i>Ex Situ</i> losses. Small particle sampling in minor flow.	[1][2]
Aerodynamic Particle Sizer	Time of Flight (Intensity)	Size, Count	0.5 – 20	10 ³ – 10 ⁴	Technique uses dilution as fundamental part of analysis. Particle loss in accelerating nozzle. Coincidence errors. Recirculation multi-counting. Droplet distortion with accelerating nozzle. Particle density uncertainty.	[1][2][4]
Fraunhofer Diffraction	Diffraction	Size, Count	1 – 1,000	<95% Obscuration	Particles outside focal length cause “vignetting” – large particle bias. Intensity attenuation errors – complex inversion algorithms.	[4][8]
Particle and Spray Analyzer	Photographic	Size, Count	3 – 18,500	Not Listed	Multiple scattering – small particle bias. Beam steering gives false large particle signals. Blurring of small particles. Poor depth of field.	[4]
3D Holography	Holography	Size, Count	5 – 10,000+	Not Listed	Significant post processing required. Not commercially available.	[4]

B.1.2.2 PDI Errors and Limitations

PDI is a single particle counting (SPC) instrument. SPCs use well defined sampling volumes using high intensity lasers to get scattering, phase, or imaging information. PDI classifies particle size based on refraction of light which is measured as high frequency signal pulses. Particle coincidence, or multiple particles passing simultaneously through the sampling volume, is the biggest source of error.

Other errors found in SPCs include total particle density errors caused by the particle trajectory (trajectory error), which is described in Chapter 3, and sizing errors due to the non-monotonic response of Lorenz-Mie scattering which is dependent on the particle shape and index of refraction. Forward scattering measurements minimize index of refraction and shape effects.

Lens imperfections, misalignment, and system limitations restrict the analytical envelope. Background scattering from gas molecules limit the lower detectable size range to about 0.05 μm . Intensity sizing instruments tend to fail under high particle concentrations because of serial scattering; although, intensity effects are made negligible by correlating the diameter to phase (PDI) rather than intensity.

For the specified size range of interest, several modifications to the standard PDI equipment had to be made including decreasing the beam width and increasing the crossing angle. These geometric modifications were necessary to extend the measurement range down to 0.1 μm ; however, the upper bound of measurable particles became fixed at 12 μm . **Figure B.2** shows range of the custom PDI in the dark orange bar and the rest of the complete measurement range for PDI as a technique in the light orange bar.

B.1.3 PDI Rationale

The PDI was ultimately chosen because it offered high fidelity measurements of particle size without the need for dilution or extraction and also provided velocity and total density measurement. As a bench scale analytical tool, the PDI is truly *in situ*; the analysis cell takes the full flow rate of the process. PDI is also commonly used in filter efficiency tests conducted in high humidity environments at pilot plant testing facilities which indicated some level of robustness as a field instrument.

ELPI can measure an order of magnitude smaller in particle diameter than the PDI. Even though the submicron region typically contains higher total densities, the mass distribution is more significant above one micron and the sources of error become more significant on the final ELPI stages. ELPI requires a very small flow rate; ELPI samples *ex situ* at all process scales.

Finally, due to the high cost of aerosol analytical equipment, only one analyzer could be chosen. Since the ELPI is being used at many pilot plants, an opportunity for advancement in aerosol measurement existed and allows for direct method comparison. For all of the reasons listed above, the PDI was selected as the aerosol analytical instrument in this work.

Appendix C: LVI Supporting Documentation

This appendix provides details covering the operation, calibration, and redesign history of the LVI hardware and controls.

C.1 LVI PERFORMANCE DATA

After the first corrosion failure of the LVI, the eductor parts were coated with SilcoTek[®] Dursan[®] protective coating in an attempt to prevent future corrosion. Even though the coating layer is 0.4–1.6 μm , and should therefore have little impact on performance, the flowrate and vacuum levels were measured against vendor data. Additionally, the flowrate was checked because the original eductor in the delivered LVI was discovered to be a different model than specified in the manual (Air Quality Analytical, 2013) and thus previously assumed flowrates had to be adjusted according to the actual, measured flow rate.

C.1.1 Eductor Flow and Vacuum

Figure C.1 shows the compensated flow rate through the LVI and the digitized curves for two eductor bodies; Air-Vac HAVR062SS is the flow body specified in the LVI manual and Air-Vac HAVR093SS is the next larger eductor design. The measured flow rate through the LVI matches the slope of the HAVR093SS curve to within 5%. It was discovered after disassembling the LVI that the actual eductor was indeed the HAVR093SS, not the HAVR062SS as specified. The decrease in flow rate can be attributed to several sources: (1) the eductor body and nozzle were coated with Dursan[®] coating to prevent corrosion, and (2) compounding error from the rotameter, pressure, and temperature measurements.

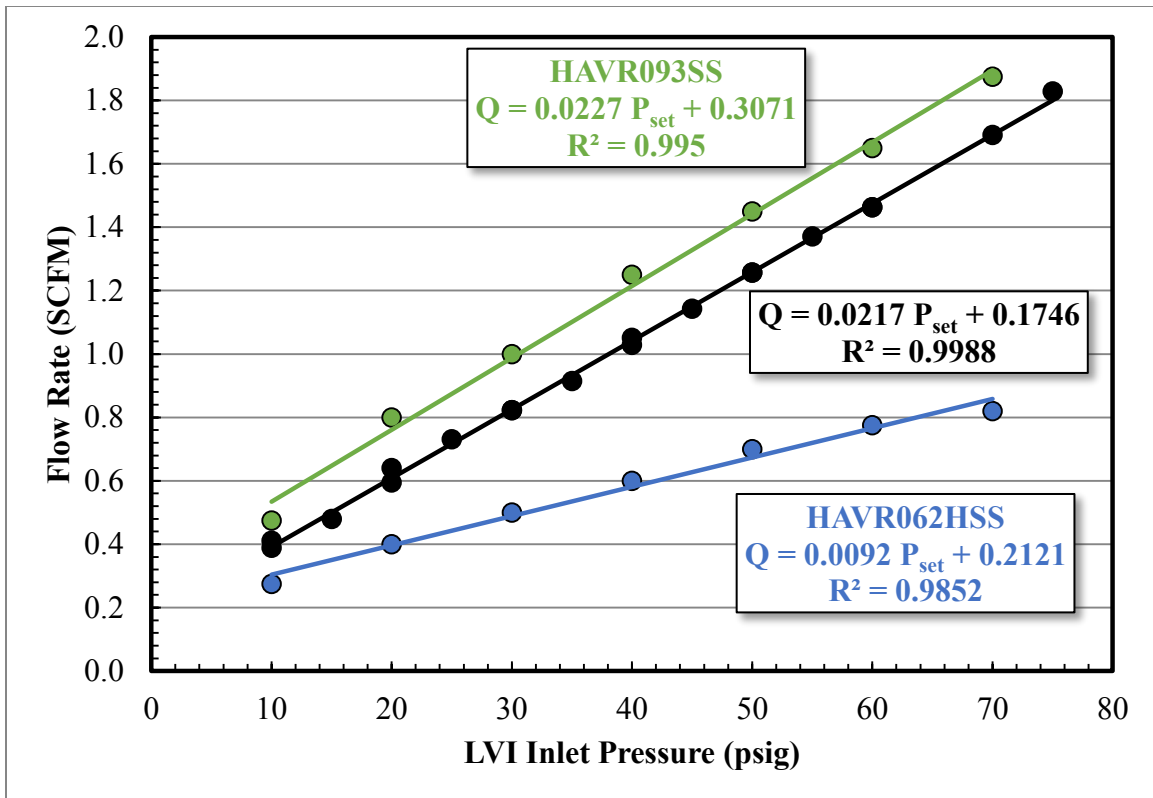


Figure C.1: Measured LVI carrier gas flow rate compared to manufacturer data. The measured flow rate was compensated for density using $P = 100$ psig and $T = 21$ °C. The black curve (●) is the measured values for the eductor in the LVI system.

The eductor vacuum was measured using the vacuum gauge mounted in the LVI enclosure. **Figure C.2** shows the comparison between the measured vacuum plotted against manufacturer data. The HAVR093SS and the HAVR062SS eductor models share the same vacuum curve. Deviations at low inlet pressure are due to: (1) lower volumetric flow rates at a given inlet pressure, and (2) the increase in absolute measurement error of the vacuum gauge. The deviations at higher inlet pressure are likely due to leakage in the vacuum line; the vacuum line has several connections between the suction measurement point and the remote gauge. Additionally, the vacuum produced is very sensitive to flowrate; therefore, very small leaks will significantly reduce actual vacuum levels.

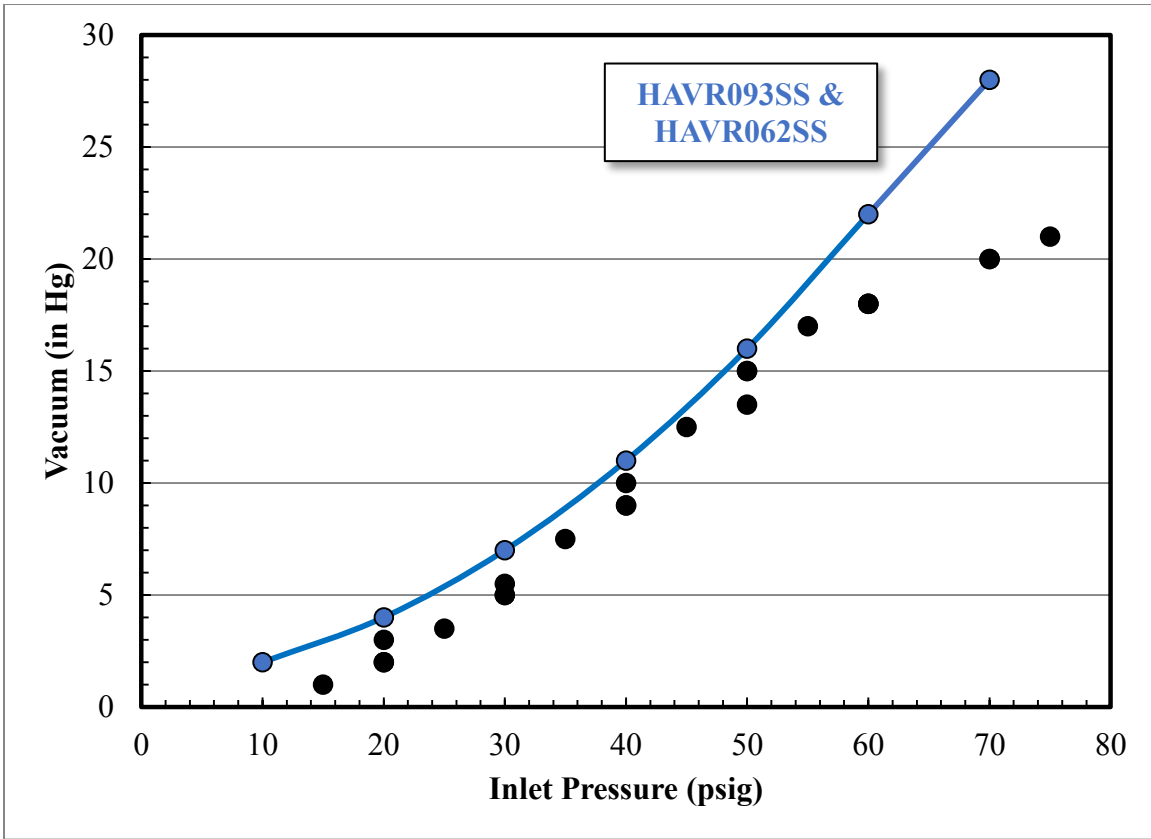


Figure C.2: LVI eductor vacuum as a function of the inlet pressure. The reported data (● blue curve) is digitized from a catalog curve while the black points (●) are measured values.

Table C.1: Flowrate and vacuum catalog data for Air-Vac model HAVR093SS and HAVR062SS eductors and actual measured values for the eductor system used in the LVI. P_{set} is the upstream motive fluid pressure.

P_{set} [psig]	Motive Fluid Flowrate (Q)			Vacuum Level (P_{vac})		
	HAVR-062HSS	HAVR-093HSS	LVI	HAVR-062HSS	HAVR-093HSS	LVI
10	0.28	0.48	0.41	2	2	--
10	--	--	0.39	--	--	--
15	--	--	0.48	--	--	1.0
20	0.40	0.80	0.64	4	4	2.0
20	--	--	0.59	--	--	2.0
20	--	--	--	--	--	3.0
25	--	--	0.73	--	--	3.5
30	0.50	1.00	0.82	7	7	5.0
30	--	--	0.82	--	--	5.0
30	--	--	--	--	--	5.5
35	--	--	0.91	--	--	7.5
40	0.60	1.25	1.05	11	11	9.0
40	--	--	1.03	--	--	9.0
40	--	--	--	--	--	10.0
45	--	--	1.14	--	--	12.5
50	0.70	1.45	1.26	16	16	15.0
50	--	--	1.26	--	--	15.0
50	--	--	--	--	--	13.5
55	--	--	1.37	--	--	17.0
60	0.78	1.65	1.46	22	22	18.0
60	--	--	1.46	--	--	18.0
60	--	--	--	--	--	18.0
70	0.82	1.88	1.69	28	28	20.0
70	--	--	--	--	--	20.0
75	--	--	1.83	--	--	21.0

C.1.2 Pump Calibration

After the original pump sleeve was replaced, a calibration curve was generated to determine the offset of the calibration dial on the pump motor. The calibration curve was generated by measuring the total volume of liquid collected in a 10 ± 0.2 mL graduated cylinder over a period of ten minutes measured by a stopwatch. Because a constant time

rather than a constant total volume was collected, the absolute of error from the graduated cylinder increases with decreasing flowrate and is the most significant source of error. An absolute error of 1 ms for the stopwatch was used for error propagation. **Table C.2** shows the raw calibration data and **Figure C.3** shows the calibration curve developed from the collected data set. Each set point was measured in duplicate. The calibration curve was not forced through zero because the pump flowrate becomes nonlinear at very low flow.

Table C.2: LVI pump calibration raw data.

Set Point (mL/min)	Volume (mL)	Time (min)	Flow Rate (mL/min)
1.00	9.5 ± 0.2	10.0	0.95 ± 0.02
	9.5 ± 0.2	10.0	0.95 ± 0.02
0.80	7.1 ± 0.2	10.0	0.71 ± 0.03
	7.2 ± 0.2	10.0	0.72 ± 0.03
0.60	4.8 ± 0.2	10.0	0.48 ± 0.04
	5.0 ± 0.2	10.0	0.50 ± 0.04
0.40	2.4 ± 0.2	10.0	0.24 ± 0.08
	2.3 ± 0.2	10.0	0.23 ± 0.09
0.30	1.1 ± 0.2	10.0	0.11 ± 0.18
	1.0 ± 0.2	10.0	0.10 ± 0.20

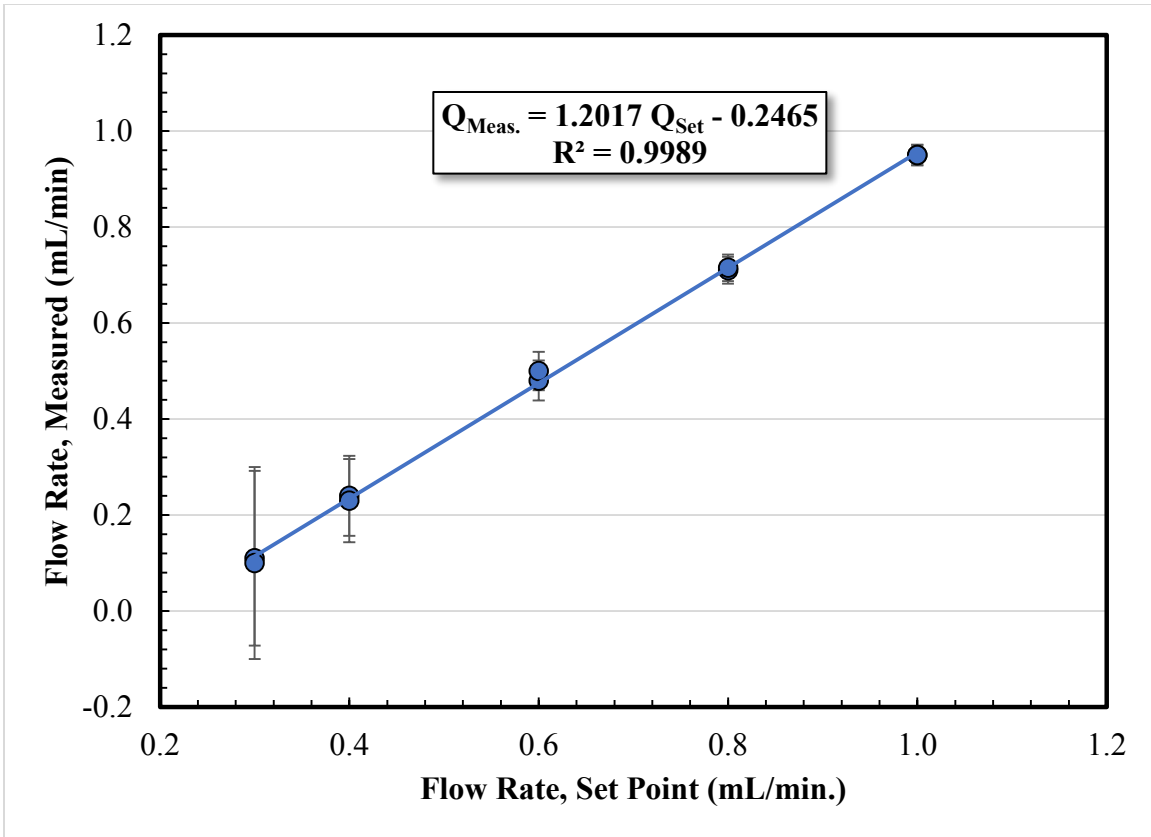


Figure C.3: LVI pump calibration curve with a new pump sleeve.

C.2 LVI TROUBLESHOOTING AND MODIFICATIONS

The original design specifications for the LVI was to produce 350–1,750 ppmv gaseous H₂SO₄ in one CFM of air or N₂. The concentrated H₂SO₄ gas was to then be mixed into 350 CFM at the SRP pilot plant to produce a total concentration of 1–5 ppmv H₂SO₄. Hot H₂SO₄ gas was to be produced by injecting 0.4–2 mL/min of 10 vol % aqueous H₂SO₄ into one CFM of air or N₂ at 275 °C. An eductor controlled the suction pressure of the H₂SO₄ stream and the flow rate of the heated carrier gas. The hot, concentrated acid would condense rapidly in the large diluent stream producing submicron, homogeneously nucleated H₂SO₄ aerosol, thus mimicking acid mist found in coal-fired boilers.

The concentration of the H₂SO₄ liquid was adjusted by dilution to serve as a nuclei source for smaller diluent stream, specifically that of the AGC (1.5–4 CFM). The pump flow rate could be adjusted; however, the rangeability of the pump was very limited (0.3–10 mL/min.)

The following sections will detail modifications and testing as problems arose using the LVI on both the bench and pilot scale. Chapter 5 describes the current state of the LVI hardware.

C.2.1 November, 2013 Campaign

The first application of the LVI was during the November, 2013 SRP campaign at The University of Texas at Austin. In that test, the LVI eductor quickly lost suction and produced a highly inconsistent and pulsating stream of aerosol at the SRP pilot plant. Severe corrosion in the eductor body, specifically the motive fluid nozzle, was observed. Partial vaporization, elevated temperature (275 °C), and the small diameter orifice in the eductor led to quick blockage of the acid delivery system and subsequent failure.

C.2.1.1 First Upgrades – Coating and Increased Temperature

Upgrades to the LVI were made following the 2013 campaign to address the corrosion issue. The fittings exposed to acid, including the eductor, were coated with Dursan[®] polymer and the carrier gas temperature was increased from 275 to 310 °C.

Figure C.4 shows the coated fittings.



Figure C.4: LVI fittings are coated in Dursan® polymer

In order to test the upgrades at pilot plant conditions (5–10 ppmv H_2SO_4 at 350 CFM), a scrubber system for the acid aerosol was built with stack sampling glassware (supplied by AECOM, formerly URS Corporation) and the delivery system was placed in a ventilated hood. The glassware consisted of a 500 mm condenser, 3 primary impingers with no constriction nozzles, a Greenburg-Smith style impinger, a glass filter with fine glass fiber filter paper, and glass wool packed into the top of the impinger bodies. A secondary condenser and impinger train was added for sampling of condensate during the testing. The impingers were filled with approximately 150 mL of 3 vol % H_2O_2 in water. The whole sampling train was placed in a large ice chest and filled with ice water prior to testing. The bath temperature was measured with a thermometer and remained constant at 2 ± 2 °C. Two submersible pumps supplied the condensers with ice water from the

bath. All glassware had ball-and-socket joints with o-ring side-seals and was clamped together using spherical joint pinch clamps. A rotameter (King Instrument Co. Models 75201102C13 and 75201102C09) was added to each of the condenser trains to compare flow rates with the LVI inlet rotameter. The line connecting the split point to the condensate sampling system was heated by heating tape controlled by a variac.

Figure C.5–Figure C.6 show a process diagram and a picture of the sampling system.

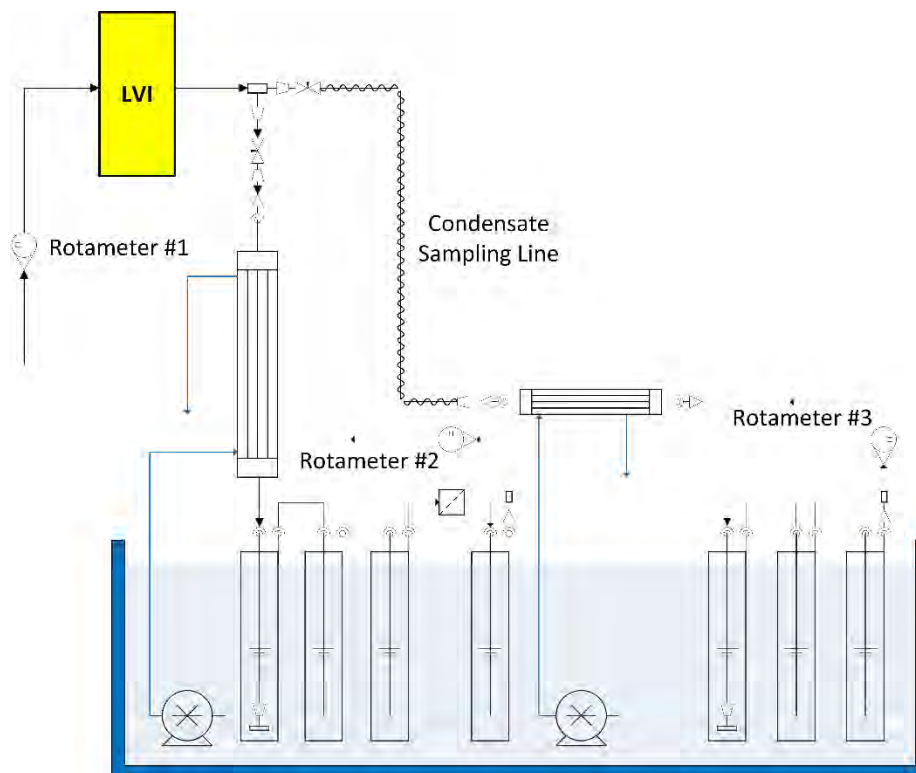


Figure C.5: LVI acid scrubbing sampler train flow diagram

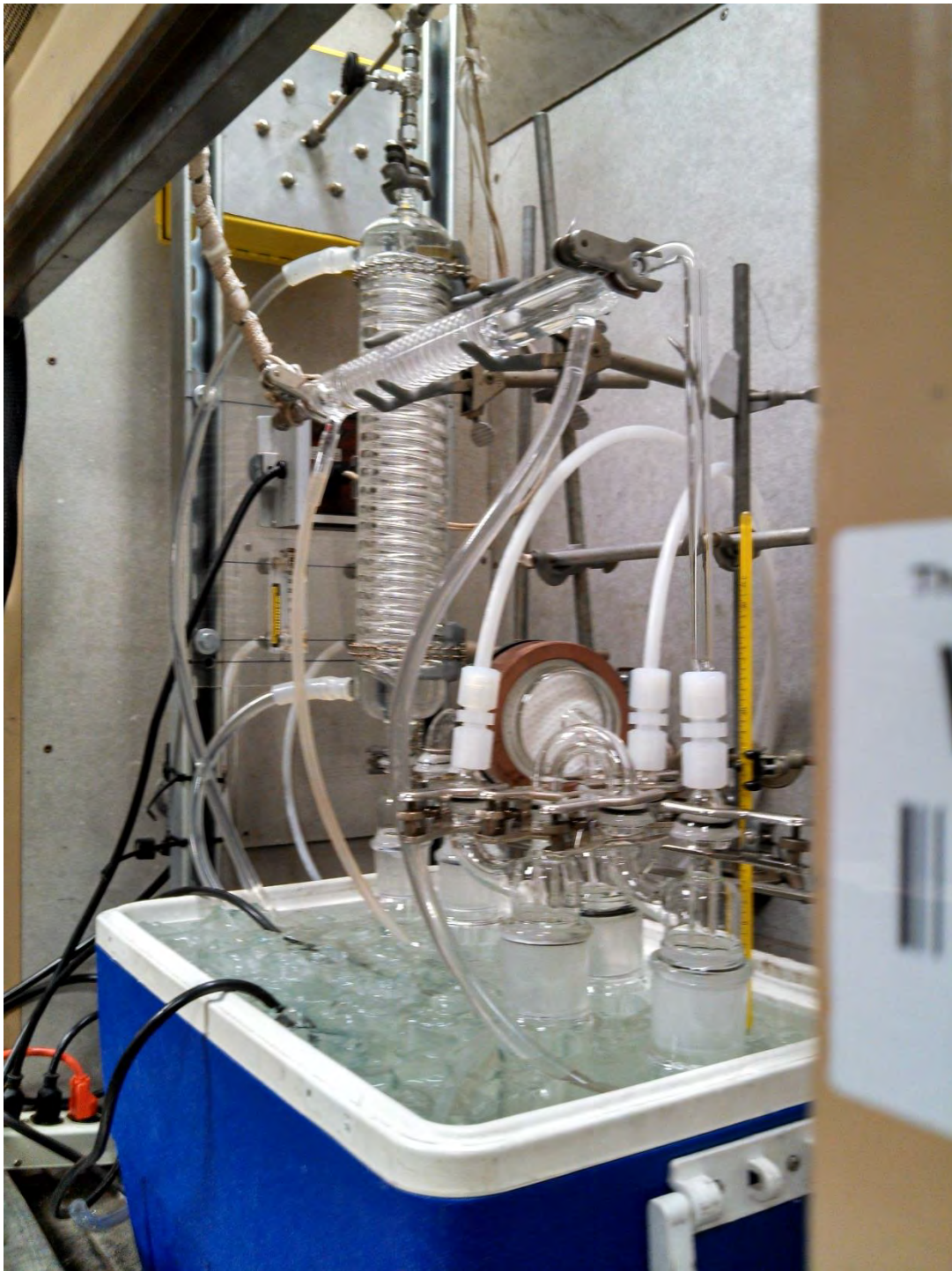


Figure C.6: First LVI test with downstream acid collection in stack sampling impinger train. Additional impingers were added after the first test which match the configuration shown in Figure C.5.

Prior to testing, the sampling/capture system was leak checked by verifying continuity of the flow measurements at different supply pressures to the LVI. **Table C.3** shows flow rate measurements recorded at different total flow rates and various split ratios between the two impinger sampling trains. The flow rate to each sampling train was varied by upstream needle valves. Rotameter #1 records the total inlet flow rate to the LVI at supply conditions (100 psig and 17 °C). Rotameter #2 and #3 measure the flow rate in the large, vertical condenser and small, horizontal condenser (condensate) sampling trains, respectively. All rotameter readings are adjusted for temperature and pressure. Rotameter #2 and #3 are assumed to be at ambient pressure.

Table C.3: LVI Sampling train flow measurements to determine system leaks

P_{LVI} (psig)	Rot. #1 (SCFH)	Rot. #2 (SCFH)	Rot. #3 (SCFH)	Rot. 2+3 (SCFH)	Diff. (SCFH)	Diff. (%)
10	24.9	27.0	0.0	27.0	2.1	8.1
10	24.9	27.2	0.0	27.2	2.3	8.8
10	24.9	15.0	11.8	26.8	1.9	7.4
20	37.3	40.0	0.0	40.0	2.7	7.0
20	37.3	21.5	18.0	39.5	2.2	5.7
30	50.4	52.0	0.0	52.0	1.6	3.1
30	50.4	29.5	24.9	54.4	4.0	7.6
30	50.4	40.0	14.0	54.0	3.6	6.9
40	63.5	65.0	0.0	65.0	1.5	2.3
40	63.5	50.0	17.3	67.3	3.8	5.8
50	76.0	76.0	0.0	76.0	0.0	0.0
60	88.4	88.0	0.0	88.0	-0.4	-0.5
65	93.9	91.5	0.0	91.5	-2.4	-2.6

Rotameter #1 (Key Instruments MR3A06SVVT) has a listed error of $\pm 5\%$ of full-scale, or 3 SCFH. The manufacturer specified error for rotameter #2 and #3 is listed as $\pm 6\%$ of full-scale, or 6 and 1.8 SCFH, respectively. Error propagation of the sum of

rotameter #2 and #3 gives a total error of ± 6.3 SCFH. Total flow measurements agreed within the expected error; therefore, leakage from the system was minimal.

The LVI system operated smoothly for about 10 minutes before the eductor vacuum level began to decrease. The suction pressure slowly increased until 10 psig was reached and the system was shut down.

During operation, a dense, blue plume was observable in the first impinger headspace indicating a submicron aerosol cloud. The plume became increasingly opaque as it passed through each impinger until it was finally collected in the filter; the gas exiting the filter was clear. Pulsation of the aerosol stream was observable and attributed to incomplete vaporization. Aerosol in the first and second impinger can be seen in **Figure C.7**.

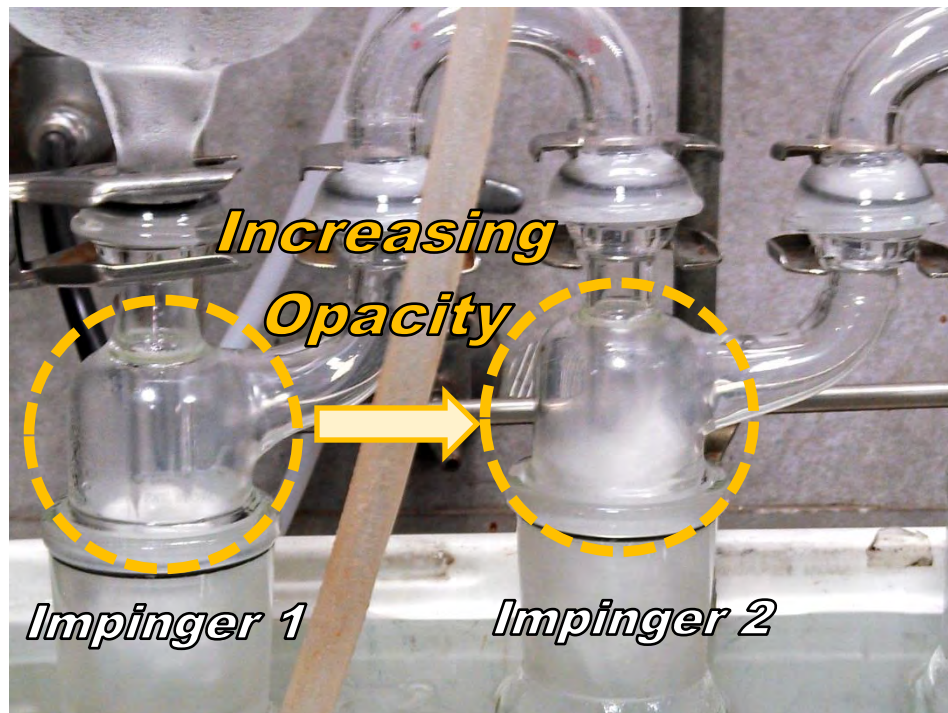


Figure C.7: Aerosols condensing through the first and second impinger cause an increase in opacity. Pulsation in aerosol production was directly observable by opacity fluctuations.

The LVI was disassembled following the test. The LVI eductor was found to be severely corroded and covered in a viscous green fluid. The Dursan[®] coating and increased operating temperature did little to prevent the onset of corrosion.

C.2.2 LVI Rebuild

C.2.2.1 Thermodynamic Analysis

Following the first unsuccessful modification, a thermodynamic analysis of the LVI system was done to determine the degree of H₂SO₄ vaporization prior to reaching the eductor suction.

First, the resulting temperature of mixing the entire N₂ stream (1 SCFM) at 310 °C and acid (1 mL/min of 10 vol % H₂SO₄ at 20 °C) was calculated using an enthalpy balance assuming complete vaporization and constant physical properties and no excess enthalpy. Physical properties were taken from the DIPPR database (DIPPR, 1998). Temperature dependent properties were averaged across temperature ranges associated with sensible heat changes. Equations (C.1)–(C.2) show the enthalpy differences for the N₂ and H₂SO₄ acid streams when mixed to the final temperature, T.

$$q_1 = \dot{m}_{N_2} Cp_{N_2}^G (T - T_1) \quad (C.1)$$

$$q_2 = \dot{m}_{H_2O} [Cp_{H_2O}^L (T_{BP} - T_2) + \Delta H_{H_2O}^{vap} + Cp_{H_2O}^G (T - T_{BP})] \\ + \dot{m}_{H_2SO_4} [Cp_{H_2SO_4}^L (T - T_2) + \Delta H_{H_2SO_4}^{vap}] \quad (C.2)$$

where:

- T = Temperature of the resulting mixture [K]
 \dot{m}_i = Molar flow rate of component i [mol/min]
 Cp_i^L = Pure component liquid-phase heat capacity of component i [J/mol·K]
 Cp_i^G = Pure component gas-phase heat capacity of component i [J/mol·K]
 ΔH_i^{vap} = Heat of vaporization of component i [J/mol]
 T_1 = N₂ inlet temperature [K]
 T_2 = Inlet temperature of H₂SO₄/H₂O solution [K]
 T_{BP} = Pure component boiling point [K]

The resulting mixture, assuming adiabatic mixing, was calculated as 1,410 ppmv H₂SO₄, 3.8 mol % H₂O, and 96.1 mol % N₂ at 236 °C. The dewpoint of the acid mixture was calculated to be between 171.5–187.1 °C at 1 atm using Equations (C.3) and (C.4), shown below. Partial pressures are atmospheres and mmHg in Equations (C.3) and (C.4), respectively. The mixture temperature is above the dewpoint and the heat input from the N₂ preheater is sufficient to fully vaporize the acid stream.

$$\frac{1000}{T^{DP}} = 1.7842 - 0.0269 \log(P_{H_2O}) - 0.1029 \log(P_{H_2SO_4}) + 0.0329 \log(P_{H_2O}) \log(P_{H_2SO_4}) \quad (C.3)$$

$$\frac{1000}{T^{DP}} = 2.276 - 0.02943 \ln(P_{H_2O}) - 0.0858 \ln(P_{H_2SO_4}) + 0.0062 \ln(P_{H_2O}) \ln(P_{H_2SO_4}) \quad (C.4)$$

where:

T^{DP} = Dew point temperature [K]

P_i = Partial pressure of component i [atm/mm Hg]

However, the acid and the preheated N₂ stream do not mix until the eductor. A small bleed of N₂ is mixed with the acid stream which is controlled by a 0.012” diameter orifice. The flow rate is estimated to be 4 SLPM at 60 psig upstream pressure. Therefore the actual heat input prior to the eductor, where the corrosion was occurring, is much less than that supplied by the full N₂ stream.

Assuming no vaporization and adiabatic mixing, the resulting mixture of liquid acid and hot bleed N₂ is 8,052 ppmv H₂SO₄, 21.7 vol % H₂O, and 77.5 vol % N₂ at 182.7 °C. Assuming complete vaporization, the resulting temperature is -88 °C when calculated using Equations (C.1)–(C.2). The dewpoint is calculated to be 211.5–220.0 °C at 1 atm total pressure. Consequently, the actual mixture is partially vaporized, and therefore below the dewpoint.

The same calculations were performed using the built in H₂SO₄ Electrolyte-NRTL model found in the Aspen Plus® V7.3 applications folder. Complete vaporization calculations matched the results of Equations (C.1)–(C.2) to within a few degrees Celsius confirming the approximations made during the previous analysis.

An adiabatic flash calculation at 1 atm for 4 SLPM at 60 psig at 310 °C mixed with 1.0 mL/min of 10 vol % H₂SO₄ in water at 20 °C produced a partially vaporized stream (vapor fraction of 0.895) at 57.1 °C. At the eductor suction pressure of 10 mmHg vacuum, the vapor fraction is 0.9 and the mixture temperature is 50.3 °C. The small bypass of hot N₂ is insufficient to fully vaporize the acid stream. Partial vaporization concentrates the H₂SO₄ liquid due to the large relative volatility of H₂O and H₂SO₄.

To prevent corrosion at the eductor suction and nozzle section, additional heat had to be applied to the stream prior to reaching the eductor. The dewpoint for the acid and hot bleed mixture was calculated to be 215.7 and 226.9 °C and required 39.55 and 40.89 W for a flash pressure of 10 mmHg vacuum and 1 atm, respectively. To mitigate acid corrosion caused by incomplete vaporization, a minimum of 41 W must be applied to the H₂SO₄ stream prior to reaching the eductor.

C.2.2.2 Second Upgrades – Acid Concentration, Tube Heater, and Enclosure

Supplemental heat was added by a Zircar[®] Ceramics model FIH-C, 1" x 3" x 6", 200W, 60V Nichrome wire resistive tube furnace. The tubing in the furnace section was constructed of SGE[™] Analytical Science 1/2" x 9.5" x 60 cm GLT[™] borosilicate glass-lined tubing swaged with graphite ferrules. The tubing was packed with refractory ceramic fish-spine beads for added transfer area and capped on both ends with quartz glass wool.

Due to the time constraint of the upcoming March, 2015 campaign and the delays in delivery of the PDI, replacing all stainless steel components with glass tubing and specifying and designing the required support components could not be procured and fabricated in time. The upstream components (stainless steel tubing and fittings) of the LVI remained unchanged. A 3D drawing of the LVI with the added tube furnace can be seen in **Figure C.8**.

The tube furnace dimensions were determined by a heat transfer calculation assuming an inlet liquid temperature of 50 °C, an outlet temperature of 310 °C, and an internal heat transfer coefficient of 300 W/m²·K to approximate the two-phase heat transfer coefficient. Conduction was assumed between the heater elements and the tube; ceramic inserts were placed in between the heater elements and the tubing to provide conduction contact and to fix the tubing at the center of the furnace geometry. The

enclosure temperature was estimated at 250 °C to calculate the heat rejected from the tube furnace outer surface. Ceramic refractory beads were added into the packed section to increase the heat exchange area in case the heat transfer coefficient had been overestimated.

The tubing between the injection point and the tube furnace inlet was 1/8" OD tubing. 1/8" diameter tubing was chosen such that the velocity of the hot N₂ bleed gas would be above the entrainment velocity of the liquid. Therefore the liquid would move through the tubing regardless of orientation and would reach the tube furnace.

Additionally, the concentration of H₂SO₄ was increased to 50 vol % to lower the amount of heat required for H₂O vaporization.

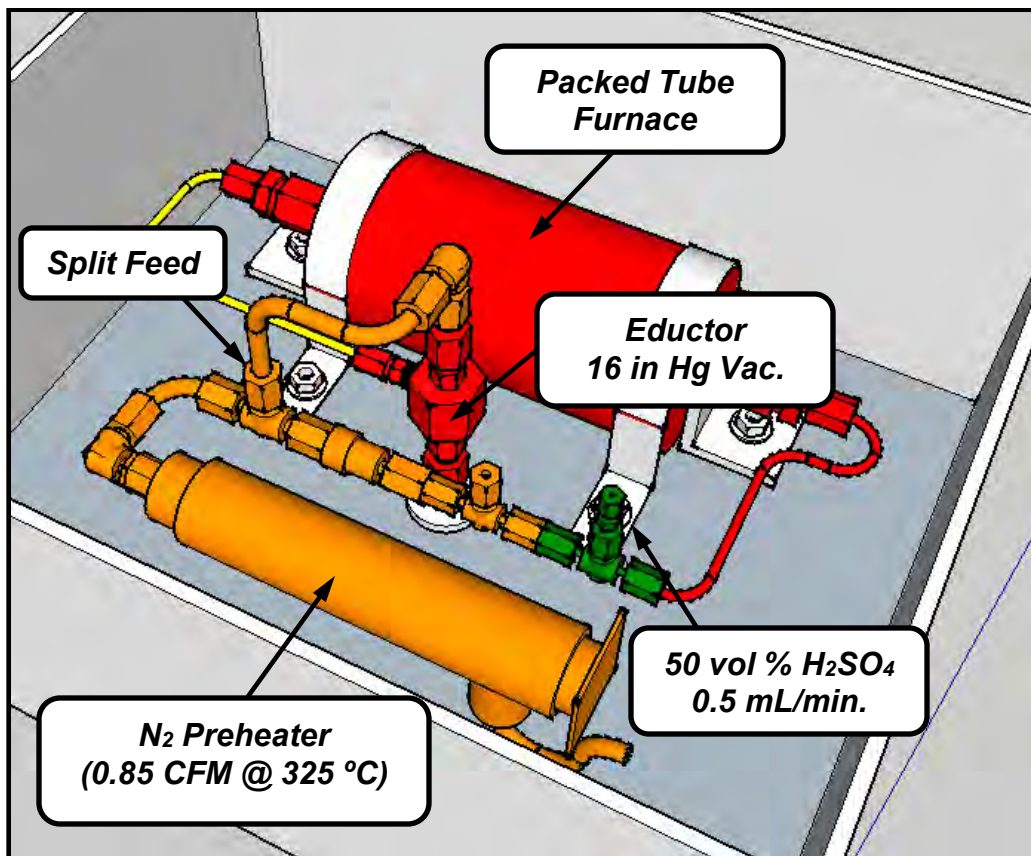


Figure C.8: 3D drawing of the upgraded LVI with added tube furnace. Acid is injected at the **green fitting**. Carrier N₂ passes through the preheater and in all of the **orange fittings**. The hot, gaseous H₂SO₄ mixes at the intersection of the **yellow tubing** and the **red** eductor.

After three separate, successful tests of over five total hours of injection, the accumulation of corrosion products from the stainless steel lines was observable in the first impinger indicated by the blur-green hue of the collected condensate (**Figure C.9**). Because the eductor did not experience any failure, it was assumed that the corrosion was in the outlet 3/8" tubing and the needle valve downstream of the LVI injection box.



Figure C.9: Condensate collected during H_2SO_4 injection in the first impinger showed significant accumulation of stainless steel corrosion products.

C.2.3 March, 2015 Campaign

Following the successful, full concentration demonstration tests at the bench scale acid scrubber, the LVI was moved into field operation during the March, 2015 SRP pilot campaign. H_2SO_4 was injected at 10–13.7 ppm for a total of 160 minutes over the duration of the campaign; however, the eductor eventually plugged and ceased operating. After disassembly, three problems were identified: (1) contaminants in the N_2 line were accumulating in the motive side of the eductor and were plugging the orifice, (2) corrosion material from the acid injection point was slowly building in the quartz wool of the tube furnace packing, and (3) the borosilicate glass lining at the cut points of the tubing was cracking and sloughing off. **Figure C.10** shows a view of the tube furnace inlet quartz wool showing significant accumulation of corroded material.



Figure C.10: The tube furnace quartz wool packing holder with accumulated stainless steel corrosion products after operation on the SRP pilot plant.

C.2.3.1 Furnace Bypass

After the March, 2015 pilot plant campaign, the tube furnace was plugged and unusable; therefore, a bypass line was added so experimentation could proceed on the AGC where a much more dilute acid could be used to generate aerosol. However, the upstream plugging of the eductor continued on the AGC even after the addition of a 2 μm filter at the N_2 supply line. A similar problem was discovered at the pilot plant when commissioning an SO_2 MFC; the actuating mechanism of the MFC was stuck in place due to the accumulation of a sticky substance in places occupied by the gas.

Fortunately a few experiments were conducted with the LVI on the AGC, but the random and unpredictable plugging of the LVI in multiple locations significantly hindered experimentation over the course of several years.

C.3 RECOMMENDATIONS

A new aerosol generation source should be used in future experiments. H_2SO_4 is extremely corrosive when used with most metals. Any cold spots or partially vaporized acid will lead to rapidly corroded surfaces and accumulation of solid and highly viscous material.

The preferred H_2SO_4 aerosol generation pathway is to catalytically oxidize SO_2 to SO_3 and provide the H_2O vapor in the diluent stream like that found in the works of Kamijo et. al (2013), Mertens et al. (2014), Wall (1982), and Roesler (2010). However, material hazards control becomes more complicated because leaks of aerosol source material would be gaseous rather than a containable liquid. It may be preferable to separate the bench and pilot scale aerosol generation activities since the safety requirements for transporting gas from outdoor cylinders across considerable distance into the lab is likely prohibitive.

Alternatively, the LVI could be fixed using the current vaporization principle, but all stainless steel tubing would need to be replaced with glass tubing with proper support apparatus for use outdoors. An eductor should be avoided to prevent corrosion of sensitive openings and to prevent upstream plugging.

C.4 SUPPORTING FIGURES



Figure C.11: Rebuilt LVI control enclosure. A second liquid reservoir was added for H₂O to use during startup and shutdown.

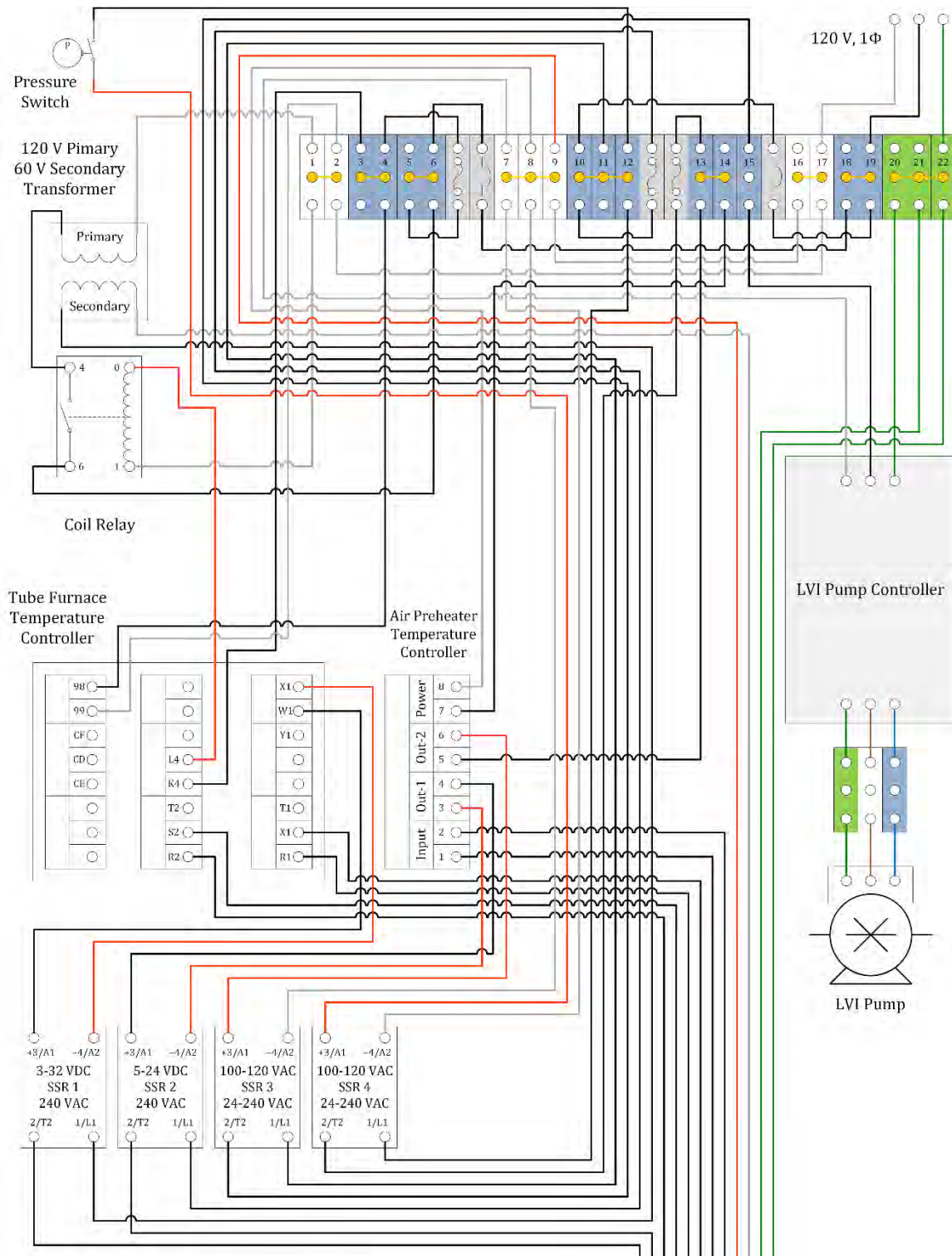


Figure C.12: Rebuilt LVI control enclosure wiring and electrical terminations.

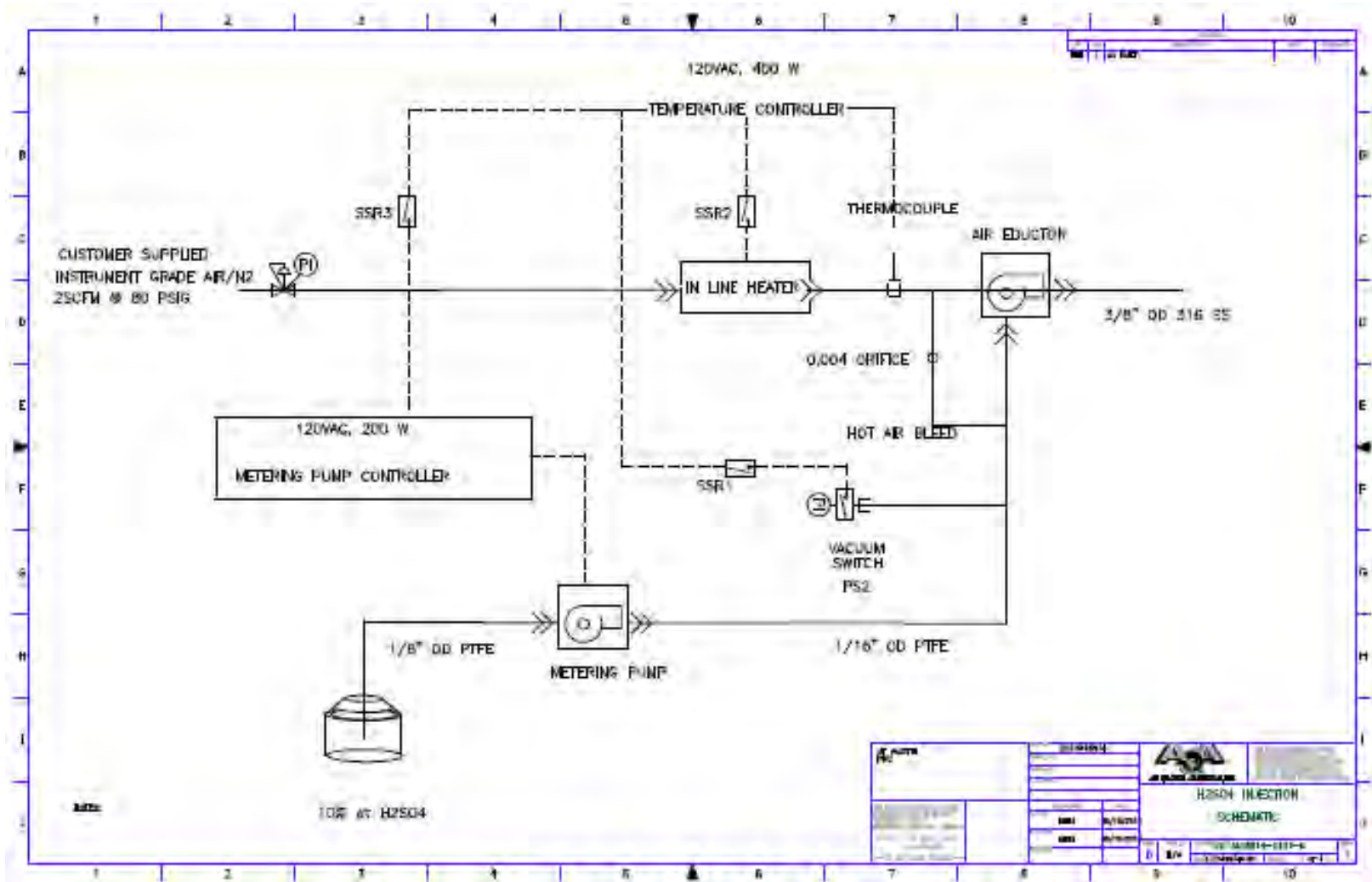


Figure C.13: Simplified schematic of the original LVI system provided by Mark Nelson of AQA.

Appendix D: FTIR Connections/Assignments and DeltaV™ Code

D.1 FTIR/DELTA V™ PHYSICAL CONNECTION

The FTIR communicates with DeltaV™ by the Modbus serial communications protocol via RS-232 interface. An RS-232 cable with a male DB9 connector (FTIR end) and stripped ends (DeltaV™ S-Series Terminal Block end) connects the FTIR and DeltaV™ terminals. A cross-over pinout diagram is shown below in **Table D.1**. The arrow colors match those of the current RS-232 cable and the arrows indicate information flow direction. The gray arrow (FTIR pin 3 to DeltaV™ pin 5) indicates a white cable.

Table D.1: FTIR RS-232 Cable to DeltaV™ S-Series Serial Interface Terminal Block Crossover Pinout

FTIR RS-232 DB-9 Cable		DeltaV™ S-Series Terminal Block	
Circuit	Pin #	Pin #	Circuit
Shield	1	1	Ground (GND)
Receive Data (RXD)	2	2	--
Transmit Data (TXD)	3	3	Transmit Data (TXD)
Data Terminal Ready (DTR)	4	4	--
Ground (GND)	5	5	Receive Data (RXD)
Data Set Ready (DSR)	6	6	--
Request to Send (RTS)	7	7	Data Terminal Ready (DTR)
Clear to Send (CTS)	8	8	Data Set Ready (DSR)

The S-Series terminal block pin connections and top and bottom views of the RS-232 cable DB9 connector can be seen in **Figure D.1–Figure D.2**.

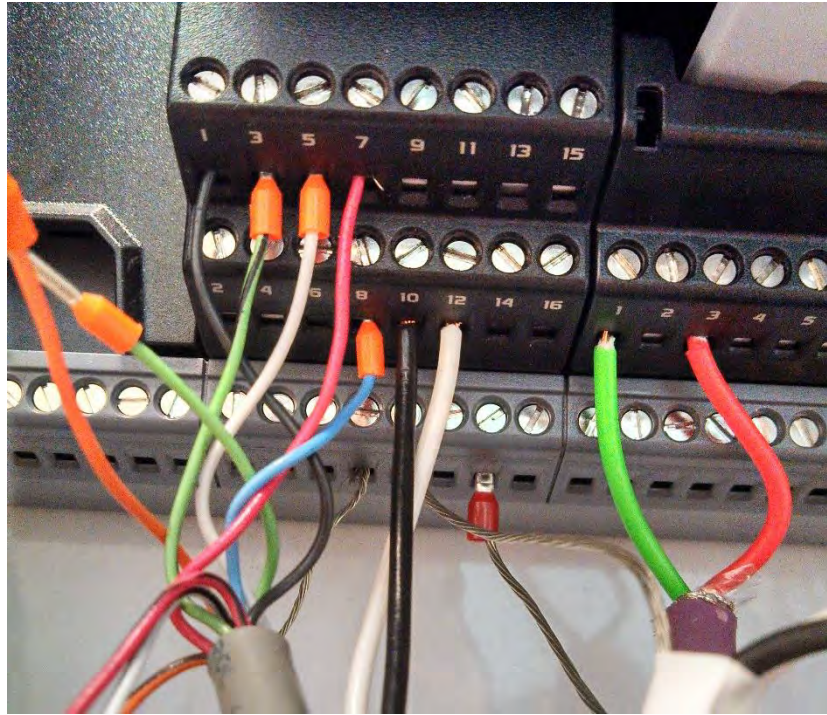


Figure D.1: DeltaV™ S-Series terminal block pin connections for FTIR input

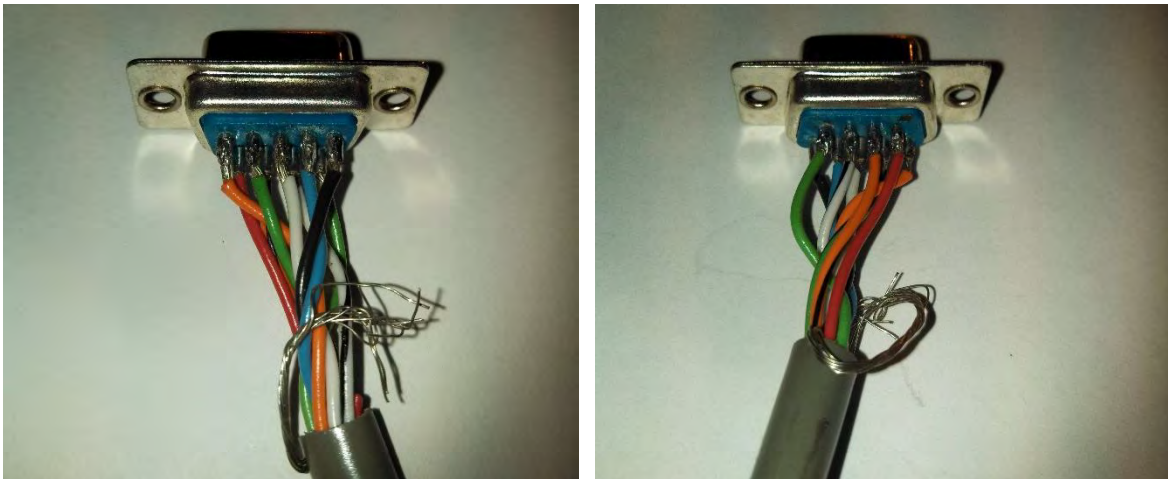


Figure D.2: Top and bottom views of the RS-232 DB9 cable pins and wire colors

D.2 FTIR MENU ASSIGNMENTS

Data is stored in a registries that are assigned contents by the user. Data registry addressing starts at 30001 on the FTIR controller card. Under the Analysis Settings

menu, the Modbus tab contains Channels which are configured for each piece of data and are assigned a registry. For example, Channel 1 on the Modbus assignment tab corresponds to registry 30001.

Figure D.3 shows the Modbus tab under the Analysis Settings menu with component names assigned to channels 1–7. The linkage to actual data is made in the Output Channel Select window (**Figure D.4**) where the component or the physical measurement index is assigned. The names of the components in this window are the same as that assigned in the Gas Components tab under the Analysis Settings menu. The Modbus channel order does not necessarily match the Gas Components channel order; the channel order is assigned by the user in both cases.

Serial output is configured under “Tools”→“Configuration”→“Serial Output”. The COM port number assignment must be for the RS-232 connection on the FTIR terminal which can be found in the Device Manager tool under the Ports (COM and LPT) collapsible menu in Windows. **Figure D.5** shows a properly configured serial output section for external communications with DeltaV™.

A screenshot of the I/O diagram for the FTIR in DeltaV™ Control Studios is shown in **Figure D.6**, below.

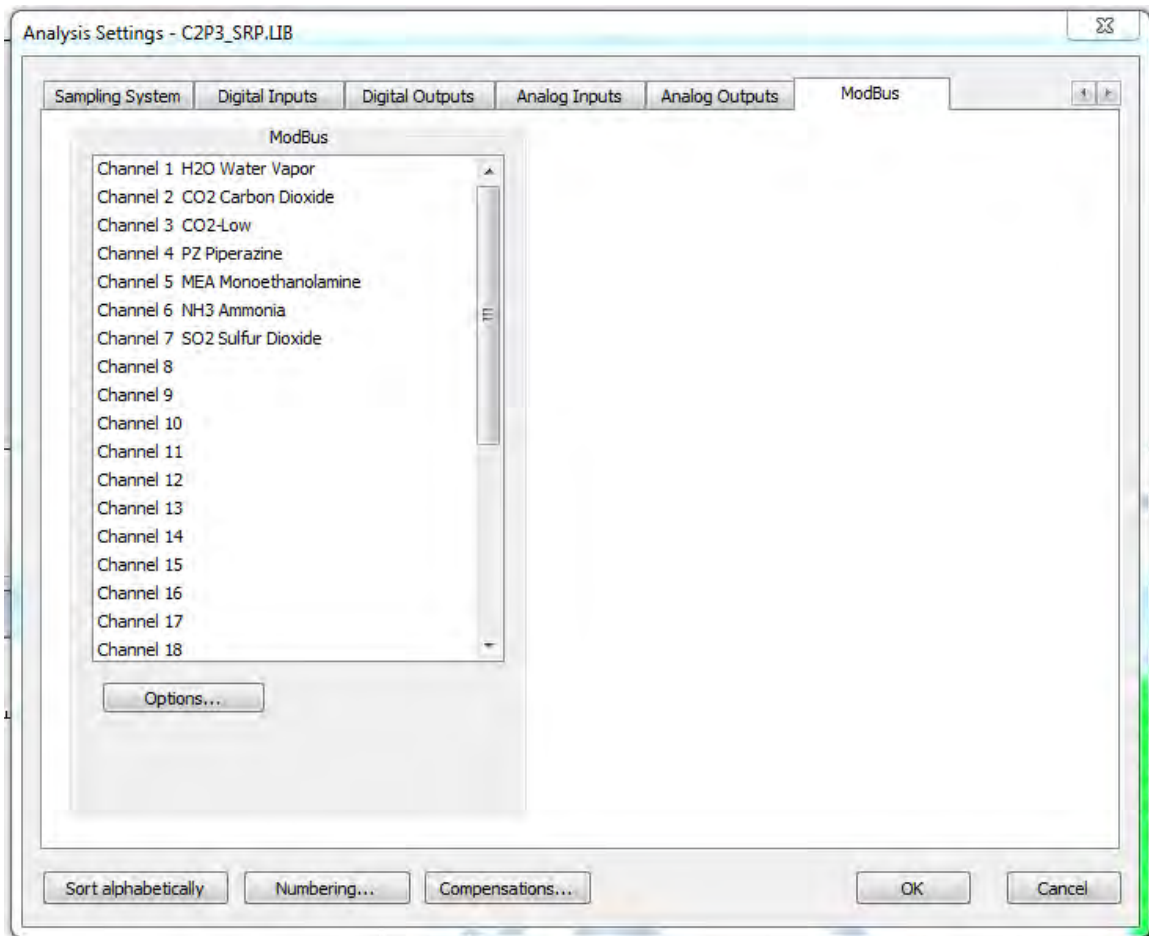


Figure D.3: Modbus output channels are configured in the analysis settings window under the Modbus tab. Up to 30 channels are configurable for any component order. The channel number corresponds to the output registry order.

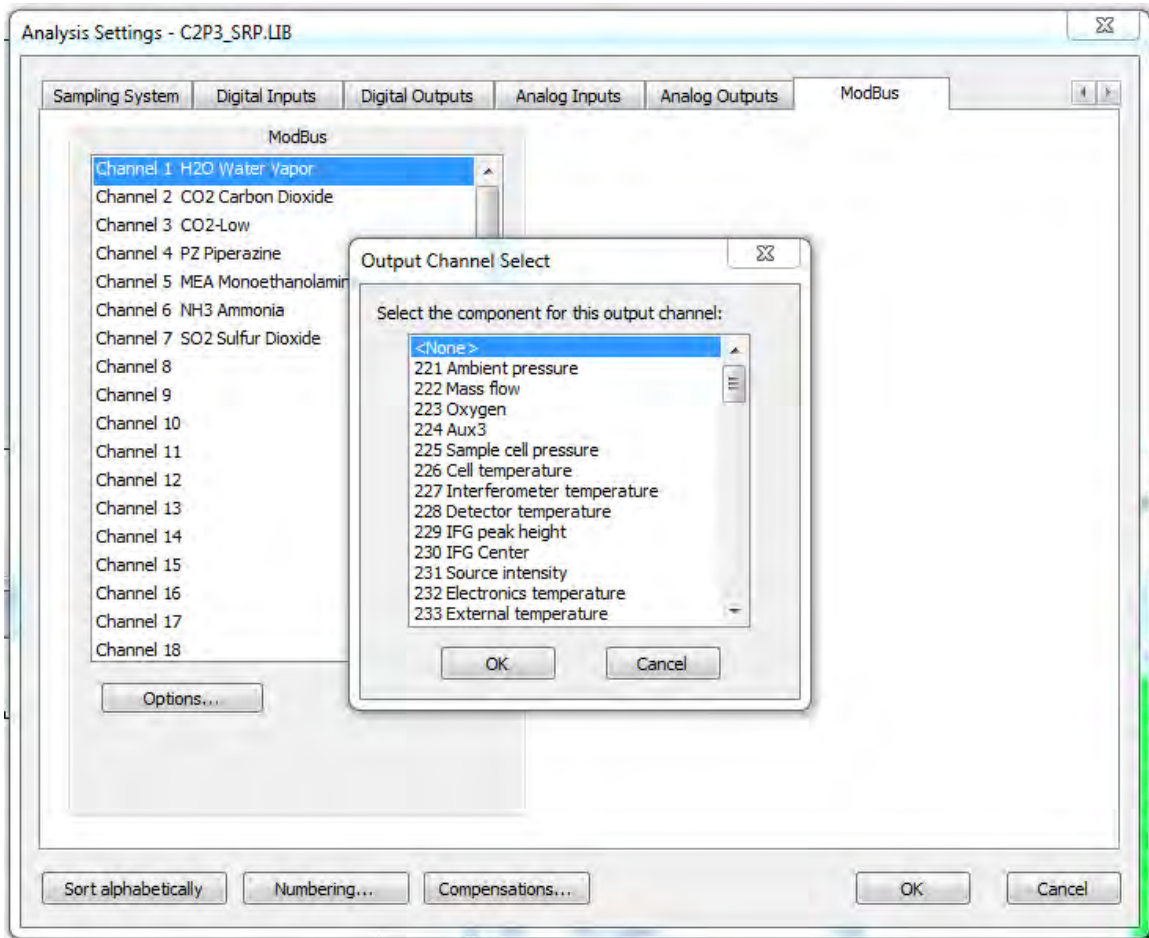


Figure D.4: Double-clicking a ModBus output channel brings up the Output Channel Select Window where the component or on-board measurement can be selected as an output. The channel number and label on the Output Channel Select window correspond to the Gas Components Analysis Settings numbering. The ModBus and the Output channel numbers do not have to be the same.

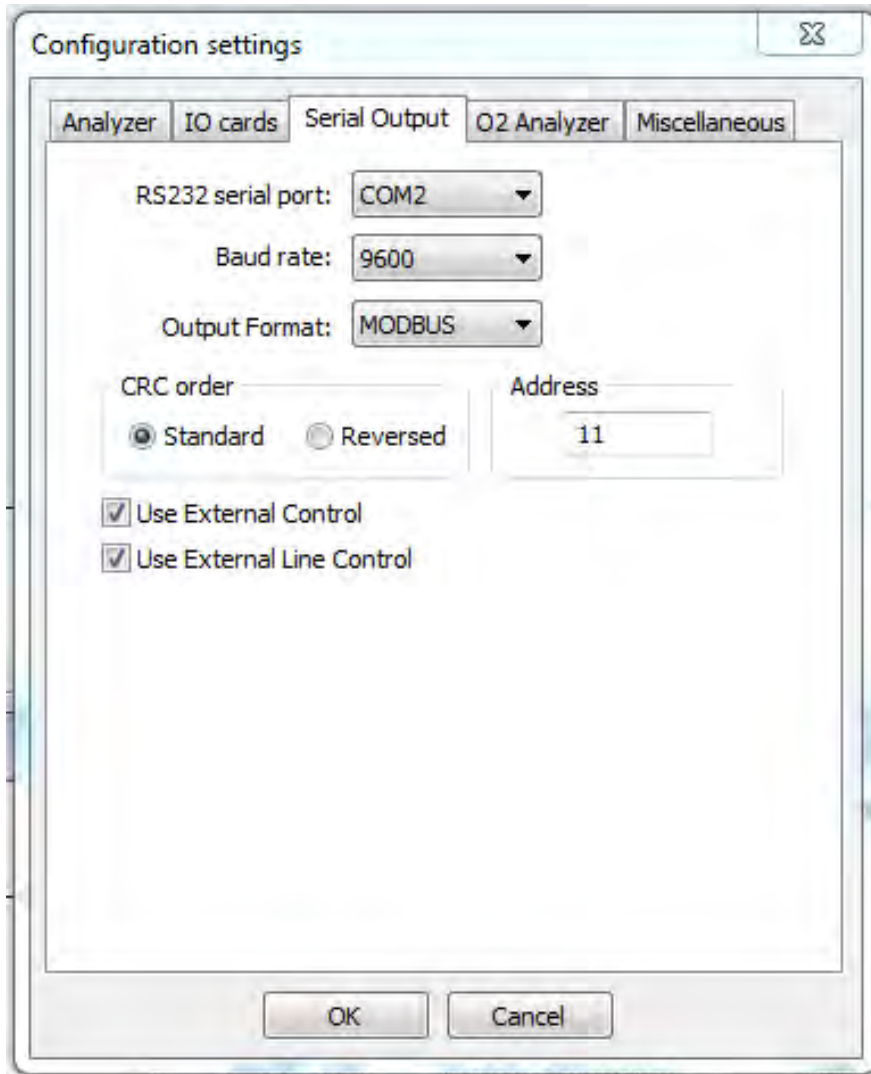


Figure D.5: The RS-232 serial output to DeltaV™ has to be configured in Calcmet. The RS-232 Serial port corresponds to the physical communications port on the FTIR computer. The baud rate is set to match DeltaV™ and the protocol is set to ModBus. Cyclic Redundancy Check (CRC) is set to standard representation. The address is the RS-232 (serial) input card address in DeltaV™.

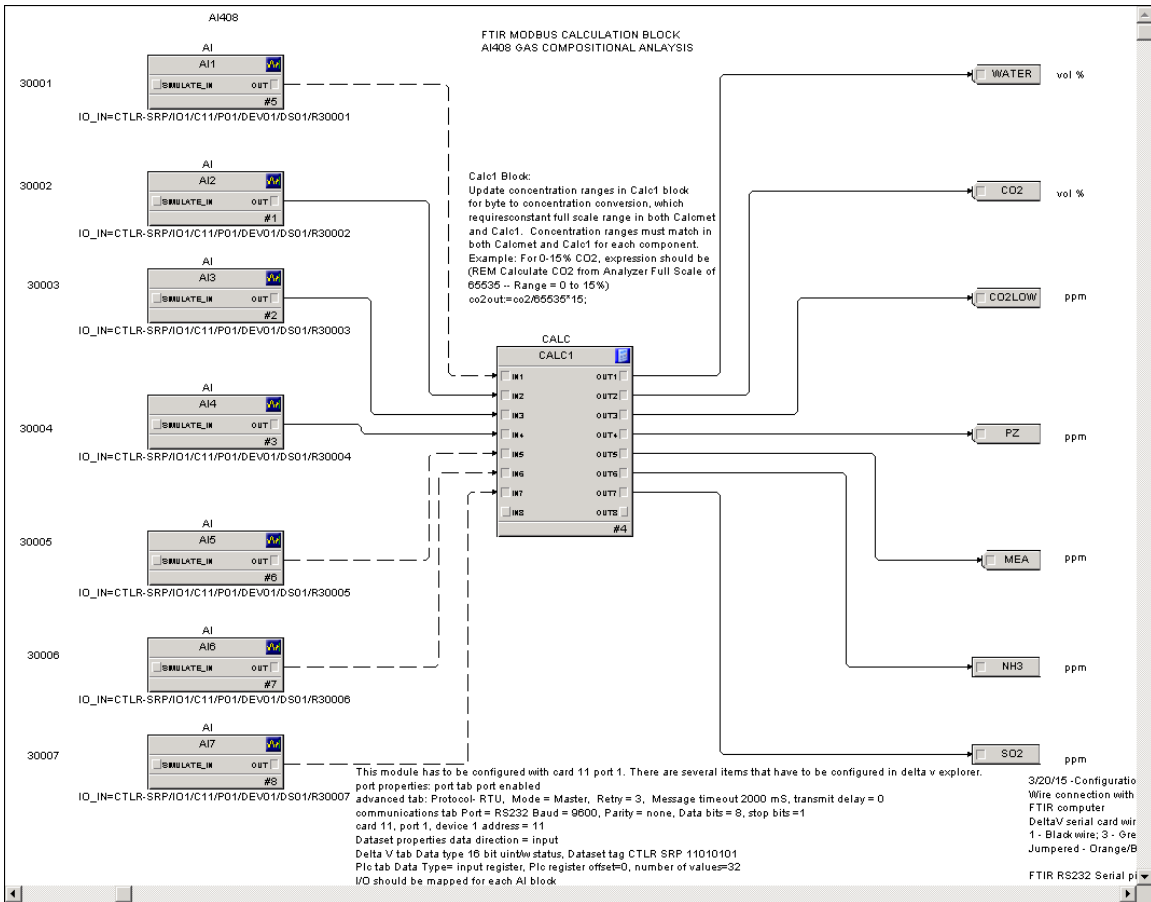


Figure D.6: I/O diagram for the FTIR in DeltaV™ Control Studios. The module is configured to card 11, port 1. The FTIR output registries begin at address 30001 which corresponds to the ModBus Output Channel 1 which is configured in Calcmet™. Seven ModBus channels are configured in this diagram. The read input values are converted to concentration numbers in the CALC1 calculation block.

D.3 CALC1 DELTA V™ CODE

The following code occurs in the calculation block (CALC1) in DeltaV™ Control Studios for digital inputs read from the FTIR. The calculation block normalizes the digital input (two bytes) read from the FTIR registry and multiplies the fraction of full scale by the specified measurement range which is set at the FTIR terminal. The measurement range is set by double-clicking on the “Ranges” bar for a component in the

Analysis Results window. The Measuring Ranges window opens and contains the input box for the maximum range. If a range is changed on the FTIR terminal, the code block has to be changed as well since the code is static.

The input section of the code assigns a variable name to the input channel number. The output is then calculated and assigned an output variable name. The output section assigns the output variable name to the output channel number.

CALC1

REM INPUT

```
water:=in1;  
co2:=in2;  
co2low:=in3;  
pz:=in4;  
mea:=in5;  
nh3:=in6;  
so2:=in7;
```

REM CALCULATIONS

REM Calculate Water from Analyzer Full Scale of 65535 -- Range = 0 to 30%

```
waterout:=water/65535*30;
```

REM Calculate CO2 from Analyzer Full Scale of 65535 -- Range = 0 to 15%

```
co2out:=co2/65535*15;
```

REM Calculate CO2low from Analyzer Full Scale of 65535 -- Range 0 to 500ppm

```
co2lowout:=co2low/65535*500;
```

REM Calculate PZ from Analyzer Full Scale of 65535 -- Range = 0 to 100ppm

pzout:=pz/65535*100;

REM Calculate MEA from Analyzer Full Scale of 65535 -- Range = 0 to 100ppm

meaout:=mea/65535*100;

REM Calculate NH3 from Analyzer Full Scale of 65535 -- Range = 0 to 20ppm

nh3out:=nh3/65535*20;

REM Calculate SO2 from Analyzer Full Scale of 65535 -- Range 0 to 50 ppm

so2out:=so2/65535*50;

REM OUTPUT

out1:=waterout;

out2:=co2out;

out3:=co2lowout;

out4:=pzout;

out5:=meaout;

out6:=nh3out;

out7:=so2out;

Appendix E: Aerosol Integration Code

E.1 AEROSOL INTEGRATION ALGORITHM OVERVIEW

The code contained in this appendix is the main script (Aerosol_x.m), the initialization routine (Initialize_x.m), the main differential equation routine (diffeql_x.m), and the stopping criteria (events_x.m). The integration algorithm (ODE23s) is called in the “Aerosol_x.m” main script. Code comments are highlighted in green.

E.2 AEROSOL_X.M

```
% Aerosol Growth Model
```

```
% Modified By: Steven Fulk
```

```
% Date Modified: 08/06/2012
```

```
%----->
```

```
% Notes:
```

```
% 1.
```

```
%----->
```

```
% The purpose of this program is to model evaporation and condensation to  
% a single liquid sphere moving at a relative velocity to a gas of varying  
% conditions. Gas-phase profiles are calculated externally in Aspen Plus  
% simulations with a combined absorber/water wash.
```

```
% Aspen Plus simulation results are copied to Excel for formatting and copied to  
% *.mat files prior to calculation. When this script is opened, load the
```

```

% *.mat files and input data into the cell arrays with the proper units.
% The program will automatically convert the cell arrays into usable
% matrices.

% This version of the aerosol growth model loads *.mat cell array files for
% correlation parameters [corr.mat], component constants such as molecular
% weight and critical temperature [compcns.mat], and the gas-phase profiles
% calculated in Aspen Plus [abspro.mat].

% The "Aerosol_x.m" script calls for two functions. The "initializex.m", which
% processes intuitive initial conditions and returns passable
% variables to the ODE functions "diffeq.m, diffeql.m, and diffeq.m."
% Differential variables are the mole fractions of each species [xi], the
% total moles in the drop [ntot], the liquid temperature [Tl], and the
% droplet velocity [momentum]. All algebraic equations are solved using the set
% of differential variables in a nested, explicit method.

%----->

clear %Clear residual variables
clc %Clear the command prompt

tic %Start computation clock.

%Run-time includes time to select resistance in user-window

```

```
%----->
```

```
% Declare global variables to pass between functions.
```

```
% The global variable list is copied into each of the functions used in this
```

```
% calculation and then unused variables are removed for cleanliness.
```

```
global g kB R Nav Ncomps N2 H2O CO2 PZ A B C D E F G Nstg hcol dcol
```

```
global height MW Tc pp Dg Tg MWgmx rhogmx kapgmx cpgmx mugmx Gvfr
```

```
global mulp Dlp rhoImxp molvp mulmxx sigp ppeqp delhH2Op cplp cplxp hnrp
```

```
global k2p Ccp d_drop molal ldg Tl vfrac holdup
```

```
%----->
```

```
% Column Information:
```

```
%----->
```

```
% The program asks for input in the command window for information related
```

```
% to the absorber or water wash column with correct units. Again, units are
```

```
% fixed in this program.
```

```
% Column diameter is fixed in this program. Variable column diameter should
```

```
% be coded as a column vector much in the same way as other column
```

```
% properties. The diameter would need to be interpolated for Reynold's
```

```
% number calculations.
```

```
% Packing and hold-up information must be included to correct the
% superficial velocity for the volume occupied by the packing and by the
% liquid. Holdup is the fraction of the free volume, meaning the total
% volume minus the fraction occupied by the packing.
```

```
% Nstg = input('Number of Aspen stages = ');
% hcol = input('Height of column from Aspen in meters = ');
% dcol = input('Diameter of column from Aspen in meters = ');
% vfrac = input('Void fraction of the packing from Aspen = ');
% holdup = input('Liquid hold-up from Aspen in fraction of free volume = ');
```

```
hcol = 3; % Column height [m]
```

```
dcol = 18.9; % Column diameter [m]
```

```
vfrac = 0.987; % Void fraction of modeled packing
```

```
holdup = 0.09402627; % Fraction of free volume occupied by liquid
```

```
%----->
```

```
% Constants, Correlation Parameters, and Column Profiles:
```

```
%----->
```

```
% Global constants are declared in fixed units.
```

```
g = 9.80665; % Acceleration of gravity [m/s^2]
```

```
kB = 1.3806503*10^-23; % Boltzman constant
```

```
[m^2*kg/s^2*K*molec]
```

```

R = 8.3144621;                                % Universal gas constant
[Pa*m^3/mol*K]
Nav = 6.0221415*10^23;                        % Avogadro's number [molec/mol]

% *.mat files are loaded as cell arrays, then numeric entries in cell arrays
% are are mapped to a new matrix. *.mat files are saved as a part of the
% script file.

load compcons.mat;
load abspro.mat;
load correl.mat;

% This step converts cell arrays into matrices.

compcons=cell2mat(compcons(2:end,3:end));
correl=cell2mat(correl(3:end,:));
abspro=cell2mat(abspro(6:end,2:end));

Nstg = size(abspro,1);

%----->
% Unpackage correlations and profiles by species:
%----->

% Declare the number of components in the gas and liquid and assign

```

% component ID's. Fortunately, correlations used in this program rely on
% apparent weight and mole fractions so speciation effects are
% implicit.

% Any future modifications to include ionic species for more rigorous
% thermodynamic calculations should follow the style of component ID's so
% code is transparent. Assigning generic number of row and columns in
% matrices is too difficult to keep track of, especially for a system which
% can contain 10+ components. The number of components is also used in
% calculations to specify the number of rows or columns used in a
% calculation such that the calculation is performed the correct number of
% times.

Ncomps = 4;

N2=1; H2O=2; CO2=3; PZ=4;

% Correlation parameters are arbitrarily ordered alphabetically but can
% certainly be changed to match preference.

A=1; B=2; C=3; D=4; E=5; F=6; G=7;

% This program uses a Lagrangian reference frame, meaning the fixed point in
% space is the center of the droplet. The calculation is a transient
% integration of a sphere surrounded by a variable gas stream. Since
% profiles from Aspen are in the Eulerian reference frame, (steady-state,

```
% fixed positions), there is a need to convert between spatial and temporal  
% variations.
```

```
% Aspen numbers calculation stages from top to bottom; however, an aerosol  
% particle moves from bottom to top. The "height" variable in this program  
% begins at the bottom of the column. The height must be normalized and  
% flipped such that interpolation of height moves from bottom to top of the  
% column.
```

```
height = (0:(Nstg-1))*(hcol/(Nstg-1));  
height = flipud(height);
```

```
% This part of the program unpackages variables from the *.mat files and  
% converts them into named column matrices. Variable names are used for two  
% reasons: 1. Code is more transparent and 2. Variables aren't confused.
```

```
MW = zeros(Ncomps,1);  
Tc = zeros(Ncomps,1);  
pp = zeros(Nstg,Ncomps);  
Dg = zeros(Nstg,Ncomps);
```

```
for i = 1:Ncomps;  
    MW(i,1) = compcons(1,i);  
    Tc(i,1) = compcons(2,i);  
    pp(:,i) = abspro(:,i+5);
```

```

    Dg(:,i) = abspro(:,i+14);
end

Tg = abspro(:,1);
MWgmx = abspro(:,10);
rhogmx = abspro(:,11);
kapgmx = abspro(:,12);
cpgmx = abspro(:,13);
mugmx = abspro(:,14);
Gvfr = abspro(:,19);

mulp = zeros(Ncomps,7);
Dlp = zeros(Ncomps,7);

rholmxp = correl(:,1)';
molvp(2:Ncomps,:) = correl(:,2:4)';
mulp(H2O,:) = correl(:,5)';
mulmxp = correl(:,6)';
sigp(2:Ncomps,:) = correl(:,7:9)';
ppeqp(2:Ncomps,:) = correl(:,10:12)';
delhH2Op = correl(:,13)';
cplp(H2O,:) = correl(:,14)';
cplp(PZ,:) = correl(:,15)';
cplxp = correl(:,16:17)';
hnryp = correl(:,18)';

```

```

Dlp(H2O,:) = correl(:,19)';
k2p = correl(:,20)';
Ccp = correl(:,21)';

%----->
% INITIAL CONDITIONS:
%----->

% The program asks for input to calculate the initial conditions of
% the droplet with correct units. Units are fixed in this program.

% Tl = input('Initial liquid temperature in C = ');
% molal = input('Initial liquid PZ concentration in mol/kg H2O = ');
% ldg = input('Initial liquid loading mol/mol alk. = ');
% d_drop = input('Initial liquid droplet diameter in micron = ');

% These conditions are used as generic inputs for quick testing of function
% output or ODE solver stability.

ldg = 0.254775;           %[Moles CO2/mol alkalinity]
Tl = 48.13755222;        %[C]
molal = 8.337;           %[Moles alkalinity/kg H2O]
d_drop = 2.051361963;    %[micron]

% The initialize function converts the intuitive initial conditions

```

```

% specified above into passable variables. The initial velocity is
% calculated using a closed-form equation assuming zero initial acceleration
% using Stoke's drag coefficient (24/ReG).

[n0] = initialize_x();

%----->
% Film-Resistance Decision:
%----->

% The program prompts via an interactive menu for input of dominating
% resistance for CO2 mass transfer. The mass transfer coefficient is
% programmed into separate functions. A switch is used to choose the
% correct function based on input.

CO2mtc=menu('Which film dominates CO2 mass transfer?','Gas','Liquid','Equilibrium');

% Tspan is the limits of integration for the independent variable. An event
% has been created to stop integration.

tspan = [0 5];

% These conditions and function call are used for open-loop checks of
% variables used in integration steps.

```

```

% n = [0; 1.7133E-08; 1.4815E-09; 2.4692E-09; 313.15; 1.8938; 0];
%
% [ret] = diffeq(n)

% This switch chooses the correct function according to the chosen
% film-resistance.

% The system of equations to be integrated is a very stiff problem. ODE45
% takes roughly 30 minutes for a 10 micron particle and creates
% semi-unstable temperature and water mass transfer profiles. ODE15s and
% ODE23s are stiff ODE solvers are much better suited for this type of
% integration, but may sacrifice some accuracy.

format long e;

options = odeset('RelTol', 1e-14,'events', @eventsX, 'InitialStep', 1e-20);

switch CO2mtc
    case 1
        [t,n] = ode15s(@diffeqg,tspan,n0);
        disp('Gas film resistance')
    case 2
        [t,n] = ode23s(@diffeqlx,tspan,n0,options);
        disp('Liquid film resistance')
    case 3

```

```

[t,n] = ode23s(@diffeq,tspan,n0);
disp('Equilibrium')
end

%----->
% Profiles and Plots:
%----->

ntot = n(:,1:Ncomps)*ones(Ncomps,1);
ldg = n(:,CO2)/(2*n(:,PZ));

xa = zeros(size(n,1),Ncomps);
xt = zeros(size(n,1),Ncomps);
wta = zeros(size(n,1),Ncomps);
rholmx = zeros(size(n,1),1);
d_drop = zeros(size(n,1),1);

for i = 1:size(n,1)
    xa(i,:) = n(i,1:Ncomps)/ntot(i);
    xt(i,:) = n(i,H2O)/(n(i,H2O)+n(i,PZ));
    wta(i,:) = n(i,1:Ncomps).*MW'./(n(i,1:Ncomps)*MW);
    rholmx(i,:) = 1000*(rholmxp(E)+rholmxp(F)*n(i,5));
    rholmx(i,:) =
rholmx(i,:)*log(rholmxp(A)*xa(i,CO2)+rholmxp(B)*xa(i,PZ)+rholmxp(C)*ldg(i)+rholm
xp(D));

```

```

    % rholmx = 1000;

    % d_drop(i,1) = 1e6*((6/pi)*n(i,H2O)*MW(H2O)*(1/(1000*rholmx)))^(1/3);

    d_drop(i,1) = 1e6*((6/pi)*n(i,1:Ncomps)*MW*(1/(1000*rholmx(i,:))))^(1/3);

end

gastemp = interp1(height,Tg,n(:,7));
colpos = n(:,7)./hcol;

CO2gas = interp1(height,pp(:,CO2),n(:,7));
PZgas = interp1(height,pp(:,PZ),n(:,7));
H2Ogas = interp1(height,pp(:,H2O),n(:,7));
% xH2OBL = interp1(height,xH2O,n(:,7));
% bulkliqT = interp1(height,TBl,n(:,7));
% figure(1);
% subplot(2,2,1)
% plot(colpos,gastemp,'-b',colpos,n(:,5),'-r',colpos,bulkliqT,'g')
% xlabel('Z/Z_t_o_t','FontSize',12)
% ylabel('Temperature [K]','FontSize',12)
% legend('Gas','Droplet')
% axis tight
% subplot(2,2,2)
% plot(colpos,n(:,2),'-b')
% xlabel('Z/Z_t_o_t','FontSize',12)
% ylabel('Water [moles]','FontSize',12)
% axis tight

```

```

% subplot(2,2,3)
% plot(colpos,n(:,3),'-b')
% xlabel('Z/Z_t_o_t','FontSize',12)
% ylabel('CO_2 [moles]','FontSize',12)
% axis tight

% subplot(2,2,4)
% plot(colpos,n(:,4),'-b')
% xlabel('Z/Z_t_o_t','FontSize',12)
% ylabel('PZ [moles]','FontSize',12)
% axis tight

% LOADING = n(:,CO2)./(2*n(:,PZ));
% MOLAL = n(:,PZ)./(MW(H2O)*n(:,H2O)/1000);

% figure(2);
% subplot(3,2,1)
% plot(colpos,LOADING)
% xlabel('Z/Z_t_o_t','FontSize',12)
% ylabel('Loading [mol CO_2/mol alk]','FontSize',12)
% axis tight

% subplot(3,2,2)
% plot(colpos,MOLAL)
% xlabel('Z/Z_t_o_t','FontSize',12)
% ylabel('PZ [molal]','FontSize',12)
% axis tight

```

```

% subplot(3,2,3)
% plot(colpos,CO2gas)
% xlabel('Z/Z_t_o_t','FontSize',12)
% ylabel('P_C_O_2 [Pa]','FontSize',12)
% axis tight
% subplot(3,2,4)
% plot(colpos,PZgas)
% xlabel('Z/Z_t_o_t','FontSize',12)
% ylabel('P_P_Z_ [Pa]','FontSize',12)
% axis tight
% subplot(3,2,5)
% plot(colpos,H2Ogas)
% xlabel('Z/Z_t_o_t','FontSize',12)
% ylabel('P_H_2_O_ [Pa]','FontSize',12)
% axis tight
% subplot(3,2,6)
% plot(colpos,xt,colpos,xH2OBL,'-r')
% xlabel('Z/Z_t_o_t','FontSize',12)
% ylabel('H_2O Mole Fraction','FontSize',12)
% axis tight

```

Toc

E.3 INITIALIZE_X.M

```
function [n0] = initialize_x()
```

% Modified By: Steven Fulk

% Date modified: 08/06/2012

%----->

% Notes:

%----->

global g N2 H2O CO2 PZ A B C D E F G Nstg dcol

global MW rhogmx mugmx Gvfr

global rholmxp

global d_drop molal ldg Tl

% This function converts intuitive initial conditions into passable

% variables for ODE solver routine

% ODE requires ni and Tl to calculate ALL process variables

% Convert Tl to correct units [K]

Tl = Tl+273.15;

% Convert d_drop to correct units [m]

d_drop = d_drop/1000000;

% Convert molal and ldg to apparent mole fractions

$$x_{\text{atot}} = (1000/\text{MW}(\text{H}_2\text{O}))/2 * \text{molal} * \text{ldg} + \text{molal};$$

$$x_{\text{a}}(\text{H}_2\text{O}) = (1000/\text{MW}(\text{H}_2\text{O}))/x_{\text{atot}};$$

$$x_{\text{a}}(\text{CO}_2) = (2 * \text{molal} * \text{ldg})/x_{\text{atot}};$$

$$x_{\text{a}}(\text{PZ}) = \text{molal}/x_{\text{atot}};$$

% Calculated average molecular weight of liquid [kg/kmol]

$$\text{MW}_{\text{lmx}} = x_{\text{a}} * \text{MW};$$

% Calculate droplet volume [m³]

$$V_{\text{drop}} = (4 * \pi / 3) * (d_{\text{drop}} / 2)^3;$$

% Calculate liquid density [kg/m³]

$$\rho_{\text{holmx}} = 1000 * (\rho_{\text{holmxp}}(\text{E}) + \rho_{\text{holmxp}}(\text{F}) * T1);$$

$$\rho_{\text{holmx}} =$$

$$\rho_{\text{holmx}} * \log(\rho_{\text{holmxp}}(\text{A}) * x_{\text{a}}(\text{CO}_2) + \rho_{\text{holmxp}}(\text{B}) * x_{\text{a}}(\text{PZ}) + \rho_{\text{holmxp}}(\text{C}) * \text{ldg} + \rho_{\text{holmxp}}(\text{D}));$$

% Calculate the total moles in the droplet [gmol]

$$m_{\text{Tot}} = V_{\text{drop}} * \rho_{\text{holmx}} / \text{MW}_{\text{lmx}} * 1000;$$

```

% Renormalize mTot to be on the order of 1

mTot = mTot/mTot;

% Simulations for water droplets require changing correlations such that
% density can be matched. If water is the only component, comment out the
% amine mixture density correlation.

% rholmx = 1000;

% Calculate initial velocity of droplet assuming acceleration is zero

% Velocity of droplet relative to the gas [m/s]

v_rel = (d_drop)^2*(rholmx-rhogmx(Nstg))*g/(18*mugmx(Nstg));

% Velocity of the gas [m/s]

v_g = 4*Gvfr(Nstg)/(pi*(dcol)^2);

% The relative velocity of the drop must be absolute so that the Reynold's
% number never goes negative. Square root operations cause imaginary
% numbers in extreme cases where the ODE solver may over-step and cause
% negative accelerations.

```

```
% Absolute velocity of the droplet [m/s]
```

```
v_drop = abs(v_g-v_rel);
```

```
% The output is a matrix ordered as components (1:4), liquid temperature  
% Tl,the absolute droplet velocity, and the starting position in the column.  
% The default is to start at the bottom. To start at another position,  
% input a value here, keeping in mind that equilibrium conditions must be  
% met for H2O and CO2 to avoid diverged, undamped oscillatory behavior  
% which diverges.
```

```
n0 = [xa mTot Tl v_drop 0];
```

```
end
```

E.4 DIFFEQL_X.M

```
function dndt = diffeql(t,n)
```

```
% Modified By: Steven Fulk
```

```
% Date Modified: 08/06/2012
```

```
%----->
```

```
% Notes:
```

```
%----->
```

```
% The diffeql.m function assumes gas-phase resistance for H2O and PZ, but
% assumes the mass transfer coefficient for CO2 is the same as kg' for a
% normal absorber-stripper calculation. Correlations are used for all
% physical properties in the liquid and profiles from Aspen are used for
% gas-phase properties.
```

```
% Declare and pass global constant values from the main script "Aerosol_2"
% for use in the ODE function. I haven't figured out how to pass dynamic
% variables or variable sets to functions to be integrated from the main
% script without declaring them as global. The global set must match the
% script in order.
```

```
global g kB R Nav Ncomps N2 H2O CO2 PZ A B C D E F G dcol
global height MW Tc pp Dg Tg MWgmx rhogmx kapgmx cpgmx mugmx Gvfr
global mulp Dlp rhoImxp molvp mulm xp sigp ppeq delhH2Op cplp cplx hnryp
global k2p Ccp vfrac holdup
```

```
% To keep consistency between variable names and the integrated matrix 'n',
% the liquid temperature, the absolute droplet velocity, and the position
% are declared before the integration calculation occurs.
```

```
%----->
```

```
% Thermal equilibrium with the gas can be assumed if the liquid temperature
% matches the gas temperature at each point. If this option is selected,
```

```
% the differential equation for energy/temperature can be commented out to  
% save computation time.
```

```
% Option #1 - energy balance option
```

```
Tl = n(5);    % Bulk liquid temperature [K]
```

```
% Option #2 - thermal equilibrium with gas-phase
```

```
% Tl = interp1(height,Tg,n(7),'spline');
```

```
%----->
```

```
v_drop = n(6); % Absolute droplet velocity [m/s]
```

```
%----->
```

```
% Stationary droplets for model validation can be simulated by turning off
```

```
% the velocity n(6) and position n(7) differential equations.
```

```
h = n(7)    % Height of droplet in the column [m]
```

```
%----->
```

```
% The ODE solver during jacobian calculations adds N2 although the
```

```
% differential equation is at all times set to zero. To bypass this, the N2
```

```
% is set to be zero before all calculations so that error is always fixed.
```

```
n(N2) = 0;    % Moles of nitrogen [moles]
```

% Compositions are calculated on an apparent and "true" species basis. The
 % "true" species basis assumes that all CO2 goes to PZ such that no
 % bicarbonate and carbonate are formed. The true species are then the total
 % H2O and PZ. Weight fractions are calculated on an apparent basis. The
 % average molecular weight is calculated on an apparent component basis.

```

ntot = sum(n(1:Ncomps));      % Total moles in droplet [moles]
ldg = n(CO2)/(2*n(PZ));      % Loading in droplet [moles CO2/mol alkalinity]
xt(H2O) = n(H2O)/(n(H2O)+n(PZ)); % True mole fraction of water
xt(PZ) = 1-xt(H2O);          % True mole fraction of PZ
xa = n(1:Ncomps)/ntot;       % Apparent mole fraction of all components
wta = (MW(1:Ncomps).*n(1:Ncomps))/(MW(1:Ncomps)'*n(1:Ncomps)); % Apparent
weight fraction of all components
MWlmx = xa*MW(1:Ncomps);     % Average molecular weight of the droplet

```

%----->

% The mixture density is calculated by correlation. The density does not
 % quite match H2O at zero loading and amine concentration. A separate
 % correlation for pure H2O must be coded.

% Option #1 - mixture density

```

rholmx = 1000*(rholmxp(E)+rholmxp(F)*Tl); % Density of the droplet [kg/m^3]
rholmx
rholmx*log(rholmxp(A)*xa(CO2)+rholmxp(B)*xa(PZ)+rholmxp(C)*ldg+rholmxp(D));

```

```

% Option #2 - pure H2O
% rho_lmx = 1000;
%----->

% Calculate droplet dimensions.

V_drop = (n(H2O)+n(CO2)+n(PZ))*MW_lmx/(1000*rho_lmx); % Volume of the droplet
[m^3]
d_drop = (6*V_drop/pi)^(1/3); % Diameter of the droplet [m]
A_drop = pi*(d_drop)^2; % Surface area of the droplet [m^2]

%----->

% Molar volume and surface tension are used to calculate corrections to
% equilibrium partial pressure for surface curvature (Kelvin effect). The
% surface tension is assumed to be independent of the particle size, meaning
% the surface concentration matches the "bulk liquid" of the aerosol
% particle.

% Molecular volume of each component [m^3/molecule]

molv(N2) = 0;
molv(H2O)
(1/(Nav*1000))*(molvp(H2O,A)+molvp(H2O,B)*Tl+molvp(H2O,C)*Tl^2+molvp(H2O,
D)*Tl^3)^-1;

```

$$\text{molv}(\text{CO}_2) = \left(\frac{1}{N_{\text{av}} * 1000} \right) * \left(\frac{\text{molvp}(\text{CO}_2, \text{A})}{\text{molvp}(\text{CO}_2, \text{B})^{1+(1-(304.21/\text{molvp}(\text{CO}_2, \text{C})))^{\text{molvp}(\text{CO}_2, \text{D}))}} \right)^{-1};$$

$$\text{molv}(\text{PZ}) = \left(\frac{1}{N_{\text{av}} * 1000} \right) * \left(\frac{\text{molvp}(\text{PZ}, \text{A})}{\text{molvp}(\text{PZ}, \text{B})^{1+(1-(T_l/\text{molvp}(\text{PZ}, \text{C})))^{\text{molvp}(\text{PZ}, \text{D}))}} \right)^{-1};$$

Tr = Tl./Tc; % Reduced temperature of all components

$$\text{sig}(\text{N}_2) = 0;$$

$$\text{sig}(\text{H}_2\text{O}) = \text{sigp}(\text{H}_2\text{O}, \text{A}) * (1 - \text{Tr}(\text{H}_2\text{O}))^{(\text{sigp}(\text{H}_2\text{O}, \text{B}) + \text{sigp}(\text{H}_2\text{O}, \text{C}) * \text{Tr}(\text{H}_2\text{O}) + \text{sigp}(\text{H}_2\text{O}, \text{D}) * \text{Tr}(\text{H}_2\text{O})^2);$$

$$\text{sig}(\text{CO}_2) = 0;$$

$$\text{sig}(\text{PZ}) = \text{sigp}(\text{PZ}, \text{A}) * (1 - \text{Tr}(\text{PZ}))^{(\text{sigp}(\text{PZ}, \text{B}) + \text{sigp}(\text{PZ}, \text{C}) * \text{Tr}(\text{PZ}) + \text{sigp}(\text{PZ}, \text{D}) * \text{Tr}(\text{PZ})^2);$$

sigmx = sig*xt'; % Surface tension of droplet [N/m]

%----->

% Calculate equilibrium partial pressures using correlations for PZ and CO2.

% The multiplier for the PZ concentration is on an apparent basis according

% to Qing's correlation. H2O is calculated using Raoult's law with the true

% concentration of H2O.

% Equilibrium partial pressure over the droplet [Pa]

$$\text{ppeq}(\text{N}_2) = 0;$$

```

ppeq(H2O) =
xt(H2O)*exp(ppeq(H2O,A)+(ppeq(H2O,B)/Tl)+ppeq(H2O,C)*log(Tl)+ppeq(H2O,
D)*Tl^ppeq(H2O,E));
ppeq(CO2) =
exp(ppeq(CO2,A)+(ppeq(CO2,B)/Tl)+ppeq(CO2,C)*ldg^2+ppeq(CO2,D)*(ldg/Tl)+
ppeq(CO2,E)*(ldg^2/Tl));
ppeq(PZ) =
xa(PZ)*exp(ppeq(PZ,A)+ppeq(PZ,B)*log(Tl)+ppeq(PZ,C)*ldg+ppeq(PZ,D)*(ldg^2
/Tl));

```

```

%----->

```

```

% The Kelvin correction can be made here by uncommenting.

```

```

ppeq(H2O) = ppeq(H2O)*exp(4*sigmx*molv(H2O)/(kB*Tl*d_drop));
ppeq(CO2) = ppeq(CO2)*exp(4*sigmx*molv(CO2)/(kB*Tl*d_drop));
ppeq(PZ) = ppeq(PZ)*exp(4*sigmx*molv(PZ)/(kB*Tl*d_drop));

```

```

%----->

```

```

%----->

```

```

% Heats of absorption/vaporization and heat capacities are used in the
% energy balance. This portion can be omitted when thermal equilibrium is
% assumed with the gas phase. The heat capacity is calculated from a
% generic correlation with binary mixing parameters regressed in Excel. The
% correlation was not stress-tested and has shown signs of major oscillatory

```

% behavior especially at high loadings.

% Heat of absorption for all components [J/mol]

delH(N2) = 0;

delH(H2O) = (1/1000)*delhH2Op(A)*(1-Tr(H2O))^(delhH2Op(B)+delhH2Op(C)*Tr(H2O)+delhH2Op(D)*Tr(H2O)^2);

delH(CO2) = -R*(ppeq(CO2,B)+ppeq(CO2,D)*ldg+ppeq(CO2,E)*ldg^2);

delH(PZ) = -R*(ppeq(PZ,B)*Tl+ppeq(PZ,D)*ldg^2);

% Heat capacity of the droplet [J/kmol*K]

cpl(H2O) = cplp(H2O,A)+cplp(H2O,B)*Tl+cplp(H2O,C)*Tl^2+cplp(H2O,D)*Tl^3+cplp(H2O,E)*Tl^4;

cpl(PZ) = cplp(PZ,A)+cplp(PZ,B)*Tl+cplp(PZ,C)*Tl^2+cplp(PZ,D)*Tl^3;

cplx1 = xa(PZ)*xa(CO2)*((cplx(1,A)+cplx(1,B)*Tl)+(cplx(1,C)+cplx(1,D)*Tl)*(xa(PZ)-xa(CO2)));

cplx2 = cplx1+xa(H2O)*xa(CO2)*((cplx(2,A)+cplx(2,B)*Tl)+(cplx(2,C)+cplx(2,D)*Tl)*(xa(H2O)-xa(CO2)));

cplx = cplx2*1000;

% Option #1 - mixture heat capacity

```
cplmx = cpl*xa+cplx;
```

```
% Option #2 - pure H2O heat capacity
```

```
% cplmx = cpl(H2O);
```

```
%----->
```

```
%----->
```

```
% The relative velocity of the particle is determined from a momentum  
% balance. The drag force is calculated using a drag coefficient (Cd) which  
% is a function of Reynold's number for hard spheres. Smaller spheres tend  
% to travel at the same velocity as the gas; therefore, the Reynold's number  
% approaches zero. At these conditions, the flow characteristics are called  
% "Stoke's Flow," meaning inertial effects are negligible. The drag  
% coefficient for this limiting condition is equal to 24/Re. However, as  
% particles approach the mean free path of the surrounding gas molecules,  
% the no-slip boundary condition that is used in continuum balances becomes  
% an inaccurate representation of the actual physics of the fluid system.  
% The Cunningham slip correction must be applied. The formulation of the  
% model thus far does not include the slip correction. The gas velocity is  
% interpolated at a given position in the column and assumes that the column  
% diameter is the same at any given point. The gas velocity calculation  
% also assumes that the packing and liquid make up a negligible amount of  
% the volume, thus the gas velocity is the superficial velocity. The  
% droplet diameter is updated at the beginning of this function, so the  
% relative velocity is simply calculated by subtracting the absolute
```

```

% velocities of the gas and drop.

% Option #1 - update the particle velocity profile

% Absolute gas velocity [m/s]
v_g = 4*interp1(height,Gvfr,n(7),'spline')/((1-holdup)*vfrac*pi*(dcol^2));

% Option #2 - assume the particle matches the gas velocity
% v_drop = v_g;

% Velocity of the droplet relative to the gas [m/s]

v_rel = (v_g-v_drop);
%----->

%----->

% The Reynold's number is calculated using the relative velocity. It is
% important to use the absolute value of the relative velocity so the
% Reynold's number is not negative. Negative Reynold's numbers result in
% imaginary results.

Re =
interp1(height,rhogmx,n(7),'spline')*v_rel*d_drop/interp1(height,mugmx,n(7),'spline');
Re = abs(Re);
%----->

```

```

%----->
% The Fuch's modification is a flux matching correction to mass transfer in
% the continuum and kinetic regimes. When the particle diameter approaches
% the mean free path of diffusing molecules, the continuum approximation of
% fluids falls apart. Kinetic theory provides a much better representation
% of the physics of mass transfer. However, kinetic and continuum theory do
% not smoothly transition from one to the other, so flux matching must be
% done by mass balance.

% The velocity of gas molecules is calculated by kinetic theory assuming a
% Maxwellian distribution of speed. The velocity calculated here is the
% arithmetic velocity. Some conventions use the root-mean square velocity
% rather than the arithmetic velocity for mean-free path calculations.

v_gmol = ((1000*Nav*8*kB*interp1(height,Tg,n(7),'spline'))./(pi.*MW)).^(1/2);    %
[m/s]
mfp = 3*(interp1(height,Dg,n(7),'spline'))./v_gmol';                            % [m]
Kn = (2*mfp/d_drop);
avgmfp = mean(mfp);                                                            % [m]
avgKn = (2*avgmfp/d_drop);
alpha = 1;
Fuchs = (0.75*alpha*(1+Kn))./(Kn.^2+Kn+0.283*Kn*alpha+0.75*alpha);

% Cunningham slip used to correct Stokes' Law.

```

```

Cc = 1+avgKn*(Ccp(A)+Ccp(B)*exp(-Ccp(C)/avgKn));
%----->

%----->

% The acceleration of the droplet is calculated from a momentum balance.
% The momentum balance uses Stokes' Law for the force of drag and applies
% the Cunningham Slip Correction for the size of the particle relative to
% the mean-free path of the surrounding fluid.

% Option #1 - update acceleration

% Acceleration of the droplet [m/s^2]

a_drop = (18*v_rel*interp1(height,rhogmx,n(7),'spline'))/(Cc*rholmx*d_drop^2)-(1-
(interp1(height,rhogmx,n(7),'spline')/rholmx))*g;
%----->

%----->

% Gas-side mass and heat transfer coefficients are calculated using the
% Frossling correlations which are adjustments made to the Sherwood and
% Nusselt number using the Reynold's number and the Prandtl number.

% Option #1 - Adjust transfer coefficients for convection

```

```

Pr =
(interpl(height,mugmx,n(7),'spline')*interpl(height,cpgmx,n(7),'spline'))/(interpl(height,
kapgmx,n(7),'spline')*interpl(height,MWgmx,n(7),'spline'));

```

```

Sc = zeros(1,Ncomps);

```

```

for i = 1:Ncomps

```

```

    Sc(1,i) =
interpl(height,mugmx,n(7),'spline')/(interpl(height,rhogmx,n(7),'spline')*interpl(height,
Dg(:,i),n(7),'spline'));

```

```

end

```

```

Sh = zeros(1,Ncomps);

```

```

for i = 1:Ncomps

```

```

    Sh(1,i) = 2+0.6*(Re.^(1/2))*(Sc(:,i).^(1/3));
end

```

```

Nu = 2+0.6*(Re.^(1/2))*(Pr.^(1/3));

```

```

% Option #2 - no convective correction - Sh = Nu = 2

```

```

% Nu = 2;

```

```

% Sh = [2 2 2 2];

```

```
hg = Nu*interp1(height,kapgmx,n(7),'spline')/d_drop;    % Heat transfer coefficient
[J/m^2*s*K]
```

```
kg = Sh.*interp1(height,Dg,n(7),'spline')/d_drop;      % Gas-side mass transfer
coefficients [m/s]
```

```
% hg = Nu*0.0254976/d_drop;
```

```
% kg = 2*0.0000244/d_drop;
```

```
%----->
```

```
%----->
```

```
% The mass transfer coefficient for CO2 is assumed to be the kg' from normal
% absorber-stripper calculations. The pseudo-first order expression of kg'
% is used. The diffusivity of CO2 in solution is equal to the diffusivity
% of CO2 in water adjusted by the ratio of pure water to solution viscosity
% raised to an adjustable power parameter. The solution viscosity is
% referenced to water such that the diffusivity of CO2 and the viscosity
% match water at dilute conditions. The Henry's constant of CO2 in solution
% is assumed to be equal to the Henry's constant of CO2 in water, such that
% the activity coefficient is neglected. The second-order reaction rate
% constant is taken from Dugas' dissertation. The concentration of PZ is
% calculated assuming one mole of CO2 removes 2 moles of PZ from the
% solution. 2PZ + CO2 <-> HPZ+ + PZCOO-. Calculated kg' values are within
% an order of magnitude for normal absorber conditions, but at high loadings
% can cause severe calculation problems because the concentration of PZ will
```

% go negative.

% Viscosity of pure water [Pa*s]

```
mul(H2O) =  
exp(mulp(H2O,A)+(mulp(H2O,B)/Tl)+mulp(H2O,C)*log(Tl)+mulp(H2O,D)*Tl^mulp(  
H2O,E));
```

% Viscosity of amine solution [Pa*s]

```
mulmx=(mulmxx(A)*wta(PZ)+mulmxx(B))*Tl+(mulmxx(C)*wta(PZ)+mulmxx(D));  
mulmx=mulmx*(ldg*(mulmxx(E)*wta(PZ)+mulmxx(F)*Tl+mulmxx(G))+1)*wta(PZ);  
mulmx=mul(H2O)*exp(mulmx/Tl^2);
```

% Diffusion coefficient of CO2 in water [m^2/s]

```
Dl(H2O) = Dlp(H2O,A)*exp(Dlp(H2O,B)/Tl);
```

% Diffusion coefficient of CO2 in amine solution [m^2/s]

```
Dlmx = (1/100^2)*Dl(H2O)*(mul(H2O)/mulmx)^0.72;
```

% Thermodynamic Henry's Law constant for CO2 in water [Pa/mole fraction]

```
henry(CO2) = hnryp(A)*exp(hnryp(B)/Tl)*101325/(100^3);
```

```
% Second-order reaction rate constant of CO2 with PZ [m^3/mol*s]
```

```
k2 = k2p(A)*exp(k2p(B)/(R*Tl));
```

```
% Free PZ concentration [mol/m^3]
```

```
% concPZ = (n(PZ)-n(CO2))/V_drop;
```

```
% concPZ = 500;
```

```
% Liquid-side mass transfer coefficient of CO2 [mol/m^2*s*Pa]
```

```
% kgprime = ((k2*concPZ*Dlmx)^(1/2))/henry(CO2);
```

```
kgprime = 1e-7;
```

```
%----->
```

```
%----->
```

```
% The differential equations are lumped in one vector (n).
```

```
% n = (N2 H2O CO2 PZ Tliq v_drop height)
```

```
dndt(1) = 0;
```

```
% Option #1 - Pure water, fixed particle, thermal equilibrium
```

```
% Change the temperature options to match the gas temperature.
```



```
dndt(2) =
Fuchs(H2O)*kg(H2O)*A_drop/(R*interp1(height,Tg,n(7),'spline'))*(interp1(height,pp(:,
H2O),n(7),'spline')-ppeq(H2O));
```

```
dndt(3) = kgprime*A_drop*(interp1(height,pp(:,CO2),n(7),'spline')-ppeq(CO2));
```

```
dndt(4) =
Fuchs(PZ)*kg(PZ)*A_drop/(R*interp1(height,Tg,n(7),'spline'))*(interp1(height,pp(:,PZ),
n(7),'spline')-ppeq(PZ));
```

```
dndt(5) = 1000*(dndt(H2O)*delH(H2O)-
dndt(PZ)*delH(PZ)+dndt(CO2)*delH(CO2)+hg*A_drop*(interp1(height,Tg,n(7),'spline'
)-Tl))/(cplmx*ntot);
```

```
dndt(6) = a_drop;
```

```
dndt(7) = n(6);
```

```
%----->
```

```
dndt = dndt(:);
```

E.5 EVENTS_X.M

```
function [value, isterminal, direction] = events_x (t,n)
```

```
% This event function stops integration at the exact time when the particle
% height matches the column height. The event requires the definition of a
```

```
% global variable.
```

```
global hcol Ncomps
```

```
% Value corresponds to a zero-point crossing, so the value is when the
```

```
% height "n(7)" matches the column height.
```

```
value = n(Ncomps+4)-hcol;
```

```
isterminal = 1;
```

```
direction = 1;
```

```
end
```

References

- Air Quality Analytical, Inc. (2013). "Liquid Vaporizer and Injector User Manual: Revision 0."
- Albrecht, H.E., Damaschke, N., Borys, M., Tropea, C. (2003). *Laser Doppler and Phase Doppler Measurement Techniques*. New York, NY: Springer - Verlag Berlin Heidelberg.
- Artium Technologies, Inc. (2015). "New Generation Phase Doppler Interferometer: An Instrument for Performing Complete Spray Characterizations Brochure."
- Artium Technologies, I. (n.d). "PDI-100 MD User Manual: Operation of the Phase Doppler Interferometer (PDI) for Spray Drop Size and Velocity Measurement."
- Artium Technologies, Inc. (n.d). "Phase Doppler Interferometer: PDI-X00SC Brochure."
- Azzi, M., Dave, N., Do, T., Jackson, P., Feron, P., Attalla, M. (2010). "CO₂ Capture Mongstad - Project B - Theoretical Evaluation of the Potential to Form and Emit Harmful Components. Task: Process Chemistry."
- Bachalo, W.D. (1980). "Method for Measuring the Size and Velocity of Spheres by Dual-Beam Light-Scattering Interferometry." *Applied Optics*. 19(3):363–370.
- Bai, H., Biswas, P., Keener, T.C. (1994). "SO₂ Removal by NH₃ Gas Injection: Effects of Temperature and Moisture Content." *Ind. Eng. Chem. Res.* 33:1231–1236.
- Biswas, P. (1985). "Impactors for Aerosol Measurements: Developments and Sampling Biases." California Institute of Technology. Ph.D. Dissertation.
- Bottoms, R.R. (1930). Process for Separating Acidic Gases. US1783901A, issued 1930.
- Brachert, L., Mertens, J., Khakharia, P., Schaber, K. (2014). "The Challenge of Measuring Sulfuric Acid Aerosols: Number Concentration and Size Evaluation Using a Condensation Particle Counter (CPC) and an Electrical Low Pressure Impactor (ELPI+)." *Journal of Aerosol Science*. 67:21–27.
- Cai, T.J., King, D.W. (2009). "Report of Raschig Super-Ring(R) No. 0.3 Test."
- Calvert, S., Englund, H. (1984). *Handbook of Air Pollution Technology*. New York, NY: John Wiley & Sons, Inc.

- Carter, T. (2012). "National Carbon Capture Center: Post-Combustion." In *2012 NETL CO₂ Capture Technology Meeting*.
- Chuang, P.Y., Saw, E.W., Small, J.D., Shaw, R.A., Sipperley, C.M., Payne, G.A., Bachalo, W.D. (2008). "Airborne Phase Doppler Interferometry for Cloud Microphysical Measurements." *Aerosol Science and Technology*. 42:685–703.
- Closmann, F.B. (2011). "Oxidation and Thermal Degradation of Methyl-diethanolamine/Piperazine in CO₂ Capture." The University of Texas at Austin. Ph.D. Dissertation.
- Crane, R.I., Evans, R.L. (1977). "Inertial Deposition of Particles in a Bent Pipe." *Journal of Aerosol Science*. 8:161–170.
- Damle, A.S., Ensor, D.S., Ranade, M.B. (1982). "Coal Combustion Aerosol Formation Mechanisms : A Review." *Aerosol Science and Technology*. 1:119–133.
- Davis, J.D. (2009). "Thermal Degradation of Aqueous Amines Used for Carbon Dioxide Capture." The University of Texas at Austin. Ph.D. Dissertation.
- Dekati Ltd. (2014). "Dekati[®] High Temperature ELPI+[™] Brochure."
- DIPPR. (1998). "DIPPR 801, Thermophysical Property Database." Provo, UT.
- Dugas, R.E. (2009). "Carbon Dioxide Absorption, Desorption, and Diffusion in Aqueous Piperazine and Monoethanolamine." The University of Texas at Austin. Ph.D. Dissertation
- Durham, M.D., Lundgren, D.A. (1980). "Evaluation of Aerosol Aspiration Efficiency as a Function of Stokes Number, Velocity Ratio and Nozzle Angle." *Journal of Aerosol Science*. 11:179–188.
- Eide-Haugmo, I., Lepaumier, H., Einbu, A., Vernstad, K., Falck da Silva, E., Svendsen, H.F. (2011). "Chemical Stability and Biodegradability of New Solvents for CO₂ Capture." *Energy Procedia*. 11(4):1631–36.
- Fine, N.A., Goldman, M.J., Nielsen, P.T., Rochelle, G.T. (2013). "Managing N-Nitrosopiperazine and Dinitrosopiperazine." *Energy Procedia*. 37:273–284.
- Frailie, P. (2014). "Modeling of Carbon Dioxide Absorption/Stripping by Aqueous Methyl-diethanolamine/Piperazine." The University of Texas at Austin. Ph.D. Dissertation.

- Frailie, P., Plaza, J., Van Wagener, D., Rochelle, G.T. (2011). "Modeling Piperazine Thermodynamics." *Energy Procedia*. 4:35–42.
- Freeman, S.A. (2011). "Thermal Degradation and Oxidation of Aqueous Piperazine for Carbon Dioxide Capture." The University of Texas at Austin. Ph.D. Dissertation
- Friedlander, S.K. (1977). *Smoke, Dust, and Haze*. New York: John Wiley & Sons, Inc.
- Friedlander, S.K. (2000). *Smoke, Dust, and Haze: Fundamentals of Aerosol Dynamics*. 2nd ed. New York, NY: Oxford University Press, Inc.
- Frössling, N. (1938). "The Evaporation of Falling Drops." *Gerlands Beiträge Zur Geophysik*. 52:170–216.
- Fuchs, N.A. (1959). *Evaporation and Droplet Growth in Gaseous Media*. Oxford: Pergamon Press.
- Fuchs, N.A. (1964). *The Mechanics of Aerosols*. Oxford: Pergamon Press.
- Fuchs, N.A., Sutugin, A.G. (1971). "Highly Dispersed Aerosols." In *Topics in Current Aerosol Research (Part 2)*., edited by G. M. Hidy and J. R. Brock, 1–200. New York, NY: Pergamon Press.
- Fujita, K., Muraoka, D., Ogawa, T., Kitamura, H., Suzuki, K., Saito, S. (2013). "Evaluation of Amine Emissions from the Post-Combustion CO₂ Capture Pilot Plant." *Energy Procedia*. 37:727–734.
- Gasmet Technologies Oy. (2009). "Calcmnet for Windows: User's Guide and Reference Manual. Analysis and Controlling Software Version 11.08."
- GASMET-USA, A.Q.A. d/b/a. (2014). "MSSH-7 Stream Switching System User Manual: Revision 0."
- Gelbard, F. (1979). "The General Dynamic Equation for Aerosols." California Institute of Technology. Ph.D. Dissertation.
- Goff, G.S. (2005). "Oxidative Degradation of Aqueous Methanolamine in CO₂ Capture Processes: Iron and Copper Catalysis, Inhibition, and O₂ Mass Transfer." The University of Texas at Austin. Ph.D. Dissertation
- Guha, A. (1997). "A Unified Eulerian Theory of Turbulent Deposition to Smooth and Rough Surfaces." *Journal of Aerosol Science*. 28(8):1517–1537.

- Hangal, S., Willeke, K. (1990). "Overall Efficiency of Tubular Inlets Sampling at 0-90 Degrees from Horizontal Aerosol Flows." *Atmospheric Environment*. 24A(9):2379–2386.
- Hanst, P.J., Hanst, S.T. (1994). "Gas Measurement in the Fundamental Infrared Region: An Applications Manual." In *Air Monitoring by Spectroscopic Techniques, Chemical Analysis Series.*, edited by M. W. Sigrist, 335–470. New York, NY: John Wiley & Sons, Inc.
- Hardalupas, Y., Liu, C.H. (1997). "Implications of the Gaussian Intensity Distribution of Laser Beams on the Performance of the Phase Doppler Technique. Sizing Uncertainties." *Prog. Energy Combust. Sci.* 23:41–63.
- Hardalupas, Y., Taylor, A.M.K.P. (1994). "Phase Validation Criteria of Size Measurements for the Phase Doppler Technique." *Experiments in Fluids*. 17:253–258.
- Heidenreich, S., Vogt, U., Büttner, H., Ebert, F. (2000). "A Novel Process to Separate Submicron Particles from Gases * a Cascade of Packed Columns." *Chemical Engineering Science*. 55:2895–2905.
- Heyder, J., Gebhart, J. (1977). "Gravitational Deposition of Particles from Laminar Aerosol Flow Through Inclined Circular Tubes." *Journal of Aerosol Science*. 8:289–295.
- Holman, J.P. (1972). *Heat Transfer*. New York: McGraw-Hill.
- IPCC. (2007). "Technical Summary. In: Climate Change 2007: Mitigation. Contribution of Working Group III to the Fourth Assessment Report of the Intergovernmental Panel on Climate Change." Cambridge, United Kingdom and New York, NY, USA.
- ISO. (2014). "Representation of Results of Particle Size Analysis -- Part 2: Calculation of Average Particle Sizes/Diameters and Moments From Particle Size Distributions."
- Jackson, P., Attalla, M. (2010). "N-Nitrosopiperazines Form at High pH in Post-Combustion Capture Solutions Containing Piperazine: A Low-Energy Collisional Behaviour Study." *Rapid Communications in Mass Spectrometry*. 24:3567–3577.
- Johannessen, T., Christensen, J.A., Simonsen, O., Livbjerg, H. (1997). "The Dynamics of Aerosols in Condensational Scrubbers." *Chemical Engineering Science*. 52(15):2541–2556.

- Kamijo, T., Kajiya, Y., Endo, T., Nagayasu, H., Tanaka, H., Hirata, T., Yonekawa, T., Tsujiuchi, T. (2013). "SO₃ Impact on Amine Emission and Emission Reduction Technology." *Energy Procedia*. 37:1793–1796.
- Khakharia, P. (2015). "Aerosol-Based Emission, Solvent Degradation, and Corrosion in Post Combustion CO₂ Capture." Technische Universiteit Delft. Ph.D. Dissertation
- Kohl, A., Nielsen, R. (1997). *Gas Purification*. 5th ed. Houston, TX: Gulf Professional Publishing.
- Kolderup, H., Hjarbo, K.W., Huizinga, A., Tuinman, I., Zahlse, K., Vernstad, K., Hyldbakk, A., et al. (2012). "WP 1 and 3 in the Project: CCM TQP Amine 6 - Emission Quantification and Reduction."
- Kulkarni, P., Baron, P.A., Willeke, K. (2011). *Aerosol Measurement: Principles, Techniques, and Applications*. 3rd ed. Hoboken, New Jersey: John Wiley & Sons, Inc.
- Laktionov, A.B. (1973). "Aspiration of an Aerosol Into a Vertical Tube From a Flow Transverse to It." *Fizika Aerozoley*. 7:83–87.
- Lee, K.W., Gieseke, J.A. (1994). "Deposition of Particles in Turbulent Pipe Flow." *Journal of Aerosol Science*. 25(4):699–709.
- Liu, B.Y.H., Agarwal, J.K. (1974). "Experimental Observation of Aerosol Deposition in Turbulent Flow." *Journal of Aerosol Science*. 5:145–155.
- Liu, B.Y.H., Zhang, Z.Q., Kuehn, T.H. (1989). "A Numerical Study of Inertial Errors in Anisokinetic Sampling." *Journal of Aerosol Science*. 20(3):367–380.
- Malvern Instruments, Ltd. (2007). "Insittec® Process Particle Sizing Brochure." *MRK967-03*.
- Mazumder, M.K., Calle, C.I., Srirama, P.K., Wilson, J.D., Zhang, J., Buhler, C.H., Ali, M. (2007). "In-Situ and Simultaneous Measurements of Size and Charge Distributions of Dust on Mars: Instrumentation and Analysis." In *Seventh International Conference on Mars*. Pasadena, California.
- Mertens, J., Brachert, L., Desagher, D., Thielens, M.L., Khakharia, P., Goetheer, E., Schaber, K. (2014). "ELPI+ Measurements of Aerosol Growth in an Amine Absorption Column." *International Journal of Greenhouse Gas Control*. 23:44–50.

- Muyshondt, A., McFarland, A.R., Anand, N.K. (1996). "Deposition of Aerosol Particles in Contraction Fittings." *Aerosol Science and Technology*. 24:205–216.
- O'Hern, T.J., Rader, D.J. (1993). "Practical Application of in Situ Aerosol Measurement." In *Halon Alternatives Working Conference*., 275–290. Albuquerque, New Mexico.
- Okazaki, K., Wiener, R.W., Willeke, K. (1987). "Isoaxial Aerosol Sampling: Nondimensional Representation of Overall Sampling Efficiency." *Environmental Science and Technology*. 21(2):178–182.
- Pierce, R. (1977). "Estimating Acid Dewpoints in Stack Gases." *Chemical Engineering*. 84(8):125–128.
- Plaza, J.M. (2012). "Modeling of Carbon Dioxide Absorption Using Aqueous Monoethanolamine, Piperazine and Promoted Potassium Carbonate." The University of Texas at Austin. Ph.D. Dissertation.
- Pui, D.Y.H., Romay-Novas, F., Liu, B.Y.H. (1987). "Experimental Study of Particle Deposition in Bends of Circular Cross Section." *Aerosol Science and Technology*. 7:301–315.
- Rader, D.J., Marple, V.A. (1988). "A Study of the Effect of Anisokinetic Sampling." *Aerosol Science and Technology*. 8(3):283–299.
- Radziemski, L.J., Solarz, R.W., Paisner, J.A. (1987). *Laser Spectroscopy and Its Applications*. Optical En. New York, NY: Marcel Dekker, Inc.
- Rao, A.B., Rubin, E.S. (2002). "A Technical, Economic, and Environmental Assessment of Amine-Based CO₂ Capture Technology for Power Plant Greenhouse Gas Control." *Environmental Science and Technology*. 36:4467–4475.
- Reist, P.C. (1993). *Aerosol Science and Technology*. 2nd ed. New York, NY: McGraw-Hill.
- Roesler, D. (2010). "Development and Field Testing of a Dynamically Spiked Controlled Condensation Train." In *Stationary Source Sampling and Analysis for Air Pollutants Conference*. Panama City, FL.
- Rohde, R., Muller, R.A., Jacobsen, R., Muller, E., Perlmutter, S., Rosenfeld, A., Wurtele, J., Groom, D., Wickham, C. (2012). "New Estimate of the Average Earth Surface Land Temperature Spanning 1753 to 2011." *The Third Santa Fe Conference on Global and Regional Climate Change*. Santa Fe, NM.

- Schwendiman, L.C., Stegen, G.E., Glissmeyer, J.A. (1975). "Report BNWL-SA-5138." Richland, WA.
- Seinfeld, J.H., Pandis, S.N. (1998). *Atmospheric Chemistry and Physics: From Air Pollution to Climate Change*. New York, NY: John Wiley & Sons, Inc.
- Sexton, A.J. (2008). "Amine Oxidation in CO₂ Capture Processes." The University of Texas at Austin. Ph.D. Dissertation
- Shah, R.K., Bhatti, M.S. (1987). "Laminar Convection Heat Transfer in Ducts." In *Handbook of Single-Phase Convective Heat Transfer.*, edited by S. Kakaç, R. K. Shah, and W. Aung. New York, NY: Wiley-Interscience, John Wiley & Sons.
- Shakal, J. (2008). "Phase Doppler Particle Analyzer: 2007 TSI LDV/PDPA Workshop and Training." TSI, Inc.
- Shale, C.C. (1973). "Ammonia Injection: A Route to Clean Stacks." In *Pollution Control and Energy Needs.*, 195–205. Washington DC.
- Sipperley, C.M., Bachalo, W.D. (2014). "Triple Interval Phase Doppler Interferometry : Improved Dense Sprays Measurements and Enhanced Phase Discrimination." In *17th International Symposium on Applications of Laser Techniques to Measure Fluid Mechanics*. Lisbon, Portugal.
- Stark, J.W., Zhang, J., Sharma, R., Adams, A.J., Mazumder, M.K. (2008). "Measurement of Electrostatic Charge and Aero- Dynamic Diameter of Sub-Micron Particles by the ESPART." In *Proc. ESA Annual Meeting on Electrostatics, Paper G3.*, 1–6.
- Thitakamol, B., Veawab, A., Aroonwilas, A. (2007). "Environmental Impacts of Absorption-Based CO₂ Capture Unit for Post-Combustion Treatment of Flue Gas from Coal-Fired Power Plant." *International Journal of Greenhouse Gas Control*. 1(3):318–342.
- Thomas, J.W. (1958). "Gravity Settling of Particles in a Horizontal Tube." *J. Air Pollut. Control Assoc.* 8:32–34.
- TSI Inc. (2015). "Aerodynamic Particle Sizer® Model 3321 Brochure P/N 1930087 Rev E."
- Van Den Moortel, T., Santini, R., Tadriss, L., Pantaloni, J. (1997). "Experimental Study of the Particle Flow in a Circulating Fluidized Bed Using a Phase Doppler Particle Analyzer: A New Post-Processing Data Algorithm." *Int. J. Multiphase Flow*. 23(6):1189–1209.

- van der Gijp, S., Huizinga, A., Kester, L., Khakharia, P., Tuinman, I., van Os, P. (2012). "Emission Reducing Technologies: Aerosols." In *The University of Texas Conference on Carbon Capture*. Austin, TX.
- Vehkamäki, H. (2006). *Classical Nucleation Theory in Multicomponent Systems*. Berlin: Springer - Verlag Berlin Heidelberg.
- Verhoff, F., Banchero, J. (1974). "Predicting Dew Points of Gases." *Chemical Engineering Progress*. 78(8):71–72.
- Voice, A.K. (2013). "Amine Oxidation in Carbon Dioxide by Aqueous Scrubbing." The University of Texas at Austin. Ph.D. Dissertation
- Wall, S. (1982). "A Monodisperse Sulfuric Acid Aerosol Generator." *Atmospheric Environment*. 16(6):1507–1512.
- Xu, Q. (2011). "Thermodynamics of CO₂ Loaded Aqueous Amines." The University of Texas at Austin. Ph.D. Dissertation.
- Zhu, J.Y. (1996). "Laser Doppler Velocimetry for Flow Measurements in Pulp and Paper Research." 618. *TAPPI Engineering Conference*. IPST Technical Paper Series. Chicago, IL.

Vita

Steven Michael Fulk graduated Allen High School in May of 2005, and attended Texas A&M University from 2005 to 2009, where he graduated with a B.S. in Chemical Engineering. During his time at Texas A&M, he worked as an undergraduate research assistant in the Mary Kay O'Connor Safety Center under supervision of Dr. M. Sam Mannan and Dr. Ray A. Menzter and also performed summer research in the NSF REU program under supervision of Dr. Mahmoud El-Halwagi. Steven entered into graduate school at The University of Texas at Austin in the Fall of 2009, working for Dr. Gary Rochelle. He has accepted a full time position at Optimized Gas Treating, Inc. in Buda, TX.

Permanent email: steven_fulk@utexas.edu

This dissertation was typed by the author.